Operando Investigations of Structure-Activity Relationships in Pd-based Model Catalysts for Methane Oxidation

Dissertation
zur Erlangung des Doktorgrades
an der Fakultät für Mathematik, Informatik und
Naturwissenschaften
Fachbereich Physik
der Universität Hamburg

vorgelegt durch

Jan-Christian Schober

Hamburg
2026

Gutachter der Dissertation:	Prof. Dr. Andreas Stierle Prof. Dr. Yuemin Wang
Zusammensetzung der Prüfungskommission:	Prof. Dr. Wolfgang J. Parak Prof. Dr. Andreas Stierle Prof. Dr. Yuemin Wang Dr. Vedran Vonk Dr. Philipp N. Plessow
Vorsitzender der Prüfungskommission:	Prof. Dr. Wolfgang J. Parak
Datum der Disputation:	27.11.2025
Vorsitzender des Fach-Promotionsausschusses PHYSIK:	Prof. Dr. Wolfgang J. Parak
Leiter des Fachbereichs PHYSIK:	Prof. Dr. Markus Drescher
Dekan der Fakultät MIN:	Prof. Dr.-Ing. Norbert Ritter

Eidesstattliche Versicherung

Hiermit versichere ich an Eides statt, die vorliegende Dissertationsschrift selbst verfasst und keine anderen als die angegebenen Hilfsmittel und Quellen benutzt zu haben.

Sofern im Zuge der Erstellung der vorliegenden Dissertationsschrift generative Künstliche Intelligenz (gKI) basierte elektronische Hilfsmittel verwendet wurden, versichere ich, dass meine eigene Leistung im Vordergrund stand und dass eine vollständige Dokumentation aller verwendeten Hilfsmittel gemäß der Guten wissenschaftlichen Praxis vorliegt. Ich trage die Verantwortung für eventuell durch die gKI generierte fehlerhafte oder verzerrte Inhalte, fehlerhafte Referenzen, Verstöße gegen das Datenschutz- und Urheberrecht oder Plagiate.

.....
Datum, Unterschrift

Abstract

The high global warming potential of CH_4 makes the catalytic conversion of residual CH_4 in exhaust gases vital for applications such as CH_4 combustion engines and turbines, power-to-gas or biomass plants. The most active heterogeneous catalyst system for complete CH_4 oxidation at low temperatures ($< 650\,K$) in lean reaction gas mixtures (overstoichiometric oxygen content) is the class of Pd-based catalysts supported by (mixed) metal oxide supports. The activity of these catalysts is closely linked to PdO content at low temperatures, as well as structure and morphology of the nanoparticles. The catalytic conversion proceeds with the Mars-van-Krevelen mechanism through numerous elementary steps which consumes lattice oxygen of PdO and produces H_2O. A persistent challenge in heterogeneous catalysis in general is catalyst deactivation, which can occur through sintering or poisoning, and these processes also affect Pd-based catalysts for CH_4 oxidation. Specifically, the inhibition by H_2O, deactivation by PdO reduction, and sintering are three of the core causes for deactivation. Strategies to address these issues are the use of oxide supports with different redox properties and the addition of other noble metals to the catalyst nanoparticles, most prominently Pt, which can alter the redox properties of the catalyst, inhibit sintering, and manage catalyst passivation by H_2O.
This work aims to elucidate the structural and morphological properties of Pd based catalysts under transient conditions during light-off. The objective is to improve the understanding of the mechanisms behind the enhancement of catalyst performance by nanoparticle support interactions and the addition of Pt. Model catalysts that combine geometric simplicity and morphological complexity were used to address these questions. This approach enables direct correlation of structural and morphological properties on the atomic scale to the catalyst's activity. The experiments were carried out in industrially relevant temperature and pressure regimes, thereby bridging the pressure and material gap between single crystal studies and conventional packed-bed or monolith reactor experiments.
α-Al_2O_3(0 0 0 1) was selected as an inert representative and CeO_2 as a redox-active support with high oxygen mobility. The CeO_2(0 0 1) model catalyst support surface was prepared by reactive physical vapor deposition of Ce in atomic oxygen atmosphere on YSZ(0 0 1), as commercially available CeO_2 substrates are unsuitable for grazing incidence X-ray scattering. The resulting CeO_2 films were thoroughly characterized by a comprehensive set of complementary techniques to ensure tight control over its properties. The CeO_2 thin films used as catalyst supports exhibited a dislocation lattice at the CeO_2/YSZ interface which enabled full coverage of the film despite the

considerable lattice mismatch. The bulk of the film was fully oxidized with a bulk-like lattice, while the surface was fully hydroxylated and covered with a molecular water level, even after annealing in ultra high vacuum under oxygen atmosphere. Two aspects of the structure and morphology were investigated: (i) the evolution under transient light-off conditions and (ii) the temporal evolution after each increment in a step-wise heating experiment. For both studies, epitaxial Pd and PdPt nanoparticles were grown by physical vapor deposition, and catalytic testing was conducted in a custom, X-ray compatible operando flow cell equipped with inline mass spectrometry. The light-off experiments conducted with Pd/Al_2O_3 and Pd/CeO_2 showed strong dependence of catalytic activity, structure and morphology from the support material. Notably, the reaction intermediates CO and CH_2O, associated with the Mars-van-Krevelen mechanism on PdO(1 0 1), were observed in the exhaust gas by mass spectrometry for the first time. These observations suggest that the migration and adsorption/desorption of surface species such as OH and CH_2O are slower than desorption of gas-phase intermediates. Consequently, complete oxidation under conventional conditions may proceed through multiple adsorption–desorption cycles. Structural and morphological data recorded in parallel by high-energy X-ray diffraction (75 keV) revealed distinct oxidation mechanisms depending on the support. The comparative analysis showed that CeO_2 inhibited sintering and stabilized the PdO phase more effectively than Al_2O_3. Furthermore, the detection of thermodynamically unstable phases under reaction conditions provided evidence for strong variations in local chemical potential at the catalyst surface. The CeO_2 thin films used in the light-off experiments contained a small amount of rectangular holes, which are associated with oxygen vacancy condensation. A statistical evaluation of SEM images revealed a pronounced size difference between NPs located on the CeO_2 film and those located in the holes of the film. These results provide evidence that Ostwald ripening is the dominant sintering mechanism on CeO_2(0 0 1) supports and that the holes act as diffusion traps, locally enhancing sintering. In the kinetic investigation, the influence of Pt on catalytic behavior was studied by comparing the activity, structure, and morphological dynamics of Pd/Al_2O_3 and $PdPt/Al_2O_3$. For the first time, HEGISAXS and HEGIXRD were combined to characterize catalysts under operando conditions. Regardless of Pt content, the epitaxial relationship between Al_2O_3 and the nanoparticles significantly inhibited their oxidation compared to the larger NPs studied in the light-off experiments. Pronounced morphological changes upon initial H_2O desorption were observed only for Pd/Al_2O_3, accompanied by significant changes in the lattice constant, ultimately leading to an overall relaxation of the lattice. In contrast, the morphology of $PdPt/Al_2O_3$ remained largely unaffected by the

initial H_2O. HEGISAXS indicated significant vertical material transport in Pd/Al_2O_3, pointing to strong reaction-induced reshaping which is consistent with the trends seen in HEGIXRD. In contrast, this was not observed for $PdPt/Al_2O_3$. Changes in the NP morphology in this system are instead attributed to the formation of PdO bulk and surface phases and slow, thermally driven sintering over the course of the experiment. While the correlation between PdO content and catalytic activity was weak, a clear relationship was observed between activity and the strain state of the metal phase. The lattice of Pd/Al_2O_3 gradually relaxed over the course of the experiment, coinciding with declining activity, whereas $PdPt/Al_2O_3$ retained a highly strained lattice, which correlated with improved performance.
In summary, these findings provide direct insight into the mechanisms of catalyst deactivation and the effects of the nanoparticle-support interactions, Pt alloying, and strain in enhancing resistance to H_2O inhibition, PdO reduction, and sintering. The use of model catalysts, combinatory X-ray techniques, and relevant pressure and temperature regimes established detailed structure-activity correlations and highlighted the role of surface diffusion, and desorption of products and intermediates of CH_4 oxidation. Overall, these results bridge the material, pressure, and complexity gap between idealized single crystal investigations and reactor studies.

Zusammenfassung

Aufgrund des starken Treibhauseffekts von CH_4 ist die katalytische Konversion von CH_4 Restgas in den Abgasen von Anwendungen wie Turbinen, Motoren, Power-to-Gas Anwendungen oder Biomasseanlagen essenziell. Für die vollständige katalytische Konversion sind vor allem Katalysatoren im Einsatz die Pd als aktive Phase und Metalloxide als Substrate verwenden. Bei niedrigen Temperaturen ist die Aktivität solcher Katalysatoren durch den PdO-Gehalt bestimmt, allerdings sind auch Struktur und Morphologie der Nanopartikel relevant fuer Aktivitaet und Deaktivierungsprozesse. Die katalytische Umwandlung verläuft über zahlreiche Elementarschritte mit dem Mars-van-Krevelen-Mechanismus bei denen Sauerstoff aus dem Kristallgitter von PdO verbraucht mit CH_4 reagiert und $CO_2 + H_2O$ gebildet wird. Eine der groessten Herausforderung in Katalysatorendesign ist die Deaktivierung die durch Prozess wie Sintern oder Vergiftung. Für Katalysatoren auf Pd Basis sind insbesondere Deaktivierung durch H_2O, Reduktion des aktiven PdO, und Sintern relevante Deaktivierungsprozesse. Strategien zur Lösung dieser Probleme sind der Einsatz von Metalloxiden mit unterschiedlichen Redox-Eigenschaften als Substrat sowie die Zugabe von weiteren Edelmetallen, insbesondere Pt, zu den Katalysatornanopartikeln. Es ist das Ziel dieser Arbeit strukturelle und morpholgoische Eigenschaften on Pd-basierten Katalysatoren waehrend des Light-Offs zu untersuchen. Dabei sollen besonders der Einfluss des Substrat, sowie die Zugabe von Pt zentrale Aspekte sein. Die erlangten Erkenntnisse sollen das Verständnis der zugrundeliegenden Mechanismen erweitern und verbessern. Zu diesem Zweck wurden Modellkatalysatoren verwendet die sich durch eine reduzierte Geometrische Komplexität auszeichnen und so eine Korrelation von Struktur und Morphologie mit der Aktivtät ermoeglichen sollen. Die Experimente wurden in industriell relevanten Temperatur- und Druckbereichen durchgeführt und überbrücken somit die Lücke zwischen Einzelkristallstudien und konventionellen Reaktorexperimenten mit Schüttgut oder Monolithen.
Es wurde α-$Al_2O_3(0\,0\,0\,1)$ als inertes und CeO_2 als redox-aktives Trägermaterial mit hoher Sauerstoffmobiliät Trägermaterial gewählt. $CeO_2(0\,0\,1)$ als Trägermaterial wurde als Dünnfilm auf YSZ$(0\,0\,1)$ realisiert, der durch reaktive physikalische Gasphasenabscheidung von Ce in atomarer Sauerstoffatmosphäre auf gewachsen, da CeO_2-Substrate für Röntgenstreuung unter streifendem Einfall ungeeignet sind. Die so hergestellten CeO_2-Filme wurden umfassend mit verschiedenen komplementären Techniken charakterisiert, um ein tiefes Verständnis der Trägereigenschaften zu gewährleisten. An der CeO_2/YSZ-Grenzfläche weissen die Dünnfilme ein Versetzungsgitter auf, wodurch der Film trotz der Gitterfehlanpassung das Substrat vollständig be-

deckte. Der Film war vollständig oxidiert und relaxiert, während die Oberfläche vollständig hodroxyliert war und selbst nach Annealing im Ultrahochvakuum in Sauerstoffatmosphäre eine Wasserschicht aufwies.
In den Katalyseexperiemnten wurden zwei Aspekte der Struktur und Morphologie: (i) die Entwicklung unter transienten Light-Off-Bedingungen und (ii) die zeitliche Entwicklung nach jedem Inkrement in einem gestuften Heizexperiment. Für beide Studien wurden epitaktische Pd und PdPt Nanopartikel durch physikalische Gasphasenabscheidung gewachsen. Die katalytischen Tests erfolgten in einer speziell entwickelten, röntgenkompatiblen Operando-Durchflusszelle mit Inline-Massenspektrometrie. Die Light-Off Experimente mit Pd/Al_2O_3 und Pd/CeO_2 wiesen eine starke Abhängigkeit der katalytischen Aktivität von Struktur und Morphologie der Nanopartikel sowie des Trägermaterials auf. Zum ersten Mal konnten mit dem beschriebenen Experimenten die Reaktionszwischenprodukte CO und CH_2O des Mars-van-Krevelen-Mechanismus auf PdO(1 0 1) anchgewiesen werden. Diese Beobachtungen legen nahe, dass die Migration sowie Desorption von Adsorbaten wie OH und H_2O langsamer erfolgen als die Desorption dieser Zwischenprodukte. Folglich kann die vollständige Oxidation in konventionellen Reaktorgeoemtrien über mehrere Adsorptions-Desorptions-Zyklen ablaufen. Parallel mittels hochenergetischer Röntgenbeugung (75 keV) aufgezeichnete strukturelle und morphologische Daten zeigten ausserdem unterschiedliche vom Substrat abhängige Oxidationsmechanismen. Die vergleichende Analyse ergab, dass CeO_2 das Sintern hemmte und PdO effektiver stabilisierte als Al_2O_3. Zudem lieferte der Nachweis thermodynamisch instabiler Phasen unter Reaktionsbedingungen Hinweise auf starke lokale Schwankungen des chemischen Potentials an der Katalysatoroberfläche.
Die in den Light-Off-Experimenten verwendeten CeO_2-Dünnfilme enthielten eine geringe Anzahl rechteckiger Löcher, die mit der Kondensation von Sauerstoffvakanzen assoziiert wurden. Eine statistische Auswertung von SEM-Bildern zeigte einen deutlichen Grössenunterschied zwischen Nanopartikeln auf dem CeO_2-Dünnfilm und Nanopartikeln die sich in den Löchern des Films befanden. Diese Ergebnisse sind indikativ dafür, dass Ostwald-Reifung der dominierende Sintermechanismus auf CeO_2(0 0 1) Oberflächen ist und die Löcher als Diffusionsfallen wirken, die das Sintern lokal verstärken.
In der kinetischen Untersuchung wurde der Einfluss von Pt auf die katalytische Aktivität untersucht indem Aktivität, Struktur und morphologische Dynamik von Pd/Al_2O_3 und $PdPt/Al_2O_3$ vergleichend analysiert wurden. Erstmals wurden hierbei HEGISAXS und HEGIXRD kombiniert, um Katalysatoren unter Operando Bedingungen zu charakterisieren. Unabhängig vom Pt-Gehalt und im Vergleich zu den größeren Nanopartikeln aus den Light-Off-Experimenten hemmte die epitaktische Beziehung zwischen Al_2O_3 und

den Nanopartikeln deren Oxidation zu PdO stark. Nur bei Pd/Al_2O_3 wurden ausgeprägte morphologische Veränderungen während der H_2O Desorption im ersten Heizschritt beobachtet die von signifikanten Änderungen der Gitterkonstante begleitet wurden die letztenendlich zu einer Relaxation des Gitters führten. Im Gegensatz dazu blieb die Morphologie von $PdPt/Al_2O_3$ durch das initiale H_2O weitgehend unbeeinflusst. Analyse der HEGISAXS Daten zeigte einen signifikanten vertikalen Materialtransport bei Pd/Al_2O_3, was auf eine starke reaktionsinduzierte Formänderung hindeutet und konsistent mit den Ergebnissen aus HEGIXRD ist. Diese Effekte wurden für $PdPt/Al_2O_3$ nicht beobachtet. Morphologische Veränderungen in diesem System wurden hingegen über die Ausbildung und Reduktion von kristallinen PdO, PdO Oberflächenphasen sowie langsamen, thermisch getriebenen Sintern über die Gesamtheit des Versuchsverlaufs begruendet. Während die Korrelation zwischen PdO-Gehalt und katalytischer Aktivität schwach war, wurde eine klare Beziehung zwischen Aktivität und Änderungen der Gitterkonstante der Metallphase festgestellt. Das Gitter von Pd/Al_2O_3 entspannte sich im Laufe des Experiments, was mit einer Abnahme der Aktivität einherging, während die Gitterkonstante von $PdPt/Al_2O_3$ nicht signifkant relaxierte und mit einer verbesserten Leistung korrelierte.
Zusammenfassend liefern diese Ergebnisse direkte Einblicke in die Mechanismen der Katalysatordeaktivierung sowie in die Effekte der Wechselwirkungen zwischen Nanopartikeln und Substrat, der Beigabe von Pt und der Änderung der Gitterkonstante auf die Erhöhung der Resilienz gegen H_2O, der PdO-Reduktion und des Sinterns. Der Einsatz von Modellkatalysatoren, der Kombination zweier Röntgentechniken sowie die industriell relevanten Drücke und Temperaturen ermöglichte detaillierte Struktur-Aktivitäts-Korrelationen und hob die Bedeutung von Oberflächendiffusion sowie der Desorption von Produkten und Zwischenprodukten der CH_4-Oxidation hervor. Insgesamt überbrücken diese Ergebnisse die Material-, Druck- und Komplexitätslücke zwischen idealisierten Untersuchungen mit Einkristallen und Studien mit konventionellen Reaktoren.

Contents

Scientific Contributions

Appendix

Preamble

1. Introduction

Methane is a critical component of the modern energy landscape and a highly valuable resource for chemical industries [1–3]. The high hydrogen density makes methane (CH_4) an excellent fuel and is commonly used in large scale power plants but also in mobile applications such as liquefied natural gas or compressed natural gas engines for cars or large cargo ships[4] (see Figure 1.1). In contrast to conventional petrol or diesel fuels, methane combusts into only CO_2 and H_2O, omitting the emission of partial oxidation products and most NO_x and SO_x emission. In chemical industries, methane, mostly in the form of natural gas, is the main feedstock for the production of methanol and more generally, a commonly used hydrogen source for a variety of industrially relevant reactions [1, 5]. Furthermore, the direct conversion of methane into chemicals with two or more carbon atoms is a heavily researched area, aiming to provide alternatives to synthesis routes from other fossil resources such as crude oil [1, 6]. Finally, large-scale infrastructure such as natural gas pipelines and power plants can be used or upgraded to work with hydrogen which makes methane an excellent candidate for transitional technologies moving away from fossil fuels [1].
While the majority of methane is currently sourced from natural gas, the production of biogas from biomass or synthetic methane (SNG) by power-to-gas applications (see Figure 1.1) are viable options for the production of green methane [2, 3, 5]. However, methane is an extremely potent green house gas, greatly exceeding the effect of CO_2: The global warming potential (GWP) is $85\times$ larger over a period of 20 years and $30\times$ larger than CO_2 over a period of 100 years [2, 3]. As a consequence, binding (inter)national legislature and voluntary initiatives such as the Global Methane Pledge [7, 8] have been passed to regulate, monitor, and reduce methane emissions (see Figure 1.1). Hence, in every step of the life cycle of methane, the production or extraction, transportation, and finally combustion or conversion, the unintentional release of methane must be prevented. Other sources of methane emissions are agriculture [2, 3], abandoned and operational oil and coal mining[2, 3] operations [9], and waste treatment.

An efficient approach to eliminate methane emissions in the case of combustion applications of methane is exhaust gas after treatment using hetero-

Figure 1.1: Pictogram highlighting the three main aspects motivating research and development of methane catalysts: National and international legislation, usage of methane for power production, extraction of methane fuels from fossil or renewable sources.

geneous catalysts [10, 11], which allow the full oxidation of CH_4 below the combustion temperature of methane. This is crucial, since otherwise large volumes of gas with a typical concentration of below 0.1 % of methane would have to be heated beyond the combustion temperature of 550 °C. Particularly under lean (oxygen rich) conditions, palladium-based catalysts demonstrate the highest activity [10, 12] due to the facile oxidation and reduction of Pd and PdO, especially in the low temperature regime at $T < 400\,°C$ [13–17]. The continued interest and research in this area discovered a number of descriptors for the performance of catalysts, such as the noble metal dispersion [18], Pd oxidation state, catalyst pretreatment [10, 19], or properties of the oxide support [20], however, mechanistic investigations of the reaction pathway have only emerged in recent years [10, 21, 22].
Crucial for the catalysts activity is the presence of PdO. Stable under lean catalytic CH_4 oxidation conditions[17, 23, 24], it has been reported to outperform Pd [15, 21]. Based on density functional theory and single crystal investigations, the PdO(1 0 1) surface was identified as the most active surface among the Pd and PdO single crystal surfaces due to its undercoordinated surface atoms [12, 25]. CH_4 is dissociatively adsorbed by the un-

dercoordinated surface palladium species and subsequently reacts with the undercoordinated lattice oxygen via the Mars van Krevelen (MvK) mechanism to CO_2. Yet, several studies have shown that the coexistence of Pd and PdO increases the activity of methane oxidation catalysts [26–28] and pretreatment of the catalyst greatly influences the activity [10, 19]. In order to enhance the activity and stability of the catalyst, other metals are often used in conjunction with palladium, the most prominent example being platinum. While platinum by itself shows only weak activity for CH_4 oxidation at higher temperatures compared to Pd/PdO [29] PdPt alloy catalyst exhibit enhanced stability [19] and maintain a higher Pd/PdO ratio [23] which has been shown to improve CH_4 dissociation. During catalytic operations, Pd and PdPt alloy catalysts undergo significant morphological changes, involving sintering, and redispersion. Under operation conditions and in controlled ultra high vacuum (UHV) experiments, alloy nanoparticles (NPs) have been reported to present Pd on the outside of the NP, while platinum diffuses to the core of the particle [30, 31].

Strong predictors for the activity such as the oxidation state or morphology of the NPs are influenced by the choice of support, modifying stability [32, 33], as well as enhance the catalytic activity [16, 17, 20, 34–38]. The support effect is attributed to stabilization effects of the Pd phase, but also direct participation of for example CeO_2 or ZrO_2 in the oxidation of CO[39] or CH_4 [40]. In industrial applications, the noble metal NPs are supported by metal-oxide supports. Al_2O_3 is the most common support as it is thermally stable under operation conditions and irreducible [33]. Generally, it does not participate actively in the reaction and only influences the dispersion, serving as a benchmark in the context of this work. In contrast, CeO_2 is easily reducible and represents the opposite side of the spectrum of supports. Generally, but also specifically for CeO_2, the improvement in activity is linked to the oxygen mobility of the support [20, 33, 41]. Specifically, the Pd/PdO ratio is larger for supports with mobile oxygen species such as CeO_2 [17]. In addition, Surface structures formed from Pd and CeO_2, for example by the embedding of Pd in the CeO_2 surface, a strongly enhanced reactivity is observed [42]. For the oxidation of CO, even direct participation of lattice oxygen of CeO_2 was observed [39] and lattice oxygen from CeO_2 was found in CO_2 [40].

In this work, model catalyst systems were employed to unravel the fundamental morphological and structural properties of Pd-based catalysts governing the activity for catalytic CH_4 oxidation. As support structures, Al_2O_3 was chosen as representatives of a stable, inert support and CeO_2 as a complex, reducible, support material actively participating in the catalytic reaction [33, 41, 43–45]. In order to investigate the catalysts under operando condi-

tions in relevant pressure and temperature regimes, an UHV based growth procedure for atomically smooth $CeO_2(0\,0\,1)$/YSZ$(0\,0\,1)$ [46], suitable for high energy grazing incidence X-ray diffraction (HEGIXRD) and high energy grazing incidence small angle scattering (HEGISAXS), was developed (Chapter 1). The $\alpha-Al_2O_3(0\,0\,0\,1)$ single crystal supports and $CeO_2(0\,0\,1)$ films were decorated with Pd or PdPt alloy nanoparticles via molecular beam epitaxy (MBE) offering great control over size and composition. The fabricated model catalysts combine a degree of complexity with structural and chemical control that allowed direct access to the morphological and structural changes during catalytic CH_4 oxidation light-off in Chapter 2 and kinetic investigations Chapter 4. In combination with inline mass-spectrometry to monitor the catalysts' activity and realistic operation conditions, structure and activity were correlated. With this approach we bridge both the material and pressure gap between fundamental investigations on single crystals in UHV and experiments with research reactors operating at atmospheric pressure or higher. Furthermore, the experiment design and flat catalyst geometry allow for a homogeneous temperature profile and eliminates readsorption events of (partial) oxidation products or prolonged dwell times of gases due to turbulence. For packed-bed reactors which are commonly utilized for catalytic investigations, these parameters are challenging to control and structural details observed in our experiments are inaccessible with powder catalysts. As a result, our experiments with model catalysts provide new insights on the dynamic structural and morphological evolution, necessary to improve the atomistic understanding of the underlying catalytic reaction mechanism [47]. In light of the dynamic structural behavior of Pd based catalysts and the complex role of metal–support interactions in methane oxidation, this work is embedded in TrackAct [48]. We aim to bridge the gap between fundamental surface science and applied catalysis by collaboration across all length and complexity scales from unsupported cluster investigations and modeling to full-fledged engine test beds and fluid dynamic modeling. By combining well-defined model catalyst systems with operando characterization techniques, the presented work provides mechanistic insight into structure–activity relationships, oxidation behavior, and sintering phenomena under reaction conditions. For this purpose, a straight-forward preparation method for atomically smooth CeO_2 films as model catalyst supports were developed. The comparative operando investigation of Pd-based catalysts supported on CeO_2 and $\alpha-Al_2O_3$ establishes a framework for understanding the influence of support properties on catalytic performance during light-off. This information is crucial as light-off experiments simulate the start-up and ramp-down of engines or reactors during which methane-slip is most pronounced. The operando kinetic investigation of Pd/Al_2O_3 and $PdPt/Al_2O_3$ highlights the dynamic

nature of catalytic CH_4 oxidation, especially the structural and morphological differences in the behavior of the catalyst due to the addition of platinum. Ultimately, this work aims to contribute to the rational design of more stable and active Pd based CH_4 catalysts, by improving atomistic understanding of the catalysts in realistic operation conditions.

2. Methodology and Theory

This chapter is subdivided into four sections covering the fundamentals of materials (Section 2.1), heterogeneous catalysis (Section 2.2), X-ray Techniques (Section 2.3) and Microscopy techniques (Section 2.4), employed in this work.
The materials section introduces fundamental properties of the metals and metal oxides used in this work, the methods used to prepare the model catalysts, and the growth and properties of nanoparticles and thin films. In the next section the scientific context of heterogeneous catalysis is set, specifically the full catalytic oxidation of CH_4 with Pd based heterogeneous catalysts. The third section covers X-ray Scattering in detail and its application in X-ray reflection, grazing incidence X-ray diffraction, grazing incidence X-ray Scattering, and X-ray photo electron spectroscopy. Emphasis is put on the application of diffraction as the main characterization technique of this work. The chapter concludes with the description of the complementary microscopy techniques that were used prior to and after the operando investigation of catalysts.

2.1 Model Catalysts on Ideal Surfaces

The inherent complexity of heterogeneous catalysis reactors makes detailed, atomistic studies under operando conditions challenging. Industrially used catalysts are made from large (cm to m) monoliths which are coated with a wash-coat containing highly dispersed (metal-) nanoparticles on a porous oxide support. The complex, hierarchical structure combined with the dynamic reaction environment under catalytic operation further limits the number of techniques that can access structural and chemical information, especially on an sub nanometer length scale. For this reason, atomistic properties such as surface structure, chemistry, and adsorption sites of reactants are often attained by studying heavily simplified model systems such as single crystals or thin films under UHV conditions [25, 49]. In order to bridge this pressure and complexity gap, the catalysts investigated in this work were prepared by UHV techniques and then investigated under realistic operation conditions.

By this approach, the complexity of the catalysts is low enough to employ surface science techniques used for the operando investigations (Chapter 2, Chapter 4), while retaining a degree of morphological heterogeneity that represents heterogeneous catalysis reactors well. The next sections describe the materials and preparation methods forming the basis of the operando studies in this work.

2.1.1 Materials

This section outlines the structure and the most crucial bulk and surface properties of the catalyst supports αAl_2O_3 and CeO_2 as well as structure and oxidation behavior of Pd, PdO, and Pt will be introduced to form a foundation for the discussion of the experimental results.

α-Al_2O_3

Al_2O_3 is one of the most used oxides in heterogeneous methane oxidation catalysts [10] and is widely regarded as inert [10, 17, 50, 51], although promotional effects have been observed as well [17, 51]. α-Al_2O_3 is the thermodynamically most stable aluminum oxide and crystallizes in the corundum crystal structure with the space group is *R-3c* [52]. The aluminum ions Al^{3+}

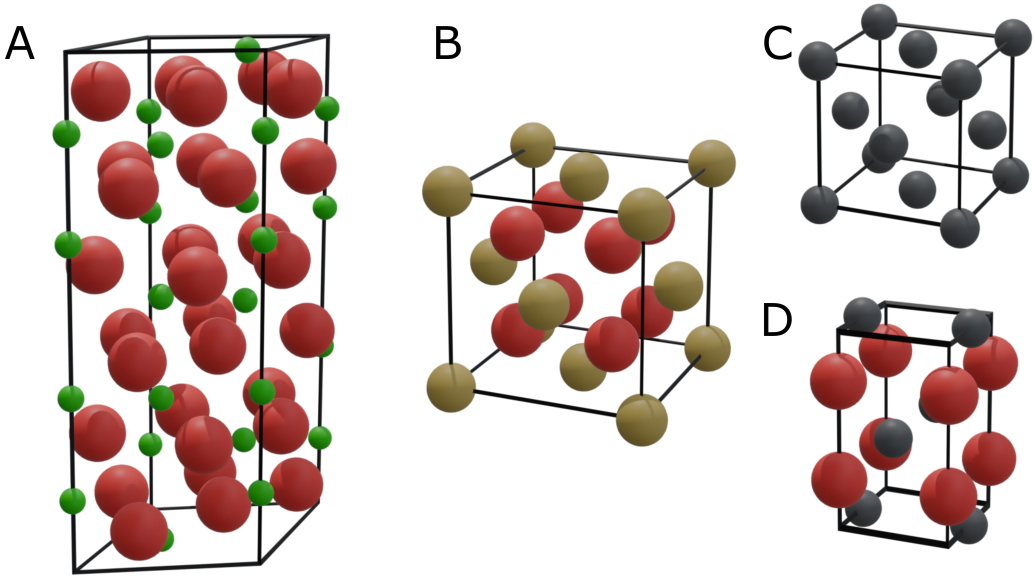

Figure 2.1: Unit cells of Al_2O_3 (**A**), CeO_2 (**B**), Pd (**C**), and PdO (**D**) shown at the same scale.

are octahedrally coordinated by six oxygen ions O^{2-}. Along the *c*-axis, the oxygen and aluminum ions are arranged in layers, where the oxygen layers are arranged in a hexagonal lattice. Overall, the oxygen lattice resembles a hexagonal close packed lattice, where $\frac{2}{3}$ of the octahedral sites are occupied by the aluminum ions. Due to the stacking of cation/anion layers of Al_2O_3 along the [0 0 0 1] direction, the Al terminated Al_2O_3 surface is stabilized by the formation of hydroxides [53]. This can for example affect nanoparticle size and shape [54], poor resistance towards H_2O inactivation [17], redox sensitivity of Pd nanoparticles [26] or enhance nanoparticle mobility [34].

CeO_2

CeO_2 as a catalyst support has come into focus of research due to its strong interaction with metal nanoparticles and promotional effects for CO and CH_4 oxidation in lean and rich reaction gas mixtures [10, 16, 20, 26, 35, 40, 55, 56]. CeO_2 crystallizes in the fluorite crystal structure in the space group $Fm\text{-}3m$ with the lattice constant $a = 5.41$ Å[57]. The Ce^{4+} ions are arranged in an fcc lattice and oxygen ions O^{2-} fill the tetrahedral sites forming squares around the Ce^{4+} ions.
Central to the advantageous properties of CeO_2 as a support for catalysts is the facile partial oxidation and reduction of the material without structural changes. Oxygen is readily bound by partially reduced CeO_{2-x} and oxygen is released from the lattice in reducing environments [35, 58–61]. Through this characteristic, CeO_2 is able to influence the stability of the equilibrium reaction $Pd + O \rightleftharpoons PdO$ and manage water poisoning [17]. In addition, direct participation by providing O to the catalytic reaction [10, 16, 35, 39, 55] or for the reoxidation of PdO [40, 56] have been reported. In addition, the promotional effects of the strong interaction between CeO_2 and noble metals allows for stabilization of single atom catalysts and highly dispersed clusters [18, 62, 63]. This approach exceptional improvement of the catalytic activity for certain reactions like CO activation, but shows poor performance for CH_4 oxidation compared to nanoparticles [63] due to the apparent necessity of extended PdO domains [17]. Also strong metal support interaction (SMI) was reported for CeO_2 supported noble metal clusters, which modified selectivity and activity, and increased the stability towards sintering [62].

An instructive example for the direct involvement of CeO_2 in the catalytic reaction relevant in the context of this work is for catalytic CO oxidation by Pt/CeO_2 [39]. The authors exposed the catalyst to CO which lead to inactivity for the Pt/Al_2O_3 catalyst when exposed to $CO + O_2$ reaction gas mixture. In contrast, Pt/CeO_2 remained active despite CO poisoning of the

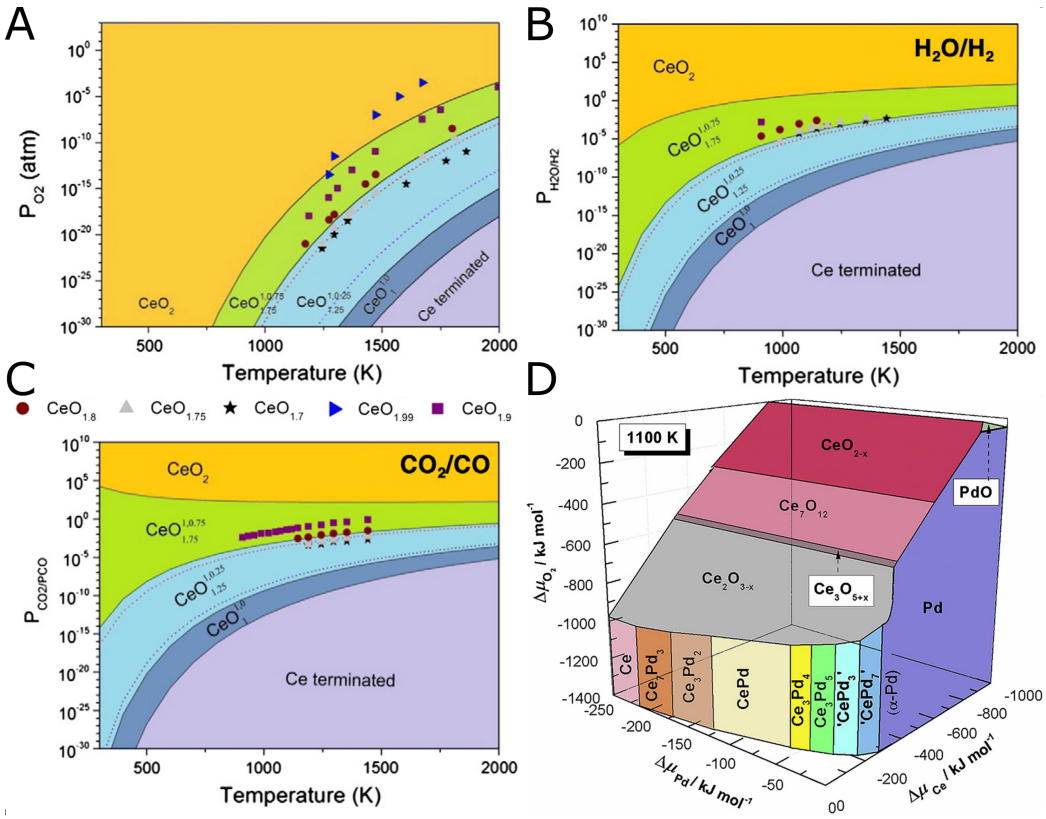

Figure 2.2: Phase diagrams of ceria in different redox environments (**A** - **C**), adapted from [64]. **D**: Pd-Ce-O tri-phase diagram at 1100 K [65].

Pt nanoparticle. The difference in behavior is explained by the inability to dissociativley adsorb O_2 on the nanoparticle as a result of CO poisoning. Activity is maintained for the CeO_2 supported catalyst by providing oxygen from the support lattice to the reaction at the support particle interface [39]. The surface phase diagrams in Figure 2.2 **A**-**C** depict the stability of CeO_2 under different oxygen partial pressures (**A**), ratio of the H_2O and H_2 partial pressures (**B**), and ratio of the CO_2 and CO partial pressures [64]. The phase diagrams were determined by density functional theory from first-principle thermodynamics without considering surface interactions. The color-coded oxidation states were calculated using Bader charges, and the datapoints in each phase diagram correspond to experimental datapoints. The phase diagram, describing the stability as a function of the oxygen partial pressure (**A**) predicts the surface to be thermally stable in the complete probed temperature range under atmospheric conditions which is confirmed by agreement with experiment (datapoints in Figure 2.2 **a**). Comparison of the phase diagrams in Figure 2.2 **B** and **C** allows several conclusions regarding the ther-

modynamic interaction of CeO_2 and reducing gas environments, as the shift of the equilibrium lines corresponds to the effective relative oxygen potential. The general trends are similar and show that CeO_2 is readily reduced by CO and H_2. The most pronounced difference is observed for the $CeO_2/CeO_{1.75}$ equilibrium line which shows that despite H_2 being the stronger reducing agent, reduction by CO occurs at larger partial pressure ratios. Since the phase diagrams in **B** and **C** show the thermodynamics of the respective redox reactions ($CO_2 \rightleftharpoons CO + O$, $H_2O \rightleftharpoons H_2 + O$) this observation implicates that already small amounts of CO are able to effectively create oxygen vacancies in the CeO_2 surface. In combination, CeO_2 can be considered thermally stable, but with the ability for facile reduction of the surface in redox gas environments.
In the previous sections, the strong interactions between CeO_2 and Pd as well as the reducibility of the surface were mentioned. Naturally, the interplay of the two properties arises for Pd/CeO_2 catalysts (see Chapter 2). The tri-phase diagram in Figure 2.2 **D** shows the relative chemical potentials of O, Pd, and Ce calculated from experimentally determined trends of the lanthanoid - palladium - oxygen systems [65]. The diagram clearly shows the extreme conditions that are required for the reduction of CeO_2. For reference, the complete phase diagrams of **A**-**C** are located within the red colored area in **D**. Experimentally, the Ce-Pd phases were confirmed by Götsch *et al.* [66]. The authors deposited first Pd, then CeO_2 on a support. The formation of $CePd_x$ alloys was observed atmosphere at temperatures above 1000 K in pure H_2. This corresponds to the parameter space at the bottom front area in Figure 2.2 **D**, namely $\Delta\mu_{Ce} < -300$ and $\Delta\mu_{O_2} < -1000$. The layer system employed also revealed a strong kinetic barrier of the alloy formation, as $CePd_5$ is formed before $CePd_3$, despite the opposite trend of the enthalpy of formation [66]. This indicates that the alloy formation is strongly dependent on the Pd diffusion length.

Pd, Pt, and PdO

The catalyst nanoparticles in this work were grown as metallic Pd or PdPt (alloy) nanoparticles. Pd and Pt both crystallize in the fcc crystal structure (space group $Fm-3m$) with lattice constants of 3.89 Åand 3.92 Å(see Figure 2.1 for structure), respectively [68, 69]. The phase diagram of the PdPt alloy has a miscibility gap with a maximum at 770 °C and the solid/liquid transition at 1500 °C which suggests the separation into Pd rich and Pt rich domains (see phase diagram in Figure 2.3) for the temperatures and alloying compositions of this work. However, the existence and relevance of this miscibility gap is highly disputed with direct evidence for full miscibility in

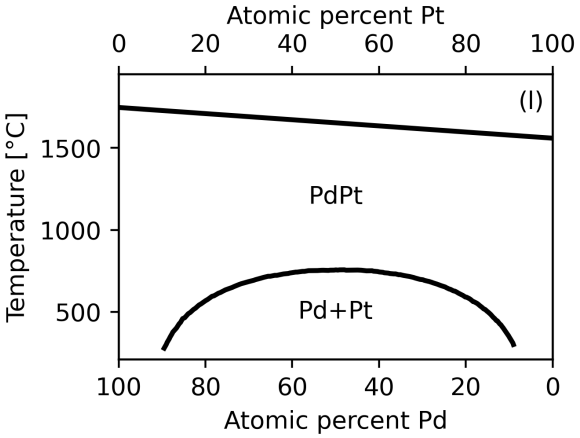

Figure 2.3: Bulk phase diagram of PdPt alloy. The straight solid line marks the phase transition to a liquid. Digitized from [67]

the nanometer regime due to kinetic barriers for dealloying [70]. Thus, PdPt alloys are considered a fully miscible alloy at any temperature within the scope of this work.
Despite full miscibility, surface segregation of Pt was observed for PdPt alloy nanoparticles as a result of exposure to hydrogen annealing at elevated temperatures [31]. The preferential surface segregation of Pt after reductive treatment and Pd after oxidative treatment was observed via the shifts of the vibrational bands of the probe molecule CO due to the different Pt or Pd dominated adsorption sites. The direct implication of this is an effect on the activity by the surface composition of the alloy nanoparticles.
In the context of this work, Pd is the material responsible for the catalytic activity towards CH_4 oxidation [10]. This is based upon the capability of Pd and specifically its (surface-) oxides for H abstraction in CH_4 [21, 25]. While platinum is active for catalytic oxidation of CH_4 [10, 29], the overall activity of Pt catalysts is poor compared to Pd catalysts [10, 23]. However, the addition of Pt seems to have a beneficial effect on the stability and selectivity of the catalyst nanoparticles [10]. As previously discussed, a major weakness of Pd based catalysts for CH_4 oxidation is the strong interaction of the active PdO(1 0 1) surface with water and hydroxile groups. Pt seems to counteract this weakness and PdPt nanoparticles show a higher resistance to poisoning by water [10, 19]. Furthermore, the oxidation and reduction of Pd is altered for PdPt based catalysts. In oxygen rich environments, the metallic Pd phase observed to be more stable for Pt containing catalysts [22].

The thermodynamics, but also kinetics of oxide formation from metallic Pd and the surface reconstructions caused by oxidation are crucial to understand for the investigation of catalysts as exposed surfaces, oxygen coverage, and morphology directly impact the catalyst's activity. For the

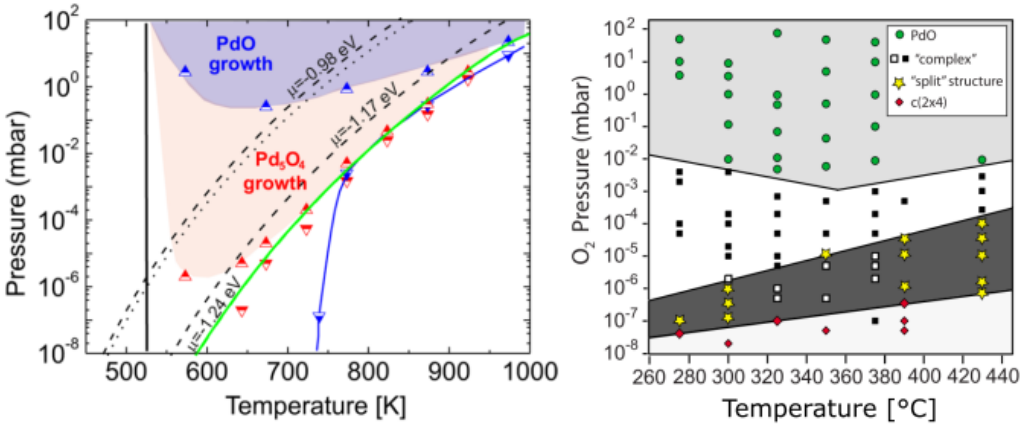

Figure 2.4: Stability diagrams of Pd and PdO phases for the oxidation of Pd(1 1 1) (**A** [49]) and Pd(1 1 0) (**B** [71]). In **A**, upward pointing triangles indicate formation, downward pointing triangles decomposition with red corresponding to surface oxide and blue to the bulk oxide.

Mars-van-Krevelen mechanism, proposed for catalytic CH_4 oxidation by Pd based catalysts, the catalysts nanoparticles must expose PdO(1 0 1) surfaces [21]. For this reason, the the following paragraphs will summarize, the behavior of (1 0 0)[72], (1 1 0)[71], (1 1 1)[49], (1 1 2)[73], and (5 5 3)[74] single crystal surfaces. This will serve as a foundation for the oxidation behavior of Pd nanoparticles (Section 2.1.3) and correlation of activity and structure of Pd based catalysts (Chapter 2, Chapter 4).
The most prominent facet for the nanoparticles investigated in the context of this work is the (1 1 1) facet which presents as a hexagonal close packed surface in UHV. Upon exposure to increasingly large oxygen pressures at temperatures above 523 K the surface first forms a two-dimensional, crystalline surface oxide with the composition Pd_5O_4. At oxygen partial pressures above 0.1 mbar, the formation of bulk PdO commences via the Stransky-Krastanov growth mode (see Section 2.1.3). The bulk oxide grows in the (1 0 0) and (1 0 1) orientations. Notably, the structures of the surface oxide and PdO(1 0 1) are nearly identical, indicating that this is the reason for the formation of the (1 0 1) oriented domains, specifically. Up until 1 mbar surface and bulk oxide coexist, followed by the formation of a rough polycrystalline bulk oxide film at $p(O_2) > 40$ mbar. An interesting observation of the study by Kasper *et al.* is the kinetic barrier for oxidation at temperatures below 523 K for which neither the formation of surface oxide, nor the formation of bulk oxide was observed. Furthermore, the formation of the surface oxide is only observed up to $T = 973$ K, which indicates that the surface oxide itself

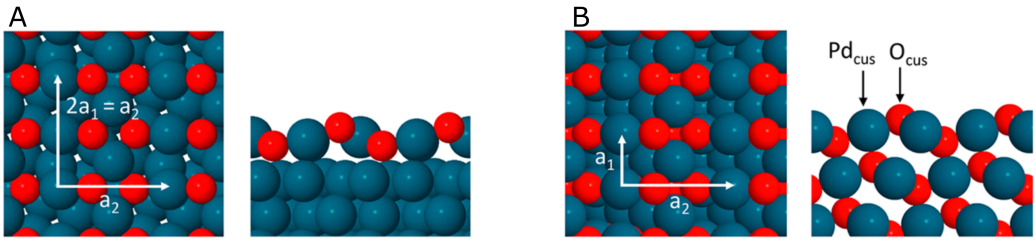

Figure 2.5: Ball models of the the Pd_5O_4 surface oxide (**A**) and the PdO(1 0 1) bulk oxide surface (**B**) in top and side, respectively. For the PdO model, the undercoordinated Pd and O sites are indicated by the subscript cus. Images taken from [76].

acts as a kinetic barrier for the growth of bulk PdO (see Figure 2.4).
Similar observations are reported for the oxidation of the (1 0 0) surface [72, 75]. Todorova *et al.* report the formation of the surface oxide on this palladium surface after exposure to $p_{O_2} = 10^{-6}$ mbar at 600 K for a period of 300 s. The structure of this surface oxide resembles that of a strained PdO(1 0 1) surface. The bulk oxide formation revealed the formation of PdO(1 0 1) at 500 K and PdO(1 0 0) at 600 K in 44 mbar O_2 and 5 mbar CO [72]. However instead of the continuous growth of bulk oxide, the (1 0 1) domains thickness saturated at 5 ML and 15 ML.
The last low-index facet (1 1 0) exhibits a completely different behavior with only the chemisorption of oxygen which leads to the formation of several meta stable surface reconstructions. Starting at 10^{-2} mbar the formation of bulk oxide was observed without the formation of a surface oxide layer.
The higher index facets (1 1 2) and (5 5 3) may be interpreted as mixed surfaces consisting of (1 1 1) facets and (1 0 0) steps (or short (1 1 3) facets in case of Pd(1 1 2)). Notably, the (5 5 3) surface forms a surface oxide at room temperature between 10^{-5} mbar and 1 mbar of oxygen partial pressure. Larger (1 1 1) facets exhibit the typical surface oxide of that surface (Figure 2.5 **A**), while the rest of the surface forms (3 3 2) facets with the same surface oxide. Beyond 1 mbar, the formation of bulk PdO was observed. From their results, the authors infer the necessity of oxygen induced shape changes as a result of the exposure to oxygen [74]. Similar surface restructuring was observed at 673 mbar for the (1 1 2) surface, which rearranges into (1 1 3) and (3 3 5) facets at 6×10^{-7} mbar. Upon exposure to 10^{-4} mbar, the surface starts the formation of a surface oxide which is followed by the formation of (0 0 1) and (1 0 0) bulk PdO.
In combination, these studies highlight the affinity for dissociative oxygen adsorption already in high vacuum and show that oxygen partial pressures in

the mbar regime and often elevated temperatures above 500 K are required to trigger the formation of bulk PdO. Comparison of the presented results also shows the dependence of the oxidation behavior of PdO with the example of the Pd(1 1 0) surface which oxidizes directly into bulk PdO. The formation of surface oxides observed for all other surfaces can kinetically limit the formation of bulk PdO (Figure 2.4), but also exemplifies that Pd readily oxidizes to PdO. In addition, the more complex surfaces exhibit immense restructuring upon exposure to oxygen, implying restructuring of nanoparticles due to the exposure to O_2, which is discussed in detail in Section 2.2.4.

2.1.2 Ultra High Vacuum Apparatus

Surface preparation, support growth and nanoparticle growth for all catalysts discussed in this work were conducted using a UHV-based approach. Two UHV chambers were used for the preparation of all samples that were investigated for this work, one for the deposition of CeO_2 thin films discussed in Chapter 1 and a second chamber used for deposition of Pd and Pt for nanoparticle growth.
For the deposition of the CeO_2 thin films relevant equipment was the e-beam heating capable of operating in oxygen atmospheres up to 1×10^{-5} mbar, the thermal cracker as a source of reactive atomic oxygen, and the e-beam evaporator for Ce evaporation. Samples for CeO_2 growth were cleaned by annealing in air and annealing in oxygen atmosphere. Deposition of CeO_2 films was achieved by evaporation of Ce metal held in a Mo-crucible of the upward facing evaporator in reactive atomic oxygen atmosphere supplied by the thermal cracker.
The metal (alloy-) nanoparticles were grown by controlled (co-) deposition of the respective metals from rods. Samples for nanoparticle growth were cleaned with the identical procedure as the CeO_2 thin films. For precise control over the amount of deposited material, the deposition rate for Pd and Pt was calibrated by growing calibration samples and determining the amount of deposited material by X-ray reflectivity (see for Figure 2.6, (description of the method in Section 2.3.2). For Pd a deposition rate of

$$f_{Pd} = 22 \times 10^{-3} \frac{\text{Å}}{\text{nA min}}$$

and for Pt a deposition rate of

$$f_{Pt} = 5.6 \times 10^{-3} \frac{\text{Å}}{\text{nA min}}$$

was determined.

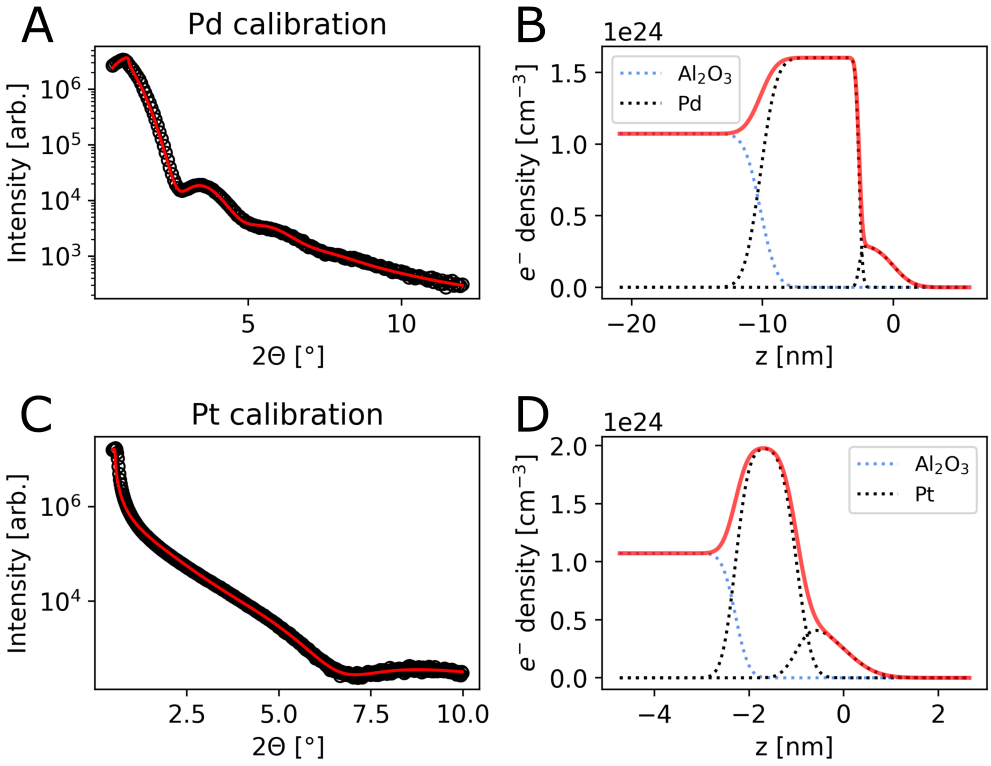

Figure 2.6: Calibration X-ray reflectivity measurements of the deposited material. **A**: Data (black circles) and fit (red line) of the Pd/Al_2O_3 calibration sample. **B**: Electron density profile from fit in **A**. **C**: Data (black circles) and fit (red line) of the Pt/Al_2O_3 calibration sample. **D**: Electron density profile from fit in **C**.

Auger Electron Spectroscopy

Auger electron spectroscopy was employed for the characterization of the CeO_2 thin film surface chemistry after growth. This technique relies on the ejection of Auger electrons by an incident electron beam. The scheme in Figure 2.7 **A** shows this process for a KLL transition. For a more detailed description and information of more advanced applications of Auger electron spectroscopy, the reader is referred to [77]. As indicated by the name of the transition, the Auger process involves three core levels of the atom that is being ionized. First, the primary electron, produced by the cathode of the Auger electron spectrometer ionizes a core level which is then filled by a second electron of a higher shell. In this example, the incident electron ionizes the K core level which is then filled by an electron of the L shell.

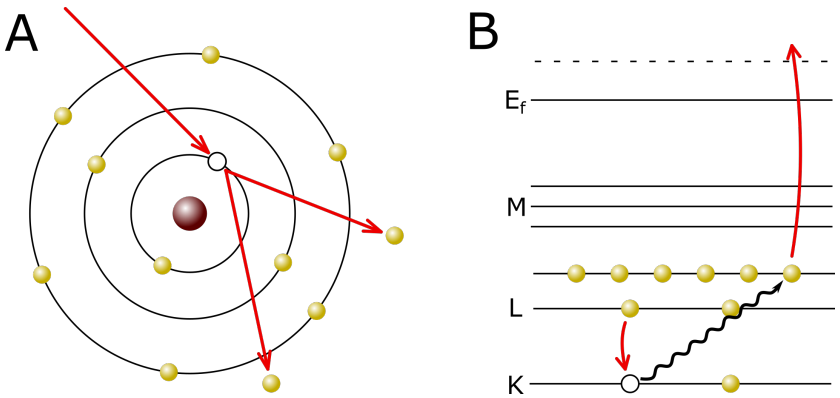

Figure 2.7: Scheme of the Auger process separated into the electron ejection visualized in the Bohr atomic model and the Auger process itself in a simplified electronic energy level scheme.

The energy difference between the two shells $E_0 - E_1$ is then used in the ionization of a third electron, which is from the $L2$ shell in this example. The energy of this electron is thus determined by the energy difference between the K and L edge, the energy of the shell from which the Auger electron originates, and the work function. The work function Φ encapsulates the sample and analyzer work function (Φ_s, Φ_a). Hence, the measured kinetic energy of an Auger electron is determined by

$$E_{kin} = E_0 - E_1 - \Phi$$

In addition to Auger electrons, a smooth, sloped background is observed in Auger electron spectroscopy. This background is caused by elastically and inelastically back scattered electrons and secondary electrons (from ionization of outer shells/valence band). In order to improve the visibility of the comparably small intensity of Auger electrons, the spectra are differentiated ($\frac{dN}{dE}$), enhancing the Auger electron signal. In case of the Auger electron spectroscopy data presented in this work, the differentiated spectra are measured directly via the Lock-In technique.

2.1.3 Nanoparticles and Thin Films

A fundamental understanding of the nucleation and growth mechanisms, the nanoparticles shape, its behavior in different gas environments, and its oxidation behavior is required to control the morphology of the catalyst supports and nanoparticles that were grown as part of this work. For this purpose, the

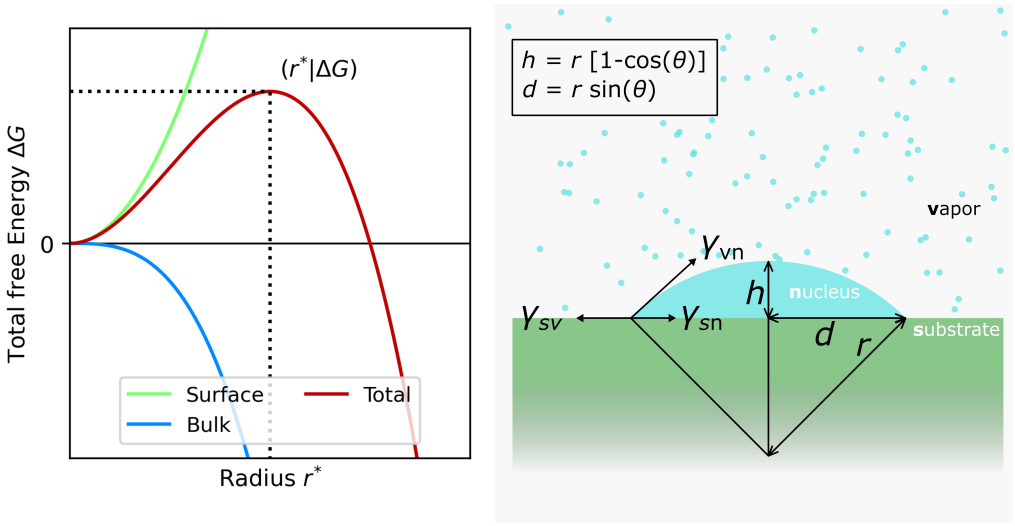

Figure 2.8: **A**: Energy diagram describing the influence of surface and bulk contribution to the particle energy. **B**: Droplet model describing the nucleus formation as a function of surface and volume energies of a droplet. Here Θ is the contact angle of the droplet.

following section first discusses general concepts of nucleation and growth of nanoparticles. This also applies to the growth of the CeO_2 thin film samples discussed in Chapter 1 as our results suggest a complex growth mechanism yielding an agglomerated particle film that is only transformed into a coherent thin film by annealing in air. Next, nanoparticle shapes will be discussed with focus on the influence of temperature, gas, and reaction induced changes, as varying activity and selectivity is observed for different facets or surfaces [25]. Finally, this section will conclude with insights into the thermal oxidation behavior of Pd nanoparticles on Al_2O_3. Further reading on general concepts in this section are found in [78]. Detailed reports on the oxidation of nanoparticles is found in [79]. Further details on the nucleation and growth of nanoparticles and thin films as well as intrinsic and interfacial defects are found in [80–82], which form the basis for the following sections.

Nucleation and Growth

In the previous section the experimental means and advantages of nanoparticle growth by MBE were discussed, but nucleation and growth were not described. During evaporation, a conical stream of atoms leaves the evaporator, pointing at the support surface. Upon reaching the surface, the evaporated material is adsorbed by the surface. Reflection off the surface and evapo-

ration or desorption can be neglected, since the sticking coefficient is unity (probability of adsorption) and the sample temperature during growth was well below the sublimation point of the evaporant for the base pressure of the chamber. Following adsorption, atoms diffuse over the surface until a point of nucleation is found. The nature of this location is in its core defined by the competition of interactions of the adatom with the support and the lateral interaction with other adatoms. The case of nucleation by the formation of clusters on terraces without the participation of surface defects is called homogeneous nucleation. However, for the material systems relevant to this work, nucleation at a surface defect such as step edges, edge atoms, terrace vacancies, edge vacancies, or color centers, called heterogeneous nucleation, is the dominating mechanism [80]. The stability of clusters is described by the Gibbs free energy which can be approximated by a droplet model considering the most important interactions at the sample surface (Figure 2.8). The simplest model for this relationship is that of a spherical particle suspended in a medium. The corresponding energy diagram (Figure 2.8 **A**) shows that an increase in volume decreases the Gibbs free energy which is essentially improving the stability of larger particles. This force is counterbalanced by the surface energy which increases with volume. Since the volume contribution scales with r^3 and the surface contribution only with r^2, at a certain radius which is defined by the interactions of the material forming the particle and the surface energy, the nucleus becomes stable and further incorporation of material further stabilizes the nucleus (vertical dotted line in (Figure 2.8 **A**). For supported nanoparticles the more interactions need to be considered leading to the surface energy being split into three components (Figure 2.8 **B**). The energy of the vapor/nucleus interface (γ_{vn}), the energy of the substrate/nucleus interface (γ_{sn}), and the energy of the substrate/vapor interface (γ_{sv}). The equilibrium contact angle of this system is given by Young's equation

$$\gamma_{sv} = \gamma_{sn} + \gamma_{vn}\cos(\Theta)$$

with Θ being the contact angle of the droplet. The specific interfacial interactions between support and deposit are described in detail in Section 2.1.3.

While this simple description considers the influence of the change in volume and surface on the Gibbs free energy the interaction with the substrate is not accurately captured. Experimentally, three growth types were observed that are tightly connected to the interaction with the substrate: 1) Volmer-Weber (island) growth, 2) Frank-van der Merwe (layer) growth, and 3) Stranski-Krastanov (island/layer) growth (see Figure 2.9). For the Volmer-Weber growth mode, the contact angle must be larger than zero, which requires

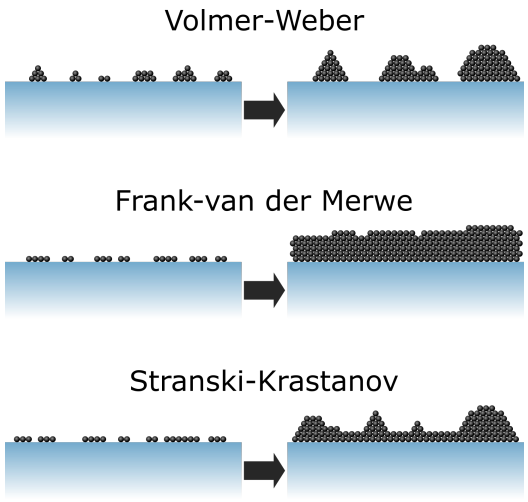

Figure 2.9: Schematics of the growth Vollmer-Weber, Frank-van der Merwe, and Stranski-Krastanov growth modes.

$\gamma_{sv} < \gamma_{ns} + \gamma_{vn}$, while for the Frank-van der Merwe growth mode, the contact angle must be zero which yields $\gamma_{sv} = \gamma_{ns} + \gamma_{vn}$. As previously stated, these relations are governed by the interaction at the interface of nucleus and support. Hence, mechanisms for this behavior is for example the lattice mismatch between support and nucleus, where a larger mismatch leads to an increase in strain and dislocations at the interface which in turn increases the γ_{ns}. For the Stranski-Krastanov growth, the relation between the surface energies changes at a certain film thickness (in Figure 2.9 this is two monolayers). An example for this could be strain accumulating with increasing layer thickness which leads to the formation of particles on top of the thin film formed in the first step.

Shape and Defects of Nanoparticles and Thin Films

Crucial for the activity of catalysts is the exposed facet of the nanoparticle [25, 83]. Hence, understanding the shape of nanoparticles and driving forces leading to this shape are vital to further improve intelligent catalyst design. Analogous to the discussion of cluster nucleation, the particle shape is governed by the surface energies of the exposed facets. In the Wulff construction, the particle shape is found by drawing planes with the distance h_{hkl} from the origin, so that the planes' normals are parallel to the vector $[h\,k\,l]$. The distance h_{hkl} is given by

$$\gamma_{hkl} = ch_i,$$

where c is an arbitrary constant and γ_{hkl} the surface energy of the $[h\,k\,l]$ surface of the nanoparticle material. Thus, the distance of the plane is pro-

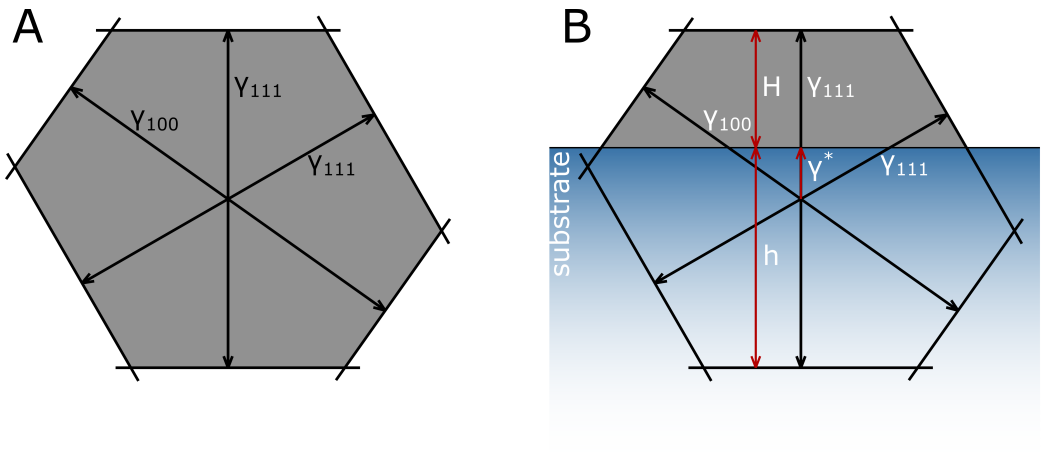

Figure 2.10: **A**: Wulff shape in the $[1\,1\,\bar{2}]/[1\,1\,1]$ plane of a nanoparticle with $\gamma_{111} < \gamma_{100}$. **B**: Nanoparticle shape according to Wulff-Kaishew theorem with strong truncation along $[1\,1\,1]$ direction.

portional to the surface energy of the plane and the smallest volume enclosed by all possible planes describes the thermodynamic equilibrium shape. An example in two dimensions ($[1\,1\,\bar{2}]/[1\,1\,1]$ plane) is given in Figure 2.10 **A**, considering only the $[1\,1\,1]$ and $[1\,0\,0]$ surfaces. The Wulff-Kaishew theorem expands on the Wulff construction, by including the adhesion energy of the particle on the substrate, which leads to a truncation h (see Figure 2.10 **B**) [84]. This truncation is given by

$$\frac{h}{h_{hkl}} = \frac{E_{ads}}{\gamma_{hkl}},$$

where the adhesion energy is given by $E_{dh} = \gamma_{np} + \gamma_{support} - \gamma_{interf}$ which is the sum of the energy gained by the formation of the interface between particle and support and the energy required for the process of interface formation. Up until now, nucleation, growth, and nanoparticle shapes were discussed independent of the structural relationship between support and film or nanoparticles and is applicable to the growth on and of single crystalline, poly crystalline, or amorphous supports and deposits.
In practice, the shape of nanoparticles is not exclusively governed by thermodynamic properties, but growth and nucleation are kinetically limited [85]. Furthermore, the nucleation and growth environment is highly anisotropic with inhomogeneous flux of the evaporant, anisotropic surface properties such as step edges or epitaxial relationships to the substrate, or differing growth rates between facets. Further sources of anisotropy influencing particle nucleation and growth are defects such as screw dislocations, mirror

planes, point defects, or grain boundaries caused by incomplete coalescence [85, 86].
The most crucial kinetic limitations are introduced by the lattice mismatch f at the particle support interface which is given by

$$f = \frac{a_s - a_f}{a_f}.$$

Generally, the lattice mismatch is non-zero and a principal parameter determining the interfacial relationship between deposit and support, governing nanoparticle growth and shape. Processes to relieve the lattice mismatch are the formation of new phases or alloying via interdiffusion, the formation of misfit dislocations and strain. However, for the growth of metals on metal oxides only the latter two processes are relevant as the substrates can be considered as inert for the applied growth conditions. The type of relaxation mechanism at the interface for a particular material system is usually governed by the magnitude of the lattice mismatch and the thickness of the film. In the case of nanoparticles, the lateral size has to be considered as well. For material systems with a small lattice mismatch, interfacial strain is often favored, as each surface atom may interact with an atom of the deposit. With increasing lattice mismatch, energy required to deform the deposit's lattice becomes larger which means that dislocations are favored instead. A similar argument explains the formation of dislocations with increasing film thickness. With each layer that is deposited, the required energy for the deformation of the deposit's lattice increases, as the necessary deformation only diminishes gradually with increasing thickness. In contrast, the energy required for the formation of misfit dislocations is independent of the film thickness. The dependence of the type of interfacial structure as a function of lateral size of nanoparticles follows the same logic: With each additional lateral layer that is added to the nanoparticle, the required deformation of the nanoparticles lattice increases which leads to the formation of dislocations starting at a critical diameter.
Comparison of the orientation of the nanoparticle ensembles in the reports [87, 88] highlights the correlation of the nanoparticle diameter with the epitaxial relationship of the nanoparticles. For small nanoparticles, below 10 nm, the ensemble exhibits exclusively cube-on-cube epitaxy [87]. Whereas, for the in diameter nearly three times larger nanoparticles, two in-plane orientations were observed. The majority ensemble still exhibits the same epitaxy as in[87] with the Pd[1 0 0] axis aligned with the MgO[1 0 0] (= cube-on-cube). However, a second, minority ensemble was observed which is rotated by 3.7 ° relative to the majority ensemble. Instructive is also the comparison of the size and the height to diameter ratio of the nanoparticles. The rotated mi-

nority ensemble exhibited an average diameter of 16.8 nm and a height to diameter ratio of 0.488. In contrast, the majority ensemble exhibits a diameter of only 14.2 nm with a height to diameter ratio of 0.62. This shows that the particle support interaction of the majority ensemble inhibits the lateral growth and promotes vertical growth while for the rotated ensemble, the lateral growth is favored.

2.2 Heterogeneous Catalysts for CH_4 Oxidation

Catalysts are materials that change the kinetics of a target reaction that modifies activation barriers in a way that allows a particular reaction to occur at thermodynamic conditions at which it would not occur without the catalyst. In addition, the catalyst material must be recoverable after reaction. The following paragraphs will first introduce general concepts of catalysis and will end with descriptions of the current understanding of the mechanism for full catalytic CH_4 oxidation and the oxidation and shape changes induced in Pd nanoparticles by oxygen. The following sections are based on [89–91].
Catalysts are generally separated in two classes: homogeneous catalysts and heterogeneous catalysts. This classification refers to the phase of the catalyst and the reactants. In homogeneous catalysis, reactant and catalyst have the same phase (i.e. liquid), whereas in heterogeneous catalysis, which is the relevant process in the context of this thesis, the catalyst is usually a solid and the reactant a liquid or gas. Heterogeneous catalysts, for example for exhaust treatment of combustion engines, are structurally complex components (see leftmost image in Figure 2.11). This is motivated by the ambition to maximize the available surface area of the catalyst while minimizing the amount of noble metal. For this purpose, the catalyst structure is optimized at each length scale. For optimal flow but also high surface areas, the catalyst is often supported on a support structure with small channels (i.e. honeycomb structure in Figure 2.11). The catalyst material is deposited on this structure in form of a slurry, containing larger ceramic or metal-oxide particles that will form the porous surface structure in the channels and the catalytically active (noble) metal nanoparticles that provide active sites. The slurry is calcined and often treated by oxidation/reduction cycles to optimize nanoparticle dispersion, porosity, and stability.
Despite the widespread use of catalysts in many applications ranging from the chemical industry to exhaust gas treatment, detailed descriptions of the atomistic processes remain elusive [10]. However, the influence of many pa-

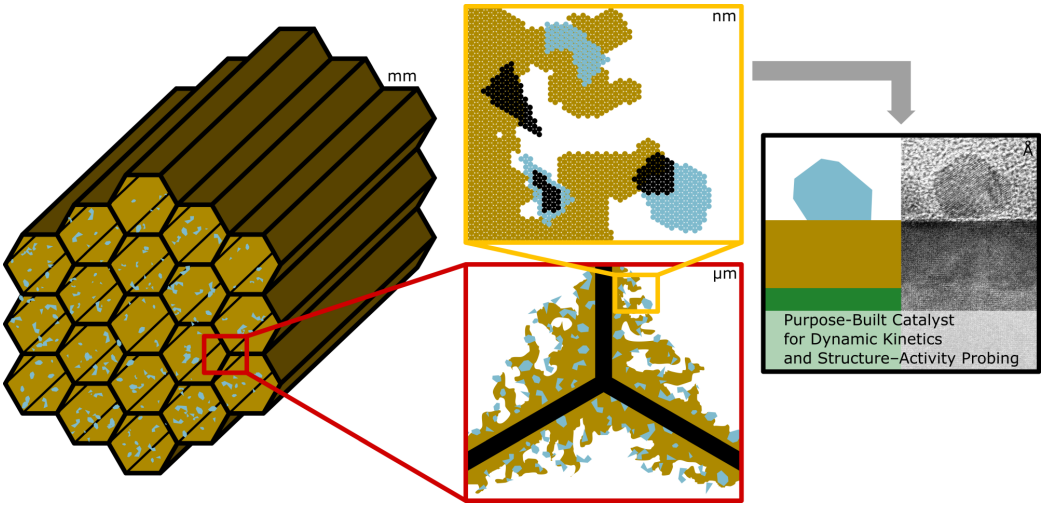

Figure 2.11: Overview of the length scales of catalyst structures with channels in the range of mm, pores in the washcoat in the range of μm, and nanoparticles in the nanometer regime. The abstracted model catalyst design, optimized for operando investigations by surface X-ray Scattering techniques.

rameters has been investigated in the past decades, giving insight into crucial properties of catalysts that govern their performance. In the context of Pd based catalysts, the PdO(1 0 1) surface has been found to be the most active surface [10, 21, 25, 92], as it provides a large number of undercoordinated surface sites required for the strong interaction between catalyst and CH_4 enabling H abstraction. Yet, the coexistence of both metallic Pd and PdO has also been reported to improve the activity [26–28]. This is commonly attributed to the ability of metallic Pd to polarize the CH_4 molecule. This shows that the shape, size, and orientation of the nanoparticles, and hence the exposed amount of different facets is crucial for intelligent design of a catalyst. In addition to the active phase itself, the supporting metal oxides or ceramics can influence the performance of catalysts directly or indirectly. Different types of supports have been shown to influence the stability of Pd and PdO respectively [20, 26]. Active participation of the support has been shown for CeO_2 which is capable of reoxidizing partially reduced PdO_{1-x} or directly provide reactive oxygen species to the reaction [10, 16, 21, 35, 55]. A crucial influence on the activity, reaction pathway, and deactivation behavior of Pd based catalysts has been observed for water [15, 21]. The degradation effect may be minimized by utilization of different types of support, which has been shown by Murata *et al.* for different types of Al_2O_3 supports [17]. Finally, the addition of Pt has been shown to improve the catalytic activity

of Pd based catalysts [19] despite pure Pt catalysts exhibiting a significantly worse activity towards full catalytic oxidation of CH_4 [10, 23]. While the exact mechanisms that improve the activity of catalysts by the addition of Pt remains unclear, an influence on the Pd/PdO ratio [19] and improvement in poisoning resistance by water [22] has been linked to the presence of Pt.
The strategy to tackle these knowledge gaps employed in this work are model catalysts (see Figure 2.11). Model catalysts employed for operando investigations in this work greatly reduce the structural complexity of the catalysts. Instead of highly complex multi-scale supports, nanoparticles are supported by atomically smooth metal oxide surfaces. The nanoparticle ensembles grown by UHV exhibit initially uniform structure and orientations. Yet, the realistic nanoparticle size distributions and realistic reaction conditions make these catalysts good approximations of industrially used catalysts.

2.2.1 Fundamental Processes in Heterogeneous Catalysis

A catalyst converts reactants into the desired products via a number of elementary steps i. The total enthalpy for a catalytic reaction is thus given by

$$\Delta H = \sum_i \sigma_i \Delta H_i$$

which sums the enthalpy changes for each elementary step. For a good catalyst, values of ΔH_i should be relatively similar, since a very negative change in enthalpy would have to be counterbalanced by a large positive change in enthalpy. This effect, depending on the order of sign in the changes of enthalpy, results in poisoning of the surface with intermediates or depletion of the catalyst surface of an intermediate and thus a small overall conversion. Figure 2.12 shows the energy diagram of catalytic CH_4 conversion over PdO(1 0 1), calculated from first-principles by DFT [92]. The initial state corresponds to CH_4 in the gas phase and the final state corresponds to CO_2 in the gas phase and a single O vacancy. The energy difference between the two states is the total enthalpy change ΔH. The inset shows the energies involved in a single elementary step. Here, E_a and E_f denote the energies of the initial and final state and the energy difference between the two states is the enthalpy change ΔH_i of the elementary step i. In between the initial and final state on the reaction coordinate x, a transition state is found. The energy difference between the initial state and the final state is the activation energy of the elementary step i.
In addition to the thermodynamic relationship between initial, final, and

intermediate states, this diagram also indicates how kinetics influence the reaction pathway. In the final steps of the energy diagram, CO is converted to $CO_{2(g)} + V$ over the course of five steps. The net change in enthalpy here is positive. In combination with the lack of investigations reporting intermediates of full CH_4 oxidation, this means that this phase of the reaction is kinetically driven. In terms of reaction coefficients this can be expressed as $k_d \ll k_r$, with k_d being the reaction rate for desorption and k_r being the reaction rate for conversion to CO_2. Hence, the desorption occurs at much lower rates than the conversion and only full oxidation products are observed.

2.2.2 Reaction Mechanisms in Heterogeneous Catalysis

In a heterogeneous catalytic reaction, reactants and products typically undergo a specific series of steps leading up to and following actual catalytic conversion at the active site of the catalyst. First, the reactants must diffuse through a boundary layer at the gas-solid interface of the catalyst. This concentration gradient is strongly dependent on the catalyst material and its interaction with the components of the reaction gas feed. Once the diffusion layer is penetrated, the catalytic reaction can take place. This process is commonly classified into three classes of reaction mechanisms depending on the

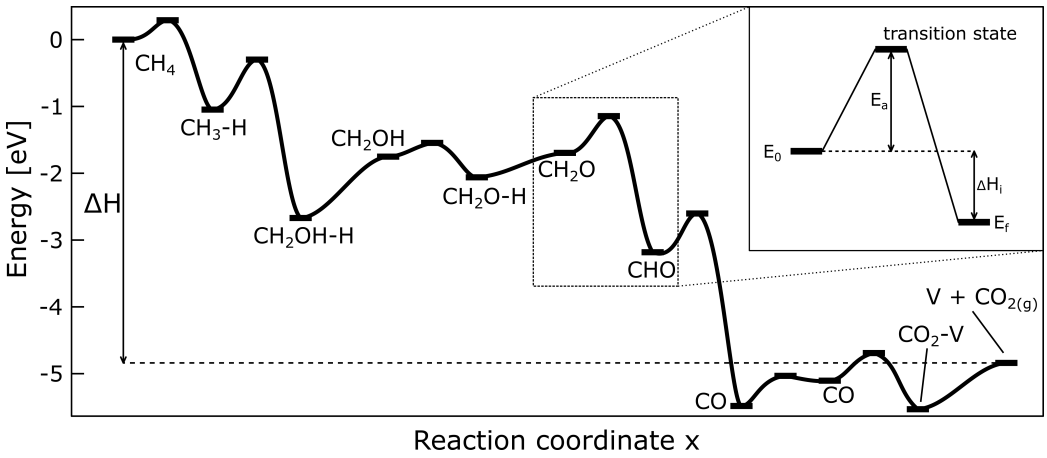

Figure 2.12: Energy diagram of the conversion of CH_4 by PdO(1 0 1) for dry gas feeds. Image adapted from [92]. V indicates an oxygen vacancy in the catalyst surface. In the inset describes the relations between initial, transitional, and final state at the example of the elementary step convertion CH_2O to CHO. The image is a reproduction from [92] which was modified with the inset and annotations.

number of adsorption (desorption) processes are required (see Figure 2.13). In the Langmuir-Hinshelwood mechanism, reactants are first adsorbed on adjacent sites on the catalyst surface. After the reaction took place, the product(s) desorb again. A prominent example for this reaction is the oxidation of CO over noble metal catalysts, such as Pt, Rh [93], or Pd [94]. In the Eley-Rideal mechanism, only one of the reactants adsorbs on the surface before the reaction takes place with the second molecule in the gas phase. Finally, the third class of reaction mechanism, the Mars-van Krevelen mechanism, is considered the main pathway for the full catalytic oxidation of CH_4 over PdO [10, 21, 92]. This pathway involves the adsorption and reaction of one of the reactants with the catalyst. The conversion of the reactants then takes place between the second reactant that is also adsorbed on the catalyst surface and the compound that has been created in the first step. In case of catalytic CH_4 conversion over Pd based catalysts, this constitutes the reaction of oxygen with palladium, forming PdO. Subsequently, CH_4 is adsorbed on the surface where a series of reactions with lattice oxygen of the PdO surface take place, which converts CH_4 to CO_2 via a number of intermediates. A detailed report of the current understanding the reaction mechanism is given in Section 2.2.3. After the catalytic conversion of the reactants, the products must desorb from the surface. This does not necessarily need to take place and can cause poisoning of the catalytic surface. These bystanders are often forming a strong bond with the catalytic surface and have a large activation energy for a possible following reaction step. Finally the desorbed products diffuse through the concentration gradient at the gas solid interface before entering the gas stream.

For the application of heterogeneous catalysis for gases with solid catalysts, the diffusion processes only become relevant at high temperatures. At low temperatures, the rate of catalytic conversion is governed by the reaction rates, which typically increase drastically with temperature. Thus, only at sufficiently high temperatures, the reaction processes become faster than the diffusion processes.

2.2.3 Full Catalytic CH_4 Oxidation Mechanism Over PdO(101)

The currently best description of the reaction mechanism of full CH_4 oxidation by Pd based catalysts is based on microkinetic modeling. A first-principle derived model was presented by van den Bossche *et al.* [92] and extending on this with experimental insights a mean field microkinetic model by Stotz *et al.* [21]. The microkinetic models were developed for the PdO(1 0 1)

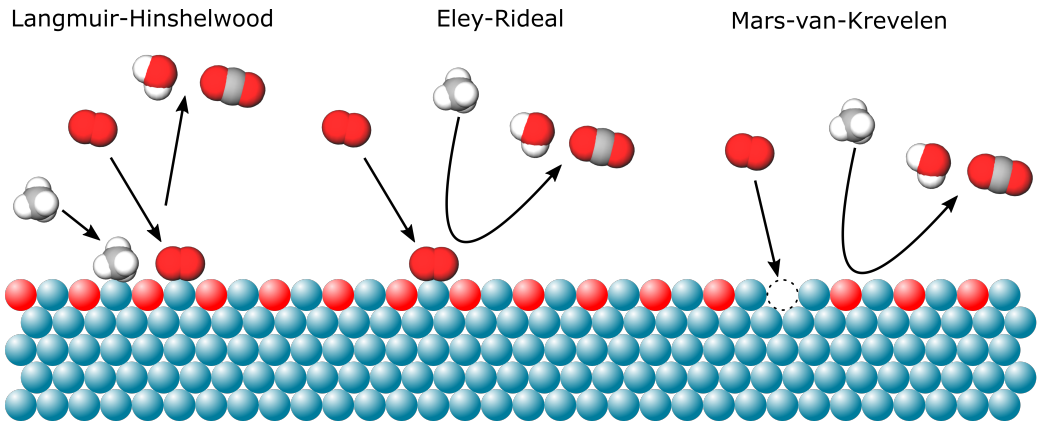

Figure 2.13: Overview over the three classes of reaction mechanisms in heterogeneous catalysis. In this example, red indicates oxygen, blue, the catalyst metal, black carbon, and white hydrogen.

surface which is ultimately motivated by numerous experiments correlating activity with the PdO(1 0 1) content [10, 14, 28, 40] and DFT calculations of the initial, final, and transition state of the first hydrogen abstraction over various Pd, PdO and Pd surface oxides [25]. From the tabular data provided in [25], Figure 2.14 was created for facile comparison of initial, transition and final state. The bulk surfaces are labeled conventionally, $\sqrt{5}$ refers to the $(\sqrt{5}\times\sqrt{5})R27°$ surface oxide discussed in Section 2.1.1, $\sqrt{5}$-Pd(1 0 0) denotes a stripe of the surface oxide supported by Pd(1 0 0), and $-r$ indicates that the surface is partially reduced.

The comprehensive calculations reveal two regimes for the final energy. The metal surfaces and the single surface oxide layer exhibit an endothermic behavior with varying activation energies. All other surfaces exhibit exothermic behavior (Pd(1 0 0)-r being the outlier with nearly isothermic behavior) with a significant spread in the activation energy and final energy state. By comparison all energy levels between the structures exhibiting exothermic behavior first insights are gained. All oxide surfaces, specifically the surfaces with a PdO]hkl(101) structure exhibit a lower initial state energy. This effect can be explained by the projected density of states (PDOS) of the $5s$ orbital of Pd. A comparison between PdO(1 0 0) and PdO(1 0 1) reveals that for PdO(1 0 1), a large portion of the PDOS is shifted above the Fermi level. These free $s-d$ hybrid orbitals interact with the methane molecule, shifting electron density from between the C–H bond closest to the surface to between the H atom and Pd. This attractive interaction is referred to as a σ-complex or precursor state and facilitates dissociative desorption by activating the CH_4 atom. Shifting attention to the activation and final state

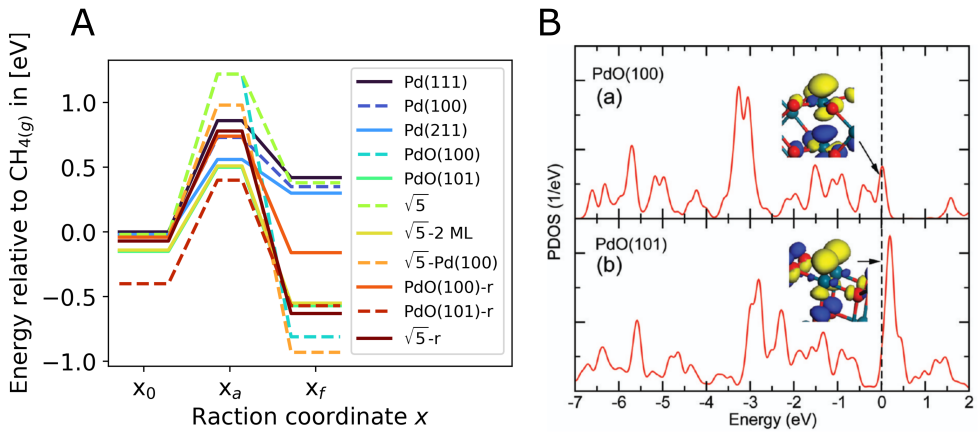

Figure 2.14: **A**: Initial, transition, and final state energies for Pd, PdO surfaces and Pd surface oxides. Energies are relative to CH_4 in the gas phase. Figure was created from the data provided in [25]. **B**: Projected density of states for CH_4 in close vicinity to PdO(1 0 1) and PdO(1 0 0). Image adapted from [25].

energies, the PdO(1 0 1) and the two monolayer surface oxide model exhibit almost identical behavior which can be rationalized by strong structural similarities of the two surfaces. As for the PdO(1 0 1)-r surface, only the initial and activation energies diminished. Overall, the three surfaces exhibit the best ratios of final and transition state energies and are thus considered the most active for the H-abstraction. The three materials that exhibit even lower final state energies have enormous activation energies over or close to 1 eV which indicates that these surfaces are unlikely to provide active sites for the first H abstraction. Overall, the low final energy states for all materials with exothermic behavior are rationalized by the stabilization of CH_3* adsorbed on Pd_{cus} (cus indicating under coordinated site) by neighboring OH groups. However, this is only true for the oxides, as adsorbed oxygen on metallic Pd increases the activation energy of the H abstraction.

Based on these results, the reaction mechanism for the (101) surface of PdO was developed from first principles [92] identifying the Pd_{cus} and O_{cus}. Furthermore, the main reaction pathways via a Mars-van Krevelen mechanism were described, where at low temperatures O is inserted forming methanol as an intermediate and at high temperatures favoring C−H fission before oxygenation of the carbon species. An extension of these findings is the mean-field approach by Stotz *et al.* which was rationalized by verification of postulated intermediates via diffuse reflectance infrared Fourier transform spectroscopy (DRIFTS) and the reproduction of the catalytic activity of

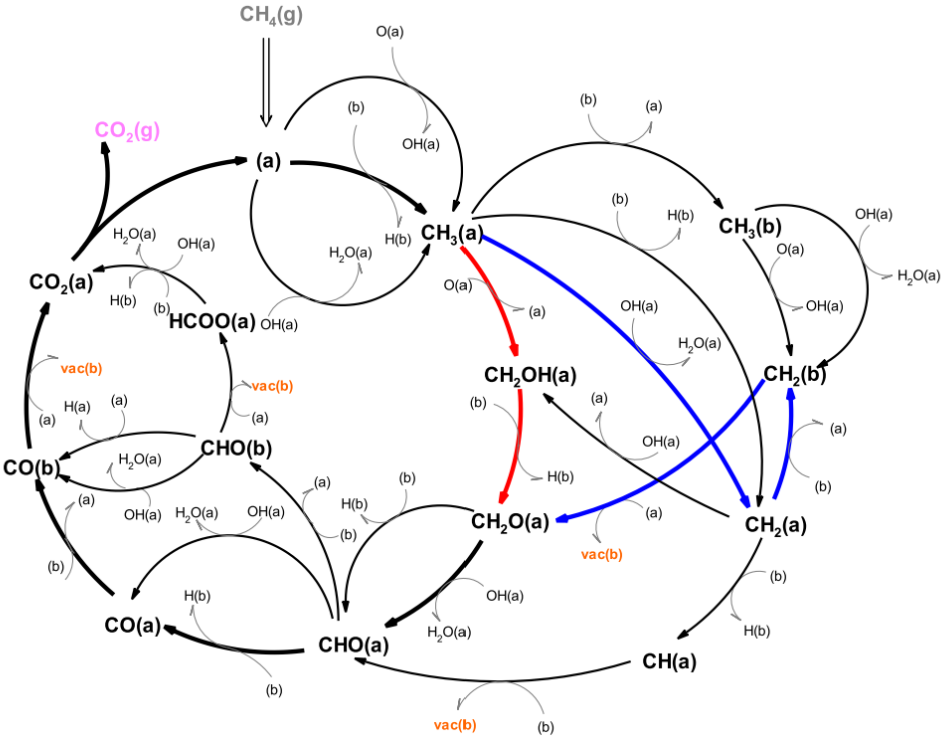

Figure 2.15: Reaction mechanism by Stotz *et al.*. Red arrows indicate the pathway in dry conditions below 400 °C (red arrows) and wet conditions and/or high temperatures above 400 °C (blue arrows). Image from [21].

Pd/Al_2O_3 powder catalysts under consideration of sintering [21]. Several assumptions were made by the authors to make calculations feasible. These include the statistical treatment of adsorbates and neglection of adsorbate-adsorbate interactions as well as the random distribution of the active sites distribution randomly distributed and identical in size. In addition to that, no support effects, no time-dependent changes or temperature changes were considered. The resulting reaction mechanism is shown in Figure 2.15, where (a) denotes the Pd_{cus} site, (b) O_{cus} site, and thick arrows indicate the preferential reaction pathway. The diagram highlights the most important findings of the mechanistic studies. Firstly, for low temperatures and high temperatures (or gas feeds without or with water), different reaction pathways are preferred, which is directly linked to the OH coverage of the surface. Secondly, the reaction proceeds via a number of stable intermediates. However, evidence for partial oxidation is only found in oxygen deficient gas feeds (severely understoichiometric O_2 content) [27, 95] and evidence for the intermediates was only partially observed by DRIFTS [21]. However, despite

the assumptions and simplifications, the presented mechanism and the reaction kinetics calculated from it were successfully applied to replicate experimentally observed activity of nanoparticles by comparably inert metal oxide supports [21, 92].

2.2.4 Shape Changes and Oxidation of Pd Nanoparticles

Thus far, the nucleation, growth and shape were discussed without consideration of interactions between nanoparticles and the surrounding environment and the catalytic activity was mainly described in the context of a perfect PdO(1 0 1) surface (or catalyst morphology that can be represented by this morphology). However, catalysts operate under dynamically changing temperature, pressure, and gas composition which induce changes in the shape, size, and oxidation state of the nanoparticles. The following section will cover the influence of oxygen, the main component of the typically lean reaction gas mixtures for catalytic CH_4 oxidation on the shape and oxidation of nanoparticles.

The driving force for the particle shape is the surface energy of the exposed facets of nanoparticles. Naturally, changes in the surface energy are expected to occur when exposed to oxygen. Indeed, shape changes have been described by DFT calculations [96] and experimentally [87, 88]. A comprehensive report on the surface energies of Pd has been published by Popa *et al.* [96] which showed that the change in surface energy of the Pd surfaces as a function of the oxygen potential is unique for each facet. Thus, a shape change of the Pd nanoparticles is expected when exposed to oxygen, provided the kinetic barriers for restructuring can be overcome. Without exposure to oxygen, they report a particle shape dominated by (1 1 1) and (1 0 0) type facets, where the (1 0 0) type facets are connected by strips of (1 1 0) type facets. With increasing oxygen partial pressure, first the (1 1 0) type facets vanish, increasing the size of the other facets. With further increase of the relative oxygen potential (up to an oxygen partial pressure corresponding to 0.3 mbar), the (1 1 1) type facets shrink in size until the particle shape resembles the shape of a die with (1 0 0) type facets dominating the shape and (1 1 1) type facets rounding off the corners.

Despite being experimentally challenging, shape changes have been observed for Pd ensembles supported by MgO(0 0 1) [87, 88]. Nolte *et al.* observed the predicted particle shape, consisting of (1 0 0), (1 1 1), and (1 1 0) type facets. By the exposure to 1×10^{-5} mbar of oxygen at 570 K, hkl(112) type facets were formed at the edge between the (1 0 0) and (1 1 1) facets. Upon

reverting to UHV conditions, the newly formed facets vanished again. In a similar experiment previously mentioned for its insights into the influence of the particle support interactions, similar observations were made. The more heterogeneous particle ensemble with generally higher index facets also present at higher temperatures formed (3 3 1) facets at the expense of (1 1 1) and (1 1 0) facets upon exposure to oxygen. This highlights not only the previously discussed the influence of the nanoparticle size and implicitly facet size on the stability or occurrence of said facet, but also the change of the particle response depending on the initial shape and size.
In addition to shape changes, the properties of support and nanoparticles have an effect on the oxidation behavior of nanoparticles. For the same sample system (Pd/MgO), oxidation of Pd nanoparticles was observed to lead to the formation of epitactic PdO. The loss of material for the metallic nanoparticles, led to a shape change towards a more pyramidal particle shape expected for small Pd nanoparticles. In addition, small amounts of polycrystalline PdO were observed to form on the top facets of the particles, which suggests that the oxidation preferentially occurs at the support particle interface [97]. Building upon this, a second study investigated the size dependence of nanoparticles by comparing oxidation of ensembles of three different size regimes. The small nanoparticles with an average size of 5 nm, full oxidized at an oxygen partial pressure of 56 mbar at 570 K [98]. Although, oxidation did occur, the required oxygen potential was roughly seven orders of magnitude larger than predicted, suggesting significant kinetic barriers in the oxidation of Pd/MgO. The nanoparticles of the medium size regime, remain partially metallic at this partial pressure, but continue to oxidize. A strong change in behavior was observed for the large nanoparticle ensemble with an average size of 20 nm. Instead of fully oxidizing, the formation of epitactic PdO was observed in pressure steps leading up to 56 mbar which is in full agreement with the observations for the smaller nanoparticles. However, the large nanoparticles start forming a polycrystalline PdO shell between UHV and 0.3 mbar which fully inhibits further oxidation. These two studies highlight the size dependence of the degree of oxidation and the mechanism of oxidation between particles that differ by only several nanometers in size.
A third oxidation experiment summarized in [79], investigated the oxidation of Pd supported by Al_2O_3(0 0 0 1) at 620 K, the same sample system investigated during CH_4 oxidation in Chapter 2 and Chapter 4. Below oxygen partial pressures of 10^{-2} mbar no oxidation or surface oxide formation was observed, but small decrease in size of the Pd nanoparticles due to chemisorption of oxygen. Similar observations were also made for Pd/MgO that showed significant changes in the strain state of the nanoparticles upon exposure to oxygen. The oxidation onset was observed at an oxygen chemical potential

roughly seven times larger than predicted. At pressures up to 3 mbar, no change in dispersion was observed and upon pumping to UHV conditions, the initial configuration was recovered. Only small amounts of oxygen induced material transport were observed, possibly the oxidation of smaller minority nanoparticles. Beyond this oxygen partial pressure, full oxidation takes place, which leads to the formation of epitactic (1 0 0) and (0 0 1) oriented PdO, accompanied by a large irreversible material transport. This study exemplifies the significance of the support particle interaction, which lead to unique behaviors of the Pd nanoparticles depending on the underlying substrate. Furthermore, the strong size dependence on the kinetic barriers for oxidation and the changed oxidation mechanisms caused by this highlight the complexity of nanoparticle oxidation.

2.2.5 Operando Catalysis Cell

Catalytic investigations were conducted using a custom, X-ray compatible operando catalysis setup entailing a gas-mixing system, the reactor, and an in-line mass spectrometry setup. The mass spectrometry section is based on [99], which is recommended for further reading and detailed information about other detector types and quantitative analysis techniques.
The computer controlled gas mixing system allows control over the the pressure, flow and mixture of up to five gases. A simplified flow scheme is displayed in Figure 2.16. The gas inlets of the gas mixer are connected to gas

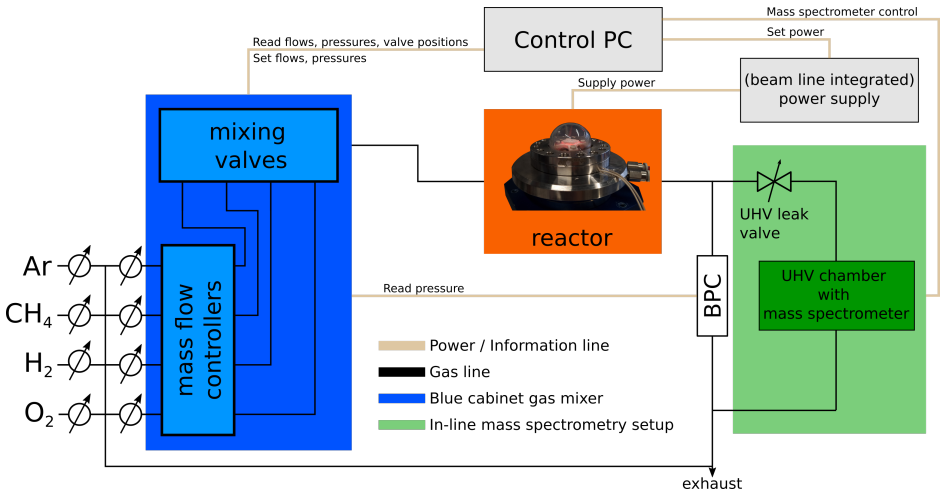

Figure 2.16: Simplified flow scheme of the operando catalysis cell set-up including gas mixing system, reaction chamber, inline mass spectrometry, and beamline integration.

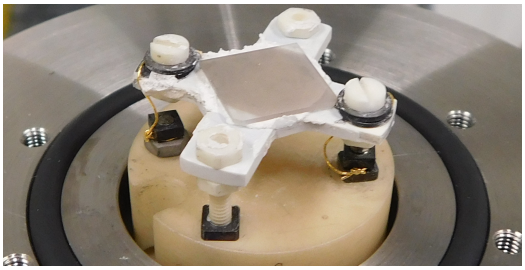

Figure 2.17: Heating cross with sample mounted in catalysis chamber.

lines providing the individual gases at a pressure between 4 to 5 bar. The flow of each gas is then controlled by individual mass flow controllers, feeding the desired gas at the desired flow to a mixing valve. From there the gases are fed to second valve used to guide the mixed gases to the shunt or directly into the reactor. For the experiments reported on in this thesis the shunt, bypassing the reactor, was used to clean gas lines and gas mixing system without contaminating the sample. For catalytic experiments, the gas flow was directed to the reactor.
The center piece of the setup is the X-ray compatible reactor, equipped with gas inlet and outlet, power connections for a heater, cooling lines, and a Be dome. The chamber allows operation under oxidizing conditions with pressures up to 1.25 bar and sample temperatures up to 1450 K. Sample heating is realized with a heating cross which consists of a flat, teflon covered graphite filament. It is mounted on a ceramic block using ceramic threads and nuts (Figure 2.17). The electrodes of the heater are connected to Mo rods by gold wires. The Mo rods are plugged into the power feedthroughs beneath the ceramic block. Vital to the use in X-ray experiments is the precise positioning of the sample which is mounted on top of the heater using BN paste. It is important to minimize thermal expansion of the chamber components, especially for operando investigations following the catalysts structure as a function of temperature using grazing incidence techniques (see Section 2.3.3). For this reason, the heating cross mounting and electrical connections for heating are separated, leaving only two mounting points for the heating cross. For ease of operation, the sample temperature was calibrated (see Figure A.1) prior to the catalytic experiments by mounting a thermocouple on top of the crystal using BN paste.
The gas mixture provided by the gas mixing system flows through the reactor, where the catalytic reaction takes place. Due to the design of the reactor, 45 % of the inlet gas passes the sample via virtual bypass before leaving the reactor [100]. From the reactor, the gas is fed to a backpressure controller, which is used to measure and control the reactor pressure. Between the

reactor and backpressure controller, the in-line mass spectrometry setup is located. It consists of a small UHV-chamber equipped with a pre-pump, turbo pump, mass spectrometry head, and a leak valve. Through the leak valve, a small portion of the catalysts exhaust gas is let into the chamber, where the composition is measured by mass spectrometry.

Mass spectrometry

In mass spectrometry of gases, the gas is first ionized by electron bombardment. The ions are then accelerated into the analyzer, where ions are separated by their $\frac{m}{z}$ ratio, where m is the mass of the ion and z is the charge of the ion. The mass spectrometer employed for the experiments presented in this thesis was equipped with a quadrupole analyzer. It consists of four symmetrically arranged metal rods or electrodes. Opposite electrodes are connected and a combination of radio frequency (RF) and direct current (DC) voltages are applied. As a result, only ions with a specific ratio mass and charge travel a stable path through the analyzer, while other ions will be deflected. By scanning RF and DC voltages, the $\frac{m}{z}$ ratio can be scanned and full mass spectra can be recorded. Finally, the ion flow is measured at the detector behind the analyzer. In this case, a channel electron multiplier (CEM) was used, which amplifies the signal by ejecting multiple secondary electrons once an ion hits the channel. Each following impact of the secondary electrons produces additional electrons which amount to a measurable current at the end of the CEM.
In practice, for each molecule, electron bombardment produces ions with a range of charges z, which leads to multiple, apparent masses for each molecule. Electron bombardment may also cause the fragmentation into multiple be destroyed by electron bombardment leading to ionized fragments. For example, CH_4 can split into fragments with the $\frac{m}{z}$ ratios 17 (due to isotopes), 16, 15, 14, 13, or 12. Hence, in qualitative mass spectrum analysis, it is vital to ensure all fragments of all educts, products and intermediates of a target reaction are considered in interpretation.

2.3 X-rays for Structure and Chemical Investigation

X-rays are electromagnetic waves with a wavelength λ of the order of atomic distances in matter. This property makes it possible to use X-rays to probe interatomic distances and electronic transitions of atoms. In this work, X-

rays were used in X-ray reflectivity (XRR), X-ray photo-emission experiments (XPS), and X-ray diffraction (XRD). For this reason, the production of X-rays and related properties as well as the interaction of X-rays with matter will be discussed in detail in the following chapter. X-ray scattering and more specifically X-ray diffraction will be in the focus as it is the main technique used in this work. A more detailed description, including more explicit mathematical derivations are found in [101–103].

2.3.1 Sources

All XRR and XPS data as well as part of the XRD data presented in this work was recorded using X-rays produced by X-ray tubes. The main component of an X-ray tube is the cathode and target material which is also the anode. Between the two, an electric field is applied, which accelerates the electrons produced by the cathode towards the target material. Typical materials for standard applications are Cu (used in this work) or Mo for XRD and XRR and Al (used in this work) or Mg for XPS. At the target material the electrons are decelerated, causing the emission of X-rays with a characteristic, smooth spectrum, called *bremsstrahlung*. If the kinetic energy of the electrons is sufficient, the target materials' core levels may be ionized. When the holes are refilled by electrons from the valence band, X-rays are produced in high intensity bands corresponding to the energy liberated by the recombination of hole and electron are characteristic for the target material. The full spectrum of X-rays radiates from the target material in 2π from the anode and is tailored to the experiment needs by X-ray optics. In the case of the experiments presented in this thesis the X-ray diffractometer source was equipped by double-mirror multilayer optics for focusing and energy selection. Due to the orders of magnitude higher intensity compared to the *bremsstrahlung*, the K_α line is commonly used, as it was in this work.
For experiments such as the operando measurements of Chapter 2 or the kinetics measurements of Chapter 4 a combination of high photon energy, flux, collimation, and coherence is required. X-rays with these properties are produced at synchrotrons. At these large-scale facilities, electrons are first accelerated to relativistic speeds and then injected into a so-called storage ring which is usually made up of straight and bent sections. In the bent sections, bending magnets are used to keep the electrons in orbit. The radiation produced by the acceleration into orbit is often used for spectroscopy application due to its smooth spectrum reaching down into the infrared regime. Higher photon flux can be achieved by wigglers and undulators in the straight sections. These are arrays of magnets with alternating poles that force the electrons into a sinusoidal trajectory. In the case of undulators, the most

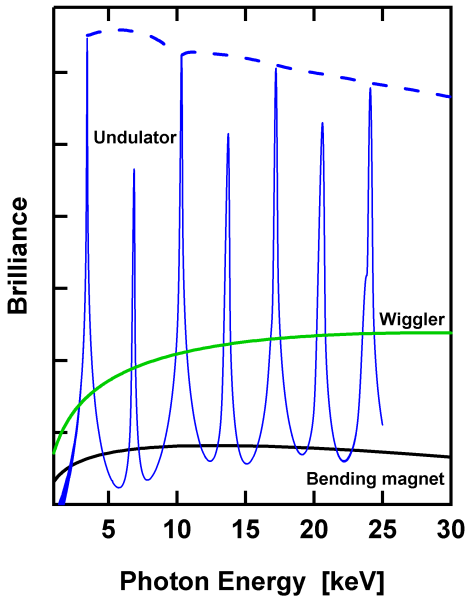

Figure 2.18: Spectra of a bending magnet (black), wiggler (green), and an undulator (blue).

common X-ray source in 3^{rd} generation synchrotrons, the electron path is modified in a way that allows for constructive interference of wave fronts produced at different positions in the device. Successive periods of pairs of magnets with opposite poles by successive periods of . The condition for constructive interference is given by

$$\lambda_{xray} = \frac{\lambda_u}{2\gamma^2}(1 + \frac{K^2}{2} + \gamma^2\Theta^2),$$

where λ_{xray} is the X-ray wavelength, λ_u the undulator period, and $\gamma = \sqrt{1 - \frac{v^2}{c^2}}^{-1}$ the relativistic electron energy. $K = \frac{e}{2\pi mc}\lambda_u B_0$ is the undulator parameter and describes amplitude of the electron oscillations as a factor for the opening angle $\approx \frac{1}{\gamma}$ of the synchrotron. Since interference of wavefronts is not limited to wavefronts produced by successive undulator periods, a spectrum like in Figure 2.18 is produced. The strongest band in the undulator spectrum is the fundamental wavelength of the undulator given by Equation 2.3.1 and harmonics of the fundamental wavelength are found at integer multiples of the energy of the fundamental wavelength. The advantageous interference in undulators is nicely illustrated in Figure 2.18, showing typical spectra for wigglers and undulators. The brilliance of an undulator (or

wiggler) depends on the the photon flux f , the source size $\Delta x \Delta y$ and the divergence $\Delta\Theta_x \Delta\Theta_y$ by

$$b \propto \frac{f}{(\Delta x \Delta y)\,(\Delta\Theta_x \Delta\Theta_y)}.$$

Due to the superior divergence and source size for undulators caused by the smaller perturbation of the electron path, the brilliance of undulator radiation exceeds that of other synchrotron sources. This makes undulator radiation the most popular synchrotron radiation as a large number of photons are available in a small angular space which allows the observation of weak (scattering) signals and fast acquisition modes.

2.3.2 Optical Interactions of X-rays and Matter

Completely analogous to interaction of visible light with matter, X-rays may be reflected, transmitted or absorbed. Due to the small interaction of X-rays with matter, the refractive index for X-rays is defined as the deviation from unity

$$n = 1 - \delta + i\beta,$$

where δ and β are the real and imaginary components. The expressions

$$\begin{aligned} \delta &= \frac{n_a r_e \lambda^2}{2\pi} f_1 \\ &= \frac{p_e r_e \lambda^2}{2\pi} \end{aligned}$$

and

$$\begin{aligned} \beta &= \frac{n_a r_e \lambda^2}{2\pi} f_2 \\ &= \frac{\mu\lambda}{4\pi} \end{aligned}$$

for the real and imaginary part of the refractive index are derived from interaction with electrons and the atomic form factor. Here, $n_a = \frac{\rho N_a}{M_a}$ is the number density, N_a the Avogadro constant, M_a the atomic molar mass, r_e the electron radius, λ the wavelength, ρ_e the electron density, μ the attenuation coefficient, and f_1 and f_2 the atomic scattering factors, describing the dispersive and absorptive interactions of X-rays with the element. Both parts of the refractive index are given as a function of the atomic scattering factor and in an alternative representation which is useful to connect the refractive index to material properties: δ depends on the electron density and β depends on the attenuation coefficient which is highly energy and element dependent.

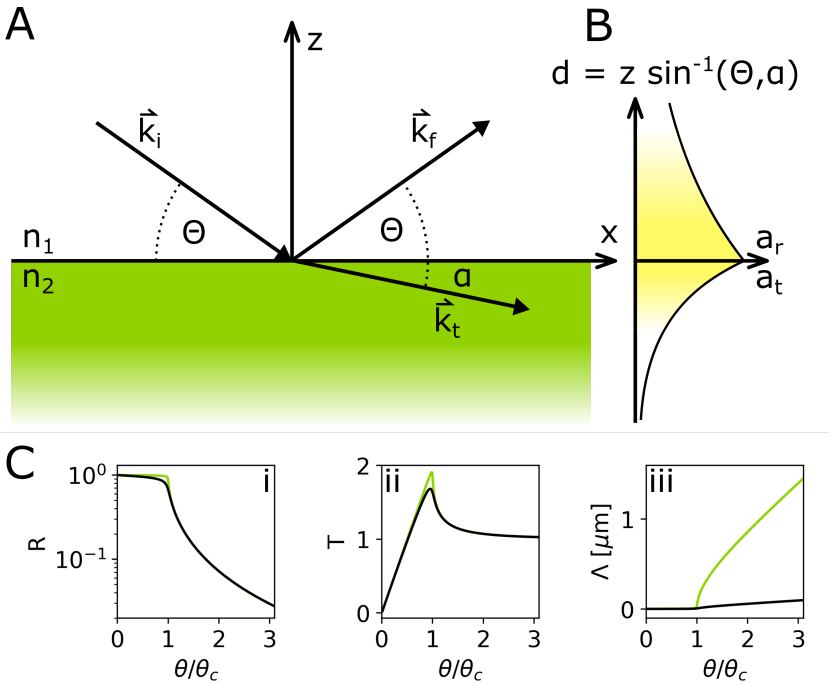

Figure 2.19: **A**: Visualization of reflection, and refraction at the interface of two materials with the refractive indices n_1 and n_2. **B**: Amplitude as a function of the traveled distance d showing the effect of absorption. **C**: Intensity of reflectivity (i), intensity of transmittivity (ii), and penetration depth as a function of θ/θ_c (iii).

Fresnel Equations

With the definition of the refractive index for X-rays, the next step is to describe the transmission, reflection, and absorption of X-rays in matter. The schematic overview over these processes in Figure 2.19 shows that the incidence and exit angle of the respective waves indicated by their wave vectors are identical (law of reflection). Notably, the transmitted wave is refracted towards the interface for the depicted case of $n_1 > n_2$, in contrast to the expected direction for visible light (Figure 2.19 **A**). Furthermore, the X-ray absorption is shown as a function of the distance d traveled in the respective mediums (Figure 2.19 **B**). The relationship between the material properties n_1 and n_2 and the incidence and refracted wave angles θ and α is derived from the continuity condition of the tangential component of the wave and its first derivative. This is a direct result of the Maxwell-Faraday equation and in this context is fulfilled if the following conditions which relate the amplitudes and wavevectors of the incidence, reflected and transmitted

wave component.

$$\begin{aligned} a_i + a_r &= a_t \\ \mathbf{k}_i a_i + \mathbf{k}_r a_r &= \mathbf{k}_t a_t. \end{aligned}$$

Here, a is the amplitude and $\mathbf{k}$ the wavevector with the indices referring to incidence (i), reflected (r), and transmitted (t) beam, leading directly to Snell's law:

$$n_1 \cos(\theta) = n_2 \cos(\alpha)$$

Analogous to visible light, the critical angle θ_c describes the point at which the wave is fully reflected ($\alpha = 0$). For the transition from air ($n_1 \approx 1$) to another, denser material the expression

$$\theta_c = \sqrt{2\delta}$$

is readily derived from Snell's law (Equation 2.3.2) and the refractive index Equation 2.3.2. The critical angle is a useful unit, since it only depends on the electron density ($\delta \propto \rho_e$) which means that it varies between materials. Furthermore, it marks the pivot point between full reflection and transmission which means that it can be easily identified in experiments.
Starting from Snell's law (Equation 2.3.2) and the complex refractive index (Equation 2.3.2), the Fresnel equations

$$\begin{aligned} r &= \frac{a_r}{a_i} = \frac{\theta - \alpha}{\alpha + \theta} \\ t &= \frac{a_t}{a_i} = \frac{2\alpha}{\alpha + \theta} \end{aligned}$$

emerge with r and t being the amplitude reflectivity and transmittivity. This concise representation is reached by the small angle approximation. This is valid since n_2 is close to unity and thus the angles become small at which refraction and reflection become relevant phenomena. The final component of the interactions is absorption (Figure 2.19 **B**) which is found from Equation 2.3.2. When using the complex refractive index for the material that is penetrated ($n_1 = 1$), α is a complex number. Hence the refracted wave becomes

$$a_t e^{ik\alpha z} = a_t e^{i\,k\,\mathrm{Re}(\alpha) z} e^{i\,k\,\mathrm{Im}(\alpha) z}$$

which shows that the penetration depth ($\frac{I}{I_0} = \frac{1}{e}$) is

$$\Lambda = \frac{1}{2k\,\mathrm{Im}(\alpha)}.$$

The expressions for the intensity of reflectivity, transmittivity as well as the penetration depth are shown for Al_2O_3 (green) and Pd (black) as a function of θ/θ_c in Figure 2.19 **C** i to iii. The behavior of each graph can be separated in three major regimes, $\theta/\theta_c << 1$, $\theta/\theta_c = 1$, $\theta/\theta_c >> 1$. At angles well below the critical angle ($\theta/\theta_c << 1$), total reflection occurs. This can be seen in Figure 2.19 **A** i which shows that the intensity for reflectivity is trending towards unity with decreasing incidence angle. Accordingly, the penetration depth is zero and the refracted and transmitted wave is of very low intensity. At the critical angle ($\theta/\theta_c = 1$), the reflectivity changes the most as this angle marks the point from which transmission can occur. Naturally, this is accompanied by a drastic increase in the penetration depth. Interesting behavior is observed for the intensity of the transmitted wave which is exploited in grazing incidence experiments (see Section 2.3.3). At these conditions, a resonant-like behavior is observed, since the phase shift of the reflected wave approaches 0 at this point. Hence, the incidence and reflected wave interfere constructively, which in turn requires the increase of the transmitted wave. For materials with lower electron densities (compare Al_2O_3, green and Pd, black in Figure 2.19 **C**), this effect is more pronounced, due to the smaller critical angles which leads to a stronger overlap of the incidence and reflected wave. Finally, at angles much larger than the critical angle, the reflectivity approaches zero as the penetration depth increases and the the intensity of the transmitted wave approaches unity. This corresponds to full transmission and no reflection.

X-ray Reflectivity

In the discussion of Snell's law and the Fresnel equations, a pronounced dependence of the X-ray matter interaction on the electron density of the material was discussed. For example, the critical angle of a material being directly linked to its electron density. Since these effects occur at every interface that the X-rays interact with, X-ray reflectivity is a powerful tool for the investigation of thin films and nanoparticles.

X-ray reflectivity relies on the interference of multiple reflection and transmission, occurring at the interfaces of a thin film samples. For the first three contributions, the reflection and transmission processes are illustrated along the beam path in the scheme in Figure 2.20. In this simple case of a single layer and only considering the three shortest interactions of reflection and transmission

$$r = r_{01} + t_{01}r_{12}t_{10}p^2 + t_{01}r_{12}r_{10}r_{12}t_{10}p^4 + ...$$

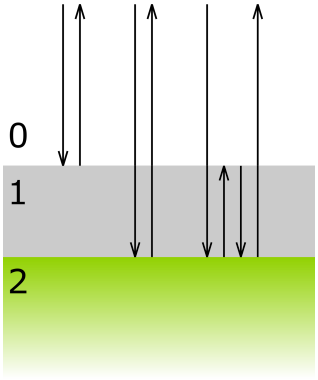

Figure 2.20: Sketch of the reflection and transmission processes in an X-ray diffraction experiment on a thin film (grey) on a substrate(green).

is attained. Here, the indices indicate the interface where the interaction takes place, and p is the phase factor which needs to be added for each transmission event. An exact expression for an arbitrary number of layers N was first described by Parrat [104]. For the bottom most layer N, the series aborted at the third contribution in Equation 2.3.2 can be expressed as

$$r_{N,N-1} = \frac{r_{N-1,N} + r_{N,s}p_s^2}{1 + r_{N-1,N}r_{N,s}p_s^2}.$$

Here, s indicates the infinite substrate below the N^{th} layer. Since no reflection is observed below this, the contribution $r_{N,s}$ can be calculated directly. For the second layer above the substrate the contribution to the total reflectivity becomes

$$r_{N,N-1} = \frac{r_{N-2,N-1} + r_{N-1,M}p_{N-1}^2}{1 + r_{N-2,N-1}r_{N-1,N}p_{N-1}^2}$$

and the following layers are expressed in the same way. The total reflectivity of an N layer system thus becomes the sum of all contributions.
In an X-ray reflectivity experiment, the angle between sample surface and source and sample surface and detector are kept equal, while the incidence angle θ_c is being varied. The varying path difference due to the varying incidence angles for the different beam paths causes oscillations in reflectivity. In Figure 2.21, simulation examples are provided that exemplify the effect of roughness (**A**), density (**B**), and thickness (**C**). For all simulation examples, the material combination of a Pd layer on Al_2O_3 and CuK_α X-ray energy were chosen, in reference to the Al_2O_3 based catalyst investigated in this work (Chapter 2, Chapter 4). In the first set of simulations a constant Pd film thickness with the roughness values of 0 Å, 5 Å, and 10 Åare compared. Accordingly, the roughness in the models on the right of Figure 2.21 **A** is indicated by the deviation from the initial state. In practice, the surface roughness is implemented as an uncorrelated Gaussian deviation of the

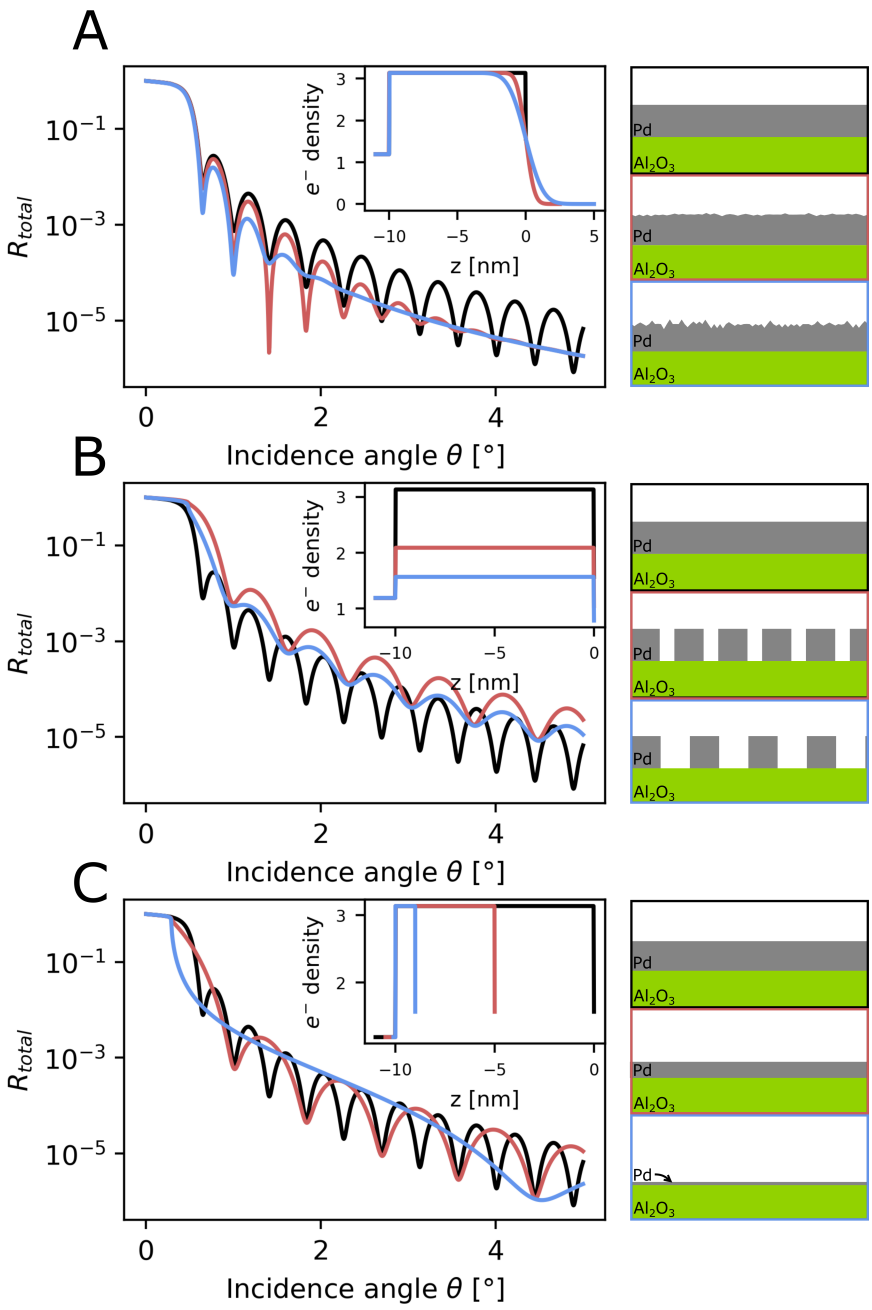

Figure 2.21: Simulation of X-ray reflectivity curves and electron densities highlighting the influence of surface roughness (**A**), density (**B**), and film thickness (**C**).

initial interface position z_0 in the Parrat formalism. The Gaussian nature is also represented in the electron density profile inset, where the increased roughness can be observed in the increasingly smeared out step at $z = 0\,\mathrm{nm}$. For the reflectivity curve, the increasing roughness causes a decrease in the amplitude of oscillations. In Figure 2.21 **B**, the effect of the relative densities of 100 %, 67 %, 50 % of Pd are shown. In the case of this simple model, the relative density of the Pd layer is equivalent to the coverage of the support with the 10 nm thick film. However, this requires a homogeneous distribution, since the X-ray-matter interaction is required to be coherent over the illuminated area. The main effect of the electron density on the reflectivity is a decreased oscillation amplitude and frequency. Similarly, the effect of the layer thickness (Figure 2.21 **C**) is a decrease in oscillation frequency. Notably, density and thickness of the layer have an immense effect on the curve just after the critical angle. Since the momentum transfer in X-ray reflectivity is parallel to the sample normal, only information along this direction is collected. Thus, nanoparticles, supported by single crystals can be analyzed in X-ray reflectivity by using a fractional electron density of the particle material (compare Figure 2.21 **B**) and large roughness values to account for the shape of the nanoparticles. Especially for three dimensional particles with large height to diameter ratios, multiple layers are often used to better approximate the shape of nanoparticles. Fitting X-ray reflectivity curves with such a model enables determination of the nominal thickness (total deposited material), surface coverage, and nanoparticle height.

2.3.3 X-ray Diffraction

In it's simplest form, the diffraction from crystals is described by Bragg's Law. In this model, lattice planes are viewed as semipermeable planes with a distance d_{hkl} at which a portion of the X-rays are reflected and a portion is transmitted. Due to the path difference between two beams reflected at different lattice planes, a phase shift is introduced, causing constructive and destructive interference:

$$n\lambda = 2d_{hkl}\sin(\Theta).$$

Here, n is an integer for the order of reflection and Θ, the incidence angle. The interplanar distance is decorated with the index hkl, referring to the Miller indices h, k, and l. These indices describe a set of equidistant crystallographic planes in a crystal. From each plane, the next is found at $(h/\mathbf{a}, k/\mathbf{b}, l/\mathbf{c})$, where **a**, **b**, **c**, are the lattice vectors of the crystal. For the crystal systems relevant to this work, the scalar expressions of the inter planar distances are

given by

$$\frac{1}{d_{hkl}^2} = \frac{h^2 + k^2 + l^2}{a^2}$$

for cubic systems (i.e. Pd),

$$\frac{1}{d_{hkl}^2} = \frac{h^2 + k^2}{a^2} + \frac{l^2}{c^2}$$

for tetragonal systems (i.e. PdO), and

$$\frac{1}{d_{hkl}^2} = \frac{4}{3}\frac{h^2 + hk + k^2}{a^2}\frac{l^2}{c^2}$$

for hexagonal systems (i.e. Al_2O_3).
While Bragg's law is useful for basic calculation of lattice spacings or diffraction angles, no statements on the intensity or intensity distribution of the diffraction signal at non-integer values of n can be made. In the following sections, this issue will be solved by treating diffraction in the more detailed picture of X-rays as electromagnetic waves interacting with electrons.

X-ray Scattering

In the broadest terms, X-rays may be scattered elastically or inelastically by electrons. The scattering processes can be separated in three phenomena: Compton scattering (inelastic), Thomson scattering (elastic) and Rayleigh scattering (elastic). Compton scattering is most prevalent in the energy range between 10 keV 500 keV and describes scattering processes of electromagnetic waves with electrons where energy is transferred to the electron without ionizing it. As Compton scattering is an incoherent scattering process and the scattered intensity only varies slowly with scattering angle, Compton scattering manifests as a smooth background in the X-ray diffraction data presented in this thesis and will be implicitly treated as such. In the following section, the kinematic approximation is applied to simplify the interaction between X-rays and matter. Within this approximation, X-rays only interact with the matter once, eliminating the need to consider multiple scattering events. This approach is only valid because the interaction between X-rays and matter is weak and thus multiple scattering events are rare. Further, more detailed description of X-ray scattering and related techniques may be found in [101–103] which were used as the base for this section.
The differential cross section $\frac{d\sigma}{d\Omega} = \frac{I_{sc}}{\psi_0 \Delta\Omega}$ defined as the ratio of scattered intensity with the incoming flux at an angle $\Delta\Omega$ is the quantity measured in an

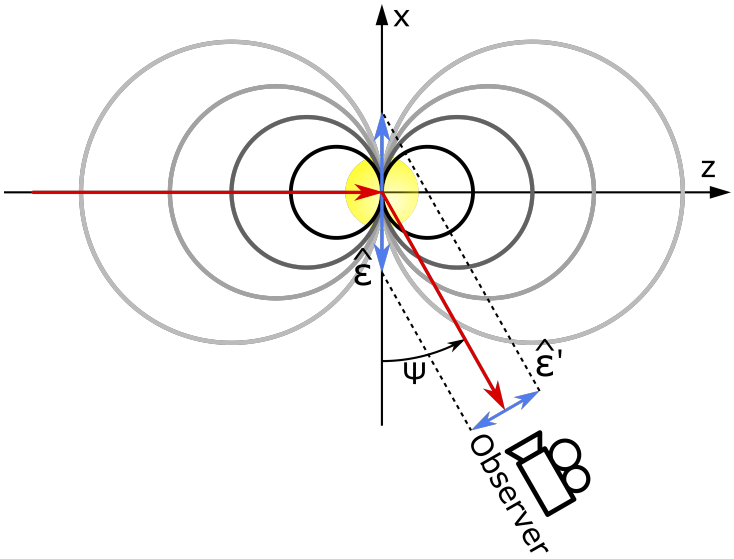

Figure 2.22: Scheme of Thomson scattering at a free electron. The beam paths are indicated by red arrows, the directions of the incidence and scattered polarization vectors in blue. The circles indicate show the shape of the scattered wavefront with different amplitudes.

elastic scattering event. In the specific case of scattering of a electromagnetic monochromatic plane wave

$$\mathbf{E}(\mathbf{r},t) \;=\; \hat{\varepsilon} E_0 e^{i(\mathbf{k}\cdot\mathbf{r}-\omega t)},$$

where $\mathbf{E}$ is the electric field, $\mathbf{r}$ the position vector, t time, $\hat{\varepsilon}$ the polarization unit vector, E_0 the the amplitude, $\mathbf{k}$ the wave vector and ω the wave frequency, this relationship can be expressed as

$$\frac{d\sigma}{d\Omega} \;=\; \frac{|\mathbf{E}_{rad}|^2 R^2}{|\mathbf{E}_{in}|^2}.$$

Here, R is the distance between scatterer and detector and $|\mathbf{E}_{rad}|^2$ and $|\mathbf{E}_{in}|^2$ are the squared modulus of the electric field vectors of the scattered and incoming electromagnetic wave, respectively. This is true, since $|\mathbf{E}_i|^2 \propto I_i$. In the simplest case, called Thomson scattering, the scatterer is a single, free electron. In the classical description the incoming electromagnetic wave will force the electron to vibrate which in turn will emit a spherical wave. Now the the acceleration amplitude of the electron can be evaluated for an observer in the plane of the polarization angle of the electric field vector. As illustrated in Figure 2.22, for a coordinate system with the incoming beam direction along z, the electric field vector along x and the observer in the

xz-plane at an angle Ψ relative to the electric field vector, the acceleration $\mathbf{a}_x = \frac{e}{m}\mathbf{E}_{in}$ becomes zero for $\Psi = 0$ and is at a maximum at $\Psi = 90$. Thus, the radiated field is given by

$$\mathbf{E}_{rad}(\mathbf{R}, t) \propto \frac{-e}{R}\mathbf{a}_x(t')\sin(\Psi),$$

where t is the observation time of the scattering event and $t' = \mathbf{R}/c$ the time of the scattering event. This relation is rearranged to

$$\frac{\mathbf{E}_{rad}(\mathbf{R}, t)}{E_{in}} \propto \frac{e^2}{m}\frac{e^{i\mathbf{k}R}}{R}\sin(\Psi)$$

using the temporal component of Equation 2.3.3. With the acceleration generalized for arbitrary observer positions as $\hat{\varepsilon}' \cdot \hat{\varepsilon} = -\sin(\Psi)$ where $\hat{\varepsilon}'$ is the polarization unit vector of the radiated wave and the factor

$$r_0 = \frac{e^2}{4\pi\epsilon_0 mc^2},$$

the classical electron radius or Thomson scattering length, emerging from equating the units in Equation 2.3.3. Combining Equation 2.3.3 and Equation 2.3.3, the Thomson cross-section for a free electron is found

$$\frac{d\sigma}{d\Omega} = r_0^2|\hat{\varepsilon} \cdot \hat{\varepsilon}'|^2.$$

In terms of X-ray diffraction experiments, maximizing the scattered amplitude is advantageous, as signal from poor scatterers can be captured and measurement times can be optimized. Hence, for an X-ray scattering experiment, the scattering plane should be chosen so that the $|\hat{\varepsilon} \cdot \hat{\varepsilon}'|^2 = 1$ which is achieved by aligning the normal of the scattering plane with the electric field vector of the incoming beam. In Figure 2.22, this is true for a plane with its normal vector aligned with the x-axis. For an unpolarized beam, the Thomson cross section becomes the average of the ideal scattering plane ($|\hat{\varepsilon} \cdot \hat{\varepsilon}'|^2 = 1$) and the plane perpendicular to that (image plane Figure 2.22, $|\hat{\varepsilon} \cdot \hat{\varepsilon}'|^2 = \cos^2(\Psi)$), yielding $\frac{1+\cos^2(\Psi)}{2}$.

Scattering from a Single Atom

In the next step, instead of scattering from a single electron, scattering from an atom with an electron density $\rho(\mathbf{r})$ is considered. When scattering from two points with a distance $\mathbf{r}$, a phase change $\Delta\phi = (\mathbf{k}' - \mathbf{k}) \cdot \mathbf{r}$ is introduced

between incidence ($\mathbf{k}$) and exit beam ($\mathbf{k}'$). From this the scattering vector is defined as

$$Q \;=\; \mathbf{k}' \,-\mathbf{k},$$

with $|\mathbf{k}| \;=\; |\mathbf{k}'|$ for elastic scattering. Integrating over all possible scattering events within $\rho(\mathbf{r})$ the total scattering length (or total scattered amplitude) becomes

$$-\,r_0 \int \rho(\mathbf{r}) e^{i\mathbf{Q}\mathbf{r}} d\mathbf{r} \;=\; -\,r_0 f^0(\mathbf{Q}).$$

The scattering behavior of an atom is thus fully captured within $f^0(\mathbf{Q})$, which is next examined for its marginal behavior. With $\mathbf{Q} \;\rightarrow\; 0$, the total scattering length becomes the ordinal number Z (= number of electrons) and for $\mathbf{Q} \;\rightarrow$ inf, the scattered fields are fully out of phase und hence, the total scattering length is 0. Up until now, the electrons of the atom were treated as free electrons within $\rho(\mathbf{r})$. Hence, the model of scattering from an atom is expanded by the dispersion corrections:

$$f(\mathbf{Q}, \omega) \;=\; f^0(\mathbf{Q}) \;+\; f'(\omega) \;+\; if"(\omega)$$

The additional terms $f'(\omega)$ and $if"(\omega)$ are found by the description of electrons as forced, charged oscillators. The terms arise due to the interaction of X-rays with bound instead of free electrons and the thus altered response of the electrons to the incoming field. Thus, both amplitude (real part) and phase (imaginary part) of the atomic form factor are corrected by the f' and $f"$, respectively.

Scattering from a Crystal

A more precise description of diffraction from a crystal than Bragg's law (Equation 2.3.3) is found by describing a crystal as a lattice with the unit cell being the repeating unit of the lattice. Within the unit cell, a number of atoms are distributed, each scattering with Equation 2.3.3. Due to the distance $\mathbf{r}_j$ from the origin of the unit cell, a phase shift is introduced making the sum of all scattered intensity from a unit cell

$$F^{UC}(\mathbf{Q}) \;=\; \sum_j f_j(\mathbf{Q}) e^{i\mathbf{Q}\,\cdot\,\mathbf{r}_j}.$$

The position of all unit cells, scattering with $F^{UC}(\mathbf{Q})$, are given by

$$R_n \;=\; n_1 a_1 \;+\; n_2 a_2 \;+\; n_3 a_3.$$

Hence, the product of the phase shift introduced by this translation of the unit cell together with the unit cell form factor describes the full crystal's scattered amplitude:

$$F^{crystal}(\mathbf{Q}) \;=\; \sum_j f_j(\mathbf{Q}) e^{i\mathbf{Q}\cdot\mathbf{r}_j} \;\cdot\; \sum_n e^{i\mathbf{Q}\cdot\mathbf{R}_n} \;=\; F^{UC} \sum_n e^{i\mathbf{Q}\cdot\mathbf{R}_n}.$$

When the structure factor in Equation 2.3.3 is evaluated explicitly for a lattice, the selection rules for that lattice emerge. The atomic positions in a unit cell of the space group Fm-3m are $(0,0,0)$, $(0,\frac{1}{2},\frac{1}{2})$, $(\frac{1}{2},0,\frac{1}{2})$, and $(\frac{1}{2},\frac{1}{2},0)$, for the example of Pd or Pt. This yields the selection rules

$$F_{hkl}^{Fm-3m} \;=\; \begin{cases} 4F^{UC} & \text{for } h,k,l \text{ all even or all odd} \\ 2F^{UC} & \text{for all other cases} \end{cases}$$

These rules also apply to YSZ, CeO_2 since they belong to the same space group. The only difference is that a different number of Wyckoff positions (the allowed positions for a symmetry group) are filled by the respective elements of the materials. Following the same logic as for the space group *Fm-3m*, for αAl_2O_3 (space group *R-3c*), the selection rules

$$\begin{cases} -h + k\; l \;=\; 3n & \text{for } |h| + |k| \neq 0 \\ l \;=\; 6n & \text{for } h \;=\; k \;=\; 0 \end{cases}$$

are found and for PdO ($P4_2/mmc$)

$$\begin{cases} \text{any } h,\, k,\, l & \text{for } |h| + |k| \neq 0 \\ l \;=\; 2n & \text{for } h \;=\; k \;=\; 0 \end{cases}$$

are found. In contrast to the space group *Fm-3m*, for the latter two space groups *R-3c* and *P4₂/mmc*, no general statement about the magnitude of the structure factor for a particular set of h, k, l. Instead the magnitude must be calculated for individual reflexes.

The Laue Condition

Since the number of unit cells is infinite ($n \;\rightarrow\; \text{inf}$) for a perfect crystal, the solution to Equation 2.3.3 can be separated in two cases. The first case being constructive interference, which occurs if the phase shift is $N \times 2\pi$ with N being an integer. In the second case, which encompasses all other possible phase shifts, $\sum_n e^{i\mathbf{Q}\cdot\mathbf{R}_n}$ becomes of the order of unity. Hence, the structure factor is extremely small compared to the first case. A more

illustrative explanation is that this phase shift adds up over the length of the infinite crystal which causes (even for very small phase shifts) destructive interference.
With knowledge of the condition for constructive interference, the reciprocal lattice can defined as

$$\mathbf{G} = h\mathbf{a}_1^* + k\mathbf{a}_2^* + k\mathbf{a}_3^*,$$

which must fulfill

$$\mathbf{a}_i \cdot \mathbf{a}_j^* = 2\pi \cdot N\,\delta_{ij}.$$

Here, δ_{ij} is the Kronecker delta, $\mathbf{a}_i$ and $\mathbf{a}_j^*$ are the real space and reciprocal space lattice vector, and h, k, and l are integers. This lattice is called the reciprocal lattice and its lattice parameters and vectors are commonly indicated by *. Upon evaluation of the condition for constructive interference with Equation 2.3.3 it becomes apparent that $\mathbf{G} \cdot \mathbf{R}_n$ also fulfills this condition. With this, the Laue condition is found, which is given by

$$\mathbf{Q} = \mathbf{G},$$

equating the diffraction geometry, i.e. the incidence and diffracted beam ($\mathbf{Q}$), with the reciprocal lattice ($\mathbf{G}$). Hence, for constructive interference and with it large solutions for Equation 2.3.3, G and Q must be aligned.

Ewald Construction

A great visualization of the Laue condition and useful tool for X-ray diffraction experiments is the Ewald construction. An illustration of an Ewald construction in two dimensions for a square lattice is given in Figure 2.23. The incidence beam's wavevector $\vec{k_i}$ with the magnitude $\frac{2\pi}{\lambda}$ with the wavelength λ is drawn towards the origin of the reciprocal lattice $(0,0)$, defining the size of the Ewald circle. In this example, the experiment geometry was chosen, so that the circumference of the Ewald circle intersects with a second node of reciprocal space. This means that the Laue condition is fulfilled and the two nodes intersecting with the circle are connected by $\mathbf{G} = \mathbf{Q}$. Hence, the direction of the diffracted beam is given by $\mathbf{k_f}$, connecting the center of the Ewald circle with the second node. When the sample is rotated around its surface normal, the reciprocal lattice is rotated around (0,0), which is equivalent to rotating the Ewald circle around the same position. This is visualized by the dotted circle in Figure 2.23 and allows access to all nodes in reciprocal space that lie within the yellow colored area.

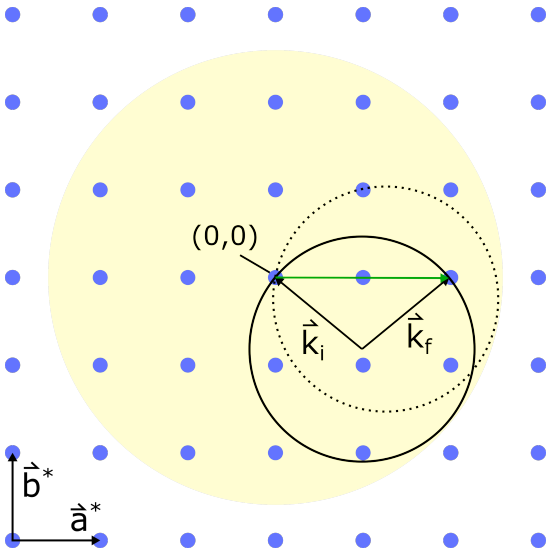

Figure 2.23: Ewald construction for a square reciprocal lattice. The solid, black line is the Ewald circle, the dotted line visualizes the sample rotation necessary to reach a second reflex. The yellow colored area visualizes the accessible part of reciprocal space by sample rotation.

Grazing Incidence Geometry

Up until now, diffraction experiments were discussed in an abstract without explicitly considering experimental configurations. However, for the investigation of thin films or nanoparticles, it is crucial to limit the information depth so that scattering intensity from the support is suppressed and intensity from the surface is enhanced. This is in the so-called grazing incidence geometry, which is visualized in Figure 2.24. Here, the sample is held at a constant incidence angle α relative to the surface normal $\vec{n}$ and the detector is positioned at the extension of k_i. By rotation of the sample around $\vec{n}$ and moving the detector, a vast section of reciprocal space is accessible. However, a small part of reciprocal space located around the specular rod ($h = k = 0$

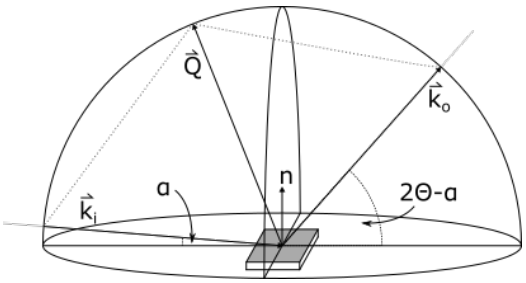

Figure 2.24: Scheme of the grazing incidence geometry in specular configuration.

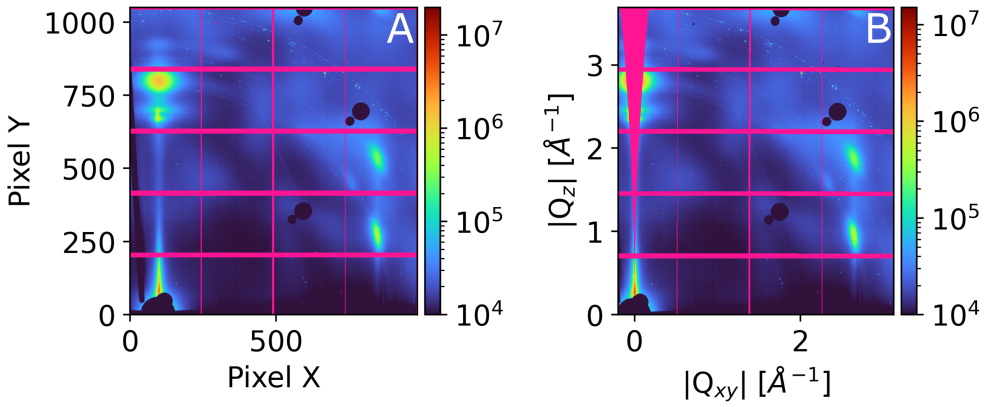

Figure 2.25: Data of epitaxial (1 1 1) oriented PdPt nanoparticles supported by a CeO_2(0 0 1)/YSZ(0 0 1) thin film. **A**: Raw 2D detector image. **B** Data of **A**, transformed into reciprocal space with the missing wedge at $Q_{xy} = 0$. All pixels with no assigned values are pink. This corresponds to panel borders in **A** and to pannel borders and missing wedge in **B**

or (0 0) rod) is not reachable because of geometrical limitations of the geometry. This is an important detail, especially for high-energy X-ray diffraction experiments utilizing 2D detectors, since the recorded detector image seem to contain diffraction signal at that location (Figure 2.25 **A**). However, upon converting from the laboratory frame into reciprocal space (Figure 2.25 **B**) a wedge appears at $Q_{xy} = 0$, called the missing wedge. The surface sensitivity of this experiment geometry is apparent upon inspection of Figure 2.19. If α is chosen just above the critical angle, the incident beam generates an evanescent-like field inside the material that decays rapidly with depth, resulting in a shallow penetration depth. Consequently, scatterers closer to the surface contribute significantly more to the total diffraction signal than the bulk support. Despite this, in many cases such as the data presented within this thesis, the bulk support still scatters significantly stronger than the nanoparticles. For this reason, the Bragg peak positions of the bulk support were covered by beamstops, allowing utilization of weaker absorbers (= higher photon flux) in the experiment (black circles in Figure 2.25).

The exceptional surface sensitivity in the grazing incidence geometry requires precise alignment of the sample surface which poses a crucial challenge in operando measurements, as presented in Chapter 2 or Chapter 4. This sensitivity is due to two factors. Firstly, the incidence angle α needs to maintained. As apparent in Figure 2.19 **C** ii, small changes in the inci-

dence angle lead to a significant decrease of the intensity of the evanescent wave. Secondly, the sample height relative to the beam position needs to maintained. The large footprint, due to the small incidence angle requires a small, vertical beam size. This is especially vital for the high energy X-ray experiments, since larger X-ray energies require a smaller incidence angle. In order to minimize time spent with alignment of the sample, in the experiments in Chapter 2 or Chapter 4, the sample height was calibrated at the beamline prior to the operando investigations (see Figure A.2). During the operando experiment, whenever the sample temperature was increased, the height was adjusted according to the calibration, followed by rapid cycles of data acquisition and height alignment. Furthermore, the incidence angle was optimized every third to fifth cycle. This approach was realized in a fully automatic manner which minimized the scan range necessary for the height and incidence angle alignment and maximized the accuracy of alignment.

Surface Characterization with CTRs

The high surface sensitivity and low penetration depth of the grazing incidence geometry poses the question whether the assumptions made for the derivation of Equation 2.3.3 are still valid. For this purpose, the scattering intensity of a semi-infinite system of infinite dimensions along x and y is evaluated along z. If $A(\mathbf{Q})$ is the scattered intensity of a single layer, the expression

$$F^{CTR} = A(\mathbf{Q}) \sum_{j}^{\infty} e^{iQ_z a_z} e^{-\beta j} = \frac{A(\mathbf{Q})}{1 - e^{iQ_z a_z} e^{-\beta}}$$

is found with the help of the series identity $\sum_0^{j=\inf} x^j = \frac{1}{1-x}$. Note that the scattering amplitude is only summed over "half of the infinite crystal" or from 0 to ∞. The second term of the exponent product accounts for absorption with $\beta = \frac{a_z \mu}{\sin(\alpha)}$ with μ being the absorption coefficient and α being the incidence angle. In Figure 2.26 **A**, the diffraction intensity due to the termination of the crystal at its surface and the effect of absorption is shown. This diffraction intensity $I^{CTR} = |F^{CTR}|^2$ which is shown in Figure 2.26 is called crystal truncation rod (CTR). A limitation of the expression for the CTR signal is revealed when expressing the scattered intensity as a function of the Miller index l and neglecting absorption:

$$I^{CTR} = \frac{|A(\mathbf{Q})|^2}{4sin^2(\pi l)}.$$

Notably, the function diverges for integer l. This shows that the expression for the intensity from the surface of a film is only valid away from the Bragg

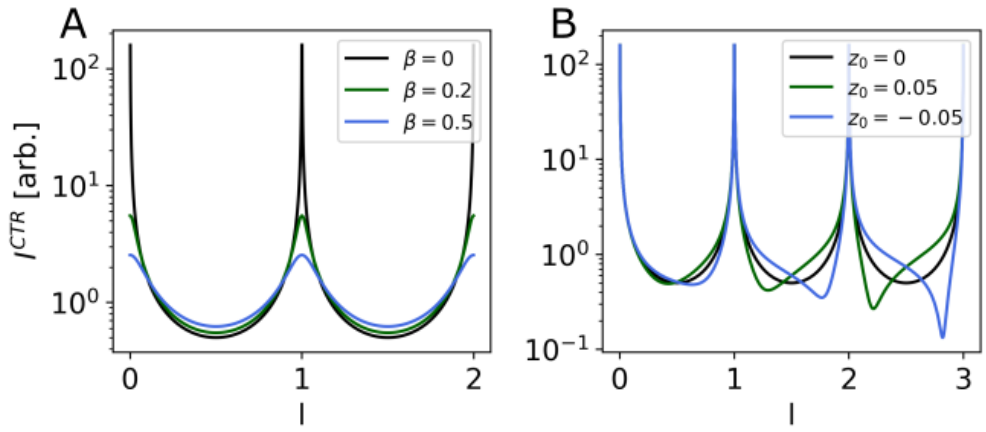

Figure 2.26: Visualization of the effect of roughness (**A**) and strain (**B**) on the CTR signal.

peak. In practice, this is reflected by masking measured intensity in the vicinity of Bragg peaks before fitting surface models to the measured intensity.
A second important phenomenon at surfaces, is the relaxation of the surface lattice planes or changes in the position of atoms near the surface compared to their bulk position. By adding a shifted layer to the expression in Equation 2.3.3, neglecting absorption, and reformulating as a function of the Miller index l,

$$F^{CTR'} = F^{CTR} + F^{top} = \frac{A(\mathbf{Q})}{1 - e^{i2\pi l}} + A(\mathbf{Q})e^{-i2\pi(1+z_0)l}$$

is obtained. Here, z_0 is the deviation of the top layer from the original position. Due to the shift in the top lattice plane, strong changes in the intensity of the diffracted signal between two Bragg peaks is observed (Figure 2.26 **B**). A positive deviation yields increased intensity just below the Bragg peak and decreased intensity just above the Bragg peak. For a negative deviation of the position of the top layer the opposite behavior is observed.

Diffraction from Nanoparticles and Thin Films

Up until now, diffraction was only discussed for infinite and semi-infinite crystals. However, nanoparticles do not fit the description of infinite or semi-infinite systems which means that the sum in Equation 2.3.3 must be evaluated for a finite number of unit cells n. If this is done along a single direction z, the structure factor for a nanoparticle simplifies to a geometric

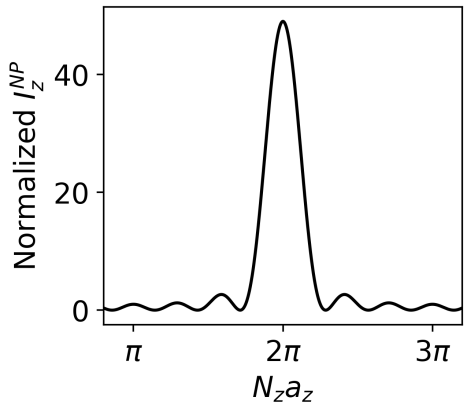

Figure 2.27: Peak broadening Equation 2.3.3 due to finite nanoparticle size. For this example, $a_z = 1$ and $N = 7$ were chosen.

series

$$F_z^{\mathrm{NP}} = \sum_{n_z=1}^{N_z} f_{n_z} e^{iQ_z a_z \cdot n_z} = \frac{1 - e^{iQ_z a_z \cdot N_z}}{1 - e^{iQ_z a_z}}.$$

From this the diffracted intensity of a nanoparticle becomes

$$I_z^{NP} = |F_z^{NP}|^2 = \frac{\sin^2(\frac{Q_z a_z \cdot N_z}{2})}{\frac{Q_z a_z}{2}}$$

which describes the peak broadening observed from a finite crystal and is often referred to as the Laue function. In Figure 2.27, the shape of Equation 2.3.3 is shown for $a_z = 1$ and $N = 7$. The graph exemplifies the similarities to slit diffraction experiment and reveals that significant diffraction intensity is only observed in the direct vicinity of $Q_z a_z N_x = 2\pi n$, with n being an integer. Since in reality N_z is significantly higher, the difference between the principle maximum of and side maxima of Equation 2.3.3 will be orders of magnitude larger. Furthermore, averaging over a number of nanoparticles with only a very small deviation in N or a immediately leads to destructive interference of the side maxima and the intensity between the principle maxima can be assumed to be zero. From the argument of the sine in Equation 2.3.3, the generalized expression for the peak width

$$N_i a_i = D_i = \frac{2\pi}{\Delta Q_i} \tag{2.1}$$

for any direction (x, y, z) is deduced. In practice, Equation 2.1 was used to determine the nanoparticle or domain size in for example Figure 2.3. However, the diffracted intensity that is observed for a nanoparticle Bragg peak

was always approximated by a Pseudo-Voigt function with a linear background instead of a slit diffraction function. This is necessary to account for the fact that in (HE)GIXRD experiments on nanoparticle ensembles a large number of nanoparticles contribute to the intensity at a single Bragg peak position. Hence, peak broadening occurs due to the finite size distribution of the nanoparticles. Crucially, the size distribution observed in XRD is weighted by N^2 (see Equation 2.3.3) which means that the diffracted intensity from a single nanoparticle is proportional to the square of the number of lattice planes along the evaluated direction. It is important to note, that Equation 2.1 only remains true as long as the instrument broadening is smaller than the peak broadening due to the domain size. This is especially relevant for thin films, where the domain size in the plane of the film may be significantly larger than along the surface normal.
For well defined, defect free nanoparticle ensembles and defect free thin films with atomically smooth surfaces, the oscillations of the Laue function (Equation 2.3.3) can no longer be assumed to be zero, giving rise to Laue oscillations. These fringes occur due to the interference of X-rays scattered at the planes of the material and are an indication for the crystallinity of the material (see Figure 1.6 **A**).

2.3.4 Grazing Incidence Small Angle Scattering

In the previous sections, X-ray scattering was treated in the context of crystalline materials. The description of scattering from an arbitrary material requires to sum over the interaction of the scattered wave of each pair n, m of scatterers. One application of this is small angle scattering (SAXS). The reader is referred to [101] for a general description of SAXS and the review article by Renaud *et al.* [105] .
For a material with only one type of molecule or atom (equivalent to the lattice basis in the description of XRD), for example a monoatomic particle

$$I(\mathbf{Q}) = f^2(\mathbf{Q}) \sum_n \sum_m e^{i\mathbf{Q}(\mathbf{r_n} - \mathbf{r_m})} = N f^2(\mathbf{Q}) + f^2(\mathbf{Q}) \sum_n \sum_{m \neq n} e^{i\mathbf{Q}(\mathbf{r_n} - \mathbf{r_m})}$$

is found. On the right side of the equation, the sum over all combinations $n = m$ are separated. By expressing this relation as a the deviation of

$\rho_n(\mathbf{r_{nm}})$ from the average electron density ρ_a the expression

$$I(\mathbf{Q}) = Nf^2(\mathbf{Q}) \tag{2.2}$$

$$+ f^2(\mathbf{Q}) \sum_n \int_V [\rho_n(\mathbf{r_{nm}}) - \rho_a] e^{i\mathbf{Q}(\mathbf{r_n} - \mathbf{r_m})} dV_m \tag{2.3}$$

$$+ f^2(\mathbf{Q}) \rho_a \int_V e^{i\mathbf{Q}(\mathbf{r_n} - \mathbf{r_m})} dV_m \tag{2.4}$$

follows. Here, $\mathbf{r_{nm}} dV_m$ is the number of scatterers at $\mathbf{r_m} - \mathbf{r_n}$. In Equation 2.4, the first term is uncorrelated scattering, the second term is sensitive to the local deviation of the average electron density ρ_a. The third term is dominant for small values of $\mathbf{Q}$ and the term for small angle scattering (SAXS). This term I_{SAXS} correlates the constant, average electron density ρ_a to the size and shape of the scatterer. From the SAXS intensity (third term of Equation 2.4) the particle structure factor is defined, so that the third term can be expressed as

$$I_{SAXS}(\mathbf{Q}) = \Delta\rho^2 V_p^2 |F(\mathbf{Q})|^2.$$

Here, $\Delta\rho$ is the electron density difference between scatterer and medium around the scatterer and V_p the scatterer volume. The particle form factor depends on the size, shape, and distance of the scatterer(s), which are the parameters that can be probed by SAXS.
For data analysis the scattered intensity is generally divided into the Porod regime with $QR \gg 1$ and the Guinier regime with $QR \ll 1$. Here, Q is the magnitude of the momentum transfer and R the particle radius. For an isolated sphere the structure factor is defined by

$$F(Q) = \frac{3J_1(QR)}{QR},$$

with J_1 being the first order Bessel function. By expansion of this term and together with Equation 2.3.4, the term

$$I(Q) \approx \Delta\rho^2 V_p^2 e^{-\frac{Q^2 R^2}{5}}$$

is found for the $QR \ll 1$ regime. By plotting the scattered intensity against Q^2, simple comparison of the slope of the scattered intensity near $Q = 0$ allows estimation of the radius R. This is illustrated for the scattered intensity of isolated spheres of two radii in Figure 2.28 (**A**). For $QR \gg 1$, the form factor for a sphere Equation 2.3.4 may be expanded and simplified to

$$I(Q) = \frac{2\pi\rho^2}{Q^4} S_p$$

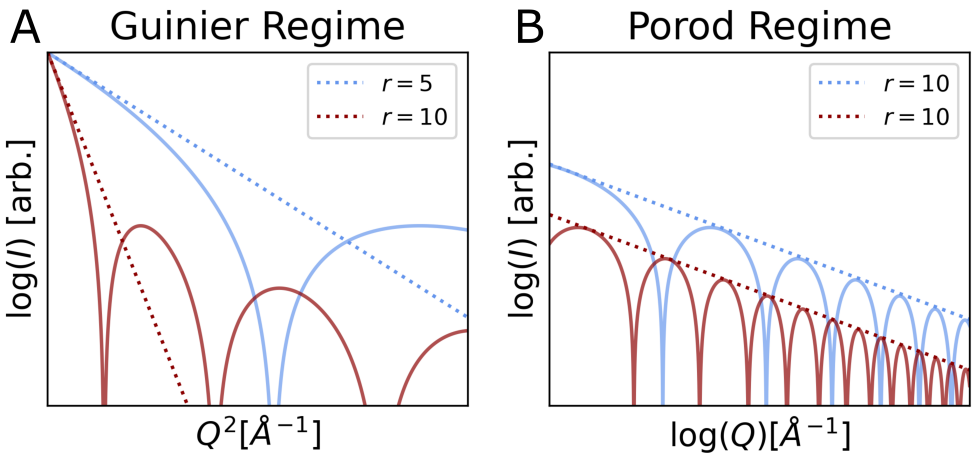

Figure 2.28: Simulations of the scattered intensity of spheres with two different radii together in the Guinier regime (**A**) and the Porod regime (B). The dotted lines are the simulated intensities including the approximations for the Guinier and Porod regimes.

with S_p being the spherical particle's surface. As for the Guinier regime, the scattered intensities of isolated spheres (solid lines) together with the simulated intensity for the Porod regime (dotted lines) is shown in Figure 2.28 **B**. Traditionally, SAXS experiments are performed in transmission geometry, which requires the particles to be suspended in a medium with significantly lower density (see Equation 2.4). In order to effectively apply the concept of SAXS to particles on a solid-state support grazing-incidence small angle X-ray scattering (GISAXS) is employed. Analogous to XRD in grazing incidence geometry (see Section 2.3.3), GISAXS exploits the interaction between X-rays and matter with incidence angles close to the critical angle to improve the surface sensitivity of the technique. However, the reflection geometry and fixed particle location and orientation lead to additional interactions and effects that need to be considered. Immediately apparent in the scheme of a (HE)GISAXS experiment (Figure 2.29) is that the resulting scattering pattern is structured and does not consist of concentric rings around the origin which is generally expected for SAXS experiments of NPs in suspension. This is a direct consequence of the fixed location of the reflection geometry and fixed spacial relationship between the particles. Due to the grazing incidence geometry, the incidence beam is both transmitted the through the sample (for simplicity refraction was neglected) giving rise to a high intensity feature at $q_x = Q_z = 0$. The second strong feature at $q_x = 0$ corresponds to

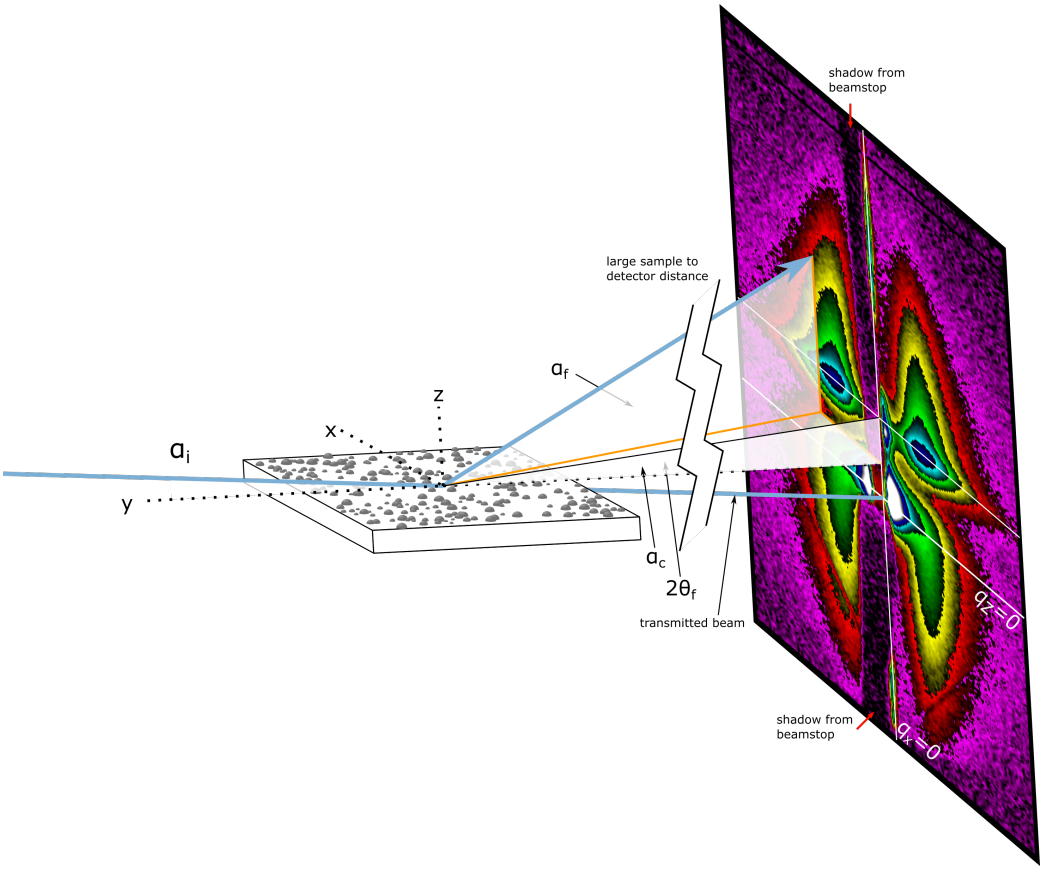

Figure 2.29: Experimental scheme of a (HE)GISAXS experiment. Here α_i is the incidence angle, α_c the critical angle, $2\theta_f$ the inplane scattering angle, and α_f the out-of-plane scattering angle. The beam path between sample is interrupted to signify the large sample to detector distance required for the small scattering angles, especially at high X-ray energies.

X-rays scattered at the critical angle. The upper, horizontal, white line in the detector image indicates the Yoneda band and stems from constructive interference of the scattered wave at the interface of the sample. At $q_x = 0$ and along q_z is the specular rod which stems from specular and diffuse scattering from the surface. Kiessig fringes may also be observed and arise from interference of rays reflected at different interfaces of the surface. Finally, at $q_x \neq Q_z \neq 0$, four features are observed that are caused by scattering from the particles on the samples surface, yielding the "butterfly shape", typical for well defined nanoparticle ensembles. The bottom two lobes are caused by X-rays scattered by particles and subsequently transmitted through the sample surface, while the top two lobes at $q_z > 0$ stem from X-rays scattered

by particles and reflected by the surface.
A common approach to gain access to the particle morphology, size, size distribution, and dispersion is the extraction of line scans along the horizontal and vertical direction of the GISAXS patterns. Crucial is the position of the horizontal line scan. Instead of extracting at the position of maximum intensity along q_z or the location of the Yoneda band, the horizontal line scan is extracted just above the Yoneda band. At this position resonant effects causing the enhanced intensity of the Yoneda band are omitted. In order to accurately describe the scattered intensity along the horizontal direction (q_x), a second term $S(Q)$ must be introduced to accurately account for interference of wavefields scattered by different particles:

$$I(q) = |F(Q)|^2 S(Q).$$

Generally, the interference term is challenging to model, especially for samples without ordered particle arrays. For this reason, interference functions are often deduced experimentally, for example by microscopy. For samples with a large difference in the horizontal dimension of the particles and distance between the particles, a good approximation for the distance between particles is $D = \frac{2\pi}{q_M}$, where q_M is the position of the first maximum in the horizontal cut of the GISAXS pattern. If the dimension of particles and distance between particles are similar, the contribution of the interference term and the scattering term contribute in the same q-range causing an overestimation of the particle distance. For the size determination of particles via GISAXS, a completely analogous approach to SAXS is employed. For isotropic particle shapes such as sphere or cylinders, the intensity from the form factor is described by Bessel functions. Hence, the particle diameter is found by $d = \frac{2qR}{q_m}$, where q_m is the position of the first minimum and qR is the position of the first minimum of the Bessel function corresponding to the selected particle shape. The same approach for the determination of the particle height is applicable, however, additional complications arise due to multiple scattering events. Hence, for a strict description of the scattered intensity along q_z, the distorted Born wave approximation is used. In this formalism, four interactions between X-rays and sample are considered: The scattering from a particle, the reflection from the surface and subsequent reflection from the sample surface, reflection from the surface an subsequent scattering from a particle, and reflection with subsequent scattering from a particle followed by reflection from the surface. Hence, transmission and reflection coefficients perturb the scattered intensity expected from the Born wave approximation, giving rise to for example the enhanced intensity at the Yoneda band. Despite this, the nanoparticle height may still be estimated by the same procedure as for the horizontal line cuts. Altogether, GISAXS

gives access to parameters that are generally hard to determine by XRD, which was used in conjunction with GISAXS in Chapter 4. The technique captures the full particle dimensions, independent of crystallinity or defects bridging the gap between reciprocal space analysis like XRD and real-space techniques such as SEM.

2.3.5 X-ray Photoelectron Spectroscopy

The chemical composition of the CeO_2 films (Chapter 1) was analyzed using X-ray photoelectron spectroscopy (XPS). The technique relies on the measurement of the kinetic energy of electrons ejected from the sample by irradiation X-rays. Since XPS was used as a complementary technique the following section will outline the theoretical background and methodology relevant to the presented data. A detailed description of the technique and the full scope of its capabilities is found in [77] and the application for thin film analysis in [106], which served as the basis for this section.

Generation and Properties of Photoelectrons in XPS

Central to XPS as a characterization technique is the photoelectric effect, the process of a photon with sufficient energy ejecting an electron from the irradiated material. With knowledge of the X-ray energy and measurement of the kinetic energy of the ejected electron (E^s_{kin}), the binding energy of the electron (E_b) is

$$E_b = h\nu - E^s_{kin},$$

where $h\nu$ is the photon energy with h being the Planck constant and ν being the frequency. In a spectrometer with a solid state sample, the ejected electrons also need to overcome the sample work function ϕ^s_w (see Figure 2.30). If the sample is conducting and grounded to the spectrometer the Fermi energies of spectrometer and sample align and the work function becomes independent of the sample and becomes an instrument specific constant ϕ_w (see Figure 2.30). With this, the binding energy, relative to the Fermi energy E_F becomes

$$E^F_b = h\nu - E_{kin} - \phi_w,$$

which means that the electron binding energy is easily calculated with knowledge of the spectrometer work function and X-ray energy.
Each core level and its corresponding peak in an XPS spectrum is denoted by its principle quantum number n = 1, 2, 3, ... and the shape of the orbital (s, p, d). The number and energy of the core levels are characteristic to the electronic configuration and environment of the atom. Generally, s-type core

levels give rise to a single peak, while all other orbitals give rise to two peaks (spin-orbit splitting). This is observed due to spin-orbit coupling expressed by the total angular momentum $j = l \pm s$. It describes the interaction of the electron spin $s = \frac{1}{2}$ and the orbital angular momentum $l = 0, 1, 2, ...$ for s, p, d, orbitals. Since $j > 0$, the total angular momentum becomes

$$\begin{aligned} j &= \frac{1}{2} \\ j &= \frac{3}{2}, \frac{5}{2} \\ j &= \frac{5}{2}, \frac{7}{2} \end{aligned}$$

for the s, p, and d core levels, respectively. Accordingly, the respective core levels are split into two components (i.e. $3p \rightarrow 3p_{5/2}, 3p_{3/2}$) with two binding energies. The energy difference between the spin-orbit split peaks depends on the the strength of the interaction and the intensity ratio of the two component is given by the number of electrons $2l + 1$ occupying the respective states. In case of larger atoms, especially for lanthanoids like Ce, an additional splitting effect occurs. This effect relies on more complex interactions, for example interaction with unpaired electrons in outer shells, inter and intra atomic electron interactions, and charge transfers [77, 107]. The number of multiplets and the energy shift relative to the original core level strongly depends on the interaction and is characteristic to the element and its oxidation state.
In addition to the number of observed multiplets, the oxidation state also has a strong influence on the position of the peak (with some exceptions such as Ce(0) and Cu(I)). Similarly, the chemical environment in covalently bonded atoms also influences the peak position. In general, a the higher oxidation state corresponds to a higher the binding energy (Ce(IV) $>$ Ce(III) or for carbon C=O $>$ C−H). In addition to the core level peaks, several other features may be observed in an XPS spectrum: Shake-up or shake-down peaks which originate from energy loss or gain of photoelectrons by interaction with outer shell electrons, inelastic scattering which is the main source for the background in XPS, and Auger electrons that are produced in the same way as explained in Section 2.1.2, except for the initial ionization occurring by irradiation with X-rays

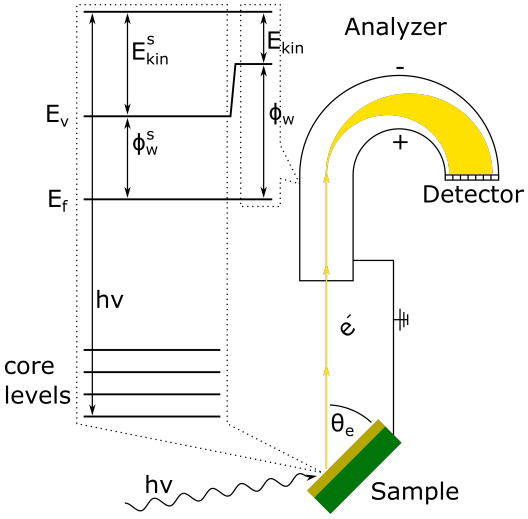

Figure 2.30: Scheme of an XPS measurement in grazing emission. The energy diagram shows the equalization of the sample/spectrometer Fermi level, work functions, and kinetic energies for sample and spectrometer reference.

Measurement Principle

In order to record an XPS spectrum, the kinetic energy is scanned and the amount of electrons for a specific kinetic energy are counted. Scanning of the kinetic energy is achieved by varying the retardation field which reduces the photoelectrons kinetic energy to the so-called pass energy E_p. Following retardation, the analyzer further discriminates the photon electron energy (see Figure 2.30). The electrons are forced onto a circular path by a homogeneous, radial electric field which is produced by the hemispherical electrodes. As indicated by the diverging electron path (yellow) and colored panels of the detector in Figure 2.30, an angular spread is introduced due to varying kinetic energy of the electrons when entering the analyzer.
The elaborate detection system employed in XPS requires great control over the X-ray energy as well. In lab sources, the X-rays are commonly produced by X-ray tubes as explained in Section 2.3.1. However, instead of traditional optics, diffraction from a quartz crystal is often used to gain more precise control over the X-ray energy. Furthermore, for insulating or poorly conducting samples such as the CeO_2 thin films in Chapter 1, electron flood guns are used to compensate for charging and to ensure alignment of the Fermi energies of spectrometer and sample Figure 2.30.

XPS Core Level Analysis

For the quantitative analysis of XPS core level spectra, the data is usually fitted using Shirley background and a peak model. In an ideal XPS experiment, the line shape of the core level peaks should be Lorentzian caused by the lifetime broadening $\frac{h}{\tau}$. However, there is a number of experimen-

tal factors such as a certain energy distribution of the X-ray beam, a finite divergence, and sample induced effects causing peak broadening. For this purpose, Pseudo-Voigt profiles defined by

$$f(x, A, \mu, \sigma, \alpha, s, c) = \frac{(1 - \alpha)A}{\sigma_g\sqrt{2\pi}} e^{-(x-\mu)^2 / 2\sigma_g^2} + \frac{\alpha A}{\pi}\left[\frac{\sigma}{(x - \mu)^2 + \sigma^2}\right] \tag{2.5}$$

are commonly used for symmetric peaks. Here, the full-width at half maximum is given by $2\sigma = FWHM$, where $\sigma_g = \frac{\sigma}{\sqrt{2\ln 2}}$, μ is the position, and α the fraction of the Gaussian and Lorentzian contribution ($\alpha = 0$ for full Gaussian peak shape). The amplitude A or intensity of the peak depends on several instrument factors, but also the atomic sensitivity factor. For comparison of intensities and the determination of species fractions from XPS, the peak areas are normalized by multiplication with the sensitivity factor. A final crucial information necessary for the interpretation of XPS spectra is the information depth of the experiment. This value is determined by the electron inelastic mean free path which is itself depending on the electrons kinetic energy and the emission angle Θ_e of the electrons (see Figure 2.30). Hence, with increasing binding energy, the electron inelastic mean free path decreases. The loss of intensity I as a function of distance x traveled in matter is described by Lambert-Beer's law

$$\frac{I(x)}{I_0} = e^{\frac{-x}{\lambda\cos(\theta)}},$$

where I_0 is the initial intensity, λ the electron inelastic mean free path, and θ the emission angle. This law was exploited in Chapter 1 to determine the thickness of the water layer that terminated the CeO_2 thin film. Detailed description of the calculations are given in Chapter B and the Python script that was used to determine the thicknesses is given in Chapter A.

2.4 Microscopy

The following sections describe the fundamental sample probe interactions of scanning electron microscopy and atomic force microscopy. These techniques were primarily used to obtain complementary, local information of the catalyst morphology before and after operando catalysis experiments. In addition, atomic force microscopy was used for surface characterization of the thin films in Chapter 1.

2.4.1 Scanning Electron Microscopy

Scanning electron microscopy is an imaging technique exploiting a variety of interactions between the probe electrons and the sample. Within the scope of this work, SEM was used as an imaging technique to investigate the size, shape, and distribution of catalyst nanoparticles and the morphology of the catalyst support. A detailed description of the technique and imaging methods is found in [108] which forms the basis of this section.
In a scanning electron microscope, electrons are produced by a cathode and accelerated by an anode to energies between a few keV up to 50 keV. Subsequently, electron optics such as slits, lenses, and condensers are used to shape the electron beam in size, divergence, and intensity. The electron beam with a probe diameter which can be as small as < 1 nm, is scanned over the sample surface by two pairs of scan coils for the x and y direction. At the sample, a large number of interactions between sample and electrons occur that allow for a large variety of analysis and imaging techniques. In Figure 2.31, a scheme of the interactions is shown. The primary electron beam hits the target and electrons penetrate the surface up to a depth of R, depending on energy, sample, and incidence angle giving rise to several contrast modes. Back scattered electrons are electrons that leave the interaction volume after multiple scattering events and are used for imaging with Z-contrast. For chemical contrast, Auger electrons (see Section 2.1.2) can be used, which are produced by either the direct beam or back scattered electrons. This technique is commonly referred to as Scanning Auger Electron Microscopy and usually requires a dedicated experimental apparatus. Another technique providing chemical contrast is energy dispersive X-ray Spectroscopy (EDX) which relies the emittance of X-rays. These are produced by ionization and subsequent recombination of the hole with an electron from a higher shell. Finally, secondary electrons (SEs) are produced by ejecting electrons from the outer shell of atoms through inelastic scattering with the primary beam. Due to the low energy (< 50 eV), imaging with secondary electrons is highly surface sensitive with an information depth of only a few nanometers. For this reason, secondary electrons are the highest resolution contrasting signal for SEM, reaching a resolution of 1 nm for the measurements in this work [109]. The imaging contrast of SEM in SE mode relies on multiple effects. The primary effects are surface tilt, shadowing, diffusion contrast, and mass thickness contrast. At tilted surfaces, the secondary electron yield is enhanced as a function of the slope of the surface. This is the main contrast which is modified additional effects. Due to the location of the detector relative to the surface normal, a shadowing effect occurs which makes "the backside" of a feature appear with lower contrast

than "the front". In the case of the SEM data in this thesis, the data was recorded using a through-lens detector, which is located behind the last lens of the optics focusing the primary electrons. Hence, this effect is only applicable for the measurements conducted at 45 ° in (Figure 2.4). Diffusion contrast describes the effect of back scattered electrons exiting the sample near a topographical feature of the surface and subsequently producing SE by inelastically scattering at the topological feature and producing SE. This effect enhances the effect of enhanced intensity at the edges of nanoparticles. Finally, mass thickness contrast describes the change in intensity due to the thickness of surface features. In the context of nanoparticles supported by metal oxides, this manifests in increased contrast for nanoparticles with a large height compared to flat nanoparticles.

In practice, imaging of metal nanoparticles on oxide supports is a challenging endeavor, due to charging of the support itself and the charging of nanoparticles, which produce a localized mirror charge at the interface to the support. Al_2O_3 is a classic insulator [110] while CeO_2 (3.0 eV[111]) and YSZ (4.23 eV [112]) are wide-bandgap semiconductors which are both prone to charging. Charging induced by the primary beam dissipates poorly due to the low electronic conductivity which causes a build up in surface po-

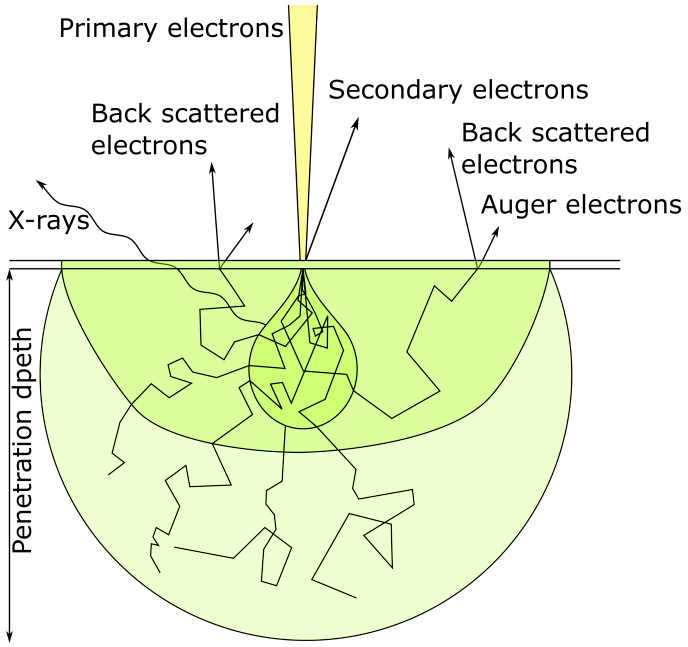

Figure 2.31: Scheme of the penetration depth of primary electrons and information depth of back scattered electrons, Auger electrons, Secondary electrons, and X-rays. Image adapted from [108].

tential. As a result, electron trajectories are perturbed and stable imaging conditions are challenging to attain. In order to mitigate these effects, samples were clamped onto a grounded sample holder using conducting clamps. High-resolution measurements were conducted close to these clamps to allow for efficient charge dissipation via the surface of the support rather than through the bulk. For SEM measurements conducted after light-off experiments, parts of the samples were additionally covered with a C film and glued to the sample holder using conductive tape to further counteract charging.
Throughout this work, SE mode SEM was used as a complementary technique for the determination of nanoparticle diameters before and after light-off experiment. Determining the nanoparticle diameters by SEM gave a direct confirmation of the approximation of the domain size determined by HEGIXRD as a nanoparticle size. The high resolution and correlation of features observed in SEM delivered additional information to the operando HEGIXRD results that allowed for a more detailed interpretation and understanding of the HEGIXRD results.
In the case of the data in Chapter 2 and Chapter 4 this was achieved using Gwyddion [113] and the built in Gaussian blur and thresholding functionality. Due to the more complex analysis routine required for nanoparticles in the holes of $CeO_2(0\,0\,1)$ thin film discussed in Chapter 3, a semi-automatic analysis script was developed (see Chapter D) which contains extended thresholding functionality and improvements that facilitated the analysis work flow.

2.4.2 Atomic Force Microscopy

Atomic force microscopy was used as an ex-situ technique to gain insight into the surface morphology of the investigated catalysts and catalyst supports. While several operation modes, techniques can be realized with an AFM instrument to probe a wide range of material properties on a nanometer scale, within the scope of this work it was exclusively used in tapping mode for the investigation of surface roughness, morphology, and nanoparticle size. Additional, more detailed information on AFM and its many applications are found in [108, 114–116], used as reference for the following section.
A simplified scheme of the working principle of AFM in tapping mode is shown in Figure 2.32 **A** and consists of five main components: the cantilever, a laser and photo diode, a piezo scanner and a feedback-loop. In tapping mode, the cantilever is being oscillated with a large amplitude in the range of 20 nm to 100 nm at or near its resonance frequency. Due to the forces resulting from the interaction between sample and tip of the cantilever, the amplitude of the oscillation is perturbed. The oscillation of the cantilever is measured by reflecting a laser from the backside of the cantilever and

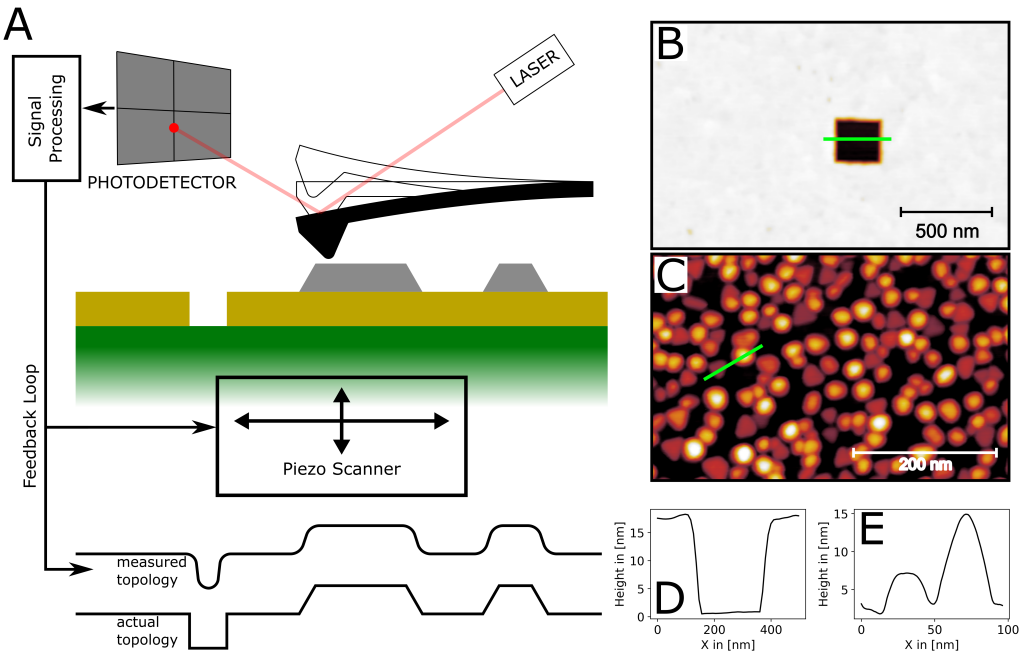

Figure 2.32: **A**: Scheme of an AFM measurement. **B**: AFM measurement of Pd nanoparticles on Al_2O_3. **C**: AFM measurement of CeO_2 on YSZ. **D**: Horizontal line scan through the hole in **B**. **E**: Line scan through two particles of **C**. Positions of the line scans in **D** and **E** are indicated by green lines in **B** and **C**.

following the intensity changes using a four-panel diode. The feedback loop is then used to adjust the vertical position of the piezo z stage to maintain a constant amplitude. Thereby, the topology of the investigated surface is recorded.
Since the lateral size of small nanoparticles is of the order of the tip radius of 8 nm [117] and deconvolution of tip and measured topology is challenging, AFM was used to determine the support roughness and topology (Figure 2.32 **B**, **D**, Chapter 1), and nanoparticle height (Figure 2.32 **B**, **C** Chapter 2, Chapter 4). With the diameters determined from SEM, the full shape of the nanoparticles could be captured from microscopy and compared to the results from HEGIXRD.

Bibliography of the Preamble

(1) Song, H. et al. *Methane Activation and Utilization in the Petrochemical and Biofuel Industries*; Springer International Publishing AG: Cham, Switzerland, 2022.

(2) Stocker, T.; Qin, D. *Climate change 2013 The Physical Science Basis*; IPCC: 2013.

(3) R., P.; Skea, S. J. *Climate Change 2022: Mitigation of Climate Change*; IPCC: 2022.

(4) Aakko-Saksa, P. et al. Reduction in greenhouse gas and other emissions from ship engines: Current trends and future options. *Progress in Energy and Combustion Science* **2023**, *94*, 101055.

(5) Szablowski, L.; Wojcik, M.; Dybinski, O. Review of steam methane reforming as a method of hydrogen production. *Energy* **2025**, *316*, 134540.

(6) Hwang, I. et al. Biological conversion of methane to chemicals and fuels: technical challenges and issues. *Applied microbiology and biotechnology* **2018**, *102*, 3071–3080.

(7) European Commission Commission Regulation (EU) 2024/1787 of 26 June 2024, `https://eur-lex.europa.eu/legal-content/EN/TXT/?uri=OJ:L_202401787`, Official Journal of the European Union, L 2024/1787, 26 June 2024, 2024.

(8) Climate & Clean Air Coalition Secretariat Global Methane Pledge, `https://www.globalmethanepledge.org/`, [Online; accessed 12-June-2025], 2025.

(9) Yang, Z. et al. Enrichment of low concentration methane: an overview of ventilation air methane. *J. Mater. Chem. A* **2022**, *10*, 6397–6413.

(10) Lott, P.; Casapu, M.; Grunwaldt, J.-D.; Deutschmann, O. A review on exhaust gas after-treatment of lean-burn natural gas engines – From fundamentals to application. *Appl. Catal. B: Environ.* **2024**, *340*, 123241.

(11) He, L.; Fan, Y.; Bellettre, J.; Yue, J.; Luo, L. A review on catalytic methane combustion at low temperatures: Catalysts, mechanisms, reaction conditions and reactor designs. *Renew. Sustain. Energy Rev.* **2020**, *119*, 109589.

(12) Trinchero, A.; Hellman, A.; Grönbeck, H. Methane oxidation over Pd and Pt studied by DFT and kinetic modeling. *Surf. Sci.* **2013**, *616*, 206–213.

(13) Datye A. K., Bravo J., Nelson T. R., Atanasova P., Lyubovsky M., Pfefferle L. Catalyst microstructure and methane oxidation reactivity during the Pd $\longleftrightarrow$ PdO transformation on alumina supports. *Appl. Catal. A Gen.* **2000**, *198*, 179–196.

(14) Chin, Y.-H.; García-Diéguez, M.; Iglesia, E. Dynamics and Thermodynamics of Pd-PdO Phase Transitions: Effects of Pd Cluster Size and Kinetic Implications for Catalytic Methane Combustion. *J. Phys. Chem. C* **2016**, *120*, 1446–1460.

(15) Velin, P. et al. Palladium dispersion effects on wet methane oxidation kinetics. *Catal. Sci. Technol.* **2020**, *10*, 5460–5469.

(16) Colussi, S.; Fornasiero, P.; Trovarelli, A. Structure-activity relationship in Pd/CeO2 methane oxidation catalysts. *Chin. J. Catal.* **2020**, *41*, 938–950.

(17) Murata, K.; Ohyama, J.; Yamamoto, Y.; Arai, S.; Satsuma, A. Methane Combustion over Pd/Al_2O_3 Catalysts in the Presence of Water: Effects of Pd Particle Size and Alumina Crystalline Phase. *ACS Catal.* **2020**, *10*, 8149–8156.

(18) Maurer, F. et al. Surface Noble Metal Concentration on Ceria as a Key Descriptor for Efficient Catalytic CO Oxidation. *ACS Catal.* **2022**, *12*, 2473–2486.

(19) Abbasi, R.; Huang, G.; Istratescu, G. M.; Wu, L.; Hayes, R. E. Methane oxidation over Pt, Pt:Pd, and Pd based catalysts: Effects of pre-treatment. *The Canadian Journal of Chemical Engineering* **2015**, *93*, 1474–1482.

(20) Farrauto, R.J. and Lampert, J.K. and Hobson, M.C. and Waterman, E.M. Thermal decomposition and reformation of PdO catalysts; support effects. *Appl. Catal. B: Environ.* **1995**, *6*, 263–270.

(21) Stotz, H. et al. Surface reaction kinetics of methane oxidation over PdO. *J. Catal.* **2019**, *370*, 152–175.

(22) Jiang, D. and Khivantsev, K. and Yong W. Low-Temperature Methane Oxidation for Efficient Emission Control in Natural Gas Vehicles: Pd and Beyond. *ACS Catal.* **2020**, *10*, 14304–14314.

(23) Jang, E. J.; Lee, J.; Oh, D. G.; Kwak, J. H. CH 4 Oxidation Activity in Pd and Pt–Pd Bimetallic Catalysts: Correlation with Surface PdO x Quantified from the DRIFTS Study. *ACS Catal.* **2021**, *11*, 5894–5905.

(24) Wu, Y. et al. Phase transformation and oxygen vacancies in Pd/ZrO_2 for complete CH_4 oxidation under lean conditions. *J. Catal.* **2019**, *377*, 565–576.

(25) Hellman, A. et al. The Active Phase of Palladium during Methane Oxidation. *Phys. Chem. Lett.* **2012**, 678–682.

(26) Nilsson, J. et al. Chemistry of Supported Palladium Nanoparticles during Methane Oxidation. *ACS Catal.* **2015**, *5*, 2481–2489.

(27) Yue, S. et al. Redox dynamics and surface structures of an active palladium catalyst during methane oxidation. *Nat. Commun.* **2024**, *15*, 4678.

(28) Carstens, J. N.; Su, C. S.; Bell, A. T. Factors Affecting the Catalytic Activity of Pd/ZrO_2 for the Combustion of Methane. *J. Catal.* **1998**, *176*, 136–142.

(29) Weng, X.; Ren, H.; Chen, M.; Wan, H. Effect of Surface Oxygen on the Activation of Methane on Palladium and Platinum Surfaces. *ACS Catal.* **2014**, *4*, 2598–2604.

(30) Nie, H.; Howe, J. Y.; Lachkov, P. T.; Chin, Y.-H. C. Chemical and Structural Dynamics of Nanostructures in Bimetallic Pt−Pd Catalysts, Their Inhomogeneity, and Their Roles in Methane Oxidation. *ACS Catal.* **2019**, *9*, 5445–5461.

(31) Dolling, D. S. et al. Probing Active Sites on Pd/Pt Alloy Nanoparticles by CO Adsorption. *ACS Nano* **2024**, *18*, 31098–31108.

(32) Murata, K. et al. Exploiting Metal-Support Interactions to Tune the Redox Properties of Supported Pd Catalysts for Methane Combustion. *ACS Catal.* **2020**, *10*, 1381–1387.

(33) Tabakova, T. et al. Effect of Support on Complete Hydrocarbon Oxidation over Pd-Based Catalysts. *Catalysts* **2025**, *15*, 110.

(34) Promhuad, P. et al. Effect of Metal Oxides (CeO_2, ZnO, TiO_2, and Al_2O_3) as the Support for Silver-Supported Catalysts on the Catalytic Oxidation of Diesel Particulate Matter. *ACS Omega* **2024**, *9*, 19282–19294.

(35) Montini, T.; Melchionna, M.; Monai, M.; Fornasiero, P. Fundamentals and Catalytic Applications of CeO2-Based Materials. *Chem. Rev.* **2016**, *116*, 5987–6041.

(36) Mi, R.; Li, D.; Hu, Z.; Yang, R. T. Morphology Effects of CeO_2 Nanomaterials on the Catalytic Combustion of Toluene: A Combined Kinetics and Diffuse Reflectance Infrared Fourier Transform Spectroscopy Study. *ACS Catal.* **2021**, *11*, 7876–7889.

(37) Guo, Y. et al. CeO_2 Facet-Dependent Surface Reactive Intermediates and Activity during Ketonization of Propionic Acid. *ACS Catal.* **2022**, *12*, 2998–3012.

(38) Spezzati, G. et al. CO Oxidation by Pd Supported on CeO_2(100) and CeO_2(111) Facets. *Appl. Catal. B Environ.* **2019**, *243*, 36–46.

(39) Gänzler, A. M. et al. Unravelling the Different Reaction Pathways for Low Temperature CO Oxidation on Pt/CeO_2 and Pt/Al_2O_3 by Spatially Resolved Structure-Activity Correlations. *J. Phys. Chem. Lett.* **2019**, *10*, 7698–7705.

(40) Ciuparu, D.; Pfefferle, L. Contributions of lattice oxygen to the overall oxygen balance during methane combustion over PdO-based catalysts. *Catal. Today* **2002**, *77*, 167–179.

(41) Chen, Y.; Lin, J.; Chen, X.; Fan, S.; Zheng, Y. Engineering multicomponent metal-oxide units for efficient methane combustion over palladium-based catalysts. *Catal. Sci. Technol.* **2021**, *11*, 152–161.

(42) Xiong, H. et al. Engineering catalyst supports to stabilize PdO_x two-dimensional rafts for water-tolerant methane oxidation. *Nat. Catal.* **2021**, *4*, 830–839.

(43) Wang, C.-M.; Thevuthasan, S.; Peden, C. H. F. Interface Structure of an Epitaxial Cubic Ceria Film on Cubic Zirconia. *J. Am. Ceram. Soc.* **2003**, *86*, 363–365.

(44) Barth, C. et al. A Perfectly Stoichiometric and Flat CeO_2(111) Surface on a Bulk-Like Ceria Film. *Scientific reports* **2016**, *6*, 21165.

(45) Wu, F. et al. Growth and Structure of Epitaxial CeO_2 Films on Yttria-Stabilized ZrO_2. *Thin Solid Films* **2008**, *516*, 4908–4914.

(46) Schober, J.-C. et al. Atomically Smooth Fully Hydroxylated CeO_2(0 0 1) Films on YSZ(0 0 1). *J. Phys. Chem. C* **2024**, *128*, 19795–19806.

(47) Chen, S.; Xiong, F.; Huang, W. Surface Chemistry and Catalysis of Oxide Model Catalysts from Single Crystals to Nanocrystals. *Surf. Sci. Rep.* **2019**, *74*, 100471.

(48) Karlsruhe Institute of Technology (KIT) TrackAct - CRC 1441, `https://www.trackact.kit.edu/`, [Online; accessed 02-July-2025], 2025.

(49) Kasper, N.; Nolte, P.; Stierle, A. Stability of Surface and Bulk Oxides on Pd(1 1 1) Revisited by in Situ X-ray Diffraction. *J. Phys. Chem. C* **2012**, *116*, 21459–21464.

(50) Lott, P.; Dolcet, P.; Casapu, M.; Grunwaldt, J.-D.; Deutschmann, O. The Effect of Prereduction on the Performance of Pd/Al_2O_3 and Pd/CeO_2 Catalysts during Methane Oxidation. *Ind. Eng. Chem. Res.* **2019**, *58*, 12561–12570.

(51) Mao, X.; Foucher, A.; Stach, E. A.; Gorte, R. J. A Study of Support Effects for CH_4 and CO Oxidation over Pd Catalysts on ALD-Modified Al_2O_3. *Catal. Lett.* **2019**, *149*, 905–915.

(52) Ishizawa, N.; Miyata, T.; Minato, I.; Marumko, F.; Iwai, S. A Structural Investigation of α-Al_2O_3 at 2170 K. *Acta Cryst. B* **1980**, *36*, 228–230.

(53) Chen, J.; Sharapa, D.; Plessow, P. N. Stability and formation of hydroxylated $\alpha-$Al2O3(0001) surfaces at high temperatures. *Phys. Rev. Res.* **2022**, *4*, DOI: `10.1103/PhysRevResearch.4.013232`.

(54) Hejral, U. et al. Composition-Dependent Alloy Nanoparticle Shape Changes under Reaction Conditions: Kinetic and Thermodynamic Effects. *J. Phys. Chem. C* **2024**, *128*, 4330–4342.

(55) Huang, F. et al. Pd or PdO: Catalytic active site of methane oxidation operated close to stoichiometric air-to-fuel for natural gas vehicles. *Appl. Catal. B: Environ.* **2017**, *219*, 73–81.

(56) Bozo, C.; Guilhaume, N.; Herrmann, J.-M. Role of the Ceria–Zirconia Support in the Reactivity of Platinum and Palladium Catalysts for Methane Total Oxidation under Lean Conditions. *J. Catal.* **2001**, *203*, 393–406.

(57) Wolcyrz, M.; Kepinski, L. Rietveld Refinement of the Structure of CeOCl Formed in Pd/CeO_2 Catalyst: Notes of the Existence of a Stabilized Tetragonal Phase of La_2O_3 in La–Pd–O System. *J. Solid State Chem.* **1992**, *99*, 409–413.

(58) Putna, E. S.; Vohs, J. M.; J., G. R. Evidence for Weakly Bound oxygen on Ceria Films. *J. Phys. Chem. C* **1996**, *100*, 17862–17865.

(59) Perrichon, V. et al. Reduction of cerias with different textures by hydrogen and their reoxidation by oxygen. *J. Chem. Soc. Faraday Transs.* **1994**, *90*, 773–781.

(60) Yang, C. et al. Chemical activity of oxygen vacancies on ceria: a combined experimental and theoretical study on CeO_2(1 1 1). *Phys. Chem. Chem. Phys.* **2014**, *16*, 24165–24168.

(61) Xiao, W.; Guo, Q.; Wang, E. G. Transformation of CeO_2(1 1 1) to Ce_2O_3(0 0 0 1) films. *Chem. Phys. Lett.* **2003**, *368*, 527–531.

(62) Yan, H.; Zhang, N.; Wang, D. Highly efficient CeO2-supported noble-metal catalysts: From single atoms to nanoclusters. *Chem. Catal.* **2022**, *2*, 1594–1623.

(63) Maurer, F. et al. Tracking the formation, fate and consequence for catalytic activity of Pt single sites on CeO_2. *Nat. Catal.* **2020**, *3*, 824–833.

(64) Botu, V.; Ramprasad, R.; Mhadeshwar, A. B. Ceria in an oxygen environment: Surface phase equilibria and its descriptors. *Surf. Sci.* **2014**, *619*, 49–58.

(65) Jacob, K. T.; Muraleedharan, S. Phase equilibria in the system Ce–Pd–O. *Calphad* **2019**, *66*, 101640.

(66) Götsch, T. et al. Formation of Pd-Ce intermetallic compounds by reductive metal-support interaction. *J. Solid State Chem.* **2018**, *265*, 176–183.

(67) Okamoto, H.; Schlesinger, M. E.; Mueller, E. M. *Alloy Phase Diagrams: ASM Handbook*, 2016; Vol. 3.

(68) Owen, E. A.; Yates, E. L. Precision Measurements of Crystal Parameters. *Philos. Mag.* **1933**, *15*, 472–488.

(69) Edwards, J. W.; Speiser, R.; Johnston, H. L. High Temperature Structure and Thermal Expansion of Some Metals as Determined by X-Ray Diffraction Data. I. Platinum, Tantalum, Niobium, and Molybdenum. *J. Appl. Phys.* **1951**, *22*, 424–428.

(70) Lee, Y.; Stender, P.; Eich, S. M.; Schmitz, G. Probing the Miscibility Gap of the Pt–Pd Binary System by Atom Probe Tomography. *Microsc. Microanal.* **2022**, *28*, 1385–1395.

(71) Westerström, R. et al. Lack of surface oxide layers and facile bulk oxide formation on Pd(1 1 0). *Phys. Rev. B* **2009**, *80*, 1000.

(72) Mehar, V. et al. Formation of Epitaxial PdO(1 0 0) During the Oxidation of Pd(1 0 0). *J. Phys. Chem. Lett.* **2023**, *14*, 8493–8499.

(73) Vlad, A. et al. Oxygen interaction with the Pd(112) surface: From chemisorption to bulk oxide formation. *Phys. Rev. B* **2012**, *86*, 1–9.

(74) Westerström, R. et al. Oxidation of Pd(5 5 3): From ultrahigh vacuum to atmospheric pressure. *Phys. Rev. B* **2007**, *76*, 1–9.

(75) Todorova, M. et al. The Pd(1 0 1)-(5×5)R27°-O surface oxide revisited. *Surf. Sci.* **2003**, *541*, 101–112.

(76) Mehar, V. et al. Understanding the Intrinsic Surface Reactivity of Single-Layer and Multilayer PdO(1 0 1) on Pd(1 0 0). *ACS Catal.* **2018**, *8*, 8553–8567.

(77) Vickerman, J. C.; Gilmore, I. S. *Surface analysis: The principal techniques*, 2nd ed.; Wiley: Chichester U.K., 2009.

(78) Cao, G. *Nanostructures & nanomaterials: Synthesis, Properties & Applications*; Imperial College Press: London, 2004.

(79) Nolte, P. In situ Oxidation Study of Supported Rh and Pd Nanoparticles, Dissertation, Stuttgart: Institue for Theoretical and Applied Physics University of Stuttgart, 2009.

(80) Baeumer, M.; Freund, H.-J. Metal deposits on well-ordered oxide films. *Prog. Quantum Electron.* **2006**, *30*, 155–296.

(81) King, D.; Woodruff, D. *The chemical physics of solid surfaces: Growth and properties of ultrathin epitaxial layers*; Elsevier: Amsterdam, 1997; Vol. 8.

(82) Lüth, H. *Solid Surfaces, Interfaces and Thin Films*; Springer Berlin Heidelberg: Berlin, Heidelberg, 2010.

(83) Schlögl, R. Heterogeneous catalysis. *Angew. Chem. Int. Ed.* **2015**, *54*, 3465–3520.

(84) Müller, P.; Kern, R. Equilibrium nano-shape changes induced by epitaxial stress (generalised Wulf-Kaishew theorem). *Surf. Sci.* **2000**, *457*, 229–253.

(85) Henry, C. R. Morphology of supported nanoparticles. *Prog. Surf. Sci.* **2005**, *80*, 92–116.

(86) Burton, W. K.; Cabrera, N.; Frank, F. C. The growth of crystals and the equilibrium structure of their surfaces. *Philos. Trans. R. Soc. Lond. A* **1951**, *243*, 299–358.

(87) Nolte, P. et al. Reversible shape changes of Pd nanoparticles on MgO(1 0 0). *Nano Lett.* **2011**, *11*, 4697–4700.

(88) Chung, S. et al. Epitaxy and Shape Heterogeneity of a Nanoparticle Ensemble during Redox Cycles. *ACS nano* **2021**, *15*, DOI: 10.1021/acsnano.1c03002.

(89) Ertl, G. *Handbook of heterogeneous catalysis*, 2nd ed.; Wiley-VCH: Chichester, 2008.

(90) van Santen, R. A. *Mechanisms in heterogeneous catalysis*; World Scientific: New Jersey, 2024; Vol. vol. 22.

(91) Kiani, D.; Wachs, I. E. Practical Considerations for Understanding Surface Reaction Mechanisms Involved in Heterogeneous Catalysis. *ACS Catal.* **2024**, *14*, 16770–16784.

(92) van den Bossche, M.; Grönbeck, H. Methane Oxidation over PdO(1 0 1) Revealed by First-Principles Kinetic Modeling. *J. Am. Chem. Soc.* **2015**, *137*, 12035–12044.

(93) Hejral, U.; Müller, P.; Balmes, O.; Pontoni, D.; Stierle, A. Tracking the shape-dependent sintering of platinum-rhodium model catalysts under operando conditions. *Nat. Commun.* **2016**, *7*, 10964.

(94) Liu, L.; Corma, A. Metal Catalysts for Heterogeneous Catalysis: From Single Atoms to Nanoclusters and Nanoparticles. *Chem. Rev.* **2018**, *118*, 4981–5079.

(95) Mouaddib, N.; Feumi-Jantou, C.; Garbowski, E.; Primet, M. Catalytic oxidation of methane over palladium supported on alumina: Influence of the oxygen-to-methane ratio. *Appl. Catal. A Gen.* **1992**, *87*, 129–144.

(96) Popa, C. et al. Structure of palladium nanoparticles under oxidative conditions. *Phys. Chem. Chem. Phys.* **2015**, *17*, 2268–2273.

(97) Kasper, N. et al. In situ oxidation study of MgO(100) supported Pd nanoparticles. *Surf. Sci.* **2006**, *600*, 2860–2867.

(98) Nolte, P. et al. Combinatorial high-energy x-ray microbeam study of the size-dependent oxidation of Pd nanoparticles on MgO(100). *Phys. Rev. B* **2008**, *77*, DOI: 10.1103/PhysRevB.77.115444.

(99) Downard, K. *Mass spectrometry*; Royal Society of Chemistry: Cambridge, England, 2019.

(100) Heitz, N. Simulation der Strömung und Verweilzeitverteilung in einer In-situ-Reaktionszelle, Ph.D. Thesis, Technische Universität Hamburg-Harburg, 2015.

(101) Als-Nielsen, J.; McMorrow, D. *Elements of Modern X-ray Physics*, 2nd ed.; Wiley: 2011.

(102) Guinier, A. *X-Ray Diffraction: In Crystals, Imperfect Crystals and Amorphous Bodies*; W. H. Freeman and Company: 1963.

(103) Warren, B. E. *X-ray Diffraction*; Dover Publications: New York, 1990.

(104) Parratt, L. G. Surface Studies of Solids by Total Reflection of X-Rays. *Phys. Rev.* **1954**, *95*.

(105) Renaud, G.; Lazzari, R.; Leroy, F. Probing surface and interface morphology with Grazing Incidence Small Angle X-Ray Scattering. *Surf. Sci. Rep.* **2009**, *64*, 255–380.

(106) Greczynski, G.; Haasch, R. T.; Hellgren, N.; Lewin, E.; Hultman, L. X-ray photoelectron spectroscopy of thin films. *Nat. Rev. Methods Primers* **2023**, *3*, DOI: 10.1038/s43586-023-00225-y.

(107) Nelin, C. J. et al. Relationships between complex core level spectra and materials properties. *Int. J. Quantum Chem.* **2010**, *110*, 2752–2764.

(108) Reimer, L. *Scanning Electron Microscopy: Physics of Image Formation and Microanalysis*, 2nd ed.; Springer-Verlag: Heidelberg, 1998.

(109) Stierle, A.; Keller, T. F.; Noei, H.; Vonk, V.; Roehlsberger, R. DESY NanoLab. *J. Large-Scale Res. Facil.* **2016**, *2*, A76.

(110) Santos, R.; Longhinotti, E.; Freire, V. N.; Reimberg, R. B.; Caetano, E. Elucidating the high-k insulator $\alpha-Al_2O_3$ direct/indirect energy band gap type through density functional theory computations. *Chem. Phys. Lett.* **2015**, *637*, 172–176.

(111) Kusmierek, E. A CeO_2 Semiconductor as a Photocatalytic and Photoelectrocatalytic Material for the Remediation of Pollutants in Industrial Wastewater: A Review. *Catalysts*, *10*, 1435.

(112) PaiVerneker, V. R.; Petelin, A. N.; Crowne, F. J.; Nagle, D. C. Color-Center-Induced Band-Gap Shift in Yttria-Stabilized Zirconia. *Phys. Rev. B* **1989**, *40*, 8555–8557.

(113) Nečas, D.; Klapetek, P. Gwyddion: an open-source software for SPM data analysis. *Central European Journal of Physics* **2012**, *10*, 181–188.

(114) Meyer, E.; Bennewitz, R.; Hug, H. J. *Scanning Probe Microscopy*; Springer International Publishing: Cham, 2021.

(115) García, R. *Amplitude Modulation Atomic Force Microscopy*, 2nd ed.; Wiley-VCH: Weinheim, 2007.

(116) García, R.; Préz, R. Dynamic atomic force microscopy methods. *Surf. Sci. Rep.* **2002**, *47*, 197–301.

(117) Inc., B. N. Bruker AFM Probes - RTESPA-300 `https://www.brukerafmprobes.com/p-3907-rtespa-300.aspx` (accessed 05/13/2025).

Scientific Contributions

1. Atomically Smooth Fully Hydroxylated CeO_2(001) Films on YSZ(001)

Outline

Status of Publication

This chapter is based on the article
Schober, J.-C.; Beck, E.E.; Kao, M.C.; Kohantorabi, M.; Creutzburg, M.; Novikov, D.M.; Keller, T.F.; Holtermann, B.; Firman, N.; Caulfield, L.; Sauter, E.; Vonk, V.; Wöll C.; Wang, Y.; Noei, H.; Eggeler, Y.M.; Stierle, A. Atomically Smooth Fully Hydroxylated CeO_2(0 0 1) Films on YSZ(0 0 1). **Journal of Physical Chemistry C** *128 (46),* 19795–19806 (2024).

Author Contribution

I am responsible for sample preparation, experiment design and execution, and the complete data analysis except HR-TEM and GPA. The beamtime experiments were carried out collaboratively with Esko Erik Beck, Ming-Chao Kao, Marcus Creutzburg, and Dmitri V. Novikov. HR-STEM and GPA were conducted and analyzed by Birger Holtermann, Nadejda Firman, and Yolita M. Eggeler. XPS measurements were carried out by Mona Kohantorabi and Heshmat Noei. FT-IR experiments were conducted by Lachlan Caulfield, Eric Sauter, Christof Wöll, and Yuemin Wang.

Copyright Notice

1.1 Abstract

CeO_2 is an important support material with redox properties interesting for heterogeneous catalysis and energy conversion applications. Here, we present a facile growth procedure for epitaxial CeO_2(0 0 1) thin films supported by YSZ(0 0 1) suitable for combined catalytic activity and structural investigations. The growth of the CeO_2 thin films was performed using standard ultra-high-vacuum (UHV) preparation techniques followed by tube furnace annealing in air. Thorough characterization prior to and after the tube furnace annealing revealed that this step induces significant restructuring of the film. Complete characterization by atomic force microscopy (AFM), X-ray reflectivity (XRR), grazing incidence X-ray diffraction (GIXRD), cross-section high-resolution scanning tunneling electron microscopy (HR-STEM), X-ray photo-emission spectroscopy (XPS), and polarization-resolved infrared reflection absorption spectroscopy (IRRAS) showed that the film is fully oxidized and atomically smooth with a coherent crystal lattice over the full film thickness. A dislocation network at the CeO_2/YSZ interface compensates the lattice mismatch between film and the YSZ support, yielding a film with bulk lattice parameters. The bulk terminated surface is found to be defect free with negligible amount of adsorption sites and stabilized by the presence of hydroxyl groups for polarity compensation.
Keywords: ceria, dislocation network, catalysis, thin film, XRR, GIXRD, HR-STEM, XPS, AFM, IRRAS

1.2 Introduction

Ceria is a complex oxide material with rich structural, chemical and catalytic properties [118–121]. Central to many applications is the fast incorporation (release) of oxygen into (from) the lattice. This is possible due to the facile and reversible change in oxidation state from Ce(IV) to Ce(III) without significant changes to the crystal structure. Prominent examples for such applications are solid oxide fuel cells (SOFC), gas sensors, and the use of ceria in heterogeneous catalysis as support or catalyst [122–125]. A large number of reports on structure, chemistry and catalytic activity [118–121, 123–134] highlight the need for detailed structural and chemical control of CeO_2 model surfaces, which also permits a direct comparison with theoretical results.
Several studies in the last decades were directed towards understanding the growth and structure of CeO_2 thin films on various oxide and metal substrates [135–140]. However, most studies only focused on single aspects of the films such as interface structure, growth mechanisms or structural and compositional changes in oxidizing (reducing) environments. For structurally well defined ultrathin CeO_2 thin films, Ru or Pt are common supports [136, 137, 141–143], however, catalytically active support crystals are inconvenient for operando catalytic studies. Films grown on inert oxides such as MgO, Al_2O_3, Pr_2O_3 or YSZ (Y stabilized ZrO_2) are frequently manufactured by pulsed laser deposition (PLD), atomic layer deposition (ALD), or molecular beam epitaxy (MBE) with varying structural and chemical control [118, 138, 139, 144, 145]. High structural and chemical control over the CeO_2 thin film can be achieved e.g. by using $Pr_2O_3(0\,0\,0\,1)$ buffer layer between the CeO_2 thin film and a $Si(1\,1\,1)$ substrate. However, sample preparation involves hazardous materials and multiple growth steps with the need to remove and reintroduce the sample from and to UHV [146]. Reports on the interface structure between CeO_2 thin films and YSZ single crystal substrates showed that the lattice mismatch between the two materials is relieved by dislocations [118, 145], but no information on the surface structure or chemistry is provided. Theoretical studies and experiments on the surface of $CeO_2(1\,1\,1)$ showed the formation of surface and subsurface oxygen vacancies [147] which are crucial for the redox properties of CeO_2 and were linked to improved catalytic activity [148] and increased stabilization of adsorbed OH species [149, 150].
In other studies CeO_2 single crystals and their behavior upon reducing or oxidizing treatments were investigated [138, 151]. Some studies report the observation of well-defined vibrations of adsorbed CO on CeO_2 single crystal surfaces distinctly different for different surface orientations revealed the presence of rather homogeneous surfaces [152–155]. In other cases poor sur-

face quality was observed, as visualized in the scanning micrograph of a freshly polished $CeO_2(1\,1\,1)$ single crystal in Figure B.1. Furthermore, in other studies CeO_2 single crystals were reported to contain significant fluorine contaminations leading to an altered surface chemistry [156, 157].
Here, we present a facile, straight-forward growth procedure for fully oxidized $CeO_2(0\,0\,1)$ thin films with atomically smooth surfaces on YSZ(0 0 1). The resulting films were prepared using standard UHV techniques which can be easily reproduced. We thoroughly characterized the films' bulk and interface structure to the substrate using GIXRD, XRR, and HR-STEM. Further information on the surface structure of the films was obtained by AFM, and crystal truncation rod (CTR) analysis, while XPS and polarization-resolved IRRAS were employed in order to understand the chemical state of the film surface. This combination of complementary techniques draws a complete picture of the chemical, structural, and morphological features of the films' bulk and surface properties.

1.3 Methods

AFM data was recorded in air using tapping mode and oxide-sharpened silicon cantilevers with a nominal tip radius of 8 nm and a resonance frequency of 300 kHz [158]. For all measurements a scanning speed of 0.5 Hz was used. To consider potential sample tilts from mounting, a polynomial plane fit was applied.
CTR data was recorded at the P23 beamline of PETRA III at an X-ray energy of 16 keV using a 5 + 2 circle diffractometer under grazing incidence with a GaAs 2D LAMBDA pixel detector. Throughout the measurement the sample was under 100 $\frac{\text{mL}}{\text{min}}$ Ar flow at a constant pressure of 100 mbar. All XRR and GIXRD data, except for the CTR data, were recorded at the DESY Nanolab[158] 6-circle diffractometer using $Cu_{K\alpha}$ radiation, a parabolic multilayer optics for focussing, and a Lambda 750K detector.
The XPS measurements were conducted at DESY NanoLab [158] using a monochromatic AlK_α source ($h\nu = 1486.6$eV) and a Phoibos 150 hemispherical energy analyzer. A flood gun was used during the measurements at an energy 2.0 eV with 20μA emission for charge compensation. Ce 3d core level spectra were recorded using a pass energy of 30 eV and a step size of 0.1 eV, the survey scan from 0 eV to 1200 eV recorded at normal emission in Figure B.9 was performed with a pass energy of 50 eV and a step size of 0.5 eV.
The polarization-dependent IRRAS experiments were conducted with an UHV apparatus combining a state-of-the-art FTIR spectrometer and a mul-

tichambered UHV system. This dedicated apparatus was built in a way that the spectrometer can be attached to the experimental chamber and guides the IR light trough the UHV chamber. Additionally, it allows performing UHV preparation as well as IR experiments on samples without exposure to atmosphere.
The crystal was placed on a sample holder specifically designed for IRRAS measurements. After introduction of the crystal into UHV (10^{-10} mbar) the CO adsorption experiments were performed for the pristine and cleaned surface. The surface was cleaned at 550 °C, for 30 min, in the presence of oxygen (O_2, 1×10^{-4} mbar) to get the fully oxidized, cleaned surface. After cooling the sample to temperatures as low as 65 K, exposure to carbon monoxide (CO) was achieved using a leak-valve-based directional doser connected to a tube of 2 mm in diameter, which is terminated 30 mm from the sample surface and 50 cm from the hot-cathode ionization gauge. The polarization-resolved IRRAS spectra were recorded with both *s*- and *p*-polarized light at a fixed grazing incidence of 80 °. All IRRAS data shown here are difference spectra obtained by subtracting the reference. The IR spectra were acquired by recording 1024 scans with a resolution of 4 cm^{-1}. Exposures are given in units of Langmuir (L) (1 L = 1.33×10^{-6} mbar s).
For the preparation of the HR-STEM specimen, the sample was first coated with 30 nm amorphous carbon in a sputter coater and then a dual focussed ion beam instrument was used to cover the selected region of interest with an amorphous protective Pt cover before milling a TEM lamella.

1.4 Results & Discussion

For CeO_2 growth, the YSZ(0 0 1) substrate single crystals with a miscut of < 0.1 ° and 9 % Y_2O_3 were used. After introduction into UHV (base pressure $< 1 \times 10^{-10}$ mbar), the substrates were heated to 600 °C with a ramp of 15 °C/min using electron beam (e-beam) heating. After degassing at 600 °C for 30 min, the substrate was further annealed for 120 min at this temperature in 5×10^{-6} mbar oxygen (99.995 % purity) to ensure a fully oxidized surface. To confirm the cleaning procedure, the Auger electron spectroscopy (AES) data shown in Figure B.2 reveals only negligible signal of carbon contamination ($\sim$ 273 eV), but strong Y and O signal. After heating the sample to the deposition temperature of 400 °C, the CeO_2 films were grown by reactive deposition at a rate of $\sim$ 1.2 Å min^{-1}. Ce metal with a purity of 99.9 % was evaporated from a crucible using an e-beam evaporator in an oxygen background pressure of 5×10^{-6} mbar, supplied through an oxygen thermal cracker providing $\sim$ 10 % atomic oxygen. The atomic oxygen back pressure

was maintained until the sample reached room temperature. Due to severe charging of the sample after the deposition, AES and low energy electron diffraction characterization could not be performed to further investigate the film before removing from UHV. Further improvement of the films' structural properties was achieved by annealing them in air in a tube furnace. The annealing procedure consisted of a single annealing step at 1100 °C for 260 min (cooling/heating ramps of 1200 °C/h).

1.4.1 Surface morphology of the CeO_2 films

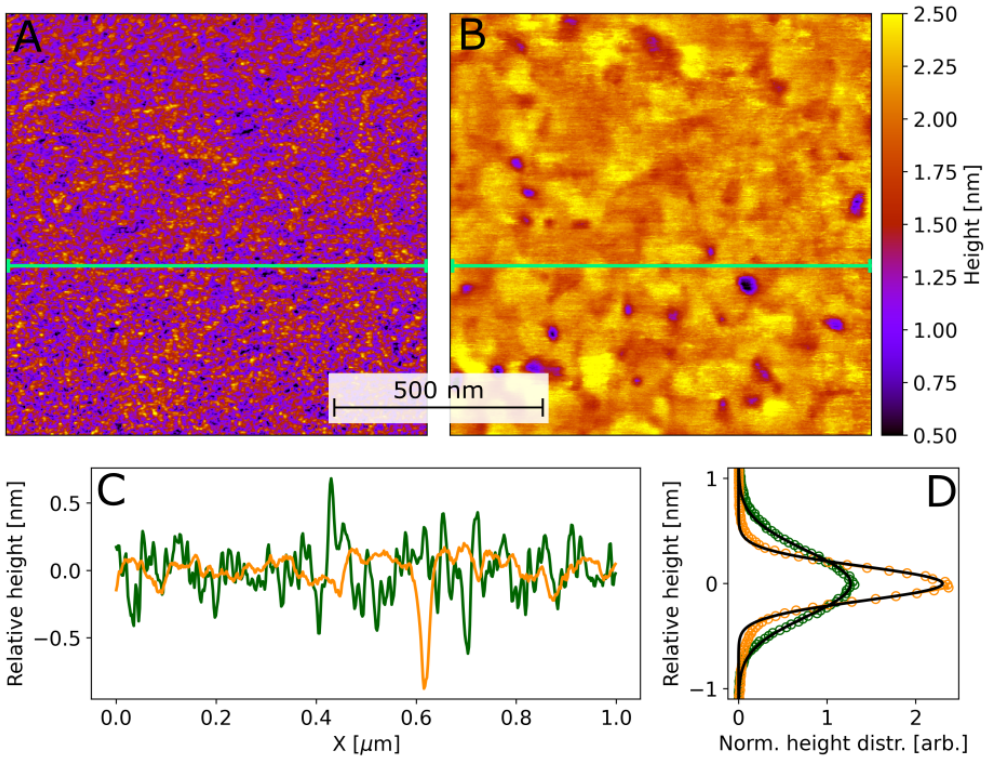

Figure 1.1: AFM images with identical height color map and lateral scale recorded before (**A**) and after (**B**) annealing in air for comparison. **C**: line scans (green: before tube furnace annealing in air, orange: after tube furnace annealing in air) indicated by the green, horizontal lines in A and B are shown. **D**: relative height as a function of the height distribution (green: before tube furnace annealing in air, orange: after tube furnace annealing in air). For both distributions the fitted Gaussian profiles are plotted in black.

The AFM height images in Figure 1.1 show the film before (A) and after (B) annealing with the as-prepared CeO_2 film likely consisting of closely packed, small crystallites fully covering the surface. For both images, line profiles with a width of 5.12 nm, corresponding to 10 pixels (Figure 1.1 (C)), height distribution profiles (Figure 1.1 (D)) showing the frequency of a given height around the mean height, and the root mean square (RMS) roughness were calculated using Gwyddion [159]. The line profiles illustrate the improvement in surface smoothness best. Before the tube furnace annealing, the surface has a peak-to-valley distance of $\sim$ 1.2 nm. Disregarding the small hole at 0.6 µm, the line profile of the sample after annealing (orange) is significantly smoother, with a peak to valley distance of 0.42 nm. The corresponding height distribution profiles reflect this as well. The FWHM of the height distribution profiles with a uni-modal Gaussian shape decreases by $\sim$ 50 % from 0.74 $\pm$ 0.002nm before the tube furnace annealing to 0.39 $\pm$ 0.002nm afterwards (see Table B.1 and accompanying text for fit parameters). The smoothness of the CeO_2 film after the tube furnace annealing is also apparent from the AFM image in Figure 1.1 (B) with much larger areas of similar height. The RMS roughness $\sigma = \sqrt{\frac{1}{N}\sum_{n=1}^{N}(z_n - \mathrm{bar}z)^2}$ (, where N is the number of height values, z_n the n-th height value and bar$z$ the average height) was calculated from the images in Figure 1.1 (A) and (B) and improved from 0.33 nm to 0.22 nm after annealing [159].
The large overview image in Figure B.3 that also contains the area of Figure 1.1 reveals that the CeO_2 film is interrupted by rectangular holes. Up to this point an area without holes was chosen to gain information on the film surface morphology without distorting statistics by the holes interrupting the film. In order to investigate the holes in detail, we performed AFM measurements on another sample with the crystal principle [1 0 0] and [0 1 0] axes aligned with the x, y image axes, as shown in Figure 1.2 (A). In Figure 1.2 (B), a 3D rendering with inverted z-axis is shown, highlighting the hole's uniform, rectangular shape, indicating $\langle 1\,0\,0\rangle$-type side facets. Figure 1.2 (C) shows a line scan of the hole at the position marked by the line with corresponding color in Figure 1.2 (A). The depth of the hole is in good agreement with the film thickness of 14.4 nm determined by XRD (see Figure B.4, Table B.2, and accompanying text), indicating that they reach down to the surface of the YSZ substrate. A possible origin of the holes will be discussed further below.

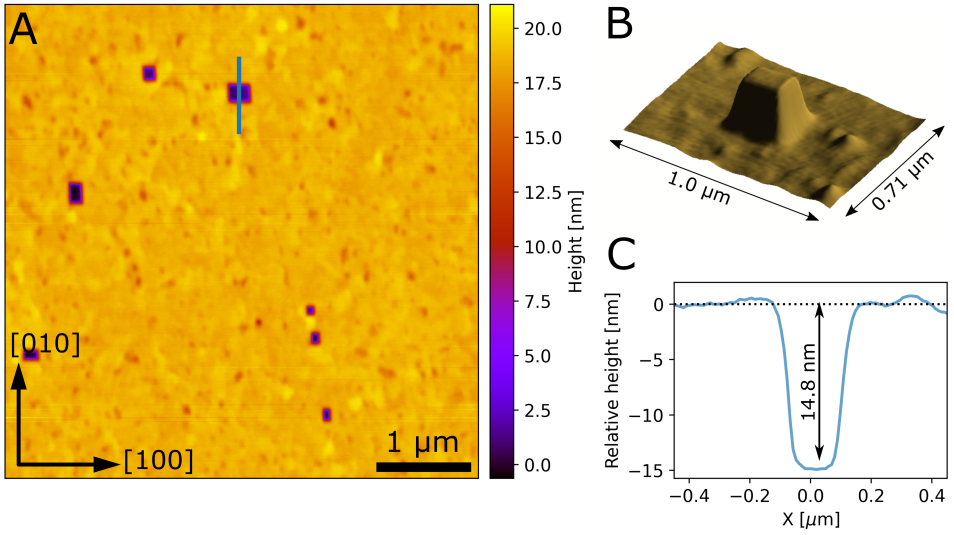

Figure 1.2: **A**: AFM image of an area of the film after annealing exhibiting holes. **B**: Inverted 3D view of one hole. **C**: Line scan through the hole.

1.4.2 Structural properties of CeO_2 films

XRR measurements were employed to gain information on film thickness, coverage, and interfacial roughness, complementary to the AFM investigations. All XRR data was fitted using the Parrat formalism [160, 161] and fit results of the material parameters are given in Table B.3. To fit the data recorded before tube furnace annealing, shown in Figure 1.3 (A), a three-layer model was chosen to accommodate three distinct features of the film: A depletion region (yellow) with reduced electron density compared to YSZ and CeO_2 at the interface to the substrate, the bulk of the film with CeO_2 bulk electron density (orange), and a top-layer with a reduced electron density (red) accommodating the rough morphology of the as-prepared film. In agreement with the height distribution profiles in Figure 1.1 (D), a Gaussian roughness model is used to smoothen the transitions between the layers. The total film thickness, as determined from XRR, is 14.9 nm. The central layer, representing the majority volume of the film, possesses the bulk electron density of CeO_2, which allows to conclude that the YSZ substrate is fully covered by the CeO_2 film, confirming the AFM observations in Figure 1.1 (A) where no interruption of the film was observed. The terminating layer of the CeO_2 film has a thickness of 2.0 nm with a surface RMS roughness of 0.95 nm, which exceeds the RMS roughness calculated from the AFM image by a factor of nearly three. The reason for this discrepancy can be of ex-

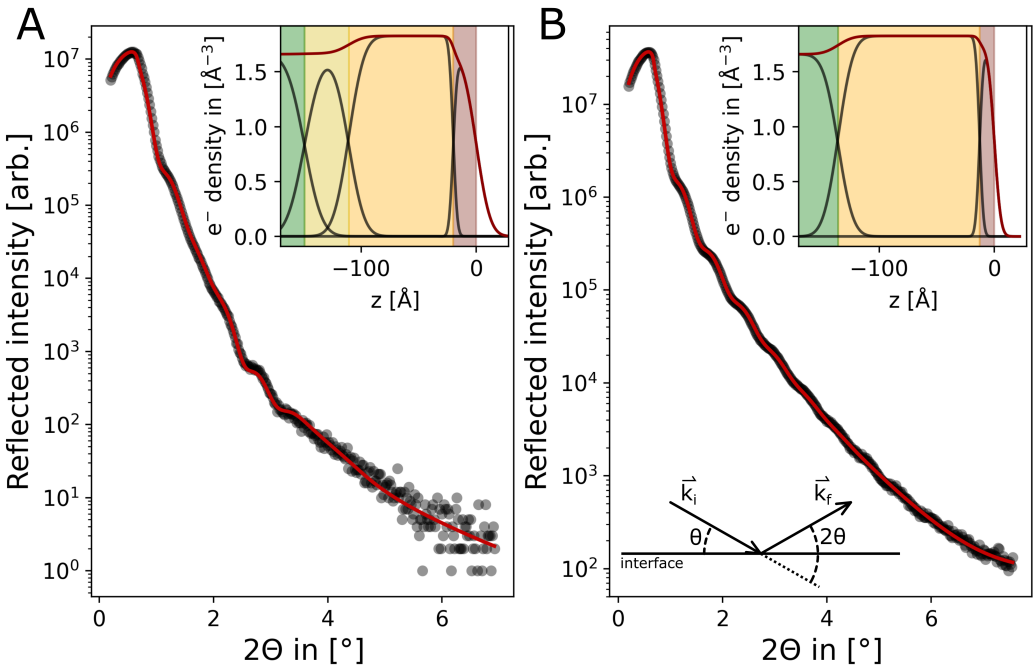

Figure 1.3: Specular reflected intensities as a function of the reflection angle 2Θ (black dots), with fitted curve (red, solid line). Inset: Electron density profile of fitted model (red line) with the components (black lines), before and after furnace anneal (**A**, **B**). Yellow, orange and red rectangles indicate CeO_2 layers, the green rectangle the YSZ substrate.

perimental and physical origin. Experimentally, the limited resolution due to convolution of the AFM tip with surface shape and inaccuracies in model choice can lead to smaller RMS roughness values in AFM and larger values in XRR analysis. However, since the roughness model fits well with the height distribution profile and the aforementioned errors cannot account for such a large difference, the top layer of the XRR model is not only reproducing morphological roughness but likely reduced density due to vacancies, loosely packed crystallites, and amorphous CeO_2.

A first, qualitative comparison of the XRR data obtained before and after the furnace annealing (Figure 1.3 (A) and (B)), confirms the observations in the AFM measurements. The most significant changes in the XRR curve after annealing (Figure 1.3 (B)) are the lack of modulation in the oscillations at $1.5° < 2\Theta < 2.5°$ and an overall intensity increase due to reduced roughness and possibly elimination of non-reflective areas. Overall, the electron density of the film is that of bulk CeO_2 before as well as after the tube furnace an-

nealing, which previously could not be observed in doped films grown by PLD [162]. This is the case despite the rectangular holes observed in AFM, indicating the holes are sparse, local features that do not contribute significantly to the average film electron density. The model could be simplified by the removal of the low density interfacial layer. It apparently restructured during the tube furnace annealing leading to the sharper substrate-film interface in the electron density profile in Figure 1.3 (B). The surface roughness of the top layer is 0.44 nm, less than half compared to before annealing (0.95 nm) and matches the AFM RMS roughness of 0.58 nm observed for the overview image, including the holes in Figure B.3. As apparent from the comparison of the electron density profiles depicted in Figure 1.3 (A) and (B), the top CeO_2 layer of the model reduced significantly in width from 2.0 nm to 1.3 nm and in electron density. This leads to a far more abrupt cut-off of the total electron density, signifying a strongly reduced surface roughness. In addition, the total film thickness is reduced from a value of 14.9 to 13.6 nm, while the thickness of the bulk CeO_2 layer increased from 9.07 ± 0.18 to 12.28 ± 0.07. We explain these changes in the film density, thickness, and roughness at both interfaces by a significant restructuring process that involves optimization of the interface structure between the YSZ substrate and the CeO_2 thin film as well as oxidation of the film at the interface.

Next we will discuss the structural properties of the CeO_2 film. In Figure 1.4 (A), rocking scans with the rotation axis along the surface normal are shown. For this, the detector position was fixed at the respective in-plane Bragg angles for (1 1 1), (2 0 0), and (2 2 0) reflections of CeO_2. These scans allow us to determine the film epitaxy and its preferential growth directions. In Figure 1.4 (A), (B), and (C), the top panel contains data recorded before the tube furnace annealing, while the bottom panel displays data obtained after. Since only the (2 0 0) and (2 2 0) rocking scans show diffraction signal and both scans have 4-fold symmetry with a 45 ° spacing between them, the film is exclusively (0 0 1) oriented. The reciprocal space maps in Figure 1.4 (B) reveal YSZ and CeO_2 (3 3 1)-type reflections in the H,K = H,L plane indicating that the film conforms to cube-on-cube epitaxy. No additional phases, such as Ce_2O_3, or metallic Ce or other orientations of CeO_2 were observed neither before, nor after tube furnace annealing. However, the peak intensity in the rocking scans increases by a factor of two while the peak width decreases in both radial and azimuthal directions (Figure 1.4 (A)). The latter indicates a change in coherent crystallite size, which was determined by line scans through the CeO_2(1 1 1) Bragg peak along the L direction (height) and H,K = H (radial) direction (lateral size), as presented in Figure 1.4 (C). Based on the fitted FWHM the coherent crystallite size D can be calculated along the respective direction using $\Delta Q = \frac{2\pi}{D}$ [163]. Before the tube

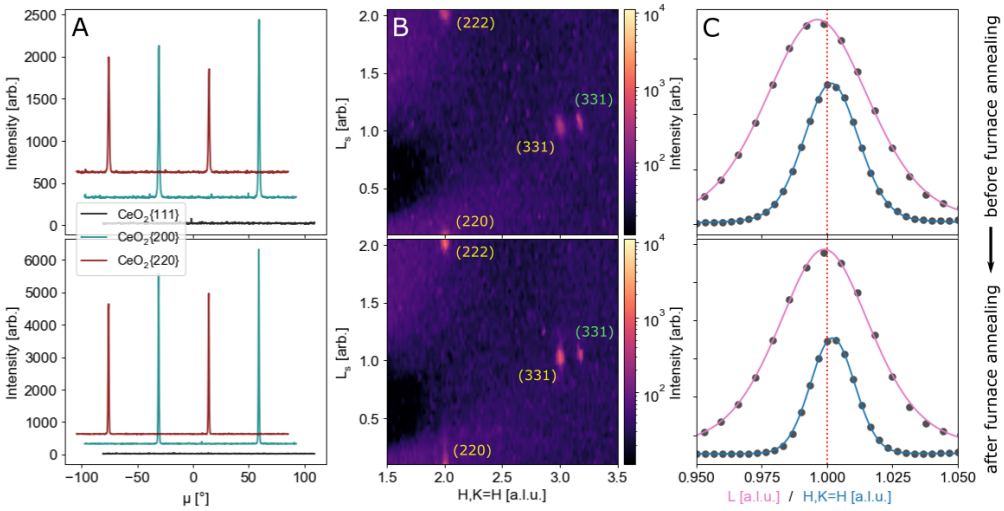

Figure 1.4: **A**: Rocking scans of the sample rotation μ, corrected for the in-plane Bragg angle, showing 45 ° spacing between in-plane (2 0 0)- and (2 2 0)-like reflections and absence of (1 1 1)-type reflections. **B**: Reciprocal space maps revealing CeO_2(0 0 1)/YSZ(0 0 1) cube-on-cube epitaxy without any other phases or orientations. CeO_2 reflections labelled in orange, YSZ reflections in green. **C**: Line scans through the CeO_2(1 1 1) Bragg peak along H,K=H (radial) and L direction (blue and pink, respectively). For all images **A** to **C**, the top image was recorded before, the bottom image after tube furnace annealing.

furnace annealing, the lateral coherent crystallite size is determined to be 25.3 nm and the coherent height is 12.9 nm. The large difference to the total film thickness of 15 nm determined by XRR, can be explained by structural heterogeneity: The film consists of CeO_2 crystallites, giving rise to the characteristic diffraction signal, as well as amorphous, (partially reduced) CeO_2 only contributing to the XRR height. After the tube furnace annealing, the coherent crystallite size grows to 14.3 nm perpendicular to the surface and laterally by roughly 25 %, to 31.6 nm. In the XRR measurement the opposite behavior, a decrease in the total film thickness, is observed, allowing the conclusion that amorphous parts of the film crystallize. In fact, the coherent crystal size with 14.3 nm is slightly larger than the observed thickness from XRR of 13.6 *nm*, but agrees within the error bars of measurements and fits. We quantified the reduction in mosaicity by the average FWHM of the in-plane (2 0 0)- and (2 2 0) rocking scans (Figure 1.4 A). For the as-prepared film the fits (see Figure B.5 for fits and Table B.6 for fit parameters) yielded

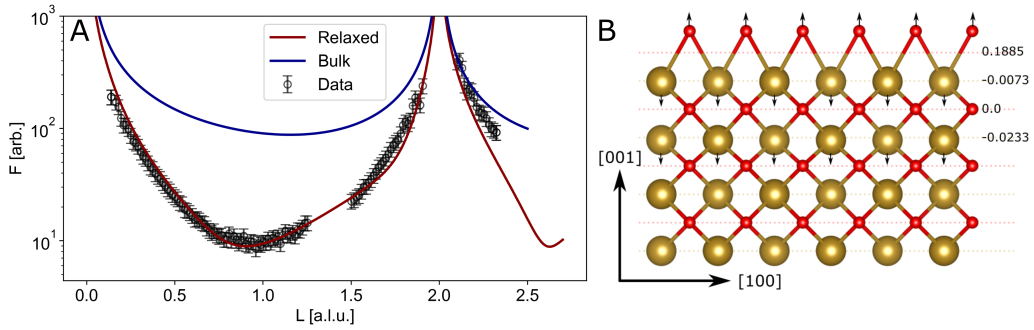

Figure 1.5: **A**: (2 2 L) rod of CeO_2(0 0 1) thin film (black circles and error bars) with CTR model of the bulk truncated model (blue) and the CTR model including relaxation of the surface layer along z (red). **B**: Model of the relaxed surface structure of the (0 0 1)CeO_2 film. The dotted lines indicate the original positions of the layers, the small black arrows the direction of the displacement.

a mosaicity distribution of 1.23 ° for the (2 0 0) type reflection, while after the tube furnace annealing the FWHM reduced by more than one third to 0.80 °. Similar values were attained for the (2 2 0) type reflection indicating, together with the increase in coherent crystallite size, a significant restructuring process during the tube furnace annealing to larger, well aligned domains.
From the peak positions in Figure 1.4 (C), the lattice parameters along the respective scan directions were calculated. The peak positions expected from the bulk lattice constant are indicated by the red, dotted lines. In-plane (H,K = H), the lattice constant increases from 5.408 ± 0.008 Å before to 5.418 ± 0.008Å (bulk lattice constant 5.4178 Å [164]) after the furnace annealing. The out-of-plane lattice constant decreases slightly from 5.46 ± 0.02 Å to 5.41 ± 0.008 Å before and after annealing, indicating a relaxation of the film towards the bulk lattice constant. The lattice constants were refined using multiple CeO_2 reflections (see Table B.5). Within these error bars, lattice parameters of the films are found to be fully relaxed to bulk stoichiometric CeO_2. The lack of uniform strain indicates that the lattice mismatch between YSZ and CeO_2 is likely relieved by dislocations.
Further information on the surface structure of the film was obtained by analysis of surface X-ray diffraction CTR data recorded at the PETRA III beamline P23. In contrast to XRR and AFM that probe the surface morphology, CTR analysis probes the termination of the crystalline lattice of the film [165]. In Figure 1.5 (A), the measured (2 2 L) CeO_2 CTR and the X-ray structure factor of two fitted surface models are shown. Since the film

surface is much smoother than its interface, a simplified model of only the top surface of the film was used. For the bulk simulation (blue curve in Figure 1.5 (A)), no parameters except a scaling factor was varied. The clear discrepancy between fitted model and data shows that the model is not representing the surface structure well. The adapted surface model includes a roughness parameter β, and relaxations of the atoms from their bulk position along the surface normal. The structural model is shown in Figure 1.5 (B) and includes the relative displacement of the atoms on the right hand-side. This simulation already yields good agreement between data and fit: The decreased scattered intensity is due to the surface roughness represented by the parameter β. For comparison with other techniques, the RMS roughness of 9.6 Å was calculated using $\sigma_{RMS}(\beta) = \frac{\beta^{0.5}}{1-\beta} \cdot d_{\perp}$, where β is the fitted roughness parameter and $d_{\perp} = \frac{a_0}{2}$ with $a_0 = 5.41$ Å is the lattice distance along the surface normal [166]. The value is in reasonable agreement with the values from XRR and AFM, inidcating that the film is fully crystalline, as only the crystalline phase contributes to β. The top O and Ce layers are relaxed from the original atomic positions, as indicated by the dotted lines and arrows. The top Ce layer is slightly compressed and the top oxygen layer is significantly expanded along the surface normal. This is in contrast to previous studies on single crystals and nanoparticles where reconstruction and massive restructuring of the (0 0 1) termination were reported [153]. We attribute the displacement of the top O layer to hydroxyl groups (see discussion below). Due to the small contribution to the electron density, H atoms were not included in the fit.

1.4.3 Interfacial dislocation network

Next we will discuss the misfit relaxation mechanism between the CeO_2 film and YSZ substrate. In Figure 1.6 (A), a reciprocal space map of the [H, K = H, L] plane in the vicinity of the in-plane CeO_2 and YSZ (2 2 0) reflections is shown. The (2 2 L) crystal truncation rod (CTR) signal of CeO_2 exhibits film thickness oscillations, which appear for atomically flat films with macroscopically coherent film thickness. Between the CTRs of CeO_2 and YSZ (split due to contributions of Cu $K_{\alpha,1}$, $K_{\alpha,2}$ radiation in the X-ray beam of the laboratory source), an additional diffraction signal can be observed. It is centered between the film and substrate (2 2 0) reflections at H = 2.06 (see line scan at L = 0.04 in the bottom panel of Figure 1.6 (A)). This satellite peak occurs due to an ordered misfit dislocation network, a long-range ordered lattice of dislocations at the interface between CeO_2 and

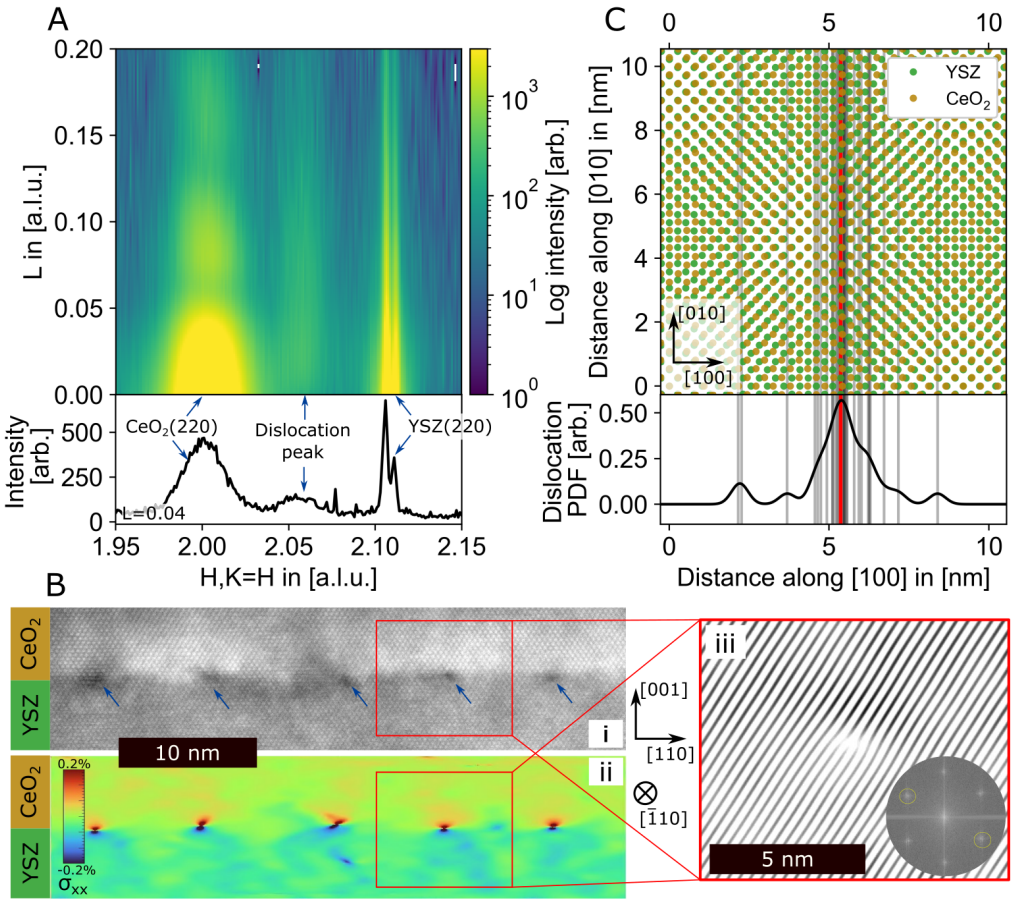

Figure 1.6: **A**: Reciprocal space map (top) and line scan (bottom) in the vicinity of the CeO_2 and YSZ (2 2 0) reflections. **B (i)**: HR-STEM image of the CeO_2 film (top) and YSZ substrate (bottom), projecting the [1 1 0] and [0 0 1] directions in the plane of the image. **B (ii)**: σ_{xx} component of the strain trensor from geometric phase analysis of the area in B(i). **B (iii)**: $\pm$(1 1 1) Bragg filtered image corresponding to the red rectangle in B (i). Crystal axes for all HR-STEM data are indicated next to the B (iii). **C**: Calculated coincidence lattice for CeO_2 (yellow) and YSZ (green). The points indicate atomic positions of metal ions in {0 0 1}-type planes (i.e. the faces of the fcc unit cell) and nicely demonstrates the deviation from a perfect coincidence lattice and hence the location of a necessary misfit dislocation.

the YSZ substrate [167]. A periodicity of 7.08 ± 0.10 nm was determined from the dislocation peak position[168], relative to the CeO_2 (2 2 0) reflection (see Figure B.6 and Table B.7 for fits and full set of fit parameters).
Further information on the misfit dislocation network was obtained by HR-STEM measurements shown in Figure 1.6 (B). For these measurements, a cross-section specimen with its normal oriented along the $[\bar{1}\,\bar{1}\,0]$ direction was prepared (see methods section). Figure 1.6 (B) shows (i) the average background subtraction filtered (ABSF) HR-STEM image, (ii) the corresponding σ_{xx} component of the strain tensor calculated by geometric phase analysis (GPA) [169, 170], and (iii) a Bragg filtered image isolating one of the misfit dislocations. In the HR-STEM image, the less scattering and hence darker bottom area corresponds to YSZ while the brighter and hence more scattering upper area corresponds to CeO_2, as labelled on the left side. The periodically darker contrast with an average distance of 7.58 ± 1.8 nm at the interface of the two materials, indicated by blue arrows, are attributed to dislocations. The highly localized opposite sided strain fields with opposing signs at those positions in Figure 1.6 (ii) confirm the assignment as dislocations. One of the misfit dislocations was investigated by Bragg filtering which shows the extra half plane at the interface of the isolated $CeO_2\{1\,1\,1\}$ and YSZ$\{1\,1\,1\}$ planes in Figure 1.6 (B, iii).
In the top panel of Figure 1.6 (C), the lattices of $\{0\,0\,1\}$ planes of CeO_2 (yellow) and YSZ (green) are shown with the circles representing the atomic positions in that plane. The gray lines are the dislocation distances, measured from two Bragg filtered images using different reflection pairs of the three images in Figure B.7. The red line is the mean dislocation distance of 7.58 ± 1.8 nm. The lines are extended into the bottom panel of Figure 1.6 (C), where the dislocation probability density function emphasize the unimodal distribution centered around the mean distribution value. All distances and the calculation is given in Table B.8 and the accompanying text. The average spacing of the misfit dislocations obtained from the HR-STEM image analysis and the value obtained from GIXRD analysis are slightly smaller than the calculated equilibrium spacing of 7.8 nm for dislocations of Burgers vector type $b = \frac{1}{2}a$ $CeO_2[110]$. In comparison with previously observed dislocation distances for this system (4.7 nm[118], 5.1 nm[145]), the dislocation network of the here presented films are in a significantly more relaxed state. A reason for the discrepancy between equilibrium spacing and the observed values could be the fact that the relaxed bulk lattices of the two materials form a Moire pattern (Figure 1.6 (C)) with a the 45 ° rotated unit cell parameter of 6.5 nm (= 18 CeO_2 or 19 YSZ $\{1\,1\,0\}$ lattice planes). The observed dislocation network spacing could be the result of these two competing interface structures.

In the vicinity of the dislocations, the σ_{xx} strain map reveals tensile strain in the CeO_2 lattice and compressive strain in the YSZ lattice. The remaining σ_{yy}, σ_{xy} and σ_{yx} strain tensor maps are presented in Figure B.8 (A), (B), and (C), respectively. The σ_{yy} strain tensor map reveals a small, relatively homogeneous expansive strain in the CeO_2 film (Figure B.8 (A)) of $\approx 0.1\,\%$, well within the errorbars of the GIXRD measurements. In addition, shear strain is also observed in the direct vicinity of the dislocation. Sign, amplitude, and location of the σ_{xy} and σ_{yx} components are nearly identical (Figure B.8 (B), (C)) and in sum, correspond to a rotation of the interface lattice in the image plane in counter clockwise direction. Shear strain was observed both along and perpendicular to the interface normal (Figure B.8 (B) and (C)) with the same sign and value indicating a rotation of the lattice along the $[1\,\bar{1}\,0]$ axis or along the image plane normal. In combination with the aforementioned rectangular holes appearing after the tube furnace annealling we deduct a complex relationship between out-of-plane strain, in-plane dislocation network, holes, and twisted CeO_2 lattice minimizing the interfacial energy between the two lattice mismatched materials. The recrystallization to larger domains observed by XRD and the increase in electron density observed by XRR indicate significant oxygen transfer through the bulk of the film from the environment. We suspect that the holes are condensated oxygen vacancies forming as the film restructuring from an oxygen deficient state (before the tube furnace annealing) to the fully oxidized state (after the tube furnace annealing) occurs. In short, the restructuring to a perfect CeO_2 film is faster than oxygen can be supplied by the environment to the film. The rectangular footprint of the holes can be rationalized by the strong interaction of the surrounding film with the substrate and the significantly stronger oxygen diffusion across $\{1\,0\,0\}$ planes compared to other directions.[171] In combination with the complex relaxation mechanism at the surface this results in a strong interaction between film and substrate at the interface which promotes the vacancy condensation to conform to the symmetry of the substrate and surrounding film leading to interruptions of the film at $\{1\,0\,0\}$ and $\{0\,1\,0\}$ planes resulting in rectangular holes.

1.4.4 Film surface composition

XPS measurements were conducted to analyze the chemical composition at the surface of the CeO_2 film after the tube furnace annealing. After introducing the sample to UHV, the sample was annealed at 450 °C with a backpressure of 5×10^{-6} mbar O_2 to remove contaminative adsorbates. The survey scan in Figure B.9 shows that the sample is free of contaminations.

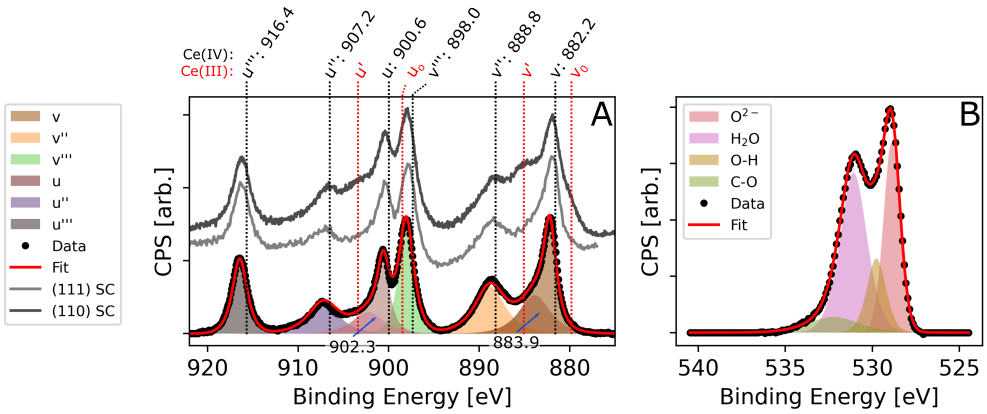

Figure 1.7: Deconvoluted Ce 3*d* (**A**) and O 1*s* (**B**) core level spectra of the thin film after tube furnace annealing at 50 ° emission angle (black dots) inlcuding fit (red line) and components (colored areas). For comparison, reference core level spectra of a (1 1 1) facetted CeO_2(110) single crystal (data provided by the authors of [172]) and an untreated CeO_2(1 1 1) single crystal, recorded at the same emission angle are shown with fitted data in **A**. In addition, the fitted peak positions of the Ce(IV) 3*d* core levels as well as the expected positions of Ce(III) 3*d* core levels from [173] are shown.

In Figure 1.7 (A), the deconvoluted Ce 3*d* core level spectrum of the film is presented alongside reference spectra obtained from CeO_2 single crystal experiments (with linear background subtracted for comparability). The light gray curve represents an untreated Ce(111) single crystal, measured in normal emission, while the dark gray curve corresponds to a {1 1 1} faceted CeO_2(1 1 0) single crystal [172] measured in grazing incidence. For the latter, the authors reported a 35 % Ce(III) content. The positions of 10 overlapping peaks of CeO_{2-x} are shown as black (Ce(IV)) and red (Ce(III)) dotted lines in Figure 1.7 (A). For both cerium oxides $Ce^{IV}O_2$ and $Ce^{III}{}_2O_3$, only doublets are observed due to the $3d_{5/2}/3d_{3/2}$ spin-orbit splitting: One doublet for the primary photo emission (v/u for Ce(IV), v_0/u_0 for Ce(III)) process, two for shake-down processes in Ce(IV) (v''/u'', v'''/u''') and one for Ce(III) (v'/u'). Overall, the XPS data of the film closely resembles the bulk spectra of the CeO_2(1 1 1) single crystal (Figure 1.7 (A), labelled (111) SC). Obvious contributions to the spectrum from Ce(III) (red dotted lines) like in the dark gray curve with 35 % Ce(III) are clearly absent. Quantification of the amount of Ce(III) species is not trivial, especially for small amounts of Ce(III), as previously described in [174–176], because of the large number of strongly overlap-

ping, symmetric, and asymmetric peaks, combined with Shirley-background subtraction. Furthermore, extreme charging because of the large band gaps of CeO_2 and YSZ (3.0 eV, and 4.23 eV respectively [177, 178]) complicated the measurement. In order to simplify the fitting procedure we chose to restrict the fit by fixing doublet spacings to 18.4 eV, the doublet area ratio to 2/3, and the FWHM to the same value. An asymmetric peak profile composed of two Pseudo-Voigt profiles was chosen for the peaks v and u[174, 175, 179]. The spacing and FWHM between the asymmetry (indicated by blue arrows and corresponding position in Figure 1.7 (A)) and the main components are equal for v and u. All components are Pseudo-Voigt line shapes with $\alpha = 0.8$ and the full set of fit parameters is given in Table B.9. The resulting best fit of the described procedure is shown in red in Figure 1.7 (A) and reproduces the data very well in all areas of the core level spectrum. No additional peaks were necessary at the expected positions of Ce(III) and including them resulted in worse agreement of fit and data, shift to Ce(IV) positions, FWHM of the order of 10 eV, or negligible peak areas, depending on the boundary conditions of the fit. In the same way, removing or reducing the asymmetry contribution to v and u did not yield improvement in the fit, independent of the inclusion or exclusion of Ce(III) components. From this, we conclude that within the error of measurement and fit, the surface of the CeO_2 film is fully oxidized. Further information on the oxidation state and surface chemistry of the film can be extracted from the O 1s and C 1s core levels shown in Figure 1.7 (B) and Figure B.10, respectively. The two dominant components of the O1s spectra are lattice oxygen at 528.98 eV[180, 181] and water at 531.18 eV[180, 181]. The spacing is in good agreement with previous studies on the surface of CeO_2(1 1 1) films supported by Pr_2O_3(0 0 0 1)/Si(1 1 1) or metal substrates, and CeO_2 single crystals [182, 183]. In order to fully reproduce the oxygen core level spectrum, an additional OH peak[184] and a carbon-related peak[185] were added at 530.16 eV and 532.73 eV, respectively. In agreement with the lack of Ce(III) signal in the Ce 3d core level spectra and the lack of a shoulder on the CeO_2 lattice oxygen peak, the addition of a lattice oxygen peak for partially reduced CeO_2 did not improve or maintain fit quality (full set of fit parameters in Table B.10 and accompanying text). In order to understand the area distribution between the H_2O, OH, and lattice O peak, a layer analysis was conducted (detailed calculation is presented the SI) which revealed that the film is terminated by a 1.8 monolayer thick water film followed by one monolayer (0.95 $\pm$ 0.09) of OH. This clearly points towards a strongly hydroxylated surface which is further stabilized by the thin H_2O overlayer.

Polarization-resolved IRRAS was employed, using CO as a probe molecule, to gain further insight into the surface chemistry of the CeO_2 film. The CO

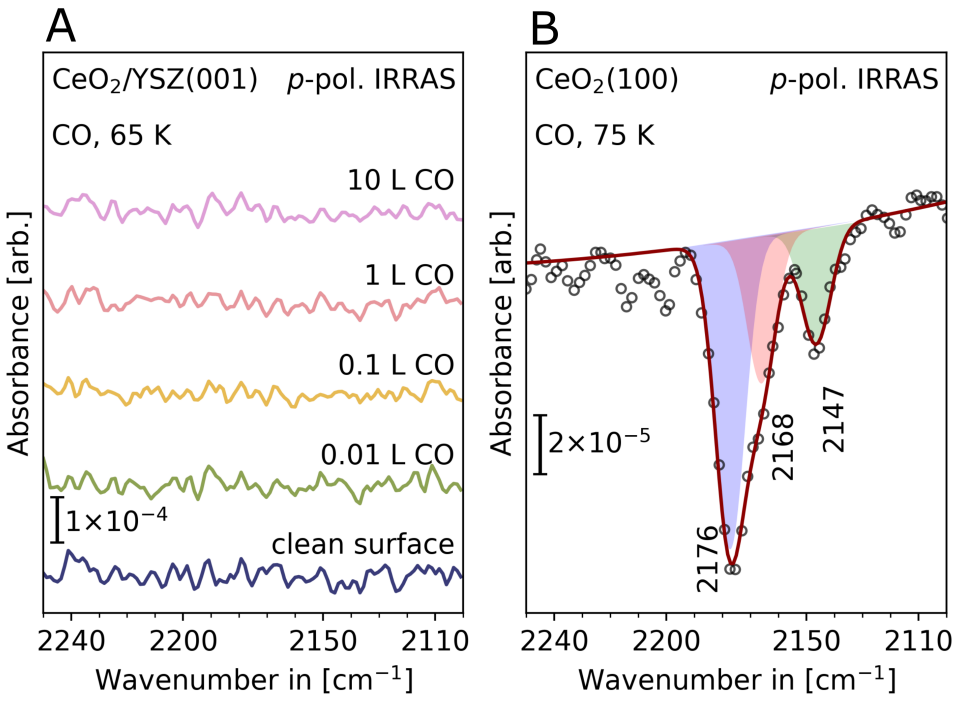

Figure 1.8: Surface structure of the oxidized CeO_2/YSZ(0 0 1) thin film characterized by polarization-resolved IRRAS. (A) p-polarized IRRAS data of CO adsorption at 65 K on CeO2/YSZ(001). (B) Reference IRRA spectrum of CO adsorption on the (2 × 2) O-terminated CeO_2(1 0 0) single-crystal surface [152].

surface ligand IR (CO-SLIR) approach[186] has been demonstrated to be well-suited for characterizing the surface structure of catalyst surfaces.[187–189] This is because the frequency of CO stretching vibrations is extremely sensitive to the chemical environment and varies significantly depending on the nature of adsorption sites. Figure 1.8 (A) shows the corresponding *p*-polarized IRRAS data as a function of CO dosage at 65 K (cooling with liquid He). Upon CO adsorption on the cleaned CeO_2/YSZ thin film, no CO-related vibrational bands were observed in the region of 2200 - 2100 cm^{-1} (the same is true for the *s*-polarized spectrum shown in Figure B.11). For comparison, the IRRAS data of CO adsorption on the oxidized CeO_2(0 0 1) single crystal surface recorded at slightly higher temperatures (75 K) is presented in Figure 1.8 (B). The bulk-truncated, polar CeO_2(0 0 1) surface is known to be inherently unstable, leading to its reconstruction into a (2 × 2) pattern for

polarity compensation [153]. As shown in Figure 1.8 (B), the charge neutral (2×2) O-terminated $CeO_2(0\,0\,1)$ surface is characterized by two CO bands at 2176 and 2147 cm^{-1}, which are respectively assigned to CO species in an on-top and a bridge configuration, as supported by theoretical calculations using the hybrid DFT (density functional theory) approach with the HSE06 functional [154]. The shoulder resolved at 2168 cm^{-1} originates from CO bound to oxygen vacancy sites as a minority species [152, 154]. We note that comprehensive IRRAS results were reported for CO adsorption on all three low-index ceria single-crystal surfaces ($CeO_2(1\,1\,1)$, $CeO_2(1\,1\,0)$, $CeO_2(1\,0\,0)$) in both oxidized and reduced forms [152–155]. These data reveal that the CO stretching band is highly facet-dependent and remarkably sensitive to the presence of O vacancies [128, 151–154]. Furthermore, blue shifts of the CO vibrations relative to the gas phase (2143 cm^{-1}) were observed for CO adsorption on all oxidized and reduced CeO_2 surfaces. Overall, the present IRRAS results provide solid evidence that the surface structure of the $CeO_2(1\,0\,0)$ thin film is rather different from that observed for $CeO_2(1\,0\,0)$ single-crystal surfaces. The absence of any CO-related IR signals, even at temperature as low as 65 K, suggests that the surface of the $CeO_2(1\,0\,0)$ thin film is stabilized by hydroxylation, where the polar instability is removed through the formation of hydroxyl groups, in line with XPS observations.

1.5 Conclusion

We present a facile, stream-lined UHV growth procedure for epitaxial, fully oxidized $CeO_2(1\,0\,0)$ thin films supported by YSZ$(0\,0\,1)$ and report on their crystallographic, chemical, and morphological properties. With the presented growth procedure we were able to reduce the number of preparation steps compared to other studies using YSZ supports [118, 145]. The films exhibit a fully coherent lattice along their surface normal over the full film thicknesses of 10 to 15 nm. The lattice is almost fully relaxed to the bulk lattice parameter, with a small tensile out-of-plane strain of $\approx 0.1\,\%$. The in-plane lattice of the film is fully relaxed via the formation of a long-range ordered dislocation network along the $[1\,1\,0]$ directions. After the tube furnace annealing, the film is completely oxidized at both interfaces and in the bulk, as no reduced electron density was observed in XRR and no significant Ce(III) population could be observed by XPS. The prepared films exhibit rectangular holes with edges aligned with the $[1\,0\,0]$ and $[0\,1\,0]$ axes. These holes are local phenomena and a result of the restructuring process occuring during the tube furnace annealing. Spectroscopic analysis by IRRAS and XPS as well as structural investigation by CTR analysis show that the point defect

free surface is hydroxylated and (0 0 1) terminated. Similar to reports on ZrO_2, the surface is found to be fully hydroxylated for charge compensation of the polar (0 0 1) surface of CeO_2 [190, 191], demonstrating its high activity towards water dissociation, occuring likely during the tube furnace annealing process [192]. The films represent an ideal support for the preparation of model heterogeneous catalysts by metal nanoparticle deposition for elucidating structure-activity relationships.

Bibliography

(118) Wang, C.-M.; Thevuthasan, S.; Peden, C. H. F. Interface Structure of an Epitaxial Cubic Ceria Film on Cubic Zirconia. *J. Am. Ceram. Soc.* **2003**, *86*, 363–365.

(119) Barth, C. et al. A Perfectly Stoichiometric and Flat CeO_2(111) Surface on a Bulk-Like Ceria Film. *Sci. Rep.* **2016**, *6*, 21165.

(120) Wu, F. et al. Growth and Structure of Epitaxial CeO_2 Films on Yttria-Stabilized ZrO_2. *Thin Solid Films* **2008**, *516*, 4908–4914.

(121) Bozo, C.; Guilhaume, N.; Herrmann, J.-M. Role of the Ceria-Zirconia Support in the Reactivity of Platinum and Palladium Catalysts for Methane Total Oxidation under Lean Conditions. *J. Catal.* **2001**, *203*, 393–406.

(122) Montini, T.; Melchionna, M.; Monai, M.; Fornasiero, P. Fundamentals and Catalytic Applications of CeO_2-Based Materials. *Chem. Rev.* **2016**, *116*, 5987–6041.

(123) Mi, R.; Li, D.; Hu, Z.; Yang, R. T. Morphology Effects of CeO_2 Nanomaterials on the Catalytic Combustion of Toluene: A Combined Kinetics and Diffuse Reflectance Infrared Fourier Transform Spectroscopy Study. *ACS Catal.* **2021**, *11*, 7876–7889.

(124) Guo, Y. et al. CeO_2 Facet-Dependent Surface Reactive Intermediates and Activity during Ketonization of Propionic Acid. *ACS Catal.* **2022**, *12*, 2998–3012.

(125) Spezzati, G. et al. CO Oxidation by Pd Supported on CeO_2(100) and CeO_2(111) Facets. *Appl. Catal. B: Environ.* **2019**, *243*, 36–46.

(126) Colussi, S.; Fornasiero, P.; Trovarelli, A. Structure-Activity Relationship in Pd/CeO_2 Methane Oxidation Catalysts. *Chin. J. Catal.* **2020**, *41*, 938–950.

(127) Liu, J.-X.; Su, Y.; Filot, I. A. W.; Hensen, E. J. M. A Linear Scaling Relation for CO Oxidation on CeO_2-Supported Pd. *J. Am. Chem. Soc.* **2018**, *140*, 4580–4587.

(128) Maurer, F. et al. Tracking the Formation, Fate and Consequence for Catalytic Activity of Pt Single Sites on CeO_2. *Nat. Catal.* **2020**, *3*, 824–833.

(129) Song, B.; Si, S.; Soleymani, A.; Xin, Y.; Hagelin-Weaver, H. E. Effect of Ceria Surface Facet on Stability and Reactivity of Isolated Platinum Atoms. *Nano Res.* **2022**, *15*, 5922–5932.

(130) Costa-Nunes, O.; Gorte, R. J.; Vohs, J. M. High Mobility of Ceria Films on Zirconia at Moderate Temperatures. *J. Mater. Chem.* **2005**, *15*, 1520.

(131) Dolcet, P.; Maurer, F.; Casapu, M.; Grunwaldt, J.-D. Insights into the Structural Dynamics of Pt/CeO_2 Single-Site Catalysts during CO Oxidation. *Catalysts* **2021**, *11*, 617.

(132) Yang, C. et al. N_2O Adsorption and Photochemistry on Ceria Surfaces. *J. Phys. Chem. C* **2022**, *126*, 2253–2263.

(133) Maurer, F. et al. Surface Noble Metal Concentration on Ceria as a Key Descriptor for Efficient Catalytic CO Oxidation. *ACS Catal.* **2022**, *12*, 2473–2486.

(134) Maurer, F. et al. Spatiotemporal Investigation of the Temperature and Structure of a Pt/CeO_2 Oxidation Catalyst for CO and Hydrocarbon Oxidation during Pulse Activation. *Ind. Eng. Chem. Res.* **2021**, *60*, 6662–6675.

(135) Wu, F. et al. Growth and Structure of Epitaxial CeO_2 Films on Yttria-Stabilized ZrO_2. *Thin Solid Films* **2008**, *516*, 4908–4914.

(136) Sauerbrey, M. et al. Cerium Oxide Epitaxial Nanostructures on Pt(111): Growth, Morphology and Structure. *Top. Catal.* **2017**, *60*, 513–521.

(137) Hasegawa, T. et al. Epitaxial Growth of CeO_2(111) Film on Ru(0001): Scanning Tunneling Microscopy (STM) and X-ray Photoemission Spectroscopy (XPS) Study. *J. Chem. Phys.* **2014**, *140*, 044711.

(138) Pieper, H. H. et al. Morphology and Nanostructure of CeO_2(111) Surfaces of Single Crystals and Si(111) Supported Ceria Films. *Phys. Chem. Chem. Phys.* **2012**, *14*, 15361–15368.

(139) Olbrich, R. et al. A Well-Structured Metastable Ceria Surface. *Appl. Phys. Lett.* **2014**, *104*, 081910.

(140) Nandasiri, M. I. et al. Influence of Growth Rate on the Epitaxial Orientation and Crystalline Quality of CeO_2 Thin Films Grown on Al_2O_3(0001). *J. Appl. Phys.* **2011**, *109*, 013525.

(141) Kaemena, B. et al. Growth and Morphology of Ceria on Ruthenium(0001). *J. Phys. Chem. C* **2013**, *117*, 221–232.

(142) Mullins, D. R.; Radulovic, P. V.; Overbury, S. H. Ordered Cerium Oxide Thin Films Grown on Ru(0001) and Ni(111). *Surf. Sci.* **1999**, *429*, 186–198.

(143) Luches, P.; Pagliuca, F.; Valeri, S. Morphology, Stoichiometry, and Interface Structure of CeO_2 Ultrathin Films on Pt(111). *J. Phys. Chem. C* **2011**, *115*, 10718–10726.

(144) Zscherp, M. F. et al. Epitaxial Growth and Structural Characterization of Ceria Deposited by Atomic Layer Deposition on High-Surface Porous Yttria-Stabilized Zirconia Thin Films. *Cryst. Growth Des.* **2020**, *20*, 2194–2201.

(145) Shi, Y. et al. Growth of Highly Strained CeO_2 Ultrathin Films. *ACS Nano* **2016**, *10*, 9938–9947.

(146) Niu, G. et al. Controlling the Physics and Chemistry of Binary and Ternary Praseodymium and Cerium Oxide Systems. *Phys. Chem. Chem. Phys.* **2015**, *17*, 24513–24540.

(147) Torbrügge, S.; Reichling, M.; Ishiyama, A.; Morita, S.; Custance, Ó. Evidence of Subsurface Oxygen Vacancy Ordering on Reduced CeO_2(111). *Phys. Rev. Lett.* **2007**, *99*, 056101.

(148) Su, Z. et al. Roles of Oxygen Vacancies in the Bulk and Surface of CeO_2 for Toluene Catalytic Combustion. *Environ. Sci. Technol.* **2020**, *54*, 12684–12692.

(149) Li, Z. et al. Interaction of Hydrogen with Ceria: Hydroxylation, Reduction, and Hydride Formation on the Surface and in the Bulk. *Chemistry* **2021**, *27*, 5268–5276.

(150) Wu, X.-P.; Gong, X.-q. Clustering of Oxygen Vacancies at CeO_2(111): Critical Role of Hydroxyls. *Phys. Rev. Lett.* **2016**, *116 8*, 086102.

(151) Caulfield, L.; Sauter, E.; Idriss, H.; Wang, Y.; Wöll, C. Bridging the Pressure and Materials Gap in Heterogeneous Catalysis: A Combined UHV, In Situ, and Operando Study Using Infrared Spectroscopy. *J. Phys. Chem. C* **2023**, *127*, 14023–14029.

(152) Yang, C. et al. Surface Faceting and Reconstruction of Ceria Nanoparticles. *Angew. Chem. Int. Ed.* **2017**, *56*, 375–379.

(153) Yang, C. et al. Surface Refaceting Mechanism on Cubic Ceria. *J. Phys. Chem. Lett.* **2020**, *11*, 7925–7931.

(154) Lustemberg, P. G.; Yang, C.; Wang, Y.; Wöll, C.; Ganduglia-Pirovano, M. V. Vibrational Frequencies of CO Bound to All Three Low-Index Cerium Oxide Surfaces: A Consistent Theoretical Description of Vacancy-Induced Changes Using Density Functional Theory. *J. Chem. Phys.* **2023**, *159*, DOI: 10.1063/5.0153745.

(155) Lustemberg, P. G. et al. Vibrational Frequencies of Cerium-Oxide-Bound CO: A Challenge for Conventional DFT Methods. *Phys. Rev. Lett.* **2020**, *125*, 256101.

(156) Esch, F. et al. Electron Localization Determines Defect Formation on Ceria Substrates. *Science* **2005**, *309*, 749–752.

(157) Kullgren, J. et al. Oxygen Vacancies versus Fluorine at $CeO_2(111)$: A Case of Mistaken Identity? *Phys. Rev. Lett.* **2014**, *112*, 156102.

(158) Stierle, A.; Keller, T.; Noei, H.; Vonk, V.; Roehlsberger, R. DESY NanoLab. *J. Large-Scale Res. Facil.* **2016**, *2*, A76.

(159) Nečas, D.; Klapetek, P. Gwyddion: An Open-Source Software for SPM Data Analysis. *Cent. Eur. J. Phys.* **2012**, *10*, 181–188.

(160) Kriegner, D.; Wintersberger, E. xrayutilities, 2023-11-06, 2023.

(161) Parrat, L. G. Surface Studies of Solids by Total Reflection of X-Rays. *Phys. Rev.* **1954**, *95*, 359.

(162) Arndt, B. et al. Structure and Stability of Gd-Doped CeO_2 Thin Films on Yttria-Stabilized Zirconia. *Thin Solid Films* **2016**, *603*, 56–61.

(163) Debye, P.; Scherrer, P. Bestimmung der Größe und der Inneren Struktur von Kolloidteilchen Mittels Röntgenstrahlen. *Nachr. Ges. Wiss. Göttingen, Math.-Phys. Kl.* **1918**, *1*, 98–100.

(164) Ma, Y. et al. Introducing Highly Redox-Active Atomic Centers into Insertion-Type Electrodes for Lithium-Ion Batteries. *Adv. Energy Mater.* **2020**, *10*, 2000783.

(165) Stierle, A.; Vlieg, E. In *Modern Diffraction Methods*; John Wiley & Sons, Ltd: 2012, pp 221–257.

(166) Robinson, I. Crystal Truncation Rods and Surface Roughness. *Phys Rev. B* **1985**, *33*, 3830–3836.

(167) G. Renbaud, P. Guenard, A. Barbier Misfit Dislocation Network at the Ag/MgO(001) Interface: A Grazing Incidence X-ray-Scattering Study. *Phys. Rev. B* **1998**, *58*, 7310–7318.

(168) Wintersberger, E. et al. Analysis of Periodic Dislocation Networks using X-ray Diffraction and Extended Finite Element Modeling. *Appl. Phys. Lett.* **2010**, *96*, 131905.

(169) Hytch, M. Geometric Phase Analysis of High Resolution Electron Microscope Images. *Scan. Microsc.* **1997**, *11*, 53–66.

(170) Kim, K.-H. Digital Micrograph Script Source Listing for a Geometric Phase Analysis. *Appl. Microsc.* **2015**, *45*, 45–101.

(171) Zhu, L. et al. Visualizing Anisotropic Oxygen Diffusion in Ceria under Activated Conditions. *Phys. Rev. Lett.* **2020**, *124*, 056002.

(172) Yang, C. et al. Surface Faceting and Reconstruction of Ceria Nanoparticles. *Angew. Chem. Int. Ed.* **2017**, *56*, 375–379.

(173) Li, Z. et al. Oxidation of Reduced Ceria by Incorporation of Hydrogen. *Angew. Chem. Int. Ed.* **2019**, *58*, 14686–14693.

(174) Świątowska, J. et al. XPS, XRD and SEM Characterization of a Thin Ceria Layer Deposited onto Graphite Electrode for Application in Lithium-Ion Batteries. *Appl. Surf. Sci.* **2011**, *257*, 9110–9119.

(175) Skála, T.; Šutara, F.; Prince, K. C.; Matolín, V. Cerium Oxide Stoichiometry Alteration via Sn Deposition: Influence of Temperature. *J. Electron Spectrosc. Relat. Phenom.* **2009**, *169*, 20–25.

(176) Alammar, T.; Noei, H.; Wang, Y.; Grünert, W.; Mudring, A.-V. Ionic Liquid-Assisted Sonochemical Preparation of CeO_2 Nanoparticles for CO Oxidation. *ACS Sustainable Chem. Eng.* **2015**, *3*, 42–54.

(177) Kusmierek, E. A CeO_2 Semiconductor as a Photocatalytic and Photoelectrocatalytic Material for the Remediation of Pollutants in Industrial Wastewater: A Review. *Catalysts* **2020**, *10*, 1435.

(178) PaiVerneker, V. R.; Petelin, A. N.; Crowne, F. J.; Nagle, D. C. Color-Center-Induced Band-Gap Shift in Yttria-Stabilized Zirconia. *Phys. Rev. B* **1989**, *40*, 8555–8557.

(179) Engelhard, M.; Azad, S.; Peden, C.; Thevuthasan, S. X-ray Photoelectron Spectroscopy Studies of Oxidized and Reduced CeO_2(111) Surfaces. *Surf. Sci. Spectra* **2004**, *11*, 73–81.

(180) Lykhach, Y. et al. Water Chemistry on Model Ceria and Pt/Ceria Catalysts. *J. Phys. Chem. C* **2012**, *116*, 12103–12113.

(181) Fu, S.-P. et al. On the wetting behavior of ceria thin films grown by pulsed laser deposition. *Appl. Phys. Lett.* **2017**, *110*, 081601.

(182) Mullins, D.; Overbury, S.; Huntley, D. Electron Spectroscopy of Single Crystal and Polycrystalline Cerium Oxide Surfaces. *Surf. Sci.* **1998**, *409*, 307–319.

(183) Kundakovic, L.; Mullins, D.; Overbury, S. Adsorption and Reaction of H_2O and CO on Oxidized and Reduced Rh/CeO_x(111) Surfaces. *Surf. Sci.* **2000**, *457*, 51–62.

(184) Chanu, W. C.; Gupta, A.; Singh, M. K.; Pandey, O. P. Group V Elements (V, Nb and Ta) Doped CeO_2 Particles for Efficient Photo-Oxidation of Methylene Blue Dye. *J. Inorg. Organomet. Polym. Mater.* **2021**, *31*, 636–647.

(185) Min, C. et al. Fabrication of Novel CeO_2/GO/CNTs Ternary Nanocomposites with Enhanced Tribological Performance. *Appl. Sci.* **2019**, *9*, 170.

(186) Wöll, C. Structure and Chemical Properties of Oxide Nanoparticles Determined by Surface-Ligand IR Spectroscopy. *ACS Catal.* **2020**, *10*, 168–176.

(187) Wang, J. et al. Dynamic Structural Evolution of Ceria-Supported Pt Particles: A Thorough Spectroscopic Study. *J. Phys. Chem* **2022**, *126*, 9051–9058.

(188) Chen, A. et al. Structure of the Catalytically Active Copper-Ceria Interfacial Perimeter. *Nat. Catal.* **2019**, *2*, 334–341.

(189) Liu, S. et al. Tuning Crystal-Phase of Bimetallic Single-Nanoparticle for Catalytic Hydrogenation. *Nat. Commun.* **2022**, *13*, 4559.

(190) Iskandarova, I. et al. First-Principle Investigation of the Hydroxylation of Zirconia and Hafnia Surfaces. *Microelectron. Eng.* **2003**, *69*, 587–593.

(191) Köck, E.-M.; Kogler, M.; Bielz, T.; Klötzer, B.; Penner, S. In Situ FT-IR Spectroscopic Study of CO_2 and CO Adsorption on Y_2O_3, ZrO_2, and Yttria-Stabilized ZrO_2. *J. Phys. Chem. C* **2013**, *117*, 17666–17673.

(192) Chen, S. et al. Structure and Chemical Reactivity of Y-Stabilized ZrO_2 Surfaces: Importance for the Water-Gas Shift Reaction. *Angew. Chem. Int. Ed.*, e202404775.

2. Complex Evolution of Oxide Supported Pd Catalysts During Methane Oxidation Light-off

Outline

Status of Publication

This chapter is based on an unpublished manuscript under preparation for submission. Publication in a peer reviewed journal is expected within this year.

Author list:
Jan-Christian Schober[1,2], Lydia Bachmann[1,2], Artem Zaidman[1,2], Esko Erik Beck[1,2], Radik Batraev[1,2], Andrea Sartori [3], Arno Jeromin [1], Vedran Vonk [1], Dmitry I. Sharapa [4], Philipp N. Plessow [4], Andreas Stierle [1,4]
[1]Centre for X-ray and Nano Science, Deutsches Elektronen-Synchrotron DESY, 22607 Hamburg, Germany
[2]Universität Hamburg, 20148 Hamburg, Germany
[3]European Synchrotron Radiation Facility, Grenoble 38000, France
[4]Karlsruhe Institute of Technology KIT, Institute of Functional Interfaces (IFG), 76344 Karlsruhe, Germany

Author Contribution

I am responsible for sample preparation, experiment design and execution, and the entirety of data analysis. The beamtime experiments were carried out collaboratively with Lydia Bachmann, Artem Zaidman, Esko Erik Beck, Radik Batraev, Andrea Sartori, and Andreas Stierle. Arno Jeromin carried out the SEM measurements. Dmitry I. Sharapa and Philipp N. Plessow contributed DFT calcuations.

Copyright Notice

Abstract

Methane-based technologies are key to a more sustainable and renewable energy future, with Pd-based catalysts commonly employed to mitigate methane slip during combustion. Despite good understanding of predictors for activity and identification of PdO(1 0 1) as the active surface, information on the transient structure during light-off is scarce. With operando grazing incidence high energy X-ray diffraction, we accessed structural information of two catalysts at transient conditions during light-off. Simultaneously monitoring the activity, Pd/Al_2O_3 showed activity for partial oxidation to CH_2O and Pd/CeO_2 for CO and CH_2O. Furthermore, the evolution of the Pd oxidation state did not follow the oxygen chemical potential and thermodynamically unstable phases were formed by reactions involving the support. Correlation of all results demonstrates that the thermodynamic condition inferred from the applied is not a reliable descriptor of the catalyst surface or active site. Instead, kinetic processes like the diffusion and desorption of surface species and reduction of PdO by the catalytic conversion of methane steer the oxidation state and available active sites of the catalyst.

2.1 Introduction

With the increasing deployment of renewable energy sources and the phase out of traditional sources, transitional technologies are required and new challenges for energy storage and energy conversion emerge. Pivotal in the transition to a fully renewable energy landscape is the compensation of power in times of excess or deficient power production. An advantage of combustion fuels such as methane in the form of biogas from biomass or e-methane from power-to-fuel applications, is that existing infrastructure and technologies such as gas turbine power plants and compressed or liquefied natural gas (CNG, LNG) engines can remain in use [193, 194]. However, the main challenge of methane combustion engines, unburned methane in the exhaust gas (methane slip) remains. A 28 times higher global warming potential compared to CO_2 with a contribution of 30 % to current global warming makes it crucial to omit methane emissions [195, 196]. For catalytic CH_4 oxidation in lean conditions, oxide supported Pd catalysts exhibit the highest activity for complete conversion to CO_2 [197, 198]. Typically operated in lean (oxygen-rich) conditions, the Pd nanoparticles (NPs) readily oxidize to PdO under operation [199]. Light-off and steady state experiments have shown that this phase is highly active for catalytic CH_4 oxidation via the Mars-van Krevelen (MvK) mechanism [198, 200, 201]. Typically, the catalysts are calcinated prior to operation, oxidizing the Pd to under common operating conditions stable PdO [199, 202, 203]. Yet, other investigations found that coexistence of metallic Pd and PdO enhances the activity [204–206]. Single crystal studies together with density functional theory were used to identify the PdO(1 0 1) surface as the most active phase [207]. This is explained by the undercoordinated Pd_{cus} and O_{cus} surface species, which are required for the dissociative adsorption of CH_4 [198, 207]. Based on the MvK mechanism on PdO(1 0 1), Stotz *et al.* were able to reproduce experimental, catalytic CH_4 oxidation light-off data for powder catalysts. By taking into account deactivation and size dependent kinetic effects, the CH_4 conversion was calculated using micro-kinetic modeling based on first-principle DFT.

While it is well established that the palladium phase provides the active site for the reaction, the support for the metal(-oxide) nanoparticles can also take part in the reaction. Different properties of the oxide support can influence Pd/PdO stability[201, 204], manage H_2O poisoning[199] or even actively participate in the reaction [198, 208–210]. For CO, an intermediate of catalytic CH_4 oxidation, direct involvement of the support in the catalytic reaction was observed [211]. Similarly, it was shown that oxygen is supplied by supports containing Ce to oxidize PdO_{1-x}[211, 212]. Despite the great

knowledge of the influence of a large number of parameters on the catalysts activity for catalytic CH_4 oxidation, detailed information on the atomic structure during light-off is limited. Furthermore, the mechanisms behind sintering of the porous support and the NPs, both of which are detrimental for the catalysts activity, are not yet established. To answer these questions, we employ model catalysts, offering a degree of complexity in good approximation to industrially used catalyst architectures, while remaining simple enough for highly sensitive measurement techniques and link well to theory [213]. We achieved meaningful correlation of structure and activity during catalytic CH_4 oxidation light-off experiments in a lean reaction gas mixture close to realistic conditions by following the structure and morphology by high-energy grazing incidence X-ray diffraction (HEGIXRD), while simultaneously monitoring the activity by inline mass spectrometry (MS). Influence of the catalyst support on structure and activity was investigated by comparing two catalysts with a $Al_2O_3(0\,0\,0\,1)$ single crystal and a $CeO_2(0\,0\,1)$/YSZ$(0\,0\,1)$ thin film[214] support as representatives for inert and active supports, respectively. Our CH_4 light-off experiments revealed distinct selectivity towards the partial oxidation products CO and CH_2O, depending on the catalyst support. These species were predicted as intermediates of the MvK mechanism [200], but de-/adsorption events were not considered. We linked the impact of adsorbates, intermediates, and the catalytic activity regimes for CO, CH_2O, CO_2, and CO_2 + CO production to the oxidation/reduction behavior of Pd and the mobility and dynamics of the NPs. Furthermore, the distinct sintering and oxidation dynamics could be linked to the availability of oxygen from the support as well as structural interaction between palladium and support phase. The HEGIXRD data further revealed a hydrolyzed alumina phase and $CePd_x$ alloys forming under reaction conditions. Overall, our experiments showed that changes in selectivity, NP oxidation state, and support structure are governed by the local chemical potential at the gas/solid interface of the catalyst and not thermodynamics, defined by operation parameters.

2.2 Results

Activity and Structure During Catalytic CH_4 Oxidation Light-off Experiment. The light-off experiments were conducted with a custom operando catalysis flow reactor with a volume of 23.5 ml, at a pressure of 100 mbar, a constant flow of 100 $\frac{\text{ml}}{\text{min}}$ (20 % O_2, 0.1 % CH_4, and 79.9 % Ar), and a temperature ramp from 411 K to 826 K (5.1 $\frac{\text{K}}{\text{min}}$). The initial state of

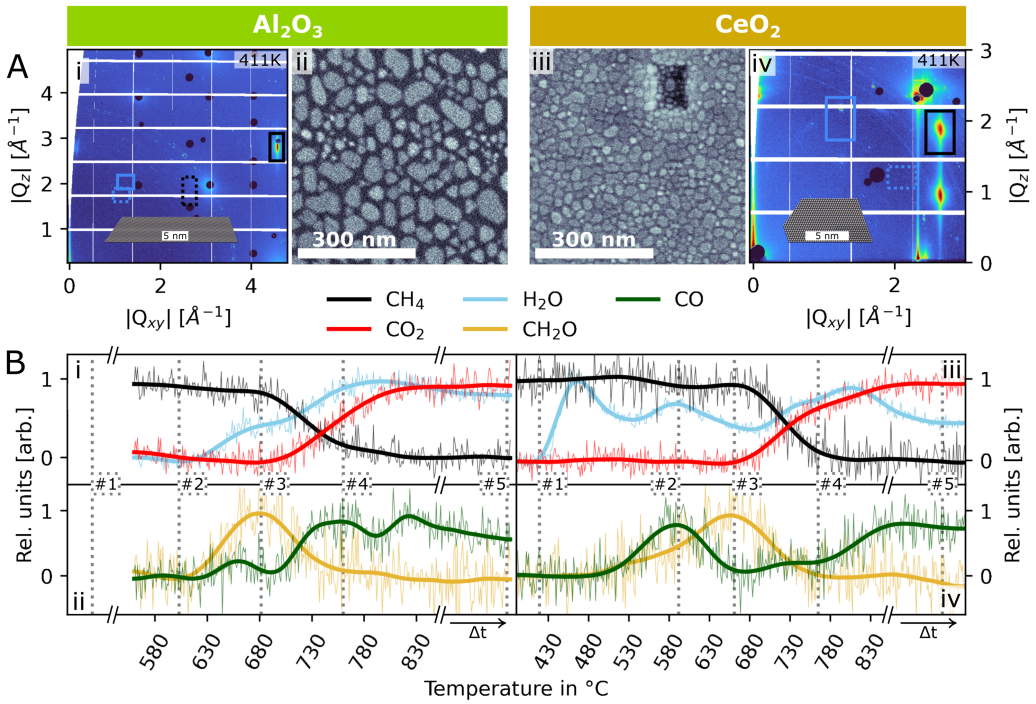

Figure 2.1: High symmetry $(1\,1\,\bar{2}\,0)/(0\,0\,0\,1)$ and $(1\,1\,0)/(0\,0\,1)$ planes (i,iv) and ex situ SEM micrographs (ii,iii) recorded prior to the light-off experiment of Pd/Al_2O_3 and Pd/CeO_2. The micrograph in ii was recorded on an identically prepared sample. The HEGIXRD data was recorded at 411 K in reaction gas mixture. The average NP shape determined from the HEGIXRD data is visualized by the insets, which were constructed by the two most stable facets [215, 216]. The partial pressures of CH_4, H_2O, and CO_2 are shown as a function of temperature in **B** i, and iii and the partial pressures of CH_2O and CO are shown in **B** ii and iv. The original data is shown as a thin line for each signal (smoothened data is shown as a thicker line in the same color). The vertical lines in **B** indicate crucial temperatures for activity and structure.

the catalyst is summarized in Figure 2.1 **A**, showing high symmetry planes of reciprocal space (i,iv) recorded by HEGIXRD at 411 K in reaction gas mixture and SEM images recorded ex situ prior to the light-off experiment (ii,iii). For $Pd/Al_2O_3(0\,0\,0\,1)$, the NP ensemble is epitaxial with the Pd[1 1 1] direction aligned with the support normal (see Section C.2). The average NP diameter and height, calculated from the (1 1 1) Bragg peak broadening, are $D = 31.4\,\text{nm}$ and $H = 5.1\,\text{nm}$ (see Figure 2.3 **B**). For $Pd/CeO_2(0\,0\,1)$ the epitaxy of the majority NP ensemble is identical (details in Section C.2), but the NP shape is distinctly different. The NP model (inset in Figure 2.1 **A** iv) highlights the much larger aspect ratio of 0.37 ± 0.02 ($H = 5.2 \pm 0.1\,\text{nm}$, $D = 14.2 \pm 0.4\,\text{nm}$) compared to the aspect ratio of 0.16 ± 0.00 for Pd/Al_2O_3. Analysis of the SEM micrographs shown in Figure 2.1 **A** ii and iii, confirmed the average diameters determined by GIHEXRD (Section C.3). In case of both catalysts crystal truncation rod signal (see Figure C.2 or movies in SI) was observed indicating the atomic flatness of both supports.
The activity of the catalysts during light-off was tracked by the relative normalized partial pressures (see methods for a detailed description) of CH_4, CO_2, H_2O, CO, and CH_2O at the exhaust line of the reactor (Figure 2.1 **B**). The light-off movies provided in the SI show the complete HEGIXRD data together with the simultaneously recorded, normalized partial pressures. For these temperatures, sections of reciprocal space highlighting the evolution of different Pd and PdO species are shown in Figure 2.2 alongside cartoons of the catalyst structure which are based on the quantitative analysis of the HEGIXRD data (Figure 2.3).

The NP ensemble of the Pd/Al_2O_3 catalyst experienced drastic structural changes already between 411 K and 598 K, prior to catalytic activity (Figure 2.2 **A** #1 to #2). The Pd(1 1 3) Bragg peak became less elongated, strong PdO(1 0 1) and PdO(1 0 0) diffraction signal and a faint Pd(1 1 1) powder ring caused by randomly oriented Pd NPs appeared. The freshly formed PdO phase exhibits the preferential, (0 1 0) and (1 0 1) orientations (see Figure C.24). From the peak broadening, the average diameters of the epitactic Pd, randomly oriented Pd and the PdO domains were determined (see methods) as 17.6 nm, 11.3 nm, and 11.9 nm, respectively. Oxidation of Pd NPs was previously observed at similar pressures and temperatures on $MgO(0\,0\,1)$ [217, 218] and Al_2O_3 [219]. However, the PdO domains' orientations under catalytic CH_4 oxidation reaction conditions do not match observations of Pd NP oxidation experiments [217, 218]. Instead, the observed orientations are similar to results reported for Pd single crystal oxidation [220, 221]. Since no conversion of CH_4 is observed at this temperature, the oxidation behavior is

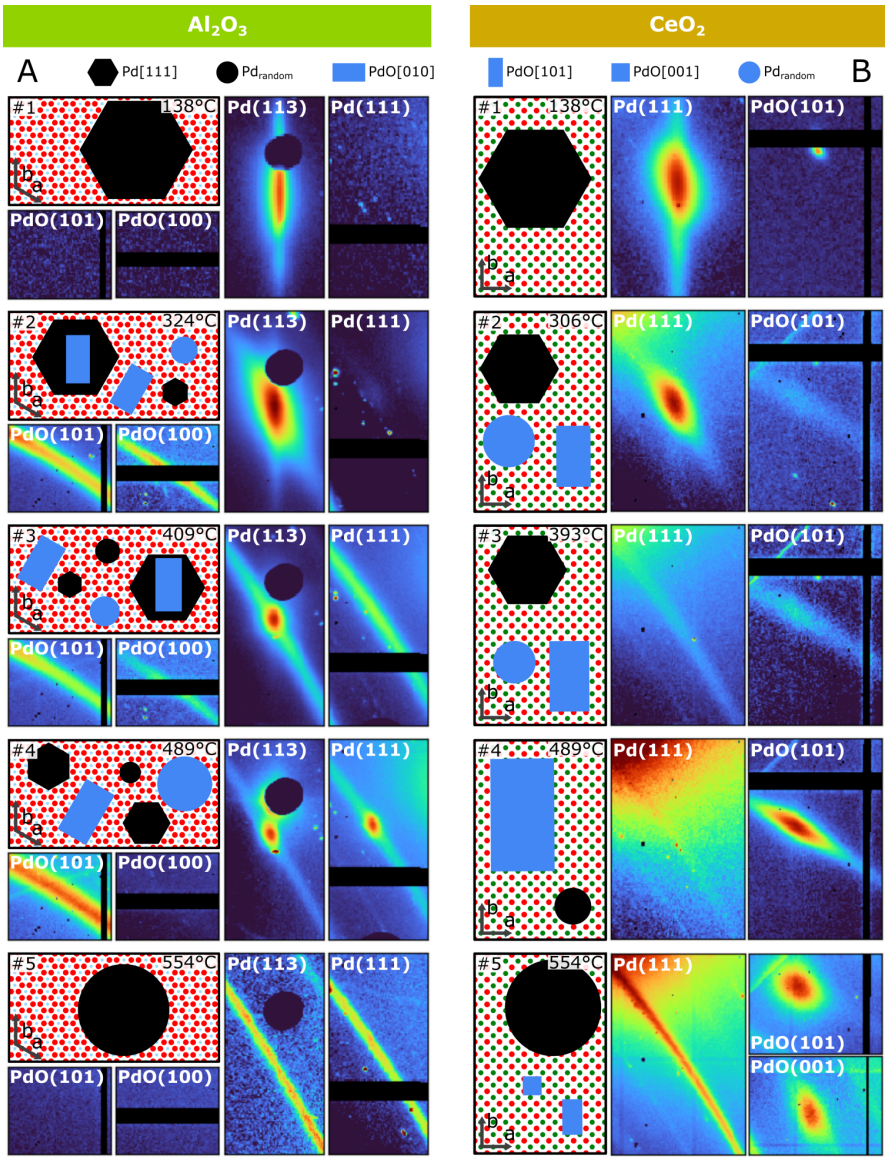

Figure 2.2: Cartoons and sections of reciprocal space extracted at the positions indicated by the rectangles in Figure 2.1. For Pd/Al_2O_3, rectangles with solid edges (black and blue respectively) represent Pd(1 1 3) and PdO(1 0 1) and dotted lines (black and blue respectively) are Pd(1 1 1) and PdO(1 0 0). The temperatures are identical with those indicated by vertical, dotted lines in Figure 2.1. The cartoons reflect the support surface termination and the type of NP domains observed by HEGIXRD (shape, color). The size of the symbols scales with the relative amount of the structural motif (Figure 2.3 **C**).

governed mainly by the applied condition and the NP size [217, 219]. Hence, we assign the (1 0 1) PdO domain to oxide formation in direct contact with metallic Pd and the tilted (0 1 0) PdO domain to full oxide NPs in direct contact with the support. For the formation of the randomly oriented Pd species, oxidation and following reduction of a full NP is required [219]. The smaller size of the randomly oriented Pd NPs may indicate that smaller NPs of the epitactic ensemble were oxidized and subsequently reduced. Since PdO is the thermodynamically stable phase, reduction should occur via interaction with Ch_4, the only reducing agent in the experiment. Thus, we propose reduction of small PdO NPs by partial oxidation of CH_4. The lack of CH_4 conversion and meaningful increase of catalytic oxidation products (OH, H_2O, CO_xH_y) indicates that the products remain on the surface, effectively blocking re-oxidation by $O_{2,g}$. With increasing temperature, partial catalytic oxidation of CH_4 to CH_2O, an intermediate of catalytic CH_4 oxidation [200, 222], is observed with the maximum yield at 682 K (Figure 2.1 **B**). In parallel, reduction of PdO to Pd takes place with a maximum Pd content at the same temperature, leading to a Pd fraction of 0.63 (Figure 2.3). The NP size of the epitactic and randomly oriented NP ensemble increased to 20.0 nm and 16.3 nm respectively, while the PdO domain size remained roughly constant at 11.6 nm. The Pd(1 1 1) diffraction signal became more pronounced and starting at 634 K, the decreasing azimuthal intensity distribution was quantified in Figure 2.3 **A** with a minimum of 12.2 ° at 682 K. Starting at 698 K the activity towards catalytic partial oxidation to CH_2O decreased and the activity regime for complete catalytic oxidation to $CO_2 + H_2O$ and catalytic partial oxidation to CO commences. With it, the azimuthal distribution of the Pd(1 1 1) signal decreases and a new epitaxial Pd species, rotated by 30 ° relative to the original orientation, is formed (Figure 2.3 #4). In addition, the PdO(1 0 0) Bragg peak vanishes by 730 K and the azimuthal distribution of PdO increases. These changes in the azimuthal intensity distribution come to their respective extremes at 747 K which coincides with T_{100} of the CO light off. The high mobility of the NPs necessary for this observation is also reflected in the dynamic behavior of the Pd and PdO NP size. The average PdO NP size first decreases down to 10.3 nm at 730 K and then recovers to 11.3 nm at 763 K while the Pd NP size reaches its maximum at 747 K before dropping again to 18.2 nm for the epitactic NPs and 19.6 nm for the new epitactic Pd NPs. These observations can only be explained by spatially separated, but simultaneous oxidation and reduction of Pd and PdO, respectively. Loss of the PdO[1 0 1], assigned to PdO in contact with Pd likely contributes to the increase in size of the Pd NPs up to 747 K [219]. In the same way, large, free standing PdO NPs with the preferential [1 0 0] orientation are being reduced contributing to the increased size of the 30 °

rotated epitactic NPs and the decrease in the PdO domain size until 730 K (see Figure 2.3). The reversal in the trends of the NP size until 763 K. Upon reversal of the trends, randomly oriented Pd NPs are being oxidized while larger Pd NPs which are better stabilized by the support/NP interface remain stable and form the well pronounced Bragg peaks (Figure 2.2 #4). At the final temperature of 827 K after 60 min time at steady state, the diffraction pattern is dominated by Pd powder rings. Due to thermal expansion of Pd, the (1 0 0) type powder ring of the Be reaction chamber dome overlaps with the Pd powder ring (Figure 2.1 **C** i, 827 K). During the ramp from 763 K to 827 K, drastic sintering was observed for Pd and PdO NPs. The PdO domain size increases to 19.5 ± 2.6 nm at 811 K, the highest temperature at which PdO was observed for Pd/Al_2O_3. Simultaneously, the Pd fraction increases, approaching nearly unity at 811 K (see Figure 2.3 **C**). The coherent NP size of Pd increases up to 38.5 ± 4.6 nm at 827 K at steady state. This is the opposite behavior as for the previous temperature step and caused by reduction of small PdO NPs, decreasing the amount of PdO while simultaneously increasing the average NP size. Despite these changes in the Pd/PdO ratio and NP size, CO_2 production continues to increase while CO production is maintained at a roughly constant level.

Upon starting the light-off experiment for Pd/CeO_2, an increase in H_2O (Figure 2.1 **B** iii) and the Pd NPs' aspect ratio from 0.36 to 0.56 (D = 9.7 nm, H = 5.4 nm) at 449 K was observed. Since thermal effects are negligible, because the growth temperature greatly exceeds the operating temperature, an adsorbate driven mechanism is likely responsible for the mass transport necessary for this shape and size. Starting at 523 K an increase in catalytic partial oxidation to CO + H_2O (not observed for Pd/Al_2O_3) with a simultaneous but more gradual increase in the production of CH_2O is observed. PdO diffraction signal consisting of a textured [1 0 0] oriented (Figure C.24) and a randomly oriented component is first observed at 561 K. At the maximum of CO production (579 K), the PdO(1 0 1) signal yielded an average coherent crystal size of 9.9 nm which remains constant up to 714 K (Figure 2.3). The average Pd domain size increased slightly to 10.2 nm at 579 K with an aspect ratio of 0.73 (see Figure C.21) caused by an increase in height while maintaining the diameter. The decrease in Pd fraction towards 0.5, and the activity for catalytic partial oxidation to CO correlate remarkably well, indicating a competition for adsorbed O_2 species for CH_4 and Pd oxidation. With increasing temperature the selectivity of the catalyst shifts from CO to CH_2O, reaching its maximum at 666 K. Between the peaks of activity for CO and CH_2O production, the conversion of CH_4 remains constant. Hence, comparable amounts of CH_4 are oxidized, which explains the reduced amount of H_2O production observed at 666 K as in the reaction

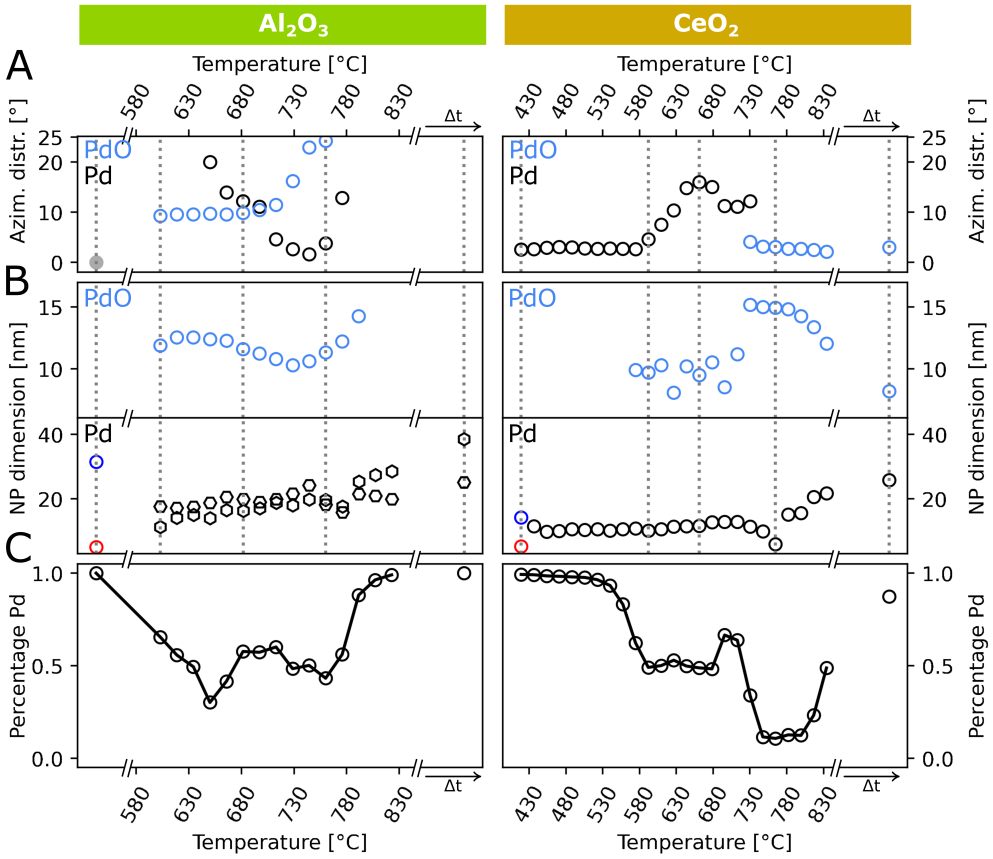

Figure 2.3: The left column of the figure shows the particle properties of Pd/Al_2O_3, the right column, the properties of Pd/Al_2O_3 during the light-off experiments, as determined from the HEGIXRD data. In panel **A** the azimuthal distribution of the Pd(1 1 1) (black) and the PdO(1 0 1) (light blue) diffraction signal around the Bragg peak powder ring is shown, giving insight into particle mobility. In **B** the PdO and Pd NP size is shown, as labeled in the graphs. Here, black markers indicate dimensions from radial, blue from horizontal, and red from vertical scans. In **C**, the ratio of the Pd(1 1 1) powder ring to the PdO(1 0 1) powder ring is shown giving insight into the relative amount of each phase.

$CH_4 + O_2 \longrightarrow CH_2O + H_2O$ only half the amount of water is produced compared to $CH_4 + 1.5\,O_2 \longrightarrow CO + 2\,H_2O$. However, the minimum in H_2O production does not coincide with the peak of CH_2O production. Likely this is due part of the by the reaction produced H_2O or OH groups remaining on the catalyst surface. In previous experiments, we found the (CeO2) thin films to be highly hydrophilic, maintaining a layer of adsorbed water even after annealing in UHV at higher temperatures [214]. Hence, migration to or involvement of CeO_2 in regard to the water balance $H_2O_{ads} \longleftrightarrow H_2O_{(g)}$ is likely. The onset, peak, and decrease azimuthal intensity distribution of the Pd(1 1 1) signal follows the evolution of the CH_2O signal indicating that the NP mobility is linked to the activity towards CH_2O production. Applying the reasoning used in the case of Pd/Al_2O_3, reduction of PdO should occur due to the consumption of PdO during CH_2O production. Reason for the lack in the change of ratio is the overlap with the activity regime for CO and CH_2O production. CO_2 light-off starts at a temperature of 672 K and T_{50} is reached at 730 K, which is both roughly 50 K lower than for Pd/Al_2O_3. Furthermore, the second CO light-off only commences at $T > T_{50}$ instead of simultaneously with the CO_2 light-off as it was observed for Pd/Al_2O_3. At the transition between activity for CH_2O production and full catalytic oxidation, the intensity ratio shifts towards Pd between 698 K and 714 K, indicating further reduction of Pd. Just as for Pd/Al_2O_3, this is due to the kinetic barrier inhibiting oxidation due to poisoning during CH_2O production which is fully lifted at 747 K when Pd is almost completely oxidized (intensity ratio < 0.15). Thus, at this temperature, O_2 incorporation is faster than the consumption by the catalytic reaction. The abrupt decrease in intensity ratio is accompanied by an increase of the PdO domain size by 50 % to 15.2 nm, while the Pd size only decreases gradually. Since the Pd NP size decreases gradually from 12.9 nm at 714 K to 763 K to 6.0 nm, the constant PdO domain size is due to an increase in the amount of PdO domains with increasingly pronounced texture. Comparison to oxidation studies shows the [1 0 0] and [0 0 1] domains are in line with fully oxidized Pd NPs directly on the support [218, 219]. In the last temperature ramp up to 827 K and $t > 60$ min at steady state, a number of structural differences to the previously discussed case for Pd/Al_2O_3 were observed for Pd/CeO_2. Once 827 K is reached a decrease in H_2O production was observed and CO, CO_2, and H_2O production equilibrate at a constant value. A change in the slope of the CO_2 light-off and the 2nd CO light-off occurs when the Pd/CeO_2 catalyst contains PdO as its majority NP phase. At the final measurement point, the Pd domain size increased up to 25.8 ± 0.6 nm and the PdO domain size decreased down to 8.2 ± 0.2 nm. Overall, the sintering is inhibited for Pd/CeO_2 as it only commences at 763 K whereas a roughly constant sintering rate of 0.75 $\frac{\text{nm}}{\text{K}}$ for Pd/Al_2O_3. Upon loss of H_2O

signal in the mass spectra, the Pd/PdO ratio increased again, but with an offset of 32 K compared to the changes in trends for Pd and PdO NP size. Notably, the decrease in H_2O signal appears to take place simultaneously with an increase in (partial) catalytic oxidation products but stagnant CH_4 conversion (see Figure 2.1). Hence, the increased water signal commencing at 666 K is due to increased desorption of surface species OH_{ads} and H_2O_{ads}. This confirms the explanation for the shift in activity from partial catalytic oxidation to CH_2O to partial catalytic oxidation CO_2. Despite the majority of the Pd being oxidized, the at first textured PdO diffraction signal becomes epitactic at the final temperature under steady state. This is nicely visualized in the decreasing azimuthal distribution (Figure 2.3 **A**). Despite the dynamic conditions in high temperatures and under reaction gas atmosphere, which lifted the epitaxial relationship of Pd, epitaxial PdO is formed. This shows that the interaction between the epitaxial PdO species and CeO_2 is stronger than the driving forces of temperature, gas feed, and catalytic reaction at the surface of the NPs, causing full reduction of Pd for Pd/Al_2O_3. This observation expands the model explaining the stabilization of PdO on CeO_2 with a structural component: In addition to the O donator/acceptor role of CeO_2[204], the beneficial interaction at the interface of CeO_2(0 0 1) with PdO(1 0 1) and PdO(0 0 1) stabilizes PdO NPs at operating conditions for which full reduction to Pd was observed for Pd/Al_2O_3. **Post-experimental Characterization**.

Complementary information on the changes of the two catalysts by AFM and SEM is provided in Figure 2.4. The data highlights the distinct influence of the supports on the NP morphology and shows the strong differences in the response of the supports to the light-off experiments.

The large particle size of 40 nm observed for Pd/Al_2O_3 at 827 K after $>$ 60 min at steady state by HEGIXRD is reflected in both the SEM and the AFM data (Figure 2.4 **A**-**C**). The SEM and AFM data reveal that NPs formed large agglomerates that can reach several hundred nanometers in diameter and up to 100 nm in height (Figure C.7). The smaller average NP size from HEGIXRD is consistent with the contrast variation within the particles and agglomerates in SEM Figure C.6, indicating multiple domains per NP and agglomerate. The formation of these large particles most likely started at 747 K when the mobility and fraction of the Pd increases abruptly (Figure 2.3). This shows that at the final temperature of 827 K, the coherent domain size determined by HEGIXRD is still representative for individual particles as parts of larger agglomerates. The support roughness increased significantly (Figure 2.4 **A**,**C**) which shows that considerable mass transport is not only observed for the NPs but also for the support.

In comparison to Pd/Al_2O_3, the SEM and AFM data of Pd/CeO_2 (Figure 2.4

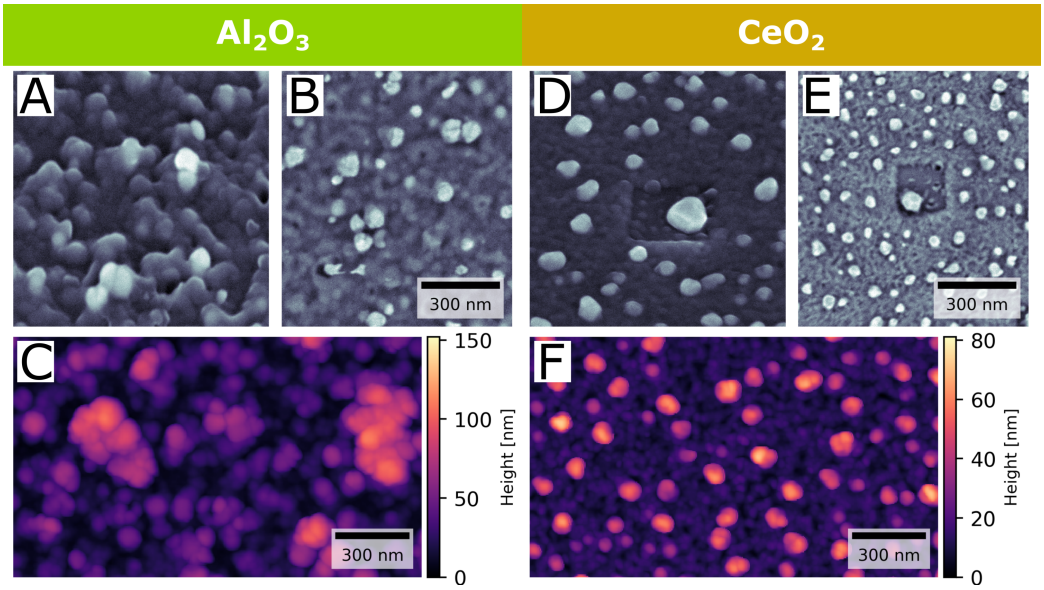

Figure 2.4: SEM micrographs (**A**,**B**,**D**,**E**) and AFM (**C**,**F**) images recorded ex-situ, after the light-off experiment. Data on the left handside of the figure (**A**-**C**) was recorded on Pd/Al_2O_3, data on the right handside (**D**-**F**) on Pd/CeO_2. The SEM micrographs in **A** and **D** were recorded with a sample tilt of 45 °.

D-**F**) reveal a more homogeneous NP distribution and smoother support (compare to Figure 2.4 **A**-**C**). Analysis of the SEM data yielded an NP diameter of 35.4 nm after the light-off experiment (Figure C.6 **D**). The slightly smaller diameter is caused by probing an average domain size of NPs with a height-to-diameter ratio < 1 (Figure 2.4 **D**) and confirms that the coherent domain size determined by HEGIXRD is an excellent approximation of the NP size. The increased surface roughness observed in Figure 2.4 was also followed qualitatively using the (1 1) rod of CeO_2 (Figure C.28). The superior support surface stability is highlighted by comparison of the AFM data. For Pd/CeO_2 a clear distinction between the comparatively smooth support and NPs is straight forward, while for Pd/Al_2O_3, the features of NPs and surface roughness cannot be distinguished from AFM alone.

Chemical Changes of the Supports.

Immense material transport is necessary for the changed surface morphology of the support (Figure 2.4). In the final temperature steps of the light-off experiments, at $Q < 1.5\text{Å}^{-1}$, new diffraction signal was observed that is linked to changes in the respective supports (see Figure 2.5). For Pd/Al_2O_3, this diffraction signal was assigned to the (1 0 1)-type reflection of diaspore (Figure 2.5 **E** i), a hydrated aluminum oxide species with the chemical formula AlO(OH) (Figure 2.5 **A**). The AlO(OH)(1 0 1) powder ring was first observed at 747 K with a domain size of 63 nm (Figure C.11, 763 K) and increases in intensity and size with temperature (98 nm at 827 K and steady state). The hydration reaction to AlO(OH) was not expected, since $\alpha-Al_2O_3$ is the thermodynamically most stable form in the temperature and O pressure regime of the light-off experiment [223, 224]. In fact, the reverse reaction was observed by annealing AlO(OH) in air at similar temperatures [225]. Therefore, we evaluated the thermodynamic stability of diaspore using density functional theory (DFT) with the PBE functional [226, 227]. Its stability is shown as a function of the chemical potential of water μ_{H_2O}, given relative to the total binding energy of one water molecule E_{H_2O} (see Figure 2.5 **B** and Section C.14). Diaspore was only found to be more stable than α-Al_2O_3 at relatively low chemical potentials of water of $\mu_{H_2O} < -0.98\,\text{eV}$. In the temperature range from 714 K to 826 K for which diaspore diffraction signal was observed, a partial pressure of 2000kbar to 30 kbar was At a partial pressure of water of 1 mbar, diaspore would only be expected to form at temperatures higher than 177 K.

For Pd/CeO_2, several powder rings that were assigned to $CePd_5$, CePd and Pd_2O were observed in the temperature range from 811 K to 827 K. Similar to the formation of diaspore, CePdx alloys were note expected to form since the ternary phase diagram of Ce, Pd, and O [228] as well as experimental observations [229] suggest that the experimental conditions in the

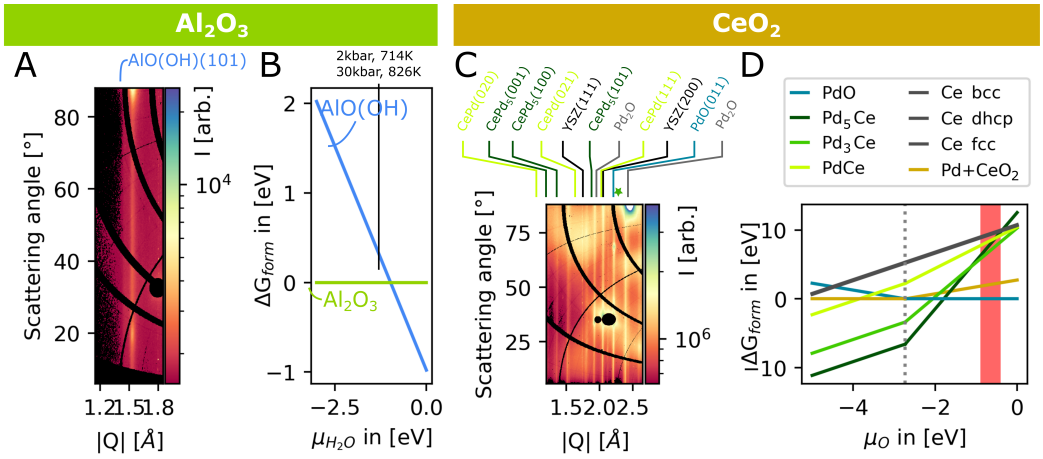

Figure 2.5: High resolution version of low Q area presented in Figure 2.1 **A** for Pd/Al_2O_3 and **C** for Pd/Al_2O_3, recorded at 827 K after dwell time as a function of the total momentum transfer and the azimuthal angle. The colormap is diverging with values above and below the limits of the colormap being colored black and white, emphasizing the weak diffraction signal. In **B** the Gibbs free energy of formation of bulk diaspore is shown as a function of the chemical potential of water and is referenced to bulk α-Al_2O_3 and gas phase H_2O. In **D**, the Gibbs free energy of formation of bulk $CePd_x$ phases is shown as a function of the oxygen chemical potential. The stability of the phases are given relative to CeO_2 and O_2(g) and the more stable of either Pd(fcc) or PdO. The optimized structures for which the Gibbs free energy was calculated are displayed in **E** i-iv. The optimized structural parameters are given in Table C.13. Notably in the AlO(Oh) Al is coordinated with three O^{2-} and three OH^-. Each of the anionic oxygen species is linked to the neighboring OH^- via a hydrogen bridging.

light-off experiment are not sufficiently reducing. In order to relate the reaction conditions in our experiment with the stability of reduced CePdx, the thermodynamic stability of several phases was calculated using PBE-DFT [226, 227] (see Figure 2.5 **D**): The Gibbs free energy of formation of $CePd_x$ phases and Ce bcc, hcp, and fcc (summarized as Ce in Figure 2.5 **D** due to nearly identical values) is given as a function of the oxygen chemical potential μ_O relative to the energy of half a molecule of oxygen in its triplet ground state ($\frac{1}{2}E(O_2)$). The results confirm that $CePd_x$ phases are not expected to be thermodynamically stable at typical partial pressures of O_2(g). For comparison, the range of chemical potential for $p_{O_2} = 20\,\text{mbar}$ probed during the light-off experiment is indicated by the red bar in Figure 2.5 **D** which illustrates that not only the formation of $CePd_x$ but also PdO is not thermodynamically, but kinetically driven.
Overall, both catalysts were active for partial and full catalytic CH_4 oxidation. The catalytic partial oxidation product CH_2O was observed ($T_{100}(CH_2O) = 666\,\text{K}$ for Pd/Al_2O_3 and $650\,\text{K}$ for Pd/CeO_2). In addition, Pd/CeO_2 exhibited low-temperature activity for CO production ($T_{100}(CO) = 579\,\text{K}$) prior to CO_2 light-off. For both catalysts, catalytic partial oxidation to CO was observed in the activity regime for full catalytic oxidation. Over the course of the light-off experiments, sintering was observed for both catalysts, but with strong differences regarding onset temperature and magnitude. In addition, the NPs of both catalysts exhibited a high mobility before and during catalytic CH_4 oxidation as evidenced by the azimuthal intensity distribution. Together with the complementary SEM and AFM data our investigation also revealed significant restructuring of the support and formation of new, thermodynamically unstable phases involving the support ($CePd_x$, AlO(OH)). These observations indicate that the oxidation state of the catalyst NPs and support surface are governed by the local chemical environment instead of thermodynamics inferred from gas feed and temperature.

Structure and Activity

The different activity and selectivity of the two catalysts together with the observed structural differences allows deep insight into the reaction mechanism beyond the scope of an idealized PdO(1 0 1) surface [200, 207]. Furthermore, the catalysts surface area and contact time of the gas feed's molecules with the catalyst surface is strongly limited in our experiment. Hence, compared to traditional packed bed flow reactors, multiple adsorption and desorption events can be excluded and intricate changes in structure and morphology can be observed. Previously, the production of CO from CH_4 (oxidation) by $PtO/Ce_xZr_{1-x}O_2$ [212] and similarly the production of CO from CO_2 (reduction) by CeO_{2-x} lattice oxygen [230] was observed in oxygen-free en-

vironments. Mouaddib *et al.* were able to observe catalytic partial oxidation in oxygen-lean gas feeds for Pd/Al_2O_3, starting at a temperature of 673 K, when the conversion of the catalyst exceeded the oxygen supply [231]. In the context of DFT calculations regarding the first H-abstraction and microkinetic modeling predicting CH_4 conversion, our observations generally implicate the presence of $(P\,d\,O)(1\,0\,1)$ surfaces for H-abstraction but also a lack of available O_{cus} sites, since CO reacts with the O_{cus} site to form $CO_{2(g)}$ and V_O [200, 222, 232]. Furthermore, catalytic CO oxidation has been observed for CO poisoned Pd/CeO_2 by active sites at the Pd/CeO_2 interface [233] indicating that at least a small amount of CO_2 should have been observed if the active site was related to metallic Pd. Similarly, lack of O_{cus} in partially reduced PdO is also an unlikely scenario, since CO is readily oxidized to CO_2 on partially reduced $PdO(1\,0\,1)$ below 573 K [232]. Hence, inhibition of full catalytic oxidation is likely related to OH-poisoning [234, 235], $HO-H_2O$ site blocking [236] or slow diffusion of $O_{cus}-H$ species from the active site which has been shown to have a detrimental effect on activity by hindering O uptake from the gas phase and O release from the catalyst [211]. Since the Pd/CeO_2 catalyst does not host any unique PdO species (see Figure 2.2) and the Pd fraction is nearly identical (see Figure 2.3), the lack of catalytic CH_4 conversion may be attributed to two effects. Firstly, poisoning by partial oxidation products that is indicated by PdO reduction before activity or stabilization of PdO through CeO_2 by providing O to the reaction or for reoxidation of PdO_{1-x} [201, 204, 208, 211]. Yet, Pd/Al_2O_3 should still exhibit activity in the same temperature regime if the support is only related to the inhibition of full catalytic oxidation. Since this is not the case, the support should also play a role in the formation of the active site. We attribute this to the hydrophilicity of $CeO_2(0\,0\,1)$ [214] and O mobility which improves H_2O resistance of catalysts with CeO_2 supports [237, 238]. This makes OH/H_2O poisoned $PdO(1\,0\,1)$ surfaces in close proximity to CeO_2 a likely candidate for the catalytic partial oxidation of CH_4 to CO. Within the reaction mechanism for $PdO(1\,0\,1)$ this would be equivalent to the favored pathway for a wet reaction gas mixture $CH_4 \longrightarrow CH_2 \longrightarrow CH_2O \longrightarrow CO$ instead of $CH_4 \longrightarrow CH_2OH \longrightarrow CH_2O \longrightarrow CO$. This is consistent with the production of CO and CH_2O, since these are the only two intermediates that are also stable, neutral molecules. The lower activity towards to catalytic oxidation to CH_2O can be explained by the fact that the catalytic process itself deactivates the local environment of the active site by reduction [205]. This increased population of V_O and $O_{cus}H$ and $Pd_{cus}-OH$ blocks CO migration from Pd_{cus} to O_{cus}, the last step before O dissociation and CO_2 desorption. Thus, the in parallel occurring Pd oxidation takes place at inactive Pd NPs. With increasing temperature, the activity towards CO

production shifts to CH_2O production for Pd/CeO_2 which is rationalized by an increasing number of adsorbates and O surface vacancies of the PdO(1 0 1) surface which limits the number of sites for H dissociation further. CH_2O production was also observed for Pd/Al_2O_3 with a maximum at 682 K (650 K for Pd/CeO_2). Considering the gas feed composition and reactor pressure, PdO should be stable [201]. This implies for Pd/Al_2O_3 that reduction of PdO to Pd and activity for catalytic partial oxidation of towards CH_2O are linked which is consistent with the MvKm in the catalytic partial oxidation reaction $CH_4 + 2\,PdO \longrightarrow CH_2O + 2\,Pd + H_2O$ [200] and other investigations [205]. On PdO(1 0 1), the intermediate CH_2O is oxidized to CHO by either OH adsorbates on Pd_{cus} ($Pd_{cus}-CH_2O + Pd_{cus}-OH \longrightarrow Pd_{cus}-CHO + Pd_{cus} + H_2O$) or by hydroxylation of a neighboring O_{cus} ($Pd_{cus}-CH_2O + O_{cus} \longrightarrow Pd_{cus}-CHO + O_{cus}-H$) [200, 222]. Thus, these pathways towards full catalytic oxidation and desorption of CH_2O must be blocked for CH_2O desorption to take place. The increasing Pd fraction (Figure 2.3 **C**) in this temperature regime indicates that PdO is being reduced during conversion but cannot be reoxidized efficiently by O_2(g). This has been shown to be due to H_2O and OH adsorbates [200, 211, 236, 239] and is especially relevant for lean reaction gas mixtures. This indicates that the local environment of the active site is strongly altered due to adsorbates produced by the catalytic partial oxidation reaction as no water was added to the gas feed. A similar argument can be made for Pd/CeO_2, where the increase in activity for CH_2O production and decrease in CO production coincides with changes in the particle morphology. Starting at 598 K the azimuthal distribution of the Pd diffraction signal increases from 3 ° for the epitaxial species to 16 ° before decreasing again at higher temperatures. The loss of epitaxy of the Pd signal implies massive mass transport and tilting of NPs, which cannot be explained by thermal effects, because the growth temperature of the particles ($T = 923\,K$) exceeds the maximum temperature during the light-off experiment. Thus, we expect the reduction of PdO to also take place for Pd/CeO_2, but the effect is masked by overlapping with the activity regime for catalytic partial oxidation to CO for which the reduction of PdO to Pd was observed. Instead, the reduction during CH_2O production is observed by the gradual loss of epitaxy, facilitated through $Pd + O \rightleftharpoons PdO$ oxidation/reduction cycles. Such oscillatory oxidation/reduction cycles were previously observed under rich CH_4 oxidation reaction conditions [205, 240]. The full catalytic oxidation product CO_2 was first observed at 666 K for Pd/CeO_2 (714 K for Pd/Al_2O_3). With increasing temperature, the Pd/PdO intensity ratio decreases, showing that the kinetic barrier for water desorption observed during CH_2O production are overcome. With it the oxidation of Pd and reoxidation of V_O of PdO may proceed and full catalytic oxidation takes

place from the point where CH_2O production stagnates. This is especially pronounced for Pd/CeO_2 which exhibits a strong decrease in the Pd fraction following CH_2O production due to the increased O mobility in CeO_2. The CO light-off commences simultaneously to the CO_2 light-off for Pd/Al_2O_3, but for Pd/CeO_2 only after $T_{50}(CO_2)$. This observation correlates with the Pd/PdO ratio which is larger for Pd/Al_2O_3 and upon close inspection, the CO light-off commences at similar Pd/PdO intensity ratios for both catalysts. The increase in the Pd/PdO intensity ratio with increasing production of CO_2 highlights that (1) the catalytic reaction consumes PdO, (2) PdO cannot be replenished faster than it is consumed, and (3) catalytic partial oxidation to CO is related to the amount of metallic Pd. Overall, full catalytic oxidation via the MvKm on PdO(1 0 1) [200] is in excellent agreement with our observations during light-off, before reaching steady state. T At 827 K and steady state, both catalysts are dominated by metallic Pd which makes a Langmuir-Hinshelwood mechanism for catalytic CH_4 oxidation via a O covered Pd surface. Especially the activity for catalytic partial oxidation of CH_4 to CO indicates a lack of O_{cus} species, in line with metallic Pd. Despite that, local oxidation of Pd and instantaneous reduction through the catalytic reaction via the MvK mechanism cannot be dismissed as the activity for catalytic partial oxidation for multiple reasons. Despite that the reaction can still take place via the MvK mechanism on surface oxides [207] which cannot be observed with the experiment design of this work. The typical consumption of PdO for MvKm was observed in the activity regimes for CO and CH_2O at lower temperatures and the degree of reduction observed in our experiments at 827 K cannot be rationalized by thermal reduction or reduction by CH_4 as the temperature is too low and the O_2/CH_4 too large [199, 201, 241]. In addition, the role of surface oxides is not elucidated since the experiments were not sensitive to it. In experiments utilizing CH_4/O_2 ratios as high as $\frac{1}{3}$ at a similar pressure, reduction of PdO was observed for a commercially available Pd NPs in the same temperature regime as our experiment. The unexpected catalytic partial oxidation of CH_4 to CO in parallel to CO_2 production and the observation of catalytic partial oxidation products prior to CO_2 light-off indicates that CH_4 oxidation does not exclusively occur via one adsorption step of CH_4 and its catalytic conversion to CO_2. Instead we propose a pathway via multiple adsorption, oxidation, and desorption steps that were previously not considered [200]. Critical to that observation is that the diffusion and desorption of OH and H_2O moieties on the PdO(1 0 1) surfaces are slow during low temperature activity. For Pd/Al_2O_3 the high concentration of water at the catalyst surface is evidenced by the hydrolysis of Al_2O_3 to Al(OH) which requires an immense H_2O chemical potential as our calculations have shown. An additional indicator are the massive ma-

terial transport leading to the extremely rough support surface observed by AFM and SEM, and the Pd sintering which largely exceeded observations for catalytic CO oxidation experiments [242, 243]. ForCeO_2, the $CePd_x$ alloys allow similar conclusions. For $CeCeO_2$ and the reaction to $CePd_x$, similar conclusions may be drawn. The alloys are thermodynamically far from stable (Figure 2.5 **D**) and the formation cannot be rationalized by the reaction gas mixture or the catalyst temperature. Instead, reduction of CeO_2 and the reaction with Pd could be facilitated via $CeO_2 + 2\,OH \longrightarrow Ce + 2\,H_2O$.

2.3 Conclusion

The HEGIXRD experiments allowed us to follow the transient structure of Pd/Al_2O_3 and Pd/CeO_2 under catalytic CH_4 oxidation up to 827 K. The strong effect of the reaction on the catalyst surface chemistry was also observed in the hydrolysis of Al_2O_3 and reduction and alloying of CeO_2. The calculated Gibbs energy of formation confirmed that the newly formed phases are not thermodynamically stable under the applied conditions. While both catalysts were active for full catalytic CH_4 oxidation, at lower temperatures than the CO_2 light-off differences in the activity for catalytic partial oxidation of CH_4 were observed. Pd/CeO_2 was active for catalytic partial oxidation to CO (579 K) and CH_2O (650 K) while Pd/Al_2O_3 did not show activity for pure CO production prior to the CH_2O activity regime (666 K). Analysis of the diffraction data revealed the highly dynamic catalyst state prior to and during activity for catalytic CH_4 oxidation with oxidation and reduction of Pd NPs taking place simultaneously, but spatially separated. Catalytic partial oxidation products were observed during light-off and in steady state in lean conditions that, to the best of our knowledge, were not reported on previously. The newly observed activity regimes for partial oxidation showed that the migration and desorption probabilities of OH and H_2O are significantly lower than the desorption probability of CO and CH_2O. This also means that if the active sites for catalytic CH_4 oxidation are limited in comparison to the amount of CH_4, the catalytic conversion of CH_4 is itself poisoning the catalyst surface. Furthermore, the absence of these observations in powder or monolithic catalyst studies [198] implicate that full catalytic oxidation may occur via multiple adsorption-reaction-desorption processes, especially at low temperature. Operation under steady state at 827 K showed parallel production of CO_2 and CO, which previously was only observed for understoichiometric reaction gas mixtures [205, 231]. Hence, the observation of CO with a lean reaction gas mixture highlights the lack of reactive oxygen in the vicinity of the active site, even at high temperatures. In addition, this strengthens the hypothesis for multiple desorption and adsorption processes in test reactors or bed reactors, as CO should be readily oxidized at much lower temperatures.

2.4 Methods

Materials.

The $CeO_2(0\,0\,1)$ thin film was grown on YSZ$(0\,0\,1)$ by reactive physical vapor deposition, is fully oxidized, and has an atomically smooth, hydroxylated surface [214]. The film is interrupted by rectangular defects that do not represent a significant portion of the support surface [214]. Prior to deposition the Al_2O_3 sample was degassed for one hour at 923 K and subsequently annealed at 573 K in 1×10^{-6} mbar of O_2. Pd was deposited at a temperature of 923 K from a rod using a EFM 3T triple evaporator. The CeO_2 thin film support was ramped to deposition temperature in 1×10^{-6} of O_2 in order to maintain the oxidation state of CeO_2. Prior to deposition, the O_2 supply was cut. Deposition commenced at a base pressure of $< 1 \times 10^{-9}$ mbar. All steps of the sample preparation were conducted at the DESY NanoLab [244].

Light-off experiments.

The light-off experiments were conducted using a custom-built, HEGIXRD compatible, water cooled operando catalysis chamber in conjunction with a gas mixing system and in-line mass spectrometry [244]. The gas-mixing system allows precise control over the inlet gas mixtures flow and pressure. All parts that are connected to the heater are either graphite (heater power connection), ceramics (heater base), gold (wires) or Mo (nuts, screws) in order to withstand the harsh chemical environment during reaction. At the exhaust the in-line mass spectrometer with a base pressure of $< 1 \times 10^{-9}$ mbar and the inlet leak set to 2×10^{-6} mbar was used to follow the activity of the model catalysts. The baseline of all masses is on the order of $< 10^{-10}$ mbar. At the initial temperature of the light-off experiments, ω-scans (scan of the sample rotation around the surface normal of the sample) were performed to capture the full sample structure. For both samples, an angular range of 100 ° was covered. For the alumina sample, the same scan was performed after the experiment as well. All ω-scans are available as movies in [245].
During the light-off experiment, the sample was heated with a resistive heater. The heating and data collection procedure consists of alternating 220 s heating intervals with a heating rate of $5.1\,\frac{\mathrm{K}}{\mathrm{min}}$ with approximately 165 s long realignment and measurement steps. The realignment and measurement step's duration is on the order of the time the sample needs to reach the target temperature. The realignment consisted of a previously calibrated change of the sample height, scans of the sample height and occasional scans of the incidence angle in order to maintain good sample alignment. For this

purpose, the integrated intensity of ROIs around specular support Bragg reflexes were used. Data collection consisted of the collection of diffraction signal of a single high-symmetry plane ($(1\,\bar{2}\,1\,0)/(0\,0\,0\,1)$ for Pd/Al_2O_3 and $(1\,1\,0)/(0\,0\,1)$ for Pd/CeO_2) of reciprocal space for a duration of 65 s.

Operando data treatment

The mass spectrometry data presented was obtained by integrating spectra with a resolution of 0.1 a.m.u. over $\pm$ 0.3 a.m.u. around the molar mass of each molecule. For CH_4, instead of the molar mass, the mass 15 a.m.u. was chosen to avoid overlap with signal from atomic O fragments from reaction educts and products. Due to fragmentation of CO_2 to CO in the mass spectrometer, the CO signal was corrected by the CO_2 signal as described in Figure C.9 and the accompanying text in the SI. Normalization and filtering of the data presented in Figure 2.1 **B** is described in Section C.5 The frames in Figure 2.1 **C** and the first datapoints in all graphs in Figure 2.3 were extracted from the rocking scans recorded before the temperature ramp of the light-off experiments. For consistency, only the frame corresponding to the angle at which the time series were recorded was used. All other frames in Figure 2.1 and datapoints in Figure 2.3 were recorded during the temperature ramp. The HEGIXRD data in Figure 2.4 are sections of reciprocal space from the last recorded dataset at 827 K after $t > 60$ min at steady state. The data was transformed to show the total momentum transfer $|Q|$ (radius in images in Q_{xy}/Q_z) on the abscissa and the azimuthal angle (angle from abscissa) on the ordinate.

SEM.

The SEM data was recorded with a high resolution field-emission SEM at the DESY NanoLab. All SEM images were recorded using an accelerating voltage of 5 kV and a concentric back-scattered (CBS) detector, achieving a lateral resolution of $\sim$ 1 nm [244].

AFM.

The AFM measurements were conducted at the DESY NanoLab using tapping mode (in air) and oxide-sharpened silicon cantilevers with a nominal tip radius of 8 nm and a resonance frequency of 300 kHz [244]. For all measurements a scanning speed of 0.5 Hz was used. A polynomial plane fit was used to account for sample tilt during the measurement.

Computational details.

Density functional theory (DFT) calculations with periodic boundary conditions were conducted using the Vienna Ab initio Simulation Package (VASP) in version 5.4.1.[246, 247] The calculations employed the PBE functional [226, 227] and the projector-augmented wave[248] (PAW) method with standard PAW potentials. An energy cutoff of 500 eV, D3 dispersion correction with Becke-Johnson damping Ref, and a Hubbard correction [249] with a value of $U = 5\,\text{eV}$ and $J = 0\,\text{eV}$ for the f-orbitals of Ce were used.

Declarations

2.4.1 Acknowledgements

This work was supported by the Deutsche Forschungsgemeinschaft, Germany (DFG, German Research Foundation) via SFB 1441, Project-ID 426888090. We acknowledge DESY (Hamburg, Germany), a member of the Helmholtz Association HGF, for the provision of experimental facilities. We acknowledge the European Synchrotron Radiation Facility (ESRF) for provision of synchrotron radiation facilities under proposal number CH6401 and we would like to thank Andrea Sartori for assistance and support in using beamline ID31. We further would like to acknowledge the work of Dennis Renner and Simon Geile for technical support in the UHV- and X-ray laboratories.

2.4.2 Competing intersts

The authors declare that they have no competing interests.

Bibliography

(193) Aakko-Saksa, P. T. et al. Reduction in greenhouse gas and other emissions from ship engines: Current trends and future options. *Prog. Energy Combust. Sci.* **2023**, *94*, 101055.

(194) Kalz, K. F. et al. Future Challenges in Heterogeneous Catalysis: Understanding Catalysts under Dynamic Reaction Conditions. *Chem. Cat. Chem.* **2017**, *9*, 17–29.

(195) *Climate change 2013: The physical science basis*; Stocker, T., Ed.; Cambridge University Press: New York, 2013.

(196) *Climate change 2022: Mitigation of climate change*; Shukla, P. R., Skea, J., Reisinger, A. R., Eds.; IPCC: 2022.

(197) Trinchero, A.; Hellman, A.; Grönbeck, H. Methane oxidation over Pd and Pt studied by DFT and kinetic modeling. *Surf. Sci.* **2013**, *616*, 206–213.

(198) Lott, P.; Casapu, M.; Grunwaldt, J.-D.; Deutschmann, O. A review on exhaust gas after-treatment of lean-burn natural gas engines – From fundamentals to application. *Appl. Catal. B Environ.* **2024**, *340*, 123241.

(199) Murata, K.; Ohyama, J.; Yamamoto, Y.; Arai, S.; Satsuma, A. Methane Combustion over Pd/Al_2O_3 Catalysts in the Presence of Water: Effects of Pd Particle Size and Alumina Crystalline Phase. *ACS Catal.* **2020**, *10*, 8149–8156.

(200) Stotz, H. et al. Surface reaction kinetics of methane oxidation over PdO. *J. Catal.* **2019**, *370*, 152–175.

(201) Farrauto, R.; Lampert, J.; Hobson, M.; Waterman, E. Thermal decomposition and reformation of PdO catalysts; support effects. *Appl. Catal. B Environ.* **1995**, *6*, 263–270.

(202) Jang, E. J.; Lee, J.; Oh, D. G.; Kwak, J. H. CH 4 Oxidation Activity in Pd and Pt–Pd Bimetallic Catalysts: Correlation with Surface PdO_x Quantified from the DRIFTS Study. *ACS Catal.* **2021**, *11*, 5894–5905.

(203) Wu, Y. et al. Phase transformation and oxygen vacancies in Pd/ZrO_2 for complete CH_4 oxidation under lean conditions. *J. Catal.* **2019**, *377*, 565–576.

(204) Nilsson, J. et al. Chemistry of Supported Palladium Nanoparticles during Methane Oxidation. *ACS Catal.* **2015**, *5*, 2481–2489.

(205) Yue, S. et al. Redox dynamics and surface structures of an active palladium catalyst during methane oxidation. *Nat. Commun.* **2024**, *15*, 4678.

(206) Carstens, J. N.; Su, C. S.; Bell, A. T. Factors Affecting the Catalytic Activity of Pd/ZrO_2 for the Combustion of Methane. *J. Catal.* **1998**, *176*, 136–142.

(207) Hellman, A. et al. The Active Phase of Palladium during Methane Oxidation. *J. Phys. Chem. Lett.* **2012**, 678–682.

(208) Huang, F. et al. Pd or PdO: Catalytic active site of methane oxidation operated close to stoichiometric air-to-fuel for natural gas vehicles. *Appl. Catal. B Environ.* **2017**, *219*, 73–81.

(209) Colussi, S.; Fornasiero, P.; Trovarelli, A. Structure-activity relationship in Pd/CeO_2 methane oxidation catalysts. *Chin. J. Catal.* **2020**, *41*, 938–950.

(210) Montini, T.; Melchionna, M.; Monai, M.; Fornasiero, P. Fundamentals and Catalytic Applications of CeO_2-Based Materials. *Chem. Rev.* **2016**, *116*, 5987–6041.

(211) Ciuparu, D.; Pfefferle, L. Contributions of lattice oxygen to the overall oxygen balance during methane combustion over PdO-based catalysts. *Catal. Today* **2002**, *77*, 167–179.

(212) Bozo, C.; Guilhaume, N.; Herrmann, J.-M. Role of the Ceria–Zirconia Support in the Reactivity of Platinum and Palladium Catalysts for Methane Total Oxidation under Lean Conditions. *J. Catal.* **2001**, *203*, 393–406.

(213) Chen, S.; Xiong, F.; Huang, W. Surface Chemistry and Catalysis of Oxide Model Catalysts from Single Crystals to Nanocrystals. *Surf. Sci. Rep.* **2019**, *74*, 100471.

(214) Schober, J.-C. et al. Atomically Smooth Fully Hydroxylated CeO_2(0 0 1) Films on YSZ(0 0 1). *J. Phys. Chem. C* **2024**, *128*, 19795–19806.

(215) Kabalan, L.; Kowalec, I.; Catlow, C. R. A.; Logsdail, A. J. A computational study of the properties of low- and high-index Pd, Cu and Zn surfaces. *Phys. Chem. Chem. Phys.* **2021**, *23*, 14649–14661.

(216) Müller, P.; Kern, R. Equilibrium nano-shape changes induced by epitaxial stress (generalised Wulf-Kaishew theorem). *Surf. Sci.* **2000**, *457*, 229–253.

(217) Nolte, P. et al. Combinatorial high-energy x-ray microbeam study of the size-dependent oxidation of Pd nanoparticles on MgO(100). *Phys. Rev. B* **2008**, *77*, DOI: 10.1103/PhysRevB.77.115444.

(218) Kasper, N. et al. In situ oxidation study of MgO(100) supported Pd nanoparticles. *Surf. Sci.* **2006**, *600*, 2860–2867.

(219) Nolte, P. In situ Oxidation Study of Supported Rh and Pd Nanoparticles, Dissertation, Stuttgart: Institue for Theoretical and Applied Physics University of Stuttgart, 2009.

(220) Kasper, N.; Nolte, P.; Stierle, A. Stability of Surface and Bulk Oxides on Pd(111) Revisited by in Situ X-ray Diffraction. *J. Phys. Chem. C* **2012**, *116*, 21459–21464.

(221) Zhang, D. et al. An In situ TEM study of the surface oxidation of palladium nanocrystals assisted by electron irradiation. *Nanoscale* **2017**, *9*, 6327–6333.

(222) van den Bossche, M.; Grönbeck, H. Methane Oxidation over PdO(101) Revealed by First-Principles Kinetic Modeling. *J. Am. Chem. Soc.* **2015**, *137*, 12035–12044.

(223) Lin, J.-F. et al. Crystal structure of a high-pressure/high-temperature phase of alumina by in situ X-ray diffraction. *Nat. Mater.* **2004**, *3*, 389–393.

(224) Liu, Y. et al. Prediction of new thermodynamically stable aluminum oxides. *Sci. Rep.* **2015**, *5*, 9518.

(225) Löffler, L.; Mader, W. Electron microscopic study of the dehydration of diaspore. *Am. Mineral.* **2001**, *86*, 293–303.

(226) John P. Perdew; Kieron Burke; Matthias Ernzerhof Generalized Gradient Approximation Made Simple. *Phys. Rev. Lett.* **1996**, *77*, 3865–3868.

(227) Perdew, J.; Borke, K.; Ernzerhof, M. Generalized Gradient Approximation Made Simple. *Phys. Rev. Lett.* **1997**, *78*, 1396.

(228) Jacob, K. T.; Muraleedharan, S. Phase equilibria in the system Ce-Pd-O. *Calphad* **2019**, *66*, 101640.

(229) Götsch, T. et al. Formation of Pd-Ce intermetallic compounds by reductive metal-support interaction. *J. Solid State Chem.* **2018**, *265*, 176–183.

(230) Sharma, S.; Hilaire, S.; Vohs, J. M.; Gorte, R. J.; Jen, H.-W. Evidence for Oxidation of Ceria by CO2. *J. Catal.* **2000**, *190*, 199–204.

(231) Mouaddib, N.; Feumi-Jantou, C.; Garbowski, E.; Primet, M. Catalytic oxidation of methane over palladium supported on alumina: Influence of the oxygen-to-methane ratio. *Appl. Catal. A Gen.* **1992**, *87*, 129–144.

(232) Zhang, F. et al. CO Oxidation on PdO(101) during Temperature-Programmed Reaction Spectroscopy: Role of Oxygen Vacancies. *J. Phys. Chem. C* **2014**, *118*, 28647–28661.

(233) Gänzler, A. M. et al. Unravelling the Different Reaction Pathways for Low Temperature CO Oxidation on Pt/CeO_2 and Pt/Al_2O_3 by Spatially Resolved Structure-Activity Correlations. *J. Phys. Chem. Lett.* **2019**, *10*, 7698–7705.

(234) Li, X.; Wang, X.; Roy, K.; van Bokhoven, J. A.; Artiglia, L. Role of Water on the Structure of Palladium for Complete Oxidation of Methane. *ACS Catal.* **2020**, *10*, 5783–5792.

(235) Zhang, F.; Hakanoglu, C.; Hinojosa, J. A.; Weaver, J. F. Inhibition of methane adsorption on PdO(101) by water and molecular oxygen. *Surf. Sci.* **2013**, *617*, 249–255.

(236) Kan, H. H.; Colmyer, R. J.; Asthagiri, A.; Weaver, J. F. Adsorption of Water on a PdO(101) Thin Film: Evidence of an Adsorbed HO–H_2O Complex. *J. Phys. Chem. C* **2009**, *113*, 1495–1506.

(237) Senftle, T. P.; van Duin, A. C. T.; Janik, M. J. Methane Activation at the Pd/CeO_2 Interface. *ACS Catal.* **2017**, *7*, 327–332.

(238) Gholami, R.; Alyani, M.; Smith, K. J. Deactivation of Pd Catalysts by Water during Low Temperature Methane Oxidation Relevant to Natural Gas Vehicle Converters. *Catalysts* **2015**, *5*, 561–954.

(239) Mihai, O.; Smedler, G.; Nylén, U.; Olofsson, M.; Olsson, L. The effect of water on methane oxidation over Pd/Al_2O_3 under lean, stoichiometric and rich conditions. *Catal. Sci. Technol.* **2017**, *7*, 3084–3096.

(240) Bychkov, V. et al. Self-oscillations during methane oxidation over Pd/Al_2O_3: Variations of Pd oxidation state and their effect on Pd catalytic activity. *Appl. Catal. A Gen.* **2016**, *522*, 40–44.

(241) Su, S. C.; Carstens, J. N.; Bell, A. T. A Study of the Dynamics of Pd Oxidation and PdO Reduction by H_2 and CH_4. *J. Catal.* **1998**, *176*, 125–135.

(242) Hejral, U.; Müller, P.; Balmes, O.; Pontoni, D.; Stierle, A. Tracking the shape-dependent sintering of platinum-rhodium model catalysts under operando conditions. *Nat. Commun.* **2016**, *7*, 10964.

(243) Hejral, U. et al. Composition-Dependent Alloy Nanoparticle Shape Changes under Reaction Conditions: Kinetic and Thermodynamic Effects. *J. Phys. Chem. C* **2024**, *128*, 4330–4342.

(244) Stierle, A.; Keller, T. F.; Noei, H.; Vonk, V.; Roehlsberger, R. DESY NanoLab. *J. Large-Scale Res. Facil.* **2016**, *2*, A76.

(245) Schober, J.-C. Light-off movies of Pd/Al_2O_3 and Pd/CeO_2 CH_4 Catalysts `https://bib-pubdb1.desy.de/record/636106`.

(246) Kresse, G.; Furthmüller, J. Efficient iterative schemes for ab initio total-energy calculations using a plane-wave basis set. *Phys. Rev. B* **1996**, *54*, 11169–11186.

(247) Kresse, G.; Furthmüller, J. Efficiency of ab-initio total energy calculations for metals and semiconductors using a plane-wave basis set. *Comput. Mater. Sci.* **1996**, *6*, 15–50.

(248) Blöchl, P. E. Projector augmented-wave method. *Phys. Rev. B.* **1994**, *50*, 17953.

(249) Anisimov, V.; Zaanen, J.; O.K., A. Band theory and Mott insulators: Hubbard U instead of Stoner I. *Phys. Rev.* **1991**, *44*, 943.

3. Methane Induced Sintering of Catalytic Nanoparticles in Spatially Confined Geometries on CeO_2 Supports

Outline

Author Contribution

I am responsible for sample preparation, experiment design and execution of the experiments. Arno Jeromin carried out the SEM measurements.

3.1 Introduction

Sintering is a deactivation process observed for Pd based catalysts for catalytic CH_4 oxidation. Especially prevalent at high temperature, the increase in nanoparticle volume and thus decrease in the surface area, causes loss in activity since the nanoparticle surfaces host the active sites for CH_4 dissociation and activation [250]. A large number of approaches to inhibit sintering have been reported [250]. One option is the addition of other metals like Pt to the Pd nanoparticles which causes the formation of a PdO shell around the Pt rich core [251, 252]. Interaction of the metallic core stabilizes the surface layer which causes the sintering inhibition. A different approach is support engineering which exploits the different interaction of NPs with the support [250, 253]. For Au/CeO_{2-x} the strong metal support interaction inhibits nanoparticle mobility whereas for Au/SiO_2 the weak interaction leads to high mobility which causes sintering by coalescence [254]. A similar effect between Al_2O_3 and CeO_2 has been exploited for Pd clusters, which exhibited great resistance to sintering. Pd clusters where isolated on CeO_2 islands on an Al_2O_3 support. Due to the weak interaction with Al_2O_3 the Pd species remained on the CeO_2 islands during CO oxidation [255].
On $CeO_2(1\,1\,1)$ different mechanisms prevail depending the NP size. For small NPs of $< 5\,\text{nm}$, Ostwald ripening is the dominating process [256] due to high mobility of single Pd atoms on CeO_2 compared to clusters [257]. Diffusion has been reported to take place via a Pd_1O_4 complex [258] under operation at low temperatures, when Pd is oxidized, whereas at high temperature a Pd_1O_2 complex facilitates diffusion. For larger nanoparticles ($> 7\,\text{nm}$) coalescence becomes the dominant process [256].
The following chapter is a case study of the Pd/CeO_2 catalyst from Chapter 2. The CeO_2 film (see Chapter 1) contains holes which penetrate the film. The formation was described as agglomeration of oxygen vacancies

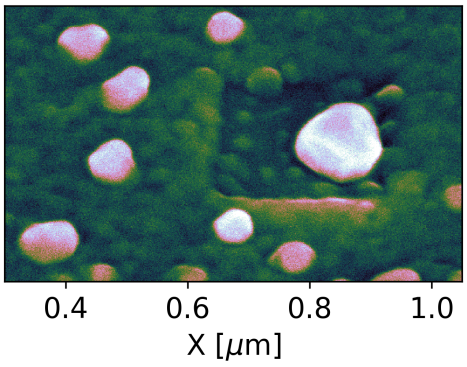

Figure 3.1: Closeup of the data presented in Figure 2.4 **D**. A dynamic colormap with constant perceived brightness was chosen to highlight the NPs without hiding the support structure.

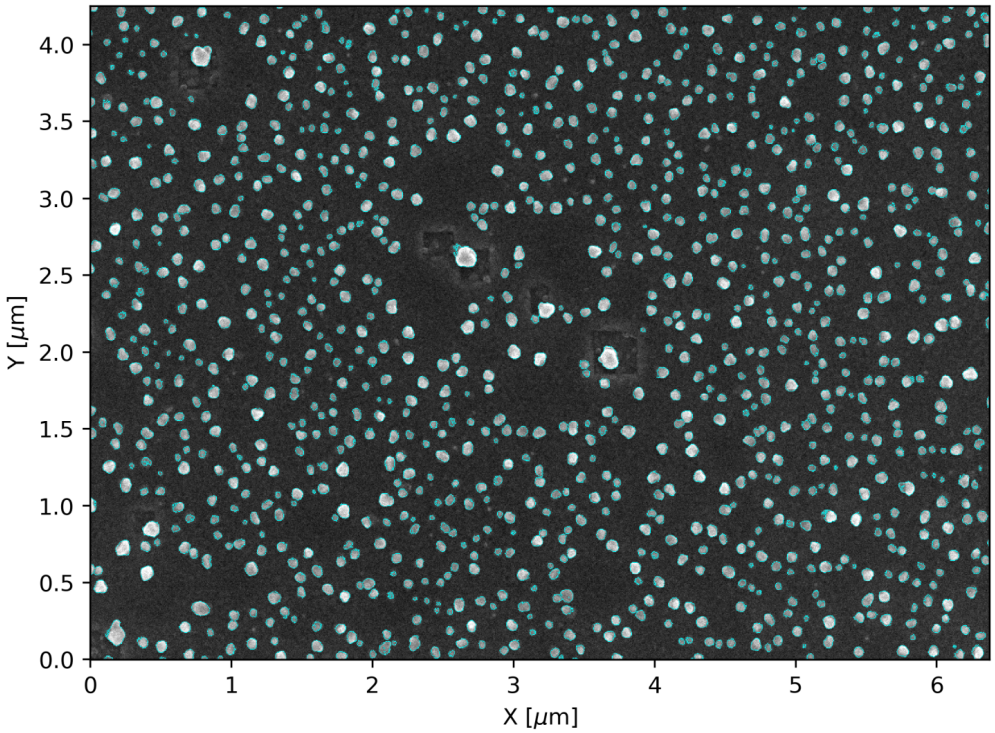

Figure 3.2: SEM image with outlines used for NP size determination of NPs on the CeO_2 film.

and offers the opportunity to study the difference in sintering between the NPs that remain on the film and NPs that are located in the holes after the catalytic experiment (see Figure 3.1). The statistical analysis revealed a pronounced size difference between the nanoparticles with NPs in the holes being significantly larger. Furthermore, holes that contain large NPs are often surrounded by a depletion area with significantly lower NP density.

3.2 Experiment & Results

Analysis of the SEM data of Pd/CeO_2 (Chapter 2) revealed a significant difference in the NP size of NPs on top of the CeO_2 film and in the holes of the CeO_2 film. In Figure 3.1 a close up SEM image is shown, recorded at an angle of 45 °. As described in Chapter 1, the holes are a scarce, local phenomenon and initially only few holes were observed at random locations on the sample. In order to quantify the apparent size difference between NPs on the film and in the holes of the film (see Figure 3.1), an extensive SEM

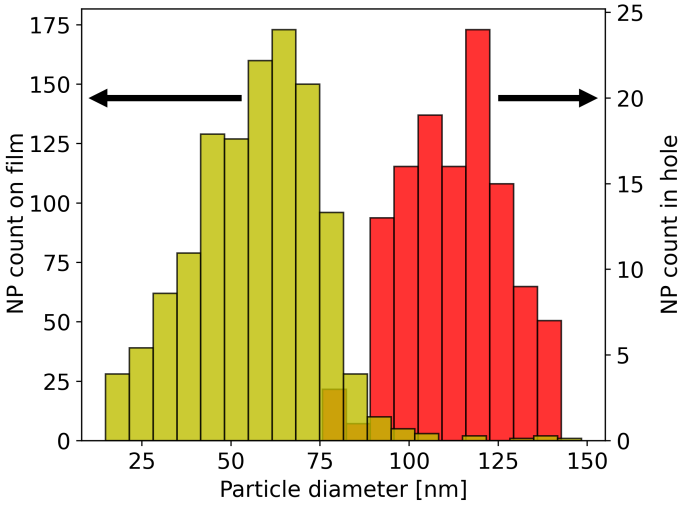

Figure 3.3: Histogram of the SEM analysis of NP diameters of NPs on the CeO_2 film (yellow) and NPs in the holes (red). The bin width of both histograms is identical.

study was conducted. The complete dataset (see Section D.3) was recorded with a high resolution field-emission SEM at the DESY NanoLab using an accelerating voltage of 5 kV and a through lens detector (TLD), achieving a lateral resolution of $\sim$ 1 nm [259]. The sample was scanned for areas with a high density of holes and a number of large overview images were recorded in order to accumulate a statistically relevant number of NPs in holes. The selected areas are shown in Section D.3 and a total of 123 NPs in holes were evaluated. In Section D.1, a detailed description of the semi automatic analysis approach is given. For the comparison with NPs on the film, a high resolution image of Figure D.9 was used (see Figure 3.2) and a total of 1095 NPs were evaluated with a total of 1081 being on the film and 14 being next to the film.

The resulting histogram shows two distributions with an average diameter of 57 nm for NPs on the film (yellow) and 113 nm for NPs in the holes. The small bars of the histogram of NPs on the film overlapping with the histogram of NPs in the holes are the NPs of Figure 3.3 that are located in the hole. The histogram of NPs on the film exhibits an untypical negatively skewed Gaussian shape and an abrupt diameter cut-off at 80 nm. The shape suggests that the sintering process is limited to this diameter for NPs on the film. In contrast, the histogram of NPs in the holes is more symmetric and seems to be positively skewed with a diameter cutoff at 90 nm at

the lower end. In comparison the histogram recorded before the experiment (Figure C.6) exhibits a typical LogNorm distribution, which is commonly observed for NPs.
The inversion of the diameter histogram of NPs on the film indicates that the maximum diameter for growth is limited and that this limitation is not relevant for the NPs in the hole. Figure 3.4 shows a proposed mechanism leading to the limited sintering of NPs on the film and the much larger NPs in the hole. Due to the very limited mobility of Pd on CeO_2 [255, 256, 258], the NPs sinter predominantly via Ostwald ripening. Coalescence would require the mobility of full NPs, which is already limited for the neutral $CeO_2(1\,1\,1)$ surface. Already starting from a cluster size of 5 Pd atoms, the detachment energy of a single Pd atom becomes smaller than the energy required for cluster migration [257]. However, in Chapter 1 it was shown that the surface is strongly hydroxylated, which is likely still the case under operation as strong evidence for OH inhibition was observed under operation [260] (see Chapter 2). While the exact mechanism and dependence of NP size and catalytic conditions of OH adsorbates on nanoparticles is still under discussion, it was shown that single atom Pd sites are stabilized by surface OH groups on CeO_2 forming a $OH-PdO_4$ complex [261]. At the same time, other adsorbates such as CO promote Pd mobility on $CeO_2\{1\,1\,1\}$ [257].
Overall, the observed NP morphology in SEM and the current state of literature suggest that the (0 0 1) terminated film increases kinetic barriers for sintering, by immobilizing atoms and NPs by the stronger interaction of the more polar (0 0 1) surface. The SEM data (see Section D.3 or Figure 3.2) supports this hypothesis, as NPs are overall homogeneously distributed and no indication of agglomeration is observed, indicating that NPs are largely immobile. Hence, sintering occurs via the diffusion of atomic Pd (Ostwald ripening), which is highly dependent on the NP size. With increasing size, the energy required for the dissolution of Pd atoms from the NP becomes larger [257]. In addition the mobility of Pd is strongly inhibited due to the hydroxylated surface [261]. Thus, the shape change of the histograms of NPs on the film before and after the light-off experiment is caused by diffusion-limited Ostwald ripening. First, larger NPs grow at the cost of smaller NPs dissolving, leading to fewer but larger NPs. As result of the increased size, less material is provided by the larger NPs and larger distances between the NPs must be overcome by OH inhibited diffusion. In combination this results in a larger number of similarly sized large NPs and fewer, smaller NPs which would slowly dissolve as a function of time. The same argument applies to the NPs in the holes, with one key difference: The holes pose a kinetic diffusion barrier which allows material transport from the film into the hole, but not vice-versa. In fact, this does not require a larger diffusion barrier

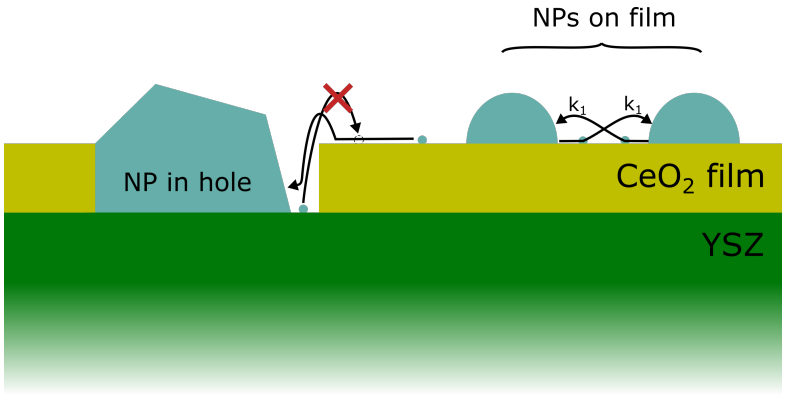

Figure 3.4: Model of proposed sintering mechanism for NPs in holes and on the CeO_2 film.

for the path from the hole onto the film, since the geometric confinement by the diffusion barrier in the hole increases the probability for recombination with the NP in the hole. Thus, the large size difference between NPs in the holes and on the films means that the hole edges pose a significant diffusion barrier which leads to a growth rate of NPs in the holes being two times the growth rate of the NPs on the film when the NPs on the film approach their size limit.

Bibliography

(250) Lott, P.; Casapu, M.; Grunwaldt, J.-D.; Deutschmann, O. A review on exhaust gas after-treatment of lean-burn natural gas engines – From fundamentals to application. *Appl. Catal. B Environ.* **2024**, *340*, 123241.

(251) Jiang, D.; Khivantsev, K.; Wange, Y. Low-Temperature Methane Oxidation for Efficient Emission Control in Natural Gas Vehicles: Pd and Beyond. *ACS Catal.* **2020**, *10*, 14304–14314.

(252) Nie, H.; Howe, J. Y.; Lachkov, P. T.; Chin, Y.-H. C. Chemical and Structural Dynamics of Nanostructures in Bimetallic Pt-Pd Catalysts, Their Inhomogeneity, and Their Roles in Methane Oxidation. *ACS Catal.* **2019**, *9*, 5445–5461.

(253) Divins, N. J. et al. Investigation of the evolution of Pd-Pt supported on ceria for dry and wet methane oxidation. *Nat. Commun.* **2022**, *13*, 5080.

(254) Liu, J.-C. et al. Metal Affinity of Support Dictates Sintering of Gold Catalysts. *J. Am. Chem. Soc.* **2022**, *144*, 20601–20609.

(255) Gashnikova, D. et al. Highly Active Oxidation Catalysts through Confining Pd Clusters on CeO_2 Nano-Islands. *Angew. Chem. Int. Ed.* **2024**, *63*, e202408511.

(256) Gholami, R.; Alyani, M.; Smith, K. J. Deactivation of Pd Catalysts by Water during Low Temperature Methane Oxidation Relevant to Natural Gas Vehicle Converters. *Catalysts* **2015**, *5*, 561–954.

(257) Su, Y.-Q.; Liu, J.-X.; Filot, I. A. W.; Hensen, E. J. M. Theoretical Study of Ripening Mechanisms of Pd Clusters on Ceria. *Chem. Mater.* **2017**, *29*, 9456–9462.

(258) Zou, C. et al. Two Distinct Oxidation Dispersion Mechanisms in Pd-CeO_2 Mediated by Thermodynamic and Kinetic Behaviors of Highly Dispersed Pd Species. *Phys. Rev. Lett.* **2025**, *134*, 218001.

(259) Stierle, A.; Keller, T.; Noei, H.; Vonk, V.; Roehlsberger, R. DESY NanoLab. *J. Large-Scale Res. Facil.* **2016**, *2*, A76.

(260) Li, X.; Wang, X.; Roy, K.; van Bokhoven, J. A.; Artiglia, L. Role of Water on the Structure of Palladium for Complete Oxidation of Methane. *ACS Catal.* **2020**, *10*, 5783–5792.

(261) An, Y. et al. Sintering resistance of Pd single atoms on steam-modified ceria: deciphering the role of hydroxyl groups. *J. Mater. Chem. A* **2023**, *11*, 21285–21292.

4. Pd_xPt_y/Al_2O_3 Nanoparticle Sintering Kinetics During Catalytic CH_4 Oxidation

Outline

Status of Manuscript

This chapter is presented in manuscript format and is based on original, unpublished research. The manuscript is currently in preparation and has not yet been submitted for peer review.

Author list:
Jan-Christian Schober[1,2], Lydia Bachmann[1,2], Daniel Silvan Dolling[1,2], Mohammad Ebrahim Haji Naghi Tehrani[1,2], Jagrati Dwivedi[1], Andrea Sartori [3], Arno Jeromin [1], Andreas Stierle [1]
[1]Centre for X-ray and Nano Science, Deutsches Elektronen-Synchrotron DESY, 22607 Hamburg, Germany
[2]Universität Hamburg, 20148 Hamburg, Germany
[3]European Synchrotron Radiation Facility, Grenoble 38000, France

Author Contribution

I am responsible for sample preparation, experiment design and execution, and the entirety of data analysis. The beamtime experiments were carried out collaboratively with Lydia Bachmann, Daniel Silvan Dolling, Jagrati Dwivedi, Mohammad Ebrahim Haji Naghi Tehrani, Andrea Sartori, and Andreas Stierle. Arno Jeromin carried out the SEM and AFM measurements.

Copyright Notice

4.1 Introduction

Catalytic CH_4 oxidation is a critical process for emission control and energy conversion due to the immense global warming potential of CH_4 in the atmosphere [262, 263]. Currently, the most effective approach are heterogeneous catalysts based on Pd NPs supported in a metal oxide or ceramic matrix for increased surface area. Pd based catalysts exhibit high conversion and excellent selectivity towards CO_2, especially under lean conditions. However, poisoning and inhibition by various contaminants of CH_4 based fuels, such as compressed or liquefied natural gas, reduce the catalysts activity over time. A persistent issue for Pd based catalysts is inhibition by water. Since H_2O is produced by the combustion of CH_4 and during the catalytic conversion in the catalyst, it is naturally present in the gas feed of CH_4 oxidation catalysts. Several approaches have been explored in the past, among them the use of Pd_3Pt_1 alloy NPs instead of pure Pd. The addition of Pt to Pd based catalysts for the catalytic oxidation of CH_4 has several effects on the activity, structure, and morphology of the catalyst. Motivating the addition of Pt despite its lesser activity towards CH_4 oxidation [264] are the beneficiary effects on the catalysts' resistivity towards poisoning by sulfur and crucially, the inhibition by water [265–267]. This positive effect of Pt has been reported for a variety of catalytic oxidation reactions [267], but the impact of Pt depends strongly on size, alloy structure, and reacting atmosphere. This is nicely illustrated by the investigations of Nie *et al.* who found optimal catalyst performance for a Pd/Pt ratio of two to one. Above this ratio, the effect of Pt diminishes, below that ratio, excess Pt only acts as a spectator [268].

The source of the positive influence of Pt on the activity is still under discussion [264], partially, because the exact mechanism, especially during transient conditions is still not fully understood (see Chapter 2). However, several studies have shown that Pt changes the electronic structure and thus oxidation/reduction behavior of the catalytically active NPs which leads to the coexistence of Pd and PdO in reaction conditions for which full oxidation would be expected [266, 269, 270]. Jiang *et al.* observed a smaller fraction of PdO for a Pd_3Pt_1 catalysts in comparison with a Pd catalyst with same amount of Pd. Furthermore, equilibration of the Pd/PdO ratio was observed for the catalysts containing Pt, indicating a larger kinetic barrier for Pd oxidation in the presence of Pt [269]. Despite smaller amount of PdO which is considered the active phase for CH_4 oxidation, the activity did not break down accordingly, which shows that the PdO fraction becomes a poor predictor for the activity Pd_3Pt_1 alloy catalysts [269]. Closely related to this are comparisons of Pd and Pd_3Pt_1 catalysts at low temperatures in lean condi-

tions. For CeO_2 and Al_2O_3 supports, the addition of Pt resulted in a smaller fraction of PdO and worse activity than for the Pd catalyst [266, 271]. Poor activity and the reduced PdO fraction were associated with inhibition of the redox cycle of Pd through the presence of Pt [271]. Initially these reports seem to be in contradiction. However, when considering that the promotional effect of Pt becomes more pronounced for higher water concentrations in the gas feed [266], a consolidating explanation is the improved resistance towards water poisoning at the cost of a smaller PdO fraction.
While the effects of Pt on the activity are relatively well understood, the structure and mechanism of the described impact of Pt are still to be elucidated. An important question that arises is on the alloy composition and differences between the surface and bulk of the NPs. While Pd and Pt mix completely at the nanoscale [272], distinct changes in the surface alloy composition were observed when alloy NPs are exposed to reducing or oxidizing environments: Exposure to H_2 causes surface segregation of Pt and exposure to O_2 leads to the surface segregation of Pd [273]. Similarly, in catalytic CH_4 oxidation conditions, the formation of a PdO shell around a Pt rich metallic core was observed [268, 269] which is driven by the much lower surface energy in oxygen of PdO compared to Pt [268]. The high activity associated with such core-shell structures was attributed to Pd^{+x} and O^{-x} undercoordinated surface species of the surface PdO layer. Our combinatory HEGIXRD, HEGISAXS and in-line mass spectrometry experiments elucidate the difference in the sinter kinetics of Pd/Al_2O_3 and Pd_3Pt_1/Al_2O_3 catalysts in a comparative manner. Furthermore, detailed, time resolved observations on the strain state of the metallic NP phase were recorded and correlated with the activity and oxidation state of the particles. Overall, our experiments reveal strong sintering inhibition for the alloy NP catalyst, and oxidation inhibition under catalytic operation. Furthermore, the influence of water on the strain state and NP shape were followed in a time-resolved manner.

4.2 Experiment & Steady State Comparison

The catalysts were prepared by standard a standard UHV approach (see Section 4.5). Pd and Pd + Pt were (co-) deposited at the deposition temperature of 923 K which is well beyond the temperatures probed during the operando experiment to exclude thermal sintering during the experiment. The investigations of NP kinetics were conducted at a pressure of 100 mbar, a constant flow of 100 $\frac{\text{ml}}{\text{min}}$ (20 % O_2, 0.1 % CH_4, and 79.9 % Ar). Between the first and second cycle of the experiment, the NPs were reduced using with 2 % H_2 in Ar at 473 K and the same pressure and flow as the catalysis reaction con-

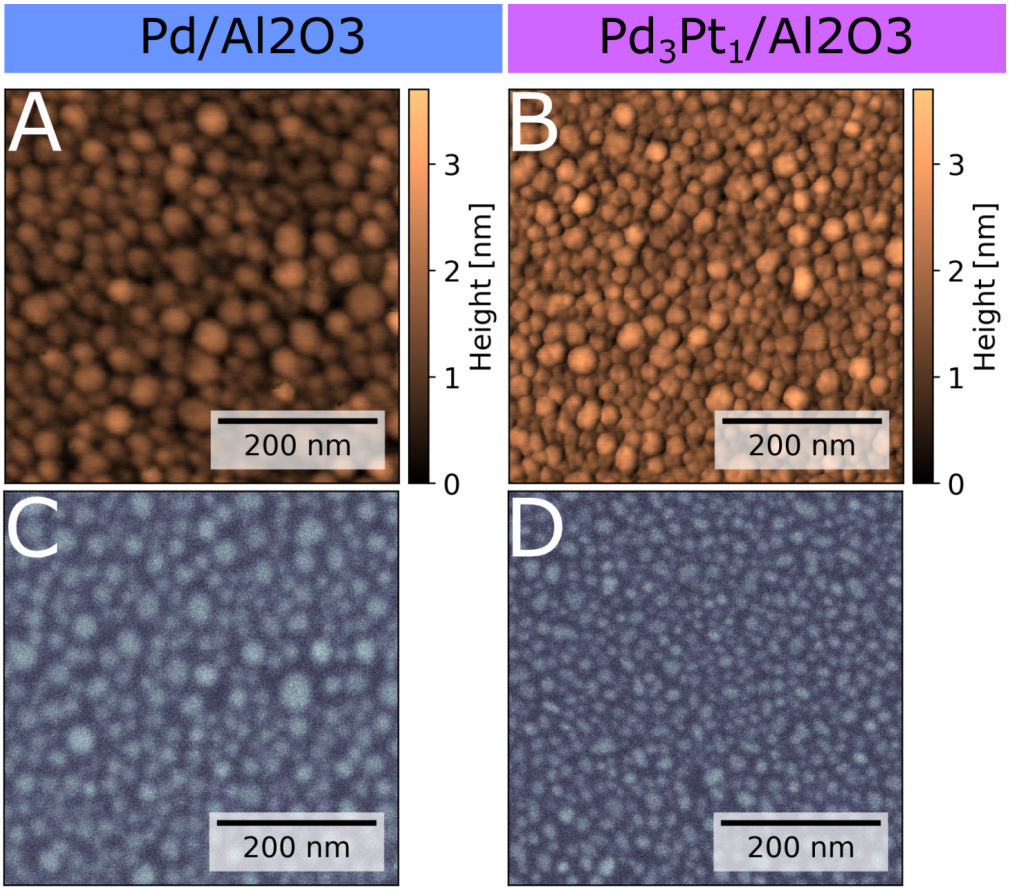

Figure 4.1: Ex situ AFM (**A**, **B**) and SEM (**C**, **D**) data of Pd/Al_2O_3 (**A**, **C**) and Pd_3Pt_1/Al_2O_3 (**B**, **D**) recorded prior to catalytic operation. The height scale of the AFM images and the lateral scale of all images are identical.

ditions. An overview of the complete experiment is given in Section E.1. NP kinetics were extracted between 573 K and 723 K in the first cycle. The second cycle concluded at 773 K.

The same amount of material was deposited for both samples, resulting in similar initial morphologies (see Figure 4.1). The AFM data (Figure 4.1 **A**, **B**) revealed slightly larger NP heights for Pd_3Pt_1/Al_2O_3 compared to the Pd/Al_2O_3 catalyst. The SEM data (Figure 4.1 **A**, **B**) revealed that the difference in height is at the expense of the nanoparticle diameters with the NPs of Pd/Al_2O_3 exhibiting slightly larger diameters. Overall, the NPs of both catalysts are still similar in size, with the Pd_3Pt_1 NPs exhibiting a slightly smaller height to diameter ratio (HDr) which is consistent with previous experiments reporting increasing HDr with increasing Pd content [274].

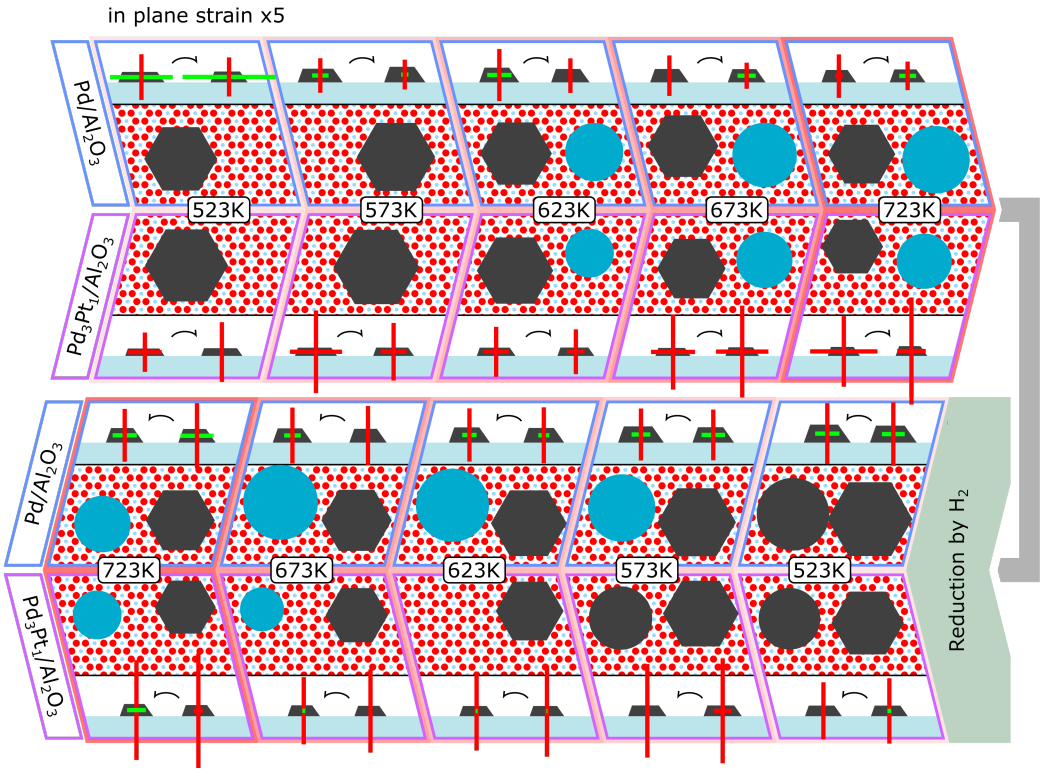

Figure 4.2: Schematic of the structural changes of Pd/Al_2O_3 (blue frames) and Pd_3Pt_1/Al_2O_3 (purple frames) as a function of temperature. The top panels pointing from left to right show the structure of the first cycle, the bottom panels pointing from right to left show the structure of the second cycle. Each panel shows the average metal NP diameter (gray shapes) and the average PdO dimension (light blue circles) in top view. The starting and ending dimensions (height and diameter) for the metal domains are shown in side view together with the average ip ($\times 5$ magnification) and oop strain, indicated as horizontal and vertical bars. Green indicates tensile strain, red compressive strain.

An overview of the catalytic activity of the catalysts is provided in Figure E.1 and Figure E.2 for Pd/Al_2O_3 and Pd_3Pt_1/Al_2O_3, respectively, showing that both catalysts are active for catalytic CH_4 oxidation. For a concise summary of the large, complex HEGIXRD datasets (Figure 4.3, Figure 4.6, Figure 4.4, and Figure 4.7) collected for the two catalysts, a schematic overview of the general trends in structure and morphology as a function of temperature is provided (see Figure 4.2). NP dimensions and lattice parameters were determined by extracting and fitting line scans along several directions of the respective diffraction signals recorded at the ESRF beam-

line. NP dimensions were determined by $d = \frac{2\pi}{\Delta Q}$ and the lattice constant by $a = \frac{2\pi}{Q_0}$, with ΔQ being the full width at half maximum of the fit and Q_0 being the peak position (detailed description in Section E.4). The upper box in Figure 4.2 contains information obtained during the first cycle of the experiments, the bottom box information obtained during the second cycle. For both cycles, the upper five panels correspond to the Pd/Al_2O_3 catalyst and the bottom panels to the Pd_3Pt_1/Al_2O_3 (blue and purple boxes). The temperature of each step is given between the panels corresponding to the respective catalysts. Each panel contains the top view, which shows the average diameter of NPs over a Al_2O_3 lattice with gray hexagons symbolizing epitaxial metallic NPs, gray circles symbolizing randomly oriented, metallic NPs, and blue circles corresponding to PdO NPs. The second component of each panel is the side view of the epitactic metallic NPs constructed from (1 0 0) and (1 1 1) facets in the $[1\,1\,\overline{2}]/[1\,1\,1]$ plane. The bars visualize the in-plane (ip) and out-of-plane (oop) strain of the NPs with compressive strain visualized by red bars and tensile strain by green bars. The respective lengths correspond to the deviation from the bulk lattice constant in percent (ip component magnified by 5x). Each panel shows two strain states corresponding to the first measurement and the last measurement at a given condition. Thermal expansion was accounted for by correcting the data with the expansion factor (detailed in Section E.2 for details). The bulk lattice constant in Figure 4.7 corresponds to the linear combination of the metal content the nominal alloy composition.

At the first temperature of 523 K, the metal NPs of both catalysts are fully epitaxial (see Figure E.6 **A** for Pd/Al_2O_3, Figure E.7 **A** for Pd_3Pt_1/Al_2O_3) and an epitaxial component is observed throughout the experiment for all temperatures ([275–278]). Notably, after reduction between the first and second cycle and before the reformation of PdO in the second cycle of the experiment, diffraction signal from randomly oriented Pd domains was observed (see circular NP representations in Figure 4.2). During the first cycle, PdO diffraction signal is observed at 573 K after 30 min in steady state (Figure 4.3, Figure 4.4) for Pd/Al_2O_3 and at 623 K for $PdPt/Al_2O_3$. This apparent inhibition for Pd oxidation is even more pronounced in the second cycle, where substantial PdO diffraction signal is observed for Pd/Al_2O_3 starting at 573 K like in the first cycle. Throughout both cycles no clear epitactic PdO diffraction signal is observed. However, the weak preferential out-of-plane orientations [0 0 1] and [1 1 2] were determined (see Section E.3). Furthermore, tilted [1 0 1] and [0 0 1] domains that were also observed previously (Chapter 2) seem to be present as well. While PdO diffraction signal is observed at the same temperature for $PdPt/Al_2O_3$, the diffraction signal

was exclusively observed in the rocking scans. This suggests a very small amount of PdO that is consumed by the reaction when ramping from 573 K to 623 K since it is not observed in the time resolved measurements of 623 K which were recorded with 10× larger integration times. The rocking scans of the ROI around the PdO(1 0 1) Bragg peak position (see Figure E.6 **B** for Pd/Al_2O_3, Figure E.7 **B** for Pd_3Pt_1/Al_2O_3) reveal a bimodal preferential ip orientation which is more pronounced for Pd/Al_2O_3 than for the alloy NP catalyst. Due to the setup with two detectors, the low index PdO diffraction signal is not included in the volume of reciprocal space that was probed by the rocking scans. Still, inspection of the diffraction patterns indicate weak preferential (1 0 1) and (0 0 1) oop orientations ([275–278]), identical to the observations of a catalyst (identical preparation technique, chamber, and gas mixture) with larger particles investigated during light-off (Chapter 2). The most prominent change in size of the metal NPs is between 723 K during the first cycle and 523 K after reduction in the second cycle. For both catalysts significant powder diffraction signal from the metal phase is observed, corresponding to the formation of randomly oriented Pd NPs from fully oxidized PdO NPs [279]. The randomly oriented Pd species is only present until PdO diffraction signal is observed (at 523 K for Pd/Al_2O_3, from 523 K to 573 K for Pd_3Pt_1/Al_2O_3). This exemplifies that the stronger support NP interaction of the epitactic species is a driving factor in the stabilization of the metallic phase. The comparison between the average NP size at the beginning of the first cycle and beginning of the second cycle gives first indications for the distinct behavior of the two catalysts. For Pd/Al_2O_3, the domain size of randomly oriented and epitaxial Pd NPs is significantly larger after reduction than at the same conditions during the first cycle. Specifically, the epitaxial NP ensemble grows from 10.98 nm to 12.8 nm in diameter, from 3.71 nm to 6.0 nm in height, and the average size of the randomly oriented NPs appearing after reduction is 12.6 nm. This indicates significant restructuring during catalytic operation and by the reduction step between the experiment cycles. In contrast, for Pd_3Pt_1/Al_2O_3 the average metal domain size at 523 K in the second cycle is roughly the same or slightly smaller than in the first cycle depending on the nanoparticle model used. The epitaxial nanoparticle ensemble evolves from a height and diameter of 2.6 nm and 12.47 nm to 3.75 nm and 10.89 nm and the average dimension of the randomly oriented NPs is 10.7 nm.

4.3 Temporal Evolution of NP Dimensions and strain

The temporal evolution of the Pd and PdO domain size and the height to diameter ratio for the Pd phase are shown in Figure 4.3 together with the normalized MS signal of water and CO_2 as a measure of activity. The left column of panels contain data collected during the first cycle, the right column data collected during the second cycle. The panels of each cycle share the same abscissa indicated at the bottom and top and the same parameter (panels in the same row) share the ordinate. The thin, red vertical bars indicate the time period during which the sample was heated. Complementary HEGISAXS data is presented in Figure 4.5, showing vertical line scans recorded during the first 15 min of data acquisition at each given temperature. The top panel contains the first and last line scan, the two dimensional plots below shows the complete dataset with an identical abscissa. Beyond the time frame shown in Figure 4.5, no temporal changes could be observed in the HEGISAXS data. In the horizontal line scans, no temporal changes could be observed for either sample. Changes between temperature steps are qualitatively shown in [280, 281]. HEGIXRD and HEGISAXS data was recorded in parallel which allows for direct comparison of results between the two techniques.

For Pd/Al_2O_3, strong changes in the average dimension of the Pd domains were observed (Figure 4.3). Starting at the first temperature of 523 K, the HDr first increases from 0.25 to nearly 0.4 before decreasing slightly to 0.3. This shape change is mainly due to the changes in the NP diameter. However, no significant increase in height is observed, which is rationalized by the formation of amorphous PdO or small PdO domains which were not resolved by our experiment. In parallel to the decrease in diameter, the always ip lattice constant's tensile strain (Figure 4.4) increases further before decreasing again when the domain diameter starts to rise again. Simultaneously, the compressive oop strain counteracts the ip tensile strain with the opposite behavior. The final data points of dimensions and lattice constant indicated by the triangle and star, were extracted from the rocking scan and show that lattice relaxes closer to the bulk value than at the beginning of this temperature step and the diameter calculated from Pd(1 1 1) recovers fully (circles and triangle). The significantly smaller diameter calculated from the second order reflex (star) indicates strong ip heterogeneous strain, consistent with the increased sensitivity of higher order reflexes to homogeneous strain. In combination with the lack of change in the HEGISAXS data (Figure 4.5), the evolution in the Pd domain size, particularly the diameter, and lattice

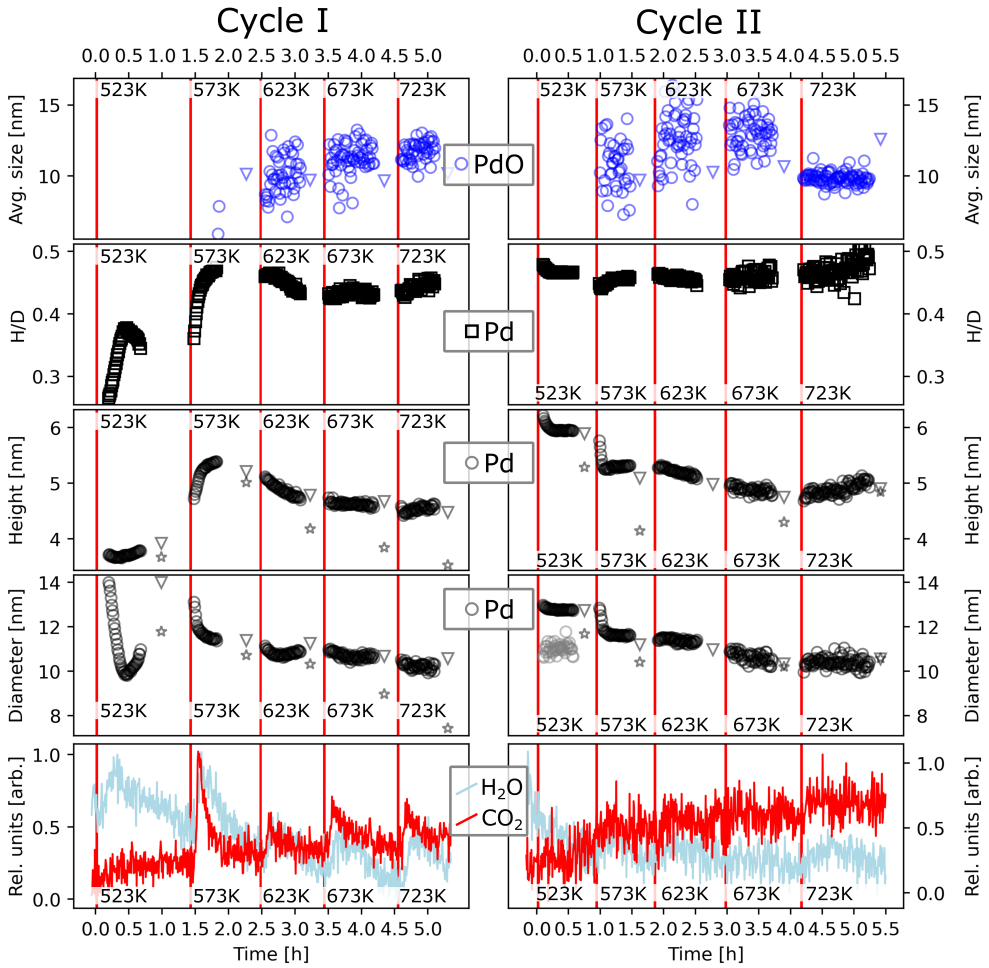

Figure 4.3: Dimensions as function of time extracted from HEGIXRD data recorded for Pd/Al_2O_3. From top to bottom, the panels contain the average PdO dimension (blue circles), the HDr (black cubes), the metal domain height (black circles), the metal domain diameter (black circles) and the normalized water (light blue line) and CO_2 (red line) MS signal as a measure of activity. For NP dimensions, additional datapoints were collected from the same plane in reciprocal space recorded during rocking scans after the time-resolved measurements. Triangles indicate dimensions from the first order Bragg peak, stars correspond to the same dimension extracted from the second order reflex (see Figure E.9) giving insight into heterogeneous strain.

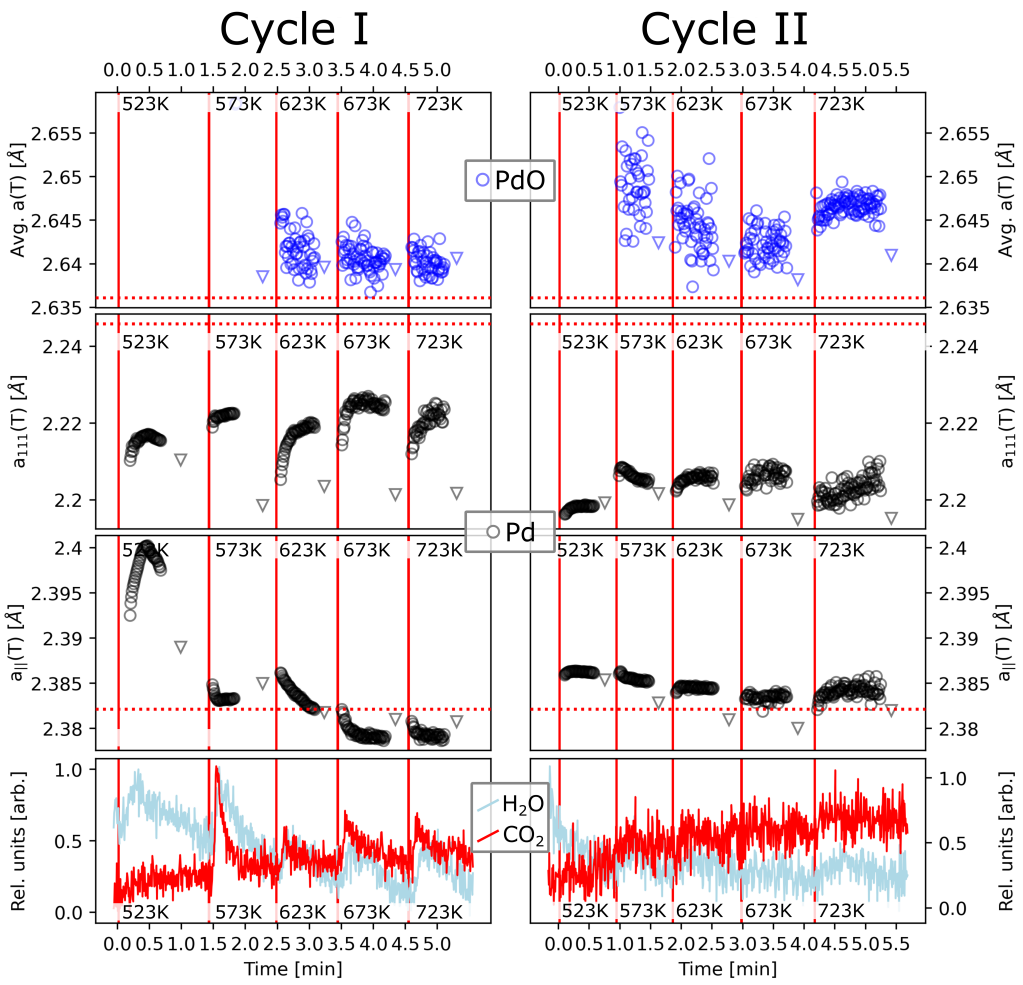

Figure 4.4: D-spacings as function of time extracted from HEGIXRD data recorded for Pd/Al_2O_3. From top to bottom, the panels contain the average PdO(1 0 1) d-spacing (blue circles), the oop component of the average Pd(1 1 1) d-spacing (black circles), the ip component of the average Pd(1 1 1) d-spacing (black circles) and the normalized water (light blue line) and CO_2 (red line) MS signal as a measure of activity. Triangles indicate data points extracted from the same plane in reciprocal space recorded during rocking scans after the time-resolved measurements.

constants suggest the formation of a disordered or highly strained surface, as water is desorbed. At this temperature, the strain can only be caused by replacement of the adsorbants (water with oxygen and methane) and surface oxidation since no bulk PdO was observed. As the diameter and lattice constant recover after the maximum H_2O signal is reached (Figure 4.3, Figure 4.4), a slight increase in the CO_2 (and CO, see Figure E.1) signal is observed. Hence, the surface structure is likely meta stable and forms after the desorption of water by incorporation of O in the NP surface, which would explain the increased activity via the MvK mechanism for PdO(101) [264, 282]. At the following temperature of 573K an abrupt increase of the HDr from 0.36 to nearly 0.5 (Figure 4.3). Surprisingly, the ip and oop lattice constant are unaffected by the shape change with only a small increase and decrease of the ip and oop lattice constants. The ip lattice is almost fully relaxed and the oop lattice experiences compressive strain (1 %). Again, the strong morphological changes coincide with the water desorption peak. In contrast to 523 K, the morphology does not recover and a strong peak in the CO_2 signal is observed. Furthermore, PdO(1 0 1) diffraction signal is observed after 45 min dwell time when the CO_2 signal approaches an equilibrium. At this temperature, first changes in the HEGISAXS pattern are observed Figure 4.5. The peak maximum of the vertical line scans shifts to larger Q_z which corresponds to a shift in the critical angle and thus an increase in the electron density contrast between NPs and substrate. In addition, the first minimum behind the critical angle shifts to lower Q_z which corresponds to an increase in the particle height. All observations combined indicate vertical reorganization of material. The appearance of PdO together with the slight decrease in height between the kinetics data (circles) and the data from the rocking scans (triangle) indicate the formation of PdO on top of the NPs, which was also observed during light-off (Chapter 2). During this restructuring and PdO formation, the catalyst becomes highly active. The flatter slope of the H_2O signal which peaks after the CO_2 signal indicates that the increase in temperature lifts kinetic barriers and restructuring frees active sites. As a result the CO_2 signal increases drastically as the activity abruptly increases. However, the catalyst surface is slowly poisoned again by H_2O produced by the catalytic reaction itself, because it desorbs significantly slower than CO_2 [283] and cannot be displaced effectively by CH_4 [284]. The strong binding of H_2O adsorbates is rationalized by stabilization via the formation of small oligomers consisting of H_2O, OH, and H adsorbates [285].
In the following temperature steps, to 623 K, 673 K, 723 K, the catalyst shows similar trends in HEGISAXS, HEGIXRD, and MS. At each temperature step, a peak in CO_2 followed by a peak in the H_2O signal was observed, but with a smaller magnitude than it was observed for 573 K. The equilibrium ac-

tivity observed during towards the end of each temperature step increases slightly with increasing temperature. The HDr remains roughly constant at 0.45 with a small decrease at 623 K and a small increase at 723 K, which is mainly due to the change in height. At the same time, the equilibrium critical angle (red line scans) observed in the HEGISAXS data (Figure 4.5) increase between temperature steps, but a decrease is observed between the last and first line scans two temperatures. This indicates decrease in the vertical electron profile during heating cycles and increase as a function of time at a set temperature. For 673 K and 723 K, the oscillation width of the vertical line scans decreases as well, which indicates particle growth as a function of time. The small changes observed HEGISAXS and opposite or absent changes in the HEGISAXS data show that during the first 10 min after reaching a set temperature, vertical material transport takes place in a disordered, or surface oxide structure which does not contribute to the coherent domain size of either Pd nor PdO. Comparison of the evolution of the NP dimensions determined from Pd(1 1 1) and Pd(2 2 2) reveal an increasing discrepancy with increasing temperature. The much smaller lattice constant at 723 K (10.6 nm and 7.6 nm ip and 4.5 nm and 3.5 nm oop) indicate that the particle is covered by an oxide layer, which has been shown to cause significant stress on the next temperature step (623 K). Thus, we conclude that Pd NPs coexist with fully oxidized Pd NPs. The PdO domain size increases form initially 6 nm to 11 nm between its first appearance at the end of 573 K and over the course of the slow increase in size over the course of 60 min at 623 K indicates that smaller Pd oxidize before, larger NPs are converted to fully oxidize first, before larger NPs oxidize. At the same time, Pd domains covered by an oxide layer coexist, as evidenced by the immense oop strain and discrepancy in the width of first and second order Pd Bragg reflexes.

As a result of the reduction process between the first and second cycle, the PdO signal fully disappeared and a Pd powder ring appeared. In Figure 4.3, the average dimension, similar to that of PdO in the previous cycle, of this species is displayed in gray. Furthermore, the average height and diameter of the epitactic ensemble increased drastically while the discrepancy between the dimensions determined from first and second order Bragg reflexes diminished significantly. The massive restructuring observed during the first cycle does not occur again, which is likely because the initially flat particle morphology was kinetically limited during growth [274].

Throughout the second cycle, the ip and oop strain are rather consistent. The ip lattice is almost fully relaxed (Figure 4.4). and the oop lattice exhibits a compressive strain of the order of 2 %. Similarly, the HDr remains roughly constant around 0.47 as well. Only at 523 K and 573 K, height and

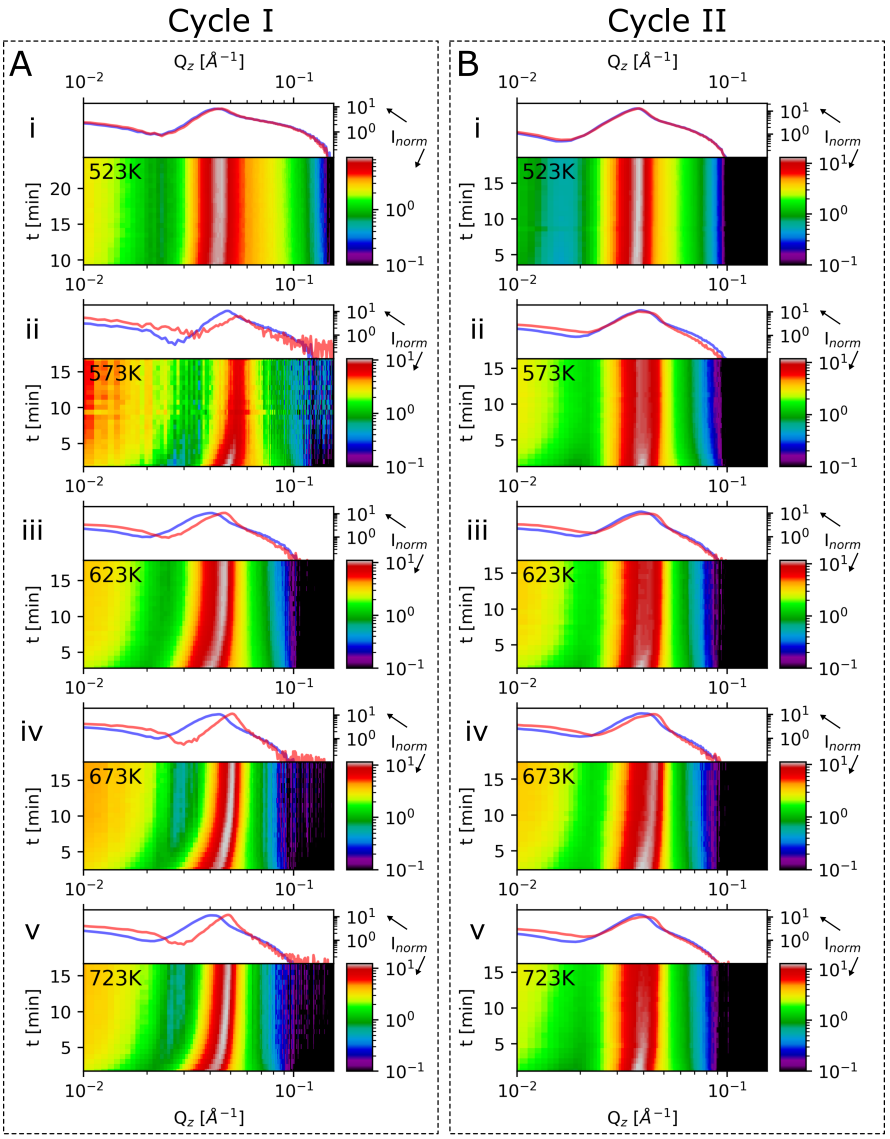

Figure 4.5: Summary of the HEGISAXS data of Pd/Al_2O_3 recorded under operation during the first cycle (**A**) and second cycle (**B**). For each temperature step of each cycle, vertical line scans of the first 15 min after commencing data acquisition is shown as false-color maps showing the intensity as a function of vertical momentum transfer Q_z and time t. The time axis shows the time t after reaching the target temperature. Additionally, the first (blue) and last (red) line scan of each false-color map is plotted on against the same abscissa.

diameter decrease in parallel. This is most likely the result of amorphous or surface oxide formation. At 573 K, the Pd powder diffraction signal vanished and instead, PdO diffraction signal is observed again. This is also reflected in the HEGISAXS data (see Figure 4.5) as the change in the critical angle is comparatively small and the slope beyond the critical is virtually unchanged throughout the second cycle. Notably, the oxidation is instantaneous which was not the case for the first cycle, indicating that the support NP interaction poses a high kinetic barrier for oxidation. The most pronounced differences in the activity between the first and second cycle is the lack of spikes in activity. Instead, the CO_2 signal remains fairly low and increases only slightly with increasing temperature. The H_2O signal conforms to that trend and only at the temperature step to 573 K and to 723 K, when discernible H_2O signal is observed, significant increase in the CO_2 production was observed. Since the PdO domains seem to behave similarly in the first and second cycle, we attribute the gradually rising CO_2 signal to the activity of fully oxidized PdO NPs and the spikes in activity during the first cycle to surface oxide species on Pd NPs and Pd/PdO grain boundaries of partially oxidized NPs. The absence of these species is rationalized by the unchanged strain state of the metal phase which is also observed in the decreasing difference in the NP size determined from first and second order Pd Bragg reflexes (triangles and stars, see Figure 4.3).

The second catalyst with alloy NPs (Pd_3Pt_1/Al_2O_3) was investigated under identical conditions as the previously discussed Pd/Al_2O_3 catalyst and analogous, the three figures Figure 4.6, Figure 4.7, and Figure 4.8 summarize the NP dimensions, lattice constants, and HEGISAXS vertical line scans. As for Pd/Al_2O_3, no temporal changes in the horizontal line scans could be observed (see Figure E.74). Upon comparison of the HDr, height, and diameter, it is apparent that the coherent domain size of the alloy NPs does not react as severely to the H_2O desorption at 523 K. The virtually identical H_2O desorption peaks, indicate that there is no significant difference in the amount or binding state of water between the two catalyst. The initial HDr of both samples is roughly the same, but no significant reaction of the HDr to H_2O desorption was observed for Pd_3Pt_1/Al_2O_3. In all following temperature steps of the first cycle, the HDr increases slowly to 0.36 which is caused by a decrease in diameter at all temperatures starting at 573 K and increase in height at 673 K and 723 K. As previously stated, PdO appears at 623 K with a domain size of 6 nm which increases to 9.9 nm over time. At 673 K and 723 K, no significant changes in the PdO domain size were observed, indicating that consumption of PdO and reoxidation of oxygen vacancies are in equilibrium. Information about heterogeneous strain is obtained by comparison of heights and diameters determined from the first

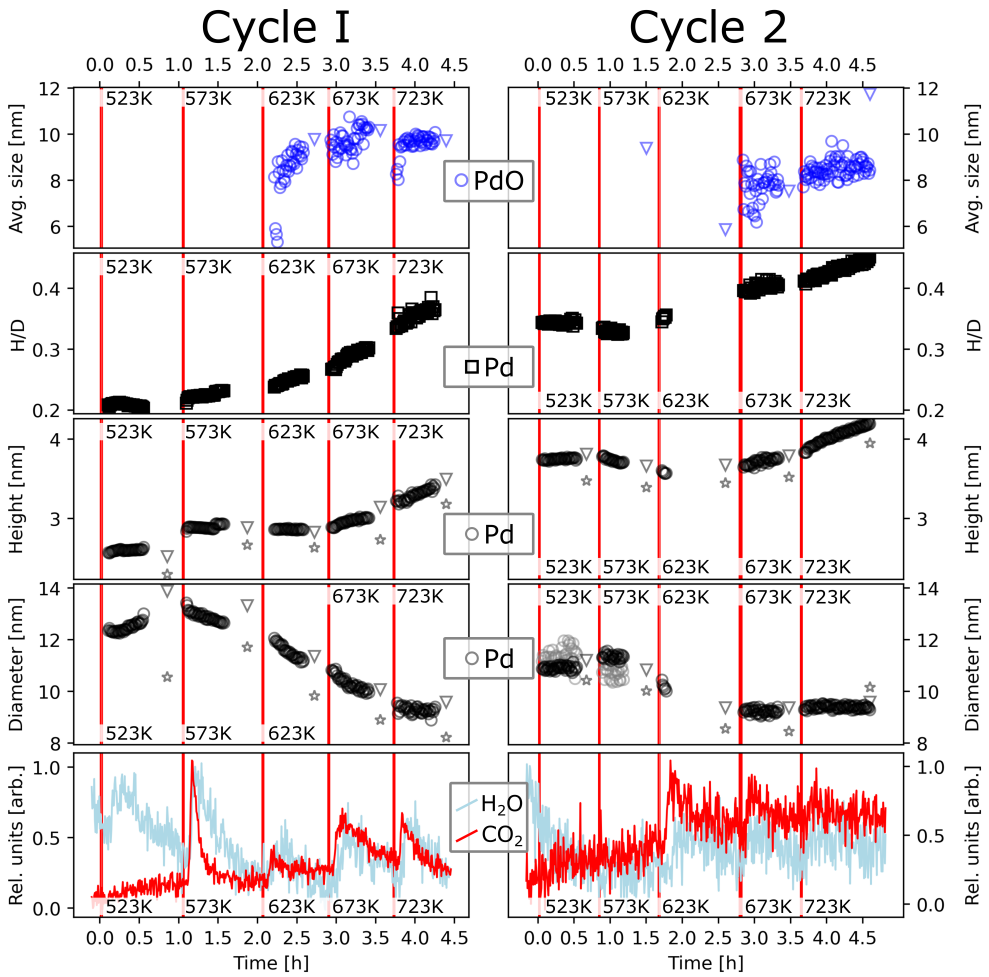

Figure 4.6: Dimensions as function of time extracted from HEGIXRD data recorded for Pd_3Pt_1/Al_2O_3. From top to bottom, the panels contain the average PdO dimension (blue circles), the HDr (black cubes), the metal domain height (black circles), the metal domain diameter (black circles) and the normalized water (light blue line) and CO_2 (red line) MS signal as a measure of activity. For NP dimensions, additional datapoints were collected from the same plane of reciprocal space recorded during rocking scans after the time-resolved measurements. Triangles indicate dimensions from the first order Bragg peak, stars correspond to the same dimension extracted from the second order reflex (see Figure E.9) giving insight into heterogeneous strain.

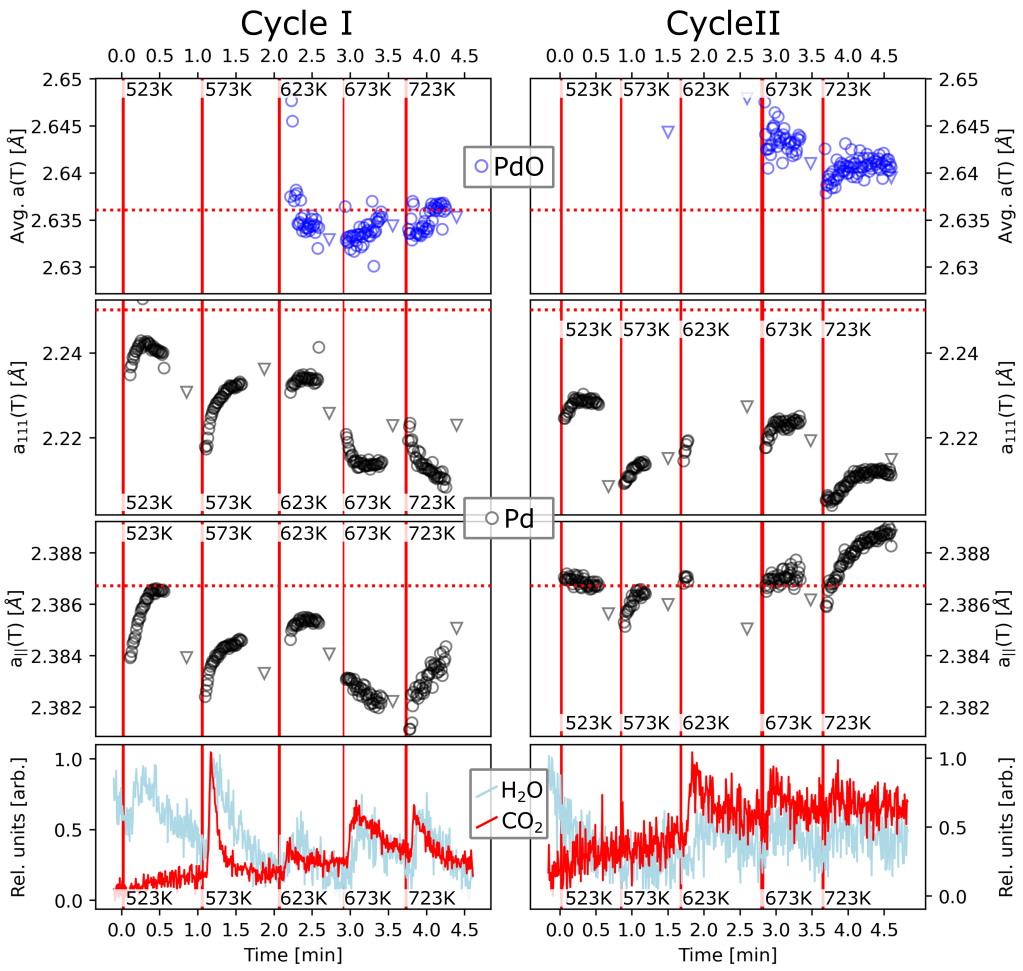

Figure 4.7: D-spacings as function of time extracted from HEGIXRD data recorded for Pd_3Pt_1/Al_2O_3. From top to bottom, the panels contain the average PdO(1 0 1) d-spacing (blue circles), the oop component of the average metal domain (1 1 1) d-spacing (black circles), the ip component of the average metal domain (1 1 1) d-spacing (black circles) and the normalized water (light blue line) and CO_2 (red line) MS signal as a measure of activity. Triangles indicate data points extracted from the same plane in reciprocal space recorded during rocking scans after the time-resolved measurements.

and second order reflexes of the metal domains (triangles and stars, see Figure 4.6). Throughout both cycles, the difference in height corresponds to 3 Å, to 4 Å (1.3 to 1, 8 monolayers). In contrast, the difference in diameter at 523 K in the first cycle is 3.4 nm, gradually diminishing to 1.1 nm during the first cycle where it remains during the second cycle. The evolution of the size, HDr and heterogeneous strain of the metal phase indicates that no significant reorganization of material is taking place during the first cycle. Instead, the loss in diameter of the metal phase indicates the formation of PdO at the edge of the particle. This is supported by the lack of change in the critical angle of the HEGISAXS data (Figure 4.8). Strong changes in the critical angle would have to be observed if the increase in the HDr was due to severe vertical reorganization of material as it was observed for Pd/Al_2O_3. Instead, the changes in the position of the first minimum between 623 K and 723 K (Figure 4.8 **A** iii, iv, v) indicate isotropic sintering of the NPs. The activity during the first cycle resembles that of Pd/Al_2O_3, but the overall activity is larger, discernible from the larger signal to noise ratio.
Overall, there seems to be no apparent correlation between the domain sizes, NP height and activity during the first cycle for Pd_3Pt_1/Al_2O_3. However, the lattice constants (Figure 4.7) exhibit a more dynamic behavior. At the first temperature (523 K), a similar behavior as for Pd/Al_2O_3 is observed: ip and oop lattice constant increase with increasing H_2O signal. However, for Pd_3Pt_1/Al_2O_3, the oop d-spacing is significantly more relaxed and the ip d-spacing $a||$ is overall less strained and approaches the bulk value (red, dotted lines in Figure 4.7). The correlation of the H_2O MS signal with d-spacings, NP size and HDr points towards H_2O desorption and replacement by oxygen as driving forces. This indicates that the presence of of Pt in Pd_3Pt_1/Al_2O_3 inhibits the restructuring. At 573 K, the evolution of the CO_2 and H_2O signal is similar between the two catalysts, however Pd_3Pt_1/Al_2O_3 is significantly more active (Figure E.3). Similarly to Pd/Al_2O_3, the oop compressively strained lattice relaxes, however for the more active Pd_3Pt_1/Al_2O_3 catalyst, the effect is significantly more pronounced. The ip d-spacing exhibits stronger compressive strain than for the previous temperature step and behaves identical to the oop lattice constant, opposite to the observations for Pd/Al_2O_3. Since no PdO diffraction signal was observed for either catalyst during the activity spike at the beginning of the temperature, a similar mechanism like catalytic conversion of CH_4 by surface oxides or multi layer surface oxides could explain the catalysts behavior since PdO is necessary for the first C−H dissociation [269, 286]. However, for Pd/Al_2O_3 PdO was observed in the rocking scan, which means that bulk oxidation already commenced. This is not observed for Pd_3Pt_1/Al_2O_3, suggesting that the stronger changes in d-spacing compared to Pd/Al_2O_3 are due to the inhibi-

tion of bulk PdO formation by Pt. The lack of bulk PdO diffraction signal at this stage further emphasizes the necessity of an active PdO surface structure [282, 286]. At 623 K, PdO is observed for the first time, and kinetics barriers for bulk PdO formation seem to be just overcome as the domain size increases rapidly at this temperature. This hypothesis is supported by the stark decrease of the PdO lattice constant which starts with an average strain of 0.5 % and ends at − 0.01 % indicating a relaxation of the lattice, consistent with the relaxation expected with increasing domain size. The compressive strain of the metallic phase exhibits a similar trend as observed for the previous temperature: A fast increase of the d-spacing in the first minutes which slows down when the maximum H_2O signal is reached. The weaker spike in activity for this temperature step compared to the previous step indicates that a surface species of the metallic NPs is indeed responsible for the activity spikes at the beginning, since the magnitude in change of the d-spacings correlates well with the activity spikes. The highly active surface species is then quickly poisoned or depleted by the reactants or products of the reaction which causes the decrease in activity. Between temperatures, the equilibrium activity which is approached at the end of each temperature increases throughout the experiment and strong increases are observed when PdO is observed. Hence, we attribute the overall gradual increase in activity at the end of the temperature step to the bulk oxide which is more stable and thus less susceptible to poisoning. In the last two temperature steps, the trends in the evolution of the d-spacing are broken. Instead of an increase in d-spacing decreasing the magnitude of compression both ip and oop, the oop d-spacing decreases in the first 15 min before stabilizing, corresponding to an increase in compression. In contrast, the ip d-spacing decreases monotonously at 673 K and increases at 723 K. Furthermore, the PdO lattice constant starts with compressive strain but recovers over a period of 45 min at both temperatures. For both catalysts, changes in d-spacing observed during the first cycle correlate with the activity of the catalyst: The spikes in activity always occur simultaneously with strong changes in d-spacing in the first 15 min of each temperature. However, for Pd_3Pt_1/Al_2O_3 the activity is significantly stronger (see Figure E.3) and the activity at 673 K and 723 K decay slower. At 673 K, this correlates with a strong decrease in diameter, indicating the formation of PdO. Since homogeneous compressive strain increases and heterogeneous strain (from comparison of the (1 1 1) and (2 2 2) diameters) increases, the strain state is likely related to chemical changes in PdO in contact with the Pt rich core of the NPs [268, 269]. The evolution of the heterogeneous strain in combination with diameter and height and the HEGISAXS data indicate that larger PdO domains which can be observed by HEGIXRD are mostly located next to the Pt rich core, since no oop ma-

terial distribution was observed in HEGISAXS and the appearance of PdO correlates with the loss in diameter.

Analogous to Pd/Al_2O_3 PdO is fully reduced in the reduction process and diffraction signal corresponding to randomly oriented metallic domains appears. Diffraction signal from the randomly oriented domains persists during the first two temperature steps (523 K and 573 K) until it becomes too weak to quantify at 623 K. The first appearance of PdO in the rocking scan at 573 K during the second cycle indicates that a kinetic barrier for PdO formation present in the first cycle is partially lifted during the second cycle. Since the randomly oriented domains are formed through reduction of PdO, the oxidation of these domains is facilitated in the second cycle, due to the lack of Pt. The loss of PdO signal in the temperature step from 573 K to 623 K indicates that the spike in activity at 623 K is due to consumption of PdO. This observation further emphasizes the earlier hypothesis that spikes during the first cycle are caused by consumption or poisoning of highly active PdO species. The overall increased activity at 623 K after the activity spike indicates the reformation of (surface) PdO, rationalized by the significant decrease in diameter between 623 K and 673 K and PdO. At the final two temperatures 673 K and 723 K, the HDr increases again, reaching 0.45 at the end of the experiment, caused by an increase in height by 5 Å. The PdO domain size is around 8 nm at both temperatures. Again, the peaks in activity are not correlated with morphological changes but instead with the changes in the strain state, consistent with the correlation of the spikes with surface species of the metallic domains.

Overall, the activity as a function of time for the set temperature steps in the first cycle evolves similarly for both catalysts, although the overall activity is higher for the alloy catalyst (Figure E.3). The activity during the second cycle is lower for both catalysts, however, the degree of sintering alone is not sufficient to explain this change. Instead, comparison of the two catalysts can provide some insight. The most striking difference between the two experiment cycles is the absence of activity spikes during the second cycle for Pd/Al_2O_3 and the massively reduced magnitude for Pd_3Pt_1/Al_2O_3. The overall activity starts increasing at lower temperatures for Pd/Al_2O_3, which we attribute to the formation of bulk PdO which is observed at 673 K for Pd_3Pt_1/Al_2O_3. The absence of spikes for Pd/Al_2O_3 indicates that the surface species to which these features where assigned during the first cycle are either poisoned or not present at all, possibly by the incorporation of H in the NP surface or the formation of aliphatic carbon by reduction of partial CH_4 oxidation products. Since the spikes are present starting from 623 K for Pd_3Pt_1/Al_2O_3, the presence of the active species is related to the influence of Pt either stabilizing the active species or preventing poisoning of the active

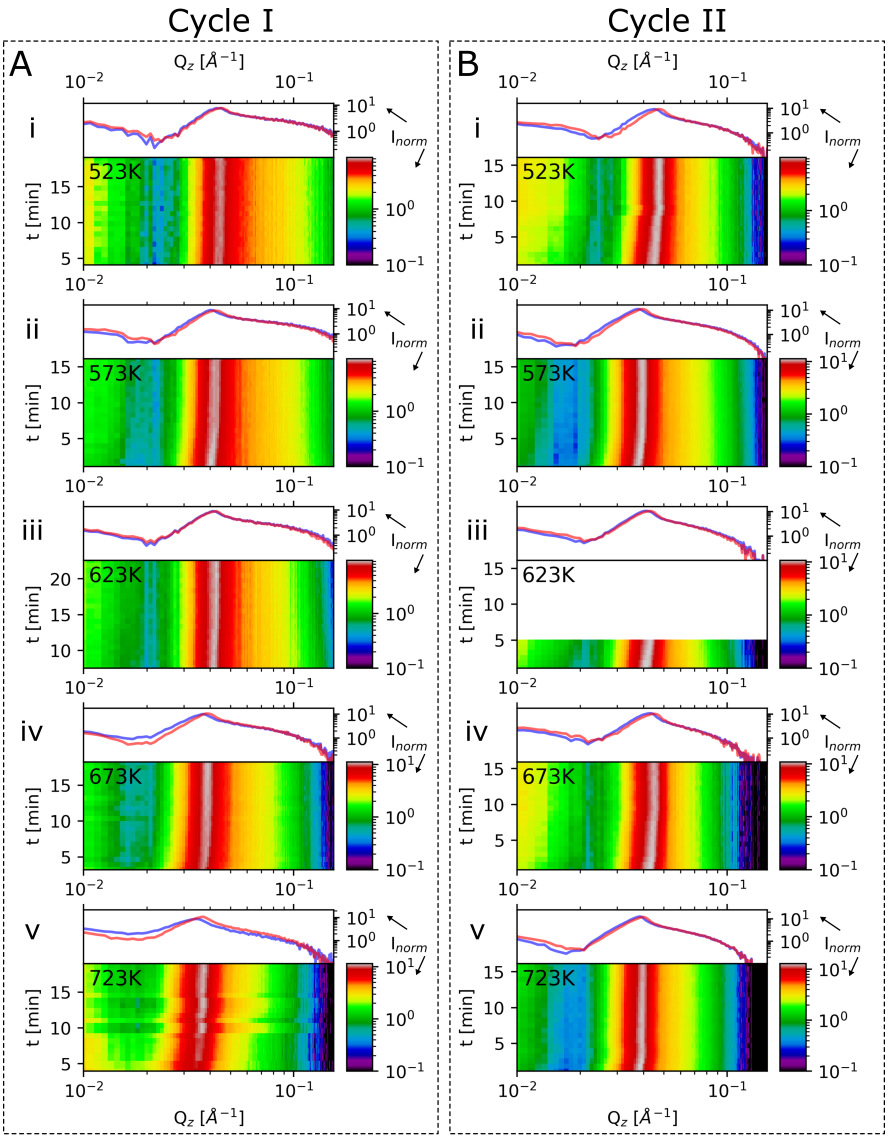

Figure 4.8: Summary of the HEGISAXS data of Pd_3Pt_1/Al_2O_3 recorded under operation during the first cycle (**A**) and second cycle (**B**). For each temperature step of each cycle, vertical line scans of the first 15 min after commencing data acquisition is shown as false-color maps showing the intensity as a function of vertical momentum transfer Q_z and time t. The time axis shows the time t after reaching the target temperature. Additionally, the first (blue) and last (red) line scan of each false-color map is plotted on against the same abscissa. Due to experimental complications, no data is available for the blank area in cycle II, 623 K. For comparability between cycles, the ordinate range of t was left at 15 min.

species. This is also clearly observed in the d-spacings of Pd/Al_2O_3 which remain roughly constant throughout the second cycle. In contrast, a more dynamic behavior is observed for Pd_3Pt_1/Al_2O_3 which is rationalized by Pd surface diffusion in reaction gas mixture at 523 K and 573 K after the reduction treatment that caused Pt surface diffusion in the metallic domains [273]. Starting at 623 K, the changes in d-spacing are again related to the activity of the surface species and the chemical changes of the surface influencing the d-spacing.

4.4 Summary & Conclusion

With this operando investigation of NP morphology and structure we elucidate NP dynamics and their influence on activity in transient temperature regimes. This was achieved by comparative analysis of a Pd/Al_2O_3 and Pd_3Pt_1/Al_2O_3 model catalyst. For the first time, simultaneous measurement of HEGIXRD, HEGISAXS, and MS were conducted on CH_4 catalysts under operation providing a unique and comprehensive dataset on the influence of Pt on NP dynamics and activity of Pd based CH_4 oxidation catalysts. Our results reveal persistent of epitaxial metal domains across all temperatures (up to 723 K) for both catalysts. In addition, the Pd/Al_2O_3 catalyst exhibits less pronounced changes in NP size compared the previous study (Chapter 2). In combination, this indicates superior stabilization of the metallic phase compared to earlier studies using larger NPs (Chapter 2) [287]. The addition of Pt further improved resistance towards adsorbent driven restructuring as NP size and HDr are stabilized for $PdPt/Al_2O_3$. This effect is particularly evident for sintering as a consequence of the reduction treatment and the initial H_2O desorption event at 523 K.
Oxidation of Pd to bulk PdO is delayed for the catalyst containing Pt, suggesting that Pt inhibits bulk oxide formation. This can be rationalized by (i) limitation of bulk oxide formation for small NPs [287], (ii) intra particle diffusion of Pd to the surface [273], and inhibition of oxidation by Pt [288]. The PdO domains did not show distinct orientations typical for PdO formation purely on the Al_2O_3 support [279] or the NPs [289], implying either rapid formation and decomposition to form mostly randomly oriented domains [279] or the formation at the NP support interface where complex interactions between metal, oxide, and support cause formation of heterogeneous domains. Furthermore, significant restructuring of the catalyst surface as observed in HEGISAXS was only present for Pd/Al_2O_3. This highlights the role of Pt in the suppression of NP growth and migration, thus serving as a powerful tool for catalyst design.

During the first cycle, strong catalytic activity was observed for both catalysts just after reaching each target temperature, starting at 573 K. This activity is attributed to highly active PdO surface species, which are slowly poisoned by OH and H_2O produced by the reaction. When the temperature is increased, the sites are rapidly freed causing a spike in activity. As a function of time, the activity decreases again due to the aforementioned poisoning effect of the reaction. The spikes are absent during the second cycle, which was explained by poisoning of the surface which did only occur for Pd/Al_2O_3. Overall, the Pd_3Pt_1/Al_2O_3 catalyst outperformed the Pd/Al_2O_3 catalyst. The superior performance is attributed to the improved stability of PdO surface species such as surface oxides or very small crystallites [288]. This is supported by the pronounced changes in the lattice constant of the metallic domain in case of $PdPt/Al_2O_3$ in both experimental cycles. In contrast, the metal and oxide domains of Pd/Al_2O_3 relax over the course of the experiment yielding a comparatively inactive catalyst. These findings underscore the importance of alloying and nanoscale structural control in designing thermally and chemically stable catalysts for dynamic oxidation environments.

4.5 Methods

Sample Preparation

The two catalyst samples were prepared with a standard UHV approach utilizing a UHV chamber with a base pressure of $< 1 \times 10^{-10}$ mbar. The $Al_2O_3(0\,0\,0\,1)$ single crystals were first annealed at 823 K in UHV by e-beam heating and then in O_2 at 523 K. Nanoparticle deposition was conducted at a temperature of 923 K with an e-beam evaporator capable of co-deposition of Pd and Pt. For consistency in regard to particle morphology both samples were grown with a rate of 0.5 $\frac{\text{Å}}{\text{min}}$ and identical nominal thickness of 1.5 nm.

MS

Inline mass spectrometer data presented in this work was recorded with a resolution of 0.1 a.m.u.. For the pressure versus time plots, spectra were integrated with a range of $\pm$ 0.3 a.m.u. around the respective molar masses of the molecules. For CH_4, instead of the molar mass, the mass 15 a.m.u. was chosen to avoid overlap with signal from atomic O fragments from reactants and products. Fragmentation of CO_2 causes increased signal in mass 28 a.m.u., assigned to CO which was corrected as described in Chapter C. Trends in the mass spectrometer signal were enhanced by normalizing to the maximum and minimum of the data presented in the respective figures.

Operando Scattering Data Acquisition

For kinetics measurements, the sample was heated rapidly by 50 °C to 100 °C. After reaching the target temperature, the sample position was corrected by the previously calibrated, expected thermal expansion of the setup. During acquisition of the scattering data (HEGIXRD and HEGISAXS), the sample position was continuously corrected, by small scans of the sample height further optimizing data acquisition. The Pilatus3 X CdTe 2M detector (172 µm pixel size) used for HEGIXRD measurements was positioned 2.8 m behind the sample and off the direct beam path to allow the small-angle scattering data to pass. The Perkin Elmer XRD 1621 detector (200 µm pixel size) was positioned at a distance of 8.3 m from the sample. Between the two detectors, a flytube was placed to minimize isotropic scattered intensity in the HEGISAXS data.
The change in sample height was calibrated prior to the first measurements, by following the height changes between the relevant temperature steps of the experiment. For the actual kinetics measurement, the data acquisition fol-

lowed a series of steps, identical for both samples and all temperature steps. First, the sample was heated to the target temperature with a temperature ramp of 20 $\frac{^\circ\mathrm{C}}{\mathrm{min}}$. Small differences of $< 5\,\frac{^\circ\mathrm{C}}{\mathrm{min}}$ between different temperature steps are due to the slightly non-linear resistance of the resistive heater.

AFM

The AFM measurements were conducted using tapping mode in air at the DESY NanoLab. Oxide-sharpened silicon cantilevers (tip radius 8 nm) with a resonance frequency of 300 kHz [290] and a scanning speed of 0.5 Hz were used for all shown AFM data. A polynomial plane fit was used to account for sample tilt during the measurement.

SEM

All SEM data was recrorded at the DESY NanoLab with a high resolution field-emission SEM. All images were recorded using a concentric backscattered (CBS) detector and an accelerating voltage of 5 kV, yielding an effective lateral resolution of $\sim$ 1 nm [290].

Bibliography

(262) *Climate change 2013: The physical science basis*; Stocker, T., Ed.; Cambridge University Press: New York, 2013.

(263) *Climate change 2022: Mitigation of climate change*; Shukla, P. R., Skea, J., Reisinger, A. R., Eds.; IPCC: Geneva, 2022.

(264) Lott, P.; Casapu, M.; Grunwaldt, J.-D.; Deutschmann, O. A review on exhaust gas after-treatment of lean-burn natural gas engines – From fundamentals to application. *Appl. Catal. B Environ.* **2024**, *340*, 123241.

(265) Abbasi, R.; Huang, G.; Istratescu, G. M.; Wu, L.; Hayes, R. E. Methane oxidation over Pt, Pt:Pd, and Pd based catalysts: Effects of pretreatment. *Can. J. Chem. Eng.* **2015**, *93*, 1474–1482.

(266) Divins, N. J. et al. Investigation of the evolution of Pd-Pt supported on ceria for dry and wet methane oxidation. *Nat. Commun.* **2022**, *13*, 5080.

(267) Large, A. I.; Bennett, R. A.; Eralp-Erden, T.; Held, G. In situ surface analysis of palladium-platinum alloys in methane oxidation conditions. *Faraday Discuss.* **2022**, *236*, 157–177.

(268) Nie, H.; Howe, J. Y.; Lachkov, P. T.; Chin, Y.-H. C. Chemical and Structural Dynamics of Nanostructures in Bimetallic Pt–Pd Catalysts, Their Inhomogeneity, and Their Roles in Methane Oxidation. *ACS Catal.* **2019**, *9*, 5445–5461.

(269) Jiang, D.; Khivantsev, K.; Wange, Y. Low-Temperature Methane Oxidation for Efficient Emission Control in Natural Gas Vehicles: Pd and Beyond. *ACS Catal.* **2020**, *10*, 14304–14314.

(270) Goodman, E. D. et al. Palladium oxidation leads to methane combustion activity: Effects of particle size and alloying with platinum. *J. Chem. Phys.* **2019**, *151*, 154703.

(271) Mussio, A. et al. Structural Evolution of Bimetallic PtPd/CeO_2 Methane Oxidation Catalysts Prepared by Dry Milling. *ACS Appl. Mater. Interfaces* **2021**, *13*, 31614–31623.

(272) Lee, Y.; Stender, P.; Eich, S. M.; Schmitz, G. Probing the Miscibility Gap of the Pt–Pd Binary System by Atom Probe Tomography. *Microsc. Microanal.* **2022**, *28*, 1385–1395.

(273) Dolling, D. S. et al. Probing Active Sites on Pd/Pt Alloy Nanoparticles by CO Adsorption. *ACS Nano* **2024**, *18*, 31098–31108.

(274) Hejral, U. et al. Composition-Dependent Alloy Nanoparticle Shape Changes under Reaction Conditions: Kinetic and Thermodynamic Effects. *J. Phys. Chem. C* **2024**, *128*, 4330–4342.

(275) Schober, J.-C. Rocking Scans Pd/Al_2O_3, Cycle I `https://bib-pubdb1.desy.de/record/636455`.

(276) Schober, J.-C. Rocking Scans Pd/Al_2O_3, Cycle II `https://bib-pubdb1.desy.de/record/636456`.

(277) Schober, J.-C. Rocking Scans Pd_3Pt_1/Al_2O_3, Cycle I `https://bib-pubdb1.desy.de/record/636453`.

(278) Schober, J.-C. Rocking Scans Pd_3Pt_1/Al_2O_3, Cycle II `https://bib-pubdb1.desy.de/record/636454`.

(279) Nolte, P. In situ Oxidation Study of Supported Rh and Pd Nanoparticles, Dissertation, Stuttgart: Institue for Theoretical and Applied Physics University of Stuttgart, 2009.

(280) Schober, J.-C. Time resolved data of Pd/Al_2O_3 `https://bib-pubdb1.desy.de/record/636458`.

(281) Schober, J.-C. Time resolved data of Pd_3Pt_1/Al_2O_3 `https://bib-pubdb1.desy.de/record/636459`.

(282) Stotz, H. et al. Surface reaction kinetics of methane oxidation over PdO. *J. Catal.* **2019**, *370*, 152–175.

(283) Ciuparu, D.; Pfefferle, L. Contributions of lattice oxygen to the overall oxygen balance during methane combustion over PdO-based catalysts. *Catal. Today* **2002**, *77*, 167–179.

(284) Zhang, F.; Hakanoglu, C.; Hinojosa, J. A.; Weaver, J. F. Inhibition of methane adsorption on PdO(101) by water and molecular oxygen. *Surf. Sci.* **2013**, *617*, 249–255.

(285) Kan, H. H.; Colmyer, R. J.; Asthagiri, A.; Weaver, J. F. Adsorption of Water on a PdO(1 0 1) Thin Film: Evidence of an Adsorbed HOH_2O Complex. *J. Phys. Chem. C* **2009**, *113*, 1495–1506.

(286) Hellman, A. et al. The Active Phase of Palladium during Methane Oxidation. *J. Phys. Chem. Lett.* **2012**, 678–682.

(287) Murata, K.; Ohyama, J.; Yamamoto, Y.; Arai, S.; Satsuma, A. Methane Combustion over Pd/Al_2O_3 Catalysts in the Presence of Water: Effects of Pd Particle Size and Alumina Crystalline Phase. *ACS Catal.* **2020**, *10*, 8149–8156.

(288) Jang, E. J.; Lee, J.; Oh, D. G.; Kwak, J. H. CH_4 Oxidation Activity in Pd and Pt–Pd Bimetallic Catalysts: Correlation with Surface PdO_x Quantified from the DRIFTS Study. *ACS Catal.* **2021**, *11*, 5894–5905.

(289) Yue, S. et al. Redox dynamics and surface structures of an active palladium catalyst during methane oxidation. *Nat. Commun.* **2024**, *15*, 4678.

(290) Stierle, A.; Keller, T.; Noei, H.; Vonk, V.; Roehlsberger, R. DESY NanoLab. *J. Large-Scale Res. Facil.* **2016**, *2*, A76.

4.6 Concluding Remarks

This dissertation explored the structure-activity relationship of Pd based catalysts with focus on the influence of the support and addition of Pt. The combination of tight control over the model catalyst supports and NPs by UHV based synthesis approaches with sophisticated operando characterization techniques contributes to the understanding of structure, morpholgoy, and dynamics in industrially relevant pressure and temperature regimes and their influence on the activity and stability of the catalysts. Four interconnected studies elucidate the support structure, NP morphology in transient conditions, the influence of geometrical constraints on sintering, and NP dynamics under catalytic operation.

In **Chapter I** a straight-forward synthesis procedure for the preparation of fully oxidized $CeO_2(0\,0\,1)$ thin films supported by YSZ$(0\,0\,1)$ is presented. The films characterized by a dislocation lattice at the interface to the support relieving the lattice mismatch between CeO_2 and YSZ, a coherent bulk lattice with minimal strain and an atomically smooth surface. Comprehensive analysis of the film revealed sparse local interruptions in the shape of rectangular holes that later revealed significantly impact on sintering behavior. Spectroscopic and structural investigation of the surface confirmed a defect free, highly polar, hydroxylated surface. The simplicity and robustness of the presented synthesis route in comparison to existing protocols yielding comparable film properties is ideal for the use as a catalyst support.

In **chapter II**, light-off experiments utilizing Al_2O_3 single crystals and the CeO_2 thin films as supports for Pd model catalysts are presented. The structure, morphology, and activity of the catalysts were monitored up to a temperature of $827,\mathrm{K}$ under catalytic operation by HEGIXRD and MS. Both catalysts exhibited complex dynamic phase transitions between Pd and PdO which occurs simultaneously, but spatially separated. Both catalysts were active for full oxidation and the partial oxidation products carbon monoxide and formaldehyde of full catalytic CH_4 conversion were observed for the first time. The results point towards oxygen mobility and support specific reactions as key factors determining activity. Moreover, OH and H_2O self-poisoning is discussed as source for diminished active site density in transient conditions. In the applied lean reaction gas mixture, the thermodynamically unstable AlO(OH) and Ce_xPd_y were observed for the Pd/Al_2O_3 and Pd/CeO_2 catalyst, respectively. In conjunction with the simultaneous production of CO and CO_2, normally associated with CH_4 rich gas feeds, these results provide novel information on the structure, activity, and local chemical potential to improve mechanistic models for heterogeneous CH_4 oxidation over Pd based catalysts.

Chapter III focuses on the sintering behavior of Pd NPs supported by the previously developed $CeO_2(1\,0\,0)$ thin films during the also previously described light-off experiment. SEM analysis revealed that sintering proceeds predominantly by Ostwald ripening, which is connected to the limited mobility of the NPs on CeO_2. The geometric confinement of NPs in the holes of the CeO_2 thin film lead to an increased NP size for the NPs in the holes of the film. A mechanistic diffusion model is proposed to explain distinct size distributions. The chapter demonstrated how support engineering at the nanometer scale can influence sintering kinetics and can potentially serve as a tool in catalyst design.
In **Chapter IV**, the role of alloying with Pt for the stabilization of NPs in Pd based catalysts was investigated by operando analysis of Pd/Al_2O_3 and Pd_3Pt_1/Al_2O_3 model catalysts. For the first time HEGIXRD, HEGISAXS, and MS measurements were combined to provide a uniquely comprehensive dataset that enabled the correlation of structural dynamics with catalytic activity. The incorporation of Pt significantly suppressed sintering and restructuring of Pd NPs. In addition, the formation of bulk PdO was inhibited. The stabilizing influence of Pt is rationalized by the inhibition of bulk oxide formation in small particles, direct stabilization of Pd by Pt and internal diffusion of Pd and Pt respectively. These results demonstrate the importance of electronic and geometric effects introduced by secondary metals, offering a strategy to enhance thermal and chemical robustness of Pd based catalysts. Altogether, the presented studies emphasize the necessity to follow structural and morphological dynamics on an atomic level to fully understand the processes occurring in heterogeneous catalysts for CH_4 oxidation. By combining intelligent catalyst design with sophisticated X-ray scattering methods, detailed structural information was extracted from catalysts under operation which are inaccessible in ex situ experiments or more conventional catalysis reactor geometries. The insights obtained from the investigation of these model system successfully bridge the temperature, pressure, and complexity gap between idealized single crystal studies and monolith reactors, which can inform intelligent design of industrial catalysts. In addition to the improvement in the understanding of processes in catalytic conversion of CH_4 through Pd based catalysts, this work also reveals limitations in conventional approaches to catalytic investigations. The inherent complexity of real-world catalysts limits the available methods for detailed atomistic structural investigation and the identification of relevant parameters for catalyst activity and stability. In contrast, insights from the investigation of idealized systems, like single crystals surfaces may not be applicable to hierarchically structured catalysts. The investigations in this work are a compromise of both, which introduces a new obstacle: The knowledge of mechanistic stud-

ies from idealized model systems and activity, deactivation, and sintering studies performed with real-world catalysts need to be reconciled. Instead of homogeneous activity of NPs the presented results point towards a nuanced, highly dynamic picture with strong local heterogeneity in oxidation state, activity, reaction intermediate desorption, and H_2O inhibition. Future avenues for research emerge directly from insights presented in this dissertation. A conservative approach could be the incremental investigation of parameter space, by variation of supports, alloying metals, or nanoparticle size. Another idea is to expand on the complexity of the system by investigating NPs on defined islands or introducing defects to the support to potentially act as anchor points for nanoparticles, simulating porous structures of hierarchical catalysts. Finally, experiments could be coupled with computational modeling to help quantify energetics in order to guide future catalysis investigations and catalyst design.

4.7 Acknowledgement

I would like to use this opportunity to thank the people involved in my journey as a PhD student. At times stressful, at times exciting, I appreciate the opportunity for the experience and everyone who made it possible.
First, I would like to thank Prof. Dr. Andreas Stierle, for offering this research project to me. I am grateful for the guidance throughout my academic journey in this group. I sincerely appreciate the way he challenged me to refine my work and grow both professionally and personally.
Next, I would like to thank my colleagues who participated in the beamtimes that led to the results presented in this work. I thank Lydia Bachmann, Esko Erik Beck, Artem Zaidman, Jagrati Dwivedi, Radik Batraev, Ming-Chao Kao and Daniel Silvan Dolling. Without their help it would not have been possible to perform the experiments successfully. I would also like to extend my gratitude to Andrea Sartori and Dmitri V. Novikov, the beamline scientists at ID31, ESRF and P23, DESY. I am gratefull for the excellent local and remote support at all times of the day (and night).
I would also like to extend my gratitude to Dr. Heshmat Noei, Dr. Vedran Vonk, Dr.-Ing. Thomas Keller, and Dr. Yuemin Wang for the many discussions. In addition, I am very grateful for the fruitful collaborations within the CRC1441: I thank Prof. Dr. Philipp Plessow and Dr. Dmitry I. Sharapa, Dr. Eric Sauter and Lachlan Caulfield, and T.T.-Prof. Dr.-Ing. Yolita Eggeler and Birger Holterman for their contributions to this work.
I am also thankful for all the support and collaboration within the DESY NanoLab and would like to thank all current and former colleagues. I would like to specifically thank Lydia Bachmann who was invaluable during beamtimes with the operando catalysis chamber and introduced me to climbing, Dennis Renner for the excellent support with UHV equipment, Dr. Marcus Creutzburg for all the scientific and non-scientific discussions, and Katharina Röper for all the administrative help at the NanoLab .
Finally, I would like to thank my family and friends for all the support and encouragement, especially in the more challenging phases. Without their support, I would not be where I am today and I am deeply thankful for all the support I was privileged to experience. I am incredibly grateful to Franzi for her unwavering support throughout this journey. Her patience, emotional support and encouragement gave me the freedom and confidence to pursue this work in my own way. I also thank my brother Nick for giving me the space to disconnect and relax, especially during the writing period. I would also like to thank Lenny for always having an open ear and for reminding me to step away from my desk once in a while. Last but not least, I want to thank my parents Martina and Micha and my grandmother Ilse for their

patience, especially when my focus on this work meant I wasn't as present as they deserved.

.....
Signature

Appendix

A. Appendix of the Preamble

A.1 Temperature Calibrations

Temperature calibrations for a variety of mounting styles and substrates are shown in Figure A.1.

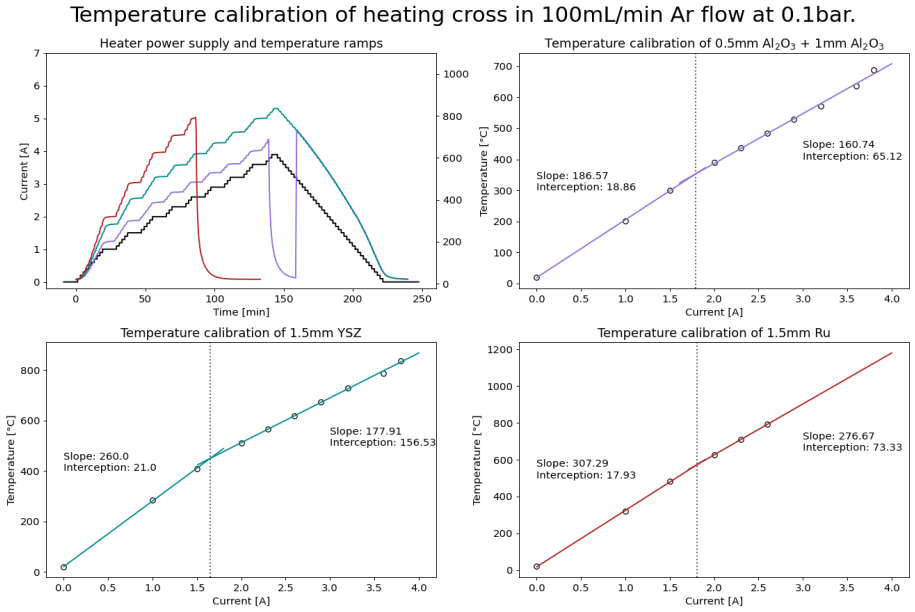

Figure A.1: Sample temperature calibration for multiple configurations.

A.2 Height Calibrations for Operando measurements

Example of a height calibration (Figure A.2) conducted for operando measurements. Previous knowledge of the expected sample z-position allows for more rapid alignment procedures leaving more time for data collection.

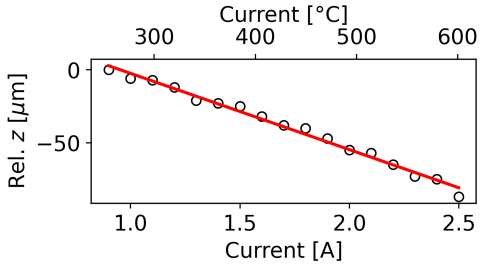

Figure A.2: Height calibration for the experiments presented in Chapter 2.

A.3 Determination of layer thickness

To estimate the thickness of layered materials from measured XPS core-level intensities, a numerical approach based on Lambert-Beer's law and a minimizing function was implemented. The approach is outlined in Section B.12.1 alongside the fit parameters used in the code below. Due to the problem being inherently non-deterministic as a result of the interdependence of the attenuation and layer thicknesses a cost function is used to minimize the deviation between simulated and experimental intensities. The following code is included as a practical example of this method so it may serve as a useful starting point for others facing similar inverse problems in surface or interface analysis.

A.3.1 Script for Layer Thickness Determination by Minimization of a Cost Function

The following pages contain the python script used for layer thickness determination by minimization of a cost function.

[ ]:
```
import numpy as np
from scipy.integrate import quad
from scipy.optimize import minimize
```

[ ]:
```
# Lambert-Beer
def attenuate(x, imfp, emissionangle):
    return np.exp(-x / (imfp*np.cos(emissionangle)))

# Compute ares from x1 and x2
def compute_areas(x1, x2):
    area_1, _ = quad(attenuate, 0, x1, args=(25,50))
    area_2, _ = quad(attenuate, x1, x2, args=(11,50))
    area_3, _ = quad(attenuate, x2, 1e3, args=(11,50))
    return area_1, area_2, area_3

# Cost function
def cost_function(x):
# Calculate the difference between the actual and target ratios
    x1, x2 = x
    area_1, area_2, area_3 = compute_areas(x1, x2)

    # Normalize the areas to compute the ratios
    actual_ratios = [area_1 / area_1, area_2 / area_1, area_3 / area_1]  #␣
↪Normalize by area_1

    # Calculate the difference between actual and target ratios
    ratio_diff = np.sum((np.array(actual_ratios) - np.array(target_ratios))**2)
    return ratio_diff  # Minimize the squared difference
```

[ ]:
```
I_h2o = 18310.81
I_o = 17839.56
I_oh = 4915.35

measurement_error = .05
err_o = np.sqrt(0.0175**2+measurement_error**2)
err_h2o = np.sqrt(0.0559**2+measurement_error**2)
err_oh = np.sqrt(0.0302**2+measurement_error**2)

# Initial guess for x1 and x2
initial_guess = [5, 6]
bounds = [(0, 1e3), (0, 1e3)] # Limits
```

[ ]:
```
#Ratios
ratio_h2o_h2o = I_h2o/I_h2o
ratio_h2o_oh = I_oh/I_h2o
ratio_h2o_o = I_o/I_h2o
target_ratios = [ratio_h2o_h2o,ratio_h2o_oh,ratio_h2o_o]
```

```
# Minimize cost function
result = minimize(cost_function, initial_guess, bounds=bounds,method='SLSQP')

# Extract the optimized x1 and x2
x1_solution, x2_solution = result.x

# Calculate the actual areas with the optimized x1 and x2
actual_area_1, actual_area_2, actual_area_3 = compute_areas(x1_solution,␣
↪x2_solution)

# Display results
print(f"Optimized Integration boundaries:")
print(f"x1 = {x1_solution} +/- {x1_solution*err_h2o}")
print(f"x2 = {x2_solution} +/- {x1_solution*err_oh}")
print(f"Actual Area 1: {actual_area_1}")
print(f"Actual Area 2: {actual_area_2}")
print(f"Actual Area 3: {actual_area_3}")

# Calculate and display the actual ratios
actual_ratios = [actual_area_1 / actual_area_1, actual_area_2 / actual_area_1,␣
↪actual_area_3 / actual_area_1]
print(f"Actual Ratios: {actual_ratios}")
print('################################################')

print(f"Number of H2O MLs = {x1_solution/3} +/- {x1_solution/3*err_h2o}") # 3 is␣
↪approximate h2o monolayer thickness
print(f"Number of OH layer without expansion = {(x2_solution-x1_solution)/(2.
↪705)}  +/- {((x2_solution-x1_solution)*np.sqrt(err_h2o**2+err_oh**2))/(2.
↪705)}")
```

```
Optimized Integration boundaries:
x1 = 5.633480835625392 +/- 0.4225039268692542
x2 = 8.216546560249817 +/- 0.32906665620566367
Actual Area 1: 5.024060404199098
Actual Area 2: 1.3485638836297038
Actual Area 3: 4.894710308783195
Actual Ratios: [1.0, 0.26842111263283724, 0.9742538733595257]
################################################
Number of H2O MLs = 1.877826945208464 +/- 0.1408346422897514
Number of OH layer without expansion = 0.9549226338722461  +/-
0.09077718769771007
```

B. SI: Atomically Smooth Fully Hydroxylated $CeO_2(001)$ Films on YSZ(001)

B.1 $CeO_2(111)$ single crystal surface.

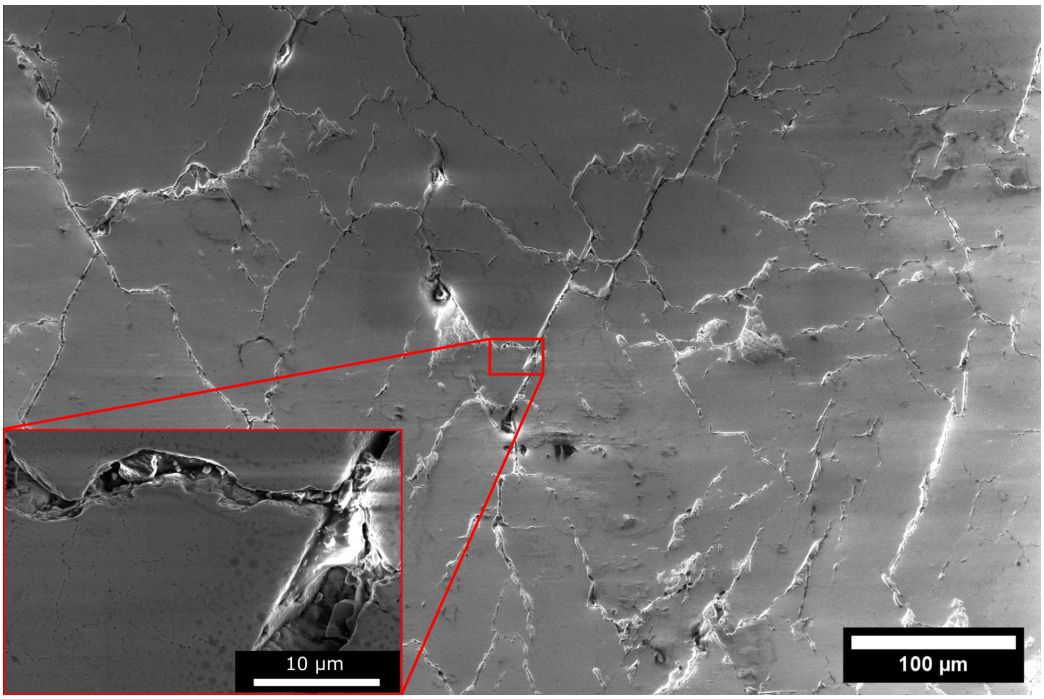

Figure B.1: SEM image of the $CeO_2(1\,1\,1)$ single crystal surface. A large number of craters, cracks, and contrast variation on the flatter areas are observed.

In Figure B.1 an overview scanning electron microscopy (SEM) image of a $CeO_2(1\,1\,1)$single crystal is shown. The inset shows a close up of the

central area marked by a the red rectangle. The images highlight the poor surface quality of commercial, polished CeO_2 single crystal substrates. While the majority of the surface is the flat areas between the cracks, the size and depth of the cracks is of the order of several µm. In addition, the flat areas are covered by larger, circular dark spots and lines of black spots. The latter appear to be small holes in the surface.

B.2 Auger Electron Spectrum of cleaned YSZ substrate.

The AES data of the cleaned YSZ single crystal, shown in Figure B.2, was measured in two parts with an overlap region between 150 eV and 200 eV in order to record high quality data with different instrument settings in both energy regimes. The left part of the spectrum was adjusted with a factor of 2.2 and an offset of 15 to match the right spectrum in the overlap region. Vertical dashed lines indicate the Mo, Zr, Y, C and O lines in the spectrum [291]. Mo lines are due to the fact that the spectrum was measured at the edge of the sample as measurements in the center of the sample were impossible due to charging. Despite that, clear Y signal at low energy (77 eV) confirms that a significant amount of the signal is from the YSZ single crystal sample. From the presented data it is clear that the majority of carbon contamination was removed by the cleaning procedure as the signal in the C region is within the error of the measurement.

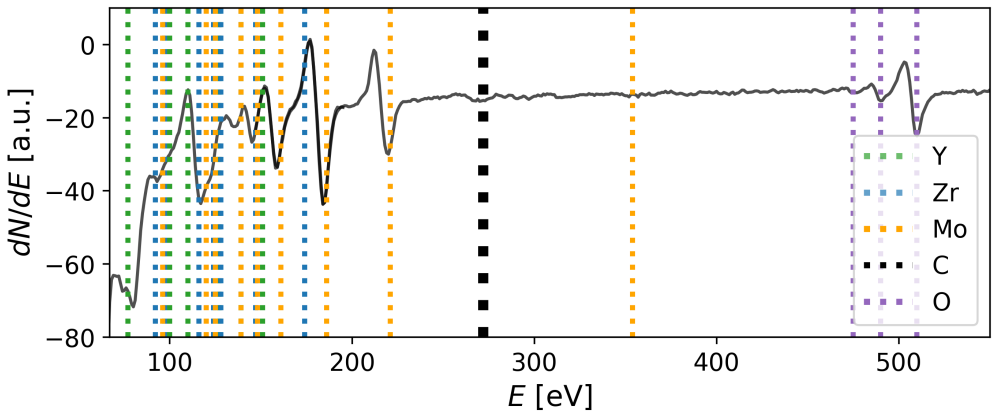

Figure B.2: AES spectrum showing typical Mo, Zr, Y and O signal indicated by the vertical, dashed lines. C signal is within the error of the measurement.

B.3 AFM overview

In Figure B.3 an overview AFM image of the same sample as Figure 1.1 is shown. The RMS roughness of the full film with the two holes in the center and the top masked, is 0.27 nm, without mask the RMS roughness is 0.58 nm, the FWHM of the height distribution profile is 0.486 nm.

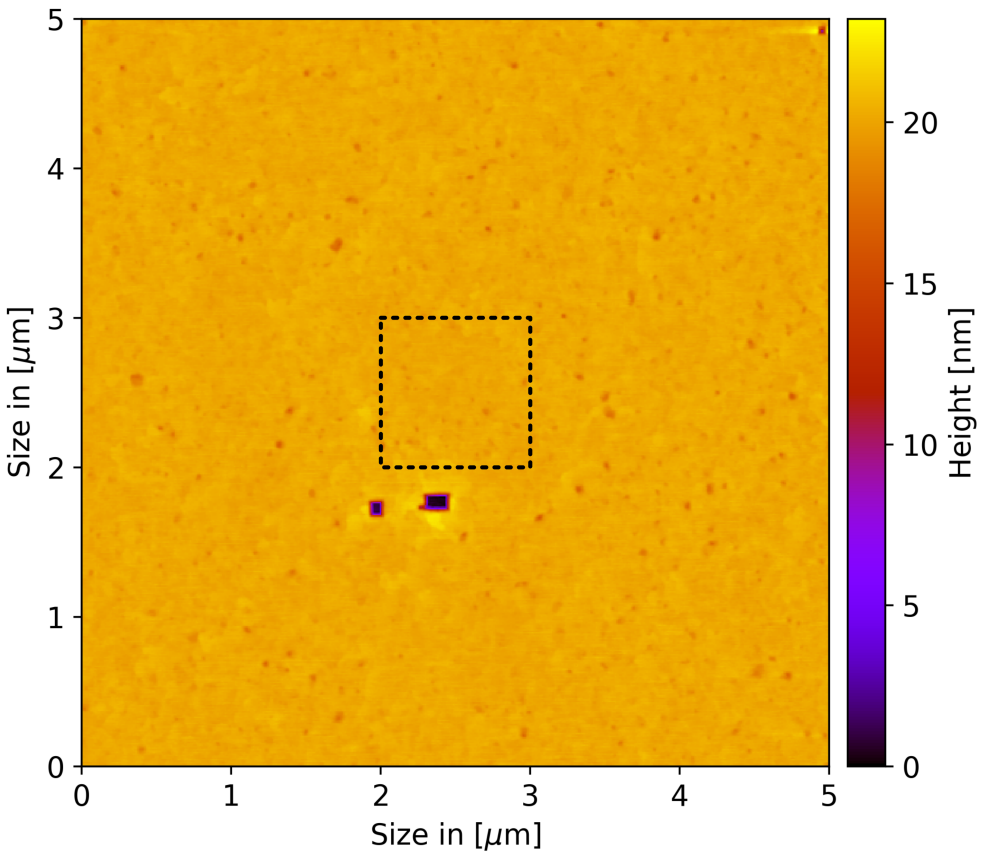

Figure B.3: Overview AFM image with the high resolution image in Figure 1.1 indicated by the dashed square.

B.4 AFM height distribution profiles

In Table B.1, the fit parameters of the height distribution profiles in Figure 1.1 and of the image in Figure B.3 are compiled. For all profiles, a single Gaussian profile was used:

$$f(x, A, \mu, \sigma) = \frac{A}{\sigma\sqrt{2\pi}} e^{[-(x-\mu)^2/2\sigma^2]}. \tag{B.1}$$

Here, A denotes the amplitude, μ the center of the Gaussian profile and $2\sigma = FWHM$.

Table B.1: Full set of fit parameters of the height distribution profile fits shown in Figure 1.1 D.

Before tube furnace annealing	
Amplitude	0.996 ± 0.003
Center	1.307 ± 0.001
FWHM	0.740 ± 0.002

After tube furnace annealing	
Amplitude	0.951 ± 0.004
Center	1.744 ± 0.001
FWHM	0.388 ± 0.002

After tube furnace annealing for the overview image in Figure B.3	
Amplitude	0.970 ± 0.003
Center	0.0157 ± 0.001
FWHM	0.486 ± 0.002

B.5 Film thickness of sample for hole analysis

In order to determine the depth of the hole, the film thickness of the sample was determined by scanning the (1 1 1) Bragg peak along the L direction. The data was fitted using one Pseudo Voigt profile to model the (1 1 1) Bragg peak and a second Pseudo Voigt profile with a constant background to account for

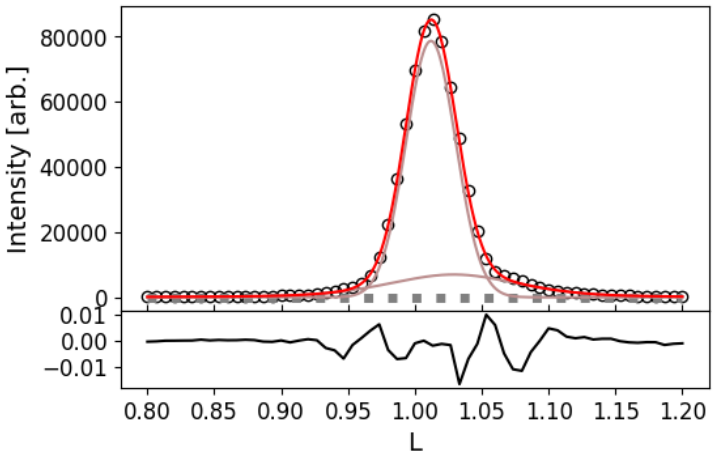

Figure B.4: Fit of the (1 1 1) Bragg peak of the sample used for the detailed investigation of the hole. The top panel shows the data as black dots, the fit as a red line and the components as brown lines. The bottom panel shows the relative residual.

diffuse scattering and the (1 1 L) CTR. Thus, full model of is

$$f(x, A, \mu, \sigma, \alpha, s, c) = \sum_{0}^{i=1} \frac{(1 - \alpha_i)A_i}{\sigma_{g,i}\sqrt{2\pi}} e^{-(x-\mu_i)^2 / 2\sigma_{g,i}^2} + \frac{\alpha_i A_i}{\pi} \left[\frac{\sigma_i}{(x - \mu_i)^2 + \sigma_i^2} \right] + c, \tag{B.2}$$

so that $\sigma_g = \frac{\sigma}{\sqrt{2\ln 2}}$ and $2\sigma = FWHM$. The variable A denotes the amplitude, α the fraction of Gaussian and Lorentzian contribution. For $\alpha = 0$ the Pseudo-Voigt profile becomes fully Gaussian, for $\alpha = 1$, the profile becomes fully Lorentzian. The full set of fit parameters is given in Table B.2.

Table B.2: Full set of fit parameters of scan through the (1 1 1) Bragg peak in Figure B.4.

(1 1 1) Bragg peak	
Amplitude	3664.935 ± 334.656
Center	1.012 ± 0.001
Fraction	0 ± 0.130
FWHM	0.044 ± 0.001

Rod and background	
Amplitude	978.688 ± 301.764
Center	1.029 ± 0.004
Fraction	0.389 ± 0.127
FWHM	0.115 ± 0.005
Y-intercept	−13.14 ± 31.25

B.6 XRR fit parameters

In Table B.3, the fit parameters of bulk and film layers corresponding to the fits in Figure 1.3 are shown. The reduced χ^2 values for the fits are 0.0178 and 6.63 $\times$ 10^{-4} before and after the furnace annealing (Figure 1.3 (A) and (B)), respectively. The density of the material is given as the real part of the refractive index in the form $n = 1 - \delta + i\beta$).

Table B.3: Fit parameters of the material for the XRR data displayed in Figure 1.3. The data in the column labeled *Before*(*after*) contains the data before (and after) the tube furnace anneal.

Layer	Parameter	Before	After
YSZ	σ in [Å]	12.04 ± 1.67	10.26 ± 0.67
CeO_2 (1)	d in [Å]	38.49 ± 4.74	
	σ in [Å]	10.7 ± 1.47	
	δ	$1.78 \times 10^{-5} \pm 7.09 \times 10^{-7}$	
CeO_2 (2)	d in [Å]	90.65 ± 1.77	122.78 ± 0.65
	σ in [Å]	2.84 ± 0.32	2.70 ± 0.137
	δ	$1.94 \times 10^{-5} \pm 5.16 \times 10^{-7}$	$1.94 \times 10^{-5} \pm 0.0$
CeO_2 (3)	d in [Å]	20.11 ± 0.39	12.87 ± 0.193
	σ in [Å]	9.51 ± 0.13	4.41 ± 0.020
	δ	$1.79 \times 10^{-5} \pm 4.91 \times 10^{-7}$	$1.84 \times 10^{-5} \pm 0.0$

B.7 Fitting results of CeO_2(111) Bragg peak profiles

In Table B.4 we present the complete fit parameters of line scans through the CeO_2(1 1 1) Bragg peak shown in Figure 1.4. Each fit was set up using a constant, linear background, and Pseudo-Voigt profile. Thus the full model of each scan is

$$f(x, A, \mu, \sigma, \alpha, s, c) = \frac{(1-\alpha)A}{\sigma_g\sqrt{2\pi}} e^{-(x-\mu)^2/2\sigma_g^2} + \frac{\alpha A}{\pi}\left[\frac{\sigma}{(x-\mu)^2+\sigma^2}\right] + sx + c, \qquad \text{(B.3)}$$

so that $\sigma_g = \frac{\sigma}{\sqrt{2\ln 2}}$ and $2\sigma = FWHM$. The variable A denotes the amplitude, α the fraction of Gaussian and Lorentzian contribution.
In Table B.5, the diffraction angles for the lattice constant refinement discussed in the main text are listed. For the in-plane lattice constant, all positions were used, for the out-of-plane lattice constant only the (1 1 1) and (1 $\bar{1}$ 1) reflections were used.

Table B.4: Full set of fit parameters for all line scans through the CeO_2 (1 1 1) Bragg peak shown in Figure 1.4. The labels *before* and *after* denote before and after the furnace annealing.

Dataset	Parameter	Value	Standard Error
L before	Slope	317.12	260.69
	Y-intercept	-398.17	258.51
	Amplitude	2175.32	22.69
	Center	0.996	0.000
	Fraction	0.420	0.024
	FWHM	0.048	0.000
L after	Slope	2142.03	952.38
	Y-intercept	-1808.07	942.19
	Amplitude	5979.56	74.27
	Center	0.999	0.000
	Fraction	0.557	0.0281
	FWHM	0.043	0.000
H before	Slope	722.24	299.51
	Y-intercept	-618.42	300.34
	Amplitude	730.31	6.78
	Center	1.002	0.000
	Fraction	0.248	0.023
	FWHM	0.025	0.000
H after	Slope	1909.03	783.34
	Y-intercept	-1620.62	784.69
	Amplitude	1289.09	14.07
	Center	1.002	0.000
	Fraction	0.024	0.031
	FWHM	0.020	0.000

Table B.5: Diffraction angles for lattice constant refinement. γ is the altitude angle, δ the azimuthal angle and θ the sample rotational angle. The subscript of the reflection indicates whether the data was recorded before or after the tube furnace annealing.

Reflection	γ	δ	θ
$(1\,1\,1)_{before}$	16.557	23.6465	17.4205
$(1\,\bar{1}\,1)_{before}$	16.561	23.5795	107.491
$(2\,0\,2)_{before}$	34.6700	34.380	0.000
$(2\,2\,2)_{before}$	51.2200	34.317	0.000
$(1\,1\,1)_{after}$	16.4468	23.66	17.6606
$(1\,\bar{1}\,1)_{after}$	16.341	23.6055	107.666

B.8 Fitting results of mosaic distribution around preferential orientations.

In order to quantify the mosaic distribution of the film crystal structure we performed fits of the diffraction peaks in Figure 1.4 A and C of the $\{2\,0\,0\}$ and $\{2\,2\,0\}$ in plane peaks. The fitted data is shown in Figure B.5, the full set of fit parameters in Table B.6. The data with the fitted model using a Gaussian model with a constant background:

$$f(x, A, \mu, \sigma) = \frac{A}{\sigma\sqrt{2\pi}} e^{[-(x-\mu)^2/2\sigma^2]} + c \tag{B.4}$$

Here, A denotes the amplitude, c the constant offset, and $2\sigma = FWHM$.

Table B.6: Full set of fit parameters of the data shown in Figure B.5.

	Fitted values			
Parameter	(2 0 0) before	(2 2 0) before	(2 0 0) after	(2 2 0) after
C:	46.30 ± 5.28	38.63 ± 3.13	57.12 ± 12.29	48.74 ± 9.25
Amplitude:	2401.71 ± 124.44	1733.04 ± 71.83	4429.89 ± 229.31	3513.74 ± 170.17
Center:	-28.31 ± 0.033	-66.14 ± 0.025	-28.55 ± 0.021	-66.36 ± 0.019
FWHM:	1.29 ± 0.077	1.225 ± 0.058	0.812 ± 0.048	0.789 ± 0.044
C:	45.58 ± 4.76	39.75 ± 3.51	54.80 ± 10.99	48.11 ± 8.83
Amplitude:	2538.77 ± 106.64	1519.48 ± 79.61	4869.54 ± 201.34	3633.95 ± 160.27
Center:	61.69 ± 0.024	23.863 ± 0.0305	61.46 ± 0.016	23.645 ± 0.017
FWHM:	1.169 ± 0.056	1.195 ± 0.072	0.783 ± 0.037	0.768 ± 0.039

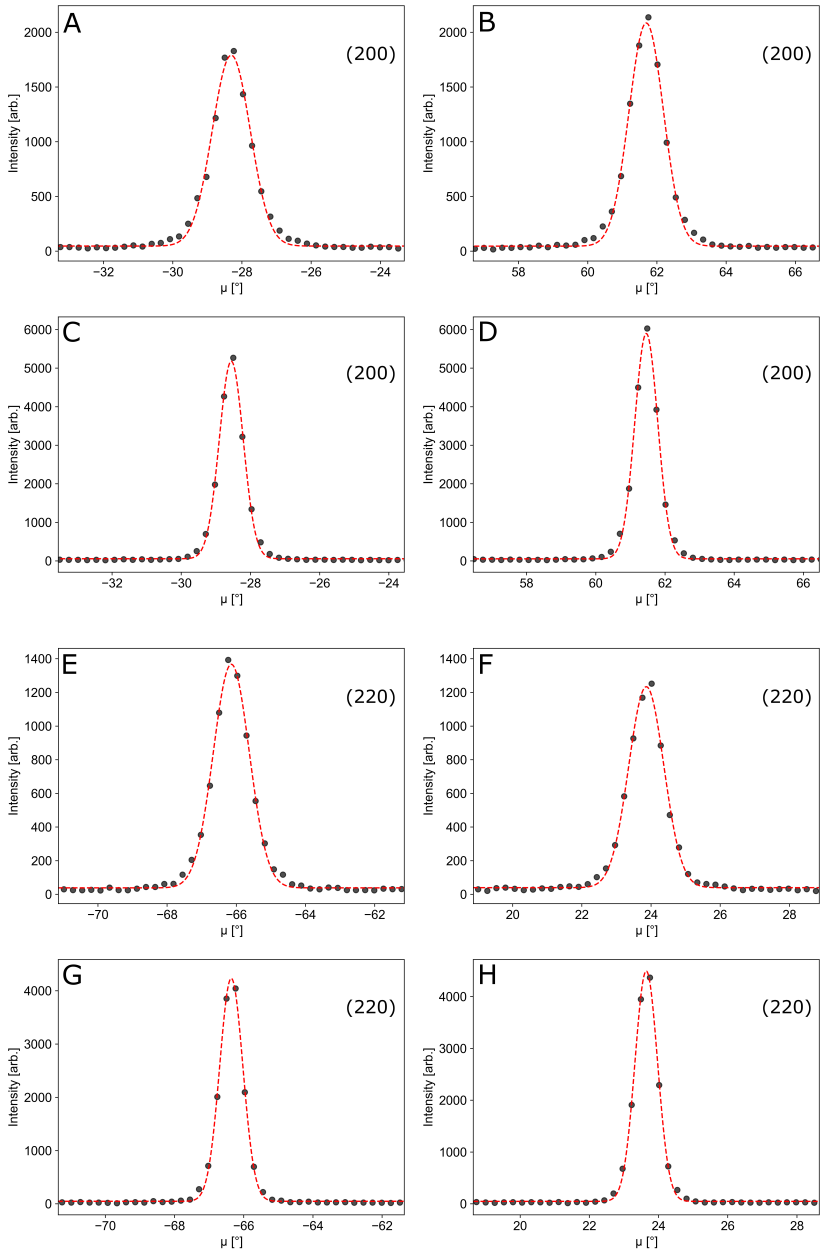

Figure B.5: Fits of the in-plane diffraction peaks of CeO_2. **A**, **B**: (2 0 0) before furnace anneal, **C**, **D**: (2 0 0) after furnace anneal, **E**, **F**: (2 2 0) before furnace anneal, **G**, **H**: (2 2 0) after furnace anneal.

B.9 Dislocation network periodicity

From the relativ distance between the film or bulk reflection to the dislocation peak, the periodicty can be calculated [292]. For this purpose, the data was fitted using two Pseudo Voigt profiles, one fore the CeO_2 (2 2 0) reflection, one for the dislocation peak. The model is identical to Equation B.2. In Figure B.6, the fitted data is shown, and in Table B.7, the fit parameters are listed for all fits.

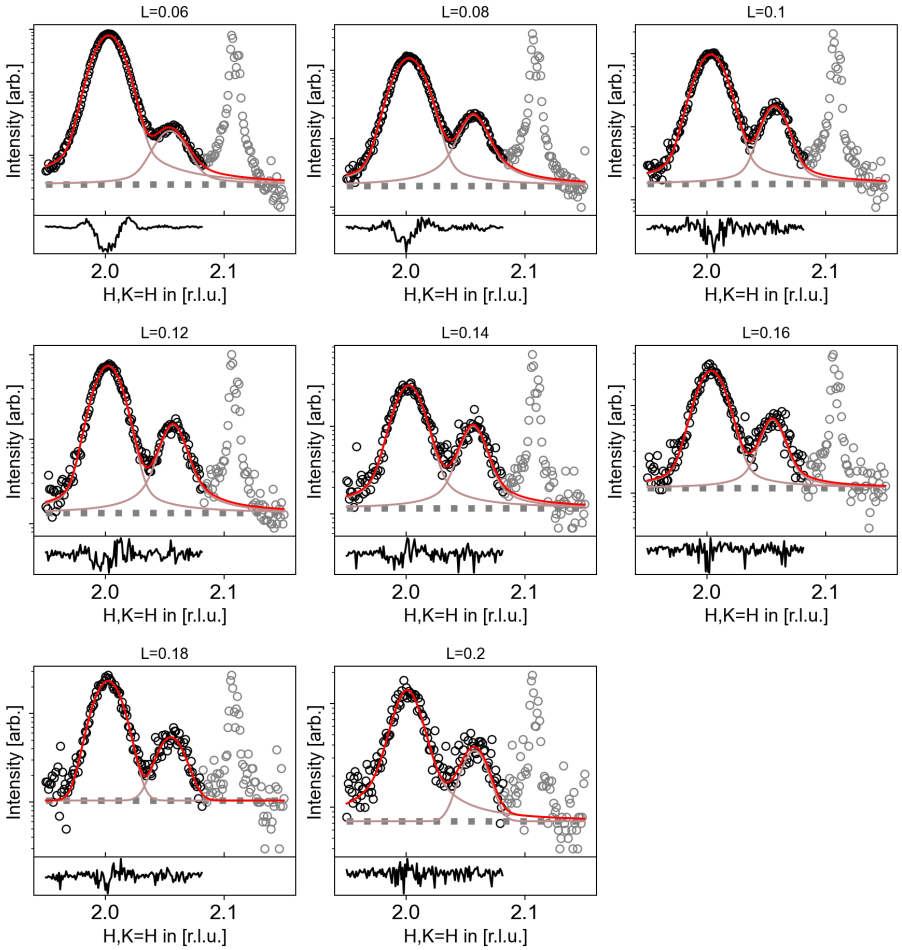

Figure B.6: Fits of the (2 2 0) of CeO_2 reflection and the dislocation peak at different values of L.

Table B.7: Full set of fit parameters of the data shown in Figure B.6.

L=0.06	Amplitude	Center	FWHM	Fraction
CeO_2(220)	232.31 ± 2.94	2.0028 ± 0.00008	0.0235 ± 0.00019	0.24 ± 0.012
Disl. peak	9.67 ± 0.487	2.0565 ± 0.00035	0.0265 ± 0.00119	1.00 ± 0.100
BG const.	−20.35 ± 5.260			
L=0.08	Amplitude	Center	FWHM	Fraction
CeO_2(220)	47.99 ± 0.85	2.0024 ± 0.00012	0.0258 ± 0.00031	0.29 ± 0.030
Disl. peak	7.23 ± 0.23	2.0574 ± 0.00026	0.0225 ± 0.00099	0.93 ± 0.084
BG const.	3.23 ± 2.8728			
L=0.1	Amplitude	Center	FWHM	Fraction
CeO_2(220)	28.64 ± 0.83	2.0032 ± 0.00017	0.0258 ± 0.00045	0.21 ± 0.051
Disl. peak	4.66 ± 0.27	2.0570 ± 0.00031	0.0216 ± 0.00097	0.43 ± 0.16
BG const.	13.89 ± 3.09			
L=0.12	Amplitude	Center	FWHM	Fraction
CeO_2(220)	21.40 ± 0.68	2.0023 ± 0.00020	0.0240 ± 0.00053	0.28 ± 0.0545
Disl. peak	4.18 ± 0.22	2.0574 ± 0.000385	0.0215 ± 0.00138	0.74 ± 0.1416
BG const.	7.03 ± 2.402			
L=0.14	Amplitude	Center	FWHM	Fraction
CeO_2(220)	8.47 ± 0.49	2.0022 ± 0.000338	0.0253 ± 0.00094	0.35 ± 0.1232
Disl. peak	2.60 ± 0.22	2.0564 ± 0.00053	0.0220 ± 0.00178	0.61 ± 0.224
BG const.	11.26 ± 2.472			
L=0.16	Amplitude	Center	FWHM	Fraction
CeO_2(220)	7.12 ± 0.47	2.0037 ± 0.00034	0.0257 ± 0.00096	0.23 ± 0.142
Disl. peak	1.58 ± 0.18	2.0553 ± 0.00065	0.0206 ± 0.00206	0.60 ± 0.289
BG const.	11.43 ± 2.343			
L=0.18	Amplitude	Center	FWHM	Fraction
CeO_2(220)	6.16 ± 0.51	2.0022 ± 0.00036	0.0260 ± 0.00097	0.00 ± 0.181
Disl. peak	1.15 ± 0.26	2.0551 ± 0.00080	0.0248 ± 0.00215	0.00 ± 0.645
BG const.	10.42 ± 2.698			
L=0.2	Amplitude	Center	FWHM	Fraction
CeO_2(220)	4.14 ± 0.31	2.0009 ± 0.00046	0.02457 ± 0.00148	0.60 ± 0.151
Disl. peak	0.71 ± 0.173	2.0575 ± 0.00085	0.02393 ± 0.00252	0.00 ± 0.698
BG const.	7.31 ± 1.765			

B.10 HR-STEM and geometrical phase analysis

In Figure B.7 we present high resolution scanning transmission electron microscopy (STEM) micrographs used for determining the misfit dislocation spacing. The micrograph in Figure B.7 (A) was filtered using an average background subtraction filter (ABSF), the micrograph in Figure B.7 (B) was filtered using a convolutional neural network filter [293]. The extracted distances are listed in Table B.8.

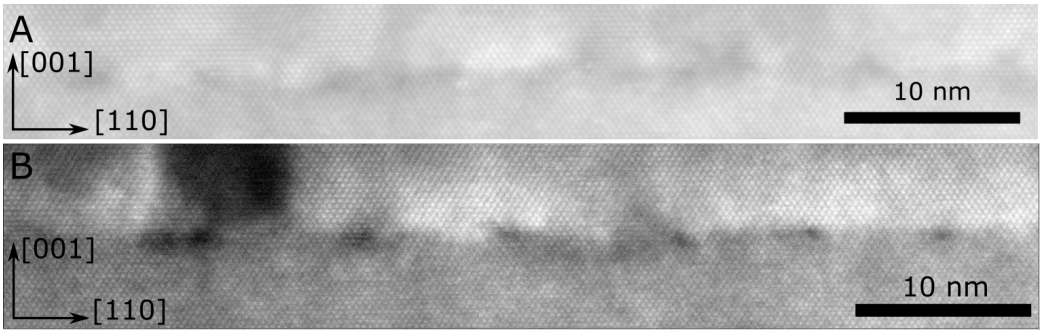

Figure B.7: HR-STEM images of the area 1 (A) and area 2 (B) of the [1 1 0]/[0 0 1] specimen.

From the distances listed in Table B.8 the probability density, shown in Figure 1.6 was calculated using

$$\rho(x) = \frac{1}{nh}\sum_{i=1}^{n} K(\frac{x - X_i}{h}), \tag{B.5}$$

where n is the number of dislocations, h is the window width, x is the dislocation distance, and K is a Gaussian profile with the property $\int_{-\infty}^{\infty} K(x)dx = 1$. The window width was chosen by halving the Scotts factor $n^{1/(d+4)}$, with $d = 1$ being the number dimensions of the dataset [294]. In Figure B.8 we present the remaining strain field vector maps of the micrograph analyzed in the main text.

Table B.8: Full set of dislocation distances extracted from Bragg filtered images depicted in Figure B.7.

Distances in area 1 [Å]		Distances in area 2 [Å]	
Reflection pair #1	Reflection pair #2	Reflection pair #1	Reflection pair #2
8.90	9.51	7.43	6.45
8.18	3.20	11.87	6.97
3.05	6.71	7.87	5.22
7.23	7.75	8.80	7.7
7.76	8.50	8.39	10.14
8.85	7.23	7.72	7.49
6.57	7.35		7.84

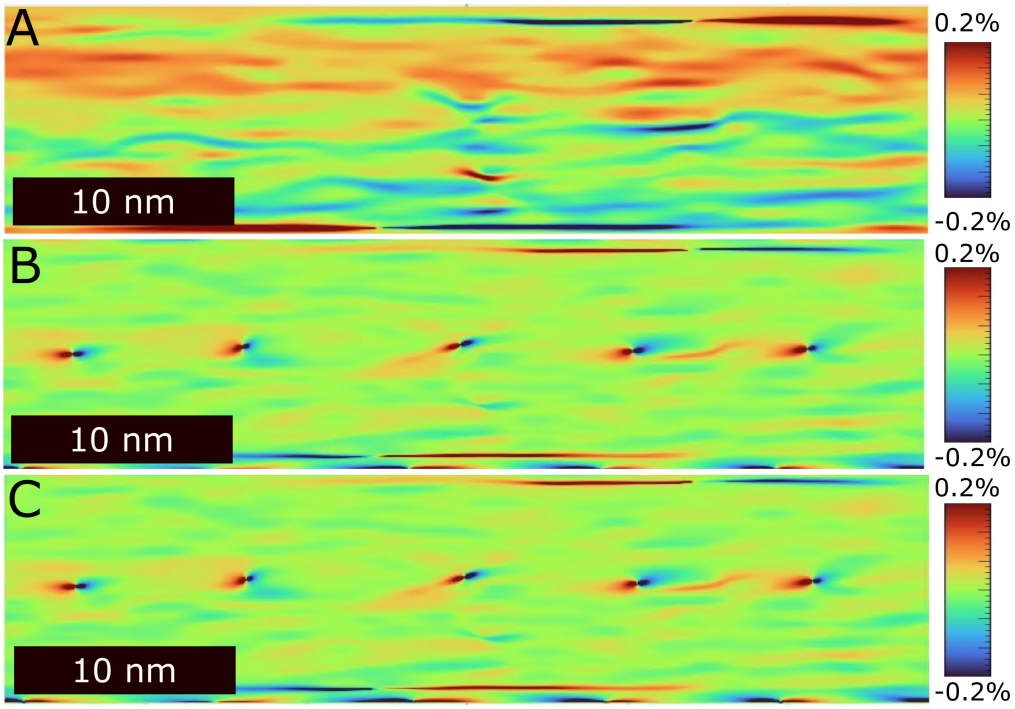

Figure B.8: Geometric phase analysis of the data HR-STEM data presented in Figure 1.6 A in the main text. A: Compressive/tensile strain along interface normal. B: Shear strain along the interface normal. C: Shear strain perpendicular to the surface normal.

B.11 XPS survey scan

This survey scan was used for the elemental analysis and confirm that the sample is clean. The data was recorded in the same experiment as the core spectra shown in Figure 1.7. Peaks were identified using [295].

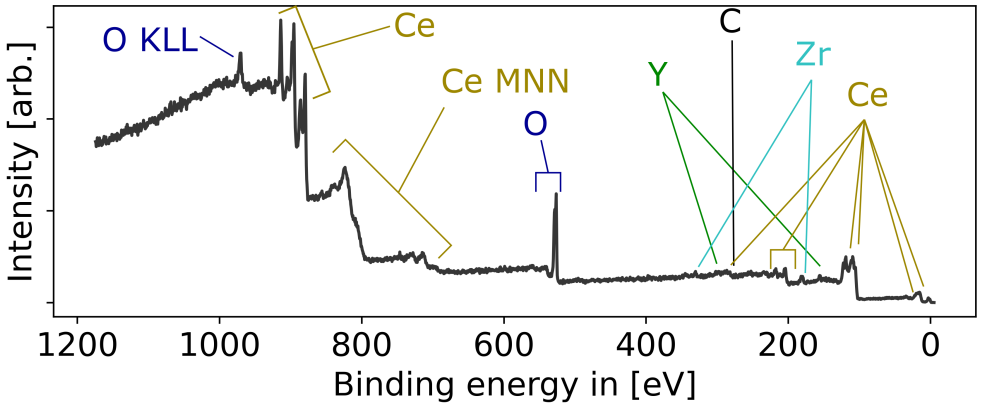

Figure B.9: XPS survey scan of CeO_2/YSZ with all contributions identified.

B.12 XPS Ce $3d$, O $1s$, and C $1s$ core levels

All XPS core levels were deconvoluted using a Shirley background and a number of Pseudo-Voigt profiles

$$f(x, A, \mu, \sigma, \alpha, s, c) = \frac{(1-\alpha)A}{\sigma_g\sqrt{2\pi}} e^{-(x-\mu)^2/2\sigma_g^2} + \frac{\alpha A}{\pi}\left[\frac{\sigma}{(x-\mu)^2+\sigma^2}\right] \tag{B.6}$$

with $\sigma_g = \frac{\sigma}{\sqrt{2\ln 2}}$ and $2\sigma = FWHM$. The variable A denotes the peak area, α the fraction of Gaussian and Lorentzian contribution.
The fit of the Ce $3d$ core level spectrum in Figure 1.7 A, described in the main text, yielded the fit parameters given in Table B.9.
For the fit of the O $1s$ core level spectrum shown in Figure 1.7 B, Pseudo-Voigt line shapes with $\alpha = 0.5$ were chosen on the basis of the tails of

Table B.9: Fit parameters of Ce $3d$ core level fit.

Name	Position	FWHM	Area
v	882.20	1.57	24251
v”	888.81	3.90	30430
v”’	898.04	1.91	35291
u	900.60	1.57	16167
u”	907.21	3.90	20286
u”’	916.44	1.91	23527
asymm 1	883.87	4.00	25125
asymm 2	902.27	4.00	14169

Table B.10: Fit parameters of O 1s core level fit.

Name	Position	FWHM	Area
O2-	528.98	1.28	6088.6
O-H	530.16	1.18	1677.6
H2O	531.18	1.70	6249.4
C-O, C-O-H	532.73	3.31	771.5

the rightmost peak at 528.98 eV. In addition, the spectrum was corrected by the sensitivity factor of 2.93 (1 for the C 1s spectrum) and the sum of the oxygen containing components from the C1s spectrum where used as an upper limit for the peak at 532.82 eV in the O 1s spectrum. The fit parameters are listed in Table B.10. For the fit of the C 1s spectrum, shown in Figure B.10, $\alpha = 0.5$ was chosen on basis of the shape of the rightmost peak at 284.82 eV. The full set of fit parameters is listed in Table B.11. We assign the rightmost component to species containing C−C and C−H and the other two components to species containing C−O and C=O in different chemical environments.

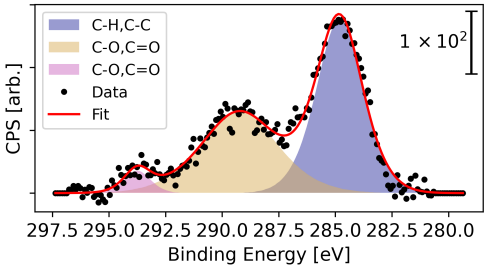

Figure B.10: C 1s core level (black dots) including fit (red line), and fitted components (colored peaks).

Table B.11: Fit parameters of C 1s core level fit.

Name	Position	FWHM	Area
C-H,C-C	284.82	2.42	1490.70
C-O,C=O	289.24	3.96	1145.43
C-O,C=O	293.75	1.37	109.79

B.12.1 XPS layer analysis

To better understand the O 1s spectrum, layer analysis based on Lambert-Beer's law

$$A_i = \frac{I_i}{I_0} = \int_{x_0}^{x_f} e^{\frac{-x}{\Lambda_i \cos(\Theta)}} \tag{B.7}$$

was carried out. Here, I and I_0 are the transmitted and initial intensity, x the distance travelled, Λ the inelastic mean free path (25 Å for H_2O[296], and 11 Å for CeO_2[297]), and Θ the emission angle. The index i denotes a layer of the model. The layer model consists of an H_2O layer ($x_0 = 0$, $x_f = x_1$), an OH layer ($x_1 = x_0$, $x_f = x_2$) terminating the surface of the thin film and the bulk O^{2-} layers ($x_0 = x_2$, $x_f = 100$). With $x_f = 100$ instead of ∞ for the final layer, the problem remains discrete and the error is negligible. The ratios of the measured intensities, given in Table B.10 are compared to the ratios of calculated intensities using Equation B.7 by

$$\frac{I(H_2O)}{I(H_2O)} = 1 = \frac{A_1}{A_1}$$

$$r_2 = \frac{I(OH)}{I(H_2O)} \stackrel{!}{=} \frac{A_2}{A_1} = R_2$$

$$r_3 = \frac{I(O^{2-})}{I(H_2O)} \stackrel{!}{=} \frac{A_3}{A_1} = R_3.$$

The solution is found by minimizing the cost function

$$C(x_1, x_2) = (R_2(x_1, x_2) - r_2)^2 + (R_3(x_1, x_2) - r_3)^2 \tag{B.8}$$

using the least mean square method. The result of Equation B.8 is $x_1 = 5.63 \pm 0.42$ Å and $x_2 = 8.22 \pm 0.33$ Å. The errors are calculated from the area uncertainties and 5 % measurement error. For the H_2O layer this corresponds to 1.83 ± 0.14 monolayers, approximating the thickness of one monolayer with 3 Å[298]. Considering the expansion of the top layer determined by CTR analysis (see Figure 1.5), the OH layer has a thickness of 0.95 ± 0.09 monolayers.

B.13 *S*-polarized IRRAS spectrum

In Figure B.11 the *s*-polarized spectrum of the 0.1 L dosing step shown in Figure 1.8 is presented. As for all other presented IRRAS spectra, no signal CO vibration could be observed.

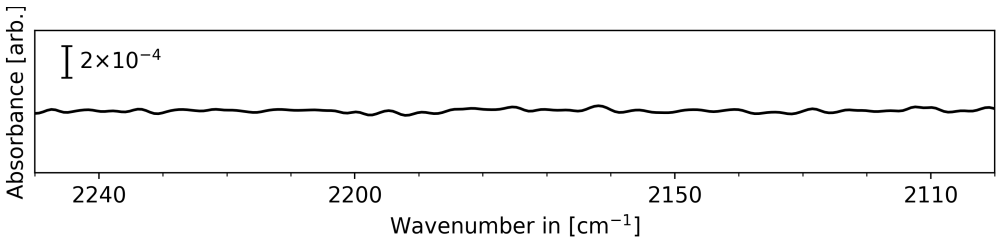

Figure B.11: *S*-polarized IRRAS spectrum of the 0.1 L dosing step shown in Figure 1.8.

C. SI: Complex Evolution of Oxide Supported Pd Catalysts During Methane Oxidation Light-off

C.1 Pd nominal thickness

The NPs of the two catalysts Pd/Al_2O_3 and Pd/CeO_2 were deposited using e-beam MBE evaporation (see Methods section in the main text). The amount of Pd was calibrated with a prior experiment, depositing Pd on $Al_2O_3(0\,0\,0\,1)$. For both catalysts, a nominal thickness of 2 nm was chosen based on the calibration shown in Figure C.1. Fit parameters are shown in Table C.1

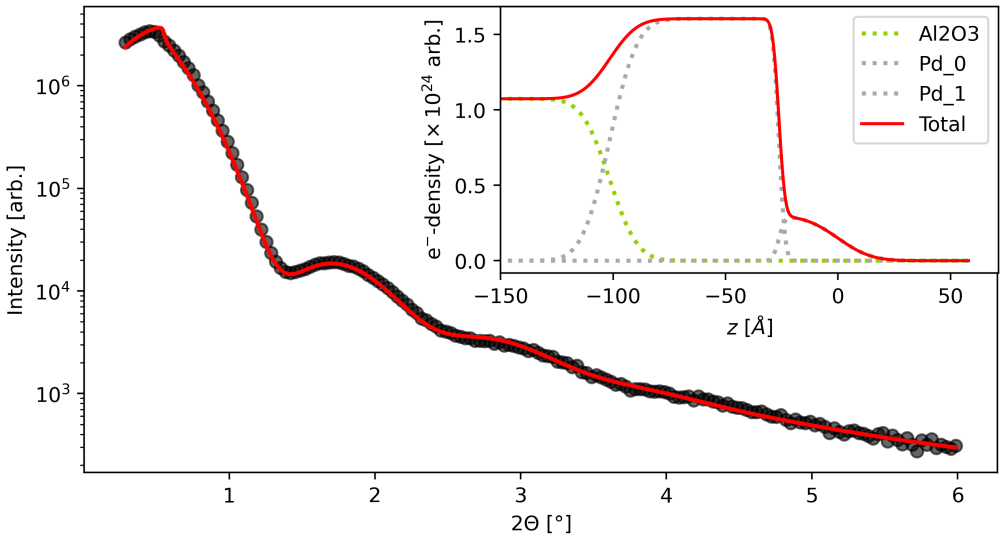

Figure C.1: X-ray reflectivity measurement of $Pd/Al_2O_3(0\,0\,0\,1)$ of the calibration sample.

Table C.1: Fit parameters for the XRR fit shown in Figure C.1

$\sigma(Al_2O_3)$	9.74 ± 0.221 Å
$d(Pd_0)$	75.195 ± 0.239 Å
$\sigma(Al_2O_{30})$	2.171 ± 0.094 Å
$\delta(Pd_1)$	$6141.511 \pm 44.275 \frac{g}{cm^2}$
$d(Pd_1)$	26.283 ± 0.845 Å
$\sigma(Pd_1)$	11.6 ± 0.0 Å
$\delta(Pd_1)$	$1143.602 \pm 36.789 \frac{g}{cm^2}$

C.2 Pd epitaxy

The Pd nanoparticle majority ensembles for both samples are (1 1 1) oriented relative to the sample normal and the in-plane $[1\,\bar{1}\,0]$-type directions are aligned with the $[1\,\bar{1}\,\bar{2}\,0]$ direction for the alumina sample and the [1 0 0] and [0 1 0] directions for the ceria sample. A second minority out-of-plane ensemble of [0 0 1] oriented particles with the $[1\,\bar{1}\,0]$ axis being aligned with the [1 0 0] axis of CeO_2 was found. Detailed description and analysis is given in the supplementary in Figure C.3 and accompanying text. In order to de-

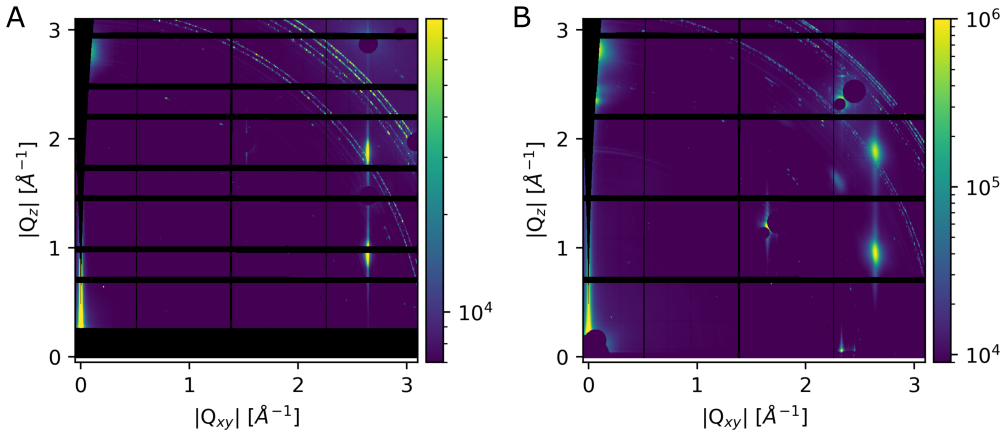

Figure C.2: Summed ω (sample rotation) scans of Pd/Al_2O_3 (**A**), and Pd/CeO_2 (**B**), recorded at 411 K.

termine the epitaxial relationship between substrate and particles, rocking scans (Figure C.2 **A** for Pd/Al_2O_3 and **B** for Pd/CeO_2) of the sample rotation were performed and ROIs around the Pd (Figure C.3 **B** and **C**) signal(s) were summed. The integrated intensities were normalized by the peak intensity of the Pd(1 1 1) Bragg peak rocking scan. In case of the alumina sample, a single Pd(1 1 1)-type Bragg peak was found over the 100 ° scan. The Bragg peak position is in line with (1 1 1) oriented nanoparticles. In the detector image in Figure C.3 **B** the CTR signal of the $(1\,\bar{1}\,0\,L)$ rod around the blocked $(1\,\bar{1}\,0\,2)$ Al_2O_3 reflection can be seen. Hence, the (1 1 1) nanoparticles in plane $[1\,\bar{1}\,0]$ direction is aligned with the $[1\,\bar{1}\,0\,0]$ direction of Al_2O_3. The epitaxial relationship of Pd and CeO_2 is more complicated with two particle orientations relative to the sample normal (black and gray ROIs in Figure C.3 **C**). The Bragg peak in the black ROI originates from (1 1 1) oriented particles, while the gray peak originates from (0 0 1) oriented particles. A plethora of peaks were observed in the rocking scan of the (1 1 1)-type Bragg peak of (1 1 1) oriented nanoparticles. The scan is dominated by 30 ° spaced peaks

corresponding to the in-plane [1 $\bar{1}$ 0] direction being aligned with the in-plane [1 0 0]-like directions of the CeO_2 substrate. In between this majority species a second set of much smaller peaks was found with 15 ° spacing in respect to the majority ensemble. These (1 1 1) oriented particles have the in-plane [1 $\bar{1}$ 0] direction aligned with the [1 1 0] direction of the substrate. The third ensemble gives rise to the small side peaks spaced 6.35 ° from the majority ensemble peaks and represent a the smallest ensemble with the [1 $\bar{1}$ 0] in plane direction at an angle of ± 6.35 ° in-plane in respect to the [1 0 0] and [0 1 0] CeO_2 directions. The largest peak of the rocking scan labelled Pd(1 1 1)* is at the same position as the CeO_2(2 2 2)-type Bragg peak which is in line cube-on-cube epitaxy, i.e. the [1 0 0] axes of CeO_2 and Pd nanoparticles are aligned.

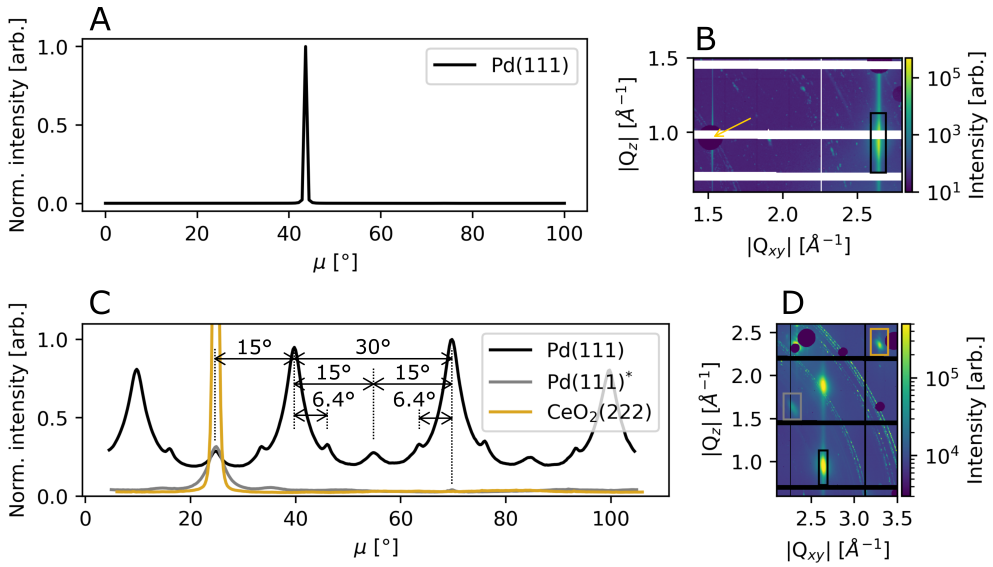

Figure C.3: Rocking scans of the sample rotation (**A**, **C**) of the alumina and ceria sample. In **B** and **D**, the respective ROIs are shown in detector images corresponding to maxima of the Pd(1 1 1) rocking scans.

C.3 NP diameters from SEM

Confirmation of good agreement between the average domain size, determined by HEGIXRD, and the NP size was achieved by comparing results from HEGIXRD and the initial and final NP shape observed by SEM (see Figure C.6 **A**-**C**). The isolating substrates and charge trapping at the NP substrate interface for metallic NPs on oxide substrates, made data pretreatment necessary before collecting NP statistics. This entailed background subtraction, by blurring the images using a gaussian filter with a width of 1.1 px, carefully masking the area between the NPs by thresholding and subsequently setting the values to zero. This procedure was repeated up to three times, until a mask which reproduced the NP size well was obtained by thresholding. Original SEM micrographs and the micrographs with the overlayed mask are shown in Figure C.4 (as prepared catalysts) and Figure C.5 (catalysts after light-off). For both images, **A** and **B** shows data for Pd/Al_2O_3 and **C** and **D** shows data for Pd/CeO_2. For both SEM micrographs of the as-prepared catalysts (Figure C.4 **A** and **C**), some NPs in the original image were not separated by the mask. In order to avoid overestimating the NP diameter, NPs that could be unambiguously be identified as isolated NPs in the original images were separated by hand. A linewidth of 1 px was chosen to avoid underestimating the NP diameter by removing significant areas in the mask. For the mask in Figure C.5, **B**, only features of the mask that can be unambiguously be identified as Pd NPs in Figure C.5 **A** were considered for the histogram in Figure C.6 **B**. Furthermore, all NPs at the edge of the images were removed from the mask in order to avoid to skewing the average size towards smaller values. The histograms in Figure C.6 show the NP diameter, calculated from the masked areas in Figure C.4 and Figure C.4, assuming a circular shape. The panels contain data for Pd/Al_2O_3 (**A** and B, before and after light-off experiment) and Pd/Al_2O_3 (**C** and D, before and after light-off experiment). The bin size was chosen at 20 % of the sample size (rounded to the nearest 10). The vertical, dashed lines show the respective mean size, the solid lines shows the coherent domain size obtained by HEGIXRD (Figure 2.3) at 411 K and 827 K and steady state in reaction gas mixture. Overall, the size determined from HEGIXRD agrees well with the diameters from SEM. Especially after light-off (**B**, **D**), the domain size determined by HEGIXRD is smaller than the NP size determined by SEM. In the case of Pd/Al_2O_3, this is due to agglomeration, in case of Pd/CeO_2 the summed domain size from Pd and PdO agrees remarkably well with the diameter obtained by SEM analysis. In sum, the comparison of SEM and HEGIXRD results confirms that the coherent domain size serves as a excellent indicator of the NP size.

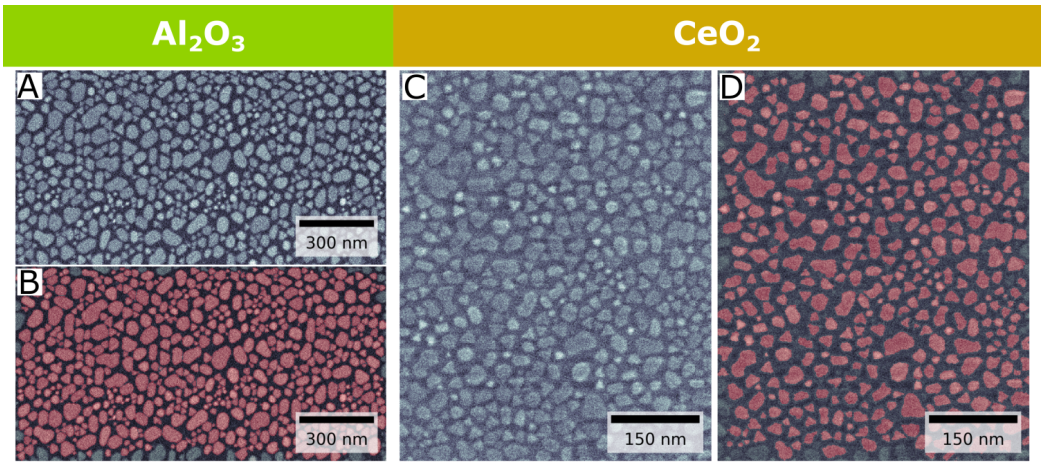

Figure C.4: SEM image of Pd/Al_2O_3 and Pd/CeO_2 (**A**,**C**) recorded ex situ before the light-off experiment. **B** and **D** show the same images with the masks used to quantify NP diameter.

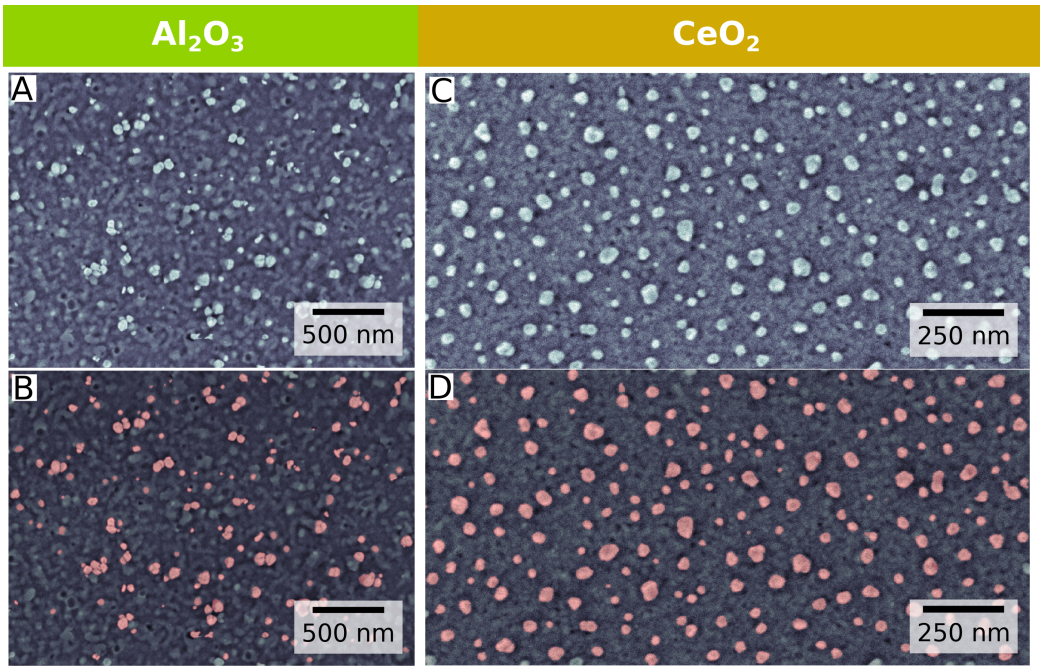

Figure C.5: SEM image of Pd/Al_2O_3 and Pd/CeO_2 (**A**,**C**) recorded ex situ after the light-off experiment. **B** and **D** show the same images with the masks used to quantify NP diameter.

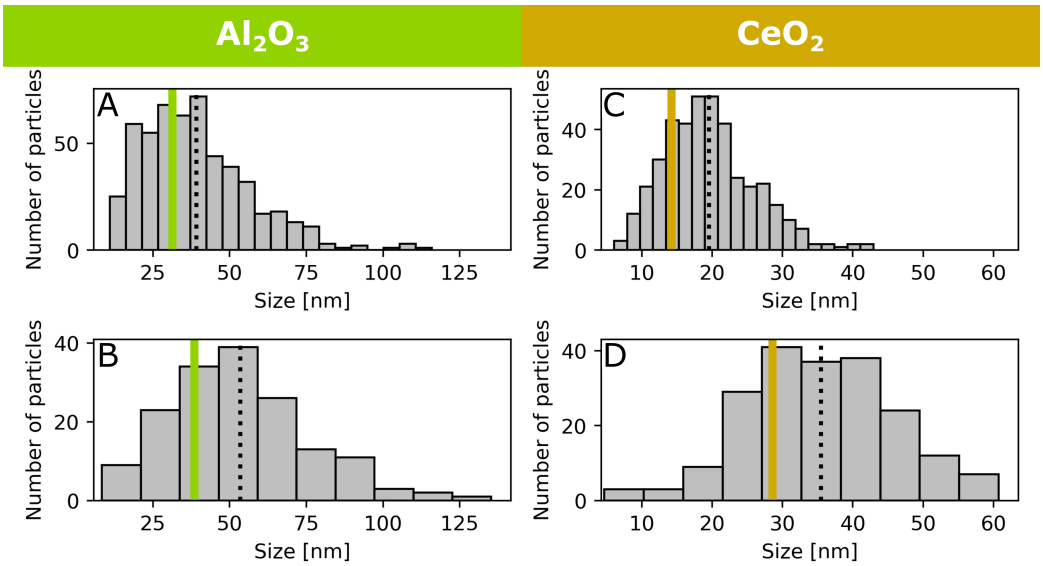

Figure C.6: Histograms of the NP diameters determined from the data presented in Figure C.4 and Figure C.5. The dotted vertical line indicates the mean diameter determined by the SEM data, the solid dotted line indicates the diameter determined at 827 K after dwell time in reaction gas mixture by HEGIXRD.

C.4 AFM line scans

An estimate of the agglomerate height of the particles of Pd/Al_2O_3 was attained by extracting line scans through the agglomerates Figure C.7. For comparison, a line scan through the smaller particles is also shown in blue.

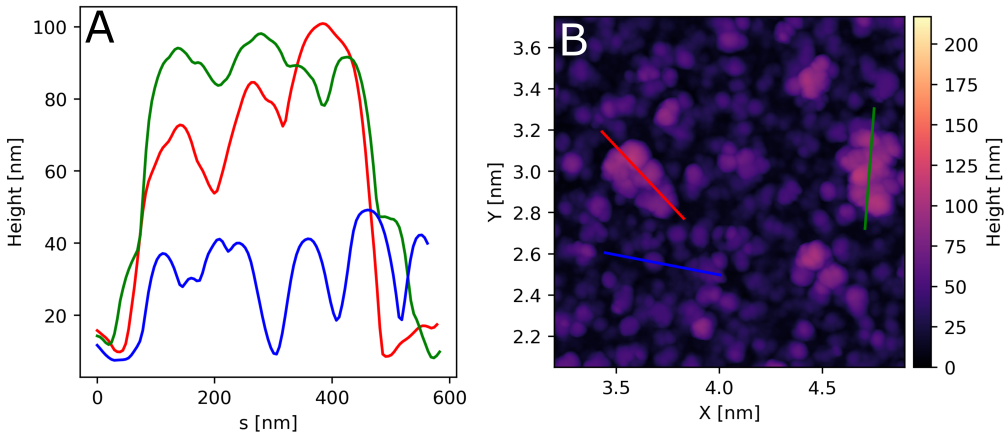

Figure C.7: Line scans (**A**) extracted from AFM image. Larger frame of the SEM in image in Figure 2.4 in the main text (**B**). The position of the line scans in **A** are indicated by lines of the same color in **B**.

C.5 Data treatment of mass Spectrometry signal

The normalization of the MS data was achieved by first subtracting a baseline value, the mean value of the 50 smallest data points, and then divided by the mean value of the 50 largest datapoints. For the purpose of clarity, the mass spectrometry data was smoothened with a Savitzky–Golay filter with the window width 50 (20 for H_2O due to more dynamic changes in the signal) and the polynomial order 3 was chosen to smoothen the data.

C.6 O_2 Mass Spectrometry signal

Due to the 100-fold higher O_2 flow throughout the experiment no relevant changes in the O_2 signal were observed (see Figure C.8). The slight changes in the O_2 mass spectra or smaller or of the the order of the error of the measurement.

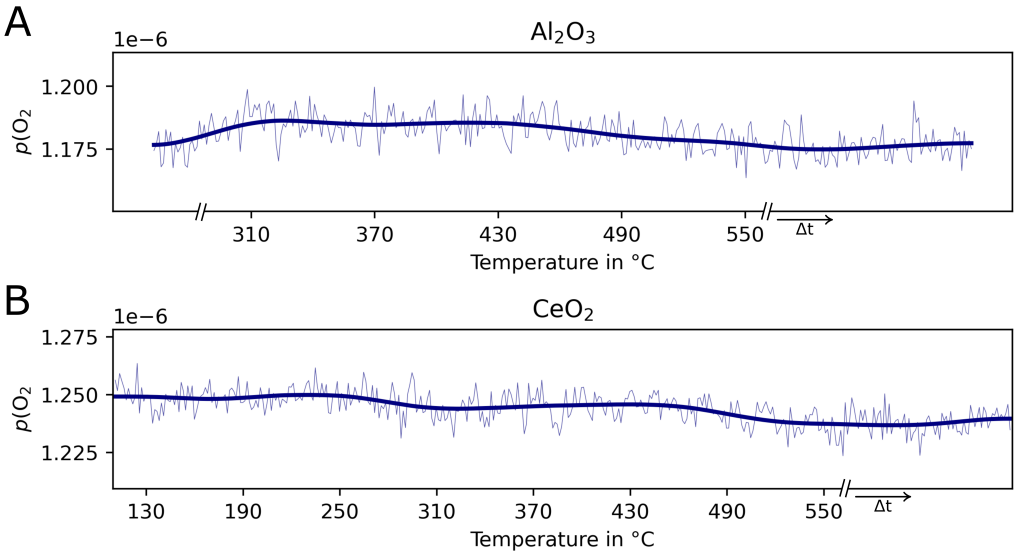

Figure C.8: O_2 mass spectrometry signal of Pd/Al_2O_3 (**A**) and Pd/CeO_2 (**B**).

C.7 CO_2 fragmentation and CO signal

An intrinsic error in mass spectrometry is the fragmentation of molecules during the measurement process. This is especially crucial in regard to CO, and CO_2. For this purpose we subtract the expected CO signal from fragmentation of CO_2 [299] from the CO signal. A comparison of the two signals is given in Figure C.9 illustrating that CO is produced by both samples during CO_2 light-off. Throughout this work the corrected intensity will be used.

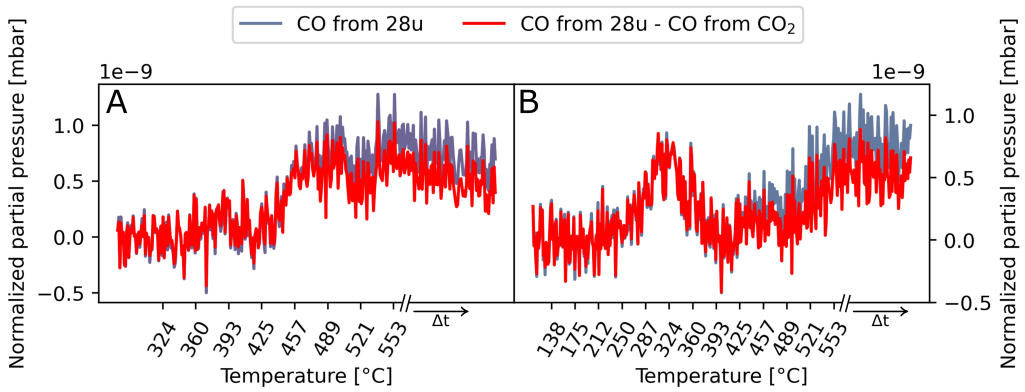

Figure C.9: Comparison of the CO and corrected CO signal for Al_2O_3 (**A**) and CeO_2 (**B**).

C.8 Identification of phases during light-off

The data presented in Figure 2.1 **A** and the data from Bragg peak analysis in Figure 2.3 was extracted from high-symmetry planes of reciprocal space, namely the $[1\,1\,0]/[0\,0\,1]$ (in CeO_2 coordinates) plane for the CeO_2 sample and the $[0\,1\,\bar{1}\,0]/[0\,0\,0\,1]$ plane (in Al_2O_3 coordinates). The full set of images is displayed in Figure C.10 and Figure C.11 for the Al_2O_3 sample and Figure C.12, Figure C.13, and Figure C.14. All panels are labeled with a running index corresponding to the order in which the data was recorded and the the temperature.

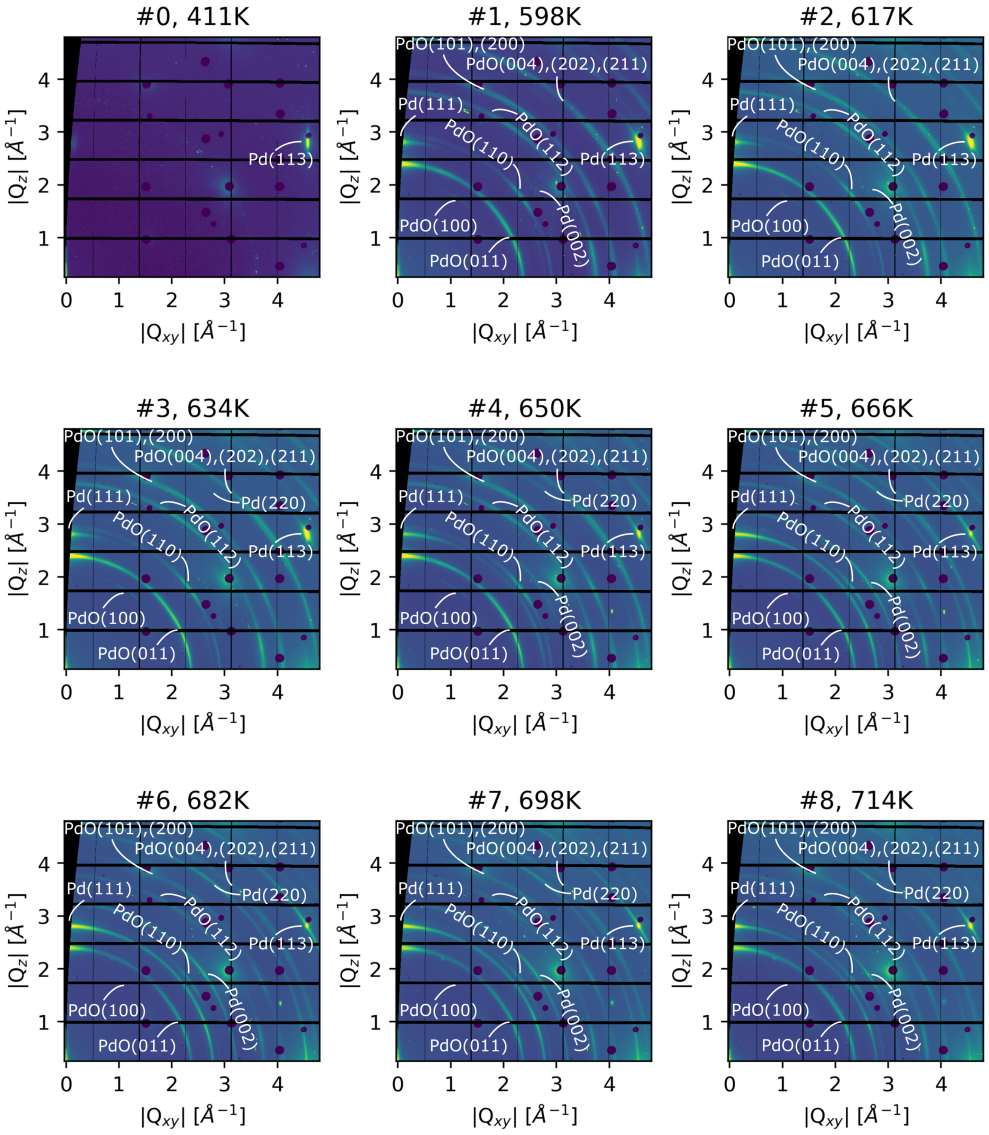

Figure C.10: Planes of reciprocal space of the Al_2O_3 sample recorded at the first 9 temperature steps of the light-off experiment.

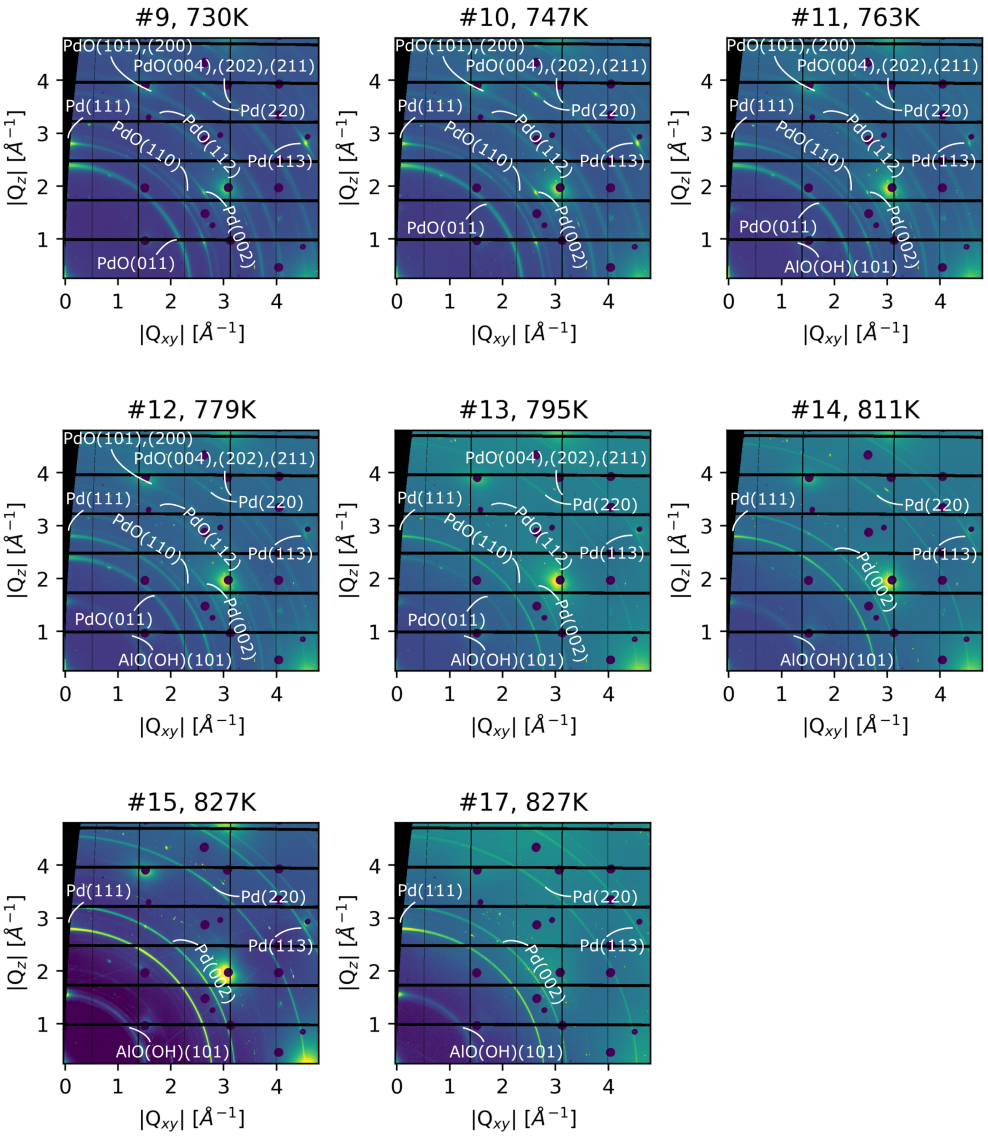

Figure C.11: Planes of reciprocal space of the Al_2O_3 sample recorded at the last 8 temperature steps of the light-off experiment.

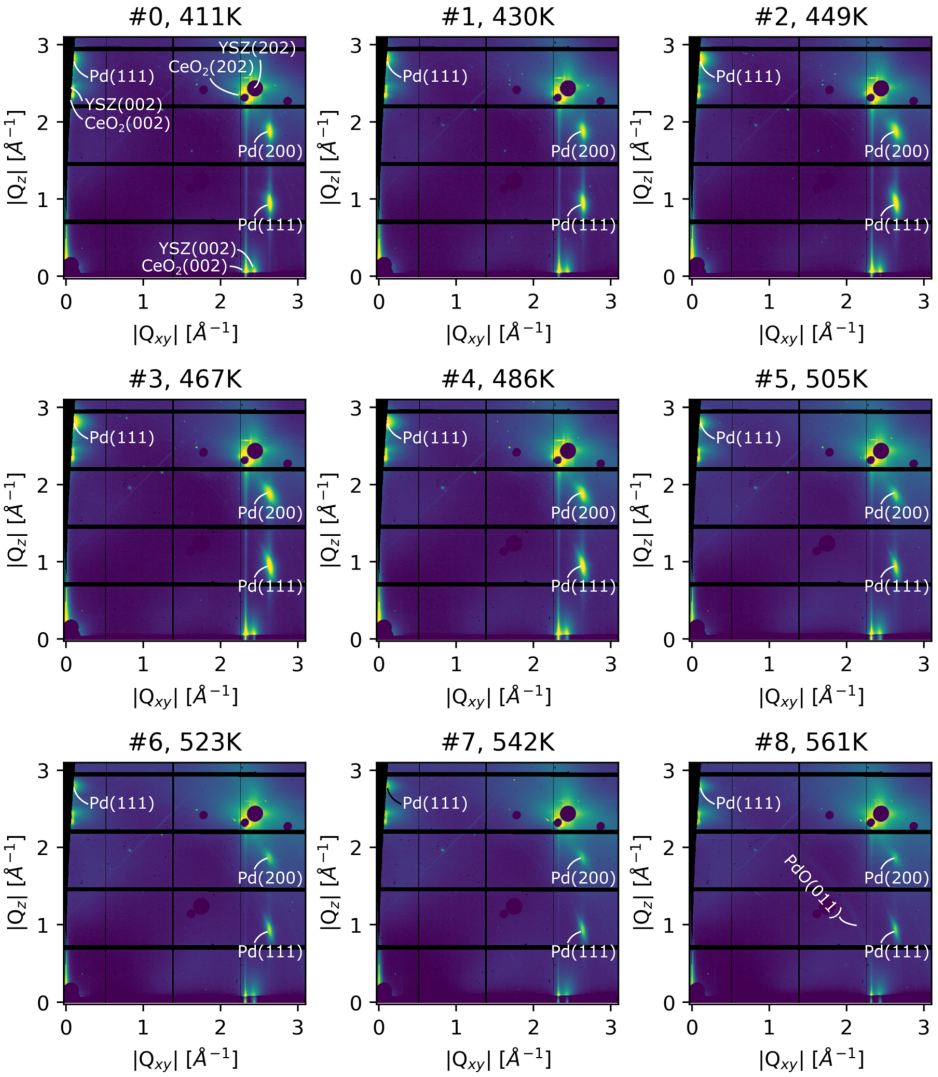

Figure C.12: Planes of reciprocal space of the CeO_2 sample recorded at the first 9 temperature steps of the light-off experiment.

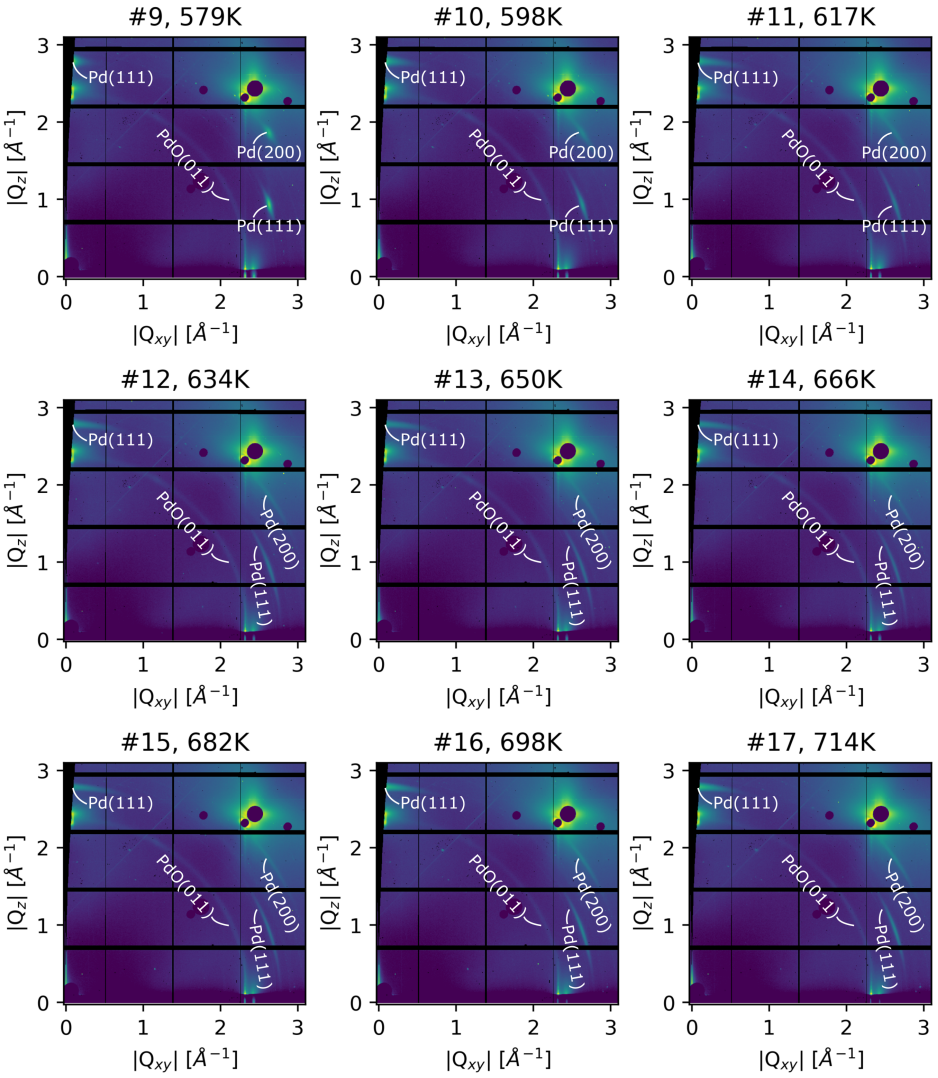

Figure C.13: Planes of reciprocal space of the CeO_2 sample recorded from the 10th to the 19th temperature step of the light-off experiment.

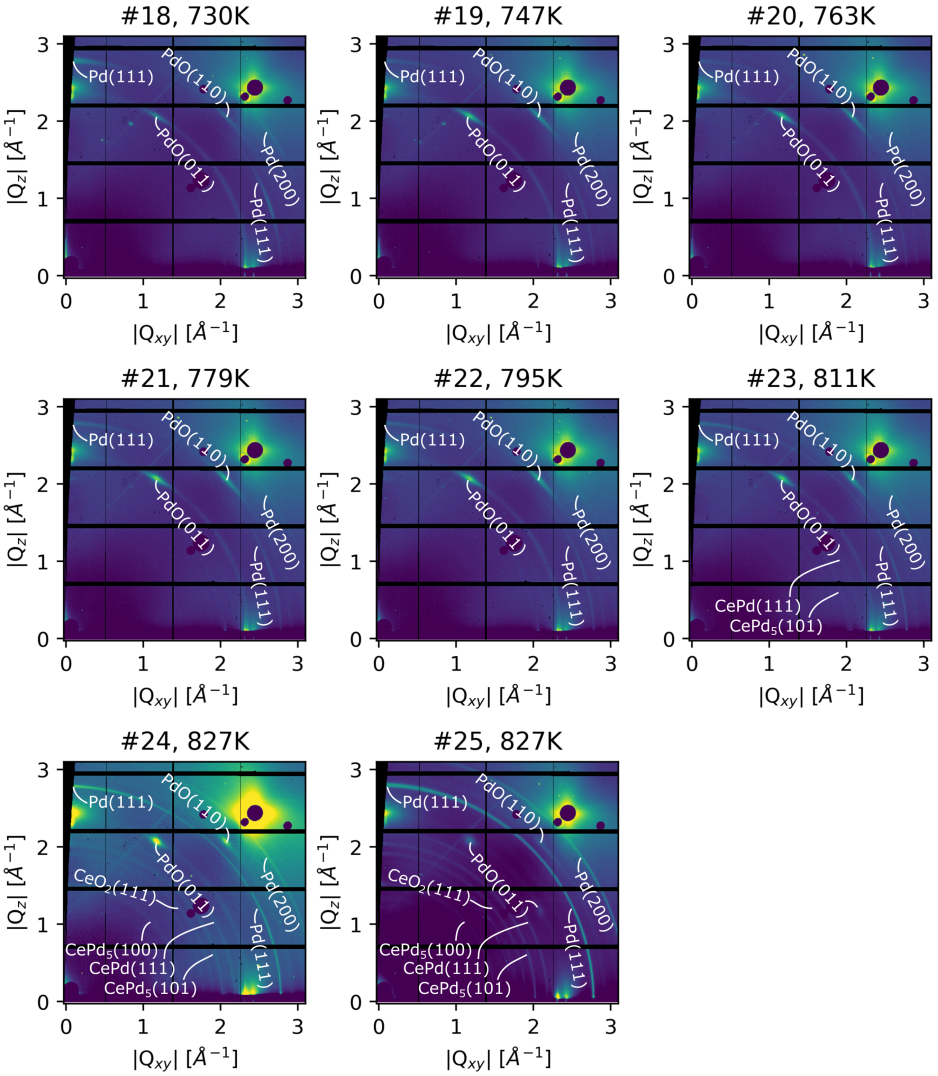

Figure C.14: Planes of reciprocal space of the CeO_2 sample recorded at the last 8 temperature steps of the light-off experiment.

C.9 Pd and PdO nanoparticle size determination

The nanoparticle size of Pd and PdO was determined from the FWHM of the (0 0 2) Bragg peak for Pd and the (0 1 1) Bragg peak for PdO using $\Delta Q = \frac{2\pi}{D}$[300]. For conditions where the investigated species is (partially) epitaxial, Bragg peak analysis was conducted in-plane as well as out-of-plane giving insight into both diameter and height of the particles (compare i.e. Figure C.15 #0). In conditions with no epitaxial relationship between particles and substrate the diffraction signal is distributed on a Debye-Scherrer ring, meaning that only a radial cut through the ring was performed giving in sight into the average particle dimension (compare i.e. Figure C.15 #1). For all fits presented in the following figures, the Bragg peaks were modeled using a linear background combined with a Pseudo-Voigt profile

$$\begin{aligned} f(x, A, \mu, \sigma, \alpha, s, c) = & \frac{(1 - \alpha)A}{\sigma_g\sqrt{2\pi}} e^{-(x-\mu)^2 / 2\sigma_g^2} \\ & + \frac{\alpha A}{\pi}\left[\frac{\sigma}{(x - \mu)^2 + \sigma^2}\right] \\ & + sx + c, \end{aligned} \tag{C.1}$$

where that $\sigma_g = \frac{\sigma}{\sqrt{2\ln 2}}$ and $2\sigma = FWHM$. The variable A denotes the amplitude, μ the peak position, α the fraction of Gaussian and Lorentzian contribution, so that for $\alpha = 0$ the Pseudo-Voigt profile becomes fully Gaussian and for $\alpha = 1$, the profile becomes fully Lorentzian. The variable s is the slope and c the constant offset of the background.
In Figure C.15 and Figure C.16, the fits through the linescans around the Pd(0 0 2) and the PdO(0 1 1) Bragg peaks of the Al_2O_3 sample are presented. Consistent with Figure C.10 and Figure C.11, the plots are labelled with a running index and the temperature. and Figure C.16

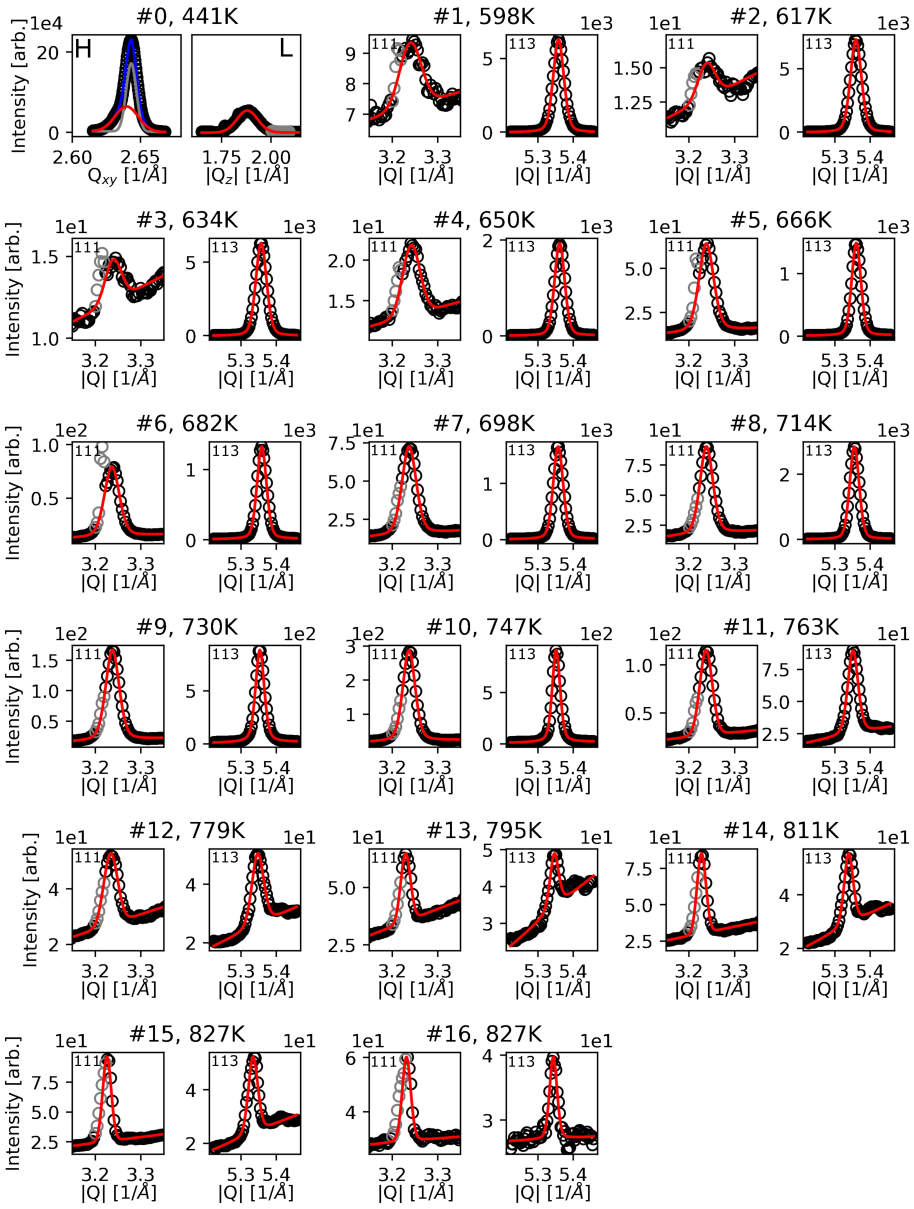

Figure C.15: Fits of linescans extracted from the Pd(0 0 2) Bragg peak of the Al_2O_3 sample along radial or in-plane and out-of-plane direction. Datapoints considered in the fit are black, datapoints that were excluded. The fit is shown in red. In the case (#1) that mulitple components are fitted, the fit is shown in blue and the component of interest (here: Pd(1 1 1)) is red.

Table C.2: Fit parameters of the data presented in Figure C.15 (#0 to #11).

ID	Parameter	Result	ID	Parameter	Result
#0	Amplitude	1328.149 ± 146.317	#6	Amplitude	3.0 ± 0.048
	Center	2.64 ± 0.0		Center	3.236 ± 0.0
	Fraction	0.0 ± 0.0		Fraction	0.0 ± 0.0
	FWHM	0.02 ± 0.0		FWHM	0.038 ± 0.0
	Amplitude	7202.421 ± 406.803		Amplitude	49.683 ± 0.554
	Center	1.879 ± 0.001		Center	5.359 ± 0.0
	Fraction	0.0 ± 0.0		Fraction	0.0 ± 0.0
	FWHM	0.124 ± 0.002		FWHM	0.032 ± 0.0
#1	Amplitude	0.125 ± 0.018	#7	Amplitude	2.525 ± 0.035
	Center	3.24 ± 0.001		Center	3.237 ± 0.0
	Fraction	0.0 ± 0.0		Fraction	0.0 ± 0.0
	FWHM	0.056 ± 0.003		FWHM	0.037 ± 0.0
	Amplitude	272.659 ± 2.446		Amplitude	64.272 ± 0.629
	Center	5.358 ± 0.0		Center	5.357 ± 0.0
	Fraction	0.0 ± 0.0		Fraction	0.0 ± 0.0
	FWHM	0.036 ± 0.0		FWHM	0.033 ± 0.0
#2	Amplitude	0.12 ± 0.027	#8	Amplitude	2.978 ± 0.036
	Center	3.238 ± 0.002		Center	3.238 ± 0.0
	Fraction	0.0 ± 1.0		Fraction	0.0 ± 0.0
	FWHM	0.044 ± 0.005		FWHM	0.033 ± 0.0
	Amplitude	319.401 ± 2.727		Amplitude	104.783 ± 1.028
	Center	5.36 ± 0.0		Center	5.355 ± 0.0
	Fraction	0.0 ± 0.0		Fraction	0.0 ± 0.0
	FWHM	0.037 ± 0.0		FWHM	0.032 ± 0.0
#3	Amplitude	0.113 ± 0.024	#9	Amplitude	6.304 ± 0.05
	Center	3.239 ± 0.001		Center	3.238 ± 0.0
	Fraction	0.0 ± 1.0		Fraction	0.0 ± 0.0
	FWHM	0.042 ± 0.004		FWHM	0.035 ± 0.0
	Amplitude	270.01 ± 2.068		Amplitude	32.289 ± 0.385
	Center	5.357 ± 0.0		Center	5.353 ± 0.0
	Fraction	0.0 ± 0.0		Fraction	1.0 ± 0.0
	FWHM	0.036 ± 0.0		FWHM	0.029 ± 0.0
#4	Amplitude	0.41 ± 0.026	#10	Amplitude	10.286 ± 0.09
	Center	3.242 ± 0.0		Center	3.237 ± 0.0
	Fraction	0.0 ± 0.0		Fraction	0.0 ± 0.0
	FWHM	0.045 ± 0.001		FWHM	0.032 ± 0.0
	Amplitude	76.189 ± 0.511		Amplitude	29.286 ± 0.364
	Center	5.361 ± 0.0		Center	5.352 ± 0.0
	Fraction	0.0 ± 0.0		Fraction	0.0 ± 0.0
	FWHM	0.033 ± 0.0		FWHM	0.026 ± 0.0
#5	Amplitude	2.293 ± 0.038	#11	Amplitude	3.143 ± 0.054
	Center	3.238 ± 0.0		Center	3.237 ± 0.0
	Fraction	0.0 ± 0.0		Fraction	0.0 ± 0.0
	FWHM	0.038 ± 0.0		FWHM	0.032 ± 0.0
	Amplitude	53.601 ± 0.558		Amplitude	2.752 ± 0.063
	Center	5.361 ± 0.0		Center	5.351 ± 0.0
	Fraction	0.0 ± 0.0		Fraction	0.0 ± 0.0
	FWHM	0.031 ± 0.0		FWHM	0.035 ± 0.0

Table C.3: Fit parameters of the data presented in Figure C.15 (#12 to #16).

ID	Parameter	Result	ID	Parameter	Result
#12	Amplitude	0.97 ± 0.046	#15	Amplitude	1.692 ± 0.045
	Center	3.234 ± 0.0		Center	3.226 ± 0.0
	Fraction	0.0 ± 0.0		Fraction	0.0 ± 0.0
	FWHM	0.036 ± 0.001		FWHM	0.022 ± 0.001
	Amplitude	1.158 ± 0.082		Amplitude	1.046 ± 0.062
	Center	5.347 ± 0.0		Center	5.334 ± 0.0
	Fraction	0.0 ± 0.0		Fraction	0.0 ± 0.0
	FWHM	0.04 ± 0.001		FWHM	0.032 ± 0.001
#13	Amplitude	0.783 ± 0.052	#16	Amplitude	0.779 ± 0.04
	Center	3.229 ± 0.0		Center	3.231 ± 0.0
	Fraction	0.0 ± 0.0		Fraction	0.0 ± 0.0
	FWHM	0.025 ± 0.001		FWHM	0.022 ± 0.001
	Amplitude	0.58 ± 0.067		Amplitude	0.374 ± 0.034
	Center	5.346 ± 0.001		Center	5.343 ± 0.0
	Fraction	1.0 ± 0.0		Fraction	0.0 ± 0.0
	FWHM	0.029 ± 0.002		FWHM	0.025 ± 0.001
#14	Amplitude	1.342 ± 0.044			
	Center	3.227 ± 0.0			
	Fraction	0.0 ± 0.0			
	FWHM	0.023 ± 0.001			
	Amplitude	0.977 ± 0.064			
	Center	5.339 ± 0.0			
	Fraction	0.0 ± 0.0			
	FWHM	0.03 ± 0.001			

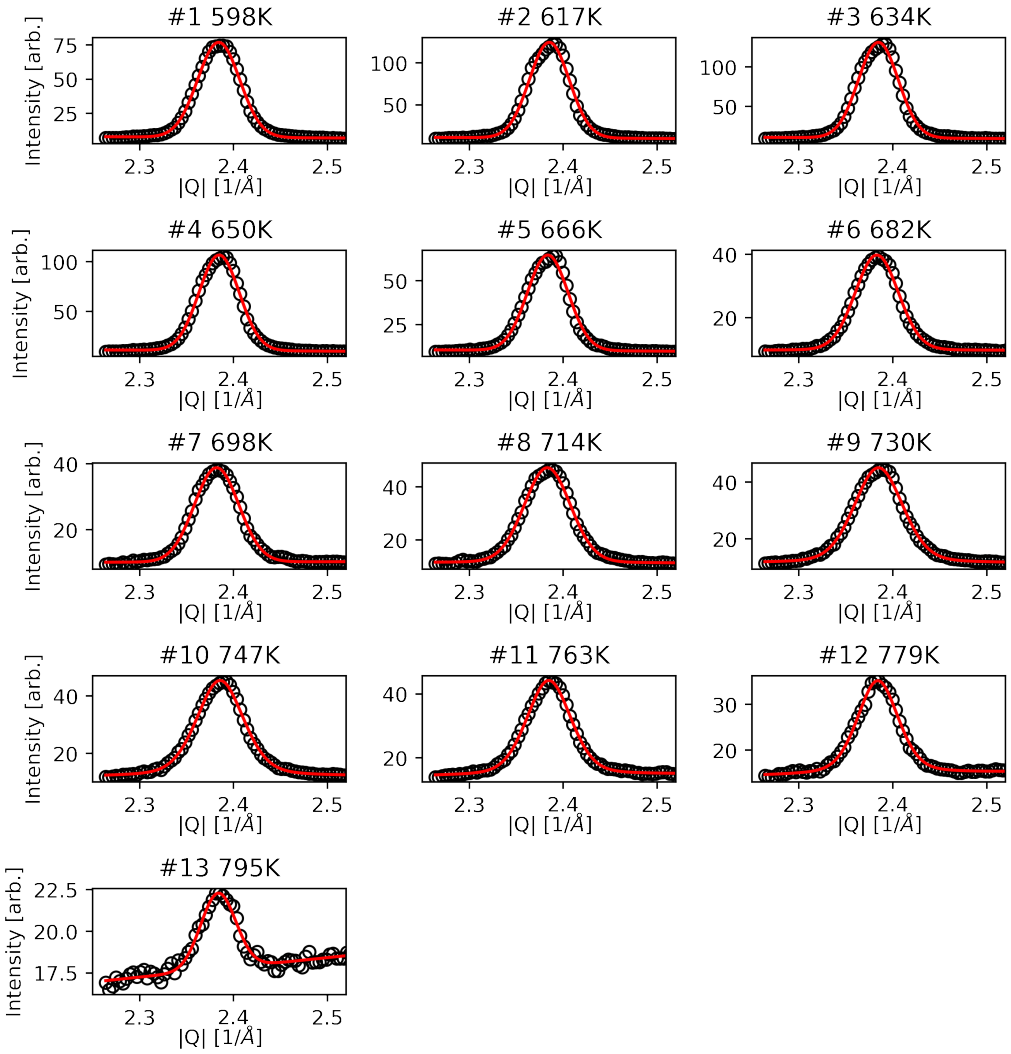

Figure C.16: Fits of linescans extracted from the PdO(0 1 1) Bragg peak of the Al_2O_3 sample along radial direction.

Table C.4: Fit parameters of the data presented in Figure C.16.

Condition	Parameter	Result	Condition	Parameter	Result
#0	Amplitude	3.9 ± 0.149	#7	Amplitude	2.294 ± 0.093
	Center	2.384 ± 0.0		Center	2.383 ± 0.0
	Fraction	0.0 ± 0.0		Fraction	0.0 ± 0.0
	FWHM	0.053 ± 0.0		FWHM	0.058 ± 0.001
#1	Amplitude	6.087 ± 0.398	#8	Amplitude	2.407 ± 0.091
	Center	2.385 ± 0.0		Center	2.385 ± 0.0
	Fraction	0.0 ± 0.0		Fraction	0.0 ± 0.0
	FWHM	0.05 ± 0.001		FWHM	0.061 ± 0.001
#2	Amplitude	6.436 ± 0.414	#9	Amplitude	2.414 ± 0.085
	Center	2.385 ± 0.0		Center	2.386 ± 0.0
	Fraction	0.0 ± 0.0		Fraction	0.0 ± 0.0
	FWHM	0.05 ± 0.001		FWHM	0.059 ± 0.001
#3	Amplitude	5.181 ± 0.263	#10	Amplitude	1.981 ± 0.064
	Center	2.385 ± 0.0		Center	2.385 ± 0.0
	Fraction	0.0 ± 0.0		Fraction	0.0 ± 0.0
	FWHM	0.051 ± 0.001		FWHM	0.056 ± 0.0
#4	Amplitude	2.949 ± 0.19	#11	Amplitude	1.294 ± 0.042
	Center	2.384 ± 0.0		Center	2.384 ± 0.0
	Fraction	0.0 ± 0.0		Fraction	0.0 ± 0.0
	FWHM	0.051 ± 0.001		FWHM	0.051 ± 0.001
#5	Amplitude	1.78 ± 0.064	#12	Amplitude	0.213 ± 0.024
	Center	2.383 ± 0.0		Center	2.384 ± 0.001
	Fraction	0.0 ± 0.0		Fraction	0.0 ± 0.0
	FWHM	0.054 ± 0.0		FWHM	0.044 ± 0.001
#6	Amplitude	1.701 ± 0.069			
	Center	2.382 ± 0.0			
	Fraction	0.0 ± 0.0			
	FWHM	0.056 ± 0.0			

Analogous to the Al_2O_3 sample, in Figure C.17 and Figure C.19, the fits through the linescans around the Pd(0 0 2) of the CeO_2 sample are presented. In Figure C.20, the line scans through the PdO(0 1 1) Bragg peaks are presented. Again, indices between Figure C.12, Figure C.13, Figure C.14 and Figure C.17, Figure C.19 and Figure C.20 are identical.

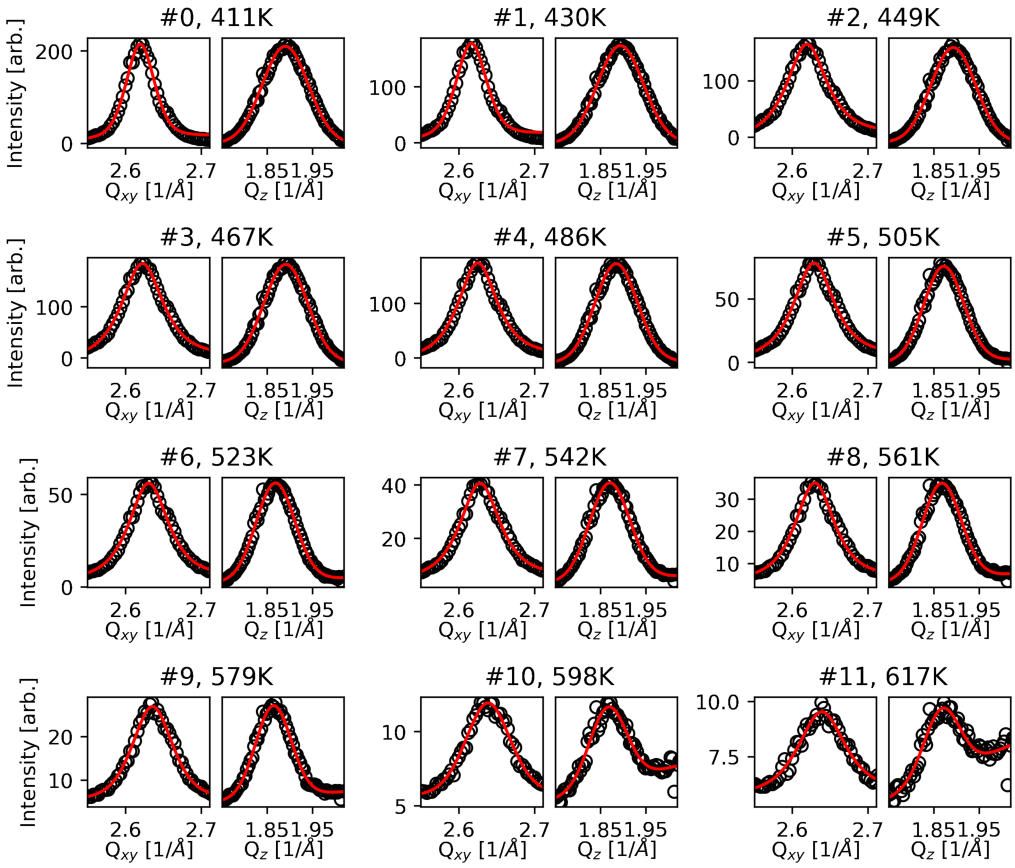

Figure C.17: Fits of linescans extracted from the Pd(0 0 2) Bragg peak of the CeO_2 sample along radial or in-plane and out-of-plane direction.

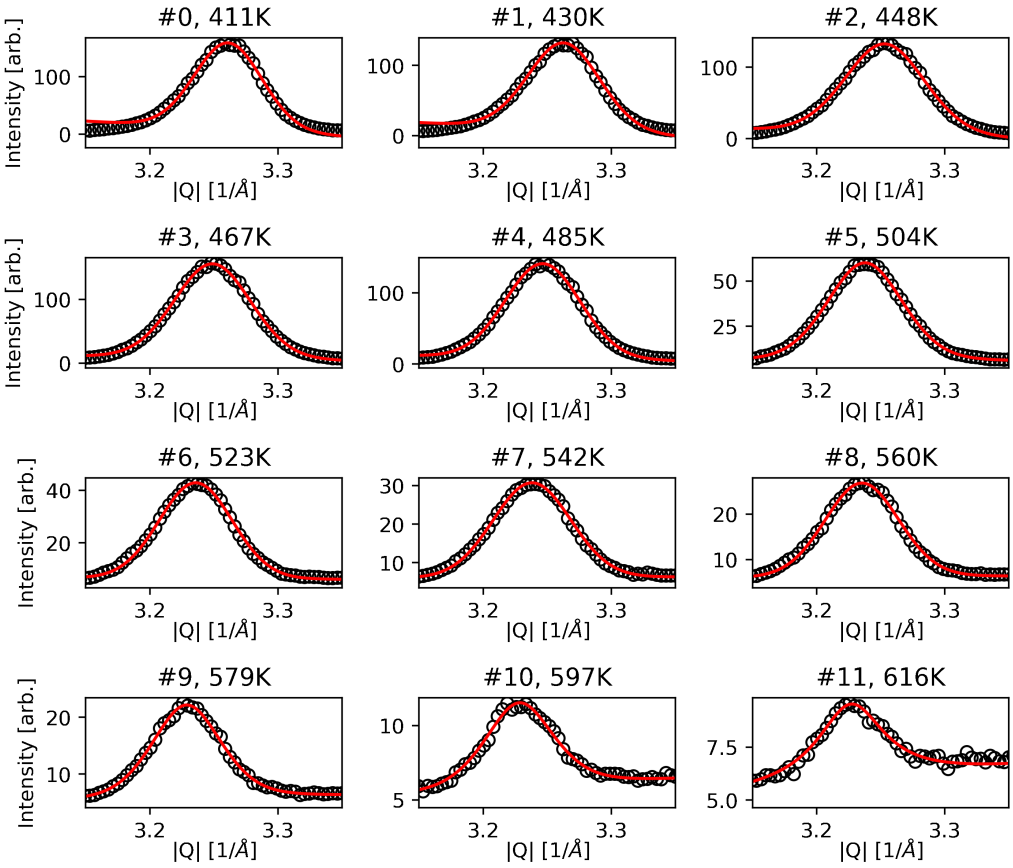

Figure C.18: Fits of linescans extracted from the Pd(0 0 2) Bragg peak of the CeO_2 sample along radial or in-plane and out-of-plane direction.

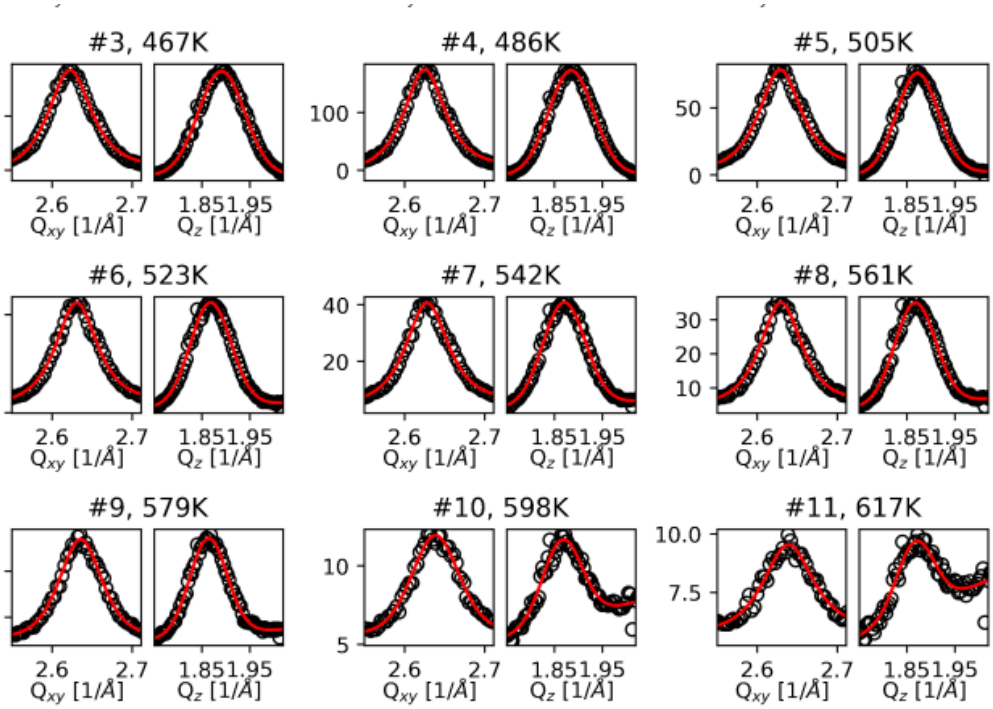

Figure C.19: Fits of linescans extracted from the Pd(0 0 2) Bragg peak of the CeO_2 sample along radial or in-plane and out-of-plane direction.

Table C.5: Fit parameters of the data presented in Figure C.17.

ID	Parameter	Result	ID	Parameter	Result
#0	Amplitude	11.575 ± 1.211	#6	Amplitude	4.947 ± 0.41
	Center	2.619 ± 0.0		Center	2.63 ± 0.0
	Fraction	0.0 ± 0.0		Fraction	1.0 ± 0.0
	FWHM	0.044 ± 0.001		FWHM	0.063 ± 0.002
	Amplitude	19.064 ± 1.57		Amplitude	5.446 ± 0.439
	Center	1.89 ± 0.0		Center	1.868 ± 0.0
	Fraction	0.0 ± 0.0		Fraction	0.0 ± 0.0
	FWHM	0.12 ± 0.002		FWHM	0.1 ± 0.001
#1	Amplitude	10.314 ± 0.923	#7	Amplitude	3.519 ± 0.243
	Center	2.616 ± 0.0		Center	2.628 ± 0.0
	Fraction	1.0 ± 0.0		Fraction	1.0 ± 0.0
	FWHM	0.048 ± 0.001		FWHM	0.064 ± 0.001
	Amplitude	15.241 ± 1.201		Amplitude	3.728 ± 0.355
	Center	1.894 ± 0.0		Center	1.87 ± 0.0
	Fraction	0.0 ± 0.0		Fraction	0.0 ± 0.0
	FWHM	0.121 ± 0.002		FWHM	0.105 ± 0.001
#2	Amplitude	17.169 ± 2.226	#8	Amplitude	2.79 ± 0.181
	Center	2.619 ± 0.0		Center	2.63 ± 0.0
	Fraction	1.0 ± 0.0		Fraction	1.0 ± 0.0
	FWHM	0.065 ± 0.003		FWHM	0.062 ± 0.001
	Amplitude	16.43 ± 1.281		Amplitude	3.127 ± 0.341
	Center	1.893 ± 0.0		Center	1.867 ± 0.0
	Fraction	0.0 ± 0.0		Fraction	0.0 ± 0.0
	FWHM	0.117 ± 0.001		FWHM	0.101 ± 0.002
#3	Amplitude	18.915 ± 2.377	#9	Amplitude	1.847 ± 0.12
	Center	2.622 ± 0.0		Center	2.635 ± 0.0
	Fraction	1.0 ± 0.0		Fraction	1.0 ± 0.0
	FWHM	0.066 ± 0.003		FWHM	0.063 ± 0.001
	Amplitude	19.521 ± 1.356		Amplitude	2.307 ± 0.182
	Center	1.891 ± 0.0		Center	1.864 ± 0.0
	Fraction	0.0 ± 0.0		Fraction	0.0 ± 0.0
	FWHM	0.114 ± 0.001		FWHM	0.093 ± 0.001
#4	Amplitude	16.903 ± 2.195	#10	Amplitude	0.543 ± 0.037
	Center	2.625 ± 0.0		Center	2.638 ± 0.0
	Fraction	1.0 ± 0.0		Fraction	0.0 ± 0.0
	FWHM	0.062 ± 0.003		FWHM	0.07 ± 0.001
	Amplitude	18.271 ± 1.356		Amplitude	0.624 ± 0.149
	Center	1.884 ± 0.0		Center	1.866 ± 0.001
	Fraction	0.0 ± 0.0		Fraction	0.0 ± 1.0
	FWHM	0.111 ± 0.001		FWHM	0.097 ± 0.003
#5	Amplitude	7.486 ± 0.735	#11	Amplitude	0.398 ± 0.037
	Center	2.628 ± 0.0		Center	2.639 ± 0.001
	Fraction	1.0 ± 0.0		Fraction	1.0 ± 0.0
	FWHM	0.064 ± 0.002		FWHM	0.074 ± 0.002
	Amplitude	7.824 ± 0.704		Amplitude	0.328 ± 0.112
	Center	1.872 ± 0.0		Center	1.867 ± 0.002
	Fraction	0.0 ± 0.0		Fraction	0.0 ± 1.0
	FWHM	0.104 ± 0.001		FWHM	0.092 ± 0.005

Table C.6: Fit parameters of the data presented in Figure C.18.

ID	Parameter	Result	ID	Parameter	Result
#0	Amplitude	10.263 ± 1.005	#6	Amplitude	2.603 ± 0.123
	Center	3.261 ± 0.0		Center	3.236 ± 0.0
	Fraction	0.0 ± 0.0		Fraction	0.0 ± 0.0
	FWHM	0.062 ± 0.001		FWHM	0.067 ± 0.001
#1	Amplitude	9.321 ± 1.014	#7	Amplitude	1.866 ± 0.085
	Center	3.263 ± 0.0		Center	3.238 ± 0.0
	Fraction	0.0 ± 0.0		Fraction	0.0 ± 0.0
	FWHM	0.067 ± 0.002		FWHM	0.071 ± 0.001
#2	Amplitude	10.857 ± 0.936	#8	Amplitude	1.557 ± 0.084
	Center	3.253 ± 0.0		Center	3.235 ± 0.0
	Fraction	0.0 ± 0.0		Fraction	0.0 ± 0.0
	FWHM	0.074 ± 0.002		FWHM	0.068 ± 0.001
#3	Amplitude	11.63 ± 0.859	#9	Amplitude	1.34 ± 0.052
	Center	3.249 ± 0.0		Center	3.229 ± 0.0
	Fraction	0.0 ± 0.0		Fraction	0.0 ± 0.0
	FWHM	0.071 ± 0.001		FWHM	0.064 ± 0.001
#4	Amplitude	9.692 ± 0.6	#10	Amplitude	0.502 ± 0.033
	Center	3.247 ± 0.0		Center	3.228 ± 0.0
	Fraction	0.0 ± 0.0		Fraction	1.0 ± 0.0
	FWHM	0.069 ± 0.001		FWHM	0.064 ± 0.001
#5	Amplitude	4.408 ± 0.155	#11	Amplitude	0.38 ± 0.03
	Center	3.238 ± 0.0		Center	3.227 ± 0.001
	Fraction	0.0 ± 0.0		Fraction	1.0 ± 0.0
	FWHM	0.069 ± 0.001		FWHM	0.064 ± 0.002

Table C.7: Fit parameters of the data presented in Figure C.19.

ID	Parameter	Result	ID	Parameter	Result
#12	Amplitude	0.306 ± 0.021	#19	Amplitude	0.161 ± 0.072
	Center	3.226 ± 0.001		Center	3.223 ± 0.003
	Fraction	1.0 ± 0.0		Fraction	1.0 ± 0.0
	FWHM	0.061 ± 0.002		FWHM	0.1 ± 0.017
#13	Amplitude	0.252 ± 0.025	#20	Amplitude	0.116 ± 0.072
	Center	3.225 ± 0.001		Center	3.226 ± 0.005
	Fraction	1.0 ± 0.0		Fraction	1.0 ± 1.0
	FWHM	0.06 ± 0.003		FWHM	0.1 ± 0.023
#14	Amplitude	0.218 ± 0.03	#21	Amplitude	0.062 ± 0.013
	Center	3.224 ± 0.001		Center	3.221 ± 0.002
	Fraction	1.0 ± 0.0		Fraction	1.0 ± 0.0
	FWHM	0.061 ± 0.005		FWHM	0.032 ± 0.006
#15	Amplitude	0.228 ± 0.022	#22	Amplitude	0.105 ± 0.047
	Center	3.223 ± 0.001		Center	3.217 ± 0.004
	Fraction	1.0 ± 0.0		Fraction	1.0 ± 1.0
	FWHM	0.053 ± 0.003		FWHM	0.073 ± 0.015
#16	Amplitude	0.338 ± 0.019	#23	Amplitude	0.059 ± 0.01
	Center	3.224 ± 0.0		Center	3.217 ± 0.001
	Fraction	1.0 ± 0.0		Fraction	1.0 ± 0.0
	FWHM	0.047 ± 0.001		FWHM	0.027 ± 0.005
#17	Amplitude	0.351 ± 0.02	#24	Amplitude	0.106 ± 0.01
	Center	3.224 ± 0.0		Center	3.219 ± 0.001
	Fraction	1.0 ± 0.0		Fraction	1.0 ± 0.0
	FWHM	0.046 ± 0.001		FWHM	0.026 ± 0.002
#18	Amplitude	0.192 ± 0.022			
	Center	3.223 ± 0.001			
	Fraction	1.0 ± 0.0			
	FWHM	0.051 ± 0.004			

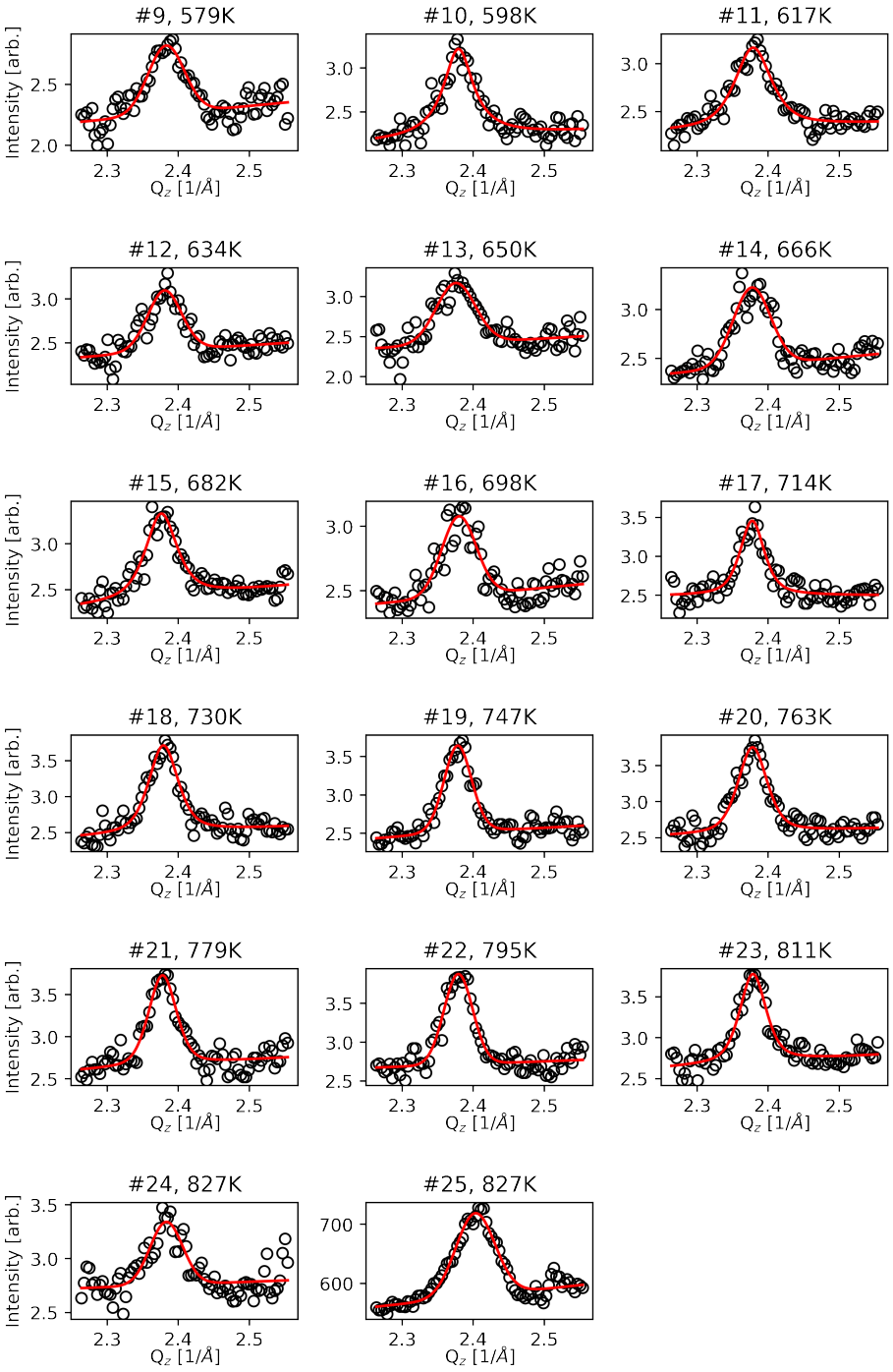

Figure C.20: Fits of linescans extracted from the PdO(0 1 1) Bragg peak of the CeO_2 sample along radial direction.

Table C.8: Fit parameters of the data presented in Figure C.20.

ID	Parameter	Result	ID	Parameter	Result
#9	Amplitude	0.036 ± 0.012	#18	Amplitude	0.081 ± 0.012
	Center	2.383 ± 0.002		Center	2.379 ± 0.001
	Fraction	0.0 ± 1.0		Fraction	1.0 ± 0.0
	FWHM	0.06 ± 0.004		FWHM	0.049 ± 0.003
#10	Amplitude	0.08 ± 0.012	#19	Amplitude	0.06 ± 0.009
	Center	2.379 ± 0.001		Center	2.378 ± 0.001
	Fraction	1.0 ± 0.0		Fraction	0.0 ± 0.0
	FWHM	0.051 ± 0.004		FWHM	0.046 ± 0.002
#11	Amplitude	0.072 ± 0.013	#20	Amplitude	0.075 ± 0.011
	Center	2.379 ± 0.001		Center	2.378 ± 0.001
	Fraction	1.0 ± 0.0		Fraction	1.0 ± 0.0
	FWHM	0.061 ± 0.004		FWHM	0.049 ± 0.003
#12	Amplitude	0.044 ± 0.013	#21	Amplitude	0.061 ± 0.01
	Center	2.381 ± 0.001		Center	2.378 ± 0.001
	Fraction	0.0 ± 1.0		Fraction	0.0 ± 0.0
	FWHM	0.057 ± 0.004		FWHM	0.046 ± 0.003
#13	Amplitude	0.052 ± 0.019	#22	Amplitude	0.059 ± 0.01
	Center	2.375 ± 0.002		Center	2.379 ± 0.001
	Fraction	0.0 ± 1.0		Fraction	0.0 ± 0.0
	FWHM	0.065 ± 0.005		FWHM	0.047 ± 0.002
#14	Amplitude	0.053 ± 0.016	#23	Amplitude	0.064 ± 0.008
	Center	2.377 ± 0.001		Center	2.378 ± 0.001
	Fraction	0.0 ± 1.0		Fraction	1.0 ± 0.0
	FWHM	0.062 ± 0.004		FWHM	0.044 ± 0.002
#15	Amplitude	0.07 ± 0.012	#24	Amplitude	0.033 ± 0.014
	Center	2.376 ± 0.001		Center	2.383 ± 0.002
	Fraction	1.0 ± 0.0		Fraction	0.0 ± 1.0
	FWHM	0.053 ± 0.004		FWHM	0.054 ± 0.005
#16	Amplitude	0.038 ± 0.013	#25	Amplitude	9.7 ± 1.666
	Center	2.38 ± 0.002		Center	2.403 ± 0.001
	Fraction	0.0 ± 1.0		Fraction	0.0 ± 0.0
	FWHM	0.057 ± 0.004		FWHM	0.065 ± 0.002
#17	Amplitude	0.054 ± 0.009			
	Center	2.377 ± 0.001			
	Fraction	1.0 ± 0.0			
	FWHM	0.041 ± 0.003			

C.10 Pd nanoparticle height, diameter, and aspect ratio

Additionally to the average dimension mostly discussed in the main text, height, diameter and the aspect ratio was determined for conditions for which Bragg peaks were observed. The results are displayed in Figure C.21. The fitting procedure and fits are presented in Section C.9

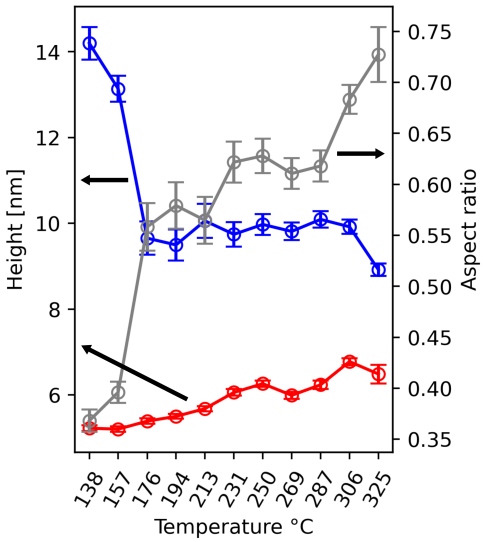

Figure C.21: Height (red), diameter (blue) and aspect ratio (gray) of the Pd NPs of Pd/CeO_2.

C.11 Azimuthal distribution of Pd and PdO

The mobility of the Pd and PdO nanoparticles was captured by analysis of the azimuthal distribution of the diffraction signal around Bragg peaks associated with the respective epitaxial species.

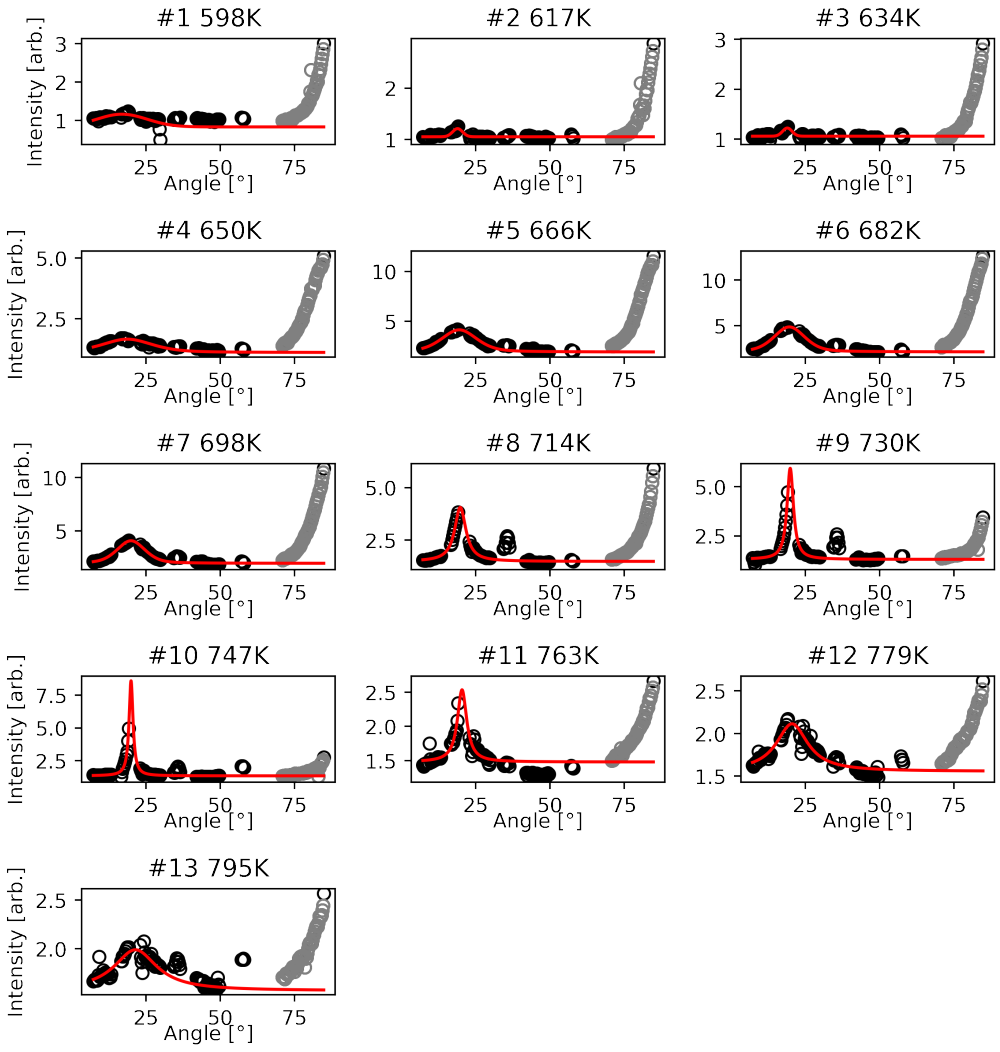

Figure C.22: Data and fits of the distribution of diffraction signal around the Pd(1 1 1) Bragg peak position. Gray datapoints were not considered during the fit.

Table C.9: Fit parameters of the data presented in Figure C.22.

ID	Parameter	Result	ID	Parameter	Result
#0	Amplitude	7.061 ± 49.167	#7	Amplitude	18.486 ± 0.596
	Center	16.873 ± 0.547		Center	19.819 ± 0.052
	Fraction	0.0 ± 4.0		Fraction	1.0 ± 0.0
	FWHM	20.0 ± 56.639		FWHM	4.558 ± 0.133
#1	Amplitude	0.665 ± 0.275	#8	Amplitude	18.751 ± 0.636
	Center	18.91 ± 0.579		Center	19.933 ± 0.059
	Fraction	0.0 ± 8.0		Fraction	1.0 ± 0.0
	FWHM	3.932 ± 1.122		FWHM	2.601 ± 0.173
#2	Amplitude	0.65 ± 0.249	#9	Amplitude	18.345 ± 2.081
	Center	18.957 ± 0.579		Center	19.945 ± 0.072
	Fraction	0.0 ± 1.0		Fraction	1.0 ± 0.0
	FWHM	3.725 ± 1.095		FWHM	1.606 ± 0.419
#3	Amplitude	14.516 ± 156.282	#10	Amplitude	6.248 ± 0.721
	Center	18.689 ± 0.193		Center	20.412 ± 0.124
	Fraction	1.0 ± 8.0		Fraction	1.0 ± 0.0
	FWHM	20.0 ± 15.718		FWHM	3.768 ± 1.065
#4	Amplitude	39.365 ± 14.044	#11	Amplitude	11.244 ± 18.227
	Center	19.45 ± 0.046		Center	20.541 ± 0.206
	Fraction	0.0 ± 0.0		Fraction	1.0 ± 0.0
	FWHM	13.968 ± 1.294		FWHM	12.829 ± 6.587
#5	Amplitude	41.552 ± 8.81	#12	Amplitude	11.61 ± 140.741
	Center	19.632 ± 0.043		Center	21.418 ± 0.333
	Fraction	0.0 ± 0.0		Fraction	1.0 ± 7.0
	FWHM	12.224 ± 0.563		FWHM	17.504 ± 74.183
#6	Amplitude	29.171 ± 4.359			
	Center	19.921 ± 0.041			
	Fraction	0.0 ± 0.0			
	FWHM	11.105 ± 0.307			

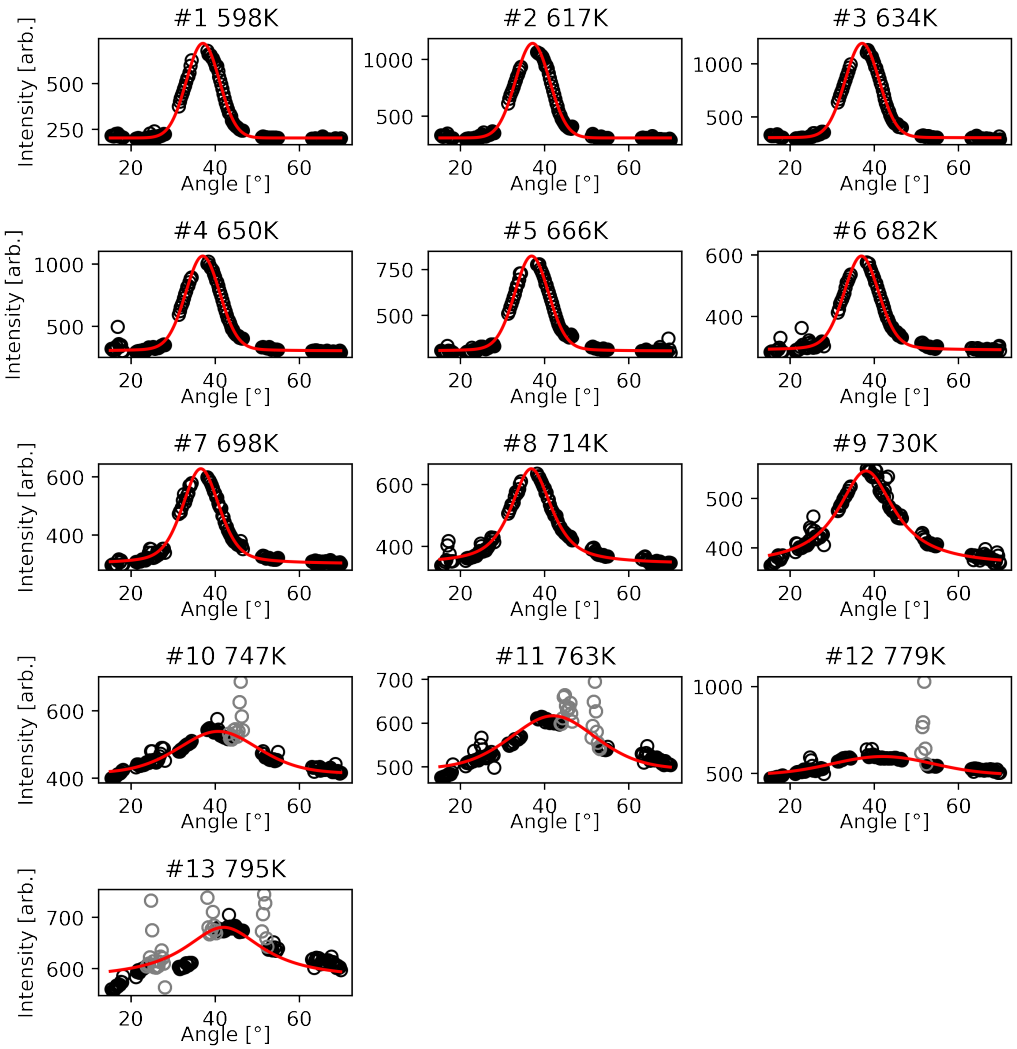

Figure C.23: Data and fits of the distribution of diffraction signal around the Pd(1 1 1) Bragg peak position. Gray datapoints were not considered during the fit.

Table C.10: Fit parameters of the data presented in Figure C.22.

ID	Parameter	Result	ID	Parameter	Result
#0	Amplitude	5093.973 ± 170.399	#7	Amplitude	5101.944 ± 202.197
	Center	37.101 ± 0.026		Center	36.796 ± 0.055
	Fraction	0.0 ± 0.0		Fraction	1.0 ± 0.0
	FWHM	9.233 ± 0.091		FWHM	11.488 ± 0.298
#1	Amplitude	8455.043 ± 249.861	#8	Amplitude	4875.615 ± 389.813
	Center	37.112 ± 0.024		Center	38.04 ± 0.12
	Fraction	0.0 ± 0.0		Fraction	1.0 ± 0.0
	FWHM	9.555 ± 0.085		FWHM	16.233 ± 0.621
#2	Amplitude	9225.788 ± 223.343	#9	Amplitude	3633.989 ± 1892.68
	Center	37.105 ± 0.021		Center	40.739 ± 0.348
	Fraction	0.0 ± 0.0		Fraction	0.0 ± 1.0
	FWHM	9.572 ± 0.073		FWHM	22.908 ± 2.313
#3	Amplitude	8312.918 ± 196.596	#10	Amplitude	3708.811 ± 3133.141
	Center	37.055 ± 0.021		Center	42.0 ± 0.917
	Fraction	0.0 ± 0.0		Fraction	0.0 ± 1.0
	FWHM	9.689 ± 0.08		FWHM	24.217 ± 4.375
#4	Amplitude	5622.922 ± 191.594	#11	Amplitude	3135.938 ± 4768.133
	Center	36.893 ± 0.029		Center	42.0 ± 2.4
	Fraction	0.0 ± 0.0		Fraction	0.0 ± 720.0
	FWHM	9.586 ± 0.117		FWHM	28.078 ± 8.801
#5	Amplitude	3545.29 ± 116.121	#12	Amplitude	3648.343 ± 5091.675
	Center	36.933 ± 0.03		Center	42.0 ± 0.11
	Fraction	0.0 ± 0.0		Fraction	1.0 ± 1.0
	FWHM	9.868 ± 0.125		FWHM	22.944 ± 10.075
#6	Amplitude	4373.658 ± 151.93			
	Center	36.605 ± 0.039			
	Fraction	1.0 ± 0.0			
	FWHM	10.43 ± 0.187			

C.12 Palladium oxide orientation

During methane oxidation, both catalysts exhibited diffraction signal from textured or epitaxial PdO. For Pd/Al_2O_3, textured PdO signal is observed between 597 K and 730 K. Between these temperatures, the signal becomes increasingly distributed on the powder ring as a function of temperature and the off-specular (1 0 1) Bragg peak vanished at 698 K. Since all PdO orientations are present at 597 K, the identification of orientations will be presented on the example of data recorded at this temperature (Figure C.24 **A**). For Pd/CeO_2, PdO occurs first at 561 K in the form of randomly oriented crystallites. Gradually, The intensity distribution on the powder ring changes and a clearly epitactic oxide species can be observed starting at a temperature of 748 K. A second species appears at prolonged operation at 827 K. Hence, for Pd/CeO_2 the last datapoint of the light-off experiment at 827 K is used for the identification of the orientations Figure C.24.

The expected PdO Bragg peak positions of three out-of-plane orientations, (1 0 1) in red, (0 0 1) in green, and (1 0 0) in light and dark blue for two

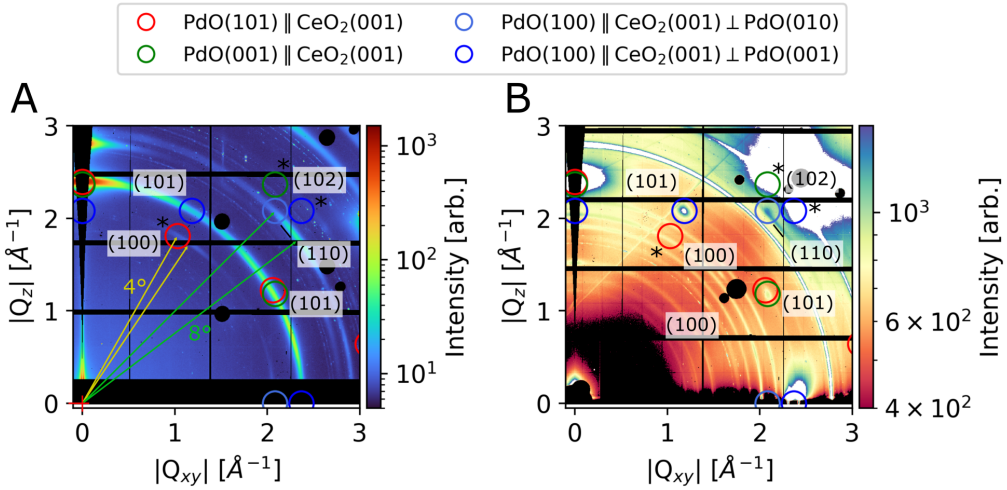

Figure C.24: High-symmetry planes of reciprocal space of Pd/Al_2O_3 (**A**) and Pd/CeO_2 (**B**) catalysts recorded under operation at 597 K (**A**) and 826 K (**B**), respectively. In **B**, a non-linear colormap with tight boundaries was chosen for better contrast. Data points below and above the colormap's limits are colored black and white, respectively. The positions of the Bragg peaks were calculated with an according to measurement temperature expanded PdO lattice [301]. Bragg peaks marked with * scatter at least two magnitudes less than unmarked Bragg peaks.

in-plane orientations are compared with the measured diffraction patterns in Figure C.24. For $PdAl_2O_3$, the low-index orientations indicated by the circles do not match the observed diffraction signal precisely. Instead, the texture is assigned to two orientations, tilted relative to the substrate normal: (1 0 1) textured PdO with a 4 ° tilt and (1 0 0) textured PdO with a tilt of 8 °. For Pd/CeO_2, a combination of (1 0 0) and (0 0 1) oriented PdO is consistent with the observed diffraction pattern. No evidence for the (1 0 1) sample could be found for this sample due to the lack of (1 0 1) Bragg peak at $Q_{xy,z} = (1.03, 1.81)$.

C.13 Analysis of Diaspore

The signal attributed to the (1 0 1)-type reflection of diaspore (Figure 2.5 **A**) emerges during the CH_4 oxidation light-off. The intensity evolution was followed by integrating intensity within a large annulus sector ROI as depicted in Figure C.25 **A** in blue. Slight misalignment and change in thermal diffuse scattering during the fast pace light-off experiment was accounted for by the background ROI close to the first ROI (Figure C.25 **A**, green). Assuming a linear change in thermal diffuse scattering, the difference between the linear fit (Figure C.25 **B**, red) and background (Figure C.25 **C**) is used as a measure of the quality of each image from which data was extracted. The fit parameters can be found in Table C.11. In Figure C.25 **D**, the intensity of the two ROIs is shown to illustrate the relative intensities after correcting the background intensity by the difference in side length and angle range of the two ROIs. In Figure C.26, the evolution of the AlO(OH)

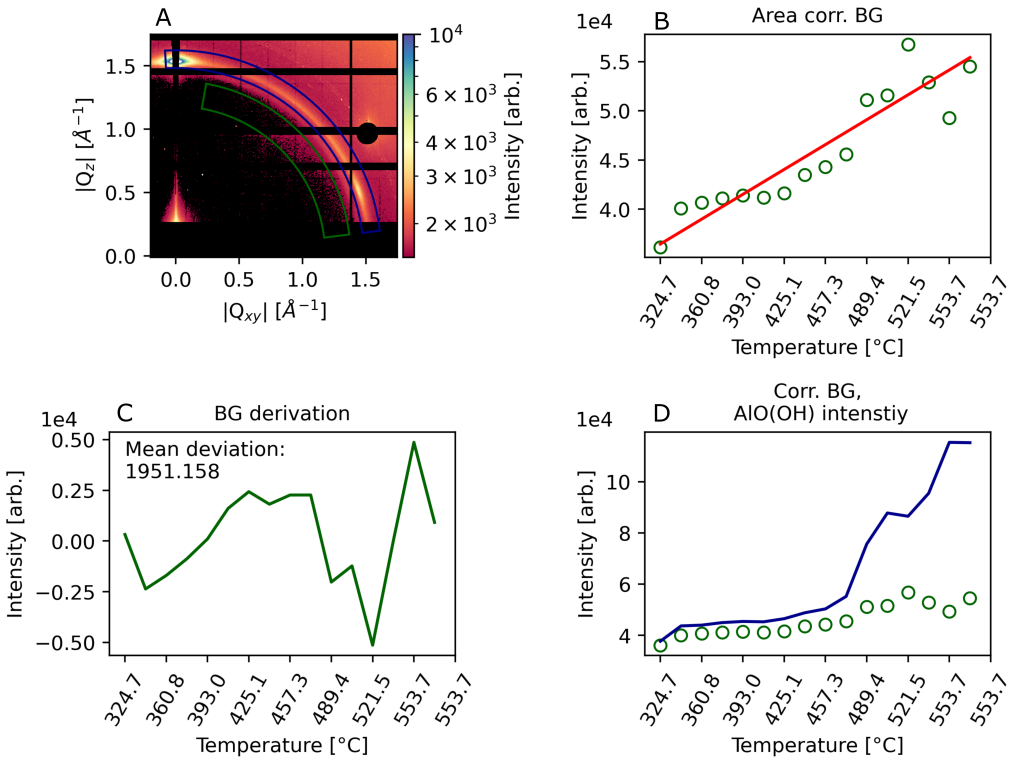

Figure C.25: **A**: ROIs used for analysis of AlO(OH) intensity evolution. **B**: Corrected background and linear fit. **C**: Deviation of background intensity from fit. **D**: Background intensity and AlO(OH) intensities.

Table C.11: Fit parameters of the data presented in Figure C.25 **B**.

Parameter	Value
Slope	1263.60 ± 127
y-intercept	36457.98 ± 1.190

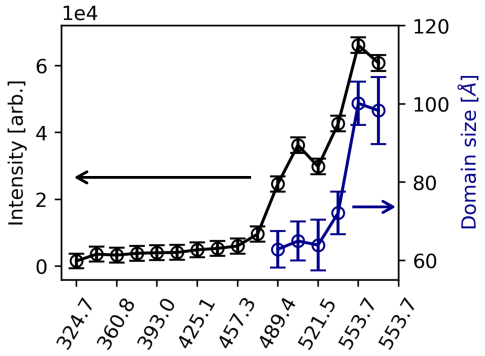

Figure C.26: Evolution of the AlO(OH) intensity after corrected background subtraction (black) and domain size (blue) calculated from the FWHMs listed in Table C.12 determined from the fits in Figure C.27.

intensity from 598 K to 827 K is shown in black. The errorbars are combined errors of the respective intensities and the measure of image quality $err = \sum \sqrt{I(AlO(OH))} + \sqrt{I(BG, corr)} + 1951.158$. In the same figure, the blue datapoints are the domain size of the diaspore which was calculated with $D = \frac{2\pi}{\Delta Q}$ from the FWHMs of the fits (modelled by Equation C.1). The fits are shown in Figure C.27, the resulting parameters are given in Table C.12.

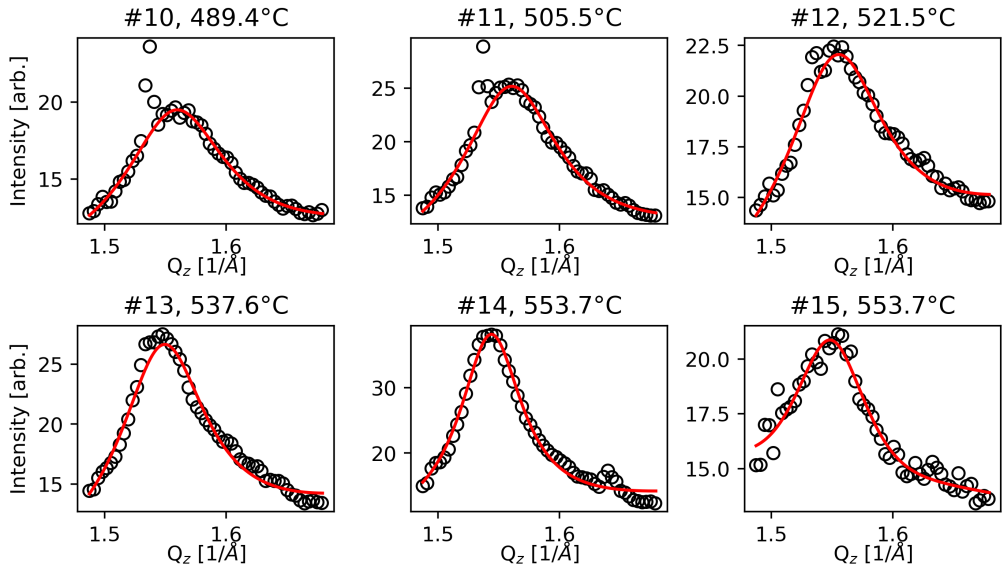

Figure C.27: Fits of radial line scans through the diaspore powder ring at the same position as the ROI in Figure C.25 **A**.

Table C.12: Fit parameters of the data presented in Figure C.27.

ID	Parameter	Result	ID	Parameter	Result
#10	Amplitude	1.413 ± 0.342	#13	Amplitude	2.303 ± 0.528
	Center	1.559 ± 0.001		Center	1.548 ± 0.001
	Fraction	1.0 ± 0.0		Fraction	1.0 ± 0.0
	FWHM	0.100 ± 0.008		FWHM	0.087 ± 0.007
#11	Amplitude	2.36 ± 0.58	#14	Amplitude	2.774 ± 0.413
	Center	1.56 ± 0.001		Center	1.544 ± 0.001
	Fraction	1.0 ± 0.0		Fraction	1.0 ± 0.0
	FWHM	0.097 ± 0.008		FWHM	0.063 ± 0.004
#12	Amplitude	1.622 ± 0.539	#15	Amplitude	0.52 ± 0.178
	Center	1.554 ± 0.001		Center	1.549 ± 0.001
	Fraction	1.0 ± 0.0		Fraction	1.0 ± 0.0
	FWHM	0.098 ± 0.011		FWHM	0.064 ± 0.006

C.14 Optimization of diaspore and reduced CePdx structures

For the calcuation of the enthalpy of formation of diaspore and reduced $CePd_x$ species (Figure 2.5 **B**, **D**), the lattice parameters of the bulk phases of a number of materials was optimized. The optimized lattice constants are listed in Table C.13.

Table C.13: Optimized unit cell parameters of all materials for which the the thermodynamic stability was calculated (see Figure 2.5 **B** and **D**).

Material	Cell type	UC parameters [Å]
Pd	cubic	$a = b = c = 4.777$
Pd_5Ce	hexagonal	$a = b = 5.259$, $c = 4.463$
Pd_3Ce	cubic	$a = b = c = 4.115$
PdCe	orthorombic	$a = 3.771$, $b = 10.799$, $c = 4.571$
Ce(bcc)	cubic	$a = b = c = 3.748$
Ce(dhcp)	hexagonal	$a = b = 3.349$, $c = 11.178$
Ce(fcc)	cubic	$a = 4.754$
PdO	tetragonal	$a = b = 3.053$, $c = 5.399$
CeO_2	cubic	$a = b = c = 5.471$
Ce_2O_3	hexagonal	$a = b = 3.817$, $c = 6.176$
AlO(OH)	orthorombic	$a = 4.382$, $b = 9.440$, $c = 2.852$
α-Al_2O_3	hexagonal	$a = b = 4.776$, $c = 13.036$

C.15 Substrate CTRs

A qualitative measure for the substrate roughness are CTRs of the substrate that were captured at the fixed detector position during light-off. While a large part of the CTR is captured due to the low curvature of the Ewald sphere, quantitative analysis would only be possible by scanning the sample rotation. Still, the scattered intensity of the (3 1) rod (Figure C.28) can serve as a measure of surface quality. Since the absolute intensity is considerably differing between images due to experimental reasons (see methods), the complete data set is presented with relative limits. The lower end of the scale is defined by the mean intensity in the bottom left corner of each image ($5\,\mathrm{px} \times x15\,\mathrm{px}$). the upper limit is defined as 10 % of the maximum intensity of each image. Up to 523 K, the CTR appears to be unchanged, indicating no changes in the overall surface quality of the film. With increasing temperature, the first CO light-off starts and the film thickness oscillations become more pronounced but the overall signal decreases, indicating a more homogeneous film thickness, but higher roughness. Starting at roughly 617 K, the signal at $Q_z = 1$, the lower end of the image vanishes and the CTR and film thickness oscillations become less pronounced until vanishing at 827 K. Overall, the qualitative analysis of the CTR could show that structural changes occur with the onset of activity of the catalyst.

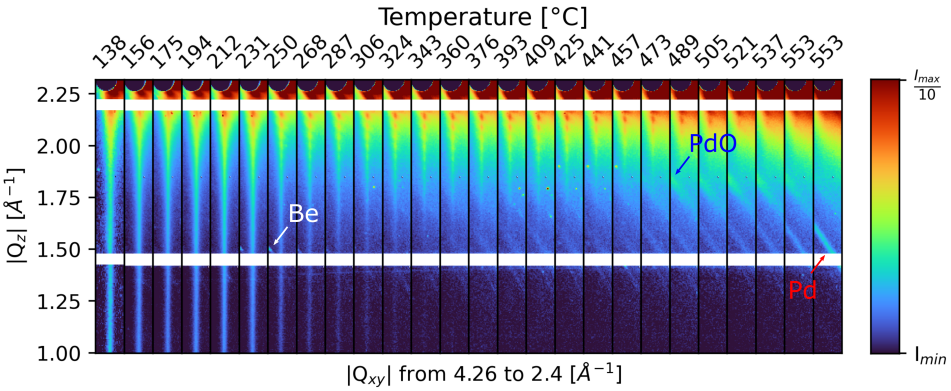

Figure C.28: Close-up of the HEGIXRD diffraction data of the (3 1) rod of the CeO_2 thin film.

D. SI: Methane Induced Sintering of Catalytic Nanoparticles in Spatially Confined Geometries on CeO_2 Supports

D.1 Semi automatic SEM analysis of NPs in CeO_2 thin film.

The following pages contain the Python code and its outputs used for semi-automatic analysis of NPs in holes of the CeO_2 thin film. This analysis routine was developed in order to cope with three issues. (1) The contrast within the individual images in Section D.3 made quantitative analysis of the NPs in holes impossible. Standard data processing procedures such as thresholding, filtering and blurring applied in consecutive order did not resolve this issue. (2) With the images extracted, individual analysis with software such as Gwyddion remains tedious. (3) While Gwyddion can be implemented in scripts, the data processing remains difficult, since processing operations first need to be concluded before another operation can commence. The script below allows simple selection of areas in big overview images and saves the image data in separate files. The second part of the script uses the images prepared before and allows for dynamic image modification using K-means clustering, gaussian blurring, thresholding, and Otsu thresholding. This means that the listed operations are applied in this order, but the respective parameters can be changed dynamically

D.1.1 Details on Usage

Note that positions of the extracted images are not stored automatically in this version and need to be added manually in the appropriate cell. Fur-

thermore, in the same cell, the resolution of each large-scale image must be given, as the individual images do not contain information on the size of the image. The current version of the script does not allow changing the order of operations without modifying core elements of the script. The following pages contain the Python script used for analysis.

[ ]:
```
%matplotlib widget

import sys
import os
from copy import deepcopy

from PIL import Image
import cv2

import numpy as np
from scipy.interpolate import interp2d
import matplotlib.pyplot as plt
import matplotlib.colors as colors
import matplotlib.gridspec as gridspec
from matplotlib.lines import Line2D

import pickle

import pylab

import ipywidgets as widgets

from jansPrettyPlots.functionality import savefigbutton, smallPreview
import xrayutilities as xu

from janspythonutility.unitconv import *
from janspythonutility.utility import printFiles, number_selector, ensureList,␣
↪pol2cart, printList, ensureList, findClosest
from janspythonutility.prettyplots.aesthetics import add_colorbar

sys.path.append('/home/schoberj/function_rep')
from roi_handler import rectROI_centered, integrateROI, showROI, mask2D,␣
↪getProfiles, roiPreview

import matplotlib as mpl
mpl.rcParams.update({'font.size': 10})
```

[ ]:
```
#Kmeans
def kmeans_color_quantization(image, clusters=8, rounds=1):
    h, w = image.shape[:2]
    samples = np.zeros([h*w,3], dtype=np.float32)
    count = 0

    for x in range(h):
        for y in range(w):
            samples[count] = image[x][y]
            count += 1
```

```
    compactness, labels, centers = cv2.kmeans(samples,
            clusters,
            None,
            (cv2.TERM_CRITERIA_EPS + cv2.TERM_CRITERIA_MAX_ITER, 10000, 0.0001),
            rounds,
            cv2.KMEANS_RANDOM_CENTERS)

    centers = np.uint8(centers)
    res = centers[labels.flatten()]
    return res.reshape((image.shape))

def find_outline(arr):
    # Get the shape of the input array
    rows, cols = arr.shape

    # Initialize the output array with zeros
    outline = np.zeros((rows, cols), dtype=int)

    # Directions for the neighboring cells (top, bottom, left, right)
    directions = [(-1, 0), (1, 0), (0, -1), (0, 1)]

    # Iterate over each cell in the input array
    for r in range(rows):
        for c in range(cols):
            # Check if the current cell has the value 255
            if arr[r, c] > 0:
                # Check all neighboring cells
                for dr, dc in directions:
                    nr, nc = r + dr, c + dc
                    # Check if the neighbor is within bounds and is zero
                    if 0 <= nr < rows and 0 <= nc < cols and arr[nr, nc] == 0:
                        # Mark the current cell in the outline array
                        outline[r, c] = 1
                        break

    return outline
```

[ ]:
```
# Load image
def to_rgb1(im):
    # I think this will be slow
    w, h = im.shape
    ret = np.empty((w, h, 3), dtype=np.uint8)
    ret[:, :, 0] = im
    ret[:, :, 1] = im
    ret[:, :, 2] = im
    return ret
```

```
# Update function
def on_button_clicked(b):
    with output:
        outline_arr = outline
        outline_file = cutfiles[currentimageidx].replace('.txt','_outline.txt')
        np.savetxt(os.path.join(cutdir,outline_file), outline_arr)
        with open(file_path, 'a') as file:
            value = diam_text.get_text().split(':')[1]
            filenumber = '_'.join(cutfiles[currentimageidx].replace('.txt','').
 ↪split('_')[-2:])
            file.write(f'{filenumber} {value}\n')
            file.close()


def updateBlur(val):

    global number_text,diam_text,area_text

    if val%2 == 1:
        (
            kmeans_im,blur_im,thresh_im,otsuthresh_im,result_im,
            original_im,outlineoverlay_im,points,sizes,outline_im
        ) = findParticles(original_image.get_array(),clusterSlider.
 ↪value,val,threshSlider.value,otsuthreshSlider.value)

        kmeans_image.set_array(kmeans_im)
        blur_image.set_array(blur_im)
        otsuthresh_image.set_array(otsuthresh_im)
        thresh_image.set_array(otsuthresh_im)
        result_image.set_array(result_im)
        #overlay_image.set_array(original_im)
        #outline_image.set_array(outline_im)
        outlineoverlay_image.set_array(outlineoverlay_im)

        number_text.set_text(f'Number of particles: {len(points)}')
        diam_text.set_text(f'Particle area: {[np.round(2 * np.sqrt(area/np.
 ↪pi),3) for area in sizes]}')
        area_text.set_text(f'Particle diameters: {sizes}')

        analyse_fig.canvas.draw()
    else:
        pass


def updateCluster(val):
    (kmeans_im,blur_im,thresh_im,otsuthresh_im,result_im,
```

```
     original_im,outlineoverlay_im,points,sizes,outline_im
    ) = findParticles(original_image.get_array(),val,blurSlider.
 ↪value,threshSlider.value,otsuthreshSlider.value)

    kmeans_image.set_array(kmeans_im)
    blur_image.set_array(blur_im)
    otsuthresh_image.set_array(otsuthresh_im)
    thresh_image.set_array(otsuthresh_im)
    result_image.set_array(result_im)
    #overlay_image.set_array(original_im)
    #outline_image.set_array(outline_im)
    outlineoverlay_image.set_array(outlineoverlay_im)

    number_text.set_text(f'Number of particles: {len(points)}')
    diam_text.set_text(f'Particle area: {[np.round(2 * np.sqrt(area/np.pi),3)␣
 ↪for area in sizes]}')
    area_text.set_text(f'Particle diameters: {sizes}')

    analyse_fig.canvas.draw()

def updateOtsuThresh(val):
    (kmeans_im,blur_im,thresh_im,otsuthresh_im,result_im,
     original_im,outlineoverlay_im,points,sizes,outline_im
    ) = findParticles(original_image.get_array(),clusterSlider.value,blurSlider.
 ↪value,threshSlider.value,val)

    kmeans_image.set_array(kmeans_im)
    blur_image.set_array(blur_im)
    otsuthresh_image.set_array(otsuthresh_im)
    thresh_image.set_array(otsuthresh_im)
    result_image.set_array(result_im)
    #overlay_image.set_array(original_im)
    #outline_image.set_array(outline_im)
    outlineoverlay_image.set_array(outlineoverlay_im)

    number_text.set_text(f'Number of particles: {len(points)}')
    diam_text.set_text(f'Particle area: {[np.round(2 * np.sqrt(area/np.pi),3)␣
 ↪for area in sizes]}')
    area_text.set_text(f'Particle diameters: {sizes}')

    analyse_fig.canvas.draw()

def updateThresh(val):
    (kmeans_im,blur_im,otsuthresh_im,thresh_im,result_im,
     original_im,outlineoverlay_im,points,sizes,outline_im
    ) = findParticles(original_image.get_array(),clusterSlider.value,blurSlider.
 ↪value,val,otsuthreshSlider.value)
```

```
    kmeans_image.set_array(kmeans_im)
    blur_image.set_array(blur_im)
    otsuthresh_image.set_array(otsuthresh_im)
    thresh_image.set_array(otsuthresh_im)
    result_image.set_array(result_im)
    #overlay_image.set_array(original_im)
    #outline_image.set_array(outline_im)
    outlineoverlay_image.set_array(outlineoverlay_im)

    number_text.set_text(f'Number of particles: {len(points)}')
    diam_text.set_text(f'Particle area: {[np.round(2 * np.sqrt(area/np.pi),3)␣
↪for area in sizes]}')
    area_text.set_text(f'Particle diameters: {sizes}')

    analyse_fig.canvas.draw()


# Function to handle button click
def on_button_click(index):
    def handle_click(button):
        global selected_image, images
        selected_image = images[index]

        global currentimageidx
        currentimageidx = index
        analyse_fig.suptitle(f'Image #{currentimageidx}')
        analyse_image = to_rgb1(selected_image/np.max(selected_image)*255)
        original_image.set_array(analyse_image)

        (kmeans_im,blur_im,thresh_im,otsuthresh_im,result_im,
         original_im,outlineoverlay_im,points,sizes,outline_im
        ) = findParticles(original_image.get_array(),
                          clusterSlider.value,blurSlider.value,threshSlider.
↪value,otsuthreshSlider.value)

        kmeans_image.set_array(kmeans_im)
        blur_image.set_array(blur_im)
        thresh_image.set_array(thresh_im)
        otsuthresh_image.set_array(otsuthresh_im)
        result_image.set_array(result_im)
        #overlay_image.set_array(original_im)
        #outline_image.set_array(outline_im)
        outlineoverlay_image.set_array(outlineoverlay_im)

        number_text.set_text(f'Number of particles: {len(points)}')
```

```
        diam_text.set_text(f'Particle area: {[np.round(2 * np.sqrt(area/np.
↪pi),3) for area in sizes]}')
        area_text.set_text(f'Particle diameters: {sizes}')

        analyse_fig.canvas.draw()

    return handle_click




def findParticles(animage,clusters,blur,scalar_threshold,AREA_THRESHOLD):

    original = animage.copy()

    # blur
    if blur %2 == 1:
        blurred = cv2.GaussianBlur(animage, (blur,blur), 0)
    else:
        blurred = cv2.GaussianBlur(animage, (blur-1,blur-1), 0)
    # kmeans segmentation
    kmeans = kmeans_color_quantization(blurred, clusters=clusters)
    # scalar thresholding
    gray = cv2.cvtColor(kmeans, cv2.COLOR_BGR2GRAY)
    gray_filter = cv2.inRange(gray, scalar_threshold[0], scalar_threshold[1])
    gray[gray_filter!=255] = 0
    gray_filtered = gray
    # otsu thresholding
    thresh = cv2.threshold(gray_filtered, 0, 150, cv2.THRESH_BINARY + cv2.
↪THRESH_OTSU)[1]

    # Find contours, remove tiny specs using contour area filtering, gather␣
↪points
    points_list = []
    size_list = []
    cnts, _ = cv2.findContours(thresh, cv2.RETR_EXTERNAL, cv2.
↪CHAIN_APPROX_SIMPLE)[-2:]

    for c in cnts:
        area = cv2.contourArea(c)
        if area < AREA_THRESHOLD:
            cv2.drawContours(thresh, [c], -1, 0, -1)
        else:
            (x, y), radius = cv2.minEnclosingCircle(c)
            points_list.append((int(x), int(y)))
            size_list.append(area)
```

```
    # Apply mask onto original image
    result = cv2.bitwise_and(original, original, mask=thresh)
    try:
        result[thresh==255] = (36,255,12)
    except:
        result = result

    # Overlay on original
    try:
        original[thresh==255] = (36,255,12)
    except:
        original = original

    global outline
    outline = find_outline(np.sum(result,axis=2))

    outlineoverlay = animage.copy()
    outlineoverlay[outline>0]=(36,255,12)


    return (kmeans,blurred,gray_filtered,thresh,result,
            original,outlineoverlay,points_list,size_list,outline)
```

1 Cutout sections

[ ]:
```
fdir,files = printFiles('./Pictures/31_sem_selection/',ftype='tif')
file = {"which": 0}
s = number_selector(files,file,width=1000)
```

1.0.1 Position selection

[ ]:
```
def on_click(event):
    # Check if the click is within the axes
    if event.inaxes is not None:
        # Store the position of the click
        positions.append((event.xdata, event.ydata))
        # Print the position0
        print(f"Clicked at x={event.xdata}, y={event.ydata}")

im = Image.open(os.path.join(fdir,file['which']))
imarr = np.array(im)[:][:1024]
fig = plt.figure(figsize=[12,8])
ax = plt.gca()
ax.imshow(imarr)
ax.set_aspect(1)
plt.tight_layout()
```

```
plt.show()

positions=[]

cid = fig.canvas.mpl_connect('button_press_event', on_click)
```

1.0.2 Extracted Positions

[ ]:
```
positions0 = [(414.99516148397134, 361.2484229360242), (192.53021766440492, 898.
↪7568896801947), (98.56986872197925, 22.714812775814153),
              (193.91198750179353, 898.7568896801947), (428.8128598578577, 531.
↪2061129348236), (251.9463206721153, 687.3461045597369),
              (544.8815261985012, 616.8758428529177), (633.3147957913725, 743.
↪99866789267), (560.0809944097759, 912.5745880540808),
              (452.3029470934641, 8.897114401927865), (854.3979697735505, 322.
↪55886748914304), (929.0135409925356, 169.18241553900702),
              (1093.4441516417805, 984.4266195982887), (1107.2618500156666, 683.
↪2007950475711), (1237.1482147301963, 721.8903504944522),
              (1203.9857386328695, 370.9208117977445), (1119.6977785521642, 381.
↪9749704968534), (1416.778293590716, 390.2655895211851)]

positions1 = [(55.73500376293222, 18.56950326364813), (46.06261490121196, 446.
↪91815285411826), (250.56455083472667, 954.0276831757392),
              (272.67286823294444, 589.2404461051453), (261.61870953383556, 314.
↪26824846481145), (185.62136847746183, 104.23923318174229),
              (356.96082831364987, 61.40436822269521), (485.46542319079083, 231.
↪36205822149464), (687.2038194495284, 25.478352450591274),
              (988.4296440002458, 837.9590168350957), (1150.0967149747137, 806.
↪1783105751576), (938.6859298542558, 727.4174298440066),
              (941.4494695290332, 120.82047123040559), (924.8682314803698, 171.
↪94595521378426), (1082.3899929426716, 86.27622529569032),
              (1122.4613182269413, 123.58401090518282), (1302.0913970874608, 242.
↪41621692060346), (1353.2168810708395, 322.5588674891429),
              (1440.268380826322, 69.6949872470268), (1517.6474917200844, 556.
↪0779700078185), (1452.7043093628197, 898.7568896801945),
              (1512.12041237053, 962.3183022000708), (1087.9170722922258, 333.
↪61302618825187)]

positions2 = [(46.06261490121196, 17.187733426259683), (155.22243205491236, 61.
↪40436822269521), (44.68084506382334, 173.32772505117293),
              (65.40739262465252, 377.8296609846876), (292.017645956385, 178.
↪8548044007273), (279.5817174198875, 369.5390419603559),
              (188.38490815223906, 691.4914140719027), (164.89482091663265, 895.
↪9933500054174), (405.3227726222513, 759.1981361039448),
              (492.374272377734, 846.2496358594274), (580.8075419706051, 701.
↪163802933623), (463.35710579257307, 580.9498270808137),
```

```
              (479.93834384123636, 539.4967319591553), (500.6648914020654, 486.
 ↪9894781383879), (540.7362166863352, 318.41355797697713),
              (537.972677011558, 148.4558679781777), (732.8022240833524, 119.
 ↪43870139301691), (579.4257721332164, 51.73197936097495),
              (689.9673591243053, 198.19958212416782), (789.4547874162854, 428.
 ↪9551449680662), (817.0901841640577, 524.2972637478805),
              (866.8338983100477, 522.9154939104918), (794.9818667658399, 789.
 ↪5970725264941), (960.7942472524734, 661.0924776493532),
              (1081.008223105283, 699.7820330962343), (1137.660786438216, 351.
 ↪57603407430383), (1147.3331752999363, 265.9063041562099),
              (1201.2221989580921, 395.7926688707395), (1168.0597228607655, 478.
 ↪6988591140562), (1248.202373429305, 299.0687802535366),
              (1112.7889293652208, 158.12825683989809), (1302.0913970874608, 167.
 ↪80064570161835), (1423.687142777659, 84.89445545830154),
              (1495.5391743218665, 521.5337240731033), (1414.0147539159384, 590.
 ↪6222159425339), (1463.7584680619286, 687.3461045597368),
              (1159.7691038364337, 792.3606122012714), (1215.0398973319782, 800.
 ↪651231225603), (1339.3991826969534, 1006.5349369965064),
              (989.8114138376344, 227.2167487093286)]

positions3 = [(178.7125192905188, 69.69498724702692), (387.35976473619934, 10.
 ↪27888423931654), (191.1484478270163, 446.91815285411826),
              (444.0123280691324, 616.8758428529177), (354.19728863887264, 813.
 ↪0871597621007), (250.56455083472667, 900.1386595175833),
              (267.14578888339, 971.9906910617912), (569.7533832714962, 844.
 ↪8678660220387), (812.9448746518921, 521.5337240731033),
              (973.2301757889712, 11.660654076704986), (1378.088738143835, 194.
 ↪05427261200202), (1517.6474917200849, 196.81781228677926),
              (1357.3621905830057, 643.1294697633012), (1502.4480235088101, 662.
 ↪4742474867419), (1360.125730257783, 757.8163662665561)]

positions4 = [(163.51305107924404, 28.241892125368622), (473.02949465429333, 220.
 ↪3078995223857), (405.3227726222513, 514.6248748861602),
              (336.23428075282067, 568.5138985443161), (258.8551698590583, 601.
 ↪676374641643), (32.24491652732581, 752.2892869170016),
              (251.9463206721153, 819.9960089490437), (850.2526602613847, 538.
 ↪1149621217667), (835.0531920501099, 381.9749704968534),
              (975.9937154637483, 445.5363830167296), (846.1073507492189, 542.
 ↪2602716339326), (887.5604458708772, 107.00277285651941),
              (1173.5868022103202, 837.9590168350958), (1501.0662536714215, 710.
 ↪8361917953433), (1472.0490870862607, 919.4834372410239)]

positions5 = [(119.29641628280842, 153.9829473277323), (261.61870953383556, 202.
 ↪34489163633373), (377.6873758744791, 227.21674870932884),
```

```
             (419.1404709961374, 138.78347911645756), (257.4734000216697, 340.
↪521875375195), (87.51571002287034, 593.3857556173111),
             (279.5817174198875, 797.8876915508259), (579.4257721332166, 621.
↪0211523650835), (660.9501925391447, 521.5337240731034),
             (1340.7809525343423, 202.34489163633373), (1438.8866109889339, 271.
↪43338350576437), (1208.1310481450353, 872.503262769811),
             (974.6119456263599, 627.9300015520265), (648.5142640026471, 54.
↪49551903575207)]

#positions6 = [(91.66101953503616, 18.56950326364813), (450.92117725607557, 8.
↪897114401927865), (193.91198750179353, 895.9933500054174),
#              (413.61339164658295, 365.3937324481901), (424.6675503456919, 528.
↪4425732600464), (518.6278992881175, 394.4108990333509),
#              (543.4997563611124, 615.494073015529), (629.1694862792065, 741.
↪2351282178928), (562.8445340845531, 907.0475087045263),
#             (673.3861210756421, 420.6645259437346), (862.6885887978822, 318.
↪41355797697713), (924.8682314803698, 159.51002667728665),
#             (1121.0795483895527, 379.2114308220762), (1192.9315799337605, 365.
↪39373244819), (1105.880080178278, 690.1096442345141),
#              (1223.3305163563102, 719.126810819675), (1092.0623818043919, 984.
↪4266195982887), (1407.1059047289957, 384.73851017163065)]

allresolutions = [3/(1497-1135), 3/(1497-1135), 3/(1497-1135), 2/(1444-1203), 2/
↪(1447-1206), 3/(1497-1135)]#, 3/(1497-1135)]

allpositions = [positions0, positions1, positions2, positions3, positions4,␣
↪positions5]#, positions6]
index = [i for i,f in enumerate(files) if file['which']==f][0]
filepositions = allpositions[index]
fileresolution = allresolutions[index]
```

1.0.3 Extract Cuts from Positions and Save

[ ]:
```
rois = []
for i,pos in enumerate(filepositions):
    rois.append([f'{i}', rectROI_centered(pos[0],pos[1],70,70)])

im = Image.open(os.path.join(fdir,file['which']))
imarr = np.array(im)[:][:1024]
fig = plt.figure()
ax = plt.gca()
ax.imshow(imarr)
showROI(ax,rois,np.full(len(rois),1500),np.full(len(rois),1500))
plt.show()
```

[ ]:
```
for f,positions,resolution in zip(files,allpositions,allresolutions):
    im = Image.open(os.path.join(fdir,f))
    imarr = np.array(im)[:][:1024]
    for i,position in enumerate(positions):
        x0,y0,x1,y1 = rectROI_centered(position[0],position[1],70,70)
        if x0<0:
            x0=0
        if x1>np.shape(imarr)[1]:
            x1=np.shape(imarr)[1]

        if y0<0:
            y0=0
        if y1>np.shape(imarr)[0]:
            y1=np.shape(imarr)[0]

        cut = imarr[int(y0):int(y1),int(x0):int(x1)]
        fname = f.replace('.tif','')
        np.savetxt(f'./Pictures/31_sem_selection/cuts/{fname}_{i}.txt', cut,␣
↪fmt='%d', delimiter=',',header=f'{resolution} um')
```

1.0.4 Load cuts and do stuff

[ ]:
```
cutdir,cutfiles = printFiles('./Pictures/31_sem_selection/cuts',ftype='txt')
cutfiles.sort()
cutfiles = [f for f in cutfiles if 'outline' not in f]

images = []
resolutions = []
for cutfile in cutfiles:
    loaded_array = np.loadtxt(os.path.join(cutdir,cutfile), delimiter=',')
    images.append(loaded_array)
    with open(os.path.join(cutdir,cutfile)) as f:
        content =  f.readlines()
    resolution = content[0].replace('\n','')
    resolutions.append(resolution)
```

[ ]:
```
fig,axs = plt.subplots(int(len(cutfiles)/6),6,figsize=(12,36))
axs = axs.ravel()

for ax,im,res in zip(axs,images,resolutions):

    sres = res.split()
    if 'um' in sres[2]:
        resolution_um = float(sres[1].replace(' um',''))
        resolution_nm = resolution_um*1e3
        x = np.linspace(0,np.shape(im)[0]*resolution_nm,np.shape(im)[0])
        y = np.linspace(0,np.shape(im)[1]*resolution_nm,np.shape(im)[1])
```

```
    ax.pcolormesh(y,x,im,cmap='gray')
    ax.set_aspect(1)
plt.tight_layout()
plt.show()
```

2 Cutout analysis

[ ]:
```
# Create buttons dynamically based on the length of images and store in buttons
buttons = []
for i in range(len(images)):
    button_layout= widgets.Layout(width='50px')
    button = widgets.Button(description=f'{i}',layout=button_layout)
    button.on_click(on_button_click(i))
    buttons.append(button)

# Display the buttons in a horizontal box
box_layout = widgets.Layout(width='100%',display='inline-flex',flex_flow='row␣
↪wrap')
carousel = widgets.Box(children=buttons, layout=box_layout)


display(widgets.VBox([widgets.Label('Select number:'), carousel]))
################################################################################

# Define image variables for analysis
currentimageidx = 0
selected_image = images[currentimageidx]
analyseimage = to_rgb1(selected_image/np.max(selected_image)*255)
clusterpar = 40
blurpar = 1
scalarthresh = (0,255)
areathresh = 70

(
    kmeans_im,blur_im,thresh_im,otsuthresh_im,result_im,
    overlay_im,outlineoverlay_im,points,sizes,outline_im
) = findParticles(analyseimage,clusterpar,blurpar,scalarthresh,areathresh)

analyse_fig = plt.figure(figsize=(8,5))
gs_datapanels = gridspec.GridSpec(2,1, height_ratios=[1,.2])
image_gs = gs_datapanels[0].subgridspec(2, 4,hspace=.5)
axs = [analyse_fig.add_subplot(image_gs[i]) for i,gs in␣
↪enumerate(list(image_gs))]
output_gs = gs_datapanels[1].subgridspec(1, 1)
oax = analyse_fig.add_subplot(output_gs[0])
oax.set_axis_off()
```

```
#Plot stuff
original_image = axs[0].imshow(analyseimage)
axs[0].set_title('Original')

blur_image = axs[1].imshow(blur_im,cmap='gray')
axs[1].set_title('Blur')

kmeans_image = axs[2].imshow(kmeans_im)
axs[2].set_title('kmeans')

thresh_image = axs[3].imshow(thresh_im)
axs[3].set_title('Threshold')

otsuthresh_image = axs[4].imshow(otsuthresh_im)
axs[4].set_title('Otsu threshold')

result_image = axs[5].imshow(result_im)
axs[5].set_title('Result')

outlineoverlay_image = axs[6].imshow(outlineoverlay_im,cmap='gray')
axs[6].set_title('Outline')

axs[7].set_axis_off()

clusterSlider = widgets.IntSlider(min=1, max=70, step=1, description='Clustering:
↪', value=clusterpar)
global clusterSlider
widgets.interact(updateCluster, val=clusterSlider)

blurSlider = widgets.IntSlider(min=1, max=50, step=1, description='Blurring:',␣
↪value=blurpar)
global blurSlider
widgets.interact(updateBlur, val=blurSlider)

threshSlider = widgets.IntRangeSlider(min=0, max=255, step=1,␣
↪description='Scalar threshold:', value=scalarthresh)
global threshSlider
widgets.interact(updateThresh, val=threshSlider)

otsuthreshSlider = widgets.FloatSlider(min=1, max=500, step=.1,␣
↪description='Area threshold:', value=areathresh)
global otsuthreshSlider
widgets.interact(updateOtsuThresh, val=otsuthreshSlider)

particle_sizes = sizes
```

```
number_text = oax.text(.5, .3, f'Number of particles: {len(points)}',
                       fontsize=12,␣
↪horizontalalignment='center',verticalalignment='center', transform=oax.
↪transAxes)
area_text = oax.text(.5, .5, f'Particle area: {sizes}',
                     fontsize=12,␣
↪horizontalalignment='center',verticalalignment='center', transform=oax.
↪transAxes)
diam_text = oax.text(.5, .7, f'Particle diameters: {[np.round(2 * np.sqrt(area/
↪np.pi),3) for area in sizes]}',
                     fontsize=12,␣
↪horizontalalignment='center',verticalalignment='center', transform=oax.
↪transAxes)

analyse_fig.suptitle(f'Image #{currentimageidx}')



file_path = './Pictures/31_sem_selection/cuts/diameters.dat'
# Make, display, and interact with button
button = widgets.Button(description='Save diameter.')
output = widgets.Output()
display(button, output)
button.on_click(on_button_clicked)

plt.show()
```

[ ]:
```
plt.figure()
plt.imshow(outline)
plt.show()
```

[ ]:
```
with open(os.path.join(cutdir,'diameters.dat')) as f:
    content = f.readlines()
    f.close()
d = []
for line in content:
    sLine = line.replace('\n','').split()[1]
    if ',' in sLine:
        values = sLine[1:-2].split(',')
        for value in values:
            d.append(float(value))
    else:
        d.append(float(sLine[1:-2]))


fig = plt.figure()
ax = plt.gca()
```

```
bins = ax.hist(np.array(d)*0.008298755186721992*1000, bins=20, edgecolor='black')
ax.set_xlabel('Particle diameter [nm]')
ax.set_ylabel('Frequency')
t = ax.text(x=80,y=16,s=f'{153-12} analyzed particles')
plt.show()
```

3 Big image analysis

[ ]:
```
def update_bigb(val):
    if val %2 == 1:
        blurred = cv2.GaussianBlur(imarr, (val,val), 0)
    else:
        blurred = cv2.GaussianBlur(imarr, (val-1,val-1), 0)
    bim.set_array(blurred)
    bfig.canvas.draw()

def update_bigk(val):
    # kmeans segmentation
    kmeans = kmeans_color_quantization(bim.get_array(), clusters=val)
    kim.set_array(kmeans)
    kfig.canvas.draw()

def update_bigts(val):

    gray = cv2.cvtColor(kim.get_array(), cv2.COLOR_BGR2GRAY)
    gray_filter = cv2.inRange(gray, val[0], val[1])
    gray[gray_filter!=255] = 0
    gray_filtered = gray

    tim.set_array(gray_filtered)
    tfig.canvas.draw()
```

[ ]:
```
file_sembig = '31_A_04_cutout2.tif'
im = Image.open(os.path.join('./Pictures/sem',file_sembig))
imarr = np.array(im)[:][:1024]
imarr.astype('uint8')
imres = 1447-1206 # for 1um
fig,ax = plt.subplots(1,1)
ax.imshow(imarr)
plt.show()
```

[ ]:
```
row_0f = [120,240]
col_0f = [170,300]

# remove roi
for i,row in enumerate(imarr):
```

```
    for j,col in enumerate(row):
        if j>row_0f[0] and j<row_0f[1] and i>col_0f[0] and i<col_0f[1]:
            imarr[i][j] = 0

imarr = imarr[300::,150::]

fig,ax = plt.subplots(1,1)
cim = ax.imshow(imarr)
plt.show()
```

[ ]:
```
bfig,bax = plt.subplots(1,1)
bim = bax.imshow(cim.get_array())
plt.tight_layout()
plt.show()

bigb = widgets.IntSlider(min=1, max=50, step=2, description='Blurring:', value=3)
widgets.interact(update_bigb, val=bigb)
```

[ ]:
```
kfig,kax = plt.subplots(1,1)
kim = kax.imshow(bim.get_array())
plt.tight_layout()
plt.show()

bigk = widgets.IntSlider(min=1, max=20, step=1, description='Kmeans clustering:
↪', value=5)
widgets.interact(update_bigk, val=bigk)
```

[ ]:
```
tfig,tax = plt.subplots(1,1)
tim = tax.imshow(kim.get_array())
plt.tight_layout()
plt.show()

bigts = widgets.IntRangeSlider(min=0, max=255, step=1, description='Scalar␣
↪threshold:', value=(100,255))
widgets.interact(update_bigts, val=bigts)
```

[ ]:
```
AREA_THRESHOLD = 5
# otsu thresholding
thresh = cv2.threshold(tim.get_array(), 0, 150, cv2.THRESH_BINARY + cv2.
↪THRESH_OTSU)[1]

# Find contours, remove tiny specs using contour area filtering, gather points
points_list = []
size_list = []
cnts, _ = cv2.findContours(thresh, cv2.RETR_EXTERNAL, cv2.
↪CHAIN_APPROX_SIMPLE)[-2:]
```

```
for c in cnts:
    area = cv2.contourArea(c)
    if area < AREA_THRESHOLD:
        cv2.drawContours(thresh, [c], -1, 0, -1)
    else:
        (x, y), radius = cv2.minEnclosingCircle(c)
        points_list.append((int(x), int(y)))
        size_list.append(area)

# Apply mask onto original image
result = cv2.bitwise_and(imarr, imarr, mask=thresh)
try:
    result[thresh==255] = (36,255,12)
except:
    result = result

# Overlay on original
try:
    imarr[thresh==255] = (36,255,12)
except:
    imarr = imarr

outline = find_outline(np.sum(result,axis=2))

outlineoverlay = imarr.copy()
outlineoverlay[outline>0]=(0,255,255)

bigfig = plt.figure()
ax = plt.gca()

plotim = cv2.cvtColor(imarr, cv2.COLOR_BGR2GRAY)

ax.pcolormesh(np.linspace(0,np.shape(plotim)[1]/imres,np.shape(plotim)[1]),
              np.linspace(0,np.shape(plotim)[0]/imres,np.shape(plotim)[0]),
              plotim,cmap='gray')
newoutline = np.full_like(outline,np.nan, dtype=np.float32)

for i,row in enumerate(outline):
    for j,val in enumerate(row):
        if val == 1 :
            newoutline[i][j] = 1
        else:
            newoutline[i][j] = np.nan

cmap = mpl.colors.LinearSegmentedColormap.from_list("", ["cyan","violet","blue"])

ax.pcolormesh(np.linspace(0,np.shape(plotim)[1]/imres,np.shape(plotim)[1]),
```

```
            np.linspace(0,np.shape(plotim)[0]/imres,np.shape(plotim)[0]),
            newoutline,cmap=cmap)

ax.set_xlabel('X [$\mu$m]')
ax.set_ylabel('Y [$\mu$m]')
plt.tight_layout()
plt.show()

savefigbutton(bigfig,'./Pictures/31_sem_selection/','outline_large.png')
```

[ ]:
```
size_large_diam = [np.round(2 * np.sqrt(area/np.pi),3) for area in size_list]

np.savetxt('./Pictures/sem/diamters_{}.txt'.format(file_sembig.replace('.
↪tif','')),size_large_diam,header=f'{imres} um')
```

D.2 NP outlines

The complete set of NPs in holes that were extracted from the images listed in Section D.3. The light blue colored outline shows the shape that is used for the diameter determination.

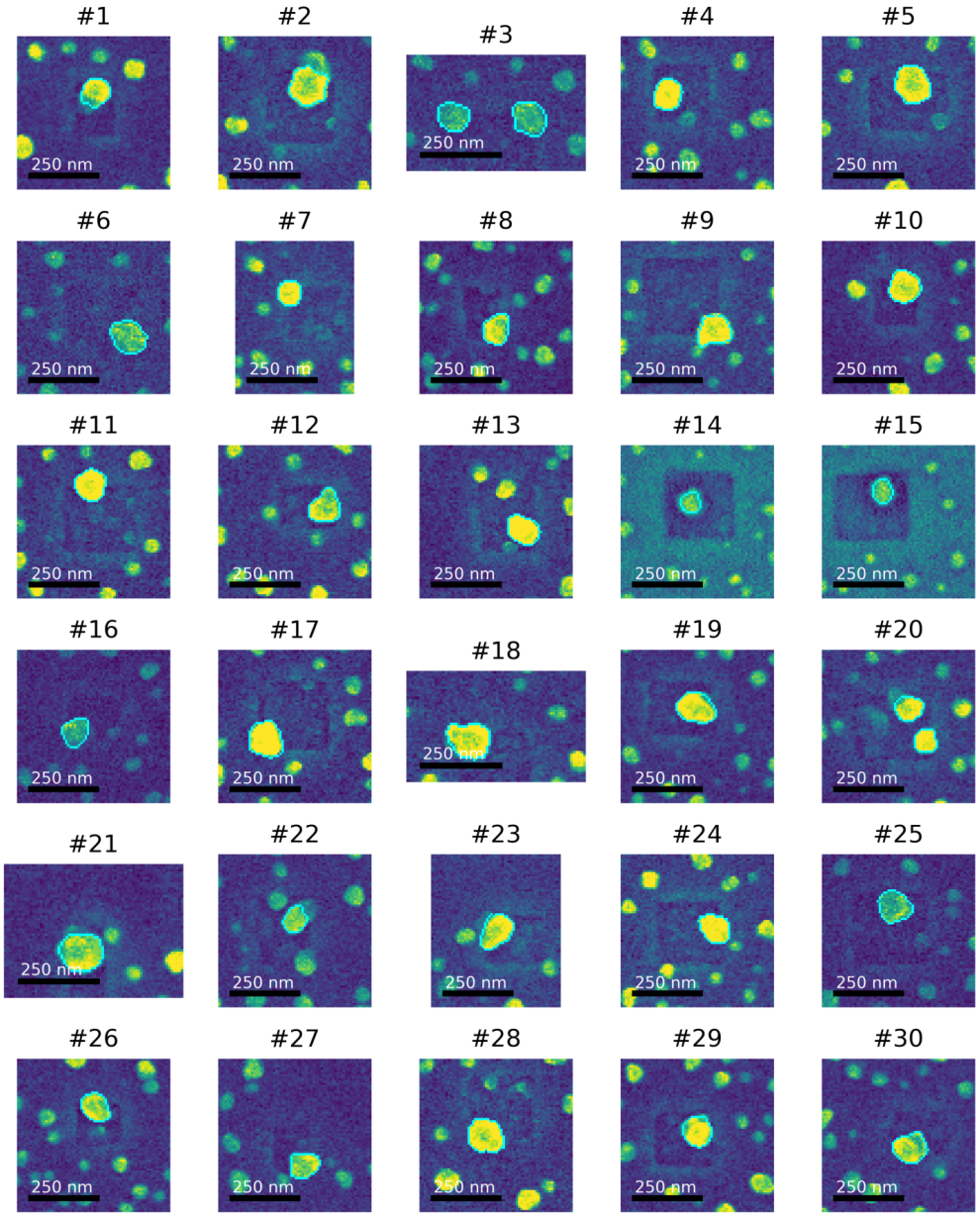

Figure D.1: Figure 1 of 5 containing the cuts taken from images in Section D.3.

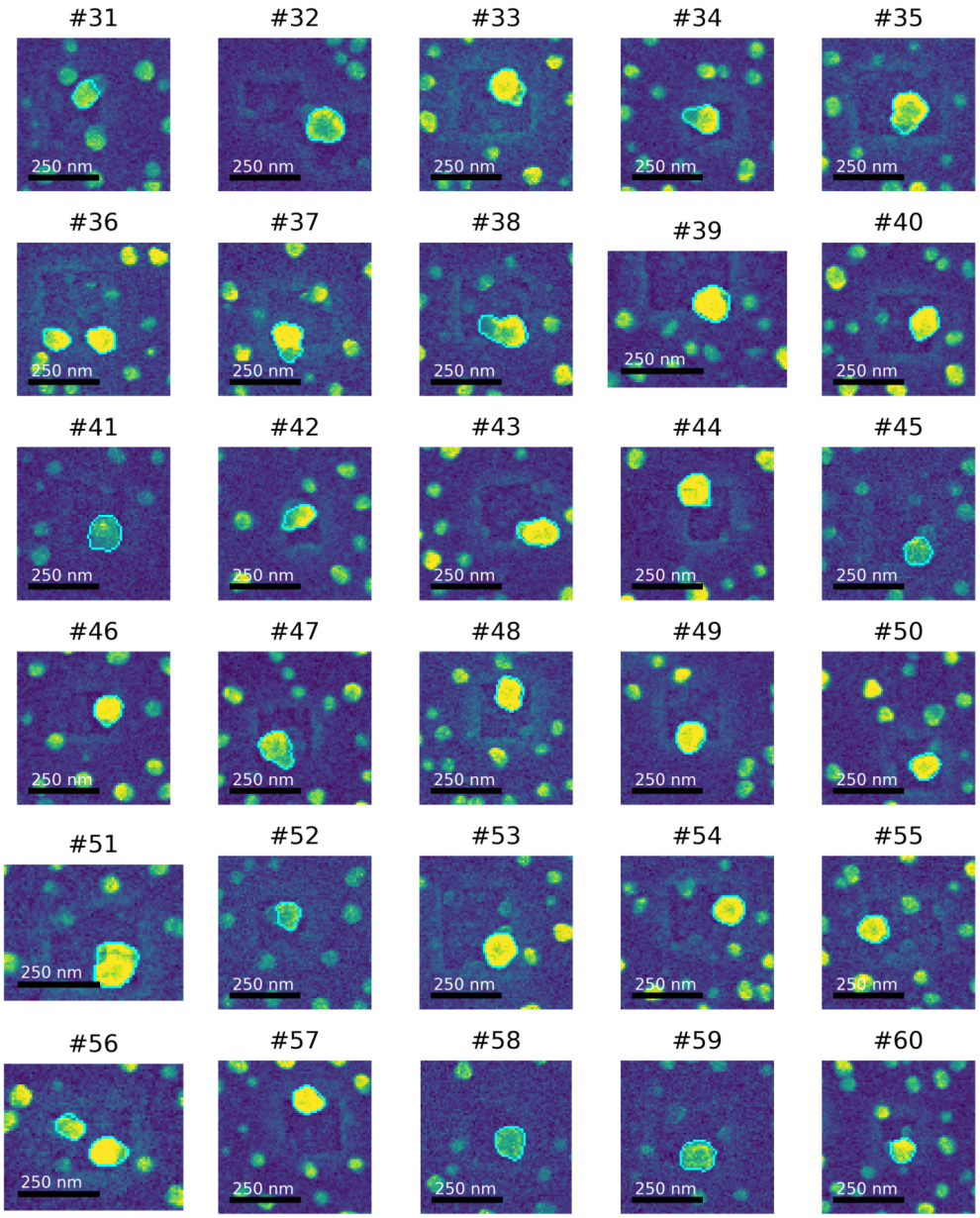

Figure D.2: Figure 2 of 5 containing the cuts taken from images in Section D.3.

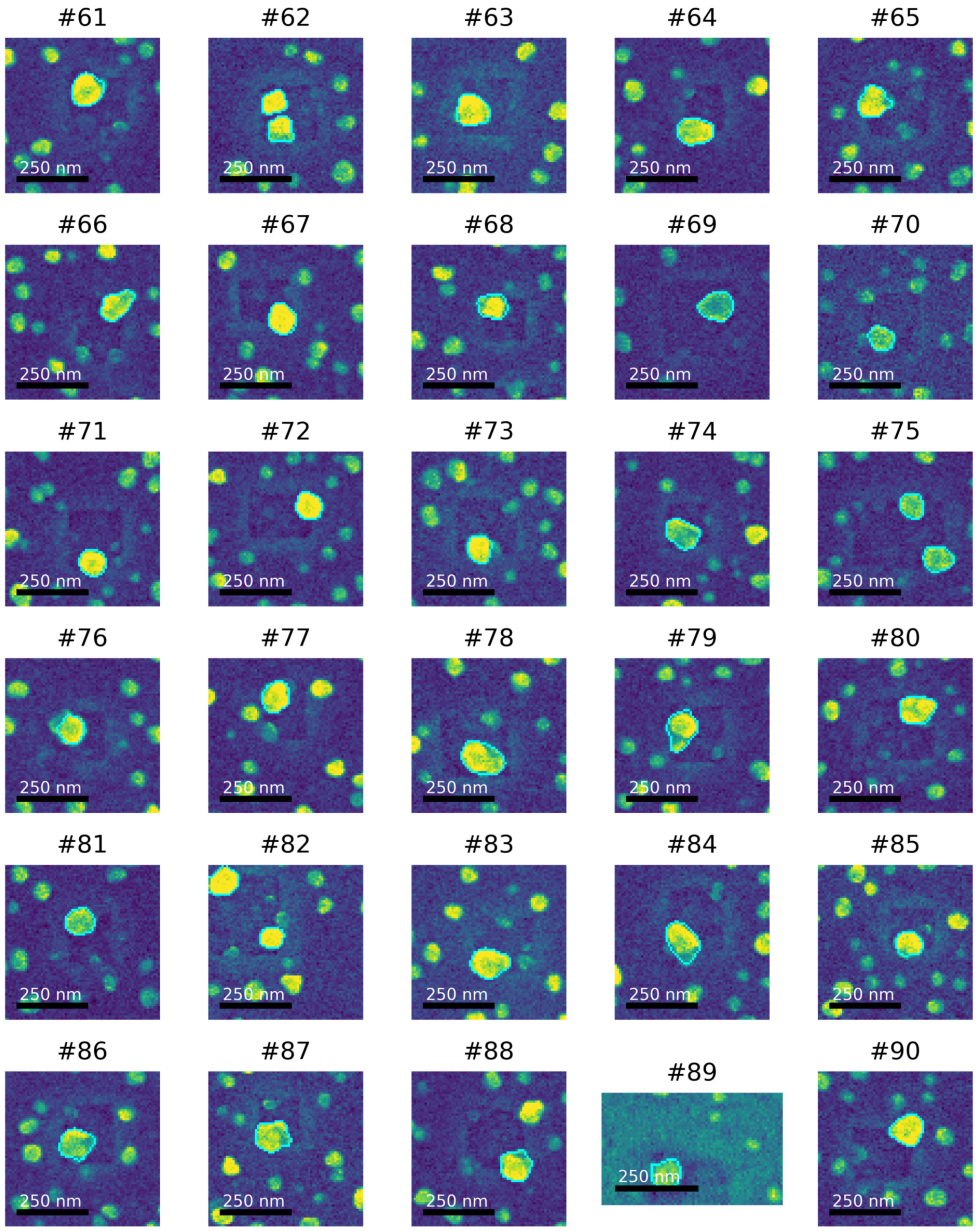

Figure D.3: Figure 3 of 5 containing the cuts taken from images in Section D.3.

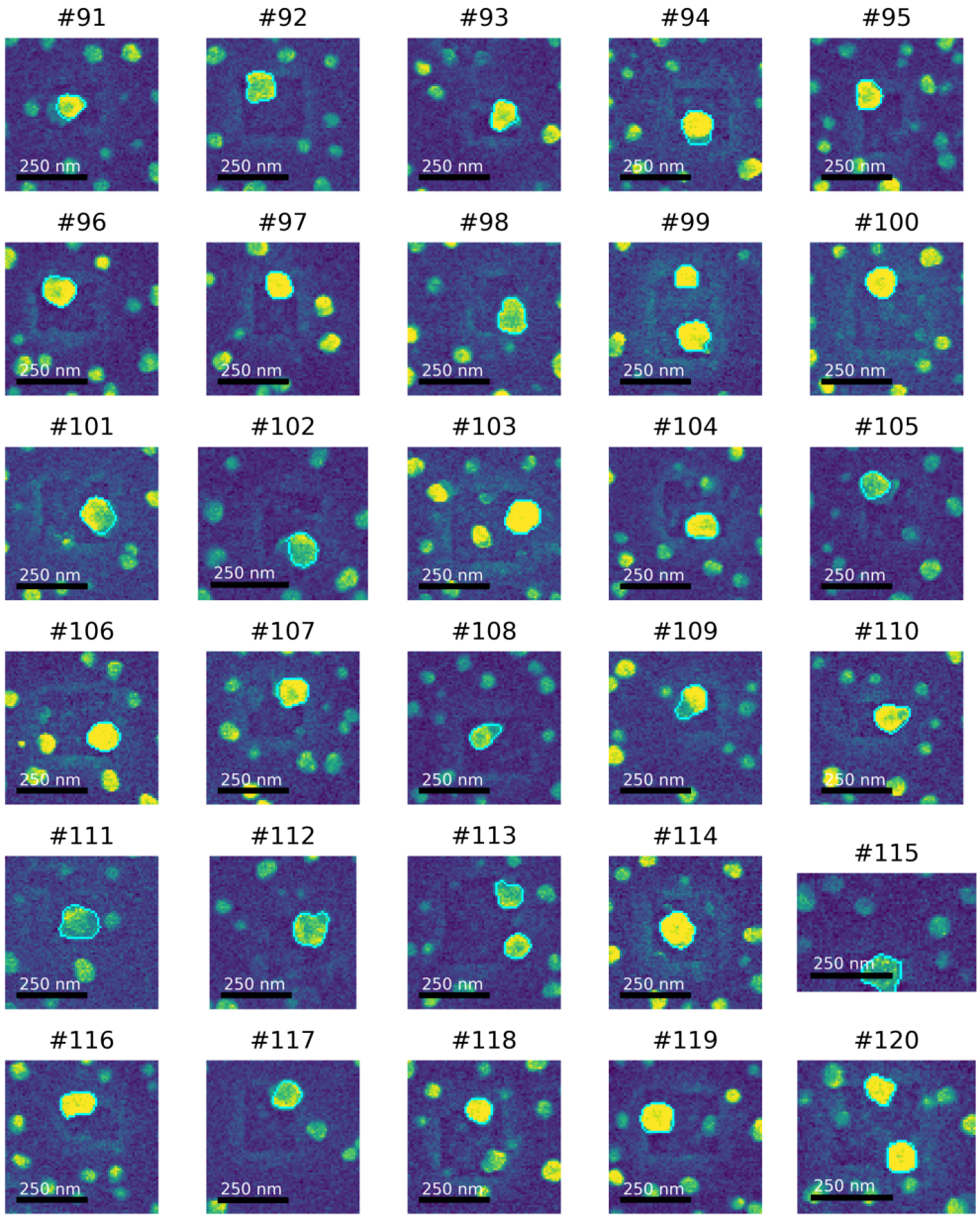

Figure D.4: Figure 4 of 5 containing the cuts taken from images in Section D.3.

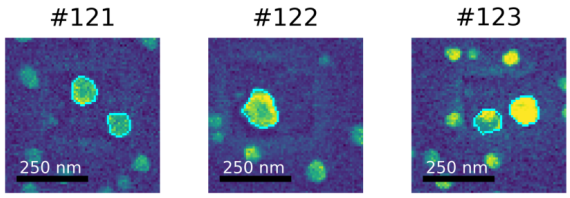

Figure D.5: Figure 5 of 5 containing the cuts taken from images in Section D.3.

D.3 SEM images of NPs in holes

This section contains the full set of SEM images from which the cutouts in Section D.2 were extracted using the code in Section D.1.1

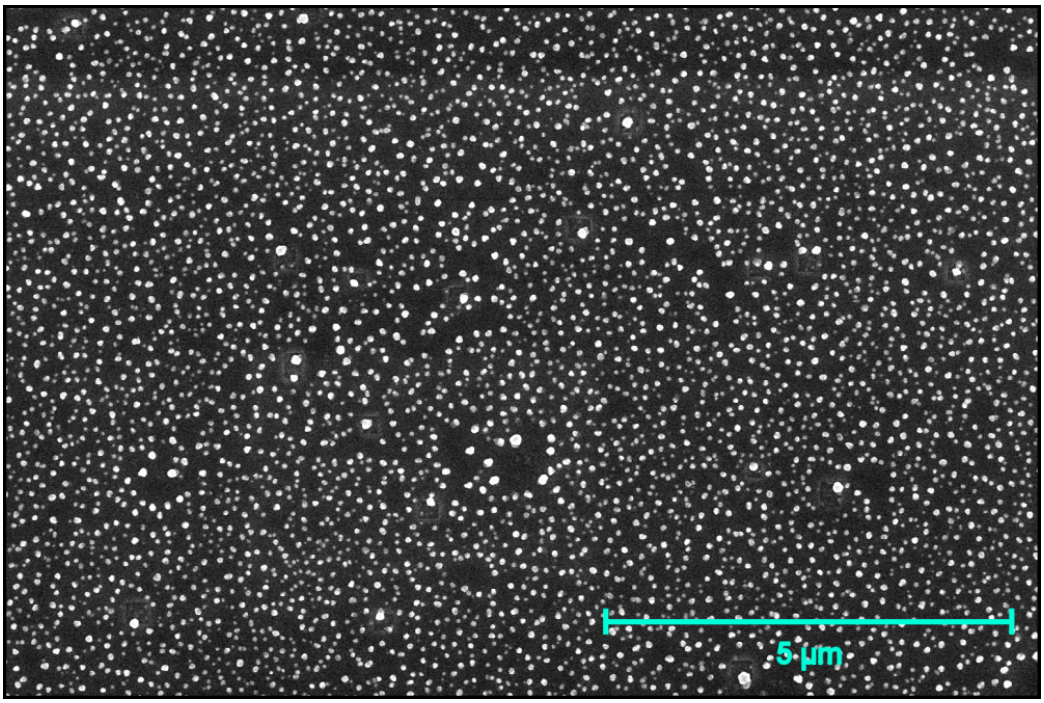

Figure D.6: Image 1 of 7 from which NP sizes of NPs in holes were extracted.

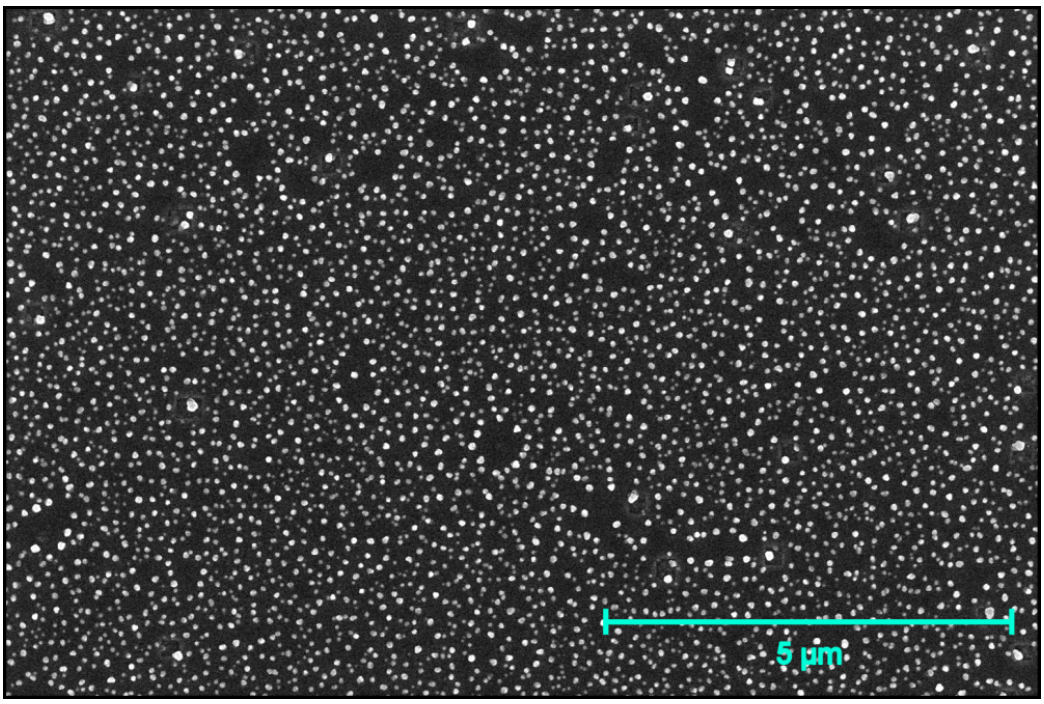

Figure D.7: Image 2 of 7 from which NP sizes of NPs in holes were extracted.

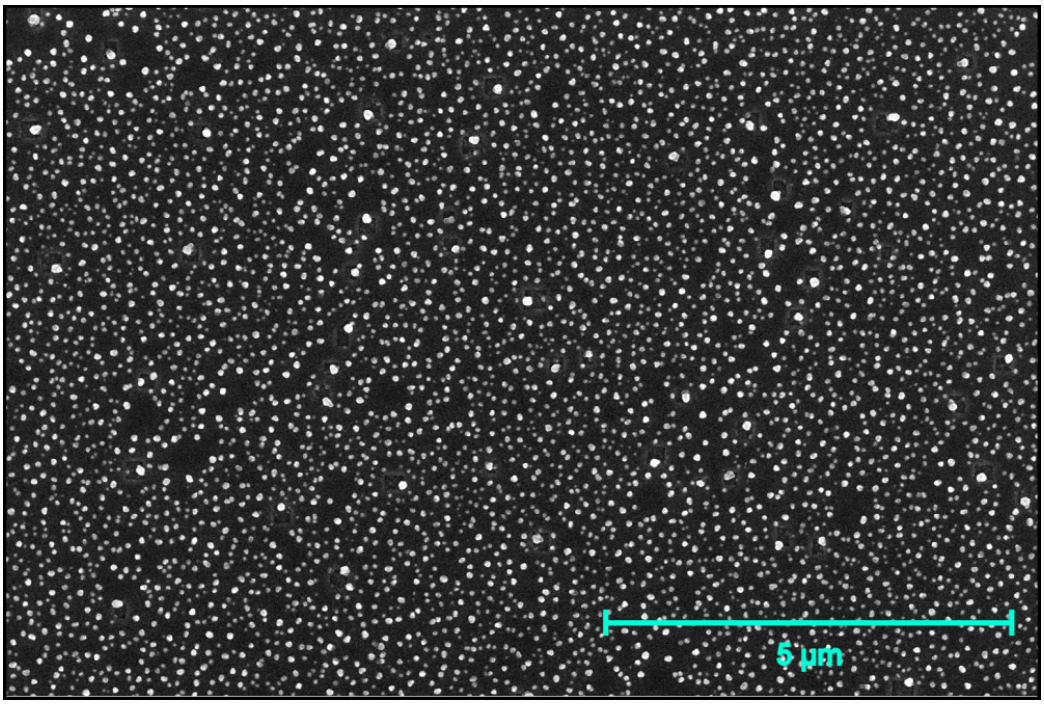

Figure D.8: Image 3 of 7 from which NP sizes of NPs in holes were extracted.

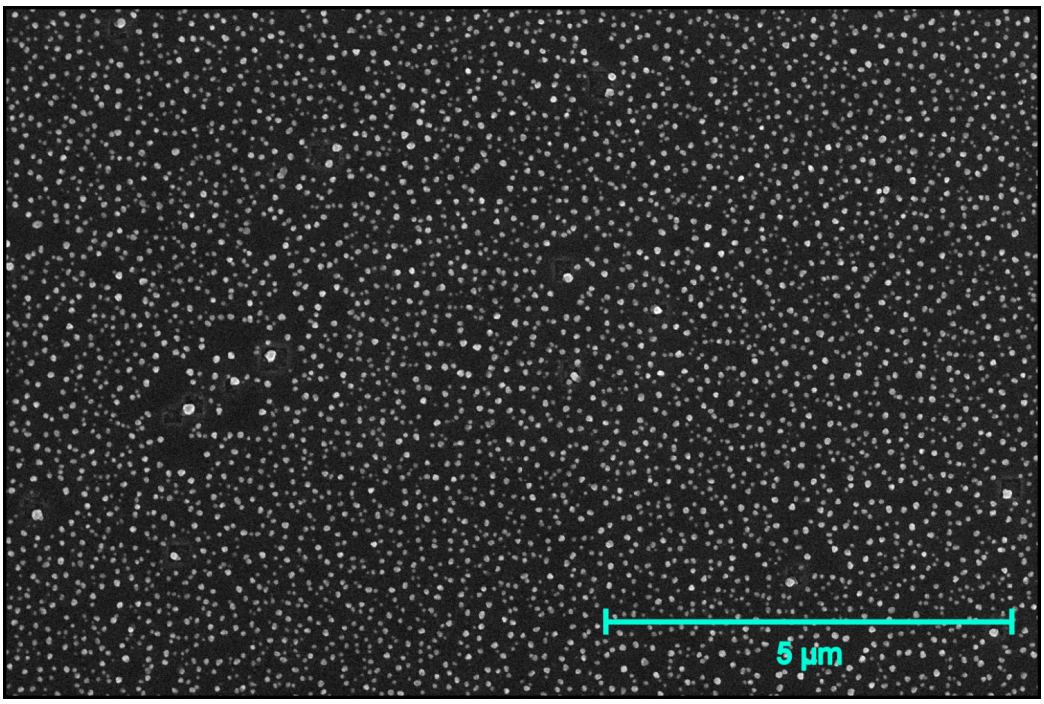

Figure D.9: Image 4 of 7 from which NP sizes of NPs in holes were extracted.

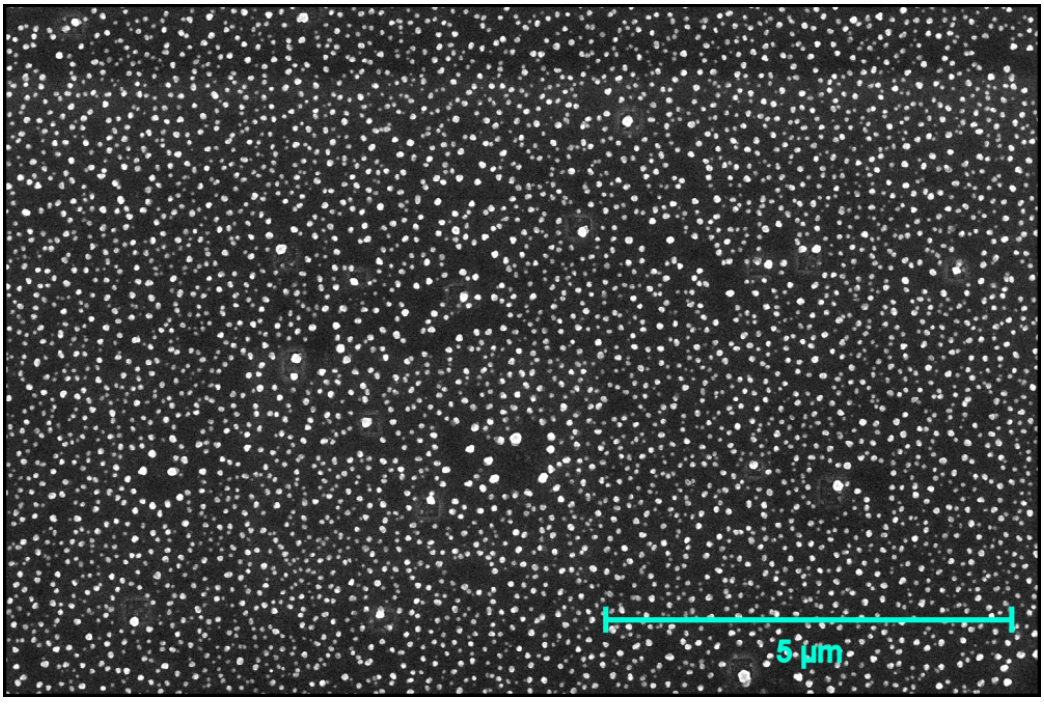

Figure D.10: Image 5 of 7 from which NP sizes of NPs in holes were extracted.

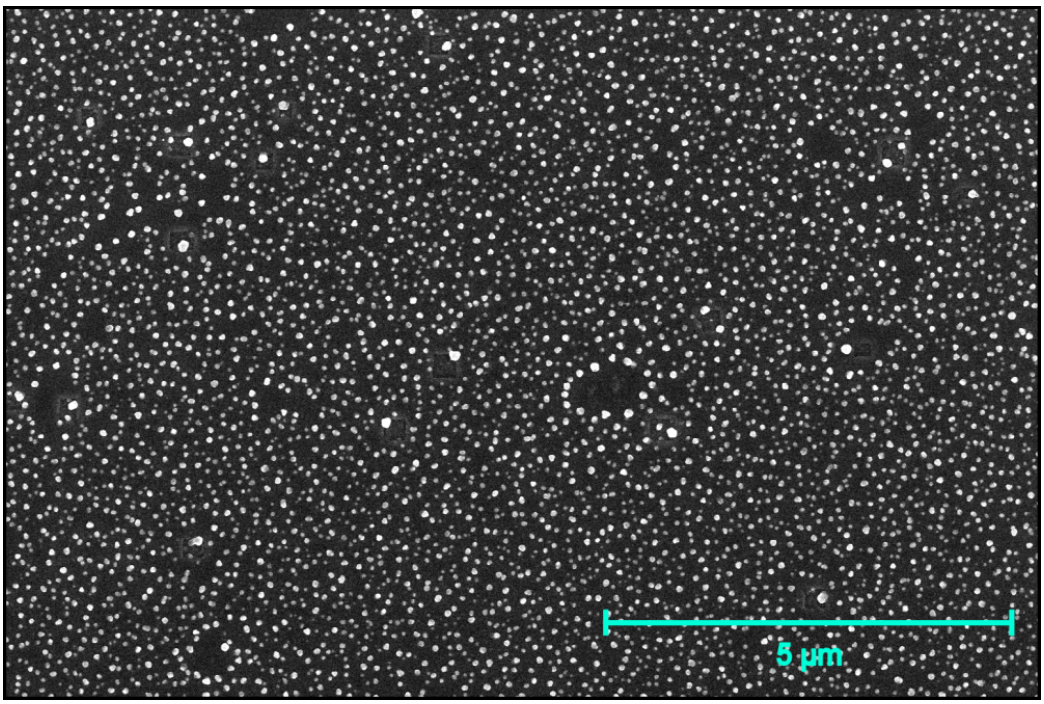

Figure D.11: Image 6 of 7 from which NP sizes of NPs in holes were extracted.

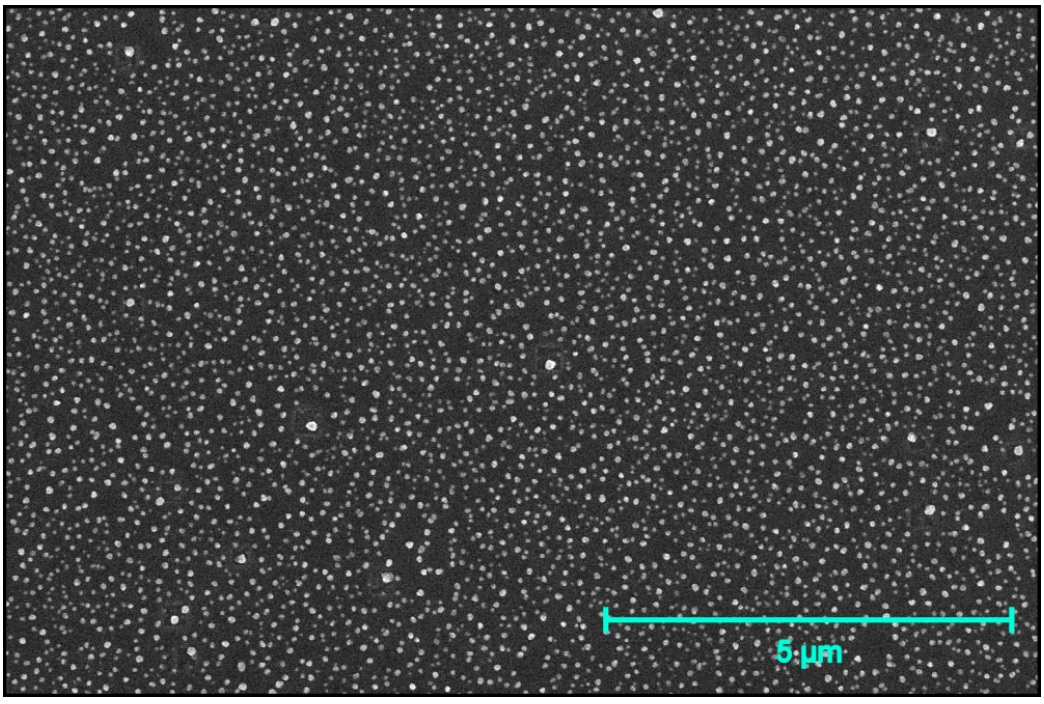

Figure D.12: Image 7 of 7 from which NP sizes of NPs in holes were extracted.

E. SI: Pd_xPt_y/Al_2O_3 Nanoparticle Sintering Kinetics During Catalytic CH_4 Oxidation

E.1 Activity Overview

An overview over the operando kinetics experiments discussed in Chapter 4 are presented in Figure E.1 and Figure E.2. Here, the temperature is indicated at the border between the top and bottom graph and by the background color becoming intenser with increasing temperature. The top panels show the evolution of CH_4, H_2O and CO_2, the main reactants and products. Partial catalytic CH_4 oxidation products CO, and CO_2 are shown in the bottom panes.
A direct comparison of the activity of the catalysts for full oxidation is shown in Figure E.3. The data is normalized to the CO_2 background pressure during reduction between the cycles.

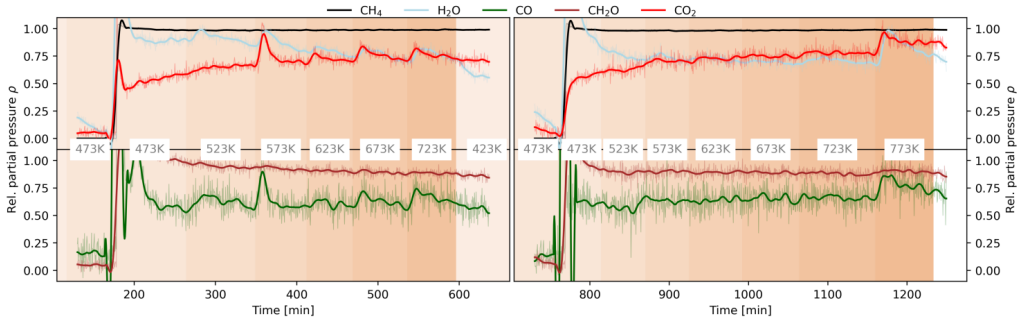

Figure E.1: Overview over the activity of Pd/Al_2O_3 from the first heating cycle (**A**) and the second cycle (**B**).

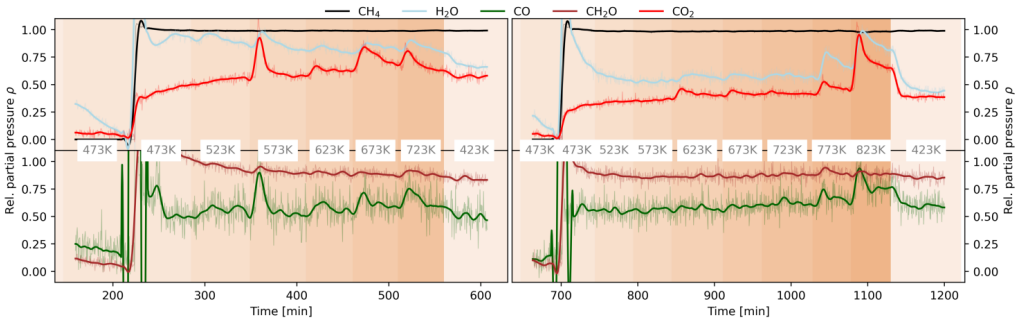

Figure E.2: Overview over the activity of Pd_3Pt_1/Al_2O_3 from the first heating cycle (**A**) and the second cycle (**B**).

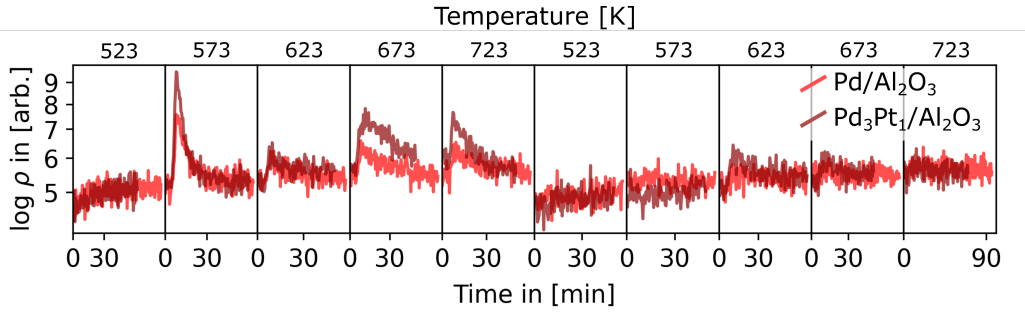

Figure E.3: Comparison of the CO_2 mass spectrometer signal recorded for Pd/Al_2O_3 (bright red) and Pd_3Pt_1/Al_2O_3 (dark red). The data is scaled and normalized to the base pressure of this mass.

E.2 Thermal Expansion

The thermal expansion of Pd was calculated based on the polynomial fit for thermal expansion reported in [302]. For the alloy nanoparticles, a weighted linear combination of the expansion factor for Pd and Pt [303] was used. The linear combination approximation introduces only a minuscule error as magnitude and curvature of the expansion factor is very similar in the probed temperature range (see Figure E.4). For the analysis described in the main text, the expansion factor of Pd was used for the Pd/Al_2O_3 catalyst and the linear combination of the expansion factors of Pd and Pt weighted by the nominal composition of the alloy NPs was used. This is illustrated in Figure E.4, which shows the expansion factors of Pd, Pd_3Pt_1 and Pt. The difference in expansion between Pd and the alloy is 0.015 % and 0.036 % at 523 K and 723 K, and the difference between the alloy and Pt is 0.046 % at 523 K and 0.107 % at 723 K. Thermal expansion is considered in Figure 4.4

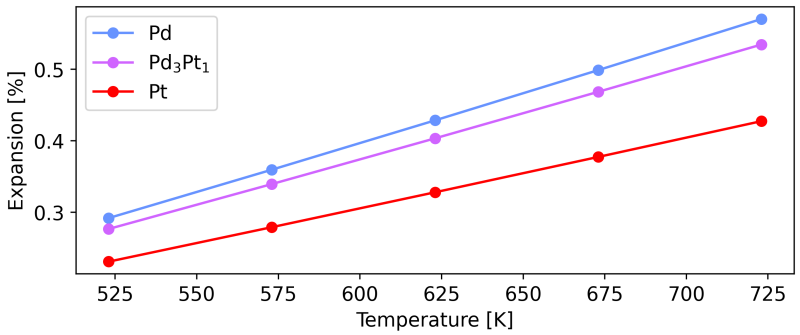

Figure E.4: Expansion in percent for the temperatures probed in the experiment.

and Figure 4.7, by correcting the lattice constant according to $\frac{1}{f_{exp}(T)}$, where $f_{exp}(T)$ is the expected expansion factor at a given temperature T.

E.3 Epitaxy of metal NPs and PdO

Rocking scans of the rotation around the sample normal were conducted to follow the epitaxial relationship of the metal nanoparticles and PdO domains. Figure E.5 shows the relevant section of the summed rocking scan recorded at 573 K with the ROI for the Pd in gray and the ROI for PdO in light blue. The rocking scans for all conditions of Pd/Al_2O_3 is shown in Figure E.6, the rocking scans of $PdPt/Al_2O_3$ are shown in Figure E.7. For both catalysts the metallic NPs are [1 1 1] oriented which is consistent with previous work (see Chapter 2). The in-plane $[1\,\bar{1}\,0]$ direction of the metal domains are aligned with the axes [1 0 0 0], and $[1\,1\,\bar{2}\,0]$ of the Al_2O_3 substrate. For Pd/Al_2O_3 another small peak is observed at $\theta \approx 162\,^\circ$ at 523 K during the first cycle. This peak corresponds to a minority ensemble with the same out of plane orientation as the main ensemble and the [1 1 0] axis of the metal domain is aligned with the $[1\,2\,\bar{1}\,0]$ axis of the Al_2O_3 substrate. The orientation of PdO is more complicated with a wide bimodal peak shape (see Figure E.6 and Figure E.7). For this purpose, two reciprocal space separated by 30 ° are compared to the expected peak positions for multiple out of plane orientations ([0 0 1], [1 0 0], [1 1 0], [1 0 1], [1 1 2]) (see Figure E.8). The weak preferential orientation observed in-plane is also observed out-of plane where PdO diffraction signal is characterized by broad altitudal distribution. Comparison of the diffraction patterns with the theoretical Bragg peak positions for the above listed out-of-plane orientations indicate coexisting preferential

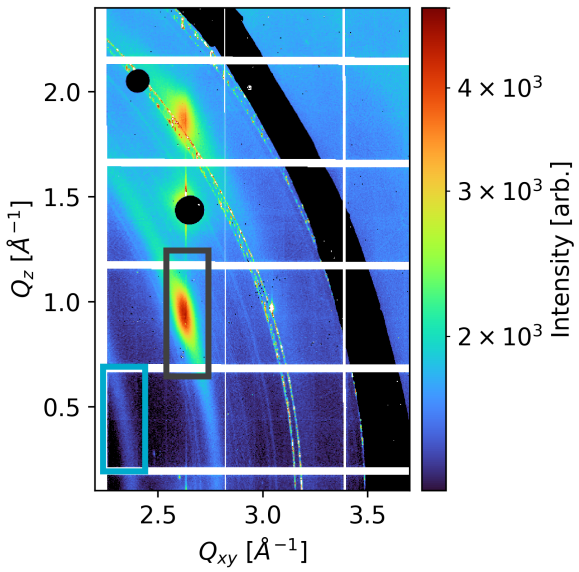

Figure E.5: Summed rocking scan of Pd/Al_2O_3 recorded at 573 K under operation with the ROIs (red rectangles).

[0 0 1] [1 1 2] orientation. Additional (1 0 1) and (1 1 0) diffraction is visible at $|Q|$ *approx* 2.38. Comparison with the diffraction data for the Al_2O_3 supported catalyst in Chapter 2 suggests that this signal belongs to tilted [1 0 1] and [0 0 1] oriented domains. For reference, the apparent angle to the in-plane direction is given for the textured (1 0 1) diffraction signal.

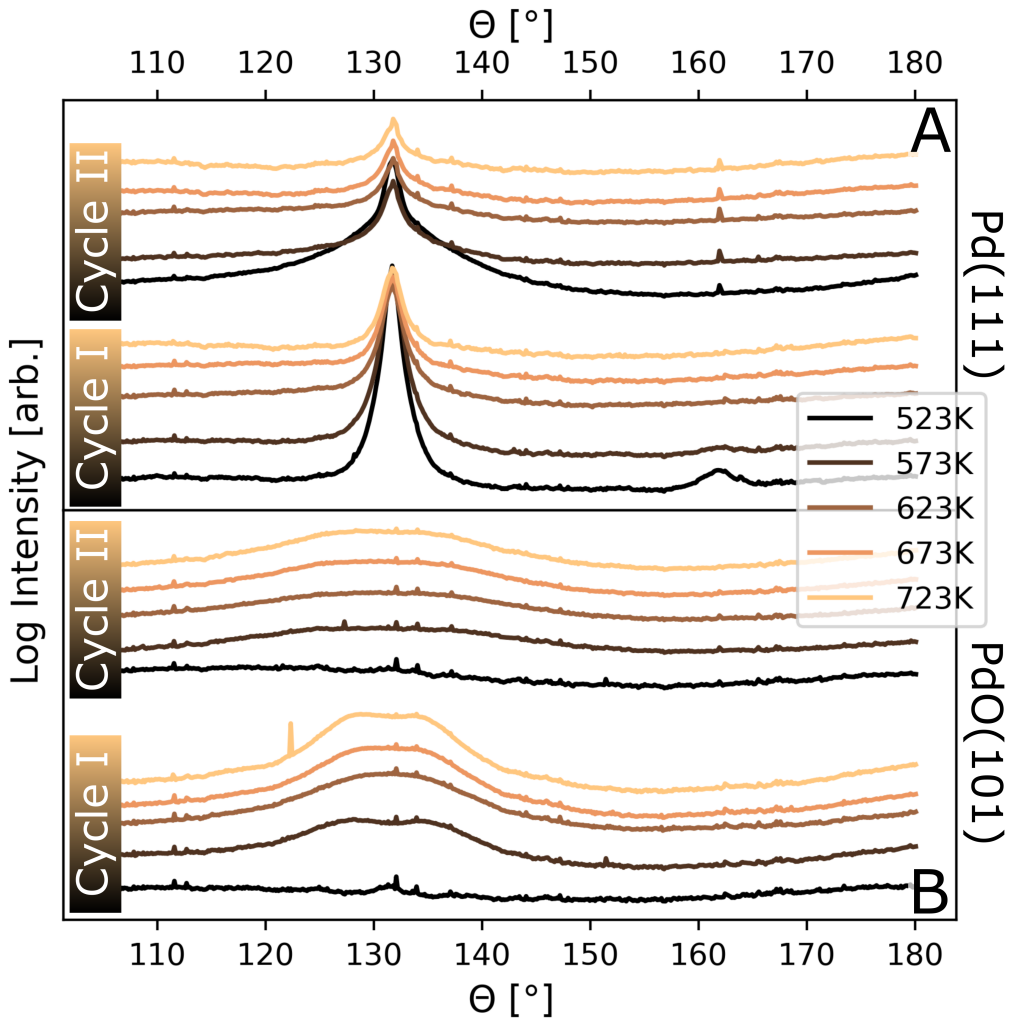

Figure E.6: Rocking scans of Pd/Al_2O_3 for all temperatures, recorded during operation (color codes of temperatures in legend). **A**: Rocking scans with the Pd(1 1 1) roi. **B** Rocking scans with the PdO(1 0 1) roi. Rectangles on the left side indicate the cycle, labels at the right edge indicate the Bragg reflex position.

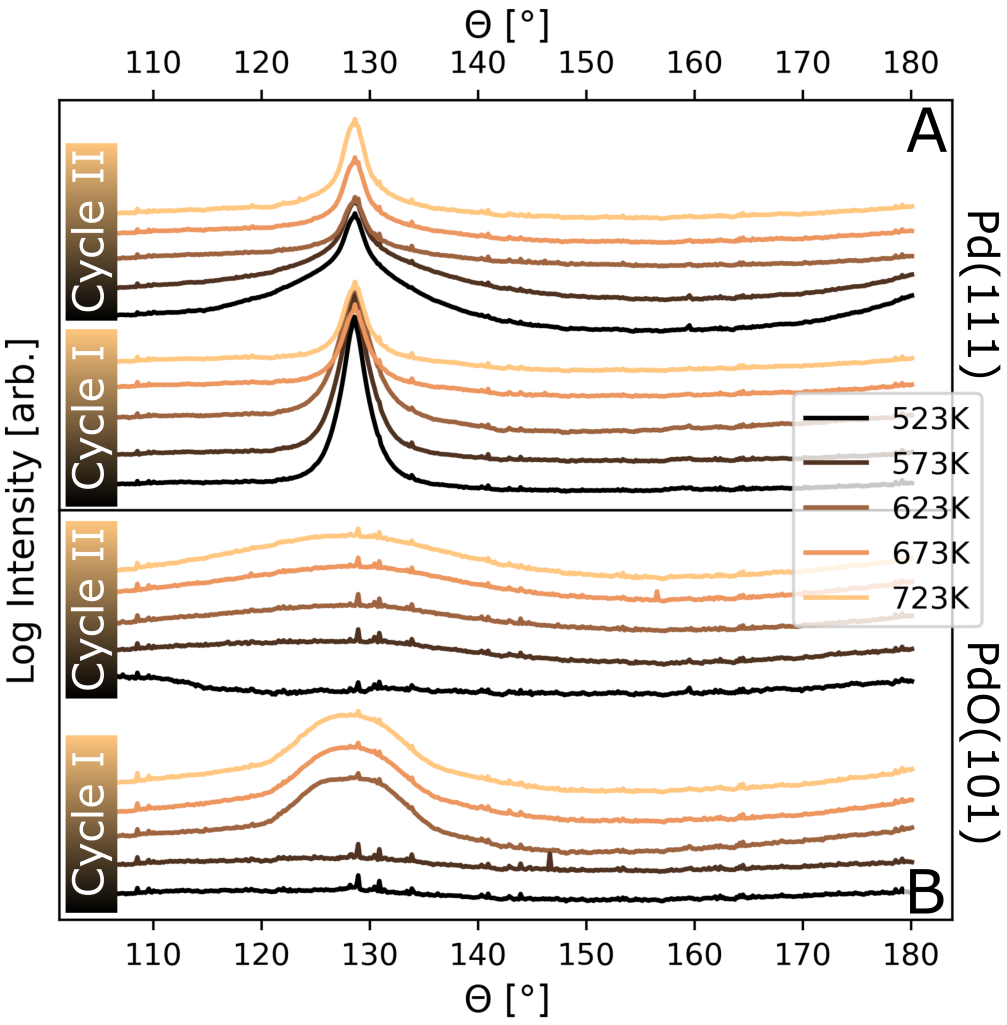

Figure E.7: Rocking scans of Pd_3Pt_1/Al_2O_3 for all temperatures, recorded during operation (color codes of temperatures in legend). **A**: Rocking scans with the Pd(1 1 1) roi. **B** Rocking scans with the PdO(1 0 1) roi. Rectangles on the left side indicate the cycle, labels at the right edge indicate the Bragg reflex position.

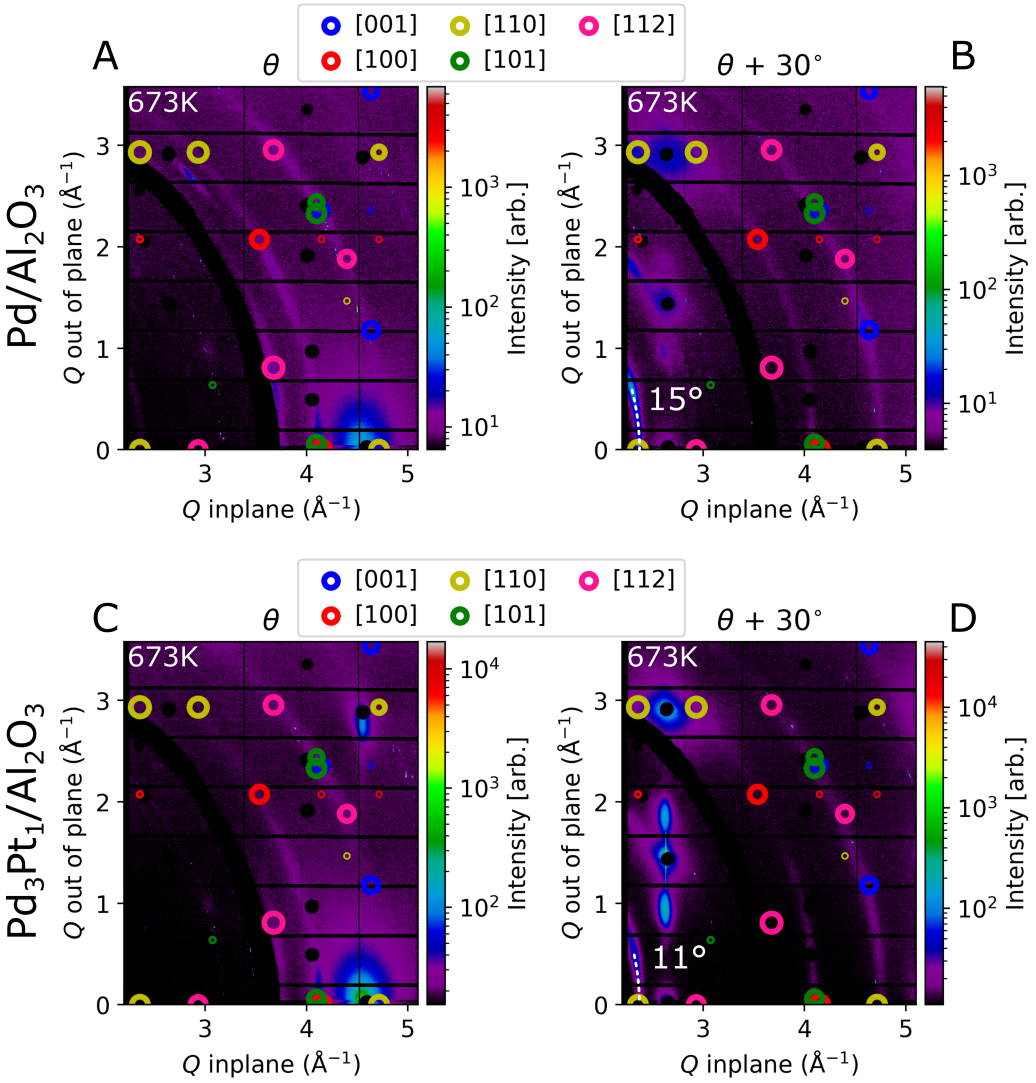

Figure E.8: Planes of reciprocal space extracted from rocking scans recorded at 573 K during the first cycle with 30 ° spacing for Pd/Al_2O_3 (**A**, **B**) and Pd_3Pt_1/Al_2O_3 (**A**, **B**).

E.4 Bragg peak analysis

Bragg peak analysis was conducted at several positions, which yielded inform for different nanoparticle ensembles (see Figure E.9). The position and length of the line scans are identical for Pd/Al_2O_3 and Pd_3Pt_1/Al_2O_3. Diffraction signal from metal of either sample will from now on be referred to as the PdPt since the experiment was not sensitive to the alloy composition. In total, line scans were extracted at four positions, corresponding to the PdPt(1 1 1) Bragg peak position (green lines), the PdPt(1 1 1) powder ring signal (yellow line), the PdO(101) powder ring (purple line), and the PdPt(2 2 2) Bragg peak (pink lines). Two lines were extracted for epitaxial diffraction signal, yielding diameter and height from horizontal and vertical line scans, whereas only an average nanoparticle dimension is deduced from the radial lines extracted for the PdO(1 0 1) or Pd(1 1 1) powder ring signal. The exact position of the lines were determined individually for each image, because static line positioning did not capture physically relevant changes but only the shift of the Bragg peak on the detector. The position of the line scans was recursively checked by comparing fitted peak positions with the estimated peak positions used to attain the data for the fits. The line width of epitaxial PdPt(1 1 1) diffraction signal is one pixel, the line width of the diffraction signal of all other lines is 3 pixel. This corresponds to linewidth of roughly $0.007\,\text{Å}^{-1}$ and $0.002\,\text{Å}^{-1}$, respectively. All line scans were modelled by a Pseudo-Voigt profile and a linear background with the expression

$$\begin{aligned} f(x, A, \mu, \sigma, \alpha, s, c) \; = & \frac{(1\,-\,\alpha)A}{\sigma_g\sqrt{2\pi}} e^{-(x\,-\,\mu)^2\,/\,2\sigma_g^2} \\ & +\; \frac{\alpha A}{\pi}\left[\frac{\sigma}{(x\,-\,\mu)^2\,+\,\sigma^2}\right] \\ & +\; sx\,+\,c, \end{aligned} \tag{E.1}$$

where that $\sigma_g = \frac{\sigma}{\sqrt{2\ln 2}}$ and $2\sigma = FWHM$. The variable A denotes the amplitude, μ the peak position, α the fraction of Gaussian and Lorentzian contribution, so that for $\alpha = 0$ the Pseudo-Voigt profile becomes fully Gaussian and for $\alpha = 1$, the profile becomes fully Lorentzian. The variable s is the slope and c the constant offset of the background. For select line scans multiple Pseudo-Voigt profiles were combined to account for crystal truncation rod signal of the substrate overlapping with the diffraction signal from the nanoparticles.

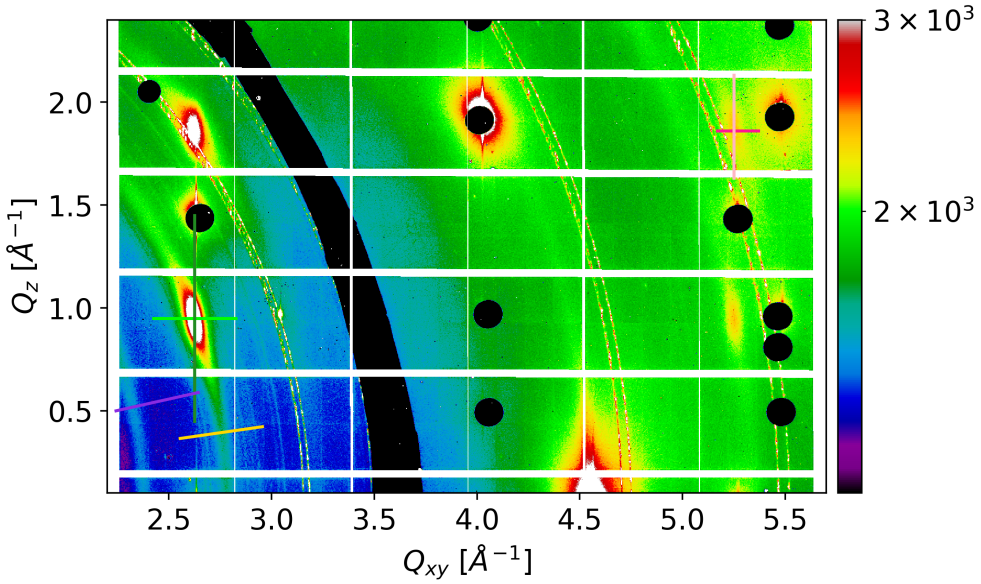

Figure E.9: Summed θ rocking scan over 75 ° of Pd_3Pt_1/Al_2O_3, recorded under operation at 573 K with lines indicating the position of the line scans that were extracted for data analysis.

E.4.1 HEGIXRD line scan analysis of Pd/Al_2O_3

Pd/Al_2O_3 - Pd(1 1 1) in plane

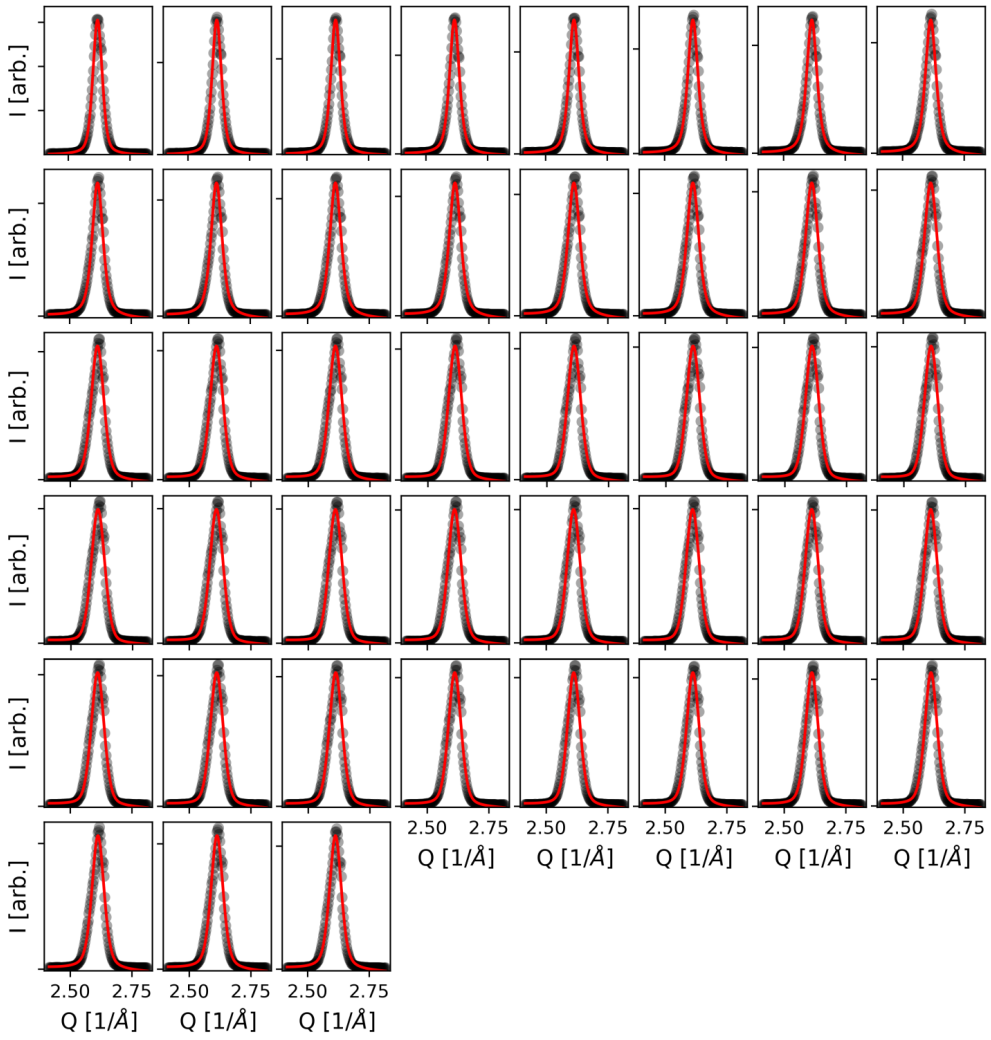

Figure E.10: In plane scans along Q_{xy}, recorded at 523 K.

Table E.1: Center and full width half maximum (FWHM) for the fits presented in Figure E.10. For fits with multiple components, only fit results of the relevant component is shown.

	Center		FWHM			Center		FWHM	
	Value	Error	Value	Error		Value	Error	Value	Error
#0	2.61853	8e-05	0.04489	0.00024	#1	2.61705	9e-05	0.04535	0.00028
#2	2.6163	9e-05	0.04614	0.00031	#3	2.61562	0.00011	0.04722	0.00037
#4	2.61503	0.00013	0.04843	0.00046	#5	2.61467	0.00015	0.04937	0.00052
#6	2.61432	0.00018	0.0502	0.0006	#7	2.61393	0.0002	0.05176	0.00069
#8	2.61352	0.00023	0.05267	0.00078	#9	2.6132	0.00025	0.0539	0.00085
#10	2.61291	0.00026	0.05485	0.00088	#11	2.61257	0.00028	0.05605	0.00094
#12	2.61218	0.0003	0.05733	0.001	#13	2.61184	0.00031	0.05814	0.00103
#14	2.61149	0.00033	0.05949	0.00107	#15	2.6112	0.00034	0.06038	0.0011
#16	2.61087	0.00035	0.06124	0.0011	#17	2.61063	0.00035	0.06187	0.00111
#18	2.61056	0.00036	0.06235	0.00113	#19	2.61032	0.00036	0.06292	0.00114
#20	2.61027	0.00038	0.06308	0.00117	#21	2.61017	0.00038	0.06383	0.00116
#22	2.61014	0.00037	0.0636	0.00114	#23	2.61017	0.00038	0.06377	0.00118
#24	2.61006	0.00037	0.06407	0.00114	#25	2.61036	0.00037	0.06363	0.00114
#26	2.6105	0.00036	0.06346	0.00112	#27	2.61082	0.00036	0.06263	0.00112
#28	2.6109	0.00037	0.06255	0.00114	#29	2.6109	0.00036	0.06292	0.00112
#30	2.61116	0.00036	0.06239	0.00112	#31	2.61136	0.00035	0.06196	0.0011
#32	2.61141	0.00035	0.06175	0.0011	#33	2.61155	0.00035	0.06153	0.00108
#34	2.61161	0.00034	0.06124	0.00106	#35	2.61154	0.00033	0.06102	0.00105
#36	2.61168	0.00034	0.06081	0.00107	#37	2.61194	0.00032	0.06051	0.00102
#38	2.61199	0.00032	0.06	0.00103	#39	2.61233	0.00032	0.05956	0.00102
#40	2.61262	0.00031	0.05835	0.00102	#41	2.61268	0.00031	0.05833	0.00102
#42	2.61306	0.00029	0.05728	0.00095					

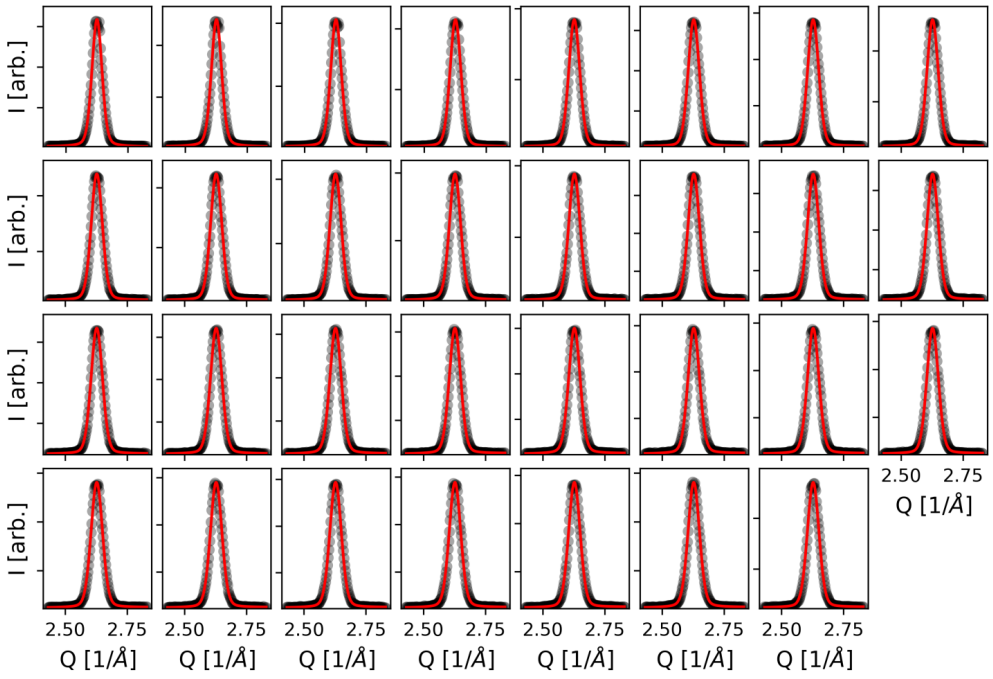

Figure E.11: In plane scans along Q_{xy}, recorded at 573 K.

Table E.2: Center and full width half maximum (FWHM) for the fits presented in Figure E.11. For fits with multiple components, only fit results of the relevant component is shown.

	Center		FWHM			Center		FWHM	
	Value	Error	Value	Error		Value	Error	Value	Error
#0	2.62515	0.0001	0.04794	0.0003	#1	2.62563	9e-05	0.04876	0.00028
#2	2.62587	9e-05	0.05014	0.00026	#3	2.62625	8e-05	0.05137	0.00023
#4	2.62658	7e-05	0.0522	0.00021	#5	2.62677	7e-05	0.05258	0.00022
#6	2.62685	8e-05	0.05294	0.00024	#7	2.62703	8e-05	0.05299	0.00023
#8	2.6271	8e-05	0.05322	0.00024	#9	2.62709	8e-05	0.05359	0.00025
#10	2.62703	9e-05	0.05367	0.00026	#11	2.62711	8e-05	0.05357	0.00025
#12	2.62706	9e-05	0.05395	0.00026	#13	2.62701	9e-05	0.05403	0.00027
#14	2.62695	9e-05	0.05416	0.00026	#15	2.62701	8e-05	0.05429	0.00025
#16	2.62693	9e-05	0.0544	0.00026	#17	2.627	9e-05	0.05456	0.00027
#18	2.62692	0.0001	0.0543	0.00028	#19	2.62685	9e-05	0.05444	0.00028
#20	2.62697	8e-05	0.05446	0.00025	#21	2.62697	9e-05	0.05483	0.00027
#22	2.62692	9e-05	0.05482	0.00026	#23	2.62694	9e-05	0.05495	0.00028
#24	2.62708	9e-05	0.05476	0.00025	#25	2.62692	0.0001	0.05496	0.00029
#26	2.62696	9e-05	0.05487	0.00027	#27	2.62694	0.0001	0.05493	0.00029
#28	2.6269	9e-05	0.05487	0.00027	#29	2.62686	9e-05	0.05471	0.00027
#30	2.62684	0.0001	0.05532	0.00029					

Table E.3: Center and full width half maximum (FWHM) for the fits presented in Figure E.12. For fits with multiple components, only fit results of the relevant component is shown.

	Center		FWHM			Center		FWHM	
	Value	Error	Value	Error		Value	Error	Value	Error
#0	2.62193	7e-05	0.05639	0.00021	#1	2.622	7e-05	0.05691	0.00019
#2	2.62229	7e-05	0.0571	0.0002	#3	2.62251	7e-05	0.05744	0.00021
#4	2.6227	7e-05	0.05739	0.00021	#5	2.62283	8e-05	0.0573	0.00024
#6	2.62289	9e-05	0.05789	0.00025	#7	2.62303	8e-05	0.0579	0.00022
#8	2.62328	8e-05	0.05817	0.00023	#9	2.6234	7e-05	0.05827	0.00021
#10	2.62349	8e-05	0.05863	0.00023	#11	2.62348	7e-05	0.05843	0.0002
#12	2.62361	8e-05	0.05834	0.00022	#13	2.62373	7e-05	0.0582	0.00021
#14	2.62396	7e-05	0.05859	0.0002	#15	2.62404	8e-05	0.05881	0.00023
#16	2.62411	7e-05	0.05869	0.00021	#17	2.62435	7e-05	0.05873	0.00022
#18	2.62431	9e-05	0.05876	0.00026	#19	2.62464	8e-05	0.0586	0.00022
#20	2.6244	6e-05	0.05815	0.00017	#21	2.62443	7e-05	0.05859	0.00021
#22	2.62478	7e-05	0.05843	0.00021	#23	2.62476	8e-05	0.05917	0.00022
#24	2.62481	7e-05	0.05856	0.00021	#25	2.62483	7e-05	0.05869	0.00019
#26	2.62505	9e-05	0.05901	0.00025	#27	2.62485	7e-05	0.05839	0.00021
#28	2.62526	7e-05	0.05838	0.00022	#29	2.62512	7e-05	0.0581	0.0002
#30	2.62525	8e-05	0.05857	0.00023	#31	2.6253	8e-05	0.05841	0.00023
#32	2.62554	7e-05	0.0584	0.0002	#33	2.62575	6e-05	0.05829	0.00018
#34	2.62564	9e-05	0.0579	0.00025	#35	2.62589	6e-05	0.05821	0.00019
#36	2.6259	8e-05	0.05777	0.00023	#37	2.62594	6e-05	0.05807	0.00019
#38	2.62603	8e-05	0.05791	0.00023	#39	2.62599	7e-05	0.05825	0.00022
#40	2.62622	7e-05	0.0581	0.00019	#41	2.62613	8e-05	0.058	0.00022
#42	2.62622	7e-05	0.05758	0.0002	#43	2.62613	7e-05	0.05741	0.00022
#44	2.62621	7e-05	0.05755	0.0002	#45	2.62631	7e-05	0.05786	0.00021
#46	2.62641	8e-05	0.05774	0.00024					

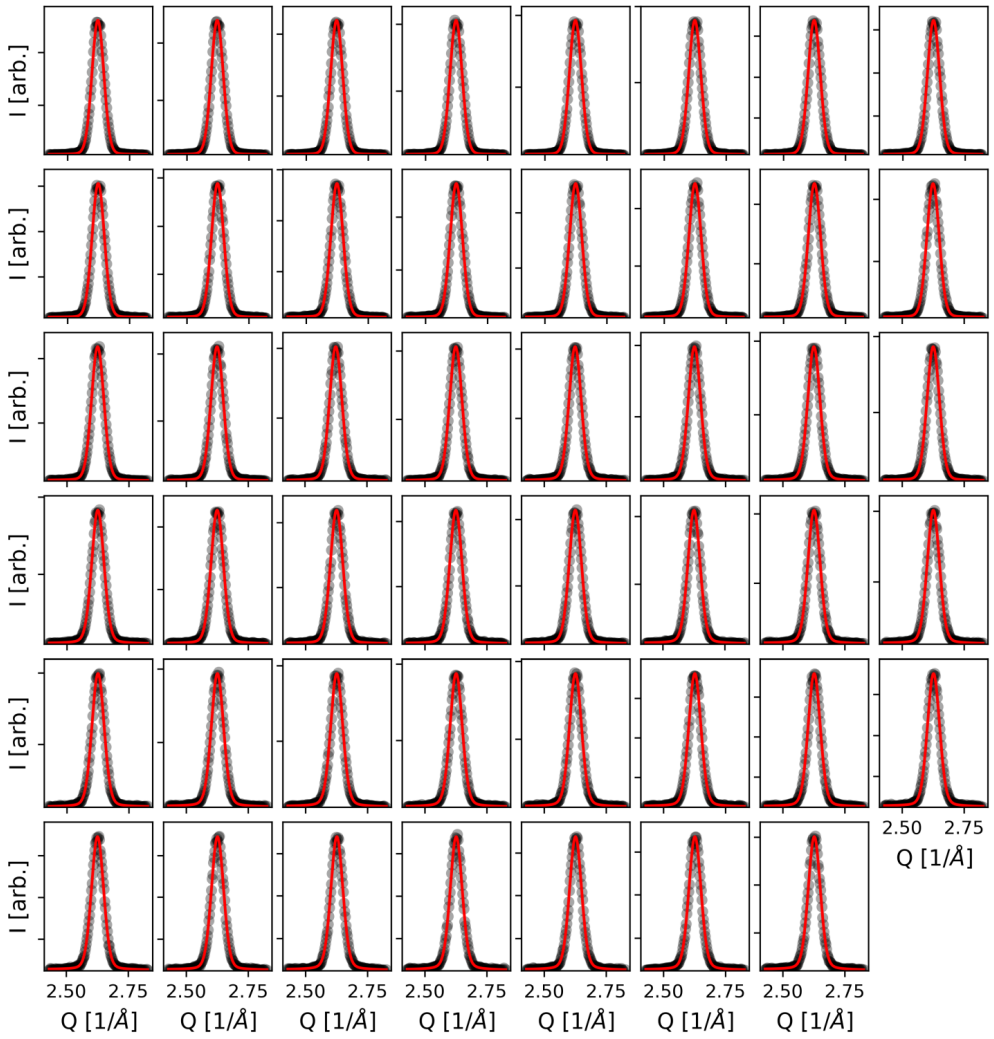

Figure E.12: In plane scans along Q_{xy}, recorded at 623 K.

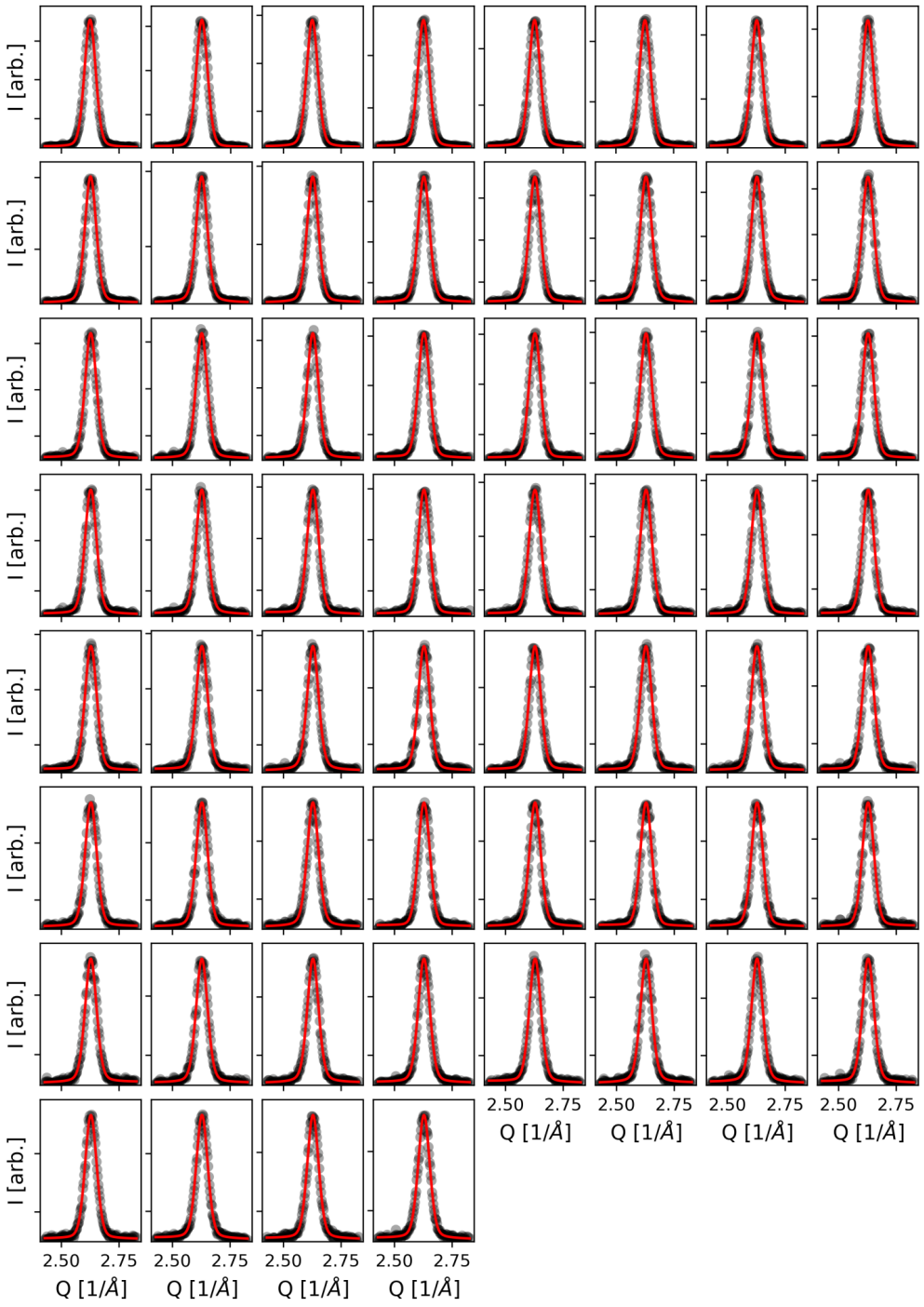

Figure E.13: In plane scans along Q_{xy}, recorded at 673 K.

Table E.4: Center and full width half maximum (FWHM) for the fits presented in Figure E.13. For fits with multiple components, only fit results of the relevant component is shown.

	Center		FWHM			Center		FWHM	
	Value	Error	Value	Error		Value	Error	Value	Error
#0	2.62456	8e-05	0.05728	0.00023	#1	2.62488	0.0001	0.05787	0.0003
#2	2.62508	9e-05	0.05706	0.00026	#3	2.62584	8e-05	0.0577	0.00025
#4	2.62597	7e-05	0.05771	0.00022	#5	2.62576	9e-05	0.05756	0.00026
#6	2.62645	9e-05	0.05756	0.00027	#7	2.62664	9e-05	0.05755	0.00026
#8	2.62667	0.0001	0.05805	0.00031	#9	2.62695	8e-05	0.05768	0.00024
#10	2.62688	0.00012	0.05799	0.00034	#11	2.62719	0.0001	0.05846	0.0003
#12	2.6271	0.00011	0.0581	0.00032	#13	2.62761	0.0001	0.059	0.0003
#14	2.62696	0.0001	0.05803	0.00029	#15	2.62717	0.0001	0.05934	0.0003
#16	2.62727	0.00011	0.05814	0.00034	#17	2.62717	0.00012	0.05845	0.00037
#18	2.62728	0.00013	0.05796	0.00038	#19	2.62777	0.00012	0.05867	0.00036
#20	2.62754	0.00012	0.05902	0.00034	#21	2.62779	0.00011	0.05849	0.00032
#22	2.62774	0.00013	0.05947	0.00038	#23	2.62769	0.00013	0.0591	0.00037
#24	2.6275	0.00015	0.05895	0.00046	#25	2.62752	0.00013	0.05886	0.0004
#26	2.62798	0.00012	0.05951	0.00036	#27	2.62801	0.00012	0.05848	0.00036
#28	2.62764	0.00014	0.06039	0.0004	#29	2.62775	0.00012	0.05941	0.00035
#30	2.6277	0.00013	0.05958	0.00038	#31	2.6281	0.00014	0.05909	0.0004
#32	2.62797	0.00013	0.05984	0.00039	#33	2.62798	0.00014	0.05893	0.0004
#34	2.62769	0.00014	0.05862	0.00042	#35	2.62811	0.00015	0.05906	0.00043
#36	2.62774	0.00014	0.05905	0.00041	#37	2.62741	0.00014	0.05968	0.0004
#38	2.62756	0.00015	0.05944	0.00043	#39	2.62811	0.00016	0.05984	0.00046
#40	2.62803	0.00017	0.05916	0.0005	#41	2.62803	0.00014	0.05894	0.00041
#42	2.62761	0.00011	0.05899	0.00032	#43	2.62804	0.00013	0.05981	0.00036
#44	2.62804	0.00016	0.05799	0.00047	#45	2.62801	0.00014	0.05858	0.00041

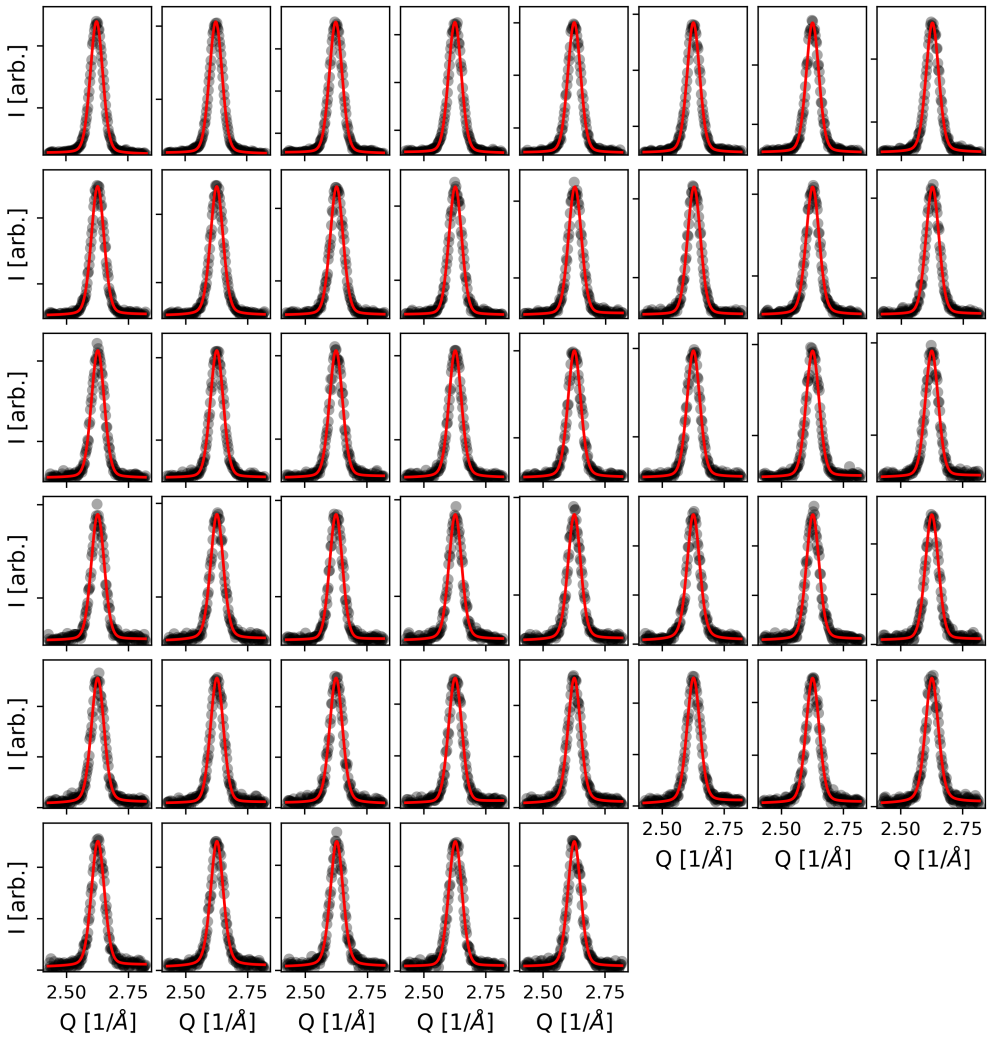

Figure E.14: In plane scans along Q_{xy}, recorded at 723 K.

Table E.5: Center and full width half maximum (FWHM) for the fits presented in Figure E.14. For fits with multiple components, only fit results of the relevant component is shown.

	Center		FWHM			Center		FWHM	
	Value	Error	Value	Error		Value	Error	Value	Error
#0	2.62411	8e-05	0.05979	0.00023	#1	2.62446	9e-05	0.06044	0.00027
#2	2.62479	9e-05	0.06081	0.00028	#3	2.62489	0.00014	0.06111	0.0004
#4	2.62543	0.00013	0.06111	0.00037	#5	2.62551	0.00013	0.05995	0.00038
#6	2.62549	0.00016	0.06074	0.00046	#7	2.62568	0.00014	0.06089	0.0004
#8	2.6256	0.00015	0.0607	0.00044	#9	2.62543	0.00014	0.06058	0.00042
#10	2.62565	0.00017	0.0619	0.00049	#11	2.62639	0.00016	0.06104	0.00047
#12	2.62573	0.00017	0.0619	0.00048	#13	2.62521	0.00017	0.06186	0.00049
#14	2.626	0.00018	0.0627	0.00052	#15	2.6258	0.00016	0.06226	0.00045
#16	2.62633	0.00015	0.06133	0.00045	#17	2.62561	0.00016	0.06154	0.00045
#18	2.62577	0.0002	0.06203	0.00058	#19	2.62597	0.00016	0.0602	0.00048
#20	2.62593	0.0002	0.06132	0.00058	#21	2.62565	0.00017	0.06152	0.0005
#22	2.6258	0.00019	0.06207	0.00056	#23	2.62578	0.0002	0.06179	0.00058
#24	2.62595	0.00022	0.06201	0.00063	#25	2.62619	0.0002	0.06115	0.00059
#26	2.6258	0.00021	0.06083	0.00059	#27	2.62634	0.00022	0.06118	0.00066
#28	2.62583	0.00021	0.06089	0.00063	#29	2.6255	0.00021	0.06106	0.00063
#30	2.62629	0.00023	0.06108	0.00066	#31	2.62615	0.00021	0.06238	0.00061
#32	2.62573	0.00021	0.06109	0.00063	#33	2.62607	0.0002	0.0619	0.00057
#34	2.62606	0.00023	0.06174	0.00068	#35	2.62579	0.00023	0.06331	0.00064
#36	2.62573	0.0002	0.06052	0.0006	#37	2.62602	0.00019	0.06193	0.00055
#38	2.62574	0.00022	0.06276	0.00064	#39	2.6262	0.00024	0.06243	0.00072
#40	2.62652	0.00023	0.06179	0.00068	#41	2.62612	0.00021	0.06068	0.00064
#42	2.62601	0.00022	0.06103	0.00067	#43	2.62643	0.0002	0.06284	0.00057
#44	2.62574	0.00024	0.06095	0.0007					

Table E.6: Center and full width half maximum (FWHM) for the fits presented in Figure E.15. For fits with multiple components, only fit results of the relevant component is shown.

	Center		FWHM			Center		FWHM	
	Value	Error	Value	Error		Value	Error	Value	Error
#0	2.62578	3e-05	0.0484	8e-05	#1	2.62567	3e-05	0.04865	8e-05
#2	2.62559	3e-05	0.04872	8e-05	#3	2.62556	3e-05	0.04877	8e-05
#4	2.62546	3e-05	0.04896	8e-05	#5	2.62542	3e-05	0.04882	8e-05
#6	2.62537	3e-05	0.04909	8e-05	#7	2.62534	3e-05	0.04908	8e-05
#8	2.62536	3e-05	0.04903	8e-05	#9	2.62536	3e-05	0.04906	8e-05
#10	2.62532	3e-05	0.04914	9e-05	#11	2.62528	3e-05	0.04913	8e-05
#12	2.62533	3e-05	0.04913	8e-05	#13	2.62528	3e-05	0.04915	9e-05
#14	2.62534	3e-05	0.04913	8e-05	#15	2.62527	3e-05	0.04909	9e-05
#16	2.62536	3e-05	0.04922	8e-05	#17	2.62534	3e-05	0.0492	8e-05
#18	2.6253	3e-05	0.04928	9e-05	#19	2.62534	3e-05	0.04931	8e-05
#20	2.62535	3e-05	0.04919	8e-05	#21	2.62531	3e-05	0.0493	9e-05
#22	2.62539	3e-05	0.04922	9e-05	#23	2.62538	3e-05	0.04918	8e-05
#24	2.62541	3e-05	0.04931	9e-05	#25	2.62537	3e-05	0.04927	8e-05
#26	2.62535	3e-05	0.04916	8e-05	#27	2.62537	3e-05	0.04916	9e-05
#28	2.62538	3e-05	0.04931	8e-05	#29	2.62539	3e-05	0.04921	8e-05
#30	2.62537	3e-05	0.04928	9e-05	#31	2.62541	3e-05	0.04924	8e-05
#32	2.62544	3e-05	0.04921	9e-05	#33	2.62544	3e-05	0.04923	8e-05
#34	2.62539	3e-05	0.04923	9e-05	#35	2.62542	3e-05	0.04924	9e-05
#36	2.62547	3e-05	0.0492	9e-05	#37	2.62547	3e-05	0.04927	9e-05
#38	2.6255	3e-05	0.04927	8e-05	#39	2.62544	3e-05	0.04913	8e-05
#40	2.62552	3e-05	0.04937	0.0001					

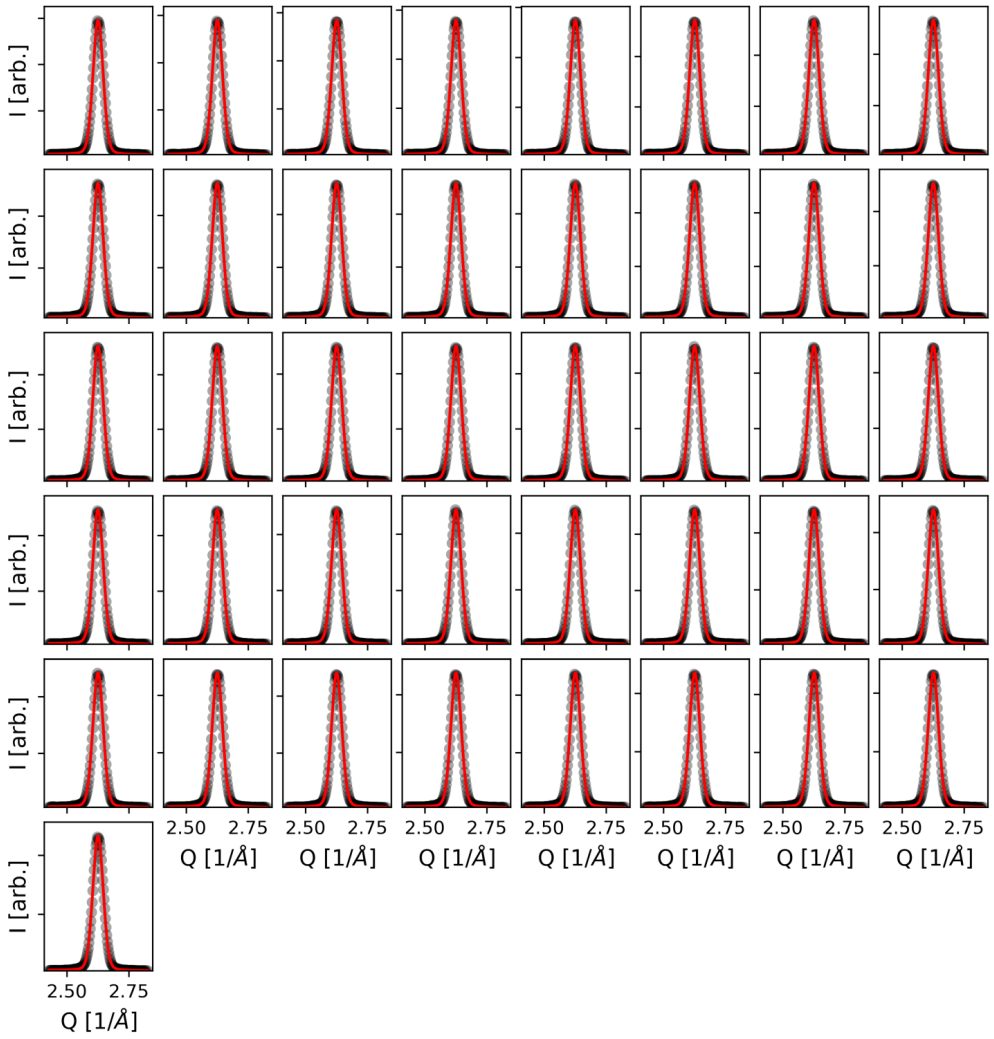

Figure E.15: In plane scans along Q_{xy}, recorded at 523 K.

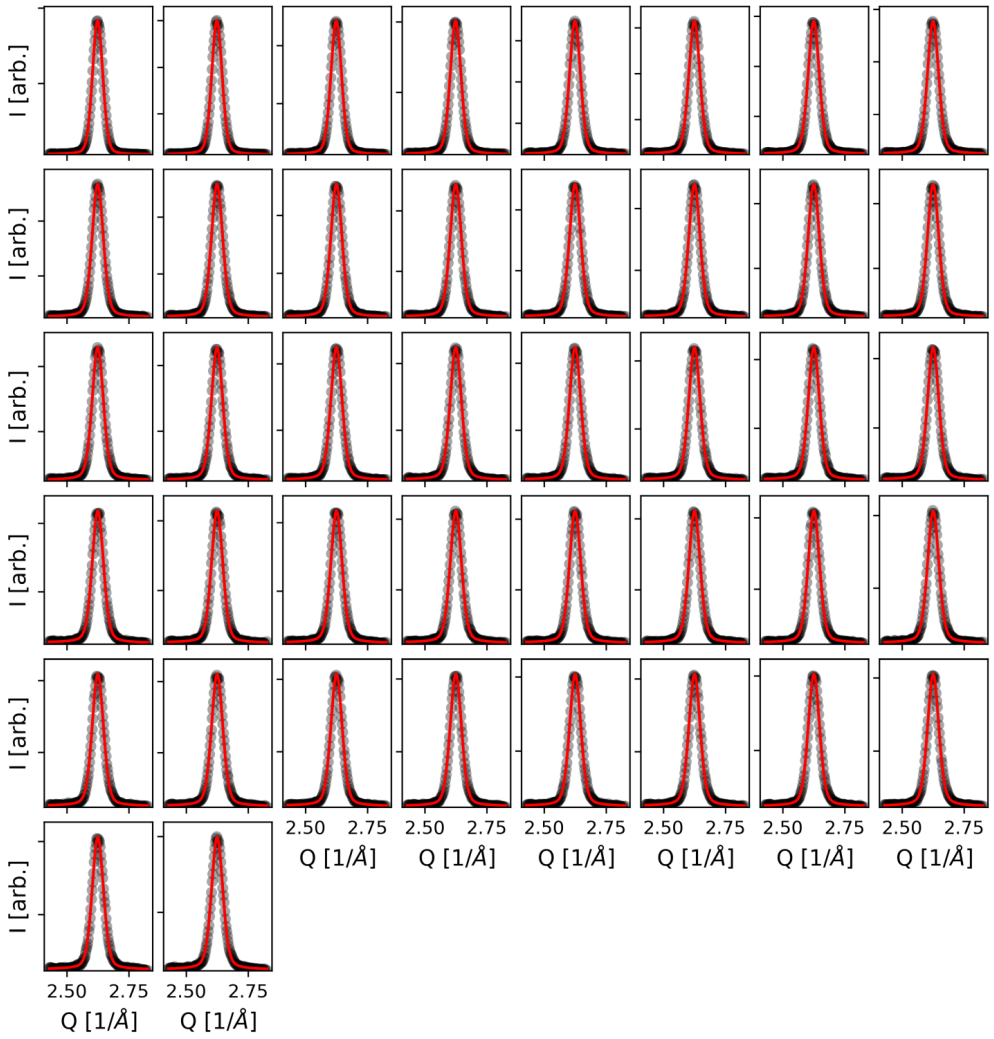

Figure E.16: In plane scans along Q_{xy}, recorded at 573 K.

	Center		FWHM			Center		FWHM	
	Value	Error	Value	Error		Value	Error	Value	Error
#0	2.62389	4e-05	0.04889	0.00011	#1	2.62366	4e-05	0.04932	0.00011
#2	2.62356	4e-05	0.05025	0.00013	#3	2.62369	5e-05	0.05104	0.00014
#4	2.62387	5e-05	0.05214	0.00014	#5	2.62408	6e-05	0.05287	0.00018
#6	2.62414	6e-05	0.05324	0.00017	#7	2.62415	6e-05	0.05337	0.00018
#8	2.62428	6e-05	0.05338	0.00017	#9	2.62431	5e-05	0.05362	0.00016
#10	2.62435	6e-05	0.05335	0.00018	#11	2.62432	6e-05	0.05375	0.00018
#12	2.62437	6e-05	0.05395	0.00019	#13	2.62434	6e-05	0.05383	0.00019
#14	2.62433	7e-05	0.05414	0.00021	#15	2.62441	6e-05	0.05416	0.00019
#16	2.62443	6e-05	0.05381	0.00018	#17	2.62431	8e-05	0.05406	0.00023
#18	2.62449	6e-05	0.05404	0.00019	#19	2.62449	6e-05	0.054	0.00018
#20	2.6244	6e-05	0.05409	0.00019	#21	2.62443	7e-05	0.0541	0.00021
#22	2.62465	6e-05	0.05391	0.0002	#23	2.62456	6e-05	0.05412	0.0002
#24	2.62475	6e-05	0.05407	0.00018	#25	2.62458	7e-05	0.05417	0.00022
#26	2.6246	7e-05	0.05411	0.00022	#27	2.62477	7e-05	0.05422	0.0002
#28	2.62456	7e-05	0.05424	0.00022	#29	2.62465	7e-05	0.05401	0.00021
#30	2.62465	7e-05	0.05413	0.00021	#31	2.62476	6e-05	0.0541	0.00019
#32	2.62474	7e-05	0.0541	0.00022	#33	2.62475	6e-05	0.05407	0.00019
#34	2.62475	8e-05	0.05408	0.00023	#35	2.62458	7e-05	0.05443	0.00021
#36	2.62476	7e-05	0.05407	0.00022	#37	2.62467	7e-05	0.05414	0.0002
#38	2.62489	7e-05	0.05433	0.0002	#39	2.62465	7e-05	0.05382	0.00021

Table E.7: Center and full width half maximum (FWHM) for the fits presented in Figure E.16. For fits with multiple components, only fit results of the relevant component is shown.

Table E.8: Center and full width half maximum (FWHM) for the fits presented in Figure E.17. For fits with multiple components, only fit results of the relevant component is shown.

	Center		FWHM			Center		FWHM	
	Value	Error	Value	Error		Value	Error	Value	Error
#0	2.62435	6e-05	0.05514	0.00019	#1	2.62424	7e-05	0.05525	0.0002
#2	2.62414	7e-05	0.05479	0.00021	#3	2.62391	6e-05	0.0549	0.0002
#4	2.62378	8e-05	0.05464	0.00024	#5	2.62366	7e-05	0.05511	0.00022
#6	2.62354	7e-05	0.05454	0.00021	#7	2.6237	6e-05	0.05464	0.0002
#8	2.62352	7e-05	0.05455	0.00021	#9	2.62376	7e-05	0.05467	0.00022
#10	2.62361	7e-05	0.05476	0.00021	#11	2.62366	6e-05	0.05464	0.00019
#12	2.62352	7e-05	0.05459	0.00021	#13	2.62372	7e-05	0.05498	0.00022
#14	2.6237	7e-05	0.05477	0.00021	#15	2.62363	7e-05	0.05478	0.00023
#16	2.62358	7e-05	0.05471	0.00021	#17	2.624	7e-05	0.05452	0.00022
#18	2.62364	6e-05	0.05473	0.00019	#19	2.62351	7e-05	0.05459	0.00023
#20	2.62363	7e-05	0.05516	0.00021	#21	2.62366	8e-05	0.05542	0.00024
#22	2.62365	8e-05	0.05516	0.00024	#23	2.62381	8e-05	0.05477	0.00023
#24	2.62368	8e-05	0.05471	0.00026	#25	2.62361	7e-05	0.05603	0.00022
#26	2.62379	9e-05	0.05579	0.00027	#27	2.6235	8e-05	0.05528	0.00025
#28	2.62362	8e-05	0.05502	0.00023	#29	2.62395	8e-05	0.05587	0.00023
#30	2.62382	8e-05	0.05531	0.00025	#31	2.62375	8e-05	0.05557	0.00024
#32	2.62359	8e-05	0.05524	0.00026	#33	2.62372	8e-05	0.05539	0.00023
#34	2.62395	8e-05	0.05477	0.00024	#35	2.62372	8e-05	0.05571	0.00024
#36	2.6238	8e-05	0.05524	0.00025	#37	2.62363	8e-05	0.05587	0.00025
#38	2.62375	9e-05	0.05522	0.00028	#39	2.62383	8e-05	0.05523	0.00024
#40	2.62373	9e-05	0.05607	0.00028	#41	2.62355	8e-05	0.05501	0.00024
#42	2.62386	8e-05	0.05525	0.00024	#43	2.62375	8e-05	0.05565	0.00023
#44	2.62377	9e-05	0.05567	0.00027	#45	2.62387	0.0001	0.05564	0.0003

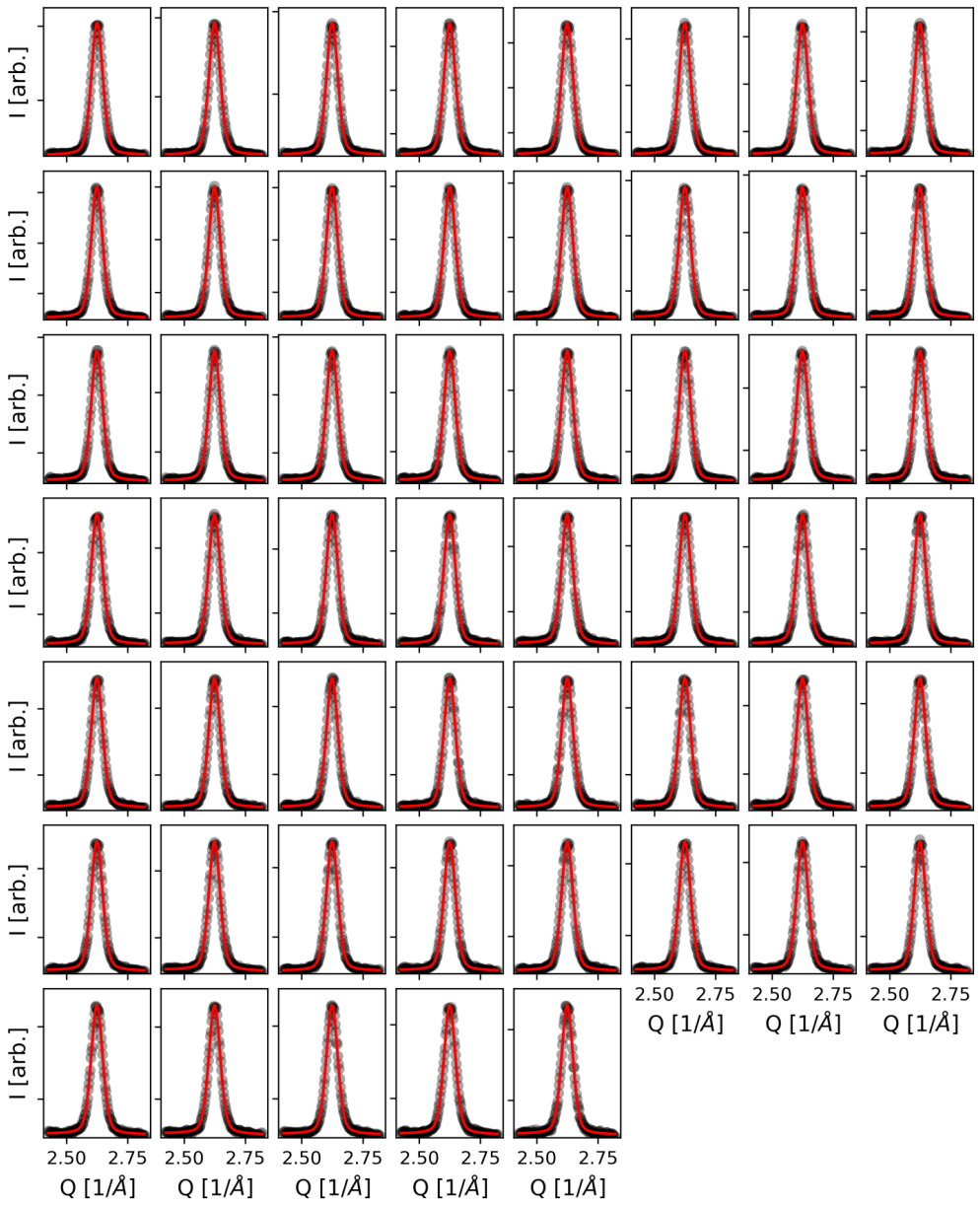

Figure E.17: In plane scans along Q_{xy}, recorded at 623 K.

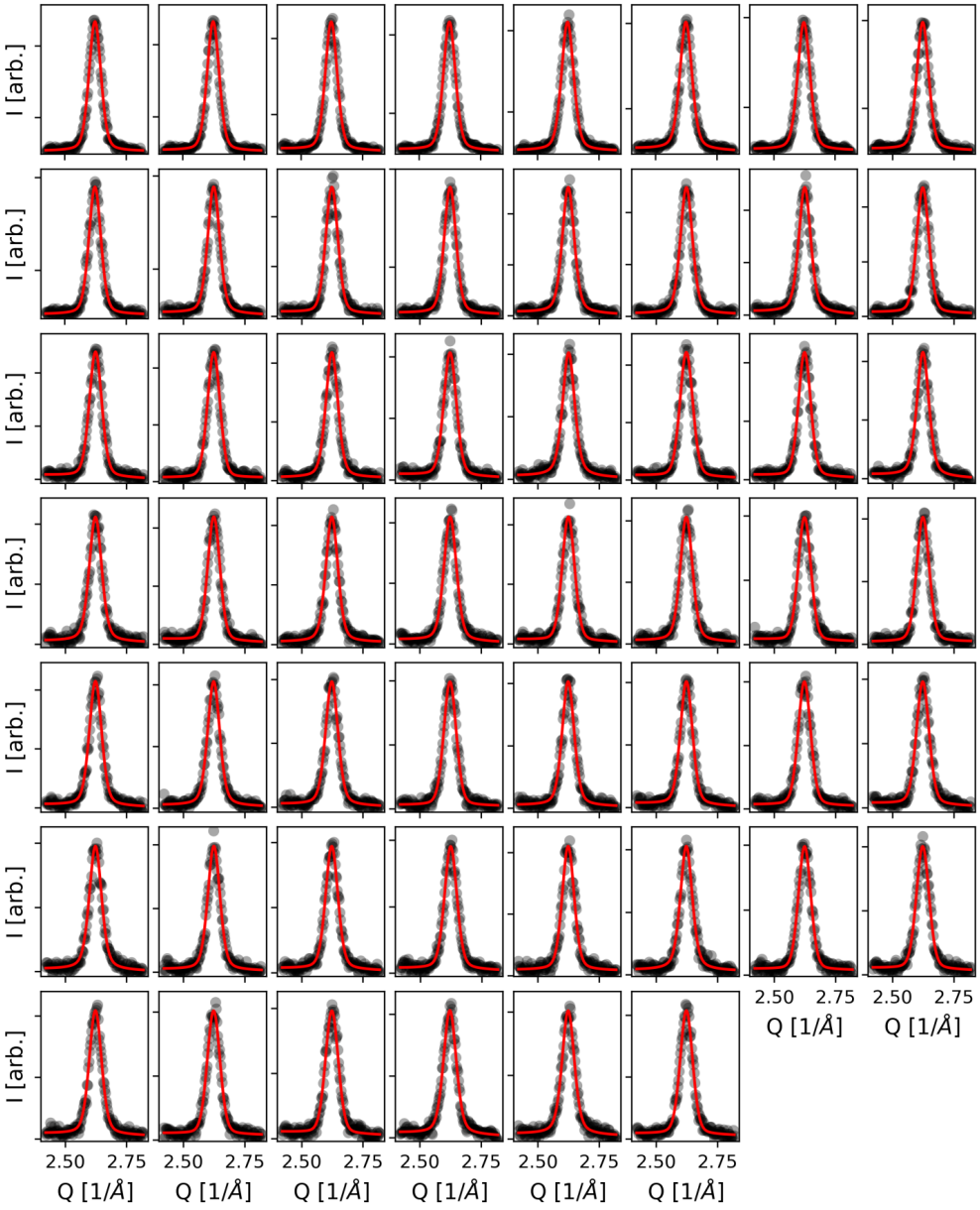

Figure E.18: In plane scans along Q_{xy}, recorded at 673 K.

Table E.9: Center and full width half maximum (FWHM) for the fits presented in Figure E.18. For fits with multiple components, only fit results of the relevant component is shown.

	Center		FWHM			Center		FWHM	
	Value	Error	Value	Error		Value	Error	Value	Error
#0	2.62325	0.00015	0.05768	0.00045	#1	2.62319	0.00012	0.05785	0.00037
#2	2.6228	0.00014	0.05705	0.00044	#3	2.62286	0.00014	0.05778	0.00041
#4	2.62276	0.00017	0.05831	0.00051	#5	2.62335	0.00017	0.05817	0.00054
#6	2.62244	0.00016	0.05927	0.00049	#7	2.62283	0.00017	0.05712	0.0005
#8	2.62297	0.0002	0.05792	0.00061	#9	2.62301	0.00018	0.05785	0.00056
#10	2.62275	0.00025	0.05877	0.00075	#11	2.62333	0.0002	0.05711	0.00059
#12	2.62323	0.0002	0.05794	0.00063	#13	2.62311	0.00019	0.05835	0.00059
#14	2.62371	0.00022	0.05741	0.0007	#15	2.62329	0.00023	0.05881	0.00069
#16	2.62321	0.00022	0.05989	0.00064	#17	2.62326	0.00022	0.05968	0.00064
#18	2.62306	0.00021	0.05859	0.00064	#19	2.62313	0.00022	0.06051	0.00064
#20	2.62478	0.00025	0.05867	0.00079	#21	2.62289	0.00026	0.0615	0.00076
#22	2.62304	0.00025	0.05865	0.00074	#23	2.62359	0.00022	0.05817	0.0007
#24	2.62284	0.00028	0.0601	0.00085	#25	2.62353	0.00022	0.05881	0.00064
#26	2.62295	0.00023	0.05847	0.00069	#27	2.6236	0.00025	0.06031	0.00075
#28	2.62376	0.00024	0.05979	0.00071	#29	2.62289	0.00028	0.05878	0.00086
#30	2.62289	0.00026	0.06055	0.00075	#31	2.62378	0.00024	0.06019	0.00071
#32	2.62292	0.00026	0.05916	0.00079	#33	2.62305	0.00022	0.05836	0.00069
#34	2.62268	0.00027	0.05975	0.00083	#35	2.62292	0.00023	0.05981	0.00069
#36	2.62283	0.00027	0.0581	0.00083	#37	2.62307	0.00025	0.05841	0.00075
#38	2.62235	0.00029	0.06017	0.00086	#39	2.62299	0.00027	0.06072	0.00081
#40	2.62276	0.00027	0.05935	0.00085	#41	2.6238	0.00027	0.05877	0.00082
#42	2.62262	0.00024	0.05969	0.00072	#43	2.62311	0.00024	0.0598	0.00072
#44	2.62282	0.00028	0.05778	0.00086	#45	2.6227	0.00026	0.05784	0.00082

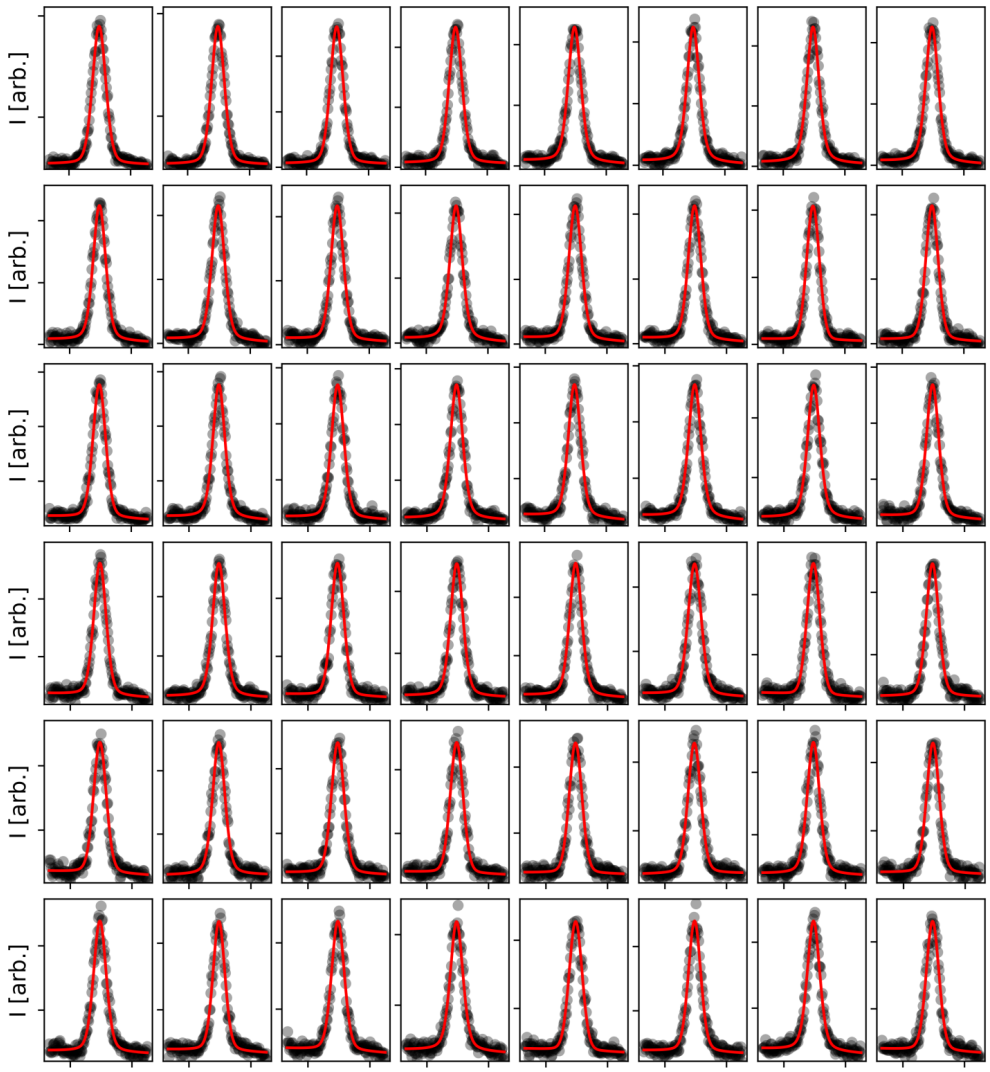

Figure E.19: First half of the in plane scans along Q_{xy}, recorded at 723 K. Continued in Figure E.20.

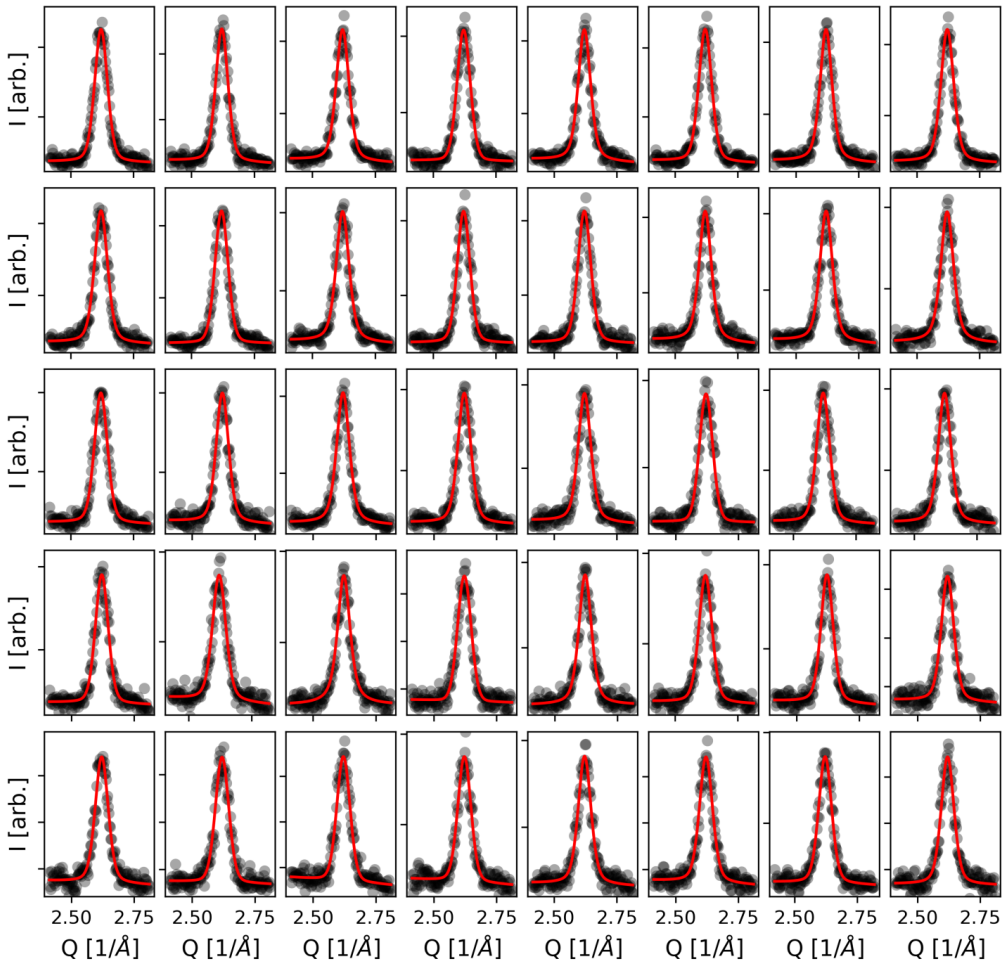

Figure E.20: Second half of the in plane scans along Q_{xy}, recorded at 723 K. Continuation of Figure E.19.

Table E.10: Center and full width half maximum (FWHM) for the fits presented in Figure E.19 and Figure E.20. For fits with multiple components, only fit results of the relevant component is shown.

	Center		FWHM			Center		FWHM	
	Value	Error	Value	Error		Value	Error	Value	Error
#0	2.62272	0.0002	0.06312	0.0006	#1	2.62214	0.00016	0.0609	0.00048
#2	2.62164	0.0002	0.06131	0.0006	#3	2.62116	0.00023	0.06147	0.0007
#4	2.62125	0.00022	0.06085	0.00068	#5	2.62219	0.00024	0.05961	0.00075
#6	2.62086	0.00022	0.05952	0.00069	#7	2.62101	0.00022	0.06052	0.00068
#8	2.62123	0.00023	0.06003	0.00069	#9	2.62063	0.00025	0.0611	0.00076
#10	2.62087	0.00024	0.06029	0.00072	#11	2.62059	0.00023	0.06003	0.00072
#12	2.62123	0.00023	0.06144	0.0007	#13	2.62017	0.00022	0.06095	0.00067
#14	2.62084	0.00024	0.06047	0.00067	#15	2.62094	0.00026	0.05943	0.00077
#16	2.62068	0.00024	0.06046	0.0007	#17	2.62064	0.00025	0.05785	0.00079
#18	2.62	0.00026	0.05979	0.00077	#19	2.61975	0.00024	0.05977	0.00075
#20	2.62088	0.00026	0.0599	0.00078	#21	2.62101	0.00022	0.06075	0.00068
#22	2.62121	0.00028	0.06004	0.00088	#23	2.62082	0.00027	0.05933	0.0008
#24	2.62051	0.00027	0.05906	0.00081	#25	2.62069	0.00022	0.0604	0.00069
#26	2.61939	0.00029	0.06072	0.00085	#27	2.62061	0.00024	0.05978	0.00071
#28	2.62045	0.00023	0.05882	0.00069	#29	2.62045	0.0003	0.0628	0.00088
#30	2.61982	0.0003	0.06143	0.00085	#31	2.62031	0.00027	0.06061	0.00079
#32	2.62046	0.00031	0.06078	0.00092	#33	2.62014	0.00029	0.05929	0.00087
#34	2.62025	0.00028	0.06067	0.00083	#35	2.62023	0.0003	0.06101	0.00086
#36	2.61986	0.00033	0.06056	0.00094	#37	2.61948	0.00032	0.06121	0.00093
#38	2.61988	0.00033	0.0598	0.00101	#39	2.61951	0.00032	0.06072	0.00093
#40	2.62045	0.00033	0.06043	0.001	#41	2.62082	0.00029	0.05702	0.00087
#42	2.62107	0.00031	0.06093	0.0009	#43	2.61996	0.00034	0.06038	0.00105
#44	2.62038	0.00029	0.06173	0.00082	#45	2.62034	0.0003	0.0592	0.0009

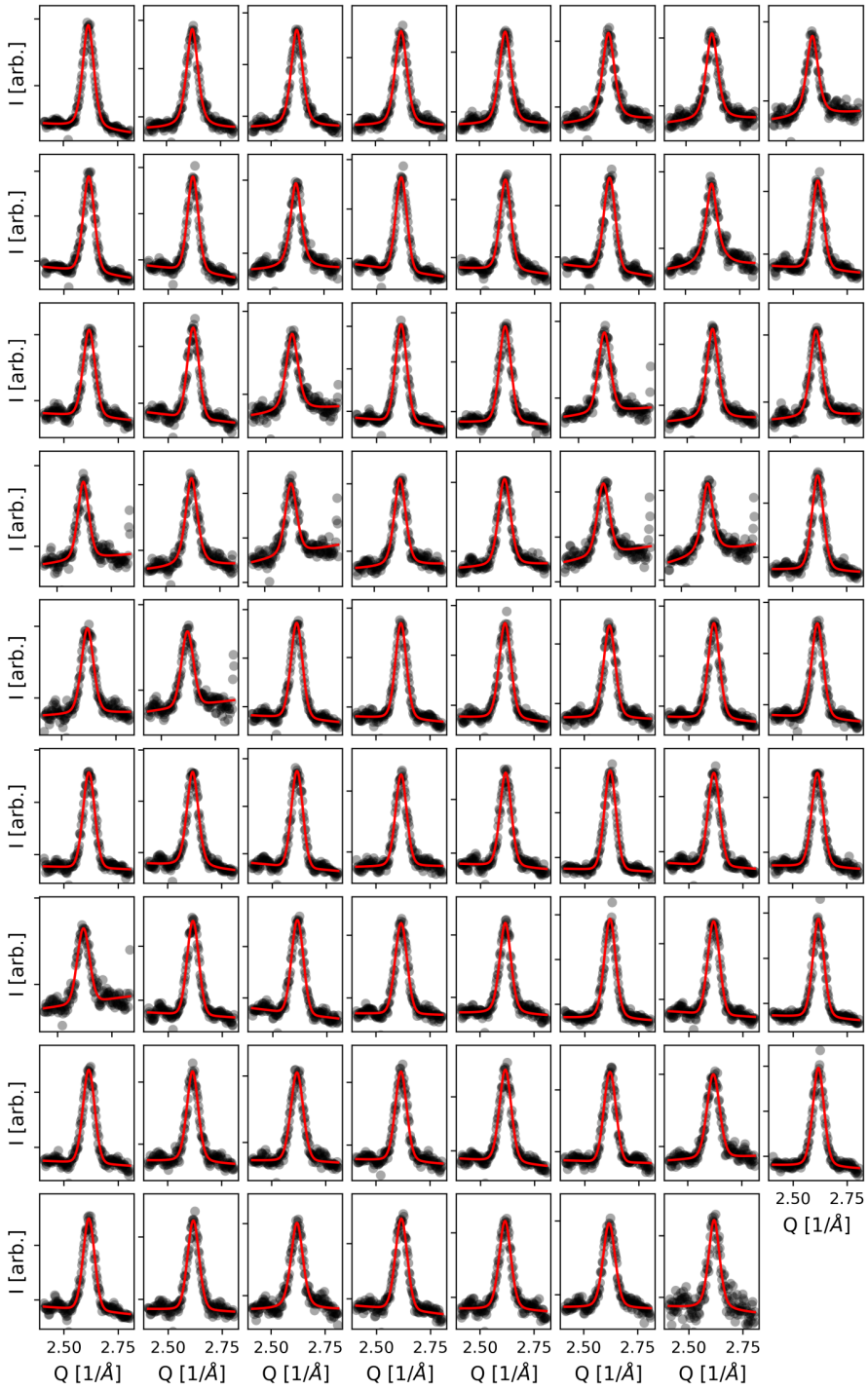

Figure E.21: In plane scans along Q_{xy}, recorded at 773 K.

Table E.11: Center and full width half maximum (FWHM) for the fits presented in Figure E.21. For fits with multiple components, only fit results of the relevant component is shown.

	Center		FWHM			Center		FWHM	
	Value	Error	Value	Error		Value	Error	Value	Error
#0	2.61472	0.00024	0.06129	0.00074	#1	2.61926	0.00038	0.06266	0.00124
#2	2.61846	0.00039	0.06296	0.00124	#3	2.61845	0.00044	0.06532	0.00135
#4	2.61854	0.00047	0.06457	0.00147	#5	2.62	0.00054	0.06571	0.00176
#6	2.61956	0.00063	0.06511	0.00206	#7	2.62095	0.00067	0.0637	0.00218
#8	2.61448	0.00033	0.06166	0.00096	#9	2.61422	0.00036	0.06005	0.00104
#10	2.61974	0.00056	0.06047	0.00191	#11	2.61449	0.00036	0.06091	0.00101
#12	2.61474	0.00044	0.06067	0.0013	#13	2.61455	0.00041	0.06299	0.00116
#14	2.62038	0.00077	0.06278	0.00299	#15	2.61445	0.00046	0.06159	0.00134
#16	2.61587	0.00052	0.06495	0.00152	#17	2.61532	0.00044	0.06278	0.00121
#18	2.62072	0.00077	0.06546	0.00249	#19	2.61381	0.00028	0.06232	0.0008
#20	2.61606	0.00039	0.06404	0.00115	#21	2.61982	0.00079	0.06525	0.00233
#22	2.61724	0.00044	0.06361	0.0014	#23	2.61955	0.00051	0.06324	0.00156
#24	2.62119	0.0009	0.06034	0.00272	#25	2.61814	0.00053	0.06557	0.00173
#26	2.62053	0.001	0.06226	0.00308	#27	2.61926	0.00053	0.06286	0.00163
#28	2.61835	0.00051	0.06643	0.00152	#29	2.62024	0.00111	0.06637	0.00332
#30	2.62093	0.00104	0.06095	0.00363	#31	2.61633	0.0004	0.06321	0.00119
#32	2.61879	0.00061	0.06606	0.0018	#33	2.62094	0.00103	0.06509	0.00292
#34	2.61516	0.00034	0.06344	0.00097	#35	2.61551	0.00035	0.0605	0.00104
#36	2.61543	0.0004	0.06466	0.00118	#37	2.61659	0.00044	0.06392	0.00131
#38	2.61544	0.00037	0.06312	0.00109	#39	2.61529	0.00035	0.06405	0.00104
#40	2.6148	0.00036	0.06359	0.00101	#41	2.61554	0.00037	0.06336	0.00111
#42	2.61431	0.00035	0.06268	0.00097	#43	2.6163	0.00042	0.06109	0.00123
#44	2.61571	0.00041	0.06193	0.0012	#45	2.6171	0.00024	0.06342	0.00069

Pd/Al_2O_3 - Pd(1 1 1) out of plane

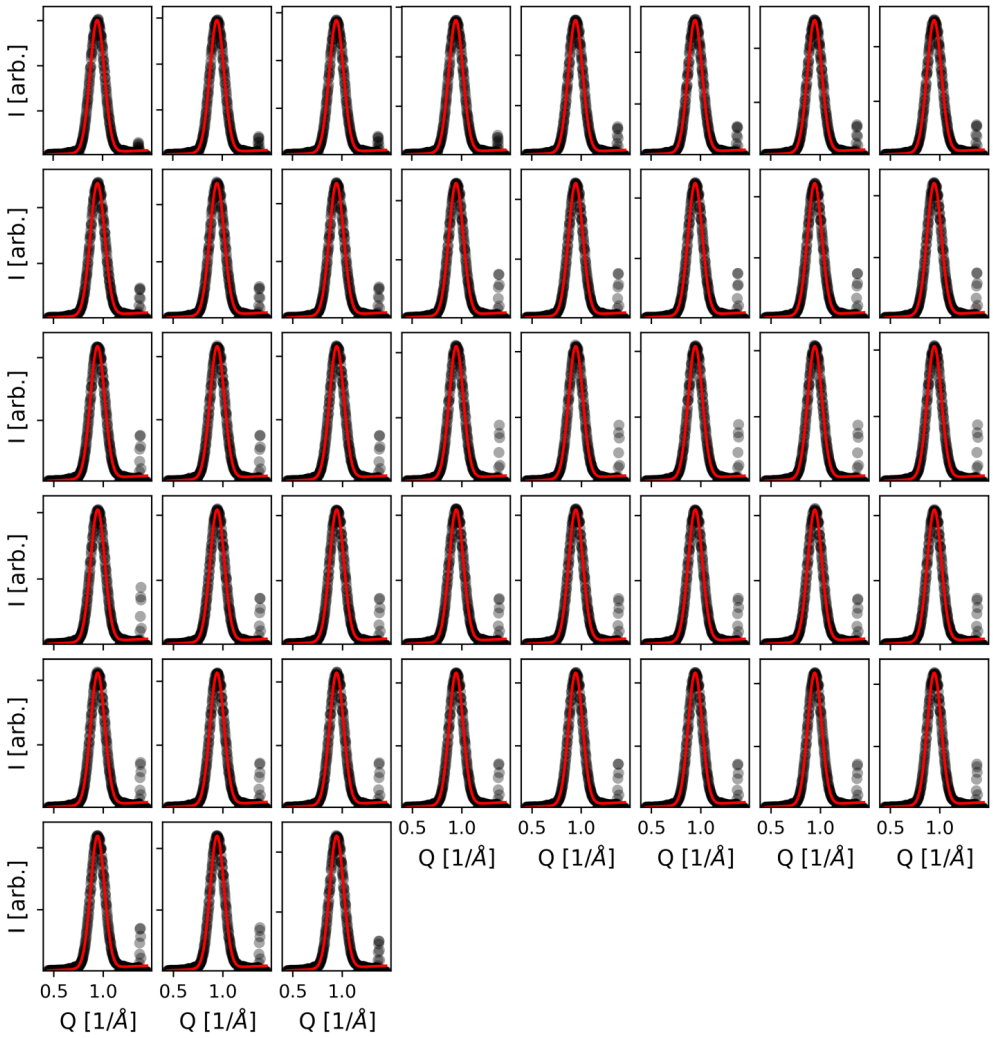

Figure E.22: Out of plane scans along Q_z, recorded at 523 K.

Table E.12: Center and full width half maximum (FWHM) for the fits presented in Figure E.22. For fits with multiple components, only fit results of the relevant component is shown.

	Center		FWHM			Center		FWHM	
	Value	Error	Value	Error		Value	Error	Value	Error
#0	0.94482	0.00015	0.16943	0.00045	#1	0.94435	0.00015	0.16893	0.00045
#2	0.9438	0.00014	0.16977	0.00043	#3	0.94318	0.00015	0.17075	0.00044
#4	0.94374	0.00016	0.16999	0.00048	#5	0.94327	0.00016	0.17022	0.00049
#6	0.94293	0.00017	0.17077	0.0005	#7	0.94287	0.00016	0.17115	0.00047
#8	0.94268	0.00016	0.17127	0.00047	#9	0.94237	0.00016	0.17154	0.00048
#10	0.94248	0.00015	0.17113	0.00045	#11	0.94277	0.00015	0.17116	0.00046
#12	0.94266	0.00016	0.17127	0.00047	#13	0.94257	0.00015	0.17123	0.00046
#14	0.94233	0.00015	0.17119	0.00045	#15	0.94222	0.00015	0.17134	0.00046
#16	0.94211	0.00014	0.17123	0.00043	#17	0.94214	0.00015	0.1717	0.00046
#18	0.9421	0.00015	0.17114	0.00045	#19	0.9421	0.00014	0.16957	0.00042
#20	0.94199	0.00014	0.16979	0.00043	#21	0.94217	0.00015	0.16969	0.00045
#22	0.94198	0.00014	0.16955	0.00043	#23	0.94196	0.00014	0.16931	0.00042
#24	0.9419	0.00014	0.16951	0.00043	#25	0.94188	0.00015	0.17026	0.00046
#26	0.94195	0.00015	0.16965	0.00046	#27	0.94204	0.00015	0.16975	0.00044
#28	0.94195	0.00014	0.16919	0.00043	#29	0.94198	0.00015	0.16935	0.00045
#30	0.94211	0.00015	0.16856	0.00045	#31	0.9421	0.00015	0.16877	0.00045
#32	0.94227	0.00015	0.16848	0.00045	#33	0.94224	0.00015	0.16795	0.00045
#34	0.94234	0.00015	0.16786	0.00045	#35	0.94229	0.00015	0.16776	0.00045
#36	0.94234	0.00015	0.16745	0.00044	#37	0.94244	0.00014	0.16709	0.00043
#38	0.94241	0.00014	0.16683	0.00042	#39	0.94251	0.00015	0.16639	0.00046
#40	0.94253	0.00014	0.1661	0.00042	#41	0.94253	0.00015	0.16574	0.00045
#42	0.94262	0.00015	0.16614	0.00045					

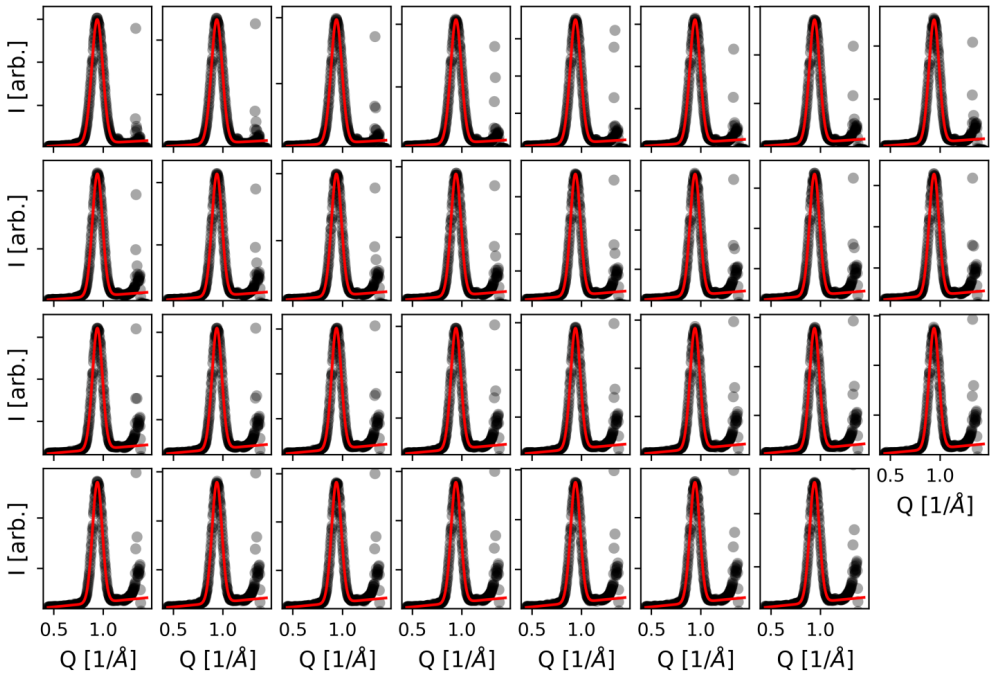

Figure E.23: Out of plane scans along Q_z, recorded at 573 K.

Table E.13: Center and full width half maximum (FWHM) for the fits presented in Figure E.23. For fits with multiple components, only fit results of the relevant component is shown.

	Center		FWHM			Center		FWHM	
	Value	Error	Value	Error		Value	Error	Value	Error
#0	0.94049	0.00011	0.13306	0.00032	#1	0.93986	0.00011	0.13088	0.00031
#2	0.93962	0.0001	0.12943	0.00028	#3	0.93982	0.0001	0.12844	0.00029
#4	0.9392	9e-05	0.12705	0.00026	#5	0.93926	9e-05	0.12514	0.00026
#6	0.93947	0.0001	0.1239	0.00028	#7	0.93934	9e-05	0.12256	0.00025
#8	0.93944	0.0001	0.12153	0.00027	#9	0.9393	9e-05	0.12111	0.00027
#10	0.9393	0.0001	0.12035	0.00027	#11	0.93925	9e-05	0.1198	0.00027
#12	0.93916	0.0001	0.11956	0.00028	#13	0.9392	0.00011	0.11916	0.0003
#14	0.93925	0.0001	0.11909	0.00029	#15	0.93915	0.0001	0.11888	0.00029
#16	0.9392	0.00011	0.11889	0.00031	#17	0.93926	0.0001	0.118	0.0003
#18	0.93903	0.00011	0.11771	0.00031	#19	0.93905	0.00011	0.11815	0.00032
#20	0.93916	0.00011	0.11758	0.0003	#21	0.93898	0.00011	0.11749	0.00032
#22	0.93897	0.00011	0.11752	0.00032	#23	0.93895	0.00011	0.11752	0.0003
#24	0.93896	0.00012	0.1172	0.00033	#25	0.93899	0.0001	0.11705	0.00029
#26	0.93904	0.00011	0.11682	0.00031	#27	0.93892	0.00011	0.11715	0.00031
#28	0.93897	0.00012	0.11678	0.00032	#29	0.93903	0.00011	0.11659	0.0003
#30	0.93893	0.00011	0.11665	0.00032					

Table E.14: Center and full width half maximum (FWHM) for the fits presented in Figure E.24. For fits with multiple components, only fit results of the relevant component is shown.

	Center		FWHM			Center		FWHM	
	Value	Error	Value	Error		Value	Error	Value	Error
#0	0.94564	0.00012	0.12277	0.00034	#1	0.94476	0.00012	0.1233	0.00034
#2	0.94399	0.00011	0.12387	0.00033	#3	0.94361	0.00013	0.12401	0.00037
#4	0.94306	0.00011	0.12434	0.00033	#5	0.94274	0.00013	0.12454	0.00037
#6	0.94226	0.00011	0.12433	0.00033	#7	0.94203	0.00012	0.12524	0.00035
#8	0.94176	0.00013	0.12557	0.00037	#9	0.9417	0.00012	0.12635	0.00035
#10	0.94147	0.00013	0.12641	0.00039	#11	0.94131	0.00012	0.12589	0.00036
#12	0.94112	0.00013	0.12661	0.00037	#13	0.94134	0.00012	0.12731	0.00035
#14	0.94094	0.00014	0.12698	0.00039	#15	0.94049	0.00015	0.12727	0.00044
#16	0.94057	0.00014	0.12765	0.0004	#17	0.94063	0.00016	0.12828	0.00046
#18	0.94017	0.00016	0.12629	0.00049	#19	0.94028	0.00015	0.12872	0.00043
#20	0.94033	0.00016	0.12811	0.00046	#21	0.94033	0.00013	0.1278	0.00039
#22	0.94049	0.00015	0.12931	0.00044	#23	0.94018	0.00018	0.12984	0.00051
#24	0.94025	0.00016	0.12907	0.00046	#25	0.94022	0.00015	0.1297	0.00045
#26	0.94031	0.00015	0.13004	0.00044	#27	0.94006	0.00016	0.12975	0.00047
#28	0.94012	0.00015	0.13067	0.00045	#29	0.93993	0.00016	0.12853	0.00048
#30	0.93969	0.00015	0.13005	0.00044	#31	0.94001	0.00017	0.1305	0.00048
#32	0.94008	0.00016	0.13018	0.00046	#33	0.93971	0.00016	0.13129	0.00047
#34	0.93992	0.00015	0.13173	0.00042	#35	0.93984	0.00015	0.1314	0.00043
#36	0.93984	0.00016	0.13242	0.00045	#37	0.93964	0.00017	0.13147	0.00049
#38	0.93937	0.00016	0.13235	0.00045	#39	0.93986	0.00018	0.13206	0.00054
#40	0.93941	0.00017	0.12983	0.00051	#41	0.93927	0.00017	0.13213	0.00048
#42	0.93964	0.00016	0.1322	0.00046	#43	0.9394	0.00016	0.1317	0.00046
#44	0.93977	0.00017	0.13245	0.00049	#45	0.93942	0.00017	0.13261	0.00048
#46	0.93987	0.00018	0.13369	0.00051					

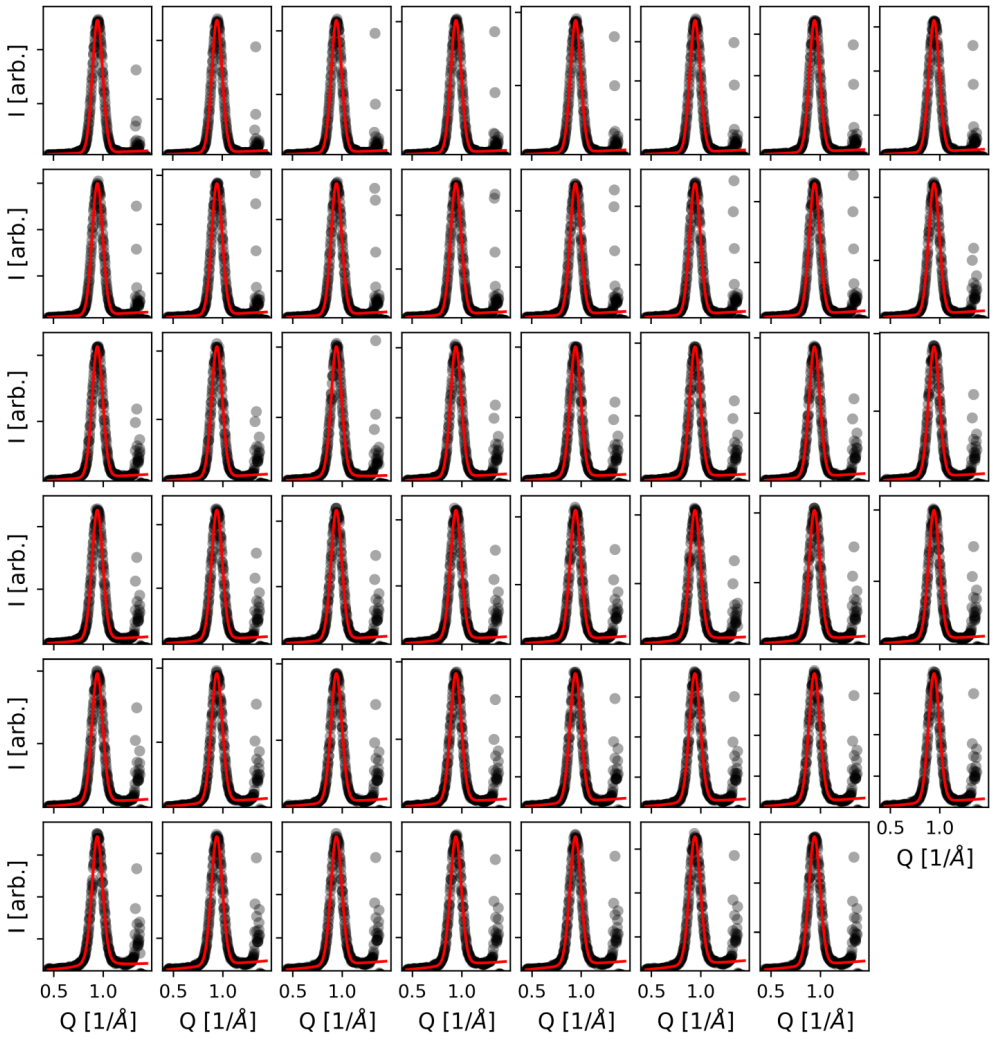

Figure E.24: Out of plane scans along Q_z, recorded at 623 K.

Figure E.25: Out of plane scans along Q_z, recorded at 673 K.

Table E.15: Center and full width half maximum (FWHM) for the fits presented in Figure E.25. For fits with multiple components, only fit results of the relevant component is shown.

	Center		FWHM			Center		FWHM	
	Value	Error	Value	Error		Value	Error	Value	Error
#0	0.94115	0.00017	0.13256	0.00052	#1	0.94055	0.00017	0.13581	0.00048
#2	0.93938	0.00018	0.13458	0.00051	#3	0.93919	0.00018	0.13494	0.00051
#4	0.93836	0.00019	0.13474	0.00056	#5	0.93743	0.00022	0.13256	0.00064
#6	0.93771	0.0002	0.13552	0.00056	#7	0.93775	0.00019	0.13533	0.00055
#8	0.93746	0.00023	0.13657	0.00065	#9	0.93692	0.00024	0.13599	0.00068
#10	0.93663	0.00021	0.1354	0.00059	#11	0.93688	0.00024	0.13585	0.00067
#12	0.93686	0.00022	0.13573	0.00061	#13	0.93667	0.00018	0.13533	0.00052
#14	0.93705	0.00025	0.13598	0.00071	#15	0.93626	0.00023	0.13486	0.00066
#16	0.9362	0.00021	0.1345	0.00059	#17	0.93601	0.00026	0.1364	0.00073
#18	0.93629	0.00023	0.13558	0.00066	#19	0.93689	0.00026	0.13497	0.00072
#20	0.93652	0.00025	0.13649	0.0007	#21	0.93654	0.00022	0.13503	0.00063
#22	0.93631	0.00024	0.13626	0.00067	#23	0.93708	0.00022	0.13518	0.00062
#24	0.93615	0.00024	0.13618	0.00069	#25	0.93619	0.00023	0.13567	0.00065
#26	0.93662	0.00027	0.13578	0.00076	#27	0.93668	0.00024	0.13604	0.00068
#28	0.9359	0.00024	0.13556	0.00067	#29	0.93663	0.00025	0.1361	0.00069
#30	0.93632	0.00026	0.13593	0.00074	#31	0.93681	0.00024	0.13603	0.00068
#32	0.93617	0.00027	0.13544	0.00074	#33	0.93599	0.00026	0.13577	0.00074
#34	0.93635	0.00025	0.13514	0.00069	#35	0.93618	0.00025	0.13491	0.00069
#36	0.93576	0.00028	0.13531	0.00077	#37	0.93602	0.00027	0.13635	0.00075
#38	0.93703	0.00027	0.13643	0.00075	#39	0.93661	0.00025	0.13616	0.00071
#40	0.93692	0.00026	0.13672	0.00073	#41	0.93614	0.00027	0.13479	0.00077
#42	0.93658	0.00028	0.13623	0.00077	#43	0.93653	0.00027	0.13625	0.00074
#44	0.93653	0.00025	0.13615	0.00071	#45	0.93678	0.00025	0.13719	0.00072

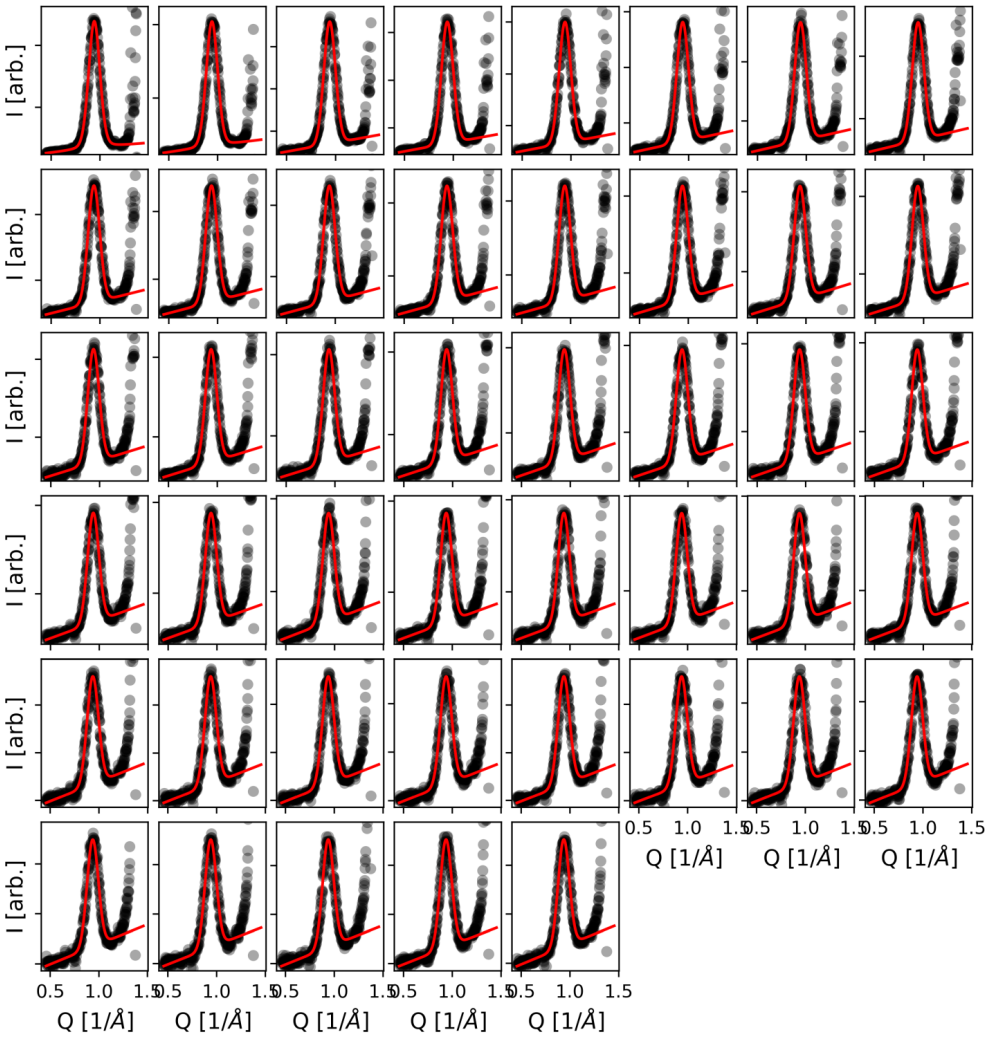

Figure E.26: Out of plane scans along Q_z, recorded at 723 K.

Table E.16: Center and full width half maximum (FWHM) for the fits presented in Figure E.26. For fits with multiple components, only fit results of the relevant component is shown.

	Center		FWHM			Center		FWHM	
	Value	Error	Value	Error		Value	Error	Value	Error
#0	0.94147	0.00019	0.13692	0.00056	#1	0.94079	0.0002	0.13802	0.00058
#2	0.94066	0.00023	0.13995	0.00066	#3	0.93967	0.00023	0.14208	0.00065
#4	0.93909	0.00025	0.14095	0.00071	#5	0.93893	0.00027	0.14059	0.00076
#6	0.9393	0.00029	0.14025	0.00083	#7	0.93949	0.00035	0.14112	0.001
#8	0.93881	0.00032	0.14023	0.00091	#9	0.93841	0.00035	0.13908	0.00099
#10	0.93968	0.00041	0.14067	0.00115	#11	0.93843	0.00035	0.13964	0.00097
#12	0.93908	0.00042	0.13843	0.00117	#13	0.93851	0.00043	0.13925	0.0012
#14	0.93817	0.00038	0.141	0.00106	#15	0.93856	0.00045	0.1394	0.00126
#16	0.93799	0.00039	0.13803	0.00108	#17	0.93668	0.00038	0.13789	0.00107
#18	0.93801	0.00039	0.13908	0.0011	#19	0.93818	0.0004	0.13819	0.00111
#20	0.93686	0.00041	0.13928	0.00115	#21	0.93819	0.00043	0.13952	0.0012
#22	0.93663	0.00042	0.13924	0.00117	#23	0.93725	0.00046	0.13574	0.00129
#24	0.93819	0.00043	0.13719	0.00119	#25	0.9381	0.00045	0.13785	0.00126
#26	0.93714	0.00049	0.13869	0.00138	#27	0.93709	0.00048	0.13696	0.00134
#28	0.93635	0.00048	0.13654	0.00134	#29	0.93705	0.00049	0.13719	0.00137
#30	0.93718	0.00052	0.13736	0.00144	#31	0.93787	0.00051	0.13698	0.00141
#32	0.93585	0.00051	0.13785	0.00141	#33	0.93694	0.00052	0.13802	0.00146
#34	0.93598	0.00051	0.13929	0.00142	#35	0.93661	0.00054	0.13854	0.00152
#36	0.93739	0.00047	0.13861	0.00131	#37	0.93709	0.00049	0.13854	0.00137
#38	0.93718	0.00056	0.13828	0.00158	#39	0.93758	0.00049	0.13642	0.00138
#40	0.9366	0.00054	0.13644	0.00152	#41	0.93792	0.00055	0.13694	0.00152
#42	0.93796	0.00059	0.13562	0.00164	#43	0.93625	0.00052	0.13858	0.00144
#44	0.93655	0.00047	0.13599	0.00132					

Table E.17: Center and full width half maximum (FWHM) for the fits presented in Figure E.27. For fits with multiple components, only fit results of the relevant component is shown.

	Center		FWHM			Center		FWHM	
	Value	Error	Value	Error		Value	Error	Value	Error
#0	0.95082	7e-05	0.10101	0.00022	#1	0.9508	7e-05	0.10192	0.00021
#2	0.95071	7e-05	0.1027	0.00022	#3	0.95057	7e-05	0.10316	0.00021
#4	0.95047	7e-05	0.10372	0.00022	#5	0.9504	7e-05	0.10382	0.00022
#6	0.95032	7e-05	0.10442	0.00021	#7	0.95022	7e-05	0.10458	0.00022
#8	0.95012	7e-05	0.10484	0.00022	#9	0.95013	8e-05	0.10502	0.00023
#10	0.95011	7e-05	0.10515	0.00021	#11	0.95011	7e-05	0.10531	0.00021
#12	0.94998	7e-05	0.10539	0.00022	#13	0.95002	8e-05	0.10558	0.00023
#14	0.94999	7e-05	0.10555	0.00022	#15	0.94987	8e-05	0.10554	0.00023
#16	0.94997	8e-05	0.10569	0.00022	#17	0.95003	8e-05	0.10554	0.00023
#18	0.94989	8e-05	0.10576	0.00023	#19	0.94989	8e-05	0.10569	0.00023
#20	0.94988	7e-05	0.10561	0.00021	#21	0.94994	7e-05	0.10557	0.00022
#22	0.94997	8e-05	0.10557	0.00023	#23	0.94997	8e-05	0.10549	0.00023
#24	0.94994	7e-05	0.10547	0.00022	#25	0.94993	8e-05	0.1057	0.00023
#26	0.94984	8e-05	0.10557	0.00023	#27	0.94983	7e-05	0.10566	0.00022
#28	0.94975	8e-05	0.10576	0.00023	#29	0.94998	8e-05	0.10571	0.00023
#30	0.94998	8e-05	0.1057	0.00023	#31	0.94981	7e-05	0.10569	0.00021
#32	0.94993	8e-05	0.10556	0.00023	#33	0.94985	7e-05	0.10553	0.00022
#34	0.94996	7e-05	0.10545	0.00022	#35	0.94987	7e-05	0.10554	0.00022
#36	0.94998	8e-05	0.10551	0.00023	#37	0.94989	8e-05	0.10565	0.00024
#38	0.94999	8e-05	0.10564	0.00023	#39	0.94994	8e-05	0.10559	0.00023
#40	0.94986	8e-05	0.10572	0.00024					

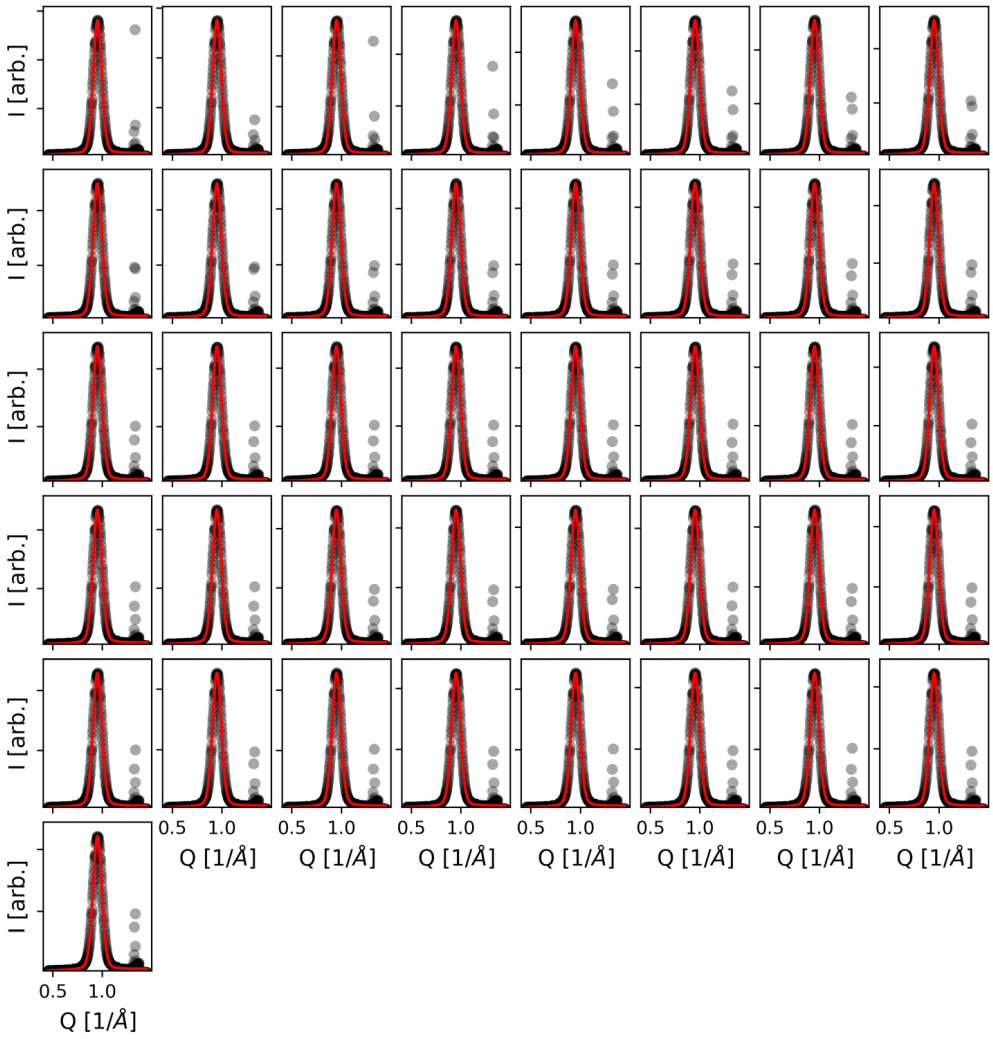

Figure E.27: Out of plane scans along Q_z, recorded at 523 K.

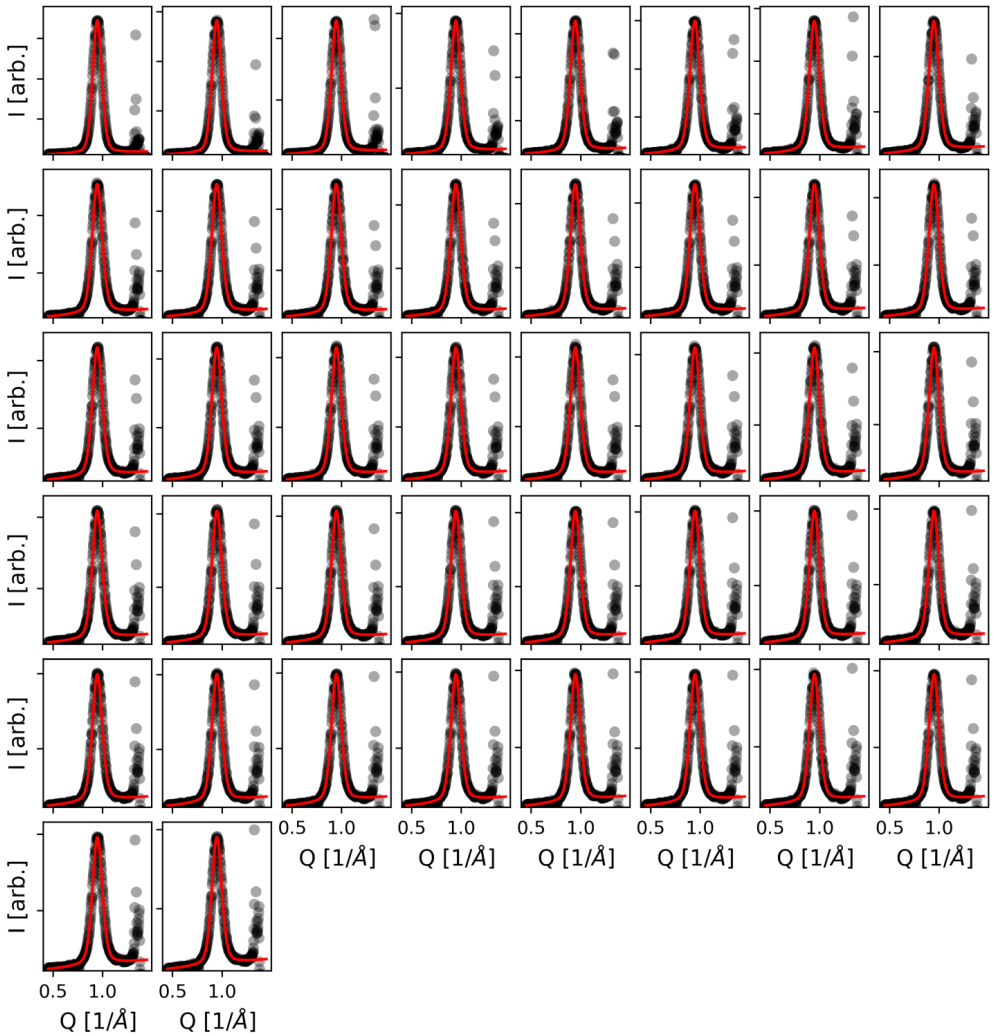

Figure E.28: Out of plane scans along Q_z, recorded at 573 K.

Table E.18: Center and full width half maximum (FWHM) for the fits presented in Figure E.28. For fits with multiple components, only fit results of the relevant component is shown.

	Center		FWHM			Center		FWHM	
	Value	Error	Value	Error		Value	Error	Value	Error
#0	0.94586	9e-05	0.10896	0.00026	#1	0.94532	9e-05	0.11117	0.00028
#2	0.94499	9e-05	0.11386	0.00029	#3	0.94494	0.0001	0.11604	0.00031
#4	0.94492	0.0001	0.11766	0.00032	#5	0.945	0.0001	0.11845	0.00032
#6	0.94502	0.00011	0.11936	0.00035	#7	0.94506	0.0001	0.11951	0.00031
#8	0.94518	0.00012	0.11967	0.00036	#9	0.94516	0.00011	0.11923	0.00035
#10	0.94545	0.00012	0.11907	0.00038	#11	0.94537	0.00012	0.11966	0.00037
#12	0.94536	0.00013	0.11914	0.0004	#13	0.94561	0.00012	0.11899	0.00038
#14	0.94535	0.00012	0.11963	0.00037	#15	0.94579	0.00012	0.11964	0.00037
#16	0.94586	0.00012	0.11862	0.00038	#17	0.94569	0.00012	0.11823	0.00037
#18	0.94595	0.00012	0.11825	0.00038	#19	0.9459	0.00013	0.1187	0.00039
#20	0.94601	0.00013	0.11839	0.00041	#21	0.94597	0.00013	0.11864	0.0004
#22	0.94611	0.00013	0.11855	0.00042	#23	0.94615	0.00012	0.11913	0.00038
#24	0.94619	0.00013	0.11837	0.0004	#25	0.94618	0.00013	0.11908	0.0004
#26	0.94647	0.00013	0.11855	0.00039	#27	0.94618	0.00013	0.11867	0.0004
#28	0.94637	0.00013	0.11887	0.00041	#29	0.94635	0.00013	0.1183	0.00041
#30	0.94619	0.00013	0.11891	0.0004	#31	0.94631	0.00013	0.11805	0.00041
#32	0.94634	0.00014	0.11842	0.00042	#33	0.94655	0.00013	0.11817	0.00042
#34	0.94633	0.00014	0.1185	0.00042	#35	0.94638	0.00013	0.11876	0.00041
#36	0.94619	0.00014	0.11806	0.00044	#37	0.9465	0.00013	0.11843	0.00039
#38	0.94641	0.00013	0.11814	0.00041	#39	0.94674	0.00013	0.11841	0.0004

Table E.19: Center and full width half maximum (FWHM) for the fits presented in Figure E.29. For fits with multiple components, only fit results of the relevant component is shown.

	Center		FWHM			Center		FWHM	
	Value	Error	Value	Error		Value	Error	Value	Error
#0	0.94694	0.00015	0.119	0.00045	#1	0.94681	0.00015	0.11889	0.00045
#2	0.94652	0.00015	0.11948	0.00045	#3	0.94646	0.00016	0.1185	0.0005
#4	0.94604	0.00016	0.118	0.00049	#5	0.94602	0.00017	0.11895	0.00051
#6	0.94617	0.00017	0.11862	0.0005	#7	0.94579	0.00017	0.11874	0.00053
#8	0.9458	0.00017	0.11933	0.00052	#9	0.94583	0.00018	0.11863	0.00054
#10	0.94564	0.00018	0.11904	0.00055	#11	0.94592	0.00018	0.11864	0.00055
#12	0.94577	0.00019	0.11955	0.00057	#13	0.94577	0.0002	0.11935	0.00059
#14	0.94536	0.00019	0.11986	0.00058	#15	0.94557	0.0002	0.12009	0.00059
#16	0.94542	0.0002	0.12009	0.00061	#17	0.94511	0.00021	0.12028	0.00063
#18	0.94563	0.00019	0.12001	0.00057	#19	0.94544	0.0002	0.12006	0.0006
#20	0.9455	0.0002	0.11999	0.0006	#21	0.94548	0.00021	0.12026	0.00063
#22	0.94538	0.0002	0.1207	0.0006	#23	0.94539	0.00021	0.11991	0.00063
#24	0.94538	0.00021	0.12039	0.00065	#25	0.94531	0.00021	0.12127	0.00062
#26	0.94539	0.00022	0.12084	0.00066	#27	0.94572	0.00021	0.12096	0.00063
#28	0.94505	0.00022	0.12115	0.00066	#29	0.94516	0.00022	0.12128	0.00067
#30	0.94514	0.0002	0.12088	0.0006	#31	0.94551	0.00022	0.12161	0.00065
#32	0.94549	0.00022	0.12105	0.00065	#33	0.94484	0.00022	0.12135	0.00066
#34	0.94506	0.00023	0.12106	0.00067	#35	0.94525	0.00022	0.12224	0.00064
#36	0.94552	0.00023	0.12145	0.00069	#37	0.94543	0.00022	0.12173	0.00066
#38	0.94522	0.00022	0.12101	0.00065	#39	0.94508	0.00023	0.12184	0.00068
#40	0.9452	0.00022	0.12223	0.00066	#41	0.94574	0.00022	0.12062	0.00066
#42	0.94532	0.00023	0.1215	0.00068	#43	0.94575	0.00022	0.12231	0.00064
#44	0.94548	0.00023	0.12199	0.00069	#45	0.94532	0.00024	0.12332	0.00069

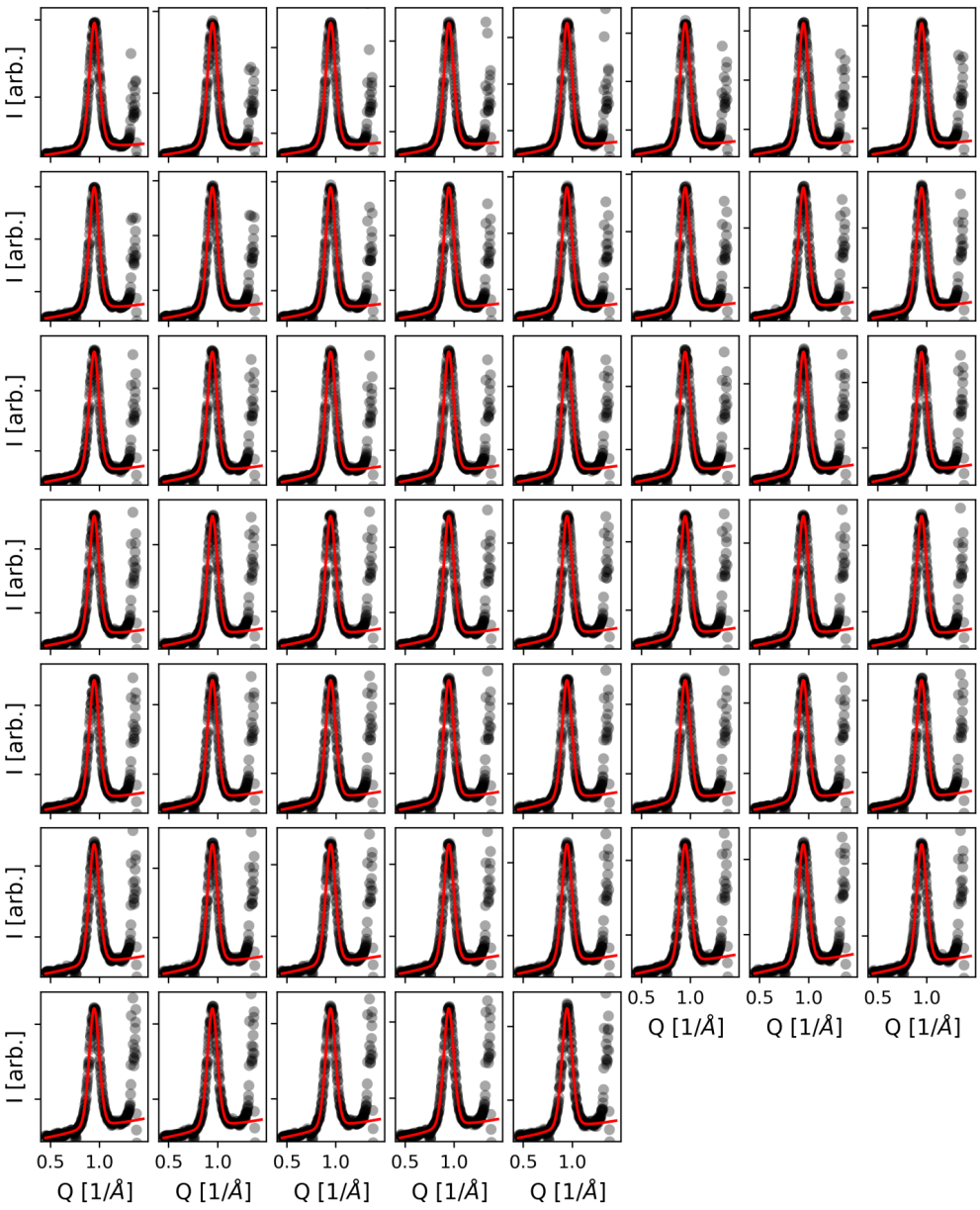

Figure E.29: Out of plane scans along Q_z, recorded at 623 K.

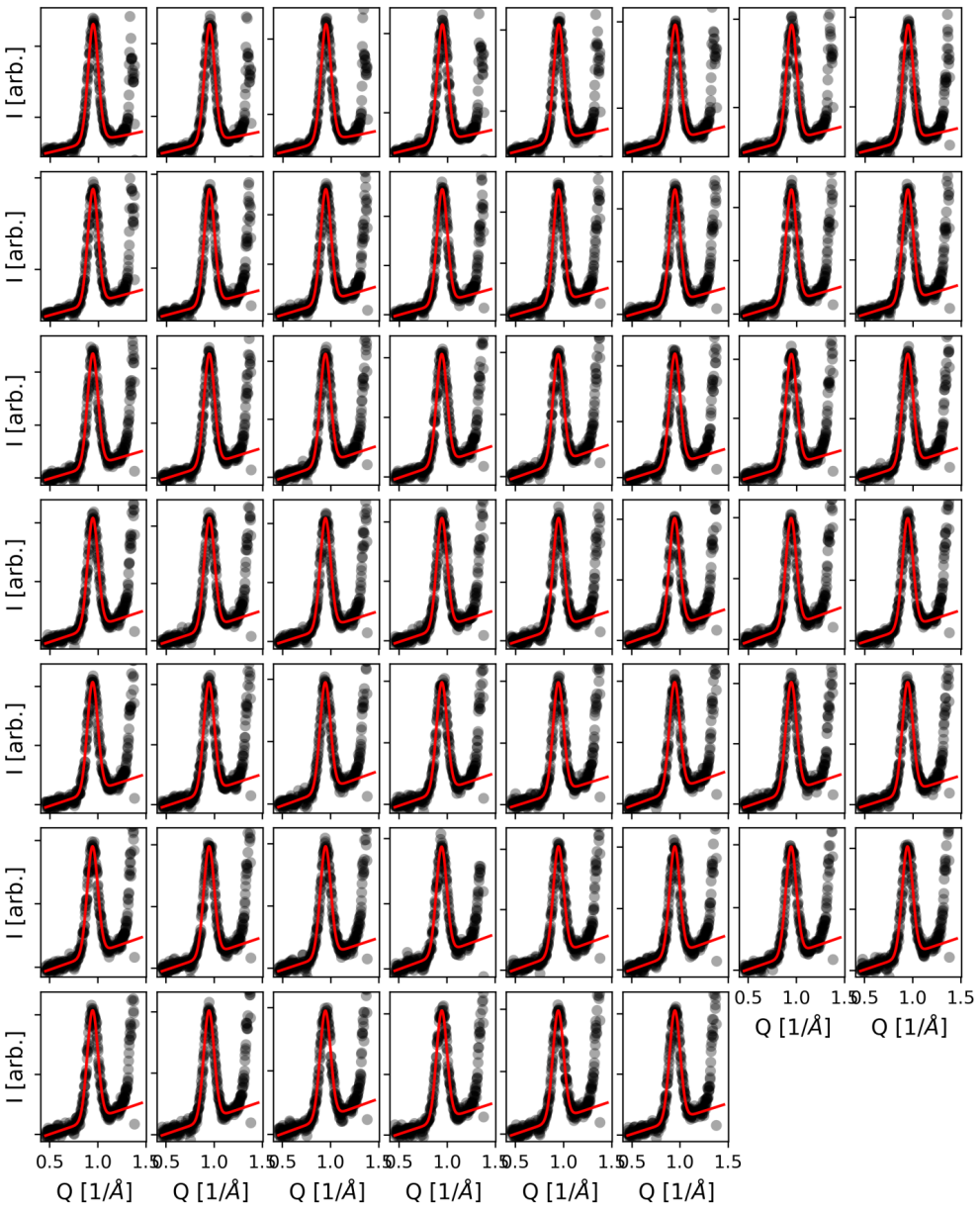

Figure E.30: Out of plane scans along Q_z, recorded at 673 K.

Table E.20: Center and full width half maximum (FWHM) for the fits presented in Figure E.30. For fits with multiple components, only fit results of the relevant component is shown.

	Center		FWHM			Center		FWHM	
	Value	Error	Value	Error		Value	Error	Value	Error
#0	0.94572	0.00039	0.12689	0.00112	#1	0.94602	0.00038	0.12576	0.00109
#2	0.94618	0.00037	0.12568	0.00106	#3	0.94533	0.00043	0.12696	0.00122
#4	0.94498	0.00039	0.12581	0.00113	#5	0.94459	0.00044	0.12995	0.00125
#6	0.945	0.00045	0.12817	0.00127	#7	0.94532	0.00042	0.12641	0.00118
#8	0.94386	0.00046	0.12647	0.0013	#9	0.94551	0.00044	0.12644	0.00122
#10	0.94504	0.00045	0.12804	0.00126	#11	0.94489	0.00047	0.12824	0.00131
#12	0.94335	0.00048	0.12624	0.00134	#13	0.94506	0.00049	0.12819	0.00136
#14	0.94469	0.00052	0.12996	0.00145	#15	0.9456	0.00053	0.12842	0.00149
#16	0.94395	0.00053	0.12853	0.00148	#17	0.94492	0.00049	0.12754	0.00135
#18	0.94398	0.00054	0.12782	0.0015	#19	0.94399	0.00057	0.12912	0.00158
#20	0.94338	0.0006	0.12853	0.00166	#21	0.94426	0.00053	0.12902	0.00149
#22	0.94455	0.00057	0.13219	0.00158	#23	0.94449	0.00057	0.12897	0.00159
#24	0.94448	0.00054	0.12874	0.0015	#25	0.94596	0.00053	0.128	0.00147
#26	0.94399	0.00054	0.12753	0.00151	#27	0.94373	0.00055	0.12828	0.00154
#28	0.94443	0.00056	0.13147	0.00156	#29	0.94344	0.00059	0.12963	0.00166
#30	0.9435	0.00062	0.12853	0.00172	#31	0.94512	0.00058	0.13065	0.00162
#32	0.94372	0.00057	0.12908	0.00158	#33	0.94365	0.0006	0.12923	0.00168
#34	0.94327	0.0006	0.12726	0.00168	#35	0.94449	0.0006	0.12965	0.00168
#36	0.94487	0.00061	0.12916	0.00171	#37	0.94423	0.00059	0.12837	0.00164
#38	0.94485	0.00058	0.13118	0.00162	#39	0.94388	0.00056	0.1304	0.00155
#40	0.94364	0.00061	0.13111	0.00169	#41	0.94483	0.00059	0.12843	0.00165
#42	0.94487	0.00059	0.12895	0.00165	#43	0.94425	0.00053	0.12777	0.00146
#44	0.94543	0.0006	0.12819	0.00168	#45	0.94516	0.0006	0.12636	0.00167

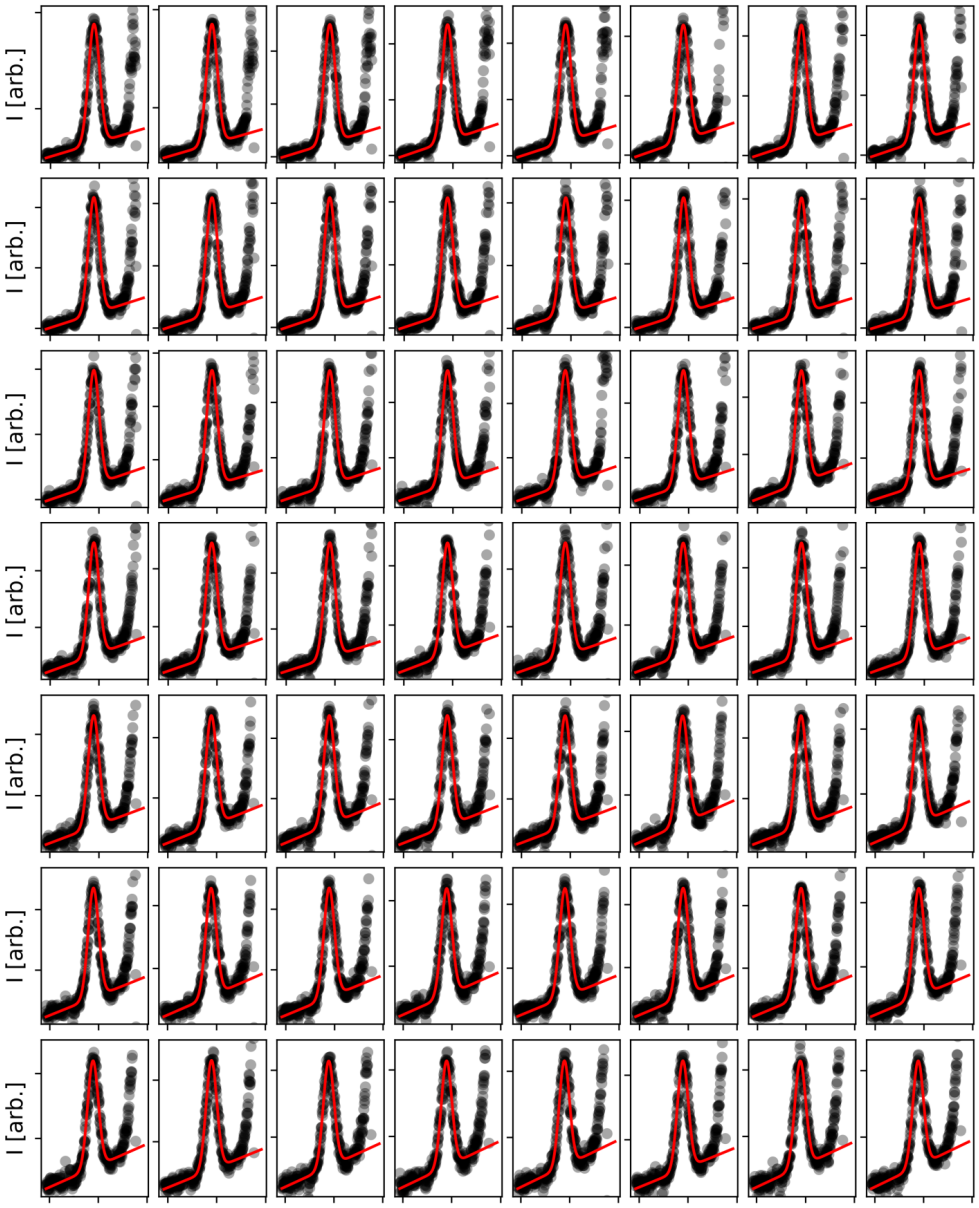

Figure E.31: Out of plane scans along Q_z, recorded at 723 K. Continued in Figure E.32.

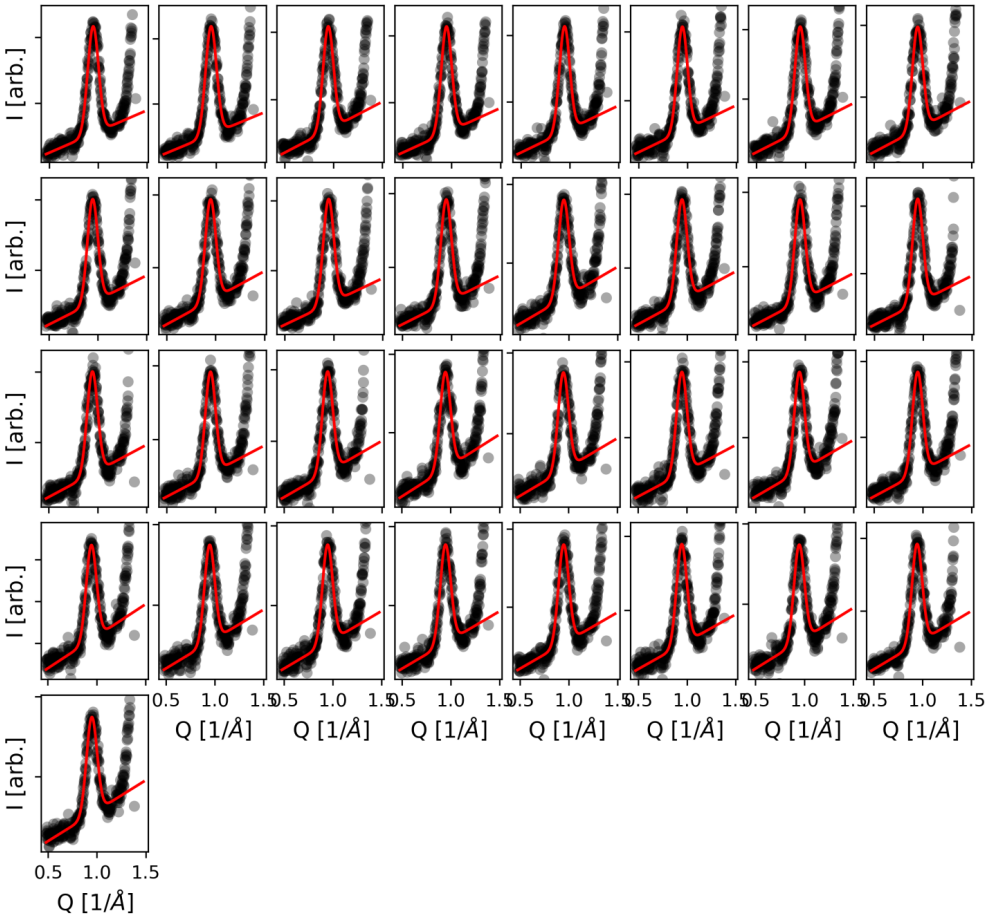

Figure E.32: Out of plane scans along Q_z, recorded at 723 K. Continuation of Figure E.31.

Table E.21: Center and full width half maximum (FWHM) for the fits presented in Figure E.31 and Figure E.32. For fits with multiple components, only fit results of the relevant component is shown.

	Center		FWHM			Center		FWHM	
	Value	Error	Value	Error		Value	Error	Value	Error
#0	0.94677	0.00045	0.13416	0.00126	#1	0.94719	0.00047	0.13252	0.00131
#2	0.94623	0.00051	0.13302	0.00143	#3	0.94519	0.00051	0.13221	0.00142
#4	0.94711	0.0005	0.13046	0.00141	#5	0.94548	0.00063	0.13281	0.00176
#6	0.9456	0.00046	0.1299	0.00128	#7	0.94577	0.00045	0.12833	0.00125
#8	0.94613	0.00043	0.1298	0.0012	#9	0.94697	0.00049	0.13242	0.00137
#10	0.94571	0.00045	0.12937	0.00126	#11	0.94526	0.00046	0.12785	0.00129
#12	0.94663	0.00051	0.12979	0.00141	#13	0.94651	0.00056	0.12808	0.00156
#14	0.94679	0.00047	0.12916	0.00131	#15	0.94695	0.0005	0.13167	0.0014
#16	0.94586	0.0005	0.13038	0.00139	#17	0.94707	0.0006	0.13036	0.00168
#18	0.94672	0.0006	0.13018	0.00167	#19	0.9463	0.00062	0.13213	0.00174
#20	0.94411	0.00065	0.13203	0.0018	#21	0.94656	0.00061	0.13113	0.00169
#22	0.94665	0.00066	0.13047	0.00184	#23	0.94716	0.00065	0.12939	0.0018
#24	0.94588	0.00067	0.1284	0.00185	#25	0.94588	0.00069	0.13126	0.00191
#26	0.94714	0.00063	0.13	0.00175	#27	0.9466	0.0007	0.1306	0.00195
#28	0.94645	0.00071	0.12967	0.00197	#29	0.94572	0.00071	0.12989	0.00196
#30	0.94752	0.00068	0.12809	0.00189	#31	0.94671	0.00065	0.12782	0.00181
#32	0.94646	0.00072	0.1308	0.002	#33	0.94539	0.00071	0.12983	0.00198
#34	0.94433	0.00075	0.12823	0.00208	#35	0.94615	0.00072	0.12645	0.00201
#36	0.94619	0.00076	0.12916	0.00212	#37	0.94416	0.00081	0.13141	0.00225
#38	0.94504	0.00074	0.13141	0.00207	#39	0.94608	0.00082	0.13006	0.00227
#40	0.94556	0.00073	0.12864	0.00204	#41	0.94393	0.00076	0.12792	0.0021
#42	0.94525	0.00075	0.12926	0.00208	#43	0.94468	0.00083	0.12858	0.00231
#44	0.9453	0.00081	0.12863	0.00225	#45	0.94577	0.00077	0.1305	0.00215

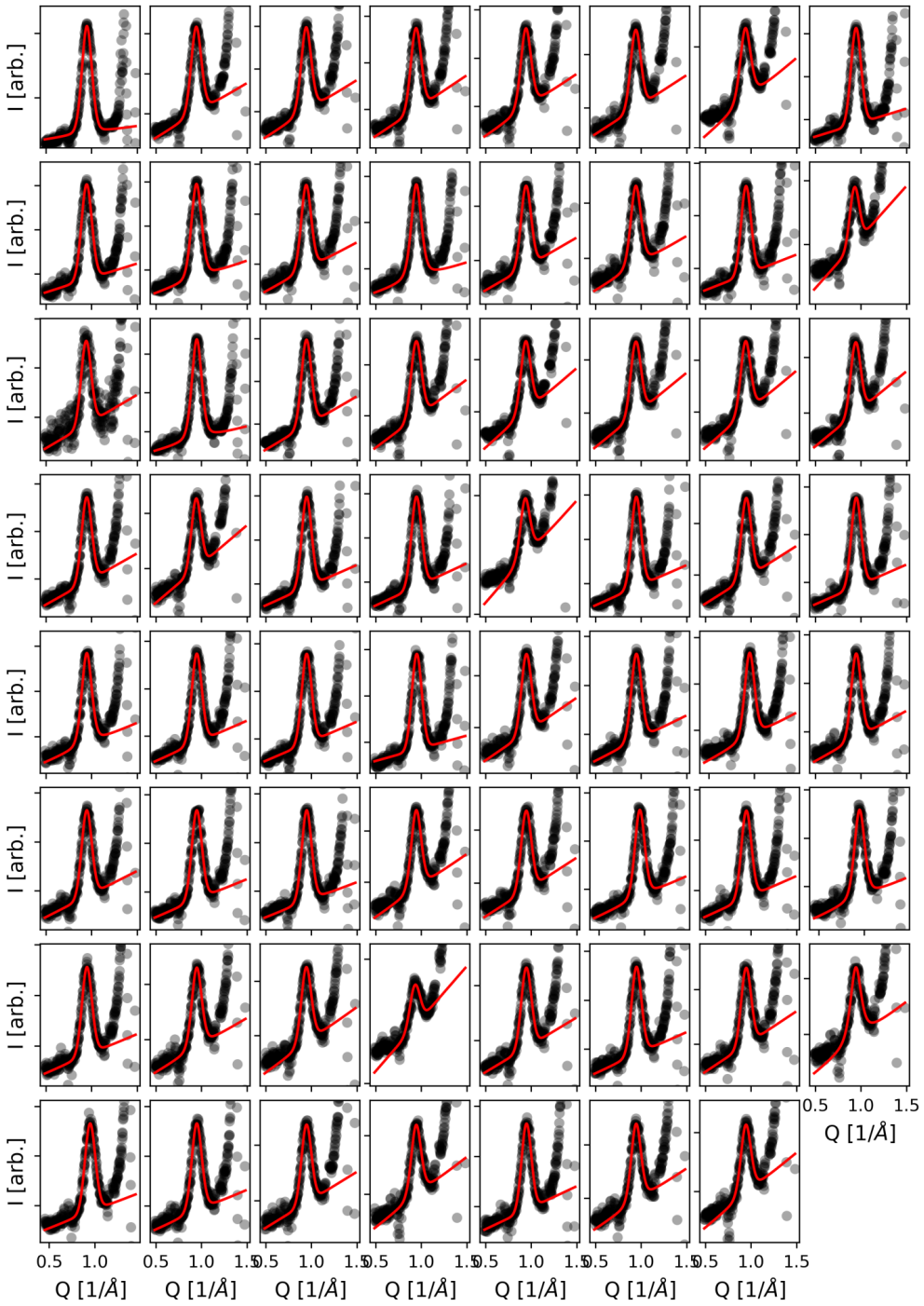

Figure E.33: Out of plane scans along Q_z, recorded at 773 K.

Table E.22: Center and full width half maximum (FWHM) for the fits presented in Figure E.33. For fits with multiple components, only fit results of the relevant component is shown.

	Center		FWHM			Center		FWHM	
	Value	Error	Value	Error		Value	Error	Value	Error
#0	0.948	0.00037	0.12849	0.00167	#1	0.94111	0.0005	0.13149	0.00234
#2	0.9413	0.0006	0.13046	0.00278	#3	0.94011	0.00063	0.13167	0.00272
#4	0.94018	0.00065	0.1325	0.00321	#5	0.93915	0.00146	0.12968	0.00442
#6	0.93651	0.00088	0.13631	0.00513	#7	0.94493	0.00049	0.12947	0.00208
#8	0.945	0.00051	0.13458	0.00238	#9	0.94425	0.00059	0.13224	0.00296
#10	0.94165	0.00067	0.12877	0.00296	#11	0.94433	0.00049	0.13201	0.0028
#12	0.94172	0.00065	0.13023	0.00276	#13	0.94026	0.00065	0.13134	0.0032
#14	0.94387	0.00063	0.12654	0.00251	#15	0.9278	0.00129	0.1197	0.00456
#16	0.93943	0.00176	0.12886	0.00734	#17	0.94772	0.00042	0.12693	0.00203
#18	0.94424	0.0005	0.12874	0.00212	#19	0.94272	0.00062	0.13285	0.00272
#20	0.93864	0.00077	0.12727	0.00342	#21	0.9399	0.00067	0.1297	0.00281
#22	0.93879	0.0007	0.12709	0.00306	#23	0.94012	0.00079	0.12628	0.00312
#24	0.9453	0.00053	0.13048	0.00227	#25	0.94028	0.00083	0.12099	0.00301
#26	0.94669	0.0005	0.12592	0.00201	#27	0.94567	0.00053	0.13105	0.00228
#28	0.93212	0.00115	0.12574	0.00536	#29	0.94578	0.00047	0.12481	0.00187
#30	0.94569	0.00064	0.12693	0.00259	#31	0.94684	0.00054	0.12736	0.00218
#32	0.94641	0.00051	0.12866	0.00242	#33	0.94712	0.00049	0.12892	0.00212
#34	0.94708	0.00054	0.12713	0.00219	#35	0.94919	0.00049	0.12722	0.002
#36	0.94569	0.00072	0.12778	0.00294	#37	0.94643	0.00053	0.13129	0.00239
#38	0.94592	0.00074	0.12703	0.00315	#39	0.94587	0.00058	0.12702	0.00245
#40	0.94589	0.00059	0.12983	0.00249	#41	0.94722	0.00057	0.13023	0.00255
#42	0.94731	0.0005	0.12681	0.00211	#43	0.94326	0.00066	0.12821	0.00293
#44	0.94377	0.00068	0.13052	0.00288	#45	0.94787	0.00067	0.12606	0.00278

Pd/Al_2O_3 - Pd(1 1 1) radial

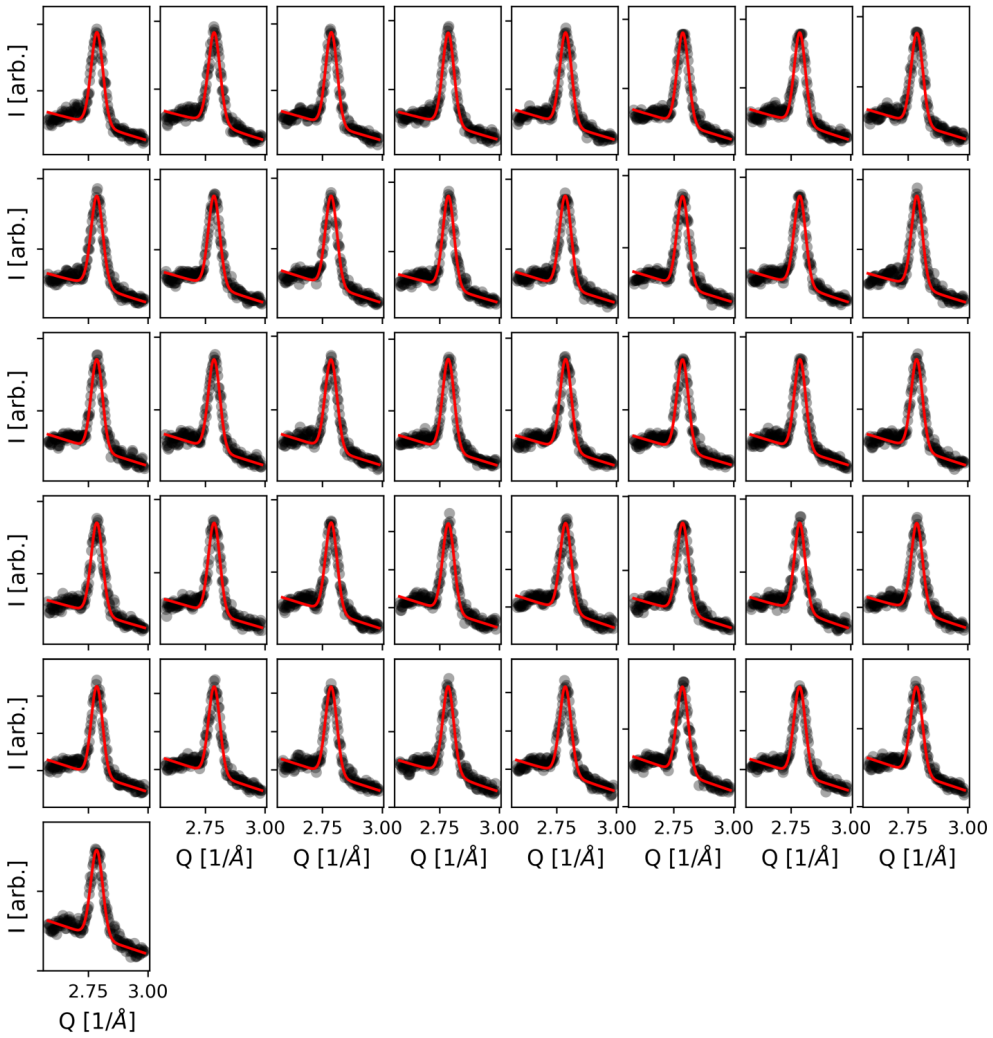

Figure E.34: Radial scans along Q_z, recorded at 523 K.

Table E.23: Center and full width half maximum (FWHM) for the fits presented in Figure E.34. For fits with multiple components, only fit results of the relevant component is shown.

	Center		FWHM			Center		FWHM	
	Value	Error	Value	Error		Value	Error	Value	Error
#0	2.78624	0.00101	0.05885	0.00285	#1	2.78658	0.00103	0.05913	0.00295
#2	2.7869	0.00094	0.05716	0.00259	#3	2.7859	0.00099	0.0565	0.00279
#4	2.78705	0.00098	0.05797	0.00268	#5	2.78722	0.00098	0.05646	0.00271
#6	2.78636	0.00099	0.05538	0.0028	#7	2.78671	0.00105	0.0578	0.00287
#8	2.786	0.00105	0.05912	0.003	#9	2.78598	0.00102	0.05701	0.00288
#10	2.78588	0.00102	0.05768	0.00282	#11	2.78666	0.001	0.0556	0.00282
#12	2.78553	0.001	0.05804	0.00276	#13	2.78634	0.00104	0.05685	0.00287
#14	2.78655	0.00104	0.05749	0.00294	#15	2.78658	0.00103	0.05535	0.00291
#16	2.78581	0.00104	0.05636	0.00287	#17	2.78624	0.00107	0.05739	0.00295
#18	2.78551	0.0011	0.05882	0.00302	#19	2.78622	0.00103	0.05719	0.00282
#20	2.78715	0.00104	0.05667	0.00291	#21	2.7861	0.00106	0.05689	0.00292
#22	2.78732	0.00103	0.05601	0.00283	#23	2.78589	0.00105	0.05667	0.00294
#24	2.78601	0.00106	0.05735	0.00296	#25	2.78642	0.00107	0.05712	0.00293
#26	2.78637	0.00107	0.05749	0.00297	#27	2.78655	0.00114	0.05671	0.00313
#28	2.78707	0.00113	0.05633	0.00317	#29	2.78665	0.0011	0.05802	0.0031
#30	2.78651	0.00105	0.05337	0.00304	#31	2.78625	0.00111	0.0569	0.00319
#32	2.786	0.00106	0.05585	0.00291	#33	2.78682	0.00114	0.05639	0.00315
#34	2.7859	0.00111	0.0567	0.00304	#35	2.78588	0.00113	0.05567	0.00327
#36	2.78583	0.00112	0.0571	0.00318	#37	2.78576	0.00117	0.05714	0.0032
#38	2.78587	0.00114	0.0571	0.00314	#39	2.78474	0.00117	0.0588	0.0032
#40	2.78539	0.00121	0.05897	0.00333					

Pd/Al_2O_3 - PdO(1 0 1) radial

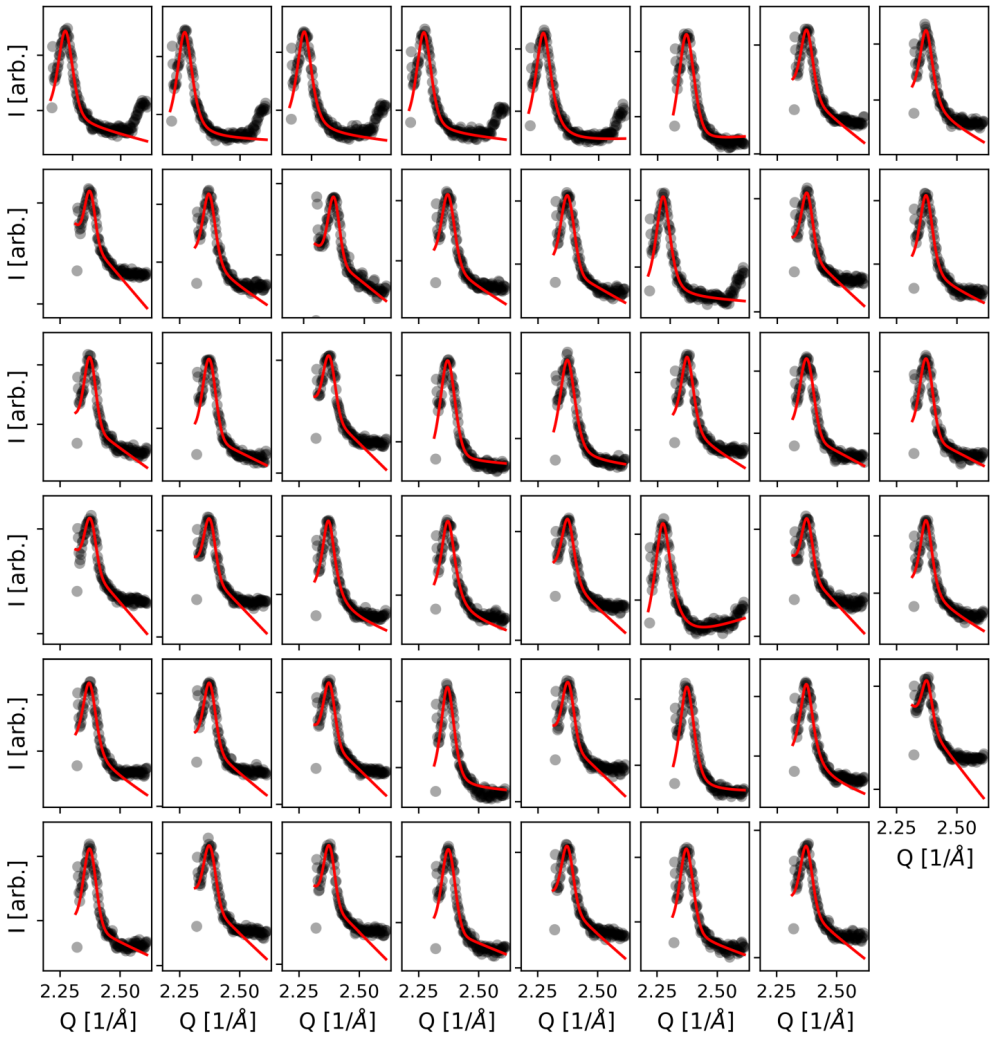

Figure E.35: Radial scans recorded at 623 K.

Table E.24: Center and full width half maximum (FWHM) for the fits presented in Figure E.35. For fits with multiple components, only fit results of the relevant component is shown.

	Center		FWHM			Center		FWHM	
	Value	Error	Value	Error		Value	Error	Value	Error
#0	2.37021	0.00052	0.07217	0.00265	#1	2.36938	0.00052	0.07598	0.00314
#2	2.3696	0.0006	0.07403	0.00357	#3	2.37004	0.00055	0.07227	0.00289
#4	2.36933	0.00054	0.08063	0.00379	#5	2.36932	0.00185	0.0764	0.00833
#6	2.37326	0.00102	0.06079	0.00481	#7	2.37261	0.00129	0.06664	0.00714
#8	2.37482	0.00086	0.04879	0.00351	#9	2.3726	0.00149	0.06217	0.00703
#10	2.3737	0.00077	0.05351	0.00299	#11	2.37229	0.00118	0.06435	0.00526
#12	2.37226	0.00149	0.06403	0.0059	#13	2.37081	0.00053	0.07071	0.00295
#14	2.37445	0.00096	0.05497	0.00416	#15	2.37262	0.00131	0.06439	0.00634
#16	2.37435	0.00106	0.05553	0.00438	#17	2.37313	0.00107	0.06253	0.00423
#18	2.37502	0.00153	0.05715	0.00608	#19	2.37071	0.00175	0.07166	0.00738
#20	2.37185	0.00198	0.07524	0.00932	#21	2.37343	0.00129	0.06217	0.00619
#22	2.37334	0.00139	0.06637	0.00525	#23	2.37269	0.00158	0.06356	0.00616
#24	2.3761	0.00103	0.05295	0.0041	#25	2.37491	0.00101	0.054	0.00405
#26	2.37221	0.00096	0.0662	0.00625	#27	2.37213	0.00138	0.07063	0.00821
#28	2.37363	0.00101	0.0609	0.00473	#29	2.36921	0.00086	0.08826	0.00713
#30	2.37487	0.00091	0.05194	0.00376	#31	2.37266	0.0009	0.06092	0.00466
#32	2.37202	0.00144	0.06611	0.00703	#33	2.37455	0.00095	0.05753	0.00418
#34	2.37539	0.001	0.05348	0.00399	#35	2.37009	0.00108	0.06613	0.00549
#36	2.37491	0.00105	0.05435	0.0042	#37	2.37153	0.00142	0.07232	0.00715
#38	2.37184	0.00125	0.0689	0.00789	#39	2.37632	0.00113	0.05061	0.00507
#40	2.3735	0.00135	0.06137	0.00565	#41	2.37506	0.00162	0.058	0.00654
#42	2.37543	0.00087	0.05143	0.00352	#43	2.37413	0.00137	0.06358	0.0054
#44	2.37386	0.00111	0.05798	0.00478	#45	2.37234	0.00135	0.06567	0.00606
#46	2.37375	0.00122	0.05953	0.0054					

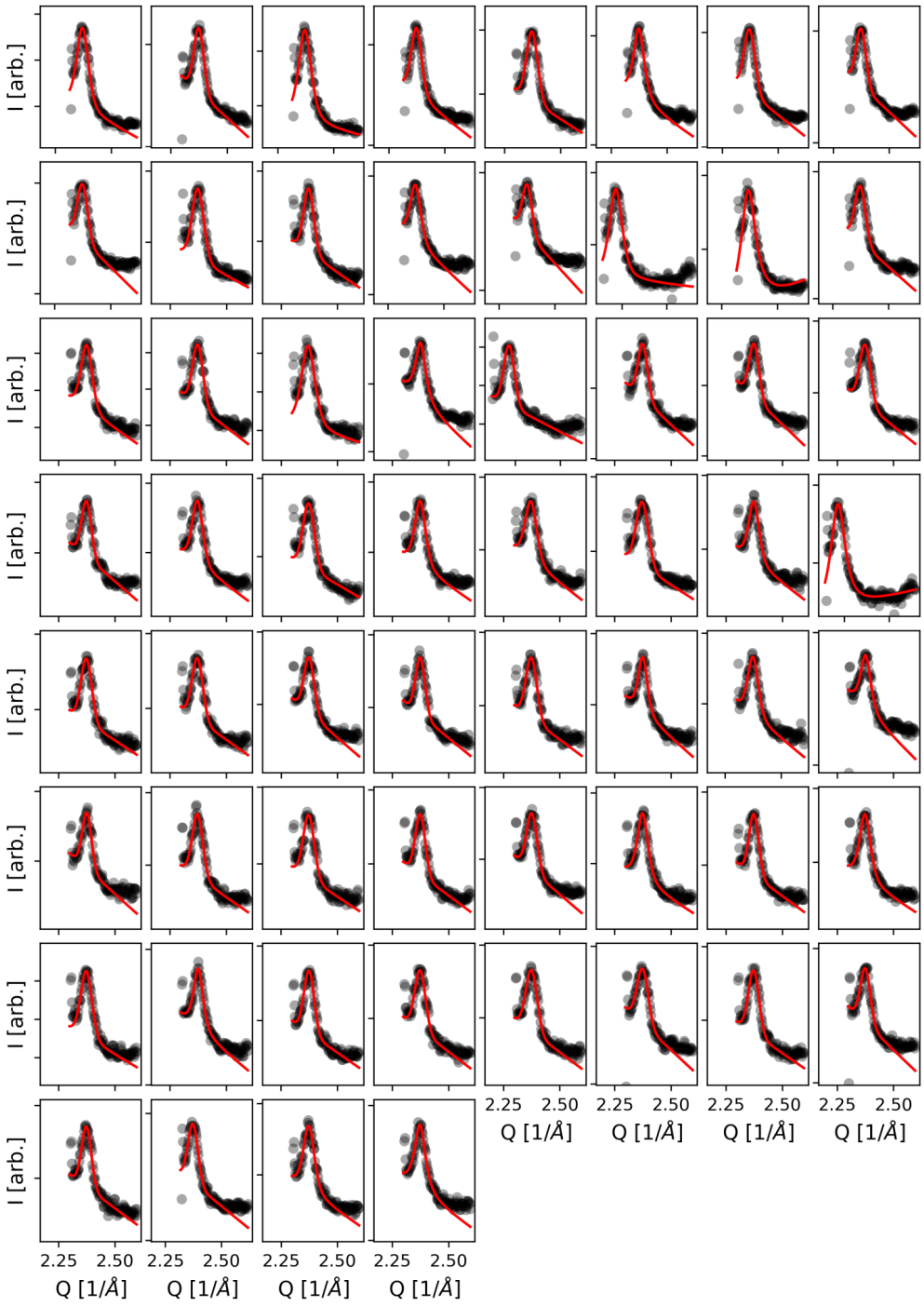

Figure E.36: Radial scans recorded at 673 K.

Table E.25: Center and full width half maximum (FWHM) for the fits presented in Figure E.36. For fits with multiple components, only fit results of the relevant component is shown.

	Center		FWHM			Center		FWHM	
	Value	Error	Value	Error		Value	Error	Value	Error
#0	2.37132	0.00092	0.06215	0.00448	#1	2.37379	0.00045	0.05137	0.00168
#2	2.37087	0.00143	0.06776	0.00763	#3	2.37247	0.00088	0.05573	0.00423
#4	2.37219	0.0007	0.05824	0.00283	#5	2.37352	0.0008	0.05803	0.00486
#6	2.37171	0.00082	0.05734	0.00346	#7	2.37321	0.00074	0.05132	0.00308
#8	2.37356	0.00099	0.05368	0.00413	#9	2.37174	0.00098	0.06066	0.00406
#10	2.37211	0.00077	0.05312	0.00306	#11	2.37309	0.0012	0.05662	0.00618
#12	2.37528	0.00102	0.04995	0.00419	#13	2.37182	0.0006	0.06884	0.0031
#14	2.36934	0.00243	0.08112	0.01881	#15	2.37259	0.00107	0.05537	0.00445
#16	2.37368	0.00087	0.05835	0.00383	#17	2.37339	0.00087	0.05457	0.00331
#18	2.36972	0.00133	0.07251	0.00725	#19	2.37512	0.00073	0.05463	0.00459
#20	2.37291	0.00059	0.05485	0.00221	#21	2.37403	0.00093	0.05018	0.00354
#22	2.37424	0.00081	0.05105	0.00295	#23	2.374	0.00085	0.05682	0.00327
#24	2.37306	0.00082	0.05046	0.00296	#25	2.37208	0.00072	0.05556	0.00323
#26	2.37214	0.00105	0.05915	0.00405	#27	2.37331	0.00087	0.05672	0.00441
#28	2.37121	0.00113	0.06072	0.00522	#29	2.37177	0.00107	0.06349	0.00418
#30	2.37354	0.00094	0.05527	0.00453	#31	2.37071	0.00072	0.07746	0.00509
#32	2.37279	0.00104	0.056	0.00398	#33	2.3719	0.00096	0.05641	0.00367
#34	2.37382	0.00077	0.05321	0.00306	#35	2.37374	0.0007	0.04915	0.0025
#36	2.37331	0.00089	0.05712	0.00341	#37	2.37426	0.00055	0.04739	0.00235
#38	2.37448	0.00079	0.0549	0.00347	#39	2.37654	0.00069	0.05384	0.00378
#40	2.37485	0.00073	0.04845	0.0026	#41	2.37239	0.00095	0.0556	0.00386
#42	2.37246	0.00121	0.05738	0.00484	#43	2.37389	0.00072	0.05115	0.00262
#44	2.37512	0.00073	0.05494	0.00278	#45	2.3735	0.00072	0.05631	0.0039

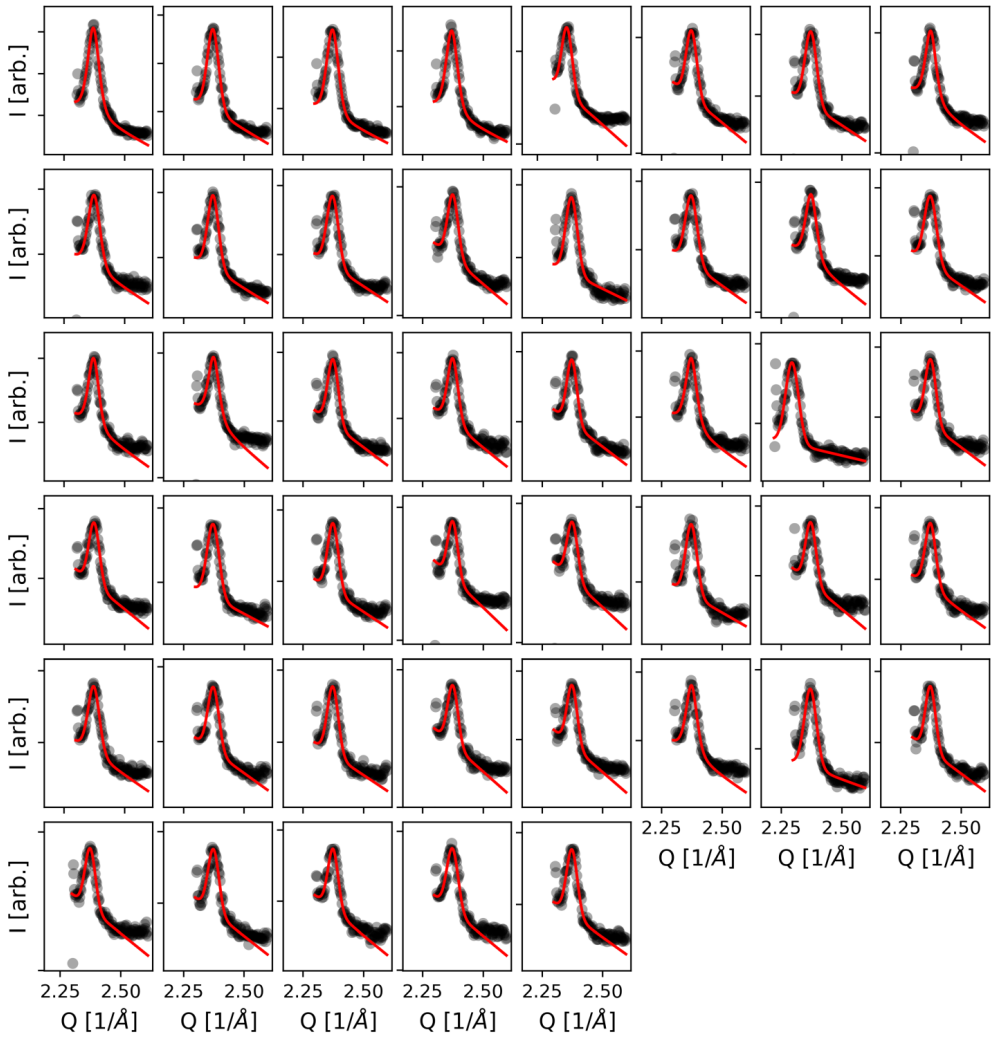

Figure E.37: Radial scans recorded at 723 K.

Table E.26: Center and full width half maximum (FWHM) for the fits presented in Figure E.37. For fits with multiple components, only fit results of the relevant component is shown.

	Center		FWHM			Center		FWHM	
	Value	Error	Value	Error		Value	Error	Value	Error
#0	2.37111	0.00045	0.05633	0.00218	#1	2.37117	0.00052	0.05617	0.00214
#2	2.37148	0.00042	0.05688	0.00178	#3	2.37027	0.00055	0.05688	0.00254
#4	2.37266	0.00063	0.05148	0.00264	#5	2.37286	0.00058	0.05219	0.00215
#6	2.37214	0.00072	0.05622	0.00275	#7	2.37356	0.00049	0.05316	0.00244
#8	2.37367	0.0006	0.05782	0.00269	#9	2.37161	0.00055	0.05377	0.00222
#10	2.37153	0.00073	0.05598	0.00277	#11	2.3746	0.00069	0.05136	0.00264
#12	2.3709	0.00076	0.05639	0.00288	#13	2.37204	0.00078	0.05764	0.0031
#14	2.37332	0.00069	0.05424	0.00312	#15	2.37261	0.00087	0.05895	0.00338
#16	2.37167	0.00058	0.05122	0.00252	#17	2.37395	0.0005	0.05339	0.00247
#18	2.37343	0.00052	0.05147	0.00192	#19	2.37421	0.00057	0.05167	0.00233
#20	2.37264	0.00059	0.04875	0.00212	#21	2.37202	0.00069	0.05498	0.00335
#22	2.37056	0.00071	0.06295	0.00288	#23	2.37317	0.00079	0.05221	0.00293
#24	2.37407	0.00073	0.05128	0.00266	#25	2.37167	0.00083	0.05799	0.0032
#26	2.37331	0.00073	0.05224	0.00272	#27	2.37432	0.00064	0.04815	0.00224
#28	2.37429	0.00083	0.05153	0.00302	#29	2.37217	0.00093	0.05451	0.00349
#30	2.3725	0.00063	0.05084	0.00229	#31	2.37269	0.00069	0.0523	0.00283
#32	2.37246	0.00073	0.05591	0.00303	#33	2.37274	0.00076	0.05378	0.00284
#34	2.37256	0.00063	0.05289	0.00234	#35	2.37444	0.00071	0.05031	0.00255
#36	2.37352	0.00065	0.04945	0.00234	#37	2.37336	0.00062	0.05416	0.00302
#38	2.37023	0.00075	0.05919	0.00301	#39	2.37269	0.00055	0.04909	0.00197
#40	2.37371	0.00071	0.05059	0.00254	#41	2.3734	0.0008	0.05287	0.00297
#42	2.37365	0.00065	0.0504	0.00247	#43	2.37322	0.00092	0.05506	0.00349
#44	2.3729	0.00082	0.05242	0.00312					

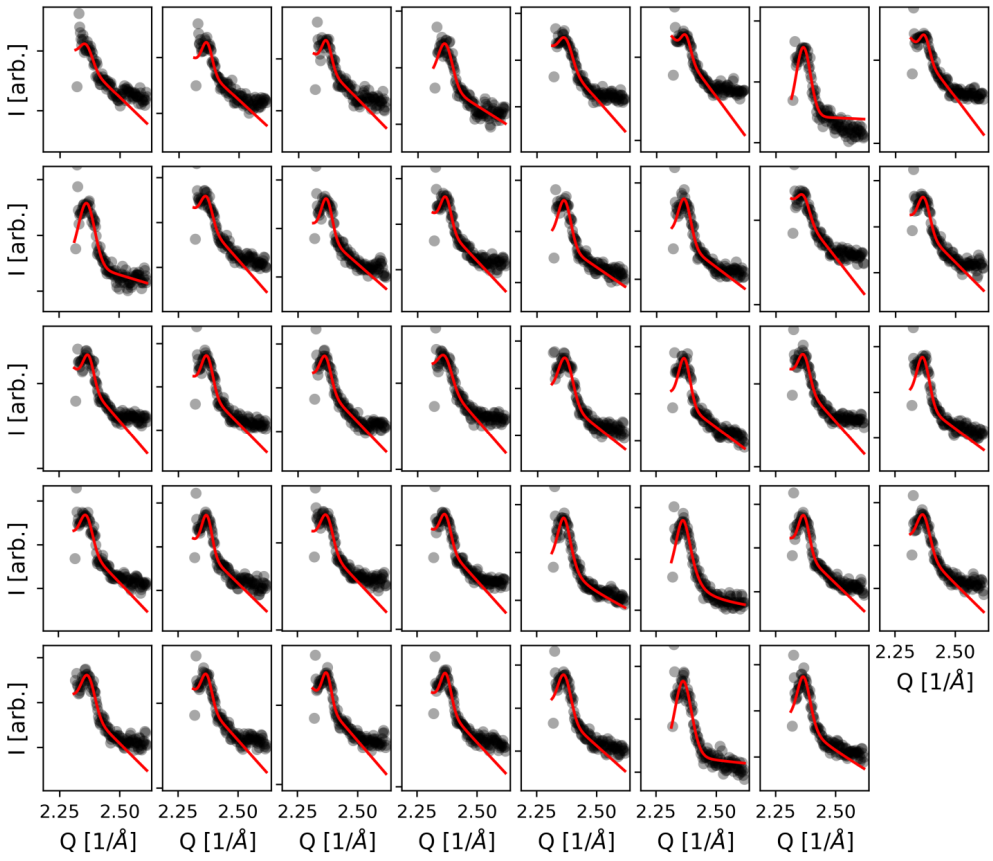

Figure E.38: Radial scans recorded at 573 K.

Table E.27: Center and full width half maximum (FWHM) for the fits presented in Figure E.38. For fits with multiple components, only fit results of the relevant component is shown.

	Center		FWHM			Center		FWHM	
	Value	Error	Value	Error		Value	Error	Value	Error
#0	2.35917	0.00645	0.06134	0.02688	#1	2.36676	0.00283	0.05018	0.01181
#2	2.36712	0.00296	0.04704	0.0123	#3	2.36319	0.00552	0.07025	0.02241
#4	2.36931	0.00463	0.06473	0.01858	#5	2.37282	0.00202	0.04638	0.00823
#6	2.36359	0.00296	0.0699	0.0121	#7	2.37215	0.00244	0.04605	0.00995
#8	2.36515	0.0046	0.07946	0.01733	#9	2.36753	0.00351	0.05511	0.01467
#10	2.3696	0.0027	0.054	0.01121	#11	2.3686	0.00224	0.05112	0.00934
#12	2.36453	0.0024	0.06211	0.01001	#13	2.3664	0.00294	0.06165	0.01221
#14	2.36496	0.00453	0.0576	0.01901	#15	2.36838	0.0028	0.05744	0.01165
#16	2.37288	0.00273	0.05167	0.01116	#17	2.36963	0.00261	0.05501	0.01085
#18	2.3644	0.00243	0.05552	0.01071	#19	2.36441	0.00615	0.0677	0.02522
#20	2.36558	0.00436	0.07036	0.01672	#21	2.36782	0.00245	0.05622	0.01026
#22	2.36781	0.00292	0.05606	0.01219	#23	2.3659	0.00233	0.0611	0.00973
#24	2.36616	0.00372	0.06034	0.01553	#25	2.3702	0.00189	0.04979	0.00785
#26	2.37136	0.00329	0.0596	0.01341	#27	2.36804	0.00223	0.0533	0.00933
#28	2.36407	0.00325	0.07098	0.01823	#29	2.36172	0.00529	0.08628	0.03439
#30	2.36789	0.00172	0.05266	0.00722	#31	2.36784	0.00254	0.06442	0.01128
#32	2.36777	0.00475	0.06616	0.01843	#33	2.3689	0.00239	0.05149	0.00995
#34	2.37157	0.00168	0.04478	0.00685	#35	2.36986	0.00185	0.05275	0.00816
#36	2.36564	0.00296	0.06399	0.0123	#37	2.36255	0.00499	0.08273	0.0207
#38	2.36652	0.00269	0.06773	0.01306					

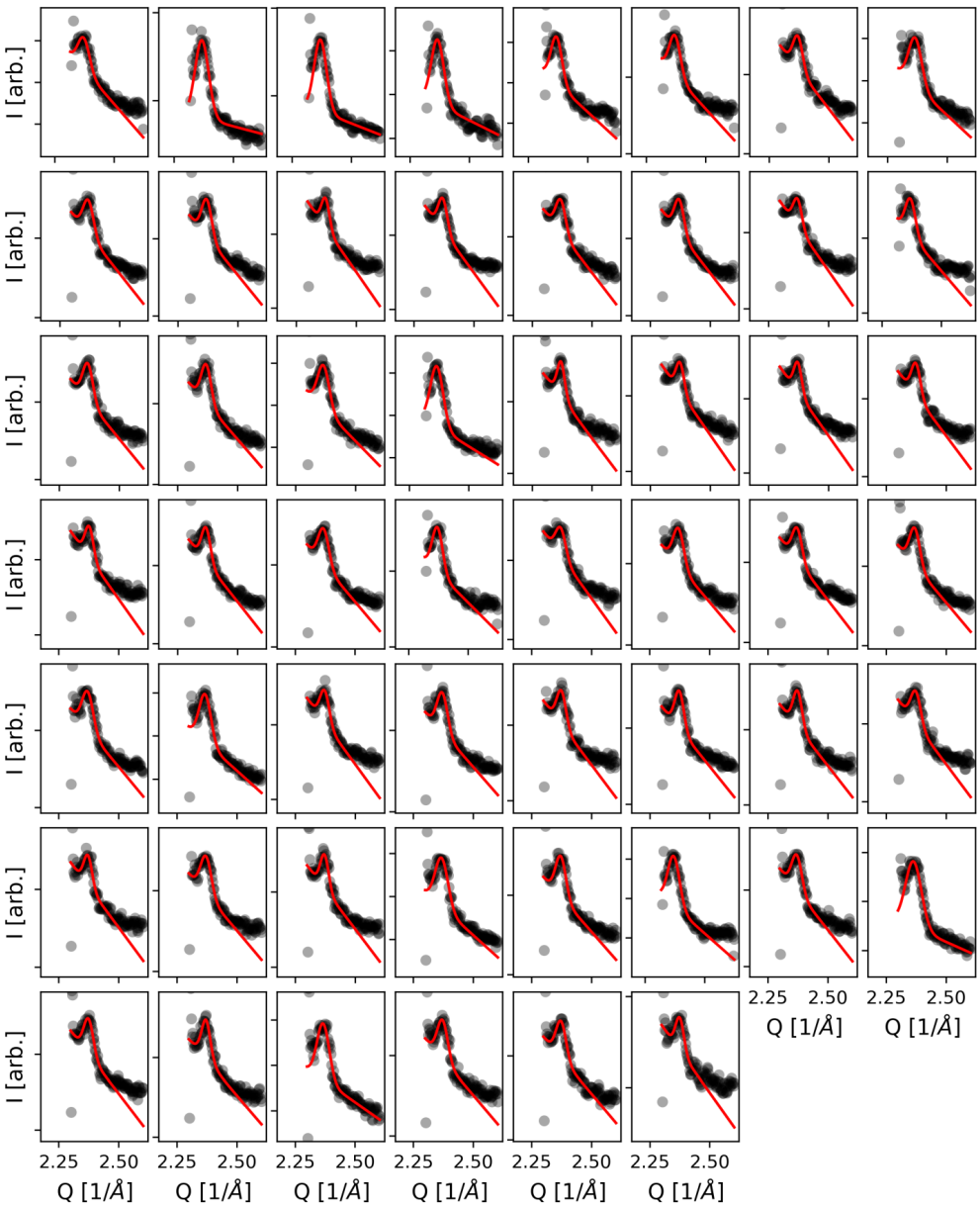

Figure E.39: Radial scans recorded at 623 K.

Table E.28: Center and full width half maximum (FWHM) for the fits presented in Figure E.39. For fits with multiple components, only fit results of the relevant component is shown.

	Center		FWHM			Center		FWHM	
	Value	Error	Value	Error		Value	Error	Value	Error
#0	2.37271	0.00286	0.0569	0.01184	#1	2.36703	0.0022	0.06748	0.00895
#2	2.36892	0.00129	0.06121	0.00535	#3	2.36539	0.00193	0.0628	0.00814
#4	2.36867	0.00189	0.05517	0.00794	#5	2.3704	0.00173	0.05484	0.00724
#6	2.36967	0.00159	0.04711	0.0056	#7	2.36608	0.00205	0.06435	0.00763
#8	2.36902	0.00178	0.05134	0.00657	#9	2.36972	0.00116	0.0489	0.00419
#10	2.37175	0.00132	0.03941	0.00402	#11	2.37029	0.00091	0.04431	0.00307
#12	2.36924	0.00162	0.0483	0.00581	#13	2.37064	0.00122	0.04692	0.00426
#14	2.37103	0.00154	0.043	0.00504	#15	2.36925	0.00199	0.05031	0.0083
#16	2.36898	0.00141	0.04991	0.00514	#17	2.36937	0.0013	0.04847	0.00468
#18	2.36581	0.00195	0.05742	0.00744	#19	2.36568	0.00156	0.06354	0.00657
#20	2.37023	0.00091	0.0383	0.00309	#21	2.37399	0.0012	0.0396	0.00357
#22	2.37212	0.00091	0.0387	0.00272	#23	2.37413	0.00148	0.04413	0.00487
#24	2.37679	0.00108	0.04137	0.00329	#25	2.36872	0.00101	0.04372	0.00346
#26	2.36852	0.00174	0.05218	0.00659	#27	2.37071	0.00138	0.0514	0.00578
#28	2.37142	0.0019	0.04934	0.0069	#29	2.36982	0.00137	0.0518	0.00513
#30	2.37158	0.00135	0.04788	0.00483	#31	2.36919	0.00148	0.05057	0.00553
#32	2.37036	0.00172	0.05422	0.00648	#33	2.36712	0.00209	0.0581	0.008
#34	2.3728	0.00131	0.04511	0.00444	#35	2.3706	0.00159	0.05164	0.00593
#36	2.37413	0.00145	0.04548	0.00487	#37	2.3731	0.00107	0.04484	0.0036
#38	2.37341	0.00115	0.04396	0.00381	#39	2.37338	0.00186	0.04911	0.0066
#40	2.37153	0.00142	0.04145	0.00465	#41	2.37086	0.00151	0.05277	0.00564
#42	2.37229	0.0011	0.04083	0.00353	#43	2.36767	0.0026	0.06293	0.00978
#44	2.37169	0.00123	0.05072	0.0045	#45	2.37017	0.00126	0.05852	0.00535

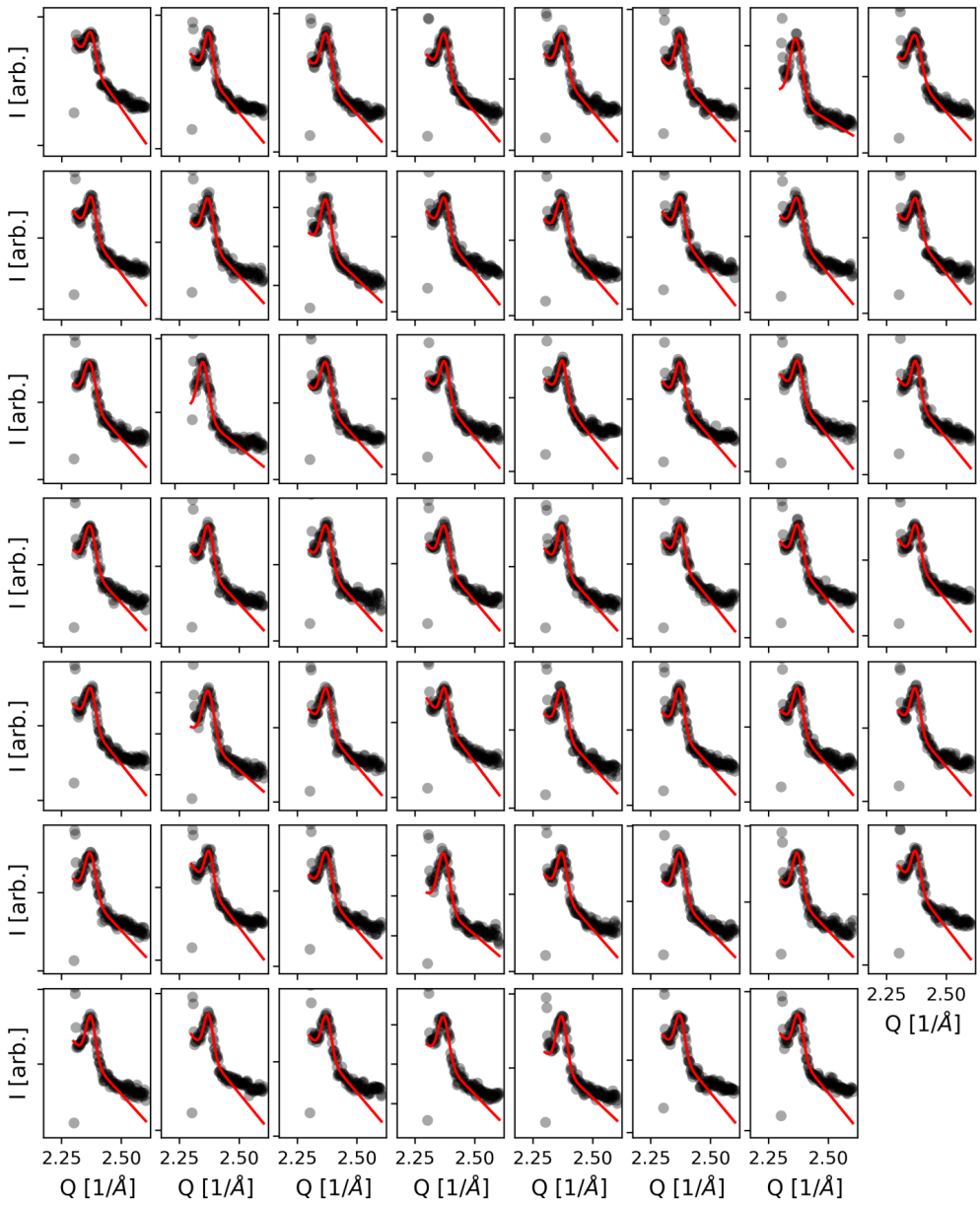

Figure E.40: Radial scans recorded at 623 K.

Table E.29: Center and full width half maximum (FWHM) for the fits presented in Figure E.40. For fits with multiple components, only fit results of the relevant component is shown.

	Center		FWHM			Center		FWHM	
	Value	Error	Value	Error		Value	Error	Value	Error
#0	2.37254	0.001	0.04629	0.00348	#1	2.37237	0.00072	0.04246	0.00239
#2	2.37149	0.00119	0.05153	0.00439	#3	2.37168	0.00091	0.04713	0.00322
#4	2.37243	0.00129	0.0506	0.00472	#5	2.37215	0.00096	0.04613	0.00334
#6	2.36897	0.00181	0.06008	0.007	#7	2.37096	0.00176	0.05809	0.00667
#8	2.37385	0.00096	0.04557	0.00325	#9	2.37049	0.0014	0.05176	0.00522
#10	2.36915	0.00129	0.05047	0.00484	#11	2.37255	0.00115	0.04593	0.00399
#12	2.3711	0.00128	0.05038	0.00472	#13	2.37446	0.00092	0.04252	0.00294
#14	2.37017	0.00154	0.05309	0.00578	#15	2.37313	0.00114	0.04912	0.00405
#16	2.36814	0.00149	0.05425	0.00569	#17	2.36953	0.00154	0.05459	0.00691
#18	2.36939	0.00157	0.05186	0.00592	#19	2.37358	0.00095	0.04618	0.00327
#20	2.3737	0.00073	0.04418	0.00285	#21	2.3717	0.00108	0.04501	0.00373
#22	2.37246	0.0011	0.04555	0.00378	#23	2.37296	0.00098	0.04383	0.00329
#24	2.36942	0.0015	0.05316	0.00567	#25	2.37032	0.0012	0.04855	0.0044
#26	2.37134	0.00137	0.05404	0.00511	#27	2.372	0.00133	0.04895	0.00478
#28	2.37205	0.00094	0.04312	0.00316	#29	2.37308	0.00087	0.04166	0.00279
#30	2.37243	0.00116	0.04717	0.00406	#31	2.37356	0.00082	0.04379	0.00271
#32	2.37152	0.00118	0.04768	0.00421	#33	2.3706	0.00149	0.05773	0.00566
#34	2.37177	0.00117	0.04841	0.00419	#35	2.37329	0.00086	0.03946	0.00264
#36	2.37032	0.00127	0.04988	0.0047	#37	2.36964	0.00102	0.04623	0.00368
#38	2.37205	0.00122	0.0481	0.00437	#39	2.37102	0.00102	0.04638	0.00361
#40	2.37011	0.00152	0.05346	0.00573	#41	2.37399	0.00093	0.04318	0.00305
#42	2.3723	0.00127	0.05182	0.00466	#43	2.3696	0.00162	0.05685	0.00615
#44	2.37138	0.00115	0.04832	0.00413	#45	2.37129	0.00114	0.0513	0.00422

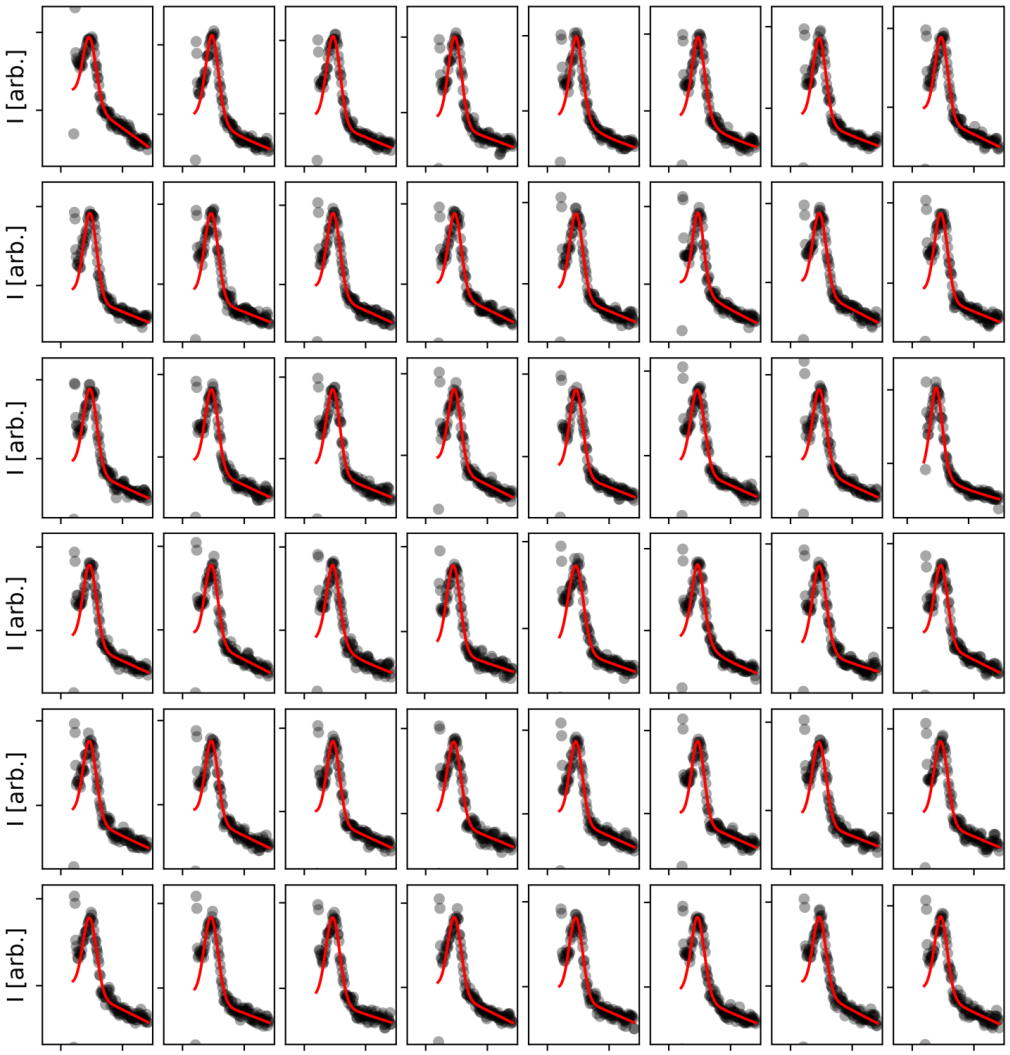

Figure E.41: Radial scans recorded at 723 K. Continued in Figure E.42.

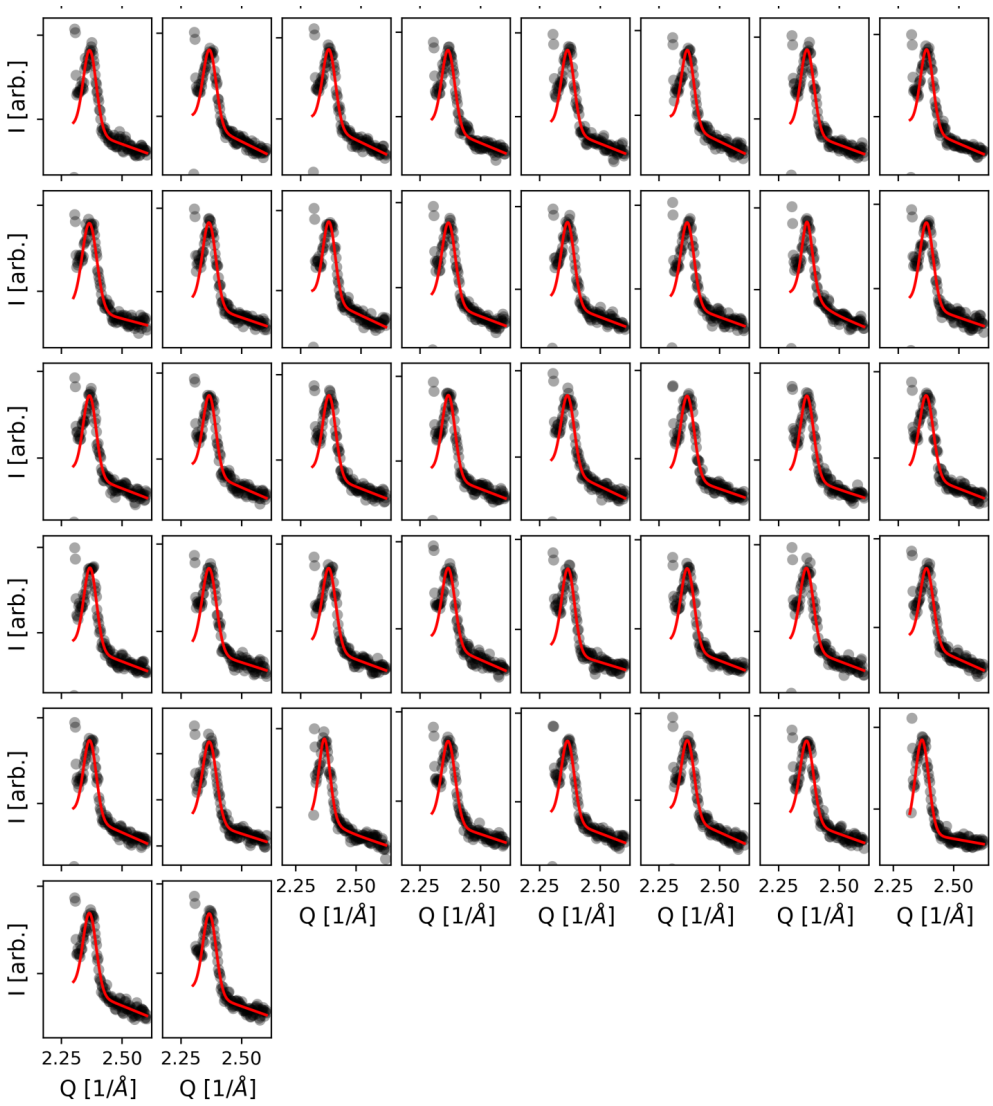

Figure E.42: Radial scans recorded at 723 K. Continuation of Figure E.41.

Table E.30: Center and full width half maximum (FWHM) for the fits presented in Figure E.41 and Figure E.42. For fits with multiple components, only fit results of the relevant component is shown.

	Center		FWHM			Center		FWHM	
	Value	Error	Value	Error		Value	Error	Value	Error
#0	2.36551	0.00069	0.06365	0.00255	#1	2.36935	0.00056	0.0643	0.00241
#2	2.36826	0.00053	0.06493	0.002	#3	2.36808	0.00067	0.06338	0.0025
#4	2.36789	0.00056	0.06249	0.00252	#5	2.36901	0.00063	0.06445	0.00286
#6	2.36699	0.0006	0.06245	0.00232	#7	2.36834	0.00063	0.06183	0.00232
#8	2.36791	0.00058	0.06256	0.00215	#9	2.36683	0.00067	0.06481	0.00249
#10	2.36834	0.00052	0.06391	0.00192	#11	2.368	0.00069	0.06219	0.00252
#12	2.36676	0.00062	0.063	0.00228	#13	2.36834	0.00057	0.05578	0.00223
#14	2.36748	0.00071	0.06445	0.00266	#15	2.36661	0.00072	0.0629	0.00266
#16	2.36778	0.00063	0.06478	0.00244	#17	2.36772	0.00067	0.06263	0.00245
#18	2.36674	0.00063	0.06515	0.00233	#19	2.36656	0.00059	0.06143	0.00215
#20	2.36712	0.0005	0.0632	0.00183	#21	2.36622	0.00069	0.06592	0.00257
#22	2.36716	0.00051	0.06473	0.00199	#23	2.36861	0.00038	0.05998	0.00141
#24	2.3668	0.00058	0.06482	0.00215	#25	2.36683	0.0007	0.06168	0.00253
#26	2.36634	0.00073	0.06588	0.00323	#27	2.36696	0.00067	0.06483	0.00245
#28	2.36571	0.00082	0.07189	0.00315	#29	2.36708	0.00057	0.06272	0.00255
#30	2.36667	0.00069	0.06778	0.00279	#31	2.36693	0.00066	0.0628	0.00243
#32	2.36605	0.00072	0.06436	0.00278	#33	2.36779	0.00066	0.0613	0.00244
#34	2.36758	0.00056	0.06084	0.00204	#35	2.36441	0.0008	0.06642	0.00297
#36	2.36632	0.00066	0.06107	0.00237	#37	2.36747	0.00066	0.06012	0.00238
#38	2.36599	0.00077	0.06595	0.00285	#39	2.36649	0.00085	0.06529	0.00318
#40	2.36641	0.00079	0.06572	0.00295	#41	2.36571	0.00068	0.06694	0.00254
#42	2.36606	0.00068	0.06828	0.00264	#43	2.36664	0.00076	0.06403	0.00282
#44	2.36587	0.00076	0.0637	0.00281	#45	2.36656	0.0007	0.06548	0.00283

E.4.2 HEGIXRD line scan analysis of Pd_3Pt_1/Al_2O_3

Pd_3Pt_1/Al_2O_3 - Pd(1 1 1) in plane

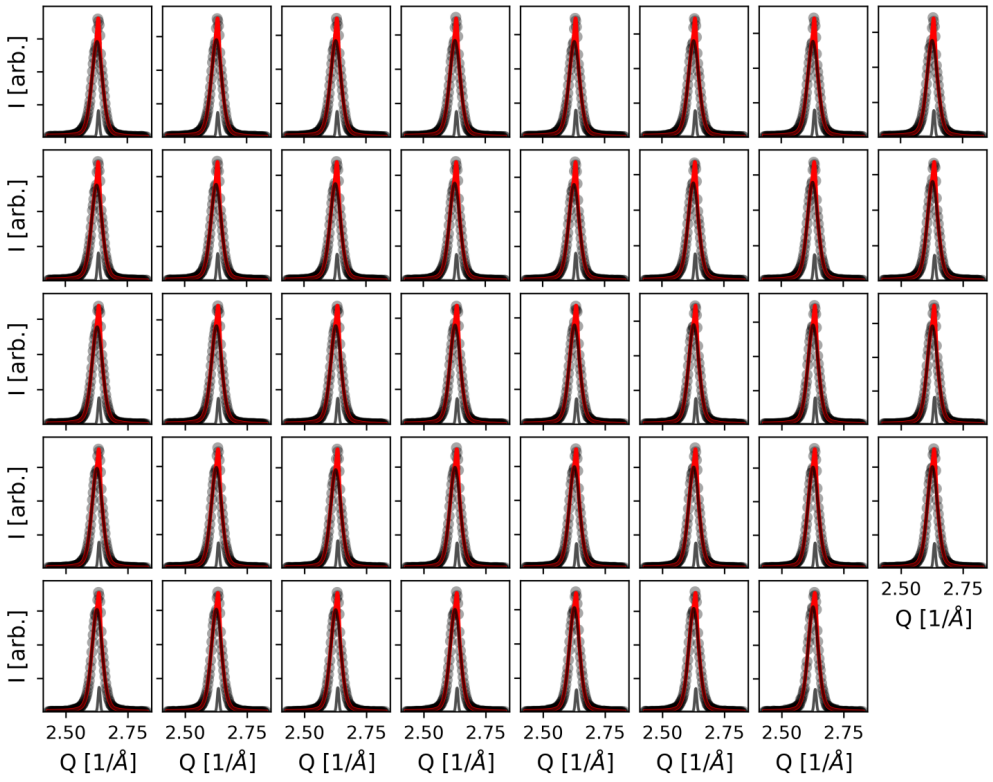

Figure E.43: In plane scans and fits along Q_{xy}, recorded at 523 K.

Table E.31: Center and full width half maximum (FWHM) for the fits presented in Figure E.43. For fits with multiple components, only fit results of the relevant component is shown.

	Center		FWHM			Center		FWHM	
	Value	Error	Value	Error		Value	Error	Value	Error
#0	2.62837	0.00018	0.05087	0.00055	#1	2.6283	0.00017	0.05047	0.00052
#2	2.62811	0.00017	0.05087	0.00052	#3	2.62776	0.00017	0.05103	0.0005
#4	2.62769	0.00017	0.05106	0.00049	#5	2.62754	0.00017	0.05112	0.00047
#6	2.62746	0.00017	0.05103	0.00047	#7	2.62717	0.00018	0.05097	0.00045
#8	2.62694	0.00017	0.05123	0.00044	#9	2.62679	0.00016	0.05093	0.0004
#10	2.62671	0.00016	0.05115	0.00039	#11	2.62666	0.00017	0.05092	0.00041
#12	2.62642	0.00015	0.05126	0.00036	#13	2.62629	0.00015	0.05078	0.00034
#14	2.62624	0.00016	0.05094	0.00034	#15	2.62618	0.00015	0.05079	0.00031
#16	2.62612	0.00016	0.05107	0.00035	#17	2.62594	0.00015	0.05065	0.00033
#18	2.62585	0.00014	0.05068	0.00031	#19	2.62583	0.00015	0.05073	0.00031
#20	2.62585	0.00015	0.0506	0.00031	#21	2.62565	0.00016	0.05006	0.00034
#22	2.62556	0.00016	0.05013	0.00032	#23	2.62553	0.00016	0.05038	0.00032
#24	2.62548	0.00016	0.05002	0.00033	#25	2.62547	0.00017	0.05	0.00034
#26	2.62561	0.00015	0.05039	0.00031	#27	2.62542	0.00015	0.05024	0.00031
#28	2.62563	0.00014	0.04983	0.0003	#29	2.62549	0.00017	0.04983	0.00034
#30	2.62541	0.00016	0.05	0.00033	#31	2.6255	0.00016	0.04956	0.00032
#32	2.62553	0.00017	0.04948	0.00033	#33	2.62546	0.00018	0.04979	0.00036
#34	2.62551	0.00016	0.04979	0.00033	#35	2.6255	0.00016	0.04969	0.00033
#36	2.62549	0.00018	0.04943	0.00035	#37	2.62547	0.00016	0.04925	0.00033
#38	2.62554	0.00019	0.04831	0.00034					

Table E.32: Center and full width half maximum (FWHM) for the fits presented in Figure E.44. For fits with multiple components, only fit results of the relevant component is shown.

	Center		FWHM			Center		FWHM	
	Value	Error	Value	Error		Value	Error	Value	Error
#0	2.62839	0.00014	0.0468	0.00033	#1	2.62815	7e-05	0.04717	0.00021
#2	2.62789	7e-05	0.04779	0.00018	#3	2.62769	7e-05	0.04788	0.00019
#4	2.62737	6e-05	0.0482	0.00018	#5	2.62724	6e-05	0.04806	0.00018
#6	2.62709	6e-05	0.04814	0.00017	#7	2.62699	6e-05	0.04798	0.00017
#8	2.62686	8e-05	0.0485	0.00021	#9	2.62692	7e-05	0.04817	0.00019
#10	2.62686	6e-05	0.0482	0.00017	#11	2.62663	7e-05	0.04845	0.00018
#12	2.62673	6e-05	0.04865	0.00018	#13	2.62661	6e-05	0.04831	0.00018
#14	2.6267	5e-05	0.04825	0.00015	#15	2.62656	6e-05	0.04876	0.00017
#16	2.62645	7e-05	0.04861	0.00019	#17	2.62654	6e-05	0.04829	0.00018
#18	2.62638	7e-05	0.04878	0.00017	#19	2.62629	7e-05	0.04867	0.00018
#20	2.62631	7e-05	0.04907	0.00018	#21	2.62626	7e-05	0.04864	0.00022
#22	2.62625	8e-05	0.04913	0.00022	#23	2.62628	7e-05	0.04918	0.00019
#24	2.62624	6e-05	0.04874	0.00018	#25	2.62619	7e-05	0.04909	0.00018
#26	2.62633	6e-05	0.04898	0.00018	#27	2.62613	6e-05	0.04904	0.00017
#28	2.62623	8e-05	0.04929	0.00023	#29	2.62616	7e-05	0.04903	0.00021
#30	2.62623	8e-05	0.04908	0.00023	#31	2.62618	9e-05	0.0493	0.00027
#32	2.6261	8e-05	0.04936	0.00023	#33	2.62618	9e-05	0.04945	0.00026
#34	2.6262	9e-05	0.04945	0.00025	#35	2.626	9e-05	0.04952	0.00024
#36	2.62607	8e-05	0.0495	0.00023	#37	2.62595	8e-05	0.04964	0.00024
#38	2.62592	7e-05	0.04972	0.0002	#39	2.626	8e-05	0.0495	0.00025
#40	2.626	9e-05	0.04967	0.00024					

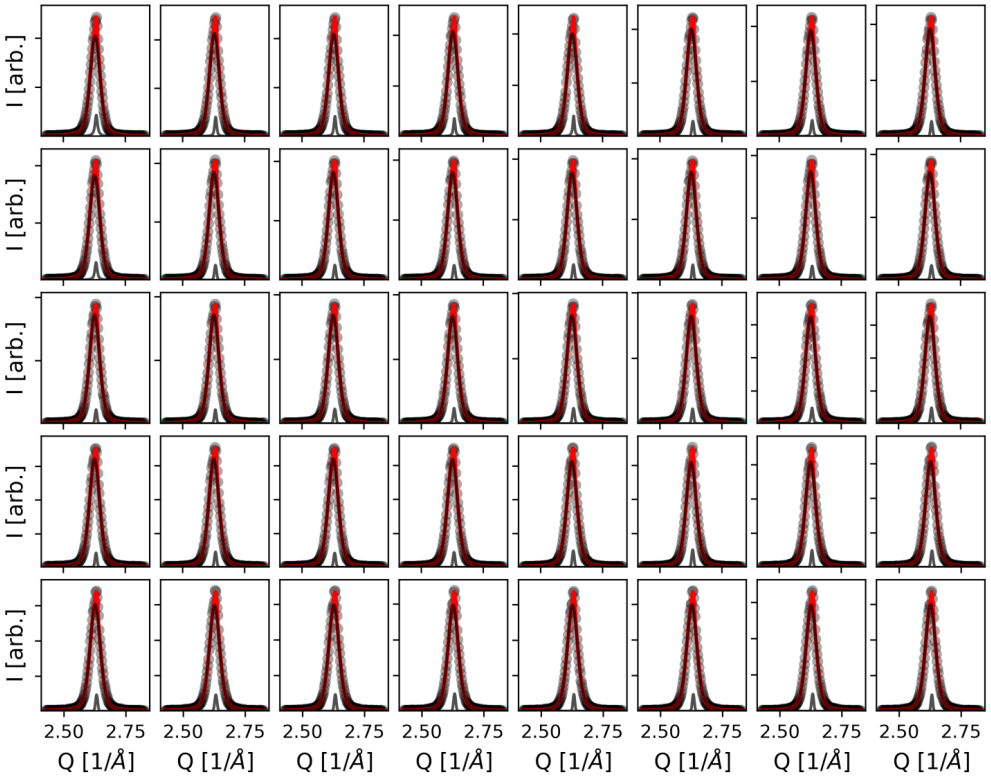

Figure E.44: In plane scans and fits along Q_{xy}, recorded at 573 K.

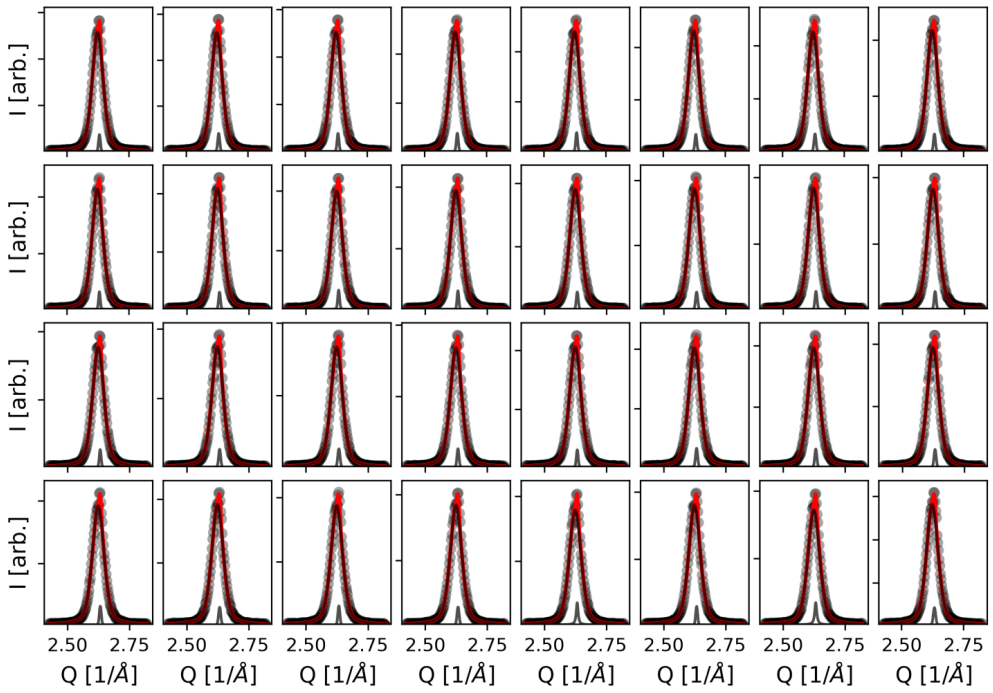

Figure E.45: In plane scans and fits along Q_{xy}, recorded at 623 K.

Table E.33: Center and full width half maximum (FWHM) for the fits presented in Figure E.45. For fits with multiple components, only fit results of the relevant component is shown.

	Center		FWHM			Center		FWHM	
	Value	Error	Value	Error		Value	Error	Value	Error
#0	2.62428	9e-05	0.05211	0.00023	#1	2.6239	0.0001	0.05265	0.00025
#2	2.62379	0.0001	0.05249	0.00024	#3	2.62369	0.0001	0.05264	0.00023
#4	2.62364	9e-05	0.05286	0.00022	#5	2.62361	0.0001	0.05306	0.00024
#6	2.62365	0.0001	0.05329	0.00025	#7	2.62368	9e-05	0.0532	0.00021
#8	2.62358	8e-05	0.05316	0.00021	#9	2.62344	0.0001	0.05339	0.00025
#10	2.62338	9e-05	0.0542	0.00024	#11	2.62347	0.0001	0.05428	0.00026
#12	2.62362	9e-05	0.05428	0.00024	#13	2.62349	0.0001	0.05456	0.00023
#14	2.62333	0.0001	0.05438	0.00023	#15	2.62343	0.0001	0.05481	0.00023
#16	2.62352	9e-05	0.05451	0.00025	#17	2.62344	0.00011	0.05474	0.00026
#18	2.62333	0.00011	0.0552	0.00025	#19	2.62338	9e-05	0.05507	0.00023
#20	2.62348	9e-05	0.05499	0.00024	#21	2.62336	0.0001	0.05558	0.00023
#22	2.62348	0.00011	0.05555	0.00027	#23	2.62342	0.0001	0.05564	0.00026
#24	2.62348	0.00011	0.05581	0.00027	#25	2.62359	0.00012	0.0556	0.00027
#26	2.6235	9e-05	0.0555	0.00023	#27	2.62343	0.0001	0.05547	0.00024
#28	2.6234	0.00011	0.05643	0.00029	#29	2.62348	0.00011	0.05558	0.00028

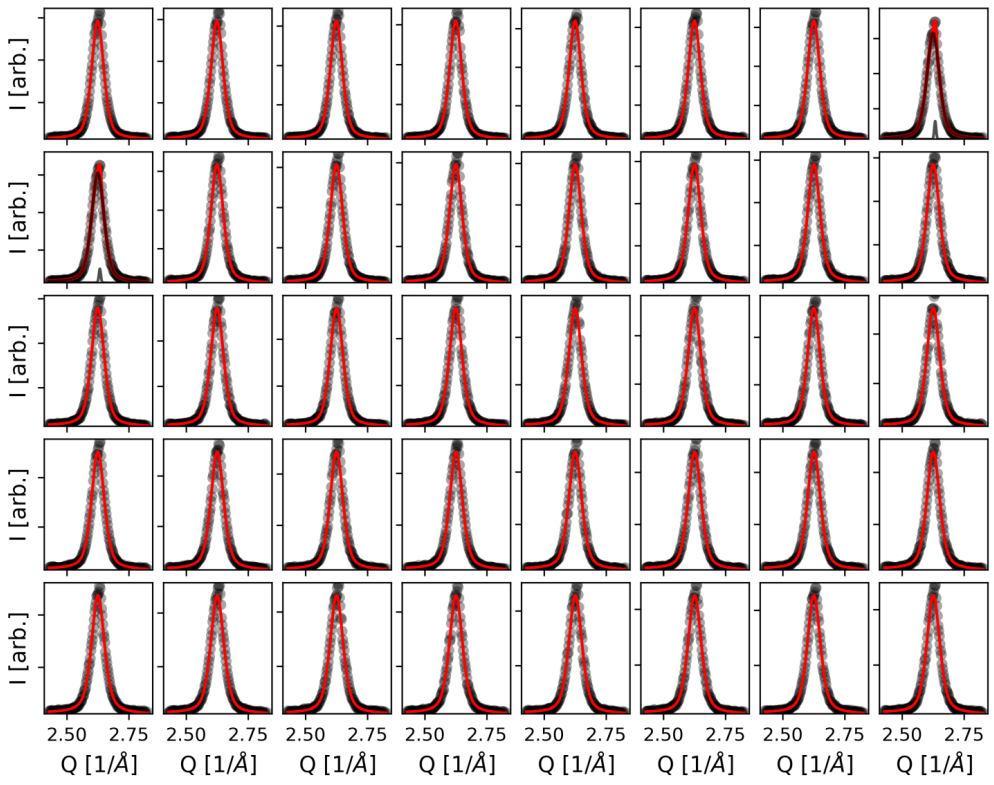

Figure E.46: In plane scans and fits along Q_{xy}, recorded at 673 K.

Table E.34: Center and full width half maximum (FWHM) for the fits presented in Figure E.46. For fits with multiple components, only fit results of the relevant component is shown.

	Center		FWHM			Center		FWHM	
	Value	Error	Value	Error		Value	Error	Value	Error
#0	2.62429	7e-05	0.05804	0.00019	#1	2.62421	5e-05	0.0582	0.00016
#2	2.62423	6e-05	0.0583	0.00016	#3	2.62428	6e-05	0.05869	0.00017
#4	2.62423	7e-05	0.05782	0.0002	#5	2.62425	6e-05	0.05846	0.00017
#6	2.62433	6e-05	0.05925	0.00019	#7	2.62443	9e-05	0.05986	0.00025
#8	2.62472	9e-05	0.0599	0.00025	#9	2.62427	7e-05	0.05947	0.00021
#10	2.62458	6e-05	0.06025	0.00017	#11	2.62446	7e-05	0.06063	0.00021
#12	2.62473	7e-05	0.05994	0.00021	#13	2.6246	9e-05	0.06044	0.00026
#14	2.62495	7e-05	0.05984	0.00022	#15	2.62478	6e-05	0.06041	0.00019
#16	2.62464	7e-05	0.06087	0.0002	#17	2.62467	8e-05	0.0616	0.00023
#18	2.62501	7e-05	0.06193	0.00021	#19	2.6245	8e-05	0.06145	0.00024
#20	2.62473	8e-05	0.06175	0.00023	#21	2.62454	8e-05	0.0618	0.00023
#22	2.62493	8e-05	0.06094	0.00023	#23	2.6249	8e-05	0.06201	0.00024
#24	2.62513	7e-05	0.06143	0.00023	#25	2.62506	8e-05	0.06149	0.00026
#26	2.62484	8e-05	0.06181	0.00025	#27	2.62535	8e-05	0.06133	0.00023
#28	2.62494	7e-05	0.06245	0.00022	#29	2.62531	8e-05	0.06271	0.00025
#30	2.6253	9e-05	0.06202	0.00027	#31	2.62514	8e-05	0.06188	0.00024
#32	2.62545	9e-05	0.06184	0.00028	#33	2.62513	7e-05	0.06299	0.00022
#34	2.62502	8e-05	0.06284	0.00024	#35	2.62523	9e-05	0.06239	0.00027
#36	2.62549	0.0001	0.06287	0.0003	#37	2.62527	8e-05	0.06331	0.00023
#38	2.62498	7e-05	0.06242	0.00022	#39	2.6253	9e-05	0.06223	0.00027
#40	2.62506	8e-05	0.06311	0.00026					

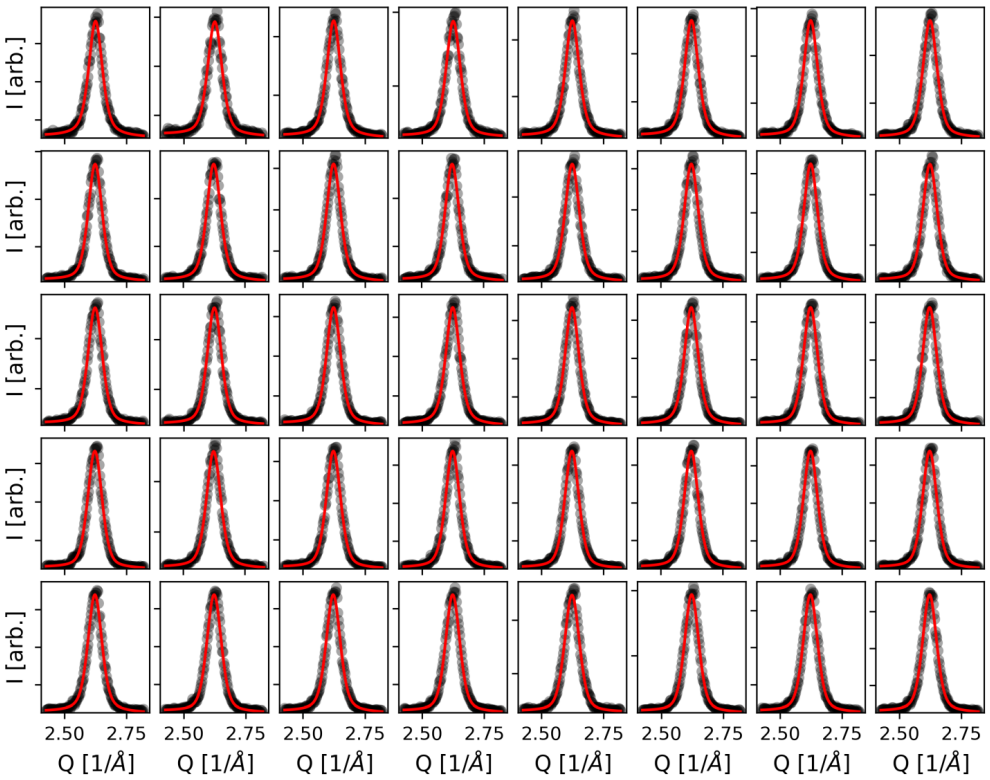

Figure E.47: In plane scans and fits along Q_{xy}, recorded at 723 K.

Table E.35: Center and full width half maximum (FWHM) for the fits presented in Figure E.47. For fits with multiple components, only fit results of the relevant component is shown.

	Center		FWHM			Center		FWHM	
	Value	Error	Value	Error		Value	Error	Value	Error
#0	2.62469	0.00016	0.0658	0.00052	#1	2.62467	0.00025	0.06869	0.00078
#2	2.62321	0.00013	0.06657	0.00039	#3	2.62441	0.00017	0.06814	0.00051
#4	2.62369	0.00013	0.06675	0.00039	#5	2.6231	0.00012	0.0664	0.00036
#6	2.6229	0.00013	0.06689	0.00037	#7	2.62327	0.00015	0.0676	0.00045
#8	2.62319	0.00013	0.06655	0.00037	#9	2.62336	0.00013	0.06723	0.0004
#10	2.62283	0.00012	0.06696	0.00034	#11	2.6228	0.00015	0.06737	0.00044
#12	2.62316	0.00012	0.06842	0.00037	#13	2.62247	0.00012	0.06806	0.00034
#14	2.62292	0.00012	0.06645	0.00036	#15	2.62315	0.00013	0.06908	0.00039
#16	2.62301	0.00014	0.06875	0.00042	#17	2.6229	0.00015	0.06818	0.00043
#18	2.62267	0.00013	0.06738	0.00037	#19	2.62234	0.00015	0.06753	0.00044
#20	2.62237	0.00012	0.0668	0.00036	#21	2.62238	0.00013	0.0667	0.00038
#22	2.62229	0.00012	0.068	0.00034	#23	2.62182	0.00012	0.06737	0.00034
#24	2.62196	0.00013	0.06832	0.00037	#25	2.62289	0.00014	0.06857	0.00041
#26	2.62211	0.00012	0.06861	0.00034	#27	2.62189	0.00012	0.06759	0.00034
#28	2.62193	0.00011	0.06777	0.00031	#29	2.62202	0.00012	0.06746	0.00035
#30	2.62228	0.00011	0.06798	0.00031	#31	2.62201	0.00013	0.06815	0.00036
#32	2.62222	0.00011	0.06732	0.00032	#33	2.62192	0.00012	0.06879	0.00034
#34	2.62144	0.00012	0.06796	0.00033	#35	2.62213	0.00012	0.06791	0.00035
#36	2.62239	0.00013	0.07064	0.00038	#37	2.62137	0.00013	0.0675	0.00035
#38	2.62179	0.00011	0.06823	0.00032	#39	2.62166	0.00011	0.06751	0.00032
#40	2.62115	0.00013	0.06685	0.00037					

Table E.36: Center and full width half maximum (FWHM) for the fits presented in Figure E.48. For fits with multiple components, only fit results of the relevant component is shown.

	Center		FWHM			Center		FWHM	
	Value	Error	Value	Error		Value	Error	Value	Error
#0	2.62494	8e-05	0.05776	0.00025	#1	2.62505	8e-05	0.05792	0.00023
#2	2.625	7e-05	0.0575	0.00021	#3	2.62478	7e-05	0.05736	0.00022
#4	2.62504	7e-05	0.0581	0.00021	#5	2.62497	8e-05	0.05805	0.00024
#6	2.62489	6e-05	0.05775	0.00019	#7	2.625	7e-05	0.05732	0.00019
#8	2.62503	7e-05	0.05774	0.00022	#9	2.62503	8e-05	0.05823	0.00022
#10	2.62522	8e-05	0.0573	0.00022	#11	2.62534	7e-05	0.05788	0.00021
#12	2.62482	8e-05	0.05807	0.00023	#13	2.62502	8e-05	0.05777	0.00024
#14	2.62492	7e-05	0.05788	0.0002	#15	2.62485	8e-05	0.05831	0.00024
#16	2.62507	7e-05	0.05755	0.00021	#17	2.62521	8e-05	0.05711	0.00024
#18	2.62509	7e-05	0.05746	0.00022	#19	2.62533	8e-05	0.05756	0.00025
#20	2.62539	0.0001	0.05696	0.00031	#21	2.62513	7e-05	0.05757	0.00021
#22	2.62484	9e-05	0.05759	0.00027	#23	2.62499	7e-05	0.05702	0.00021
#24	2.62519	8e-05	0.05725	0.00023	#25	2.62512	8e-05	0.05756	0.00024
#26	2.62528	7e-05	0.05766	0.00021	#27	2.62534	8e-05	0.0581	0.00023
#28	2.62527	7e-05	0.05709	0.00021	#29	2.62533	8e-05	0.05718	0.00024
#30	2.62544	8e-05	0.05753	0.00024	#31	2.62515	8e-05	0.05761	0.00023
#32	2.62541	6e-05	0.05722	0.00016	#33	2.62526	7e-05	0.0582	0.00021
#34	2.62511	7e-05	0.05814	0.00021	#35	2.62534	7e-05	0.05861	0.00021
#36	2.62528	7e-05	0.05637	0.00021	#37	2.62528	7e-05	0.05734	0.00021
#38	2.62513	7e-05	0.05801	0.00022	#39	2.62533	8e-05	0.05768	0.00022
#40	2.62525	8e-05	0.0574	0.00023					

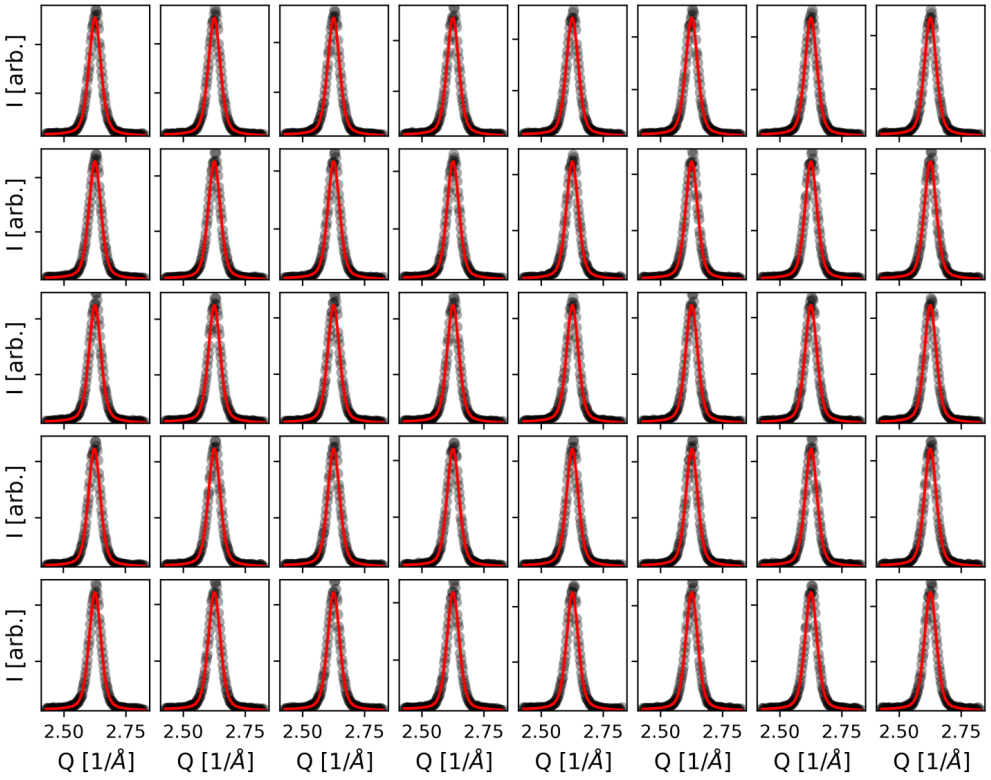

Figure E.48: In plane scans and fits along Q_{xy}, recorded at 523 K.

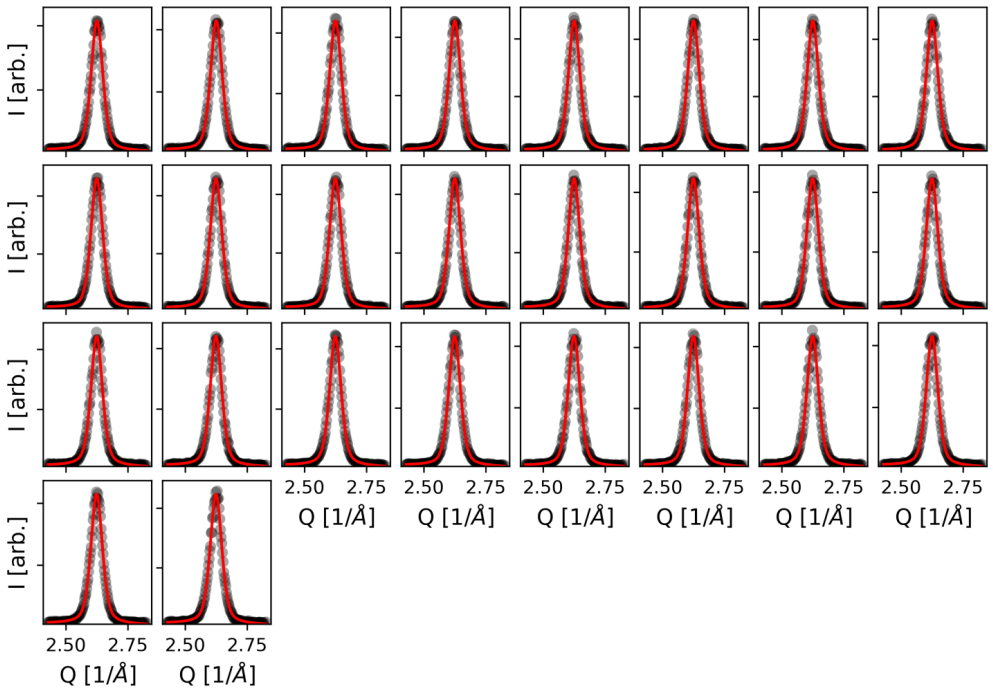

Figure E.49: In plane scans and fits along Q_{xy}, recorded at 573 K.

Table E.37: Center and full width half maximum (FWHM) for the fits presented in Figure E.49. For fits with multiple components, only fit results of the relevant component is shown.

	Center		FWHM			Center		FWHM	
	Value	Error	Value	Error		Value	Error	Value	Error
#0	2.62521	0.0001	0.05552	0.00032	#1	2.62539	8e-05	0.05548	0.00027
#2	2.62488	0.0001	0.05578	0.00032	#3	2.62472	8e-05	0.05459	0.00027
#4	2.62476	9e-05	0.0549	0.00028	#5	2.6247	8e-05	0.05517	0.00027
#6	2.62462	9e-05	0.05433	0.0003	#7	2.62433	9e-05	0.05496	0.00029
#8	2.62453	8e-05	0.05582	0.00025	#9	2.62406	9e-05	0.05537	0.00029
#10	2.62431	0.00011	0.05612	0.00034	#11	2.62448	9e-05	0.0554	0.0003
#12	2.62416	8e-05	0.05508	0.00025	#13	2.62407	9e-05	0.05581	0.00028
#14	2.62386	0.0001	0.0558	0.00032	#15	2.62387	0.00012	0.05538	0.00039
#16	2.62408	0.00011	0.05515	0.00036	#17	2.62384	0.0001	0.05549	0.00031
#18	2.62408	0.0001	0.0549	0.00032	#19	2.6238	0.00011	0.0558	0.00034
#20	2.62417	0.00012	0.05635	0.00038	#21	2.6239	0.00011	0.05578	0.00034
#22	2.62397	0.00011	0.05502	0.00036	#23	2.62402	0.0001	0.05568	0.00033

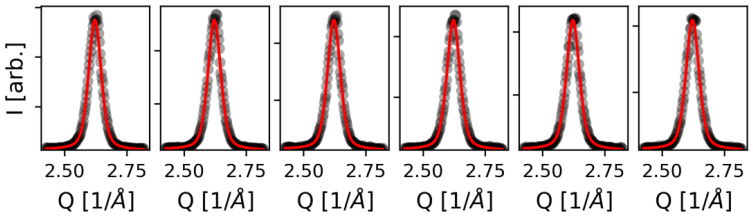

Figure E.50: In plane scans and fits along Q_{xy}, recorded at 623 K.

Table E.38: Center and full width half maximum (FWHM) for the fits presented in Figure E.50. For fits with multiple components, only fit results of the relevant component is shown.

	Center		FWHM			Center		FWHM	
	Value	Error	Value	Error		Value	Error	Value	Error
#0	2.62188	8e-05	0.06012	0.00021	#1	2.62158	8e-05	0.06126	0.00022
#2	2.62164	9e-05	0.06165	0.00026	#3	2.6216	8e-05	0.06231	0.00021

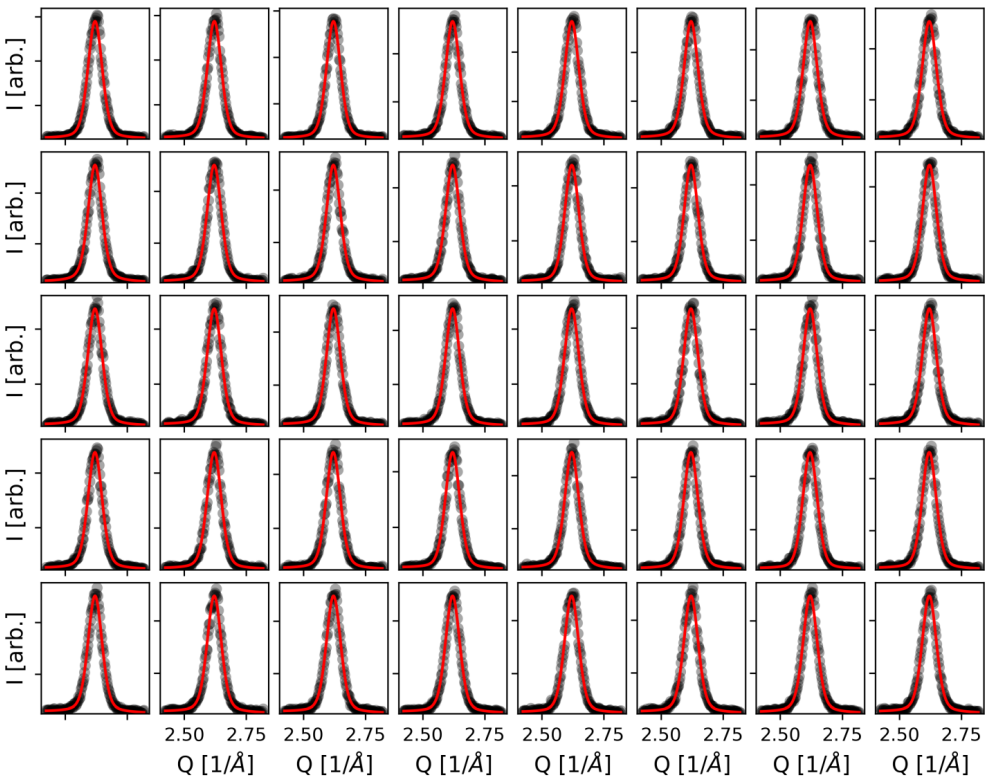

Figure E.51: In plane scans and fits along Q_{xy}, recorded at 673 K.

Table E.39: Center and full width half maximum (FWHM) for the fits presented in Figure E.51. For fits with multiple components, only fit results of the relevant component is shown.

	Center		FWHM			Center		FWHM	
	Value	Error	Value	Error		Value	Error	Value	Error
#0	2.62027	0.0001	0.06834	0.00026	#1	2.62052	0.00011	0.06768	0.00029
#2	2.62037	0.0001	0.06739	0.00028	#3	2.62001	0.00011	0.06797	0.00029
#4	2.61999	0.00012	0.06804	0.00034	#5	2.62029	0.00012	0.06732	0.00034
#6	2.61999	0.00014	0.06797	0.00037	#7	2.61972	0.00014	0.06906	0.00039
#8	2.62003	0.00012	0.06727	0.00033	#9	2.61989	0.00015	0.06807	0.00041
#10	2.61999	0.00014	0.06704	0.00037	#11	2.62	0.00014	0.06776	0.00038
#12	2.62008	0.00014	0.06789	0.00037	#13	2.62015	0.00013	0.06695	0.00034
#14	2.61983	0.00013	0.06892	0.00036	#15	2.62031	0.00013	0.06777	0.00034
#16	2.62002	0.00013	0.06855	0.00035	#17	2.61999	0.00015	0.06877	0.00041
#18	2.62022	0.00012	0.06684	0.00033	#19	2.62006	0.00014	0.06756	0.00037
#20	2.61957	0.00013	0.06943	0.00035	#21	2.61955	0.00016	0.06907	0.00043
#22	2.61989	0.00015	0.06762	0.00039	#23	2.61994	0.00013	0.06837	0.00034
#24	2.61992	0.00013	0.06813	0.00036	#25	2.61992	0.00015	0.0683	0.00039
#26	2.61958	0.00013	0.06792	0.00035	#27	2.61984	0.00013	0.06895	0.00036
#28	2.61999	0.00012	0.0677	0.00034	#29	2.61973	0.00012	0.06811	0.00032
#30	2.61935	0.00013	0.06936	0.00035	#31	2.61952	0.00011	0.06789	0.00028
#32	2.62009	0.00012	0.06728	0.00033	#33	2.62023	0.00015	0.06786	0.00041
#34	2.62039	0.00012	0.06806	0.00033	#35	2.62	0.0001	0.06803	0.00027
#36	2.61917	0.00014	0.06828	0.00038	#37	2.62006	0.00017	0.06873	0.00045
#38	2.61989	0.00014	0.06827	0.00036	#39	2.61971	0.00015	0.06832	0.00039

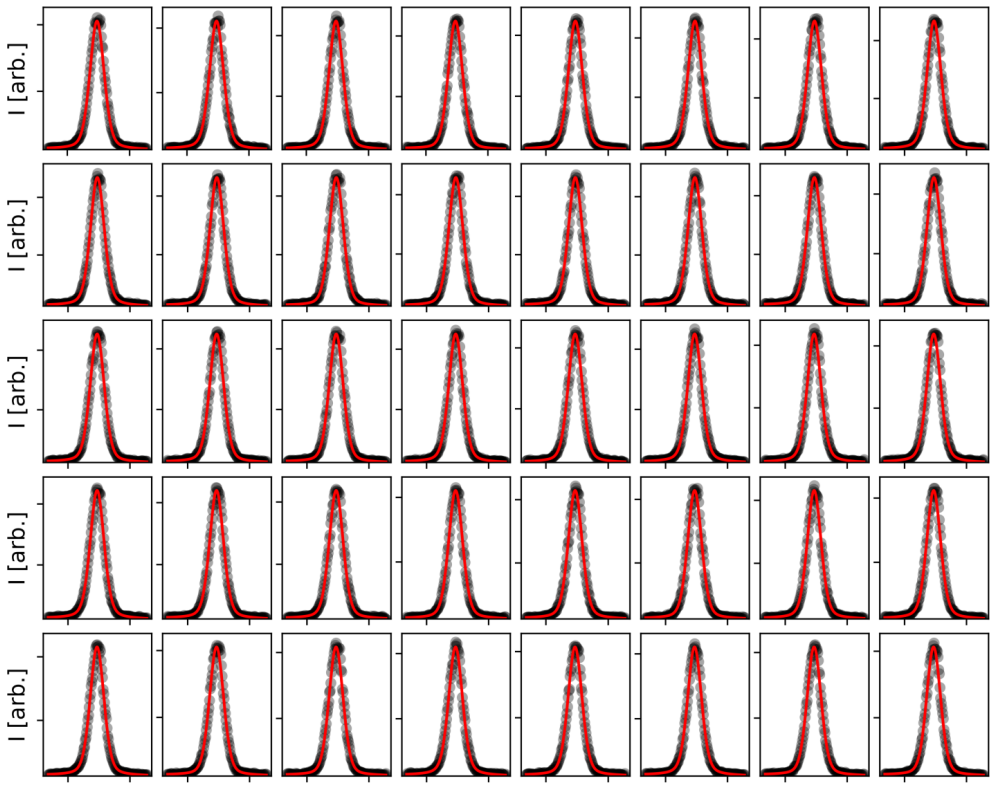

Figure E.52: In plane scans and fits along Q_{xy}, recorded at 723 K.

Table E.40: Center and full width half maximum (FWHM) for the fits presented in Figure E.52. For fits with multiple components, only fit results of the relevant component is shown.

	Center		FWHM			Center		FWHM	
	Value	Error	Value	Error		Value	Error	Value	Error
#0	2.6194	8e-05	0.06756	0.00022	#1	2.61945	0.00011	0.06752	0.00029
#2	2.61926	9e-05	0.06667	0.00025	#3	2.61874	9e-05	0.06794	0.00023
#4	2.61833	9e-05	0.0671	0.00022	#5	2.61848	9e-05	0.0665	0.00023
#6	2.61861	8e-05	0.06709	0.0002	#7	2.6186	8e-05	0.06654	0.00021
#8	2.61847	8e-05	0.06639	0.0002	#9	2.61844	8e-05	0.06656	0.00021
#10	2.61823	9e-05	0.06712	0.00023	#11	2.61832	8e-05	0.06743	0.00021
#12	2.61816	0.0001	0.06647	0.00027	#13	2.61832	0.0001	0.06618	0.00025
#14	2.61805	7e-05	0.06713	0.00017	#15	2.61813	0.0001	0.06731	0.00027
#16	2.61774	0.0001	0.06708	0.00026	#17	2.61773	8e-05	0.067	0.00021
#18	2.61773	8e-05	0.06702	0.0002	#19	2.61765	9e-05	0.06664	0.00022
#20	2.61756	8e-05	0.06715	0.00021	#21	2.61743	9e-05	0.06594	0.00022
#22	2.61701	0.0001	0.06595	0.00025	#23	2.61727	9e-05	0.06622	0.00024
#24	2.61761	9e-05	0.06645	0.00022	#25	2.61734	9e-05	0.06634	0.00023
#26	2.61752	0.0001	0.0665	0.00025	#27	2.61734	8e-05	0.06691	0.00022
#28	2.61738	0.00011	0.06644	0.00028	#29	2.61716	0.0001	0.06685	0.00026
#30	2.61717	9e-05	0.06609	0.00023	#31	2.61707	8e-05	0.06661	0.00021
#32	2.61725	0.0001	0.06611	0.00025	#33	2.61722	0.0001	0.06781	0.00025
#34	2.6171	0.00011	0.06751	0.00027	#35	2.6171	0.00013	0.06632	0.00033
#36	2.61685	9e-05	0.06722	0.00022	#37	2.61688	8e-05	0.06631	0.00022
#38	2.61687	9e-05	0.06711	0.00024	#39	2.61677	9e-05	0.06721	0.00022
#40	2.61675	0.0001	0.0672	0.00027	#41	2.61662	9e-05	0.06739	0.00024
#42	2.6168	0.0001	0.06692	0.00024	#43	2.61673	9e-05	0.06718	0.00023
#44	2.61694	9e-05	0.06649	0.00024	#45	2.61661	9e-05	0.06662	0.00024

Pd_3Pt_1/Al_2O_3 - Pd(1 1 1) out of plane

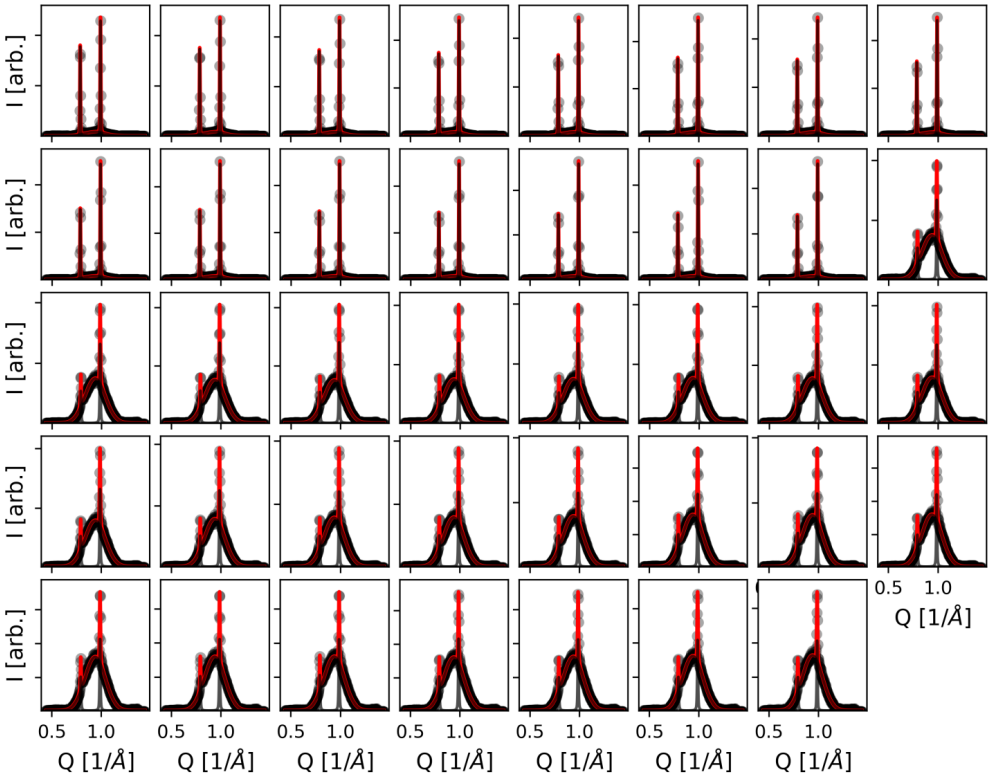

Figure E.53: Out of plane scans and fits along Q_z, recorded at 523 K.

Table E.41: Center and full width half maximum (FWHM) for the fits presented in Figure E.53. For fits with multiple components, only fit results of the relevant component is shown.

	Center		FWHM			Center		FWHM	
	Value	Error	Value	Error		Value	Error	Value	Error
#0	0.93456	0.00369	0.24427	0.00961	#1	0.93377	0.00387	0.24509	0.01067
#2	0.93355	0.00387	0.24415	0.01062	#3	0.9328	0.00387	0.24331	0.01054
#4	0.93299	0.00374	0.24253	0.01015	#5	0.93254	0.00386	0.24271	0.01044
#6	0.9322	0.00366	0.24232	0.00985	#7	0.93226	0.00372	0.2422	0.01002
#8	0.932	0.00366	0.24183	0.00979	#9	0.93174	0.00368	0.24171	0.00982
#10	0.93162	0.00358	0.24089	0.00949	#11	0.93144	0.00358	0.24099	0.00949
#12	0.93117	0.00374	0.24077	0.00988	#13	0.93188	0.00359	0.24042	0.0095
#14	0.9311	0.00361	0.24069	0.00952	#15	0.93572	0.00053	0.24172	0.00141
#16	0.93539	0.00054	0.24213	0.00142	#17	0.93553	0.00053	0.24149	0.0014
#18	0.93563	0.00053	0.24184	0.00142	#19	0.93526	0.00053	0.24172	0.0014
#20	0.93547	0.00055	0.24147	0.00146	#21	0.93544	0.00051	0.24174	0.00134
#22	0.93554	0.00051	0.24183	0.00135	#23	0.93575	0.00051	0.24134	0.00136
#24	0.93616	0.00051	0.24137	0.00136	#25	0.93599	0.00052	0.24102	0.00139
#26	0.93575	0.0005	0.24143	0.00132	#27	0.93606	0.00051	0.24115	0.00135
#28	0.93618	0.00051	0.24097	0.00135	#29	0.93599	0.00051	0.24134	0.00135
#30	0.93616	0.00052	0.24096	0.00137	#31	0.93626	0.0005	0.2402	0.00133
#32	0.93634	0.00052	0.24093	0.00136	#33	0.9362	0.00051	0.24109	0.00135
#34	0.93642	0.00052	0.2409	0.00137	#35	0.93631	0.0005	0.24077	0.00133
#36	0.93659	0.00051	0.24069	0.00136	#37	0.93637	0.00051	0.24056	0.00135
#38	0.93791	0.00055	0.23799	0.00138					

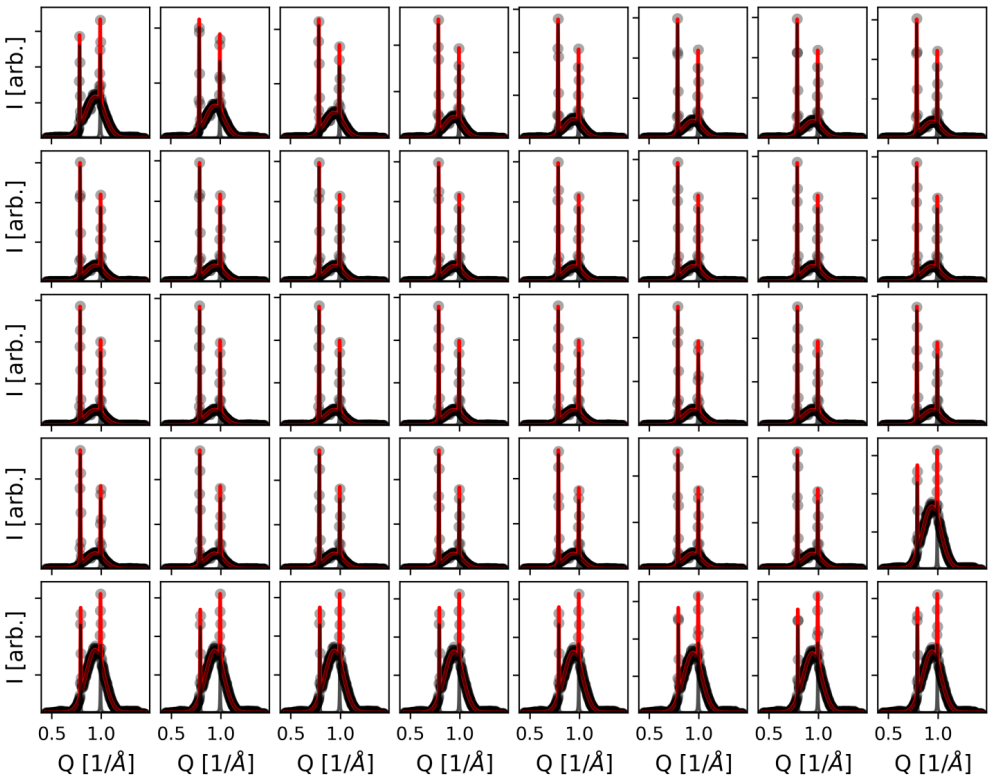

Figure E.54: Out of plane scans and fits along Q_z, recorded at 573 K.

Table E.42: Center and full width half maximum (FWHM) for the fits presented in Figure E.54. For fits with multiple components, only fit results of the relevant component is shown.

	Center		FWHM			Center		FWHM	
	Value	Error	Value	Error		Value	Error	Value	Error
#0	0.94109	0.00084	0.22136	0.00219	#1	0.94132	0.00084	0.21845	0.00219
#2	0.94102	0.00105	0.21717	0.0027	#3	0.94021	0.00124	0.21677	0.00318
#4	0.93931	0.00139	0.21727	0.00354	#5	0.93876	0.00148	0.21686	0.00377
#6	0.93818	0.0015	0.21758	0.00382	#7	0.93793	0.00154	0.21729	0.00393
#8	0.93762	0.00154	0.21761	0.00391	#9	0.9373	0.00153	0.21729	0.0039
#10	0.93723	0.00154	0.21739	0.0039	#11	0.93704	0.00155	0.21743	0.00393
#12	0.93676	0.00156	0.21752	0.00393	#13	0.9367	0.00153	0.21748	0.00387
#14	0.93669	0.00154	0.21754	0.00389	#15	0.93642	0.00153	0.21775	0.00386
#16	0.93638	0.00153	0.21766	0.00386	#17	0.93621	0.00153	0.21794	0.00386
#18	0.93612	0.00156	0.21797	0.00392	#19	0.93615	0.00155	0.21826	0.00391
#20	0.9358	0.00155	0.2179	0.00389	#21	0.9355	0.00151	0.21849	0.00378
#22	0.9358	0.00154	0.21828	0.00386	#23	0.93559	0.00154	0.21825	0.00385
#24	0.93538	0.00149	0.21857	0.00373	#25	0.93535	0.00154	0.21809	0.00384
#26	0.93533	0.00153	0.21863	0.00383	#27	0.935	0.00154	0.21854	0.00384
#28	0.93508	0.00154	0.21913	0.00383	#29	0.93512	0.00151	0.21863	0.00375
#30	0.93517	0.00151	0.2186	0.00376	#31	0.93726	0.00052	0.21456	0.00131
#32	0.93737	0.00051	0.21393	0.00128	#33	0.93709	0.00052	0.21424	0.00131
#34	0.93708	0.00051	0.21477	0.0013	#35	0.93723	0.00052	0.21436	0.00132
#36	0.93697	0.00053	0.21473	0.00135	#37	0.9369	0.00052	0.214	0.00132
#38	0.93675	0.00051	0.21426	0.0013	#39	0.93703	0.00053	0.21408	0.00134
#40	0.93697	0.00053	0.21439	0.00135					

Table E.43: Center and full width half maximum (FWHM) for the fits presented in Figure E.55. For fits with multiple components, only fit results of the relevant component is shown.

	Center		FWHM			Center		FWHM	
	Value	Error	Value	Error		Value	Error	Value	Error
#0	0.93511	0.00097	0.21932	0.00247	#1	0.93439	0.00111	0.21899	0.00279
#2	0.93447	0.0011	0.21901	0.0028	#3	0.93416	0.0011	0.21907	0.00279
#4	0.93427	0.00112	0.21958	0.00284	#5	0.93426	0.00112	0.21914	0.00283
#6	0.93396	0.0011	0.21873	0.00279	#7	0.93387	0.0011	0.21928	0.00278
#8	0.93365	0.00113	0.21898	0.00287	#9	0.93758	0.00043	0.21902	0.00112
#10	0.93707	0.00041	0.21921	0.00103	#11	0.93766	0.00044	0.21897	0.00113
#12	0.93738	0.00043	0.21854	0.00109	#13	0.93724	0.00042	0.21932	0.00107
#14	0.93697	0.00043	0.21969	0.00111	#15	0.93724	0.00041	0.21815	0.00107
#16	0.93733	0.00044	0.21893	0.00116	#17	0.93741	0.00046	0.21935	0.00114
#18	0.93729	0.00045	0.21973	0.00118	#19	0.93756	0.00042	0.21976	0.00113
#20	0.93736	0.00046	0.21983	0.00117	#21	0.93731	0.0004	0.21891	0.00106
#22	0.93694	0.00044	0.21961	0.00112	#23	0.93749	0.00042	0.21994	0.00113
#24	0.93733	0.0004	0.21887	0.00107	#25	0.93754	0.00044	0.22005	0.00114
#26	0.93785	0.00044	0.21962	0.00117	#27	0.93746	0.00041	0.21904	0.00107
#28	0.93776	0.0004	0.21884	0.00107	#29	0.93736	0.00043	0.21962	0.0011

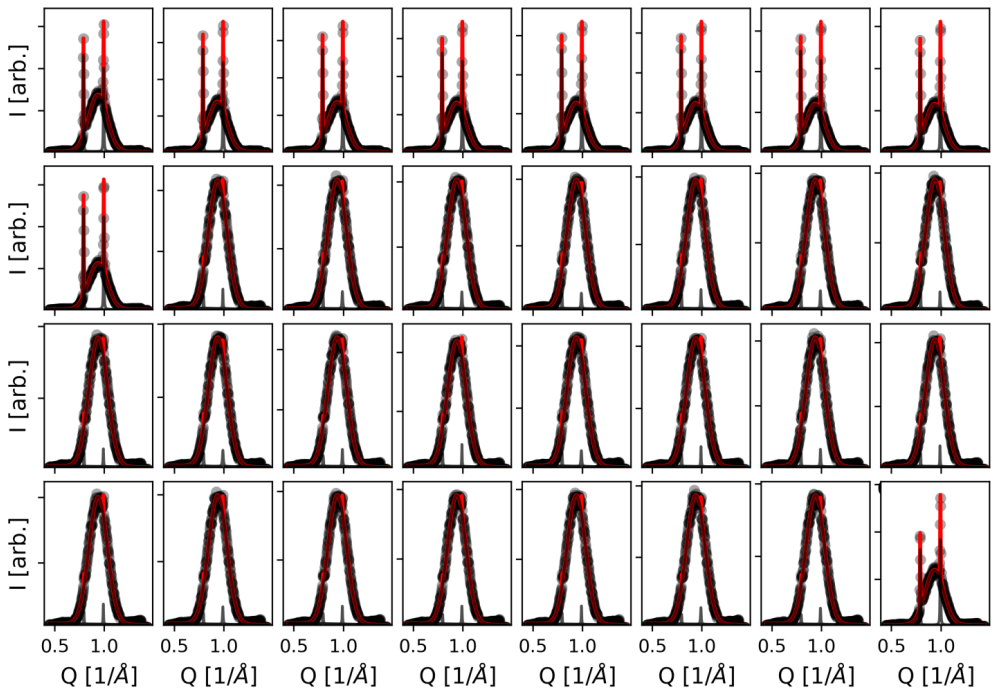

Figure E.55: Out of plane scans and fits along Q_z, recorded at 623 K.

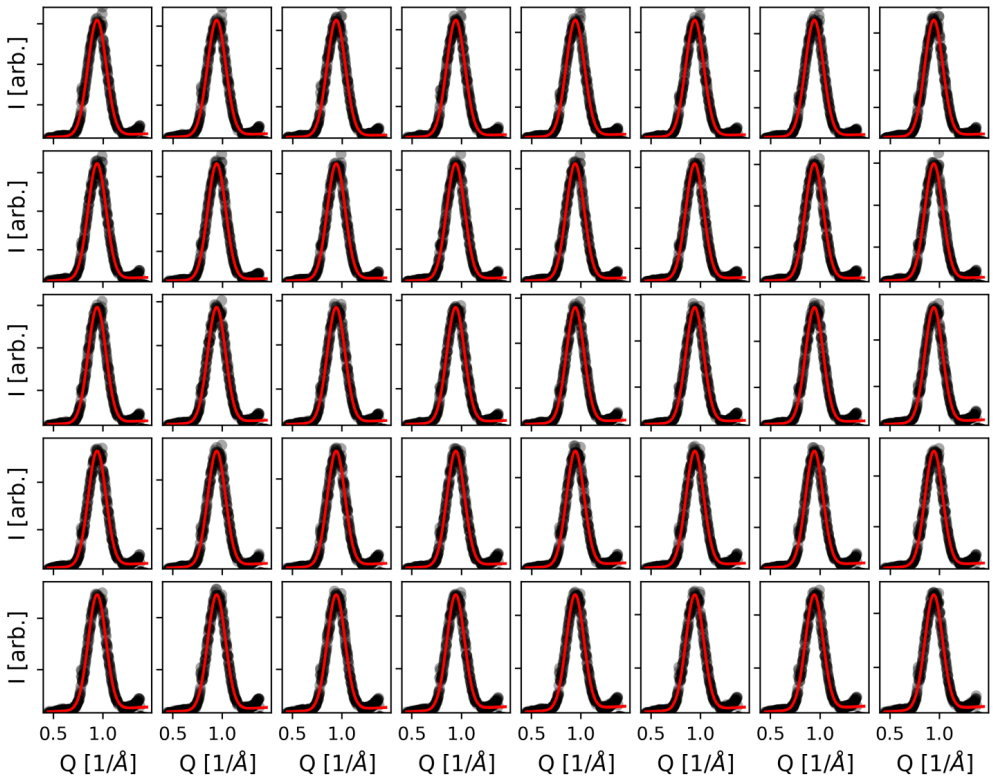

Figure E.56: Out of plane scans and fits along Q_z, recorded at 673 K.

Table E.44: Center and full width half maximum (FWHM) for the fits presented in Figure E.56. For fits with multiple components, only fit results of the relevant component is shown.

	Center		FWHM			Center		FWHM	
	Value	Error	Value	Error		Value	Error	Value	Error
#0	0.93865	0.00062	0.21736	0.00166	#1	0.93896	0.00063	0.21759	0.00173
#2	0.93944	0.00058	0.21782	0.00156	#3	0.94006	0.00059	0.21743	0.00158
#4	0.94026	0.00059	0.217	0.00156	#5	0.94088	0.00056	0.21573	0.0015
#6	0.94075	0.00057	0.21531	0.0015	#7	0.94069	0.00049	0.21508	0.00135
#8	0.94143	0.0005	0.21422	0.00134	#9	0.94137	0.00049	0.21376	0.00131
#10	0.94127	0.00048	0.21302	0.00128	#11	0.94141	0.0005	0.2139	0.00134
#12	0.94127	0.00049	0.21304	0.0013	#13	0.94198	0.00046	0.21264	0.00121
#14	0.94194	0.00047	0.21356	0.00126	#15	0.94191	0.00045	0.21304	0.0012
#16	0.94156	0.00045	0.2114	0.0012	#17	0.94126	0.0004	0.21212	0.00106
#18	0.94156	0.00048	0.21168	0.00128	#19	0.94158	0.00044	0.21138	0.0012
#20	0.94175	0.00046	0.20979	0.00125	#21	0.94185	0.00044	0.21138	0.00118
#22	0.94177	0.00046	0.21103	0.00124	#23	0.94179	0.00048	0.21016	0.00133
#24	0.9417	0.00047	0.21061	0.00128	#25	0.9412	0.00044	0.21071	0.00116
#26	0.94176	0.00047	0.21	0.00127	#27	0.94213	0.00046	0.20996	0.00125
#28	0.9416	0.00044	0.20945	0.00116	#29	0.94169	0.0005	0.21131	0.00132
#30	0.94166	0.00045	0.20791	0.00122	#31	0.94174	0.00049	0.20998	0.0013
#32	0.94168	0.00049	0.2098	0.00131	#33	0.94167	0.00051	0.20993	0.00133
#34	0.94168	0.00052	0.20964	0.00138	#35	0.9416	0.00046	0.20879	0.00126
#36	0.94123	0.00048	0.20827	0.0013	#37	0.94189	0.00051	0.20911	0.00136
#38	0.94161	0.00052	0.20839	0.00137	#39	0.94148	0.0005	0.20907	0.00132
#40	0.94143	0.00052	0.20888	0.0014					

Table E.45: Center and full width half maximum (FWHM) for the fits presented in Figure E.57. For fits with multiple components, only fit results of the relevant component is shown.

	Center		FWHM			Center		FWHM	
	Value	Error	Value	Error		Value	Error	Value	Error
#0	0.93866	0.00137	0.19479	0.00361	#1	0.93726	0.00069	0.19529	0.00182
#2	0.9369	0.0008	0.19119	0.00213	#3	0.93867	0.00052	0.19732	0.00138
#4	0.93856	0.00067	0.19448	0.00178	#5	0.93937	0.00053	0.19559	0.00139
#6	0.93975	0.00046	0.19619	0.00121	#7	0.9403	0.00047	0.19468	0.00124
#8	0.94042	0.00046	0.19497	0.00121	#9	0.94115	0.00047	0.19388	0.00123
#10	0.93971	0.00073	0.19626	0.00192	#11	0.94068	0.00045	0.19435	0.00117
#12	0.93984	0.00071	0.19465	0.00186	#13	0.94101	0.0005	0.19169	0.00131
#14	0.94096	0.00043	0.19214	0.00114	#15	0.9414	0.00044	0.19261	0.00115
#16	0.94101	0.00052	0.18877	0.00138	#17	0.94143	0.00053	0.19089	0.0014
#18	0.94145	0.00047	0.19018	0.00123	#19	0.94105	0.00042	0.19142	0.0011
#20	0.94144	0.00043	0.19054	0.00113	#21	0.94157	0.0004	0.1901	0.00104
#22	0.94158	0.00041	0.18854	0.00107	#23	0.9417	0.00044	0.18977	0.00116
#24	0.94159	0.00041	0.1902	0.00109	#25	0.94174	0.00039	0.18915	0.00102
#26	0.94082	0.00063	0.18839	0.00165	#27	0.94194	0.00043	0.18859	0.00113
#28	0.94233	0.00041	0.18865	0.00109	#29	0.94213	0.00042	0.18754	0.0011
#30	0.9419	0.00038	0.18771	0.00101	#31	0.94248	0.00043	0.188	0.00112
#32	0.94238	0.00041	0.18667	0.00108	#33	0.94228	0.00043	0.18683	0.00113
#34	0.94239	0.00043	0.18665	0.00114	#35	0.94184	0.00041	0.18627	0.00108
#36	0.94235	0.00039	0.18572	0.00102	#37	0.94176	0.00054	0.18343	0.00142
#38	0.94326	0.00037	0.18823	0.00106	#39	0.94249	0.00041	0.1845	0.00109

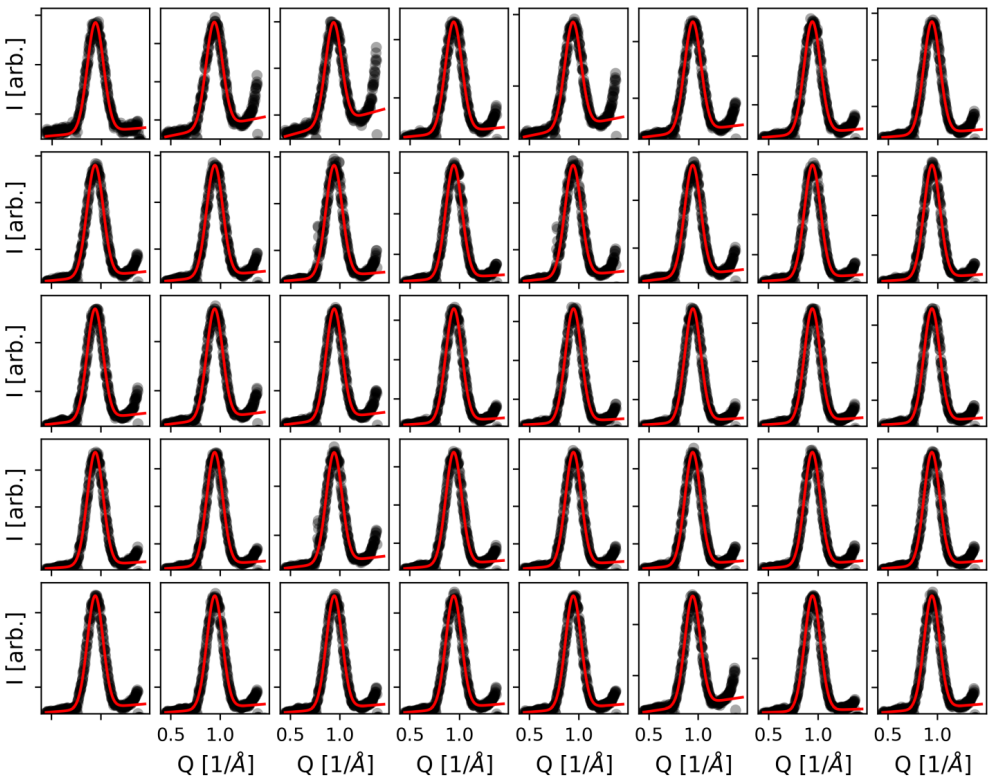

Figure E.57: Out of plane scans and fits along Q_z, recorded at 723 K.

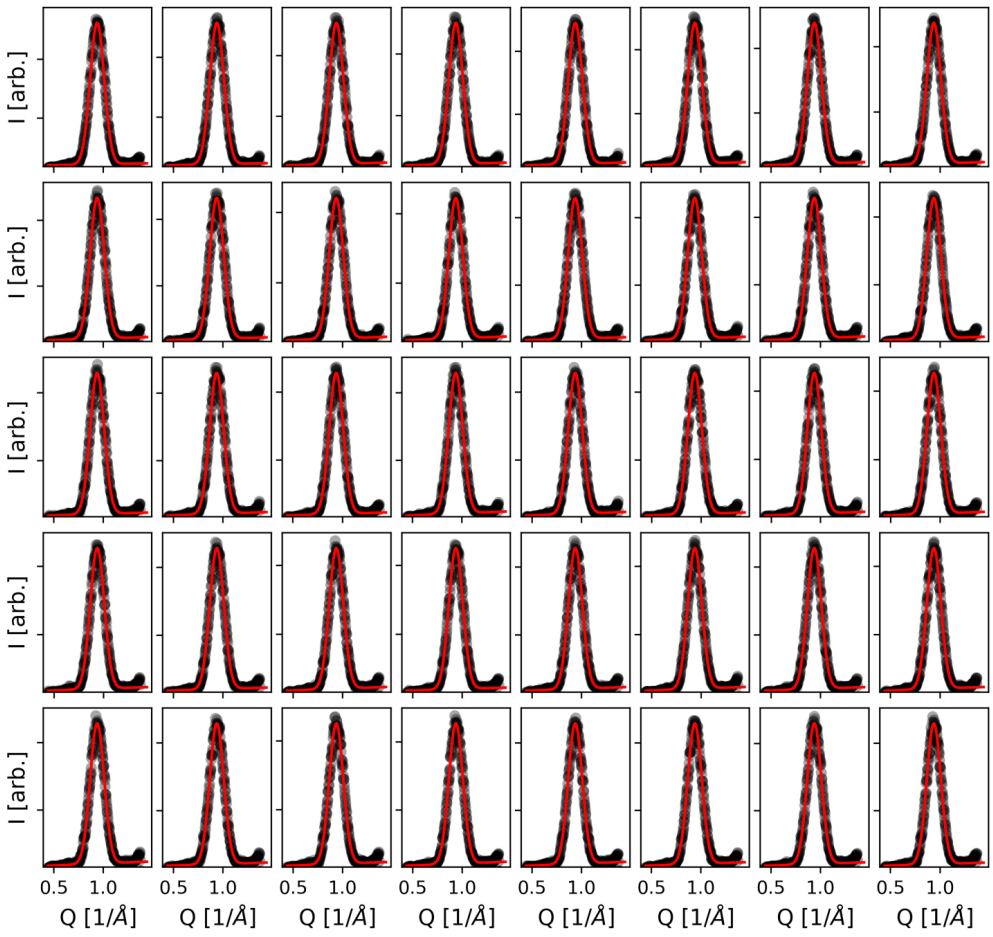

Figure E.58: Out of plane scans and fits along Q_z, recorded at 523 K.

Table E.46: Center and full width half maximum (FWHM) for the fits presented in Figure E.58. For fits with multiple components, only fit results of the relevant component is shown.

	Center		FWHM			Center		FWHM	
	Value	Error	Value	Error		Value	Error	Value	Error
#0	0.93881	0.00022	0.168	0.00059	#1	0.93886	0.00024	0.1683	0.00063
#2	0.93859	0.00024	0.16807	0.00064	#3	0.93844	0.00024	0.1674	0.00063
#4	0.93816	0.00027	0.16851	0.00072	#5	0.93783	0.00027	0.16802	0.00071
#6	0.93828	0.00024	0.16815	0.00063	#7	0.93762	0.00023	0.1681	0.00061
#8	0.93772	0.00027	0.1689	0.00071	#9	0.93742	0.00026	0.16802	0.0007
#10	0.93736	0.00027	0.16749	0.0007	#11	0.93675	0.00025	0.16733	0.00067
#12	0.93697	0.00028	0.16774	0.00075	#13	0.93691	0.00026	0.16771	0.00068
#14	0.93706	0.00025	0.16738	0.00065	#15	0.93732	0.00022	0.16835	0.00059
#16	0.93708	0.00025	0.1678	0.00066	#17	0.93688	0.00026	0.1675	0.0007
#18	0.93709	0.00025	0.16728	0.00066	#19	0.93726	0.00027	0.16768	0.00071
#20	0.93706	0.00027	0.16718	0.00072	#21	0.93708	0.00026	0.16763	0.0007
#22	0.93645	0.00024	0.16714	0.00063	#23	0.93701	0.00025	0.16682	0.00067
#24	0.93716	0.00025	0.16743	0.00067	#25	0.93733	0.00024	0.16746	0.00063
#26	0.937	0.00026	0.16818	0.0007	#27	0.93726	0.00025	0.1674	0.00066
#28	0.93723	0.00025	0.16639	0.00067	#29	0.93686	0.00026	0.16748	0.00068
#30	0.93689	0.00028	0.16741	0.00075	#31	0.93737	0.00026	0.16708	0.00068
#32	0.93723	0.00027	0.16682	0.0007	#33	0.93703	0.00026	0.16713	0.00069
#34	0.93688	0.00028	0.16701	0.00074	#35	0.93727	0.00024	0.16693	0.00064
#36	0.93723	0.00025	0.16672	0.00066	#37	0.93729	0.00024	0.16676	0.00064

Table E.47: Center and full width half maximum (FWHM) for the fits presented in Figure E.59. For fits with multiple components, only fit results of the relevant component is shown.

	Center		FWHM			Center		FWHM	
	Value	Error	Value	Error		Value	Error	Value	Error
#0	0.9448	0.00021	0.16627	0.00059	#1	0.94472	0.00022	0.16571	0.00062
#2	0.94463	0.00022	0.16589	0.00064	#3	0.94451	0.0002	0.16621	0.00059
#4	0.94406	0.00022	0.16767	0.00062	#5	0.94413	0.0002	0.167	0.00057
#6	0.94416	0.00022	0.16698	0.00063	#7	0.94407	0.00021	0.16745	0.0006
#8	0.94407	0.0002	0.16829	0.00058	#9	0.94334	0.00021	0.16754	0.00061
#10	0.94322	0.00021	0.16778	0.0006	#11	0.94334	0.00023	0.16821	0.00065
#12	0.94312	0.0002	0.16908	0.00059	#13	0.9432	0.00021	0.16827	0.00059
#14	0.94312	0.00023	0.16822	0.00067	#15	0.94326	0.00021	0.16858	0.00061
#16	0.94296	0.0002	0.16862	0.00058	#17	0.94291	0.00022	0.1694	0.00064
#18	0.94265	0.00022	0.16926	0.00062	#19	0.94272	0.00022	0.16959	0.00064
#20	0.94276	0.00021	0.16986	0.0006	#21	0.94275	0.00023	0.17006	0.00067
#22	0.94294	0.00021	0.1695	0.00061	#23	0.94258	0.00021	0.16982	0.0006

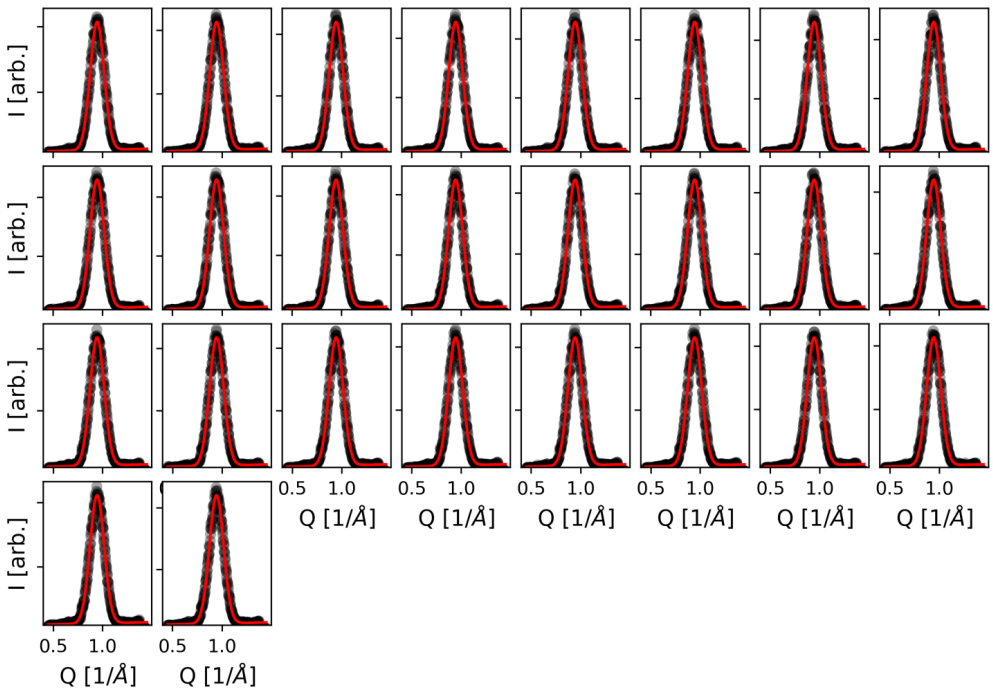

Figure E.59: Out of plane scans and fits along Q_z, recorded at 573 K.

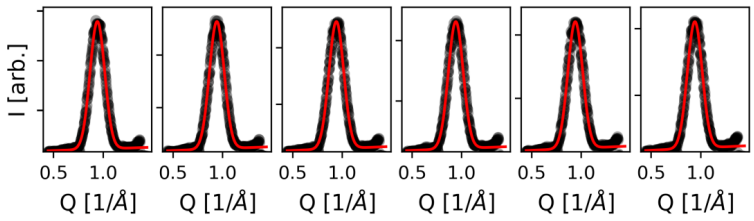

Figure E.60: Out of plane scans and fits along Q_z, recorded at 623 K.

Table E.48: Center and full width half maximum (FWHM) for the fits presented in Figure E.60. For fits with multiple components, only fit results of the relevant component is shown.

	Center		FWHM			Center		FWHM	
	Value	Error	Value	Error		Value	Error	Value	Error
#0	0.94192	0.00028	0.17429	0.00073	#1	0.94107	0.00029	0.17519	0.00076
#2	0.94091	0.0003	0.17545	0.0008	#3	0.94026	0.00031	0.17602	0.00082

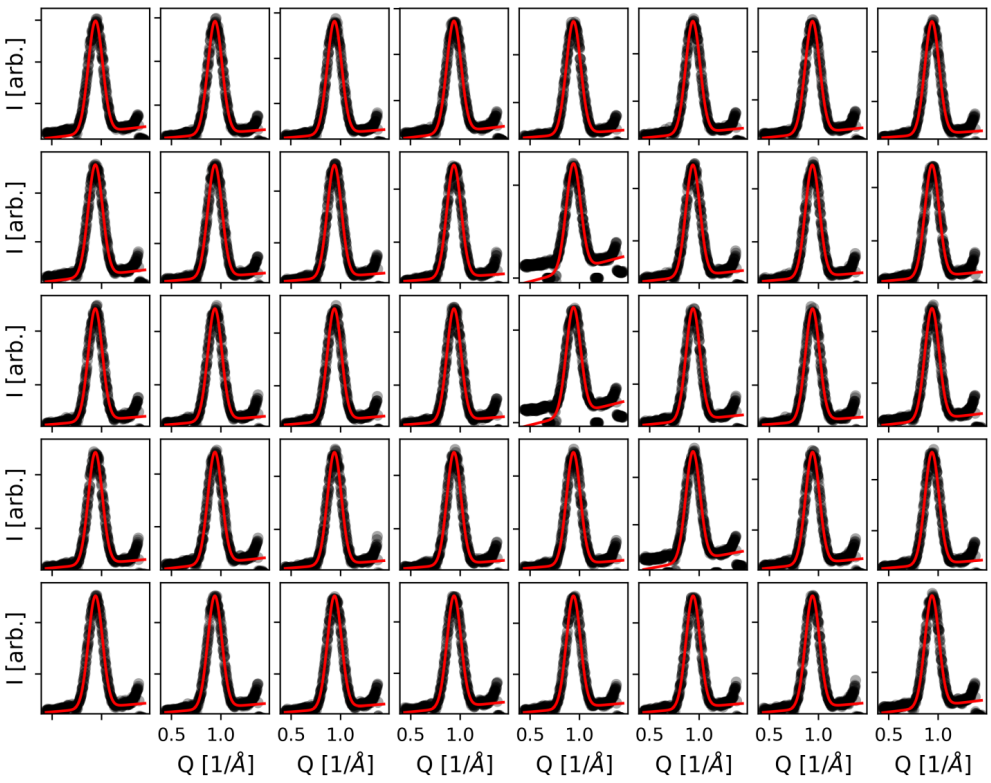

Figure E.61: Out of plane scans and fits along Q_z, recorded at 673 K.

Table E.49: Center and full width half maximum (FWHM) for the fits presented in Figure E.61. For fits with multiple components, only fit results of the relevant component is shown.

	Center		FWHM			Center		FWHM	
	Value	Error	Value	Error		Value	Error	Value	Error
#0	0.93998	0.00095	0.17236	0.00251	#1	0.93996	0.00071	0.17084	0.00189
#2	0.93906	0.00069	0.171	0.00182	#3	0.93891	0.00093	0.17127	0.00245
#4	0.93923	0.00056	0.17157	0.00148	#5	0.93836	0.00077	0.17087	0.00202
#6	0.93817	0.00082	0.17158	0.00216	#7	0.93871	0.00061	0.17043	0.00162
#8	0.93806	0.00096	0.17176	0.00254	#9	0.93779	0.00062	0.17001	0.00164
#10	0.93743	0.0006	0.16939	0.00161	#11	0.93797	0.00059	0.17067	0.00158
#12	0.93747	0.00168	0.17265	0.00438	#13	0.93729	0.00081	0.16838	0.00214
#14	0.93766	0.00069	0.16854	0.00184	#15	0.93744	0.00069	0.16953	0.00183
#16	0.93711	0.00069	0.16856	0.00183	#17	0.93778	0.00073	0.16916	0.00194
#18	0.93735	0.00062	0.16824	0.00166	#19	0.93792	0.00065	0.16814	0.00173
#20	0.93742	0.00161	0.17112	0.0042	#21	0.93815	0.00084	0.16658	0.00223
#22	0.93772	0.00062	0.16839	0.00164	#23	0.93734	0.00093	0.16966	0.00247
#24	0.93775	0.00063	0.16755	0.00167	#25	0.93801	0.0009	0.16954	0.00239
#26	0.938	0.00061	0.16666	0.00163	#27	0.9382	0.0007	0.16694	0.00185
#28	0.93728	0.00064	0.16711	0.0017	#29	0.93768	0.00131	0.16998	0.00343
#30	0.9378	0.00078	0.16739	0.00206	#31	0.93746	0.0007	0.16857	0.00185
#32	0.93749	0.00071	0.16827	0.00187	#33	0.93709	0.0007	0.16865	0.00186
#34	0.93734	0.00061	0.16786	0.00163	#35	0.93723	0.00076	0.16705	0.00201
#36	0.93752	0.00069	0.16731	0.00182	#37	0.93723	0.00066	0.16716	0.00175
#38	0.93748	0.0007	0.16775	0.00185	#39	0.93756	0.00092	0.16768	0.00244

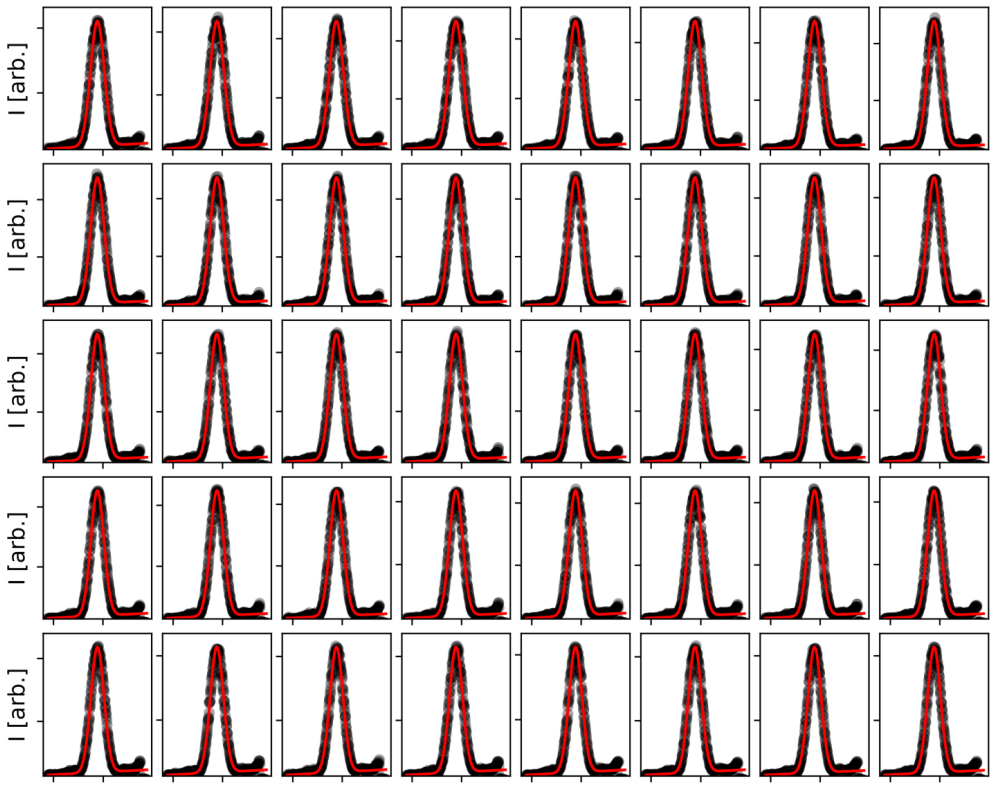

Figure E.62: Out of plane scans and fits along Q_z, recorded at 723 K.

Table E.50: Center and full width half maximum (FWHM) for the fits presented in Figure E.62. For fits with multiple components, only fit results of the relevant component is shown.

	Center		FWHM			Center		FWHM	
	Value	Error	Value	Error		Value	Error	Value	Error
#0	0.94461	0.00046	0.16391	0.00122	#1	0.94472	0.00043	0.16407	0.00114
#2	0.94415	0.00043	0.16387	0.00113	#3	0.94429	0.00044	0.16369	0.00117
#4	0.94436	0.00035	0.16221	0.00094	#5	0.94455	0.00033	0.16137	0.00088
#6	0.94484	0.00035	0.1616	0.00093	#7	0.94516	0.00033	0.16097	0.00088
#8	0.94466	0.00034	0.1607	0.00091	#9	0.94446	0.00035	0.16089	0.00093
#10	0.94455	0.00034	0.16039	0.00091	#11	0.94443	0.00035	0.16041	0.00093
#12	0.94445	0.00034	0.16013	0.0009	#13	0.94447	0.00036	0.16038	0.00096
#14	0.94421	0.00034	0.15982	0.0009	#15	0.94419	0.00034	0.15916	0.0009
#16	0.94361	0.00033	0.15856	0.00089	#17	0.9434	0.00035	0.15839	0.00092
#18	0.94337	0.00034	0.15848	0.00091	#19	0.9436	0.00035	0.15839	0.00092
#20	0.94375	0.00036	0.1587	0.00095	#21	0.94316	0.00034	0.15817	0.00091
#22	0.9433	0.00033	0.15754	0.00087	#23	0.94328	0.00036	0.15727	0.00095
#24	0.94317	0.00034	0.15647	0.0009	#25	0.94285	0.00033	0.1565	0.00088
#26	0.94307	0.00033	0.15705	0.00088	#27	0.94271	0.00033	0.15724	0.00086
#28	0.94221	0.00037	0.15684	0.00097	#29	0.94235	0.00034	0.15632	0.00091
#30	0.94276	0.00034	0.15634	0.00091	#31	0.94248	0.00034	0.15673	0.00091
#32	0.94238	0.00036	0.15669	0.00094	#33	0.94173	0.00036	0.1562	0.00095
#34	0.94222	0.00035	0.1561	0.00094	#35	0.94234	0.00034	0.15509	0.0009
#36	0.94225	0.00036	0.15552	0.00097	#37	0.94177	0.00035	0.15491	0.00093
#38	0.94213	0.00034	0.15551	0.00091	#39	0.94196	0.00034	0.15409	0.00089
#40	0.94236	0.00037	0.15402	0.00097	#41	0.94216	0.00036	0.15554	0.00096
#42	0.94164	0.00035	0.15464	0.00094	#43	0.9419	0.00034	0.15419	0.0009
#44	0.94192	0.00034	0.15393	0.00091	#45	0.9421	0.00035	0.15421	0.00094

$\mathbf{Pd_3Pt_1/Al_2O_3}$ - $\mathbf{Pd}(1\,1\,1)$ radial

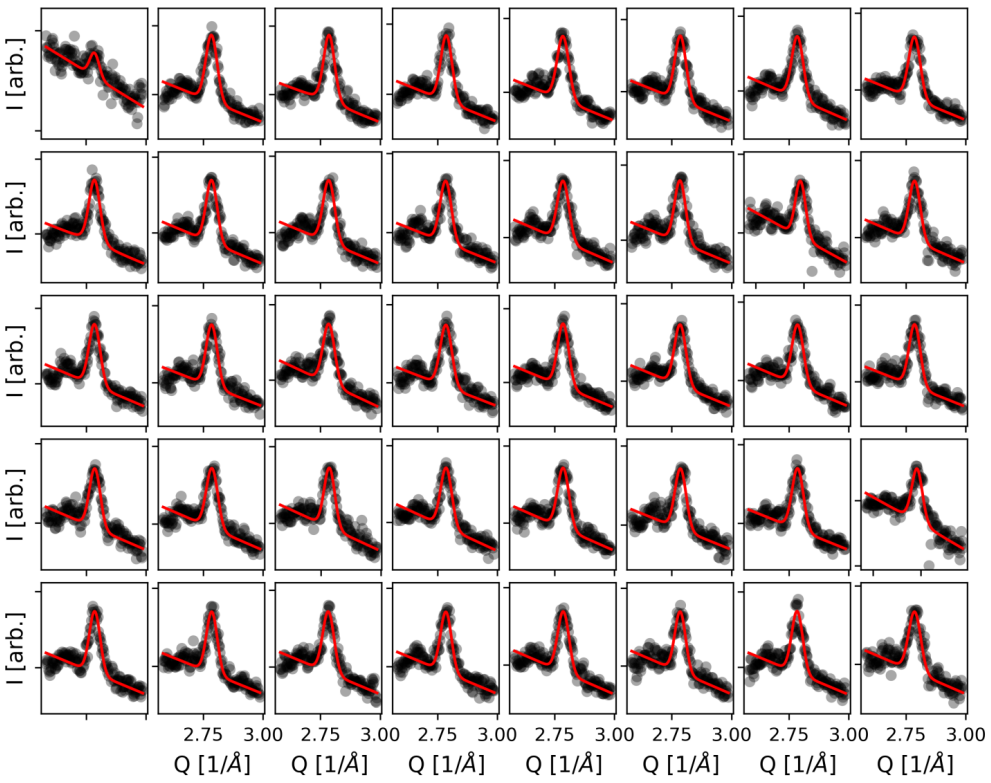

Figure E.63: Radial scans and fits recorded at 523 K.

Table E.51: Center and full width half maximum (FWHM) for the fits presented in Figure E.63. For fits with multiple components, only fit results of the relevant component is shown.

	Center		FWHM			Center		FWHM	
	Value	Error	Value	Error		Value	Error	Value	Error
#0	2.78473	0.00705	0.04669	0.01948	#1	2.78389	0.00156	0.05625	0.0043
#2	2.78599	0.00162	0.05512	0.00466	#3	2.78663	0.00162	0.05557	0.00446
#4	2.78435	0.0018	0.05813	0.00496	#5	2.78556	0.00162	0.05545	0.00446
#6	2.78526	0.00184	0.05664	0.00505	#7	2.78475	0.0018	0.05733	0.00495
#8	2.78448	0.00183	0.05543	0.00529	#9	2.78439	0.00176	0.05432	0.00483
#10	2.785	0.00189	0.05709	0.0052	#11	2.78379	0.00197	0.05548	0.00541
#12	2.78488	0.002	0.05714	0.00549	#13	2.78407	0.0019	0.05414	0.00521
#14	2.7852	0.00213	0.05011	0.00585	#15	2.78542	0.00201	0.05569	0.00551
#16	2.78472	0.00194	0.0554	0.00531	#17	2.78479	0.00192	0.05515	0.00528
#18	2.78475	0.00196	0.05726	0.00537	#19	2.78516	0.00201	0.05706	0.00551
#20	2.7851	0.00179	0.05549	0.00491	#21	2.78458	0.0019	0.05658	0.00522
#22	2.7861	0.00197	0.05687	0.0054	#23	2.78559	0.0019	0.05544	0.00521
#24	2.78596	0.00202	0.05375	0.00556	#25	2.78609	0.00202	0.05671	0.00555
#26	2.78501	0.00192	0.05252	0.0053	#27	2.78578	0.00196	0.05518	0.00539
#28	2.78542	0.00195	0.05612	0.00537	#29	2.78602	0.00206	0.05485	0.00565
#30	2.78625	0.00193	0.05599	0.0053	#31	2.78311	0.00237	0.05254	0.0068
#32	2.78563	0.00178	0.05326	0.00489	#33	2.78535	0.00186	0.05289	0.00512
#34	2.78293	0.00191	0.05567	0.00524	#35	2.78491	0.00195	0.05391	0.00538
#36	2.78584	0.00191	0.05575	0.00524	#37	2.78474	0.0019	0.05296	0.00524
#38	2.7842	0.00185	0.05433	0.00508	#39	2.78556	0.00213	0.05987	0.00581

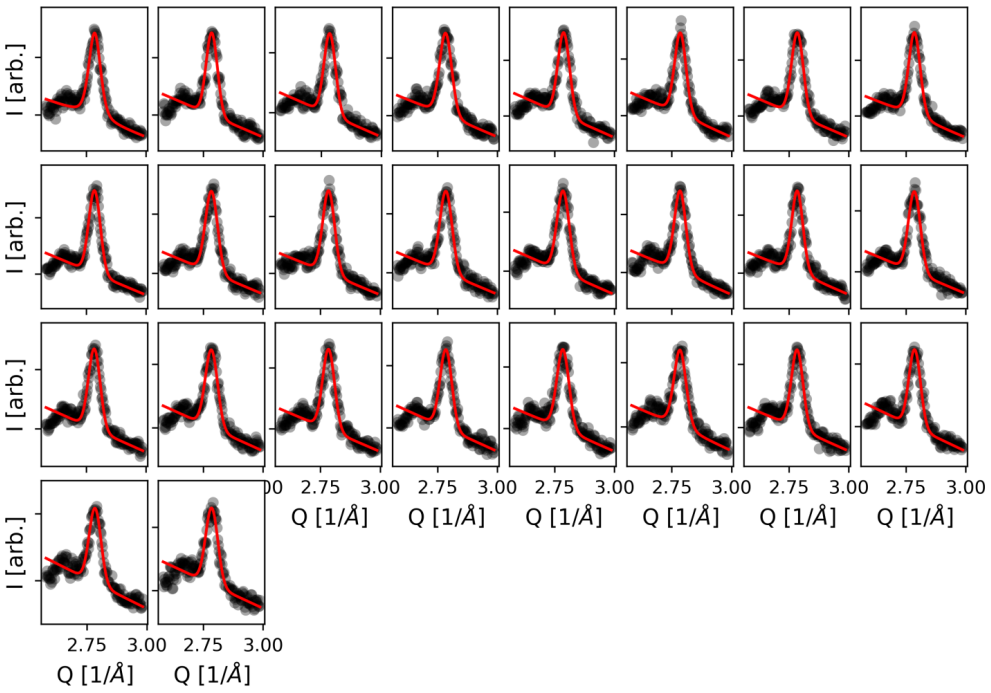

Figure E.64: Radial scans and fits recorded at 573 K.

Table E.52: Center and full width half maximum (FWHM) for the fits presented in Figure E.64. For fits with multiple components, only fit results of the relevant component is shown.

	Center		FWHM			Center		FWHM	
	Value	Error	Value	Error		Value	Error	Value	Error
#0	2.78529	0.00115	0.05851	0.00358	#1	2.78504	0.00112	0.0555	0.00309
#2	2.78498	0.00117	0.05691	0.0032	#3	2.78342	0.00117	0.06008	0.00328
#4	2.78739	0.0011	0.05792	0.00301	#5	2.78516	0.00113	0.05679	0.0032
#6	2.78503	0.0011	0.05815	0.00304	#7	2.78459	0.00107	0.05689	0.00307
#8	2.78463	0.00107	0.05701	0.00293	#9	2.78381	0.0012	0.06	0.0033
#10	2.78423	0.0011	0.05861	0.00305	#11	2.78474	0.00118	0.06026	0.00325
#12	2.78476	0.00117	0.06064	0.00321	#13	2.78417	0.00118	0.05725	0.00337
#14	2.78456	0.00115	0.05582	0.00331	#15	2.78432	0.00121	0.05904	0.00331
#16	2.78375	0.00117	0.05805	0.0032	#17	2.78357	0.00134	0.06054	0.00367
#18	2.78387	0.00122	0.05874	0.00336	#19	2.78468	0.00124	0.05825	0.0034
#20	2.78409	0.00132	0.06018	0.00369	#21	2.78391	0.00141	0.06023	0.00407
#22	2.784	0.00132	0.05769	0.0037	#23	2.78565	0.00129	0.05733	0.00355

$\mathbf{Pd_3Pt_1/Al_2O_3}$ - $\mathbf{PdO}(1\,0\,1)$ radial

Table E.53: Center and full width half maximum (FWHM) for the fits presented in Figure E.65. For fits with multiple components, only fit results of the relevant component is shown.

	Center		FWHM			Center		FWHM	
	Value	Error	Value	Error		Value	Error	Value	Error
#0	2.37666	0.00308	0.07708	0.01273	#1	2.36753	0.0039	0.10629	0.01636
#2	2.36946	0.00269	0.11106	0.01288	#3	2.36636	0.00321	0.11798	0.0134
#4	2.37707	0.00144	0.07124	0.00586	#5	2.37655	0.00129	0.0754	0.00533
#6	2.37603	0.0016	0.08176	0.00673	#7	2.37635	0.00132	0.07996	0.00598
#8	2.37927	0.00118	0.07094	0.00482	#9	2.37935	0.00119	0.07423	0.00568
#10	2.37912	0.00129	0.07797	0.00542	#11	2.37702	0.00095	0.07912	0.005
#12	2.37871	0.00101	0.07473	0.0044	#13	2.37996	0.0007	0.0725	0.00313
#14	2.37935	0.00079	0.06904	0.00371	#15	2.37849	0.00076	0.07493	0.00372
#16	2.37964	0.0008	0.07257	0.00356	#17	2.38005	0.00063	0.07295	0.0031
#18	2.3797	0.00058	0.06772	0.00275	#19	2.37971	0.00063	0.06801	0.00283
#20	2.37926	0.00062	0.07141	0.00273	#21	2.37993	0.00069	0.07211	0.00296
#22	2.37952	0.00057	0.06557	0.00259	#23	2.37881	0.00044	0.06868	0.00196
#24	2.3785	0.00051	0.07365	0.00243	#25	2.37952	0.0005	0.06739	0.00214
#26	2.37935	0.00053	0.06922	0.00235	#27	2.3801	0.00047	0.06629	0.00191
#28	2.37883	0.00044	0.06941	0.00208	#29	2.37948	0.0005	0.07028	0.00217

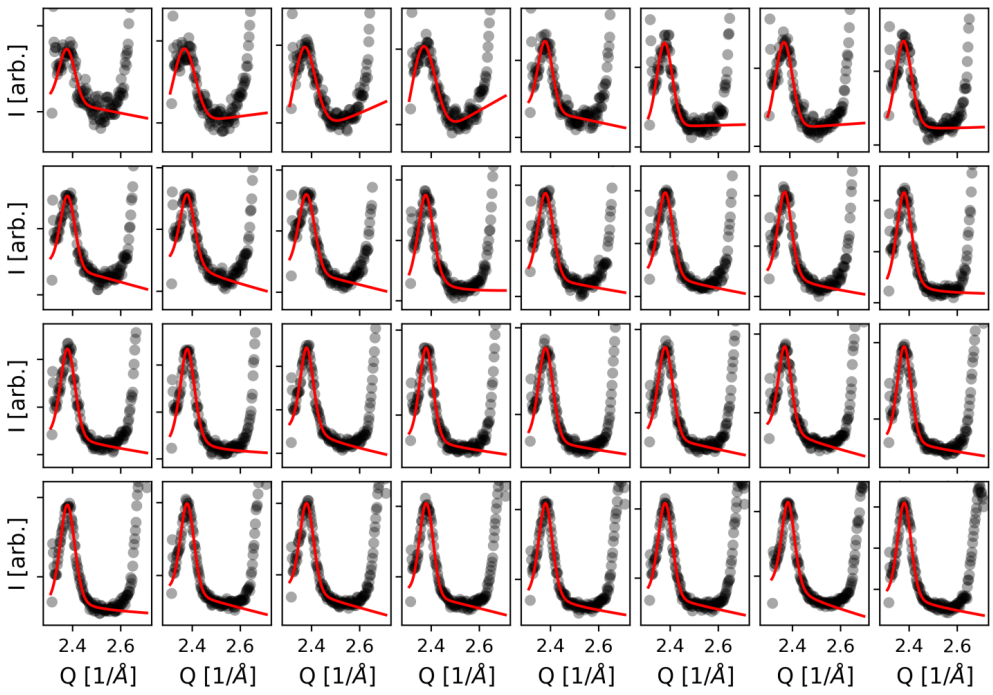

Figure E.65: Radial scans recorded at 623 K.

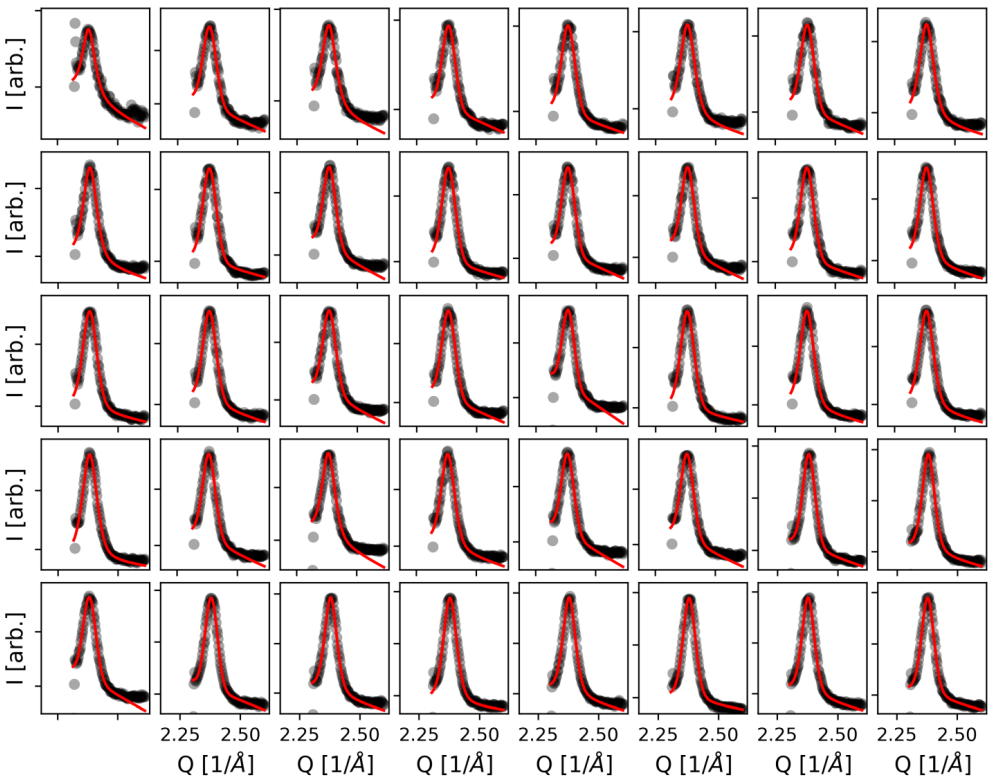

Figure E.66: Radial scans recorded at 673 K.

Table E.54: Center and full width half maximum (FWHM) for the fits presented in Figure E.66. For fits with multiple components, only fit results of the relevant component is shown.

	Center		FWHM			Center		FWHM	
	Value	Error	Value	Error		Value	Error	Value	Error
#0	2.37993	0.00078	0.06433	0.00469	#1	2.38321	0.00056	0.06569	0.00236
#2	2.38291	0.00053	0.06876	0.00315	#3	2.38341	0.00055	0.0629	0.00217
#4	2.38332	0.0005	0.06649	0.00217	#5	2.3828	0.00044	0.07124	0.00226
#6	2.38406	0.00057	0.06497	0.00242	#7	2.38277	0.00038	0.06988	0.00213
#8	2.38289	0.00038	0.06766	0.00212	#9	2.38273	0.0004	0.06698	0.00171
#10	2.38426	0.00031	0.06235	0.0014	#11	2.38288	0.00035	0.06686	0.00151
#12	2.38324	0.00035	0.06317	0.00142	#13	2.3837	0.00036	0.06323	0.00165
#14	2.38263	0.00045	0.06554	0.00189	#15	2.38259	0.0004	0.06603	0.00185
#16	2.3819	0.00032	0.06896	0.0015	#17	2.38262	0.00026	0.06654	0.00118
#18	2.38384	0.00041	0.06484	0.00189	#19	2.38287	0.00036	0.06591	0.00149
#20	2.38363	0.00044	0.05841	0.00173	#21	2.38195	0.00032	0.06714	0.00141
#22	2.38252	0.00044	0.06735	0.0021	#23	2.38242	0.00026	0.06846	0.00127
#24	2.38168	0.00041	0.0719	0.00201	#25	2.38222	0.00038	0.06387	0.00168
#26	2.38276	0.00027	0.06396	0.00149	#27	2.38164	0.00038	0.06727	0.00188
#28	2.3828	0.00034	0.06125	0.00143	#29	2.38237	0.00035	0.06394	0.00156
#30	2.37943	0.00022	0.06029	0.00106	#31	2.37907	0.00024	0.0603	0.0013
#32	2.38253	0.0003	0.06282	0.00128	#33	2.37929	0.00019	0.05952	0.00082
#34	2.37917	0.00017	0.06015	0.00096	#35	2.37795	0.00018	0.06558	0.00105
#36	2.3783	0.00019	0.06099	0.00103	#37	2.37825	0.00017	0.06155	0.00088
#38	2.37774	0.00024	0.06104	0.00122	#39	2.378	0.00021	0.06112	0.00104

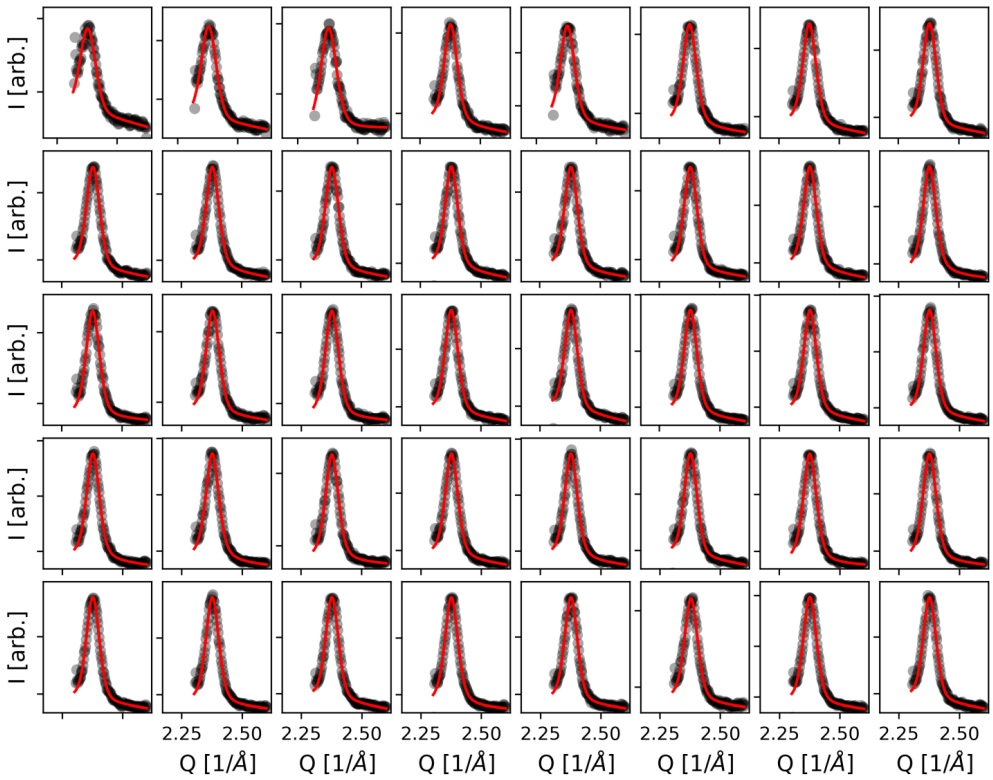

Figure E.67: Radial scans recorded at 723 K.

Table E.55: Center and full width half maximum (FWHM) for the fits presented in Figure E.67. For fits with multiple components, only fit results of the relevant component is shown.

	Center		FWHM			Center		FWHM	
	Value	Error	Value	Error		Value	Error	Value	Error
#0	2.3782	0.00052	0.07589	0.00225	#1	2.37862	0.00042	0.07404	0.00185
#2	2.37858	0.00041	0.07823	0.00201	#3	2.3772	0.00027	0.06574	0.00127
#4	2.37925	0.00032	0.07119	0.00147	#5	2.37554	0.00022	0.06648	0.00108
#6	2.3758	0.0002	0.06619	0.00095	#7	2.3788	0.00018	0.06487	0.00081
#8	2.37857	0.00019	0.0659	0.00086	#9	2.37861	0.0002	0.06417	0.00096
#10	2.3787	0.00023	0.06594	0.00108	#11	2.37812	0.00018	0.06379	0.00084
#12	2.37875	0.00022	0.06457	0.001	#13	2.37883	0.0002	0.06482	0.00093
#14	2.37803	0.00019	0.06419	0.00089	#15	2.3779	0.00014	0.0649	0.00069
#16	2.37844	0.00022	0.0663	0.00101	#17	2.37744	0.00024	0.06579	0.00109
#18	2.37665	0.0002	0.06623	0.00092	#19	2.37814	0.00017	0.06467	0.00079
#20	2.37845	0.00017	0.06272	0.00078	#21	2.37818	0.00019	0.06397	0.00088
#22	2.37789	0.00015	0.06306	0.00073	#23	2.37645	0.00018	0.06334	0.00081
#24	2.37616	0.00021	0.06453	0.00101	#25	2.37579	0.00021	0.06613	0.00109
#26	2.37738	0.0002	0.06501	0.00096	#27	2.37625	0.00015	0.06346	0.00073
#28	2.37597	0.00017	0.06343	0.0008	#29	2.37643	0.00019	0.06344	0.00084
#30	2.37577	0.00016	0.06578	0.00078	#31	2.37612	0.00015	0.06531	0.0007
#32	2.3762	0.00017	0.06437	0.00076	#33	2.37586	0.00017	0.06451	0.00081
#34	2.37645	0.00017	0.06343	0.00078	#35	2.37572	0.00015	0.06542	0.00078
#36	2.37578	0.0002	0.06362	0.00092	#37	2.37821	0.00026	0.06538	0.00123
#38	2.37569	0.00013	0.0656	0.00061	#39	2.37649	0.0002	0.06401	0.00093

Table E.56: Center and full width half maximum (FWHM) for the fits presented in Figure E.68. For fits with multiple components, only fit results of the relevant component is shown.

	Center		FWHM			Center		FWHM	
	Value	Error	Value	Error		Value	Error	Value	Error
#0	2.36687	0.00196	0.07066	0.00682	#1	2.36993	0.00084	0.09305	0.00626
#2	2.37133	0.00073	0.0797	0.00336	#3	2.37138	0.00101	0.08117	0.0046
#4	2.37316	0.00081	0.07279	0.0038	#5	2.37131	0.00083	0.07503	0.0039
#6	2.37099	0.00124	0.09431	0.00584	#7	2.37189	0.00075	0.07461	0.00411
#8	2.37092	0.00088	0.08451	0.00493	#9	2.36937	0.00081	0.07493	0.00382
#10	2.3693	0.00101	0.08014	0.00503	#11	2.36908	0.00093	0.09241	0.00755
#12	2.36786	0.00121	0.09647	0.00764	#13	2.37045	0.0009	0.08075	0.00429
#14	2.3699	0.00111	0.09737	0.00801	#15	2.3711	0.0009	0.0832	0.00586
#16	2.36827	0.00115	0.10151	0.00991	#17	2.37052	0.0008	0.07792	0.0031
#18	2.37017	0.00081	0.08025	0.00544	#19	2.37075	0.00099	0.09047	0.00716
#20	2.37265	0.00087	0.07221	0.00341	#21	2.36997	0.00083	0.08204	0.0044
#22	2.36936	0.00093	0.08725	0.0064	#23	2.37044	0.00089	0.07952	0.00472
#24	2.37028	0.0009	0.07945	0.00347	#25	2.37131	0.00083	0.07911	0.00585
#26	2.37082	0.00072	0.07792	0.00373	#27	2.37066	0.00105	0.07682	0.00405
#28	2.37072	0.00084	0.08067	0.00518	#29	2.37162	0.00083	0.07219	0.00396
#30	2.37197	0.00066	0.07525	0.00383	#31	2.37083	0.00081	0.07843	0.00563
#32	2.3707	0.00078	0.08027	0.00363	#33	2.37182	0.00073	0.07142	0.00329
#34	2.37147	0.00081	0.08022	0.00437	#35	2.37034	0.00093	0.08385	0.00477
#36	2.37	0.00078	0.08303	0.00497	#37	2.37047	0.00088	0.07814	0.0044
#38	2.37018	0.00103	0.08073	0.00442					

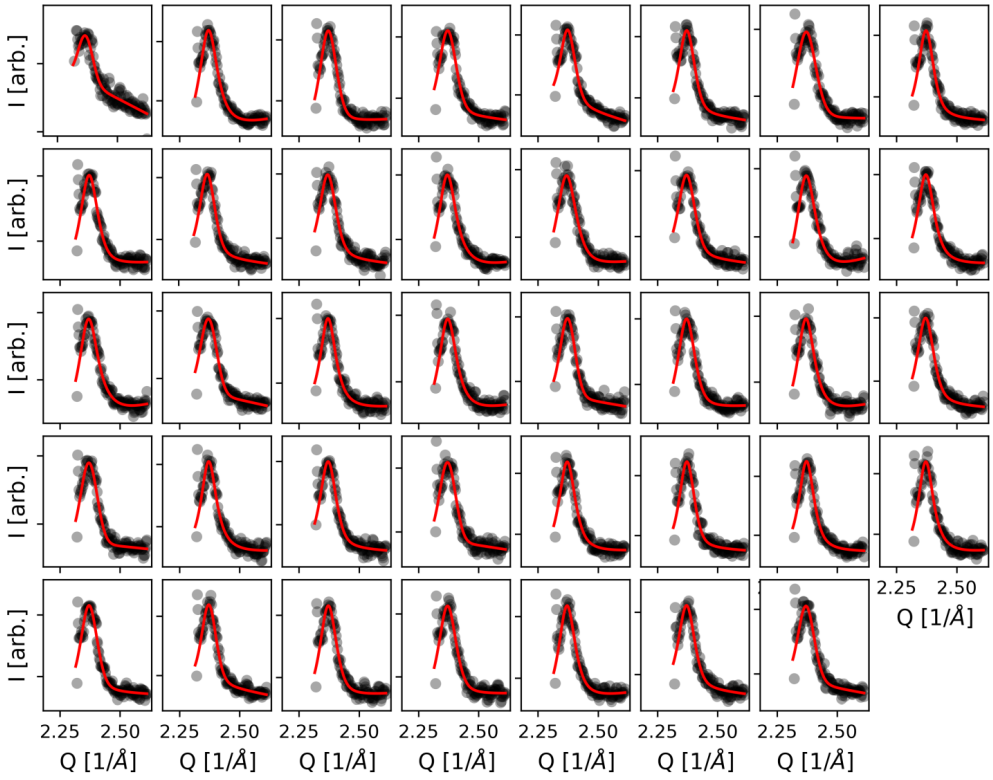

Figure E.68: Radial scans recorded at 673 K.

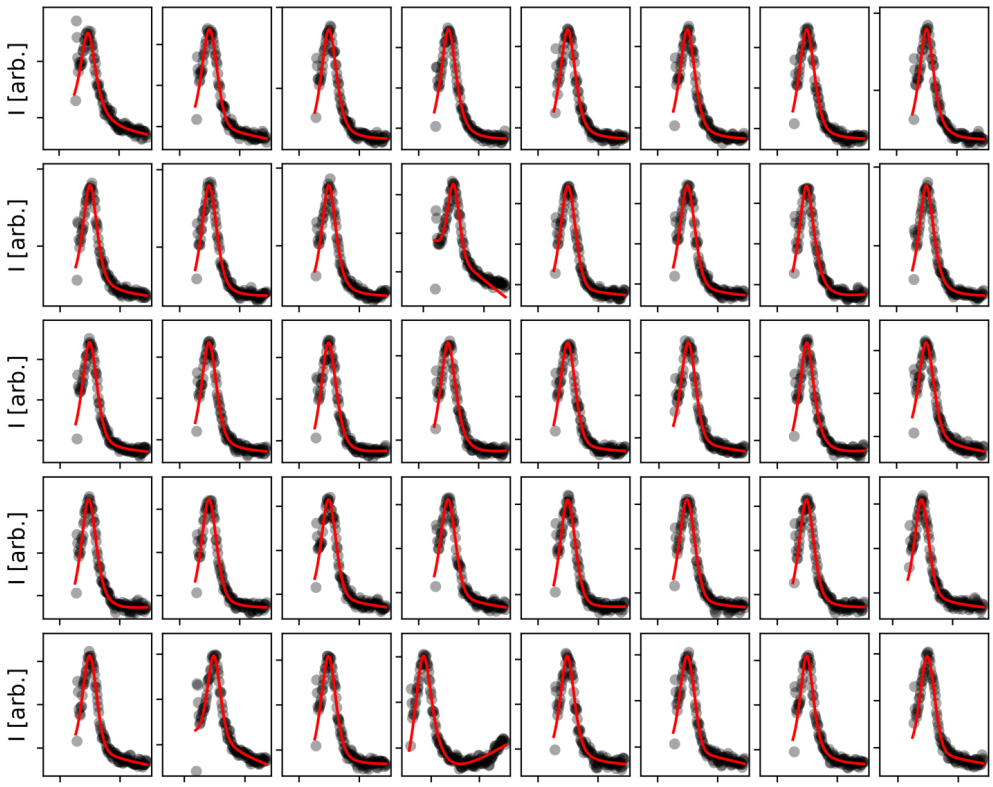

Figure E.69: Radial scans recorded at 723 K.

Table E.57: Center and full width half maximum (FWHM) for the fits presented in Figure E.69. For fits with multiple components, only fit results of the relevant component is shown.

	Center		FWHM			Center		FWHM	
	Value	Error	Value	Error		Value	Error	Value	Error
#0	2.37052	0.00066	0.08143	0.00441	#1	2.37474	0.00047	0.07484	0.00213
#2	2.37399	0.00041	0.0769	0.00224	#3	2.374	0.00036	0.07828	0.00214
#4	2.37311	0.00044	0.07623	0.00234	#5	2.37341	0.00047	0.07561	0.00249
#6	2.37295	0.00046	0.0777	0.00242	#7	2.37381	0.00039	0.07416	0.00235
#8	2.37426	0.00041	0.07124	0.00218	#9	2.3727	0.00044	0.07739	0.00239
#10	2.37353	0.00044	0.07284	0.00252	#11	2.37456	0.00052	0.05695	0.00235
#12	2.3742	0.00039	0.07333	0.00175	#13	2.37348	0.00048	0.07516	0.00235
#14	2.37155	0.00043	0.07941	0.00269	#15	2.373	0.00038	0.07484	0.0022
#16	2.37307	0.00037	0.07345	0.00189	#17	2.37222	0.00041	0.07527	0.00208
#18	2.37232	0.00044	0.07827	0.00249	#19	2.37186	0.00047	0.08031	0.00297
#20	2.37265	0.00047	0.07552	0.00219	#21	2.37201	0.00052	0.0734	0.0024
#22	2.3726	0.00039	0.0751	0.00246	#23	2.37265	0.00045	0.07596	0.00229
#24	2.37002	0.00045	0.0785	0.00268	#25	2.37215	0.00047	0.07586	0.00234
#26	2.37287	0.00051	0.0726	0.00234	#27	2.37217	0.00052	0.07398	0.00238
#28	2.37282	0.00045	0.07581	0.00215	#29	2.37226	0.00049	0.07668	0.00218
#30	2.37176	0.00044	0.07387	0.00225	#31	2.37059	0.00044	0.07104	0.00201
#32	2.37318	0.00041	0.06961	0.00181	#33	2.37231	0.00052	0.06471	0.00249
#34	2.37194	0.00043	0.07506	0.00221	#35	2.36726	0.00052	0.09798	0.00344
#36	2.37191	0.00054	0.07256	0.00292	#37	2.37322	0.00047	0.07029	0.00182
#38	2.37288	0.00042	0.06945	0.00237	#39	2.37229	0.0005	0.07131	0.00215
#40	2.37139	0.00054	0.07924	0.00259	#41	2.37066	0.00046	0.07933	0.00319
#42	2.37263	0.00044	0.06955	0.00218	#43	2.37226	0.00048	0.07622	0.00236
#44	2.37227	0.00046	0.07315	0.00232	#45	2.37141	0.00048	0.07238	0.00264

E.4.3 HEGIXRD line scan analysis from rocking scans of Pd/Al_2O_3

Table E.58: Center and full width half maximum (FWHM) for the fits presented in Figure E.70.

T [K]	Scan	Cycle I				Cycle II			
		Center		FWHM		Center		FWHM	
		Value	Error	Value	Error	Value	Error	Value	Error
523	H, Pd(111)	2.622	0.0	0.045	0.001	2.626	0.0	0.049	0.0
	L, Pd(111)	0.945	0.0	0.161	0.001	0.95	0.0	0.107	0.001
	H, Pd(222)	5.25	0.0	0.053	0.0	5.256	0.0	0.054	0.001
	L, Pd(222)	1.867	0.0	0.171	0.002	1.878	0.0	0.119	0.001
573	H, Pd(111)	2.625	0.0	0.055	0.001	2.627	0.0	0.056	0.001
	L, Pd(111)	0.949	0.0	0.121	0.0	0.948	0.0	0.123	0.001
	H, Pd(222)	5.253	0.0	0.059	0.001	5.263	0.001	0.06	0.004
	L, Pd(222)	1.879	0.0	0.125	0.001	1.872	0.001	0.152	0.008
	PdO(101)	2.377	0.001	0.062	0.008	2.373	0.002	0.065	0.008
623	H, Pd(111)	2.627	0.0	0.056	0.001	2.628	0.0	0.057	0.002
	L, Pd(111)	0.946	0.0	0.131	0.001	0.948	0.0	0.126	0.001
	H, Pd(222)	5.258	0.0	0.061	0.002	5.265	0.002	0.088	0.037
	L, Pd(222)	1.872	0.001	0.15	0.003	1.878	0.003	0.14	0.008
	PdO(101)	2.375	0.001	0.065	0.004	2.374	0.001	0.061	0.009
673	H, Pd(111)	2.626	0.0	0.059	0.001	2.627	0.0	0.061	0.002
	L, Pd(111)	0.947	0.0	0.135	0.001	0.949	0.001	0.132	0.002
	H, Pd(222)	5.256	0.001	0.07	0.004	5.262	0.002	0.062	0.007
	L, Pd(222)	1.875	0.001	0.164	0.006	1.88	0.003	0.146	0.02
	PdO(101)	2.374	0.001	0.065	0.005	2.375	0.001	0.059	0.006
723	H, Pd(111)	2.624	0.0	0.059	0.002	2.623	0.0	0.06	0.002
	L, Pd(111)	0.946	0.0	0.141	0.001	0.949	0.001	0.128	0.002
	H, Pd(222)	5.254	0.001	0.085	0.017	5.252	0.004	0.059	0.012
	L, Pd(222)	1.864	0.002	0.178	0.012	1.873	0.005	0.13	0.015
	PdO(101)	2.372	0.001	0.062	0.004	2.372	0.001	0.05	0.003

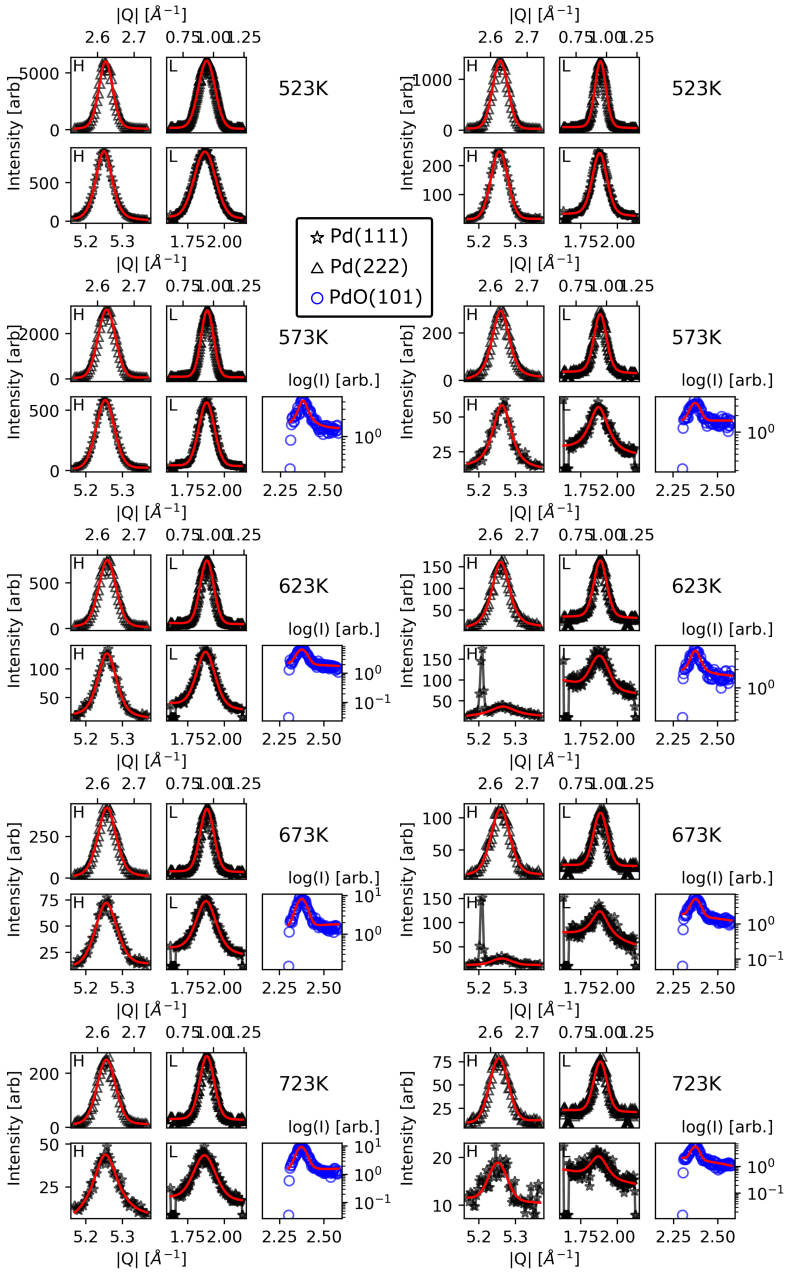

Figure E.70: Scans extracted from rocking scans and their fits for all temperatures. Black triangles corresponds to data from Pd(111), black stars to data from Pd(222), and blue circles to data from PdO(101). No PdO signal is observed for either cycle at 523 K.

E.4.4 HEGIXRD line scan analysis from rocking scans of Pd_3Pt_1/Al_2O_3

Table E.59: Center and full width half maximum (FWHM) for the fits presented in Figure E.71.

T [K]	Scan	Cycle I				Cycle II			
		Center		FWHM		Center		FWHM	
		Value	Error	Value	Error	Value	Error	Value	Error
523	H, Pd(111)	2.628	0.0	0.045	0.001	2.627	0.0	0.056	0.001
	L, Pd(111)	0.936	0.001	0.249	0.004	0.946	0.0	0.165	0.001
	H, Pd(222)	5.262	0.0	0.06	0.001	5.256	0.0	0.06	0.001
	L, Pd(222)	1.842	0.001	0.274	0.011	1.873	0.001	0.181	0.003
573	H, Pd(111)	2.627	0.0	0.047	0.001	2.624	0.0	0.058	0.001
	L, Pd(111)	0.933	0.0	0.218	0.001	0.942	0.0	0.172	0.001
	H, Pd(222)	5.257	0.0	0.054	0.0	5.251	0.0	0.063	0.002
	L, Pd(222)	1.854	0.001	0.236	0.005	1.866	0.001	0.185	0.004
623	H, Pd(111)	2.625	0.0	0.055	0.001	2.624	0.0	0.067	0.002
	L, Pd(111)	0.937	0.0	0.222	0.002	0.937	0.001	0.171	0.002
	H, Pd(222)	5.251	0.0	0.064	0.001	5.252	0.001	0.074	0.004
	L, Pd(222)	1.86	0.001	0.239	0.008	1.864	0.002	0.182	0.008
	Pd(101)	2.381	0.001	0.064	0.003	2.367	0.004	0.107	0.028
673	H, Pd(111)	2.625	0.001	0.062	0.003	2.621	0.0	0.067	0.001
	L, Pd(111)	0.938	0.0	0.2	0.002	0.939	0.0	0.166	0.002
	H, Pd(222)	5.255	0.001	0.071	0.004	5.244	0.001	0.074	0.004
	L, Pd(222)	1.86	0.002	0.23	0.016	1.86	0.001	0.179	0.006
	PdO(101)	2.379	0.0	0.062	0.002	2.373	0.001	0.083	0.009
723	H, Pd(111)	2.62	0.0	0.066	0.002	2.616	0.0	0.066	0.001
	L, Pd(111)	0.937	0.0	0.18	0.002	0.941	0.0	0.149	0.001
	H, Pd(222)	5.244	0.001	0.076	0.005	5.237	0.0	0.062	0.002
	L, Pd(222)	1.858	0.001	0.198	0.007	1.86	0.001	0.159	0.003
	PdO(101)	2.377	0.0	0.065	0.002	2.373	0.001	0.054	0.003

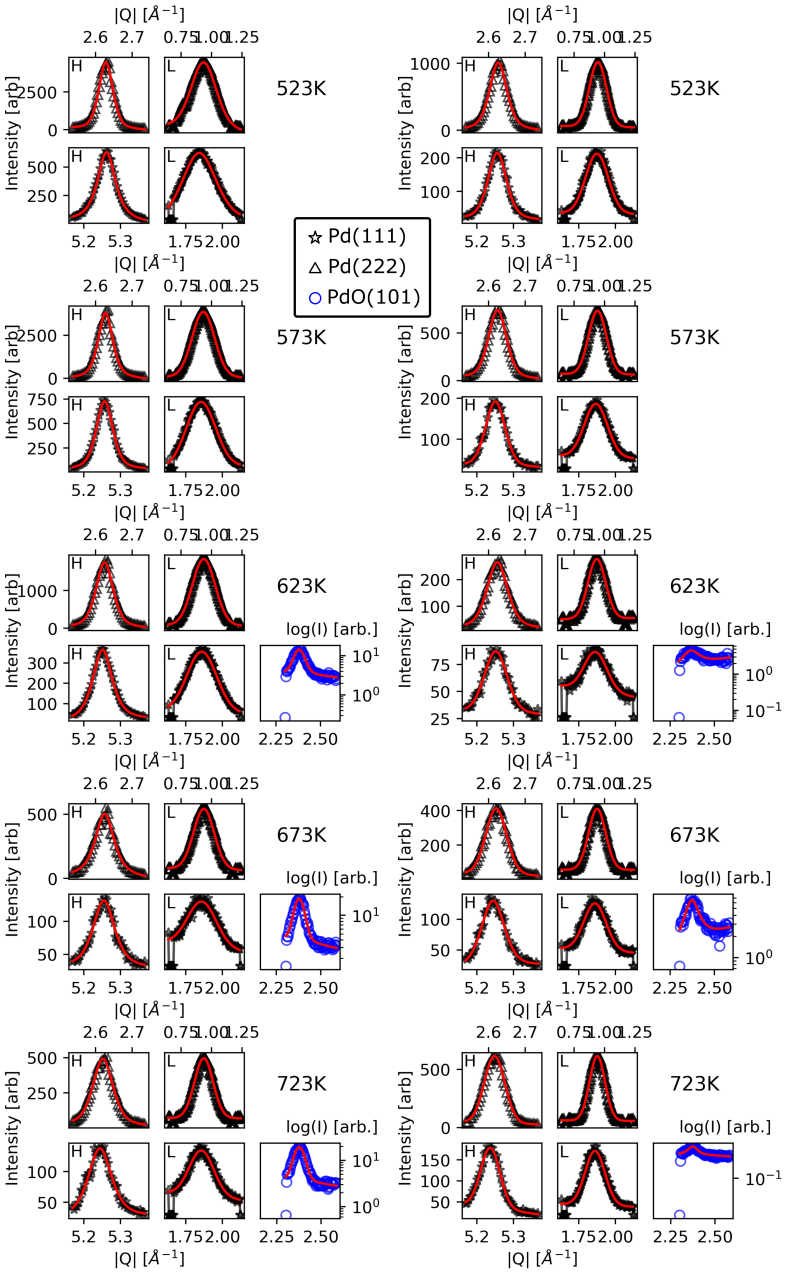

Figure E.71: Scans extracted from rocking scans and their fits for all temperatures. Black triangles corresponds to data from Pd(111), black stars to data from Pd(222), and blue circles to data from PdO(101). No PdO signal is observed for either cycle at 523 K and 573 K.

E.5 HEGISAXS analysis

Line cuts were extracted from the time resolved HEGISAXS data shown in [280, 281] in order visualize the subtle changes. The position of the line cuts was determined by the position of the maximum intensity of the scattered, off-specular scattering signal. The vertical line cuts were extracted at the Q_x position of the maximum, the horizontal line cuts were extracted just above the Q_z position of the maximum (see Figure E.72). All line scans were extracted with an integration width of 0.0015 Å, corresponding to 3 px. All

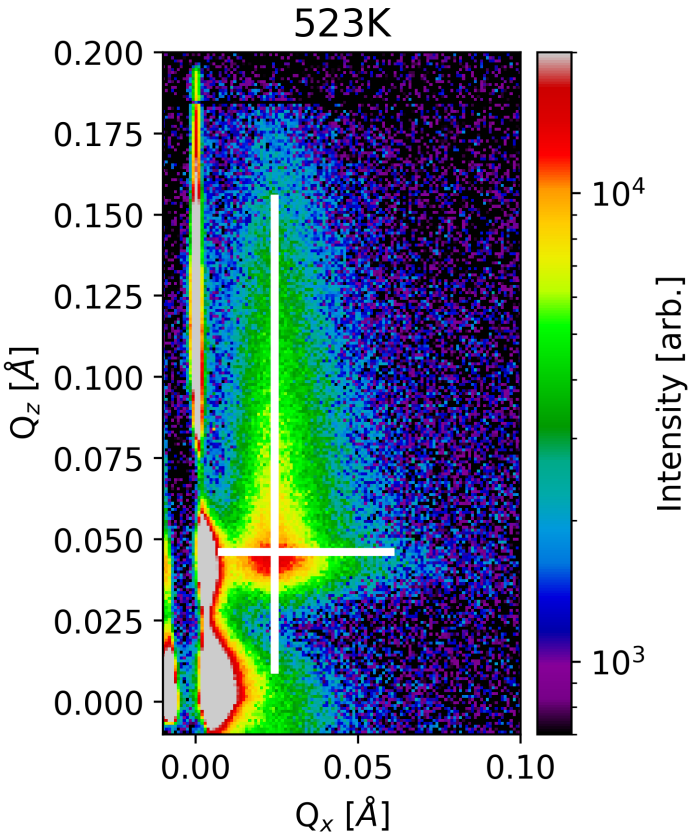

Figure E.72: HEGISAXS data recorded under operation for Pd_3Pt_1/Al_2O_3 catalyst at 523 K. White lines indicate the positions of the vertical and horizontal cuts. The width of the lines correspond to the integration width and the length to the Q range of the extracted lines.

line scan data is treated with z-score normalization which is given by

$$I_{norm} = \frac{I(q) - \mu}{\sigma} \tag{E.2}$$

with μ being the mean of $I(Q)$ and σ being the standard deviation of $I(Q)$.

E.6 HEGISAXS Horizontal Cuts

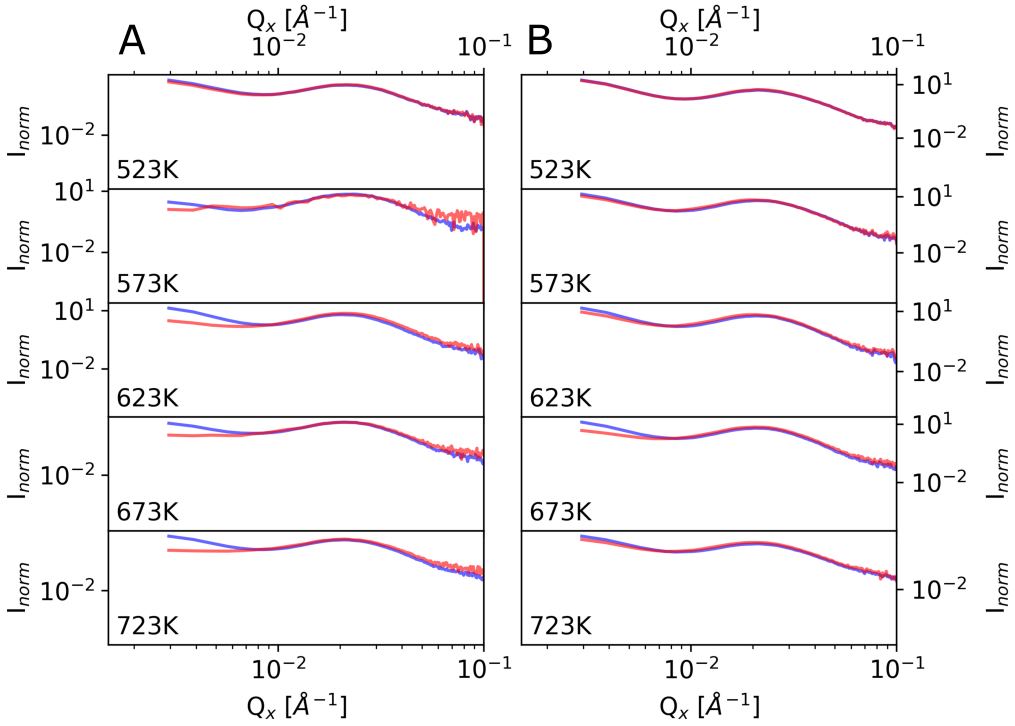

Figure E.73: Horizontal line cuts recorded under operation with the Pd/Al_2O_3 catalyst. Data recorded during the first cycle is in **A**, data recorded during the second cycle in **B**. The blue lines correspond to the first data point recorded at each given temperature (indicated in the bottom left corner of each panel), the red line to the data point recorded 15 min later.

As mentioned in the main text, no significant changes were observed in the horizontal cuts at a given temperature. This is likely due to the heterogeneity of size of the NPs and distance between the NPs leading to a broad distribution of scattering vectors. As a result, the sum of the incoherent contributions mask sharp features. In Figure E.73 and Figure E.74 are the

horizontal cuts for all conditions of the first and second cycle of Pd/Al_2O_3 and $PdPt/Al_2O_3$, respectively. The blue line corresponds to the first datapoint, the red line to the data point recorded 15 min afterwards.

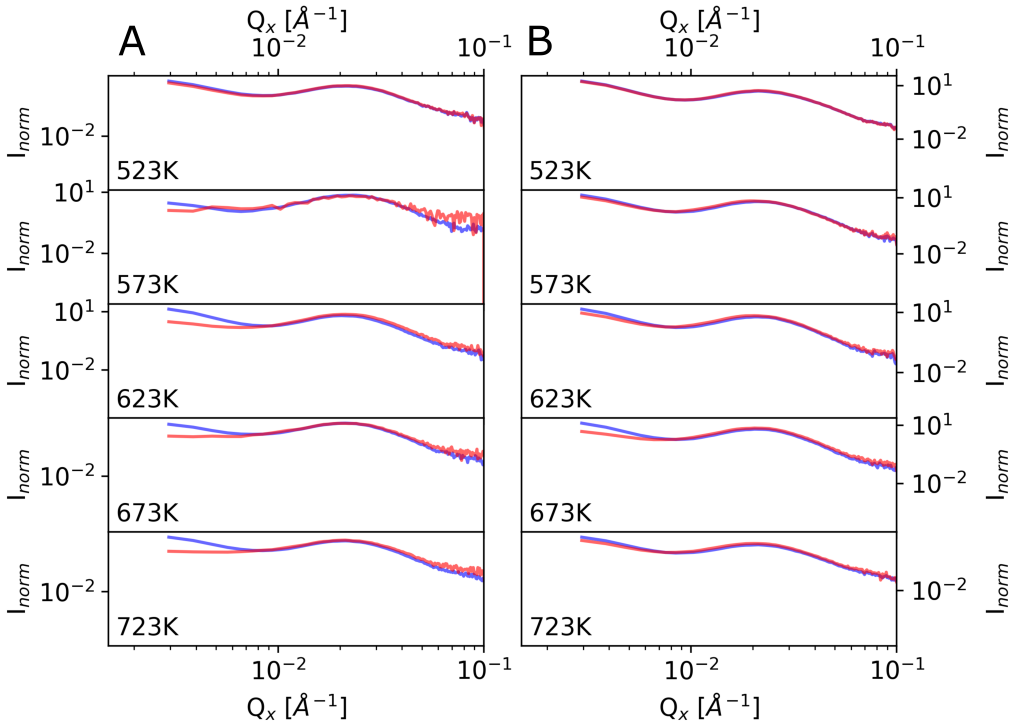

Figure E.74: Horizontal line cuts recorded under operation with the Pd_3Pt_1/Al_2O_3 catalyst. Data recorded during the first cycle is in **A**, data recorded during the second cycle in **B**. The blue lines correspond to the first data point recorded at each given temperature (indicated in the bottom left corner of each panel), the red line to the data point recorded 15 min later.

Biblography

(280) Schober, J.-C. Time resolved data of Pd/Al_2O_3 `https://bib-pubdb1.desy.de/record/636458`.

(281) Schober, J.-C. Time resolved data of Pd_3Pt_1/Al_2O_3 `https://bib-pubdb1.desy.de/record/636459`.

(291) Palmberg, P. *Handbook of Auger Electron Spectroscopy*; Physical Electronics Industries: Virginia, USA, 1972.

(292) Wintersberger, E. et al. Analysis of Periodic Dislocation Networks using X-ray Diffraction and Extended Finite Element Modeling. *Applied Physics Letters* **2010**, *96*, 131905.

(293) Lobato Hoyos, I.; Friedrich, T.; Aert, S. Deep Convolutional Neural Networks to Restore Single-Shot Electron Microscopy Images. *NPJ Comput. Mater.* **2024**, *10*, 1–19.

(294) Silverman, B. W. Density Estimation for Statsitics and Data Analysis. *Monogr. Stat. Appl. Probab.* **1986**, 1–22.

(295) Moulder, J.; Stickle, W.; Sobol, P.; Bonnoth, K. *Handbook of X-Ray Photoelectron Spectroscopy*; Perkin-Elmer Coporation: USA, 1992.

(296) Nguyen-Truong, H. T. Low-energy electron inelastic mean free paths for liquid water. *J. Phys. Condens. Matter* **2018**, *30*, 155101.

(297) Krawczyk, M.; Holdynski, M.; Lisowski, W.; Sobczak, J. W.; Jablonski, A. Electron inelastic mean free paths in cerium dioxide. *Appl. Surf. Sci.* **2015**, *341*, 196–202.

(298) Verdaguer, A. et al. Growth and Structure of Water on SiO_2 Films on Si Investigated by Kelvin Probe Microscopy and in Situ X-ray Spectroscopies. *Langmuir* **2007**, *23*, 9699–9703.

(299) Zavilopulo, A. N.; Chipev, F. F.; Shpenik, O. B. Ionization of nitrogen, oxygen, water, and carbon dioxide molecules by near-threshold electron impact. *Tech. Phys.* **2005**, *50*, 19–24.

(300) Scherrer, P.; Debye, P. Bestimmung der Grösse und der inneren Struktur von Kolloidteilchen mittels Röntgenstrahlen. *Nachr. Ges. Wiss. Göttingen* **1918**, 98–100.

(301) Bayer, G.; Wiedemann, H. G. Formation, Dissociation and Expansion Behavior of Platinum Group Metal Oxides (PdO, RuO_2, IrO_2). *Thermochim. Acta* **1975**, *11*, 79–88.

(302) Arblaster, J. W. Crystallographic Properties of Palladium. *Platin. Met. Rev.* **2012**, *56*, 181–189.

(303) Edsinger, R.; Reilly, M. L.; Schooley, J. F. Thermal Expansion of Platinum And Platinum-Rhodium Alloys. *J. Res. Natl. Bur. Stand.s* **1986**, *91*, 333–356.